The role of eIF2Bα in the integrity of eIF2B bodies

Madalena Isabel Ribeiro de Oliveira

A thesis submitted in partial fulfilment of the requirements of
Sheffield Hallam University
for the degree of Doctor of Philosophy

September 2023

Candidate Declaration.

I hereby declare that:

1. I have not been enrolled for another award of the University, or other academic or professional organisation, whilst undertaking my research degree.
2. None of the material contained in the thesis has been used in any other submission for an academic award.
3. I am aware of and understand the University's policy on plagiarism and certify that this thesis is my own work. The use of all published or other sources of material consulted have been properly and fully acknowledged.
4. The work undertaken towards the thesis has been conducted in accordance with the SHU Principles of Integrity in Research and the SHU Research Ethics Policy.

The word count of the thesis is 64582.

Name	Madalena Isabel Ribeiro de Oliveira
Award	Doctor of Philosophy (PhD)
Date of submission	11 September 2023
Faculty	Health and Wellbeing
Director of studies	Dr Liz Allen

Contents

Covid Impact Statement

On the 17th of March of 2020, due to the COVID-19 pandemic, the Sheffield Hallam University was forced to close its facilities, which included the BMRC. The laboratory access during approximately 6 months was prohibited. Although, restricted laboratory-based activities resumed on the 22nd of September of 2020, strict COVID-19 measures were taken until the April of 2021, where a 3-day-a-week rota booking system was in place.

As this project was entirely laboratory-based, the closure of the laboratory halted any collection and analysis of data. While non-laboratory work, which consisted of RF2 submission process and literature review, took place during the closure of the BMRC, pre-existing data was scarce since the project had only begun in November 2020; and analysis of this pre-existing data was not possible due to the lack of specialised computers/software. As such, a bioinformatic study was initiated during this time in order to obtain data, which was then incorporated into the original project aims.

Furthermore, during the 3-day-a-week rota period, most experiments consisted of optimising protocols to accommodate a limited work schedule, which proved itself to be challenging and ineffective, with most techniques requiring more than three days to be completed. Particularly, any experiments that required cell culture were unfeasible with the work schedule and this project required extensive cell culture work. Specialised computers and software remained highly restricted and PhD students did not have a dedicated office space throughout this period. This led to a delay in data analysis, which in turn delayed plans for follow-up experiments. Due to this time constraint, experiments were cut short or discarded and subsequently data collection was labours and more time consuming. As such, due to the COVID-19 pandemic, 6 full months of laboratory time were lost, combined with approximately 9 months of restricted/limited work.

Abstract.

The eukaryotic initiation factor 2B (eIF2B) is a multisubunit protein composed of two sets of five subunits (α-ε) forming a heterodecamer. eIF2B is a guanine exchange factor (GEF) recycling inactive eukaryotic initiation factor 2 (eIF2) to its active state, being an essential checkpoint for translational control. Following induction of stress, kinases phosphorylate eIF2α, activating the integrated stress response (ISR), subsequently inhibiting eIF2B activity. Mutations within the eIF2Bα-ε subunits can lead to vanishing white matter disease (VWMD) and eIF2Bα variants may cause permanent neonatal diabetes mellitus (PNDM). VWMD and PNDM mutations, primarily affect glial cells and pancreatic β-cells, respectively, suggesting cell type-specific functions of eIF2B.

eIF2B bodies are cytoplasmic bodies containing the eIF2B protein. In this study, we highlight bioinformatic tools to optimise the immunocytochemistry detection of eIF2Bα-ε foci. We investigated cell type-specific localisation of eIF2B subunits within neuronal and glial cell types, showing that oligodendrocytes and neuronal cells possess additional eIF2Bα foci, independent of other eIF2B subunits. Additionally, eIF2Bα has been found to be essential for eIF2B foci formation. We have further revealed that eIF2Bα spatially interacts with G3BP-containing stress granules (SGs), induced by endoplasmic reticulum (ER) and oxidative stress in a p-eIF2α-dependent manner. *EIF2B1*$^{L100P/WT}$ mutant cell line shows decreased formation of SGs following p-eIF2α induction, while SG assembly independent of p-eIF2α was not impacted.

Our study showed that in cells depleted of eIF2Bα, large eIF2Bβ-ε foci were not able to form. ISRIB, a molecule known to stabilise the decamer, was able to rescue large foci assembly, establishing a similar functional role to eIF2Bα regarding eIF2B foci formation. Additionally, the assembly of SGs and the localisation of eIF2Bα to these aggregates appeared to play an important role in eIF2B subcomplex formation during ISR activation and the sensing of stress through the p-eIF2α pathway.

Acknowledgments.

This is going to be a long one, so buckle up!

I would like to thank Dr Liz Allen and Dr Susan Campbell for being such great supervisors and mentors throughout my PhD journey. Your passion for research greatly inspired and motivated me to pursue new opportunities and to not be afraid of experimenting! I would also like to thank Dr Alison Cross for your advice throughout my PhD and to Dr Rachel Hodgson for always having time to come and rescue me in the lab. To Dan English and Dr Celine Souilhol, you were always friendly faces that I could count on for a quick chat or quick question. Thank you so much for your help.

I would like to firstly thank my family for their support. I owe everything to you. Mãe e pai, vocês deram-me muito apoio e eu sei que sofreram muito por eu não estar por perto. Sei que o vosso coração esteve muitas vezes apertado durante estes anos. Mãe, obrigada por não me teres deixado desistir no primeiro ano do PhD sem um plano B. Como o doutoramento era o plano A até Z, tu abraçaste-me e desejaste-me boa sorte cada vez que me deixavas no aeroporto, sabendo que estavas a fazer o melhor para mim. Tu és uma mulher incrível e lutadora. Herdei de ti a minha ética de trabalho e devo muito da pessoa que sou hoje a ti. Os sacrifícios que fazias no teu dia-a-dia para depois chegares a casa e ainda teres que cuidar de uma pirralha … esteriei eternamente em tua dívida. Tu és uma mulher cheia de amor para dar, mas sempre escolheste dar um extra para mim. Obrigada por atenderes as minhas chamadas, mesmo quando a única coisa que fazia era chorar ou queimaxar-me. Adoro-te até ir ao céu e voltar milhões e milhões de vezes. Pai, obrigada por seres a pessoa calma e pacifica que és. No meio do caos, tu és sempre capaz de pensar tranquilamente. Obrigada por encorajares-me a viajar e a seguir os meus sonhos. Tu aproveitaste a tua vida ao máximo, mesmo quando as oportunidades eram escassas. Para quem não andou no liceu, tu agora és uma pessoa bem sucedida, que sabe muitas línguas e que viajou quase o mundo todo. Espero ter a tua coragem e motivação.

'Mom and Dad, you gave me a lot of support and I know you suffered a lot because I wasn't next to you. I know that your heart has been heavy many times during these years. Mom, thank you for not letting me give up in the first year of my PhD without a plan B. Since the PhD was plan A to Z, you hugged me and wished me good luck every time you dropped me

off at the airport, knowing that you were doing what's best for me. You are an incredible woman and a fighter to the core. I inherited my work ethic from you and I owe a lot of the person I am today to you. The sacrifices you made in your day-to-day life only to get home and still have to take care of a little brat... I will forever be in your debt. You are a woman full of love to give, but you always chose to give a little extra to me. Thank you for answering my calls, even when the only thing I did was cry or complain. I love you to the moon and back millions and millions of times. Dad, thank you for being the calm and peaceful person that you are. In the midst of chaos, you are always able to think calmly. Thank you for encouraging me to travel and follow my dreams. You made the most of your life, even when opportunities were scarce. For someone who didn't go to high school, you are now a successful person, who knows a thousand languages and has traveled almost the entire world. I hope I have your courage and motivation.'

I want to thank my sister, Joana, and my brother, João. You both put up with a little brat, while you were teenagers trying to make sense of the world. I want to thank you for always trying to make things fun and lighthearted, for being understanding about me not being able to come and see you and your family, and for still making sure that my nieces and nephews know that I exist. My best memories as a kid are of being with you two during my summer breaks, thinking about how cool it was to hang out with my big brother and sister. The music, the laughter and the sun are always the things that I think about when I think about you two. You have shaped the person that I am today, and I wouldn't be here without you two. You are both incredible parents and always put your family first, making sure to create a better and more beautiful world for them. I know that Tomás, Afonso, Eva and Carolina will be amazing people (they already are!) because they were raised by you guys.

I would like to show some love to my friends from back home, Luísa, Mariana, Yenine, who mean the world to me. Luísa, you are one of the funniest people that I know, and you can always put me in a good mood when I am around you. You are a compassionate, intelligent, and resilient woman. What you do for your family and loved ones goes above and beyond, and I am so grateful to call you a friend. Mariana, we have known each other since we were in our mothers' wombs, and I hope to always have you by my side. Through trials and tribulations, you have never wavered, and when you set your mind to something I know that you will get it done! Yenine, you are the sweetest, most chilled person I know (maybe in the world?). Your kind heart and mind have always kept me on track and encouraged me to be a better person. The way

that you love and adore everyone, but especially the people close to you, is inspiring. You girls have supported me and have been my biggest cheerleaders. Through drunken nights, European trips, and late-night texting, you have always made me feel like even if I was far away, I was always close to you girls. I have always kept you all in my heart and I hope to have many more journeys together!

I would like to express my love and gratitude to the people who have accompanied me throughout these years in the BMRC.
Laura, my sister from another mister, you are truly a gem of a person, and I am so glad that you are part of my life. You are hilarious and have made me laugh in my darkest times (you have literally made me laugh so much I had to lie down). Thank you for always opening your house to me to watch scary movies or talk about life. Thank you for the hour-long chats in the corridors, for the dance breaks inside the cold room and for always knowing exactly what to say. You have made such an impact on my life, and I can't imagine a world without you in it. Your intelligence and work ethic are something to behold. I can't even imagine the amazing future that you will build, and I hope to be by your side to see it come true. Muna, Italian Ice Spice was correct, I do believe we are soulmates. You are one of the most giving humans in the world, your heart is full of love, and you are so kind to everyone you meet. Your listening ear, office dance parties and endless coffee breaks have kept me going through these years. Thank you for the expensive lattes and for the brunch dates, but most importantly, thank you for always having a little time for me. You are always able to put a smile on my face and you give the best advice! I want to thank you for the international trips, for the talks about our future, for always having my back and for believing in me, even when I didn't. You work so hard, and in everything you do you always give 100 %. You are a genius and I know that your future is going to be so bright! The litty committee will be reunited soon and I hope to always have you both in my life.

Filipe, you have one of the greatest scientific minds and one of the kindest souls. I want to thank you for giving this shy and introverted girl a chance, and for making me part of your family. You always made time to answer my stupid

questions and to listen to my rants. I will never forget the dancing (so much dancing!), the long days in the lab and our good morning choreo. You will always be the Brenda to my Karen, and I already miss you not seeing you every day. Your confidence and presence within this world have shaped the woman and scientist that I am, and I aspire to be like you. My Portuguese crew, Cristiana, Filipa, and Nelma, you will always be in my heart. Cristiana, starting this experience with you made it less lonely and scary. Thank you for letting me spend more time in your first flat than in my own house and thank you for making it a place where we could share our fears and hopes for the future. Filipa, our singing-walks will always be a highlight of my PhD. Thank you for making the beginning of this journey less dauting. I still cannot say '*Vanishing White Matter'* without hearing your voice, and every time that '*Don't Call Me Angel'* plays I think about you. Nelma, my scientific idol, you are absolutely brilliant. You are one of the smartest and fiercest people that I know. The passion and wisdom that you have about science, but also about the people around you, is inspiring. Thank you for listening to my rants about academia, for late-night dancing to *Pimba* and for taking time to travel with me. Now we just need to plan our trip to Greece.

Emerald, my Canadian sister, I am forever in gratitude for your time and patience. Thank you for feeding me when I didn't have time to cook, thank you for checking up on me and for reminding me that there is more to life than the office/lab. I want to thank you for always listening to me and always having time for a catch up. You are a strong, funny and exceptional person, and I am lucky to call you a friend.

Lastly, I want to thank Adem. I want to thank you for watching the stars (and bats) with me, and for letting me drag you to every bookshop in the UK. For talking through my panic attacks, for listening to my poster presentations and bioforum talks (I bet 40 minutes never felt so long!), and for showing my work to your family and friends. Thank you for making honey-chicken and rice, so you were sure that I ate something, and for bringing me treats when I was sad. Thank you for singing silly songs and making noises every single moment of the day (AAAAAA) and for dancing to the crosswalk lights. Thank you for making me a cup of coffee every morning, making breakfast every weekend, getting the Sunday paper so I can do the sudoku, and bringing me flowers every week, which brought a bit of colour to

my life even on rainy days. Thank you for all the memes, for our inside jokes that would have us in stitches for hours, and for driving me to work even if that meant that you got loads of traffic. Thank you for all these little things and the big things that made my time during the PhD filled with love, laughter and light. You are one of the funniest, most caring and intelligent people I know. You are incredibly astute, always trying to see every side and thinking things through. You are an amazing person, and I am very honoured to have you in my life. I also want to thank the Slater family for taking me in, a lost Portuguese girl, into their home and hearts. You made my first Christmas in Sheffield less lonely and ever since then you have always given the best hugs and always made me feel like I was part of your family. You all made my mum feel like I had a family looking out for me, and you made me feel at home every time that I visited. Dino, the cutest and sweetest dog in the world, thank you for letting me cuddle you even when I know you don't like it. You have been my screen saver for most of my PhD, and you have always brought me comfort. I will be giving you treats until the end of time!

List of figures.

List of tables.

List of abbreviations.

By alphabetical order:

4E-BPs – eIF4E-binding proteins
a.u. – arbitrary units
AGS – astrocyte growth supplement
AM – Astrocyte Medium
APS - Ammonium persulphate
ATF4 – activating transcription factor 4
BiP – binding immunoglobulin protein
BSA - Bovine serum albumin
CHOP – C/EBP homologous protein
CHX – cycloheximide
CNS – central nervous system
DAPI - 4,6-diamidino-2-phenylindole
DMEM – Dulbecco's modified Eagle's medium
DMSO – dimethyl sulfoxide
DNA - deoxyribonucleic acid
dsRNA – double-strand RNA
E.coli – Escherichia coli
eEFs – eukaryotic translation elongation factors
EF-T – Elongation factor-T
EF-Tu – Substrate of elongation factor-T
eIF2 – eukaryotic initiation factor 2
EIF2Aks – eIF2α family of protein kinases
eIF2B – eukaryotic initiation factor 2B
eIF2α – Alpha subunit of eIF2
eIFs – eukaryotic initiation factors
ELISA – enzyme-linked immunosorbent assay
ER – endoplasmic reticulum
eRFs – eukaryotic release factors
ESP – eIF2 stimulating protein
FBS – fetal bovine serum
fluorescent protein
FRAP – fluorescence recovery after photobleaching
g - gravitational force
G3BP - Ras-GTPase-activating protein (SH3 domain) binding protein
GADD34 – growth arrest and DNA damage-inducible protein
GAP – GTPase-activating protein
Gcd- - general control derepressible
Gcn- - general control nonderepressible
GCN2 – general control non-derepressible 2
GDF – GDI displacement factor
GDI – GDP dissociation inhibitor
GDP – guanine diphosphate
GEF – guanine exchange factor
GFAP – glial fibrillary acidic protein
GFP – green fluorescent protein
GTP – guanine triphosphate
h – hours
H_2O_2 - hydrogen peroxide
HA – human primary astrocytes
HCl – hydrochloric acid

HRI – heme-regulated eIF2α kinase
ICC – immunocytochemistry
IMS – industrial methylated spirit
iPSC – induced pluripotent stem cell
IRES – internal ribosome entry site
ISR – integrated stress response
ISRIB – ISR inhibitor
LB – Lysogeny broth
LLPS – liquid-liquid phase separation
M – Molar
m^6A – N^6-methyladenosine
m^7G – 7-methylated-guanosine
MBP – myelin basic protein
MEM – minimum essential medium
Met-$tRNA_i$ – initiator methionyl-tRNA
MFC – multifactor complex
mGFP – Monomeric green
min – minutes
mM – Millimolar
MO3.13 – human glial oligodendrocytic hybrid cell line
MRI – mass resonance imaging
mRNA – messenger ribonucleic acid
mRNP – messenger ribonucleoprotein
MS – mass spectrometry
ms – milliseconds
MTT - 3-(4,5-Dimethylthiazol-2-yl)-2,5-Diphenyltetrazolium Bromide
NaF - Sodium fluoride
NEAA – non-essential amino acids
NeuN – neuronal nuclei
nm – Nanometre
ROI – region of interest
ns – Non-significant
NT - nucleotidyl-transferase
^oC – Celsius
OD – optical density
p – P-value
P/S – penicillin/streptomycin
PABP – poly(A)-binding protein
P-bodies – processing bodies
PBS – phosphatase-buffered saline
PDB – protein data bank
p-eIF2α – Phosphorylated eIF2α
PERK – PKR-like ER kinase
PFA – paraformaldehyde
Pi – inorganic phosphatase
PI – propidium iodide
PIC – preinitiation complex
PKR – double-stranded RNA-dependent protein kinase
PMSF - Phenylmethylsulfonyl fluoride
PNDM – permanent neonatal diabetes mellitus
poly(A) – polyadenoside
RBPs – RNA binding proteins
RFP – Red fluorescent protein
RNA - ribonucleic acid
RNA - ribonucleic acid
RNP – ribonucleoprotein
RocA - rocaglamide A
ROS - reactive oxygen species
RPMI – Resewell Park Memorial Institute medium
RT – Room temperature
s – seconds
s.d. – standard deviation

SA – sodium arsenite
SDS - Sodium dodecyl sulfate
SDS-PAGE – SDS-polyacrylamide gel electrophoresis
SGs – stress granules
SH-SY5Y – human neuroblastoma cell line
SKOV3 – human ovarian adenocarcinoma cell line
t1/2 – Half-life
TBF – transformation buffer
TBS - Tris-buffered saline
TBST – TBS/Tween-20
TC – ternary complex
TEMED - N,N,N′,N′-Tetramethyl ethylenediamine
Tg - Thapsigargin
tGFP – Turbo green fluorescent protein
tRNA – transfer RNA
U373-MG – human glioblastoma astrocytoma cell line
uORFs – upstream open reading frames
UTR – untranslated region
v/v – Volume/volume
VWMD – vanishing white matter disease
w/v – Weight/volume
α – Alpha
β – Beta
γ – Gamma
δ – Delta
ε – Epsilon
μM – Micromolar

Chapter 1. General introduction.

1.1. Overview of eukaryotic translation.

Cellular responses to external signals are harmoniously coordinated through the interaction of transcriptional and translational regulatory mechanisms. These two processes are highly conserved and controlled. Within the intricacies of the transcriptional process, genetic information is meticulously transcribed into messenger RNA (mRNA) molecules. These molecules feature particular sequences allowing for ribosomal assembly and translation of proteins.

The translation process is divided into four stages: initiation, elongation, termination, and recycling. During the initiation step, the ternary complex (TC) is formed consisting of initiator methionyl-tRNA (Met-tRNA$_i$) and eIF2 bound to guanine triphosphate (GTP). This complex binds to a small (40S) ribosomal subunit, promoted by eukaryotic initiation factors (eIFs), forming the 43S preinitiation complex (PIC). PIC binds near the 5' cap of the mRNA and scanning for the start codon is initiated (Jackson *et al*., 2010; Hinnebusch, 2014). Recognition of the AUG start codon triggers downstream events in the pathway, including hydrolysis of eIF2, converting it into a guanine diphosphate (GDP) bound state. When eIF2 is in its inactive status and other eIFs are released, the large (60S) subunit binds to the PIC, producing the 80S initiation complex. These 80S ribosomes move progressively along mRNAs, mediating transfer RNA (tRNA) codon base-pairing synthesising the encoded protein. This elongation activity is coordinated through aminoacyl-tRNAs and the eukaryotic translation elongation factors (eEFs). In the termination step of translation, at the end of the open reading frame the termination codon is recognized, and the nascent protein is realised from the ribosome, which is mediated by eukaryotic release factors (eRFs). During the recycling stage, the ribosome complex is recycled to the 40S and 60S subunits and a new round of translation is set to being (Demeshkina *et al*., 2012; Loveland *et al*., 2017; Hellen, 2018).

eIF2 plays a key role in translation and its control. For continuous translation initiation to occur, eIF2 in its active GTP-bound state is required. As such, the eIF2B, a guanine nucleotide exchange factor (GEF) replenishes eIF2-GTP allowing for subsequent rounds of translation. This protein complex regulates translation initiation by controlling levels of GTP-bound eIF2, and during adverse

stimuli can lead to the inhibition of its activity (Marintchev & Ito, 2020), which will be discussed in more detail later in this introduction.

1.1.1. Synthesis of mRNA.

Through the transcription process, genes are transcribed from deoxyribonucleic acid (DNA) to mRNA. In eukaryotic cells, pre-mRNAs undergo co-transcriptional modifications to become a fully translatable mRNA – capping at the 5' end, addition of a polyadenoside (poly-A) tail at the 3' end and splicing of non-coding introns. A 7-methylated-guanosine (m^7G) cap is linked to phosphates present at the 5'end of ribonucleic acid (RNA) polymerase II nascent transcripts (20–25 nucleotides in length). This capping process safeguards degradation by 5'-3' exonucleases. Once in the cytoplasm, cap-binding protein complex eIF4F mediate the recruitment of 43S PIC to the 5'end of mRNA via cap recognition (Chowdhury & Tharun, 2009; Shatkin & Manley, 2000; Tharun & Parker, 1999).

The spliceosome, which is a large ribonucleoprotein (RNP) complex comprised of small nuclear RNPs and several proteins, recognises specific splice junctions and introns are spliced out of the mRNA. A hydroxyl (OH) group in the 3' end of the exon attacks the phosphodiester bond at the 3′ splice site, resulting in ligation of the two exons and excision of the intron lariat (Proudfoot *et al*., 2002; Valadkhan & Manley, 2001; Will & Luhrmann, 2011).

Prior to the addition of the poly(A) tail, the pre-mRNA is cleaved at a highly conserved U- or GU-rich motif at the 3'end. Following this, poly(A) polymerase adds a chain between 100 and 250 residues long of adenine nucleotides, forming a more stable molecule, preventing its degradation and enhancing cap-dependent translation (Colgan & Manley, 1997; Y. Zhang *et al*., 2021; Zhao *et al*., 1999).

The result is a mRNA which can be divided into 5 major regions: cap structure, 5' untranslated region (UTR), coding sequence, 3' UTR and poly(A) tail. These main transcriptional processes allow the creation of mature mRNA molecules prepared for translation steps.

1.2. Translation Initiation.

1.2.1. Formation of the 43S PIC.

The preliminary steps of translation initiation involve the assembly of the TC. An essential component of this complex is the eIF2, a heterotrimeric G protein that contains of three subunits – α, β and γ. This protein, in its active state (eIF2-GTP),

binds to Met-tRNA$_i$ having a higher affinity than bound to GDP, thus assembling the TC (Gordiyenko *et al*., 2019; Schmitt *et al*., 2012). It has been found that while the eIF2γ subunit directly interacts with the Met-tRNA$_i$ through its guanine binding sites, the other subunits are required to stabilise this interaction (Naveau *et al*., 2013).

Several eIFs participate in the recruitment of 40S ribosome to the TC, forming the 43S PIC. The eIF1, eIF1A and eIF3 alters the 40S ribosomal structure promoting the association of the TC (Maag & Lorsch, 2003; Majumdar *et al*., 2003; Passmore *et al*., 2007). Additionally, eIF5 facilitates the interaction between eIF2 and eIF3, with all these eIFs forming an intermediary multifactor complex (MFC) (Sokabe *et al*., 2012). It is of note that MFC is not rate-limiting for the delivery of Met-tRNA$_i$ to the 40S ribosome subunit, but it has been found to be essential for 80S ribosome assembly and eIF2 release (Sokabe *et al*., 2012). These steps lead to the formation of the 43S PIC, a structure capable of scanning the 5'UTR of mRNAs to locate the first AUG start codon (**Figure 1.1**).

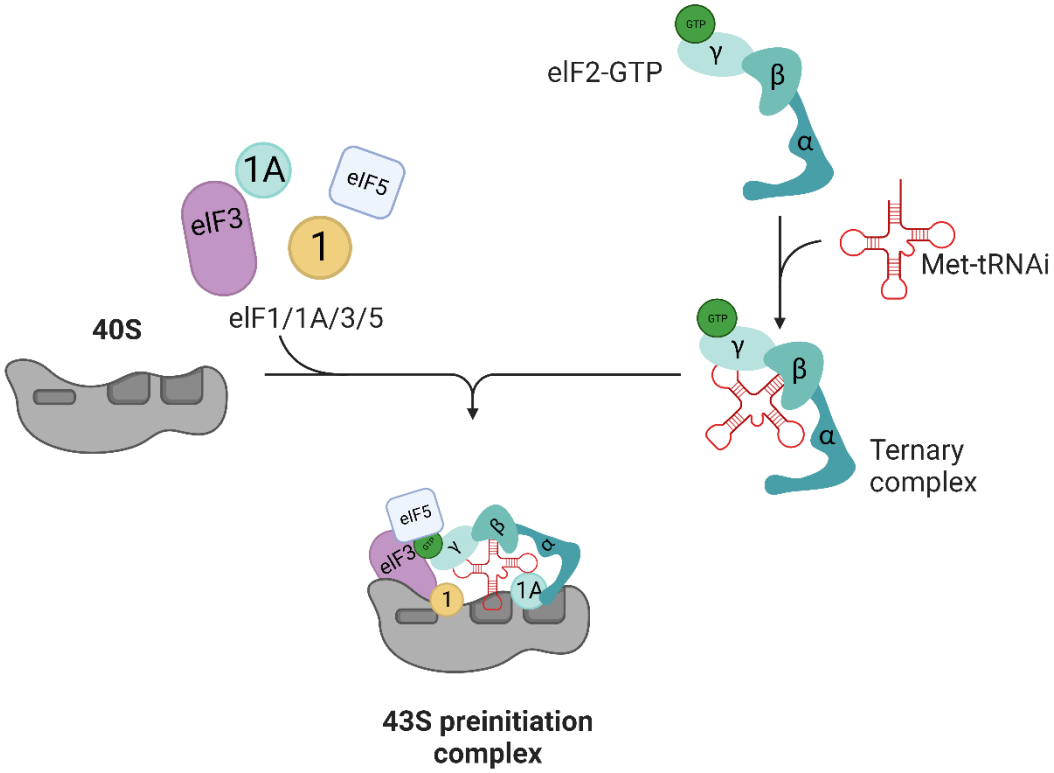

Figure 1.1. Formation of the 43S PIC.

eIF2-GTP binds to Met-tRNA$_i$ forming a TC. The TC binds to the small 40S ribosomal subunit, facilitated by eIF1, eIF1A, eIF3 and eIF5. This in turn forms the 43S PIC. Image designed in BioRender.

1.2.2. mRNA recruitment and scanning.

1.2.2.1. Cap-dependent translation.

Cap dependent translation is highly regulated and an extremely complex process, with the involvement of 10 eIFs. The eIF4F cap binding complex comprised of eIF4E, eIF4A and eIF4G, associates with the 5' end of fully mature mRNA molecules possessing m^7G cap. The presence of intricate secondary structures within the mRNA 5' UTR poses a formidable challenge, requiring the intervention of the eIF4A, a DEAD box ATP-dependent RNA helicase, which produces a single stranded regions near the 5’ cap. This in turn, removes docking-disruptive secondary structures, thus allowing ribosome binding (Mayberry *et al*., 2009; SVITKIN *et al*., 2001). The eIF4G has a scaffold function, orientating eIF4A in the correct position to unwind the mRNA structure (Gross *et al*., 2003; Hilbert *et al*., 2011; Schütz *et al*., 2008). This in turn enhances the interaction between eIF4E with the mRNA cap. eIF4G also stabilises the 43S PIC and mRNA binding by eIF3 interaction. Additionally, eIF4G interacts with the poly(A)-binding protein (PABP) present at the 3' end of the transcript (Villa *et al*., 2013; Yanagiya *et al*., 2009). These processes produce a closed loop complex, which is thought to enhance ribosome re-initiation (Vicens *et al*., 2018).

Once these interactions occur, the 43S PIC complex scans in a 5'- 3' direction to find the optimal AUG start codon complementary to the anticodon present in Met-tRNAi. For this process to occur the appropriate release of TC-associated inorganic phosphate (Pi) is necessary (Passmore *et al*., 2007; SVITKIN *et al*., 2001) (**Figure 1.2**).

1.2.2.2. Cap-independent translation.

While the canonical form of translation involves cap-dependent translation initiation, alternative modes of cap-independent translation initiation also exist. During stress conditions, the canonical translation initiation is affected, and global protein synthesis is decreased while increasing selective stress response mRNAs. These stress-responsive proteins can be produced through translational reprograming mechanisms, one of which is cap-independent translation (Shatsky *et al*., 2018). It is of note that non-canonical translation initiation can also occur via a cap-dependent but scanning-free mechanism (Kwan & Thompson, 2019).

The most commonly reported cap-independent mode of translation initiation involves the recruitment of 40S ribosomal subunits into a location upstream of the start codon via a unique internal ribosome entry site (IRES) motif, bypassing the

need for eIF4E binding (Van Eden *et al*., 2004). Although IRES was previously assumed to be a unique feature of viruses, subsequent studies discovered similar elements in eukaryotic mRNA transcripts. In particular, this was found in transcripts encoding key proteins for cell differentiation, apoptosis and cellular responses to abnormal conditions (Liberman *et al*., 2015; Shi *et al*., 2016; Vaklavas *et al*., 2016). It was previously thought that IRES-mediated ribosome recruitment was independent of eIFs, but evidence has highlighted that eIF involvement varies between mRNA transcripts, with eIF4G and PABP enhancing mRNA expression. Additionally, secondary structures of IRES have been found to aid interactions between the mRNA and the translational machinery (Gilbert *et al*., 2007; Lozano *et al*., 2018). Moreover, N^6-methyladenosine (m^6A) is a reversible base modification which occurs frequently under stress conditions. m^6A is present in the mRNA 5'UTRs and it is able to bind to eIF3, which in turn is enough to recruit the 40S ribosome under stress in an eIF4F-independent manner (Coots *et al*., 2017; Meyer *et al*., 2015).

1.2.3. Start codon selection & 80S ribosome assembly.

Normally, the first AUG triplet from the mRNA's 5' end is recognized as the start codon by base-pairing with the anticodon present in Met-$tRNA_i$ (Basu *et al.,* 2022). Additional eIFs display an essential role in promoting appropriate initiation codon scanning, with the eIF1 and 43S complex facilitating a favorable scanning-competent conformation, rejecting possible codon-anticodon mismatches and stops premature eIF5 hydrolysis of eIF2-GTP (Cheung *et al*., 2007; Pisarev *et al*., 2006). Furthermore, the alpha subunit of eIF2 (eIF2α) and the 18S ribosomal RNA component of the 40S ribosomal subunit, associate with particular nucleotides near the AUG codon. This in turn, has shown to increase the efficiency for start codon selection (Pisarev *et al*., 2006). AUG recognition leads to the irreversible hydrolysis of GTP bound to eIF2, which is dependent on the GTPase-activating protein (GAP) eIF5.

Concomitantly, eIF1 dissociates from the 40S ribosome, promoted by eIF5, releasing Pi molecules from eIF2 (Algire *et al*., 2005; Llácer *et al*., 2018). These processes collectively lead to a conformational change of the 43S PIC stalling further scanning (Llácer *et al*., 2018). eIF2 bound to GDP has a lower affinity for Met-$tRNA_i$, which is further reduced by the binding of PIC components eIF5 and eIF3 (Sokabe *et al*., 2012). This inactive GDP-bound eIF2 is released from the 43S PIC in complex with eIF5 (Algire *et al*., 2005; Singh *et al*., 2006), leaving the

Met-tRNA$_i$ in the P-site of the ribosome. For subsequent rounds of translation initiation to occur, eIF2 bound to GDP is recycled to its active state by eIF2B, which will be discussed in more detail in **section 1.2.6 and 1.4.1**.

eIF5B bound to GTP catalyzes the second GTP dependent stage of translation initiation. eIF5B-GTP interacting with eIF1A and eIF3 leads to its hydrolysis, which consequently results in a conformation change, releasing eIF5B, eIF3 and eIF1A, promotes the association of the small (40S) and large (60S) ribosomal subunits, (Chukka *et al*., 2021; Fringer *et al*., 2007; Unbehaun *et al*., 2004) (**Figure 1.2**).

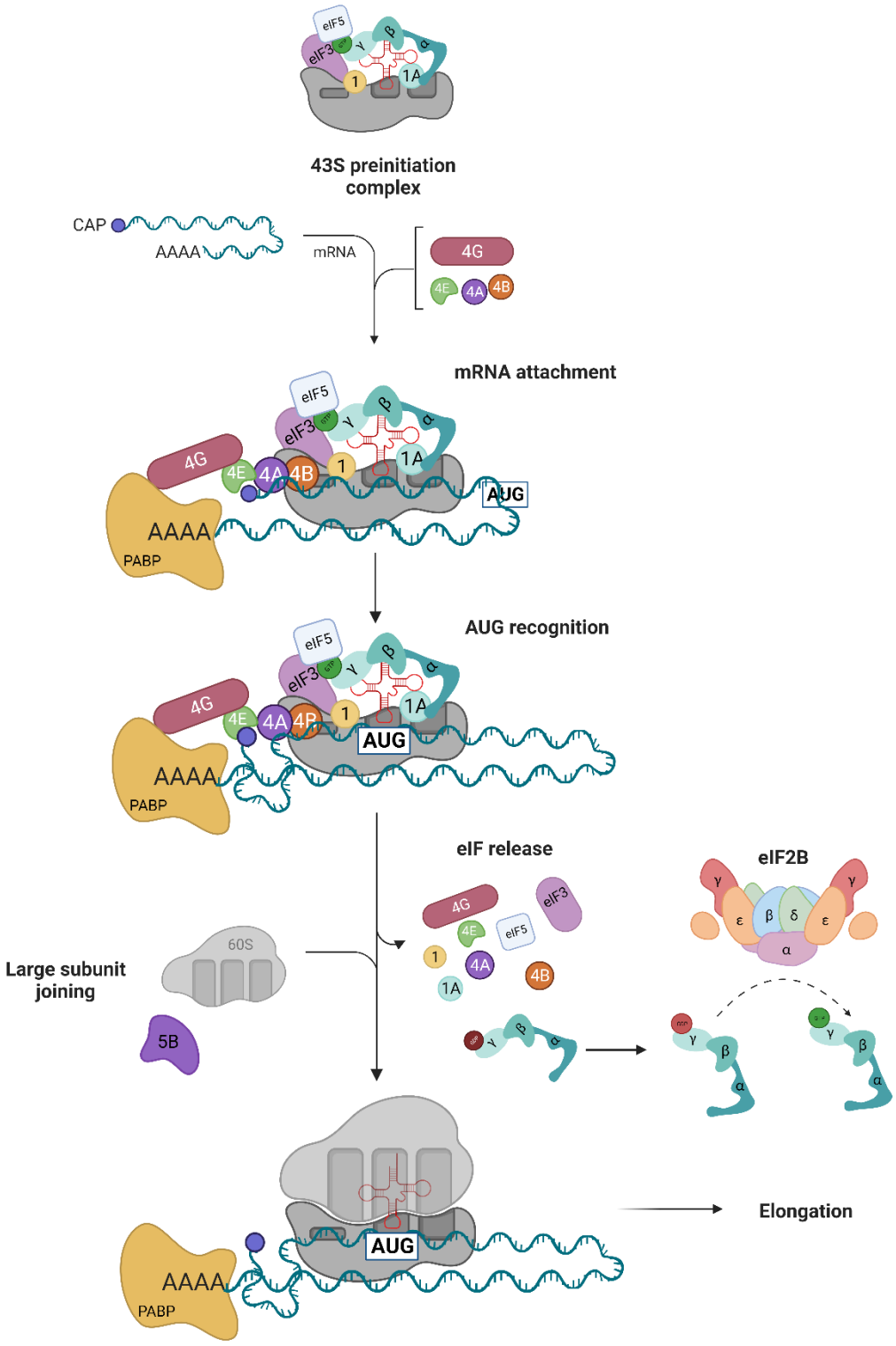

Figure 1.2. Start codon selection and 80S ribosome assembly.

The mRNA and eIF4 factors (eIF4A, eIF4B, eIF4E and eIF4G) bind to the 43S PIC and scanning for the AUG start codon initiates. Following AUG recognition eIF2-GTP is hydrolysed to eIF2-bound to GDP and the dissociation of eIFs occurs. For subsequent rounds of translation, eIF2B carries out its GEF activity and recycles inactive eIF2-GDP to eIF2-GTP. eIF5B facilitates large 60S ribosomal binding to form elongation-competent 80S ribosome. Image designed in BioRender.

1.2.4. Translation elongation

Translation elongation is a process of synthesizing the polypeptides by progressively adding amino acids to the growing polypeptide chain every 1/6th of a second (Noeske & Cate, 2012). The 80S ribosome moves along the ORF in a 5'-3' direction, with the ribosome movement and aminoacyl-tRNA selection being mediated by eEFs. eEF1A bound to GTP delivers aminoacyl-tRNAs forming a TC, binding to the A-site of the ribosome. Once base-pairing is established, GTP is hydrolyzed and the inactive complex of eEF1A is released from the ribosomal structure, accommodating the aminoacyl-tRNA into the A site (Dever & Green, 2012; Gromadski *et al*., 2007). eEF1A-GDP is recycled to its active state through the GEF eEF1B (Dever *et al*., 2016).

The peptidyl transferase activity of the large ribosomal subunit forms a peptide bond, which is catalyzed between the aminoacyl-tRNA in the A-site and the aminoacyl-tRNA in the P-site (Beringer & Rodnina, 2007). These transitions create hybrid states with the growing peptidyl chain being transferred onto the A-site, leaving the aminoacylate-tRNA in the P-site of the ribosome. Subsequently, increasing movement of the ribosomal complex results in changes of conformation and rearrangement of ribosomal functional sites, positioning the acceptors end of the tRNAs located in the P and the A-site moving to the P and E sites, respectively (Ben-Shem *et al*., 2010; Zhou *et al*., 2014). With a vacant A-site, a new aminoacylate-tRNA can occupy this position, repeating subsequent rounds of elongation. It is important to note that eEF2-GTP promotes the tRNA translocation into the canonical P and E sites (Agirrezabala *et al*., 2012; Ratje *et al*., 2010). Through this repetitive cycle, the synthesis of polypeptide chains complementary to the mRNA coding sequence is carried out.

1.2.5. Translation termination and ribosome recycling

Translation termination is supported by eRF, which are triggered by the recognition of stop codons: UAA, UGA, or UAG (Eliseev *et al*., 2011). eRF3 active state binds to eRF1 and functions as a GTP dissociation inhibitor, by guiding eRF1 to the A-site of the ribosome. This interaction leads to the hydrolysis of eRF3-GTP which in turn positions eRF1 in the peptidyl transferase center of the ribosome through Rli1p interaction, combining stop codon recognition and peptide release (Alkalaeva *et al*., 2006; Fan-Minogue *et al*., 2008).

Recycling of post-termination ribosomes is initiated by ABCE1, which

following release of eRF1, mRNA and de-acylated tRNA, recycles vacant 80S ribosomes and stalled ribosomal elongation complexes (Kärblane *et al*., 2015; Pisarev *et al*., 2010). Additionally, the combination of eRFs and eIFs facilitate ribosome recycling at specific Mg^{2+} concentrations. eRF1 and eRF3 promote ribosomal subunit dissociation which combined with eIF3 interaction to the 40S ribosome leads to its disassembly from 60S subunit (Pisareva *et al*., 2011; Shoemaker *et al*., 2010). eIF1 has been also found to induce de-acylated tRNA release, followed by mRNA dissociation (Pisarev *et al*., 2010).

1.2.6. Recycling of eIF2-GTP

For subsequent rounds of translation initiation to occur two major key players in translation need to be recycled to the translationally active GTP-bound form – eIF2-GDP and eIF5B-GDP. While eIF5B nucleotide exchange appears to be spontaneous, therefore not requiring a nucleotide exchange factor (Chukka *et al*., 2021; Lee *et al*., 2002), eIF2 recycling occurs via the GEF eIF2B (Erickson & Hannig, 1996). The eIF2 complex results from 1:1:1 association of its three subunits: eIF2α, eIF2β, and eIF2γ. These subunits appear to have distinct roles: eIF2α has a regulatory role, which following stress is a target for eIF2-specific protein kinases; eIF2β displays lysine blocks in its N-terminus, thought to be essential for the eIF2B and GAP eIF5 binding (Luna *et al*., 2012). Additionally, it presents zinc binding motifs near its C terminus, which appears to play a role in the regulation of GTP hydrolysis (Browning & Bailey-Serres, 2015). eIF2γ plays a part in the binding of Met-$tRNA_i$ and to the catalytic domain of eIF2Bε (Marintchev & Ito, 2020; Roll-Mecak *et al*., 2004; Shin *et al*., 2011; Vanselow *et al*., 2022).

The ratio between GDP and GTP, which it has been found to be 1:10 in cells (Walton & Gill, 1975; Zhigailov *et al*., 2020), should theoretically play a part in the activity of eIF2, but the affinity of eIF2 for GDP is 100 folds higher than for GTP (Bogorad *et al*., 2017; Dever *et al*., 2016; Walton & Gill, 1975). Therefore, spontaneous rates of nucleotide exchange of eIF2 are not sufficient, thus requiring eIF2B to carry out its GEF activity, demonstrating that the availability of eIF2-GTP can become rate limiting for translation initiation.

Following hydrolysis of eIF2-GTP catalyzed by eIF5, eIF2 bound to GDP is released. eIF5 functions hinders GDP release from eIF2, functioning as a GDP dissociation inhibitor (GDI). It has been found that eIF2B competes with

eIF5 for eIF2-GDP interaction. Before carrying out its GEF activity, eIF2B acts as a GDF, releasing eIF5 from the inactive eIF2 complex (Jennings *et al*., 2013; Jennings & Pavitt, 2010, 2014). Following this displacement, eIF2B activity as a GEF is essential, exchanging GDP for GTP, an action which is highly regulated within the cell. This will be explored further in **section 1.4**.

1.3. Control of protein synthesis via translation initiation

Protein synthesis is an energetically expensive activity, and adequately reprogramming cellular metabolism under stress or suboptimal growth conditions is a critical component of cell survival and repair of stress-induced damage. This process involves a myriad of coordinated alterations, and the reprogramming of mRNA translation involves stress-activated kinases. These kinases target components of the translation initiation machinery, with the overall goal of global inhibition of translation whilst concomitantly promoting translation of stress-responsive proteins (Gebauer & Hentze, 2004; Hershey *et al*., 2019). Regulation of the cyclic process of translation initiation can occur at any step of protein synthesis - initiation, elongation, termination, and ribosome recycling. The most prevalent regulatory events happen at the initiation stage, which involves synchronised action of multiple trans-acting components, leading to a tight regulation of translation (Jackson *et al*., 2010; Wang & Proud, 2008). Inhibition of translation initiation is mediated by key regulatory mechanisms: phosphorylation of eIF2α, eIF4G cleavage and dephosphorylation of p-eIF4E-binding proteins (4E-BPs) (Elia *et al*., 2017; Sharma *et al*., 2016; Willcocks *et al*., 2004). Additionally, specific RNA-binding proteins play a role in regulating translation of a selected subset of mRNAs. Here, we will focus on the ISR, a collection of stress sensing pathways which regulate translation via the common mechanism of eIF2 phosphorylation.

1.3.1. The ISR

The ISR is an intricate and complex signalling pathway, which is an integral component of eukaryotic cells' stress detection and adaptation process. The outcome of this pathway is designed to repair cellular damage, restore homeostasis, or alternatively, to induce apoptosis. Extrinsic and intrinsic stresses are able to activate the ISR, with particular kinases responding to distinct environmental and physiological factors, reflecting their unique regulatory

systems, while converging at a singular point, which is phosphorylation of the eIF2α subunit on serine 51.

1.3.1.1. Activation of the ISR and attenuation of global protein synthesis

In eukaryotes, the eIF2α family of protein kinases (EIF2AKs) plays a pivotal role in regulating protein synthesis in response to specific stress stimuli. This in turn, serves the dual purpose of conserving resources while also reconfiguring gene expression to facilitate stress adaptation. Alternatively, under certain conditions, these kinases can trigger apoptosis, presenting a complex regulatory mechanism (Wek *et al*., 2006). Four distinct eIF2 kinases have been identified, each possessing a diverse array of regulatory domains that endow them with the ability to detect various stimulatory cues (Dey *et al*., 2007). Through their remarkably similar catalytic domains, their signalling cascades transmit a potent inhibitory signal that disrupts translation initiation by selectively phosphorylating a common cellular substrate, eIF2α, at the critical serine 51 site (Muaddi *et al*., 2010; Uppala *et al*., 2018). These kinases are the following: PKR-like ER kinase (PERK) (Kaufman, 1999), double-stranded RNA-dependent protein kinase (PKR) (Nanduri, 2000), general control non-derepressible 2 (GCN2) (Vazquez De Aldana *et al*., 1994) and heme-regulated eIF2α kinase (HRI) (Han, 2001) (**Figure 1.3**). Amidst stress conditions, the activation of eIF2α kinases ensues, initiating a conformational shift towards a dimer configuration of their catalytic kinase domains and autophosphorylation (Lavoie *et al*., 2014; Pakos-Zebrucka *et al*., 2016).

PERK, a constituent of the ER stress response, is positioned within the ER lumen, wherein it forms complexes with the chaperone binding immunoglobulin protein (BiP), tightly orchestrated to maintain cellular proteostasis. Under conditions of ER stress, characterised by the accumulation of misfolded proteins in the ER lumen, the dissociation of BiP occurs, unlocking the gateway to PERK oligomerization and, subsequently, culminating in the activation of its C-terminal cytoplasmic eIF2α kinase domain (Bertolotti *et al*., 2000; Cui *et al*., 2011; Wang *et al*., 2018).

Within the N-terminal segment of PKR there are two double-strand RNA (dsRNA) binding domains. Binding of dsRNA instigates dimerization and subsequent kinase activation (Nanduri, 2000). Additionally, expression of PRK is induced by interferon, thereby highlighting this kinase as a pivotal component within the

cellular antiviral defence apparatus, while also participating in ER stress (Onuki *et al*., 2004), cytokine signalling, bacterial surface proteins (Goh, 2000) and oxidative stress pathways (García *et al*., 2006).

GCN2 stands as the sole eIF2α kinase in yeast, regulating the ISR in response to amino acid deprivation. Remarkably, GCN2 is highly conserved from yeast to mammalian cells (Castilho *et al*., 2014), with its response being activated by amino acid deficit, innate antiviral response (Berlanga *et al*., 2006) and proteasomal inhibition (Jiang & Wek, 2005).

The discovery of HRI emerged from investigations conducted in reticulocytes, where its crucial role in impeding protein synthesis within heme-deprived lysates was initially identified (Han, 2001). Subsequently, it was unveiled to not only be activated under heme-deprivation but also in response to diverse stressors such as heat shock, osmotic stress, and oxidative stress through arsenic treatment in cells (Lu *et al*., 2001; McEwen *et al*., 2005).

Phosphorylation plays a pivotal role in converting eIF2 from a substrate into an inhibitor of eIF2B, effectively curbing the cellular abundance of active GTP-bound eIF2. Consequently, the scarcity of active eIF2 significantly constrains the supply of Met-tRNA$_i$ to the ribosomes, culminating in a dual effect on translation initiation. Firstly, this deficiency leads to a global attenuation of translation initiation, exerting a sweeping impact on the cellular translational environment. Secondly, this also brings about a selective and targeted up-regulation of translation for a specific subset of mRNAs (Hinnebusch & Lorsch, 2012; Palam *et al*., 2011). The upregulation of these stress responsive proteins allows for an adaptive response to the specific stress. The regulation of these stress responsive mRNA is prominently governed by the presence of upstream open reading frames (uORFs) in the 5' UTR of target transcripts. The abundance of TCs plays a key role in determining the fate of uORF-mediated translation. When TCs are abundant, the scanning ribosome tends to initiate translation at uORFs. However, when TCs levels are depleted, the scanning ribosome is unlikely to bind a TCs by the time it reaches a uORF. Consequently, the ribosome continues to scan the transcript until a TC joins, leading to a higher likelihood of bypassing uORFs and initiating translation at the coding ORF, a phenomenon known as leaky scanning (Ferreira *et al*., 2014).

One of the most extensively characterised mRNAs regulated through this mechanism is the transcription factor, activating transcription factor 4 (ATF4)

(GCN4 – yeast equivalent; Lu *et al*., 2004). Human ATF4 mRNA has two uORFs, the second of which overlaps the start codon of the protein-coding sequence (Ghezala *et al*., 2012; Vattem & Wek, 2004). Under normal cellular conditions, these up-stream uORFs function as re-initiation sites. After stop codon recognition, the 60S ribosome dissociates, while the 40S ribosome remains associated. In the presence of ample TCs, the scanning 40S ribosome swiftly acquires a new TC, allowing for the efficient re-initiation of translation at the next uORF. Crucially, the second uORF sequence overlaps with the coding sequence of ATF4, albeit in an out-of-frame manner, and thus, the translation of uORF2 inhibits the translation of ATF4 (Lu *et al*., 2004; Marasco *et al*., 2022; Vattem & Wek, 2004). Under cellular stress, the phosphorylation of eIF2α generates a reduction in the availability of TCs, intricately modulating translation dynamics. Consequently, the scanning ribosome encounters delays in being recharged with Met-tRNA$_i$ in a timely fashion to efficiently translate uORF2. This delay-induced effect disrupts the typical translational trajectory, bypassing the scanning ribosome from engaging with uORF2. Instead, the ribosome persists in its scanning process until it eventually reaches the main ORF of ATF4 (Vattem & Wek, 2004).

ATF4 emerges as a multifaceted regulator, capable of inducing pro-survival or pro-apoptotic pathways. For long-term survival, a crucial strategy unfolds, wherein translationally upregulated transcription factors, exemplified by ATF4, seize the opportune moment to drive the expression of adaptive genes. This 'window of opportunity' presents a critical temporal phase during cellular stress responses, enabling the orchestrated activation of gene expression programs that bolster the cell's adaptive capacity (Neill & Masson, 2023; Wortel *et al*., 2017). In this view, to restore cellular homeostasis, ATF4 sets in motion crucial downstream events by activating the transcription factor C/EBP homologous protein (CHOP). CHOP drives the transcription of growth arrest and DNA damage-inducible protein (GADD34). This protein recruits protein phosphatase 1 which together act as a stress-induced eIF2α phosphatase (Choy *et al*., 2015). By dephosphorylating eIF2α, GADD34 effectively counteracts the translational inhibition caused by the ISR, allowing for renewed translation and facilitating the cell's path toward regaining normal physiological functions. Indeed, while ATF4 adeptly orchestrates pro-survival mechanisms as discussed earlier, it can also initiate apoptosis, cell-cycle arrest, and senescence (Frank *et al*., 2010; Han *et*

al., 2013; Lin *et al*., 2010). The CHOP:ATF4 interaction has been implicated in pro-apoptotic pathways, through the up-regulating of expression of death receptors, including DR5 (Zhou *et al*., 2008) and ATF5-mediated transcription of cell death genes (Teske *et al*., 2013).

Amidst the complex terrain of cellular stress responses, the activation of the ISR serves as a pivotal balancing act, characterised by two distinct periods: the transient 'acute' ISR and the prolonged 'chronic' ISR. During the 'acute ISR' phase, eIF2α undergoes phosphorylation, leading to a global suppression of translation to mitigate the immediate stress onslaught. Simultaneously, this phase triggers the expression of genes devoted to bolstering cellular recovery, fostering the cell's journey back to homeostasis. However, a shift to the 'chronic' phase represents a paradigm shift, indicating a delayed adaptation to prolonged stress (Korneeva, 2022). While initially adaptive, sustained activation of the ISR can eventually propel cells toward a pro-apoptotic trajectory. Pathological manifestations, such as neurodegeneration in chronic PERK activation (as observed in Parkinson's disease), underscore the critical importance of a finely tuned ISR for cellular health and function (Mercado *et al*., 2018; Talukdar *et al*., 2023). Navigating this delicate balance between the acute and chronic stress responses holds profound implications for cellular fate.

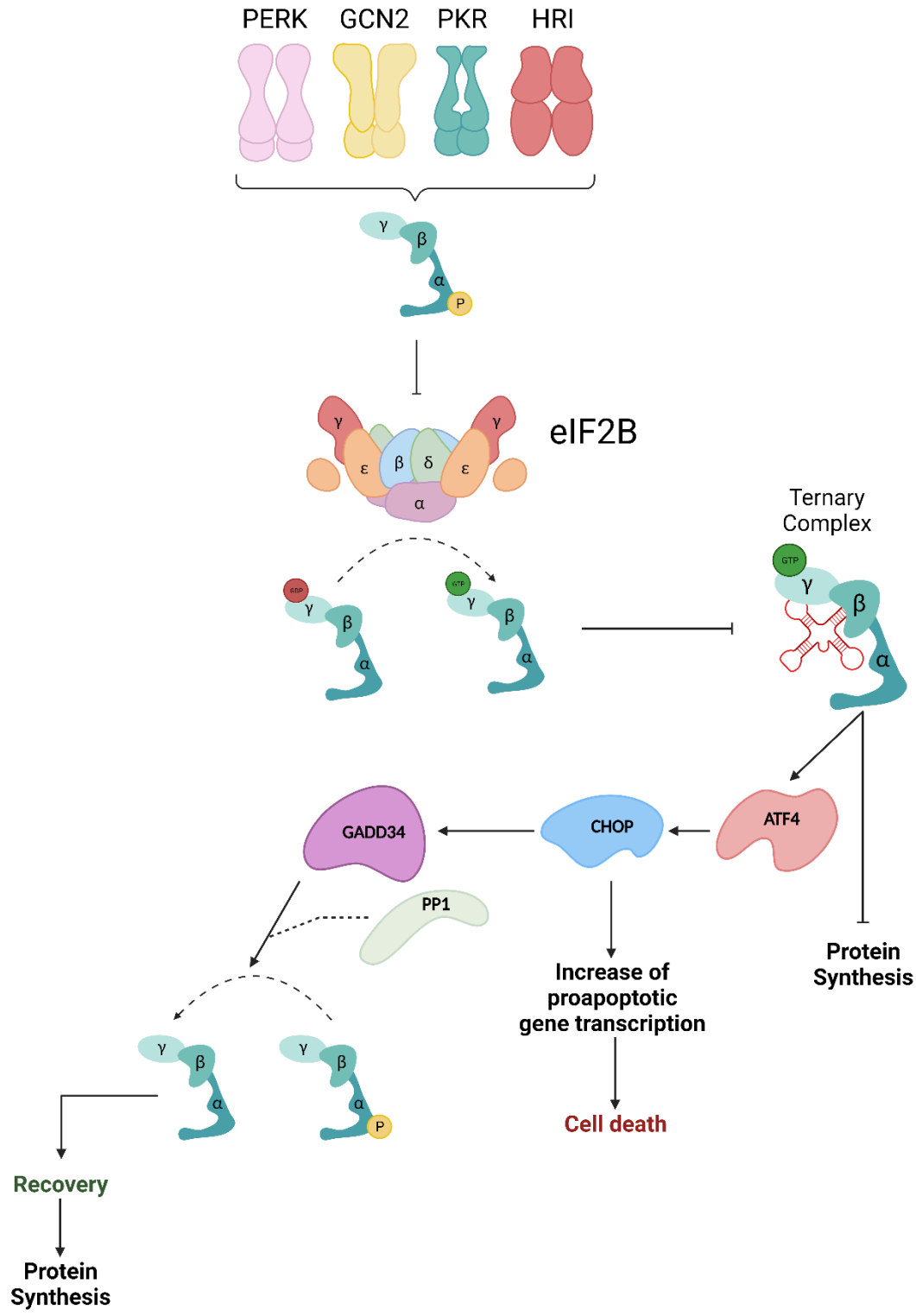

Figure 1.3. ISR pathway activation.

In response to cellular stress, eIF2α kinases are activated through dimerization and autophosphorylation. Subsequently, eIF2α is phosphorylated at serine 51, which acts as a competitive inhibitor of eIF2B GEF activity. This leads to global protein synthesis inhibition and translation of stress-specific response mRNAs, such as ATF4. To restore homeostasis, ATF4-mediated activation of CHOP induces the transcription of GADD34, which in turn dephosphorylates eIF2α. If cells are unable to recover, CHOP promotes proapoptotic gene expression. Image designed in BioRender.

1.3.1.2. eIF2B inhibition

Converging at a pivotal point, the ISR kinases phosphorylate eIF2α, which in turn transforms eIF2 from a substrate for eIF2B into a potent eIF2B inhibitor. This regulatory switch marks a crucial turning point in translational control, dictating the fate of translation initiation and cellular response to diverse stress stimuli.

Recent publications have provided insights into the complex interaction between eIF2B and eIF2 complexes (Adomavicius *et al*., 2019; Gordiyenko *et al*., 2019; Kashiwagi *et al*., 2019; Kenner *et al*., 2019). The eIF2 binds across the surface of eIF2B in an elongated conformation, interacting with the eIF2B complex at four interfaces (IF1-IF4) each playing a distinct role in the eIF2B•eIF2 interaction. The IF1 and IF2 sites interact with eIF2γ, binding it between eIF2Bε's catalytic and core domains, fostering the GTP binding site's stabilization and unravelling, thus facilitating nucleotide exchange. Meanwhile, IF3 and IF4 connect eIF2α to the twofold symmetry interface of eIF2B, binding to eIF2Bβ and eIF2Bδ. However, the pivotal transformation occurs upon serine 51 phosphorylation of eIF2α, wherein eIF2 assumes an entirely new binding mode. Phosphorylated eIF2α (p-eIF2α) now establishes a binding site between eIF2Bα and eIF2Bδ, distinct from the eIF2α binding surfaces in the original state (Bogorad *et al*., 2017; Gordiyenko *et al*., 2019). This in turn, highlights eIF2Bα essential role in sensing of eIF2α phosphorylation, which will be expended on in **1.4.3**. This phosphorylation-driven change remarkably renders p-eIF2α incompatible with the IF3/IF4 binding that facilitates normal substrate engagement. Subsequently, p-eIF2α assumes an inhibitory role.

Both eIF2 and p-eIF2 protein complexes bind to the eIF2B complex composite interaction surfaces (Kashiwagi *et al*., 2019; Kenner *et al*., 2019). The binding mode is primarily determined by eIF2α, which serves as the anchor for both eIF2 and p-eIF2α at their respective binding sites. A recent steric clash-based model has been proposed, where the binding position of eIF2γ, in its phosphorylated structure, prevent non-phosphorylated eIF2 substrate from interacting with eIF2Bε's catalytic activity (Kashiwagi *et al*., 2019; Kenner *et al*., 2019). However, conflicting studies propose that the eIF2α C-terminal domain's flexibility might allow eIF2γ to avoid the proposed clash. These studies suggest that allosteric competition, rather than steric clash, might play a significant role in p-eIF2α-mediated inhibition (Adomavicius *et al*., 2019; Schoof *et al*., 2021).

Research revealed that the binding of eIF2 and p-eIF2 is inversely related, even in the presence of only the α subunit of p-eIF2, thus binding of unphosphorylated and phosphorylated at the opposing tetrameric is not possible. As a consequence of p-eIF2α binding, substrate binding is impeded, despite the considerable distance (~50 Å) between the two binding sites (Schoof *et al*., 2021). Additionally, the phosphorylated form of eIF2α alone is capable of inhibiting GEF activity by reducing both substrate affinity and the catalytic efficiency of eIF2B. Depending on the concentration levels, this inhibition of eIF2B's inherent catalytic activity may be the primary factor responsible for the limiting of TC levels. ISRIB, a molecule able to modulate the ISR, and eIF2 when bound to eIF2B stabilize the active A-state conformation, while p-eIF2α interaction with eIF2B stabilizes the inactive I-state conformation characterised by reduced GEF activity and eIF2 binding (Schoof *et al*., 2021).

Previous studies have shown that eIF2 is approximately 3 to 5 times more abundant than eIF2B within the cell. This significant difference highlights the fact that even a minor presence of p-eIF2α can have a substantial impact on reducing eIF2B's GEF activity, leading to the inhibition of translation initiation (Merrick & Pavitt, 2018).

1.4. eIF2B

eIF2B is a GEF, initially identified as a protein factor capable of counteracting the inhibition of protein synthesis instigated by HRI kinase, without influencing the phosphorylation state of eIF2α. Consequently, it earned the moniker "anti-inhibitor" or "anti-HRI" (Amesz *et al*., 1979).

In a separate discovery, eIF2B was also unveiled as an eIF2 stimulating protein (ESP), a complex factor that facilitates the formation of the TC (de Haro & Ochoa, 1978; Siekierka *et al*., 1981). Subsequently, the once-disparate proteins of anti-HRI and ESP were found to be embodied by the same multifunctional protein, capable of facilitating GDP release from eIF2, leading to the increase of TC formation, a pivotal step in the complex machinery of protein synthesis initiation. Consequently, this protein earned the title of "eukaryotic recycling factor 2B" or "eIF2B" (Salimans *et al*., 1984).

Despite sharing functional similarities with other guanine nucleotide exchange factors, eIF2B stands out as a remarkably intricate entity within its structure. This protein complex is comprised of five nonidentical subunits, denoted by α-ε, and

these subunits are encoded the genes *EIF2B1-EIF2B5*, respectively. In its native conformation, eIF2B adopts a heterodecameric assembly, with two copies of each of its five subunits (Gordiyenko *et al*., 2014; Wortham *et al*., 2014). However, within mammalian cells, eIF2B reveals forms subcomplexes of various compositions, housing varying degrees of individual eIF2B subunits (Hanson *et al*., 2023; Hodgson *et al*., 2019; Wortham & Proud, 2015).

1.4.1. eIF2B function

To date, the principal role attributed to eIF2B is the facilitation of GDP/GTP exchange on eIF2, a process akin to the prokaryotic substrate of elongation factor-T/elongation factor-T (EF-Tu/EF-Ts) system (Schmitt *et al*., 2010). In both yeast and mammalian cells, the enzymatic activity of eIF2B results in the augmentation of eIF2-GTP binary complexes, thereby fostering the assembly of the GTP-eIF2•Met-tRNAi-TC. Similar to other GEFs, eIF2B triggers the initiation of GDP dissociation through elaborate conformational alterations within the nucleotide-binding pocket of eIF2, coupled with the destabilization of Mg^{2+} ion coordination (Bogorad *et al*., 2017).

The conventional enzymatic reaction orchestrated by eIF2B can be illustrated through the following chemical equation:

eIF2-GDP + GTP + eIF2B <-> eIF2-GTP + GDP + eIF2B.

Within this biochemical interaction, eIF2 engages in a transitory interaction with eIF2B, leading to a modulation of eIF2's affinity for GDP, consequently inducing a reduction in said affinity (Boone *et al*., 2022).

A conventional assay for evaluating eIF2B's GEF activity involves monitoring the exchange of radioactively or fluorescently labelled GDP for its unlabelled counterpart. This approach is rooted in the fact that the rate of eIF2-GDP dissociation from eIF2B is approximately an order of magnitude faster than that of eIF2-GTP dissociation (Williams *et al*., 2001). Furthermore, a recent report underlines that yeast eIF2B exhibits comparable affinities for both *apo*-eIF2 (lacking bound nucleotide) and nucleotide-bound eIF2 (GDP or GTP), hinting at the possibility that the directionality of the nucleotide exchange reaction facilitated by eIF2B may hinge upon the presence of Met-$tRNA_i$ (Bogorad *et al*., 2017).

Additionally, an auxiliary role of eIF2B contributes to this exchange process. Initially, this mechanism entails the dissociation of eIF2 from the eIF2-GDP●eIF5 complex, achieved by eIF2B through its capacity for GDI displacement of eIF5. Following this initial step, nucleotide exchange transpires. This intricate

mechanism is further enriched by the competition between Met-tRNA$_i$ and eIF2B for binding to eIF2-GTP (Jennings *et al*., 2017; Kershaw *et al*., 2021). Upon the assembly of the TC, eIF5 is recruited to reconstitute a quaternary arrangement involving eIF2-GTP, Met-tRNA$_i$, and eIF5 (eIF2-GTP●Met-tRNA$_i$●eIF5), which serves the purpose of inhibiting the association of eIF2B (Jennings *et al*., 2017). The eIF2Bγ and ε subunits, recognized as integral constituents of a catalytic subcomplex, establish interactions with eIF2 and exhibit GEF activity (Kershaw *et al*., 2021). Supporting biochemical investigations have demonstrated that eIF2Bε possesses independent catalytic activity, albeit substantially reduced (~100-fold) compared to its activity within a fully assembled complex. On the other hand, eIF2Bγ, when considered individually, does not exhibit guanine exchange activity; nevertheless, it reinforces the interactions between eIF2 and eIF2Bε (Kashiwagi *et al*., 2019; Kenner *et al*., 2019; Schoof *et al*., 2021).

The precise mechanism by which the facilitation of guanine exchange occurs remains elusive and lacks a well-defined explanation. The proposed substitutional mechanism posits that the dissociation of GDP takes place upon the formation of the eIF2B●eIF2 complex. The sequential mechanism involves the successive assembly of a TC comprising eIF2B●eIF2 and GDP/GTP, facilitated by the eIF2B●eIF2-GDP/GTP intermediate. Supporting this mechanism are observations that eIF2B cannot displace GDP from eIF2 without the presence of GTP (Kershaw *et al*., 2021; Manchester, 2001). Additionally, GTP, but not GDP, is required for the dissociation of eIF2 from eIF2B (Goss *et al*., 1984; Kershaw *et al*., 2021), and GTP demonstrates binding affinity to eIF2B irrespective of the presence of eIF2 (Dholakia & Wahba, 1989), with the availability of GTP regulating eIF2B GEF activity. Studies have demonstrated a transfer of GTP from eIF2Bγ to eIF2γ, as these two subunits exclusively possess GDP/GTP-binding domains (Circir *et al*., 2022; Jennings *et al*., 2013; Kershaw *et al*., 2021). It is of note that the binding of GTP to eIF2Bγ exclusively occurs when it is in complex with eIF2Bε (eIF2Bγε), and this interaction, in turn, is thought to promote the displacement of GDP from eIF2 (Kershaw *et al*., 2021). The eIF2B regulatory subunits undertake the task of modulating eIF2B activity levels, influenced by the intricacies of the cellular environment. Given that eIF2 exhibits a greater affinity for GDP, the extent of GEF activity executed by eIF2B plays a pivotal role in governing the overarching rates of cellular translation.

1.4.2. eIF2B structure

In comparison to other GEFs, eIF2B operates within a more intricate structural framework, distinguished by its heterodecameric architecture in its native conformation. This decameric arrangement is composed of two sets, each containing five distinct subunits denoted as α, β, γ, δ, and ε, corresponding to the genes *EIF2B1*-5 in ascending order of size (Gordiyenko *et al*., 2014; Wortham *et al*., 2014) (**Figure 1.4**). Upon its initial isolation from rabbit reticulocytes, eIF2B was commonly found in conjunction with the three subunits of the eIF2 complex within cells, which could be dissociated by increasing salt concentration (Konieczny & Safer, 1983; Salimans *et al*., 1984; Siekierka *et al*., 1981). The subunits of eIF2B can be categorized based on their roles: catalytic and regulatory. The eIF2Bγ and ε subunits were shown to drive the catalysis of GDP/GTP exchange, while the eIF2Bα, eIF2Bβ, and eIF2Bδ subunits oversee GEF activity modulation in response to cellular cues (Kimball *et al*., 1998; Pavitt *et al*., 1997; Williams *et al*., 2001).

The catalytic subunits, eIF2Bγ and ε, contain nucleotidyl-transferase (NT) domains along with a β-helical barrel that arises from a region of repeated motifs enriched in isoleucine (referred to as the I-patch). These structural elements serve as pivotal components in their interchange with one another as well as with the other subunits (Wang *et al*., 2012). Moreover, within eIF2Bε, distinct NF motifs (Asparagine-Phenylalanine) and HEAT domains have been discerned on its distal facet, contributing to its multifaceted functionality (Boesen *et al*., 2004; Kashiwagi *et al*., 2016). The C-terminal domain of eIF2Bε plays a crucial role in forging the connection between the complex and eIF2β and eIF2Bγ (Asano, 1999; Mohammad-Qureshi *et al*., 2007). Furthermore, the HEAT domain takes on the responsibility of catalysing the nucleotide exchange process, the swiftness of which gains augmentation upon the collaborative incorporation of other eIF2B subunits. This is notably facilitated by eIF2Bγ's affinity for GTP, culminating in the stabilization of the interaction between eIF2 and eIF2Bε (Gomez *et al*., 2002; Gordiyenko *et al*., 2014; Williams *et al*., 2001). In a synchronized fashion, eIF2Bγ assumes a role in displacing eIF5 from the eIF2-GDP complex (Jennings & Pavitt, 2014).

The regulatory α, β, and δ subunits of eIF2B exhibit a remarkable degree of sequence homology yet are distinguished by their distinctive N-terminal domains, which bestow upon them their individuality. Their structural compositions are

characterised by the presence of alpha helical domains and C-terminal Rossmann-fold-like domains (Kuhle *et al*., 2015; Paddon & Hinnebusch, 1989). Structural analysis has revealed that the three regulatory subunits forming the hexameric core of eIF2B construct a central cavity, perceptible when viewed from the apex of the subcomplex. This cavity has been hypothesized to have the potential to interact with eIF2α (Kashiwagi *et al*., 2016).

It is noteworthy that the balanced stoichiometric expression of eIF2B subunits, as well as their regulation, plays a part in the complex's precision and efficiency within cellular processes. Although no discernible alterations concerning the levels or transcription of their corresponding mRNAs were unveiled, it became apparent that the absence of co-expression precipitates a reduction in the expression of specific subunits. There is requirement for the co-expression of specific counterparts to ensure the expression of certain subunits – eIF2Bε expression hinges upon the simultaneous presence of eIF2Bγ, whereas the maintenance of eIF2Bδ expression necessitates the simultaneous participation of eIF2Bβ and the eIF2Bγ+ε subunits (Wortham *et al*., 2016). Changes in expression levels are due to degradation through the ubiquitin-proteasome system.

The formation of this heterodecameric structure has had varied proposed assembly pathways, some investigations suggesting that assembly is orchestrated through the catalytic subunits $(\gamma\varepsilon)_2$ (Gordiyenko *et al*., 2014), while others indicated the involvement of the regulatory $(\alpha\beta\delta)_2$ core (Bogorad *et al*., 2014; Wortham *et al*., 2014). In recent years, a paradigm shift has emerged, centering on the concept of eIF2Bβδγε coexistence and the alignment of two sets facilitated by eIF2Bα_2 homodimer (Tsai *et al*., 2018; Wortham *et al*., 2014). As eIF2Bε expression is under the regulatory influence of eIF2Bγ levels and due to their potential for dimerization, initial assembly involves the formation of heterodimers between eIF2Bγ and ε. In a similar manner, eIF2Bβ and δ can establish heterodimeric interactions, subsequently binding with the eIF2Bγε heterodimer, thereby progressing to an intermediate state characterised by an eIF2Bβδγε tetramer. eIF2Bα exhibits the capability to form homodimers, and the incorporation of this subunit serves as the culminating step of decamer eIF2B formation, bringing together two opposing tetramers and effectively generating the complete eIF2B$(\alpha\beta\delta\gamma\varepsilon)_2$ holocomplex (Schoof *et al*., 2021; Wortham *et al*., 2016a).

The eIF2B sub-complexes described exhibit notable stability, enabling their presence in what is potentially an intermediate state. This scenario postulates the coexistence of eIF2B(βδγε) and eIF2B(γε) sub-complexes within mammalian cells, and these entities manifest progressively diminishing GEF activity in comparison to the complete holocomplex, with approximately 50 % and 20 % efficiency, respectively (Liu *et al*., 2011; Wortham *et al*., 2014). A potential role for these subcomplexes has been proposed wherein these eIF2B sub-complexes form eIF2B bodies with varying affinities for p-eIF2α. This arrangement potentially furnishes distinct sub-populations of GEF hotspots, which exhibit divergent responses during episodes of cellular stress, adding a layer of complexity to their regulatory dynamics (Hodgson *et al*., 2019).

The investigation of the molecular architectures of eIF2B in both mammalian and *Schizosaccharomyces pombe* systems (Kashiwagi *et al*., 2016; Tsai *et al*., 2018; Zyryanova *et al*., 2018) has revealed an intricate assembly. The imperative interaction between the catalytic subunits, eIF2Bγ and ε, and their fellow eIF2B subunits is substantially facilitated by the NT domains, as previously explained. Furthermore, the AT-like domain nestled within the eIF2Bε subunit also emerges as an indispensable element of binding interactions with the regulatory subunits (Koonin, 1995; X. Wang *et al*., 2012).

It is noteworthy that the constituent subunits of the regulatory subcomplex exhibit intriguing homology to sugar-phosphate isomerases found in archaeal organisms, while the structural features of the catalytic subcomplex subunits display compelling resemblances to sugar transferases (Kashiwagi *et al*., 2016). Although the structural investigations on human eIF2B have not yielded direct evidence of nucleotide occupancy within its architecture (Anand & Walter, 2020), the prospect that eIF2B might engage with nucleotides or sugars in a manner that orchestrates functionality is still open.

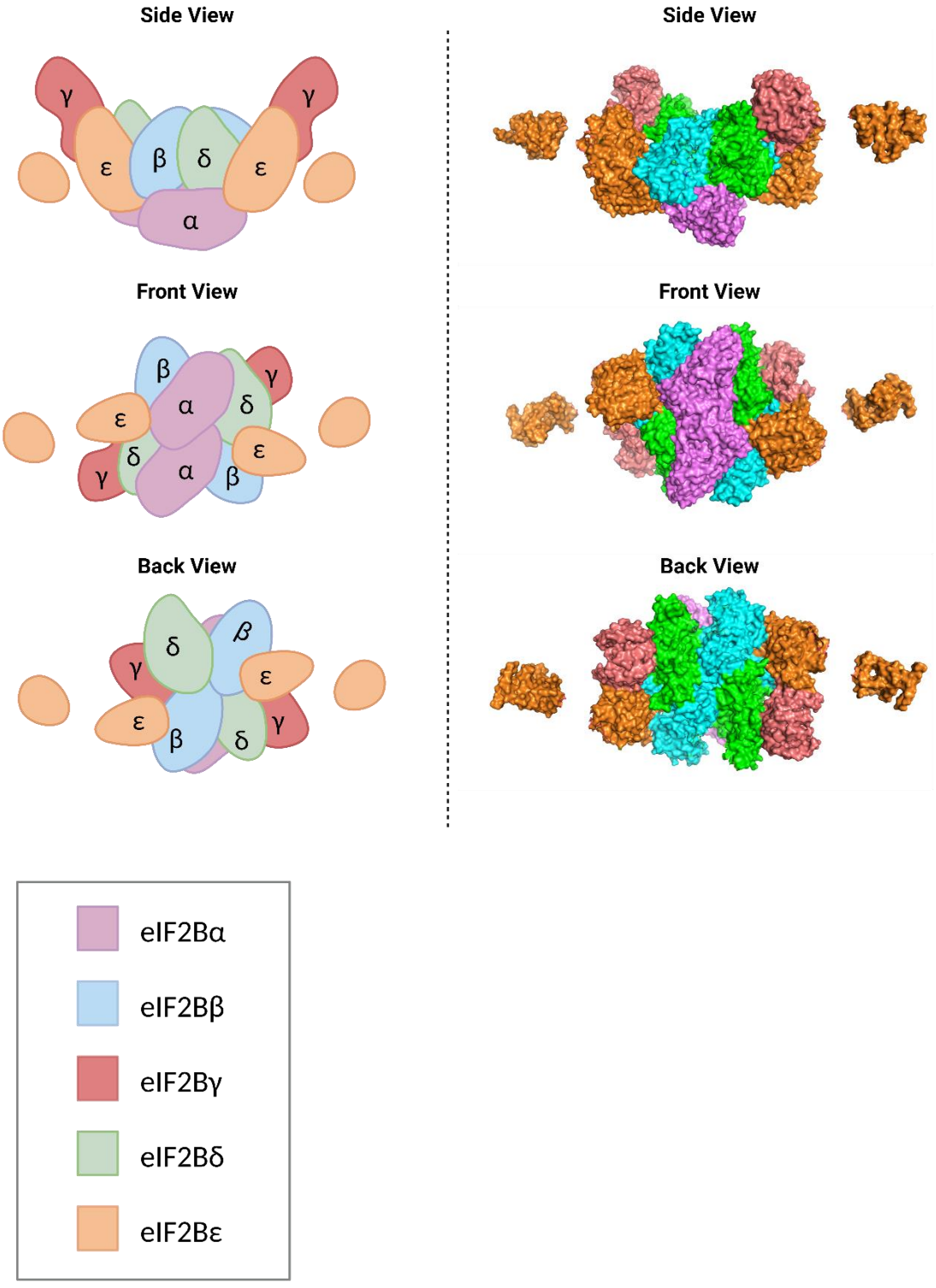

Figure 1.4. The cryogenic electron microscopic structure of mammalian eIF2B.
In its native conformation eIF2B exists as a decamer comprised of two copies of each eIF2Bα-ε. The regulatory subunits (eIF2Bα, eIF2Bβ, and eIF2Bδ) reside in the centre of the decamer, with the catalytic subunits (eIF2Bγ, and eIF2Bε) flanking either side of the regulatory core. The images on the right are cartoon representations of the cryogenic electron microscopic structure of mammalian eIF2B.The images on the left panel are resolved crystal structure of mammalian eIF2B (protein data bank - PDB: 6O81, in PyMOL). Image designed in BioRender.

1.4.3. eIF2Bα

As stated previously, the eIF2B complex can be divided into catalytic and regulatory categories. From three-dimensional structural work, the regulatory core was found to form a central cavity, binding to eIF2α (Kashiwagi *et al*., 2016). This highlights the regulatory role of eIF2B regulatory subunits in mediating levels of the eIF2B activity through sensing of phosphorylated eIF2α, particularly in the case for the eIF2Bα subunit, a 30-kDa protein. Additionally, as stated previously, the eIF2B decameric structure strongly relies on the presence of eIF2Bα dimers to join eIF2Bβγδε tetramers together (Schoof *et al*., 2021; Wortham *et al*., 2016) (**Figure 1.5**).

In yeast, the eIF2Bα subunit encoded by the *GCN3* gene, is non-essential and it has been found to be dispensable for the eIF2B complex GEF activity (Bushman *et al*., 1993; Gomez *et al*., 2002; Hannig *et al*., 1990; Hannig & Hinnebusch, 1988; Yang & Hinnebusch, 1996). However, it still maintained its essential role in sensing the status of eIF2α phosphorylation. The same was not found in mammalian cells, with rates of guanine exchange being considerably decreased when eIF2Bα is absent from the eIF2B complex (Liu *et al*., 2011; Wortham *et al*., 2014), demonstrating a key role, not only in sensing of stress but also functionally important for the activity of the complex. This potential divergence between yeast and mammalian cells may suggest that a higher degree of eIF2 phosphorylation is necessary to effectively inhibit eIF2B's activity in yeast (Dever *et al*., 1992). This observation might be indicative of the distinct eIF2:eIF2B ratio variations between yeast and mammalian cells, potentially leading to a higher ratio in the latter. Alternatively, it is plausible that yeast eIF2B(βγδε) tetramers exhibit enhanced efficacy compared to their mammalian counterparts. It's worth considering that the more robust yeast eIF2B(βγδε) tetramers could potentially manifest as eIF2B$(\beta\gamma\delta\varepsilon)_2$ octamers (Gordiyenko *et al*., 2014), potentially operating independently without necessitating the presence of eIF2Bα as a bridging component.

Additionally, under physiological conditions, eIF2Bα homodimerizes at its C-terminus and under higher concentrations of purified protein, eIF2Bα can form larger structures, such as octamers (Bogorad *et al*., 2014; Kashiwagi *et al*., 2016). In these same studies, eIF2Bβ was not capable of forming these complex arrangements, showing a monomeric structure. Thus, the potential of the eIF2Bα subunit to form stable higher order complexes was not an experimental artefact.

After encountering cellular stress and the subsequent interaction between p-eIF2α and eIF2Bα, a subsequent alteration in conformation ensues. This conformational transition intricately dampens the catalytic activity of eIF2B, thereby leading to a reduction in TCs levels. As a consequence of this mechanism, global protein synthesis encounters inhibition, which in turn impacts the translation of mRNAs specifically linked to stress responses (Kashiwagi *et al*., 2021; Zyryanova *et al*., 2021) (**Figure 1.5**). Alterations within the yeast eIF2Bα (Gcn3p), triggered translation or derepression of GCN4, thought to be due to curtailed GEF activity that imitated the binding interaction between eIF2B and p-eIF2α (Hannig *et al*., 1990). This condition mirrors the scenario that typically arises when the cell is subjected to stress.

VWMD is a disorder which is caused by mutations in all five eIF2B subunits, which will be expanded on in **1.6.1**. Only a minimal count of mutations are detected within eIF2Bα, constituting a mere fraction of ≤ 1 % of VWMD patients (Pronk *et al*., 2006). This observation potentially serves as compelling evidence regarding the indispensability of this subunit in orchestrating other functions that remain veiled in the realm of the undiscovered.

eIF2Bα VWMD mutations are thought to have an impact on eIF2B complex structure and sensing of stress. Interestingly, in yeast models eIF2Bα regulatory variants, general control nonderepressible (Gcn-) mutations, demonstrated a dispersed pattern of eIF2B bodies throughout the cytoplasm similar to that observed in eIF2Bα null strains. On the other hand, the catalytic mutants, denoted as general control derepressible (Gcd-) mutations, exhibited the formation of distinct microbodies (Norris *et al*., 2021). eIF2Bα^{N208V} mutation, which is present in a region that binds to p-eIF2α, displayed increased GEF activity, and eIF2Bα^{V183F}, was shown to prevent eIF2Bα homodimerisation and subsequently resulted in decreased GEF activity (Wortham *et al*., 2014; Wortham & Proud, 2015).

In yeast, insect and mammalian models, instances involving null or genetically altered eIF2Bα/Gcn3 strains have been studied, revealed that cellular growth remains unaltered (Elsby *et al*., 2011; Fabian *et al*., 1997; Kimball *et al*., 1998; Norris *et al*., 2021; Pavitt *et al*., 1997). However, eIF2Bα^{T41A} point mutation exhibited the capability to overcome the translation suppression triggered by amino acid deficiency. Notably, the absence of eIF2Bα or the introduction of

variants into mammalian cells effectively counteracts the outcomes of p-eIF2α, rendering normal cells susceptible to viral infection (Elsby *et al*., 2011).

As mentioned earlier, the hexameric regulatory core eIF2B$(\alpha\beta\delta)_2$ bears similarity to the hexameric core of archaeal ribose-1,5-bisphosphate isomerase (Kuhle *et al*., 2015; Nakamura *et al*., 2012). Recently, eIF2Bα has been found to bind to various sugar phosphate metabolites to conserved regions, possibly enhancing decamer formation (Hao *et al*., 2021). This eIF2Bα feature may also contribute to the eIF2B complex formation and eIF2B body localisation, which could have an implication of VWMD mutations.

Furthermore, eIF2Bα has been found to be associated with α_2A-, α_2B-, α_2C-, and β_2-adrenergic receptors, with eIF2Bα exhibiting co-localisation exclusively within regions of the plasma membrane that establish contact with the extracellular medium of human embryonic kidney 293 cells, alongside various receptors (Klein *et al*., 1997). Although subsequent investigations were not pursued, it remains plausible that eIF2Bα might augment receptor-mediated signalling by impeding established receptor desensitization mechanisms. Alternatively, the interaction between this protein and receptors could potentially contribute to an additional layer of translational regulation.

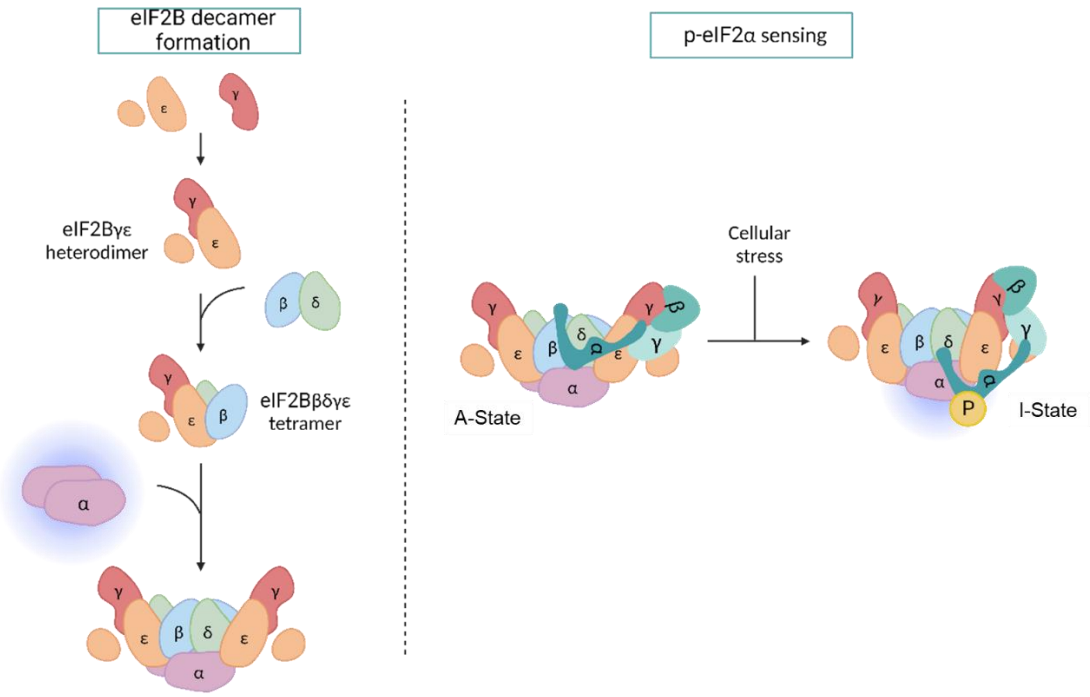

Figure 1.5. eIF2Bα known functions.

eIF2Bα has two main known functions. (Left panel) eIF2Bα participates in the final stage of the eIF2B decameric structure formation, by binding two eIF2Bβγδε tetramers together, thus stabilising the eIF2B complex and perhaps facilitating eIF2B body formation. (Right panel) Under normal conditions, eIF2α primarily binds to eIF2Bβ and eIF2Bδ in the regulatory pocket of the eIF2B complex in its A-state (active state). Under the presence of stress, eIF2•eIF2B complex undergoes structural modifications, and p-eIF2α interacts with eIF2Bδ and eIF2Bα, in its I-state (inhibited state). Image designed in BioRender.

1.4.4. ISRIB

Recently, the compound ISR inhibitor (ISRIB) was pinpointed through a cell-based screening designed to identify inhibitors of PERK activity (Sidrauski *et al*., 2013). ISRIB exhibits the remarkable ability to reverse the translational repression triggered by phosphorylated eIF2α (Halliday *et al*., 2015; Sidrauski *et al*., 2013, 2015; Zyryanova *et al*., 2021). This action is achieved by restoring eIF2B activity (Sekine *et al*., 2015; Zyryanova *et al*., 2021). ISRIB's mechanism of action was found to be centred around its capacity to stabilize the eIF2B decamer, as evidenced by size-exclusion chromatography studies (Sekine *et al*., 2015). ISRIB's interaction with the eIF2B complex was found to engage identical residues of opposing eIF2Bβδ dimers, effectively occupying a symmetrical interface pocket (**Figure 1.6**). This unique binding arrangement leads to the dimerization of two eIF2Bβδγε tetramers into eIF2B$(\beta\delta\gamma\varepsilon)_2$ octamers, facilitating the subsequent assembly of eIF2Bα_2 dimers to form the complete eIF2B decamers (Schoof *et al*., 2021; Tsai *et al*., 2018; Zyryanova *et al*., 2018). The introduction of ISRIB to eIF2B decamers has been shown to inhibit the binding of two p-eIF2α substrates (Zyryanova *et al*., 2021). As the p-eIF2α•eIF2B•p-eIF2α complex displays an altered ISRIB-binding pocket structure, the presence of ISRIB discourages the assembly of the eIF2B complex with two p-eIF2α substrates, while favouring all other potential states, each characterised by partial or complete catalytic activity (Zyryanova *et al*., 2021). Nonetheless, the effectiveness of ISRIB seems to be contingent on the concentrations of p-eIF2α, as elevated levels can supersede the equilibrium achieved by ISRIB in regulating the interaction between eIF2 and eIF2B (Anand & Walter, 2020; Hanson *et al*., 2023; Hodgson *et al*., 2019; Rabouw *et al*., 2019; Zyryanova *et al*., 2021).

Moreover, in the absence of eIF2Bα, ISRIB retains its ability to facilitate the assembly of eIF2B$(\beta\delta\gamma\varepsilon)_2$ octamers (Schoof *et al*., 2021), thereby exhibiting analogous functional outcomes to those attributed to eIF2Bα (**Figure 1.6**).

Hence, ISRIB could potentially exert a potent impact on eIF2Bα mutations that disrupt the stability of eIF2B assembly. Furthermore, mutations located beyond the ISRIB binding site, resulting in impaired GEF activity, might also find solution through ISRIB's capacity to promote the formation of decameric complexes. VWMD mutations showing resistance to ISRIB effects might be those directly influencing ISRIB binding or significantly hampering dimerization or eIF2 binding.

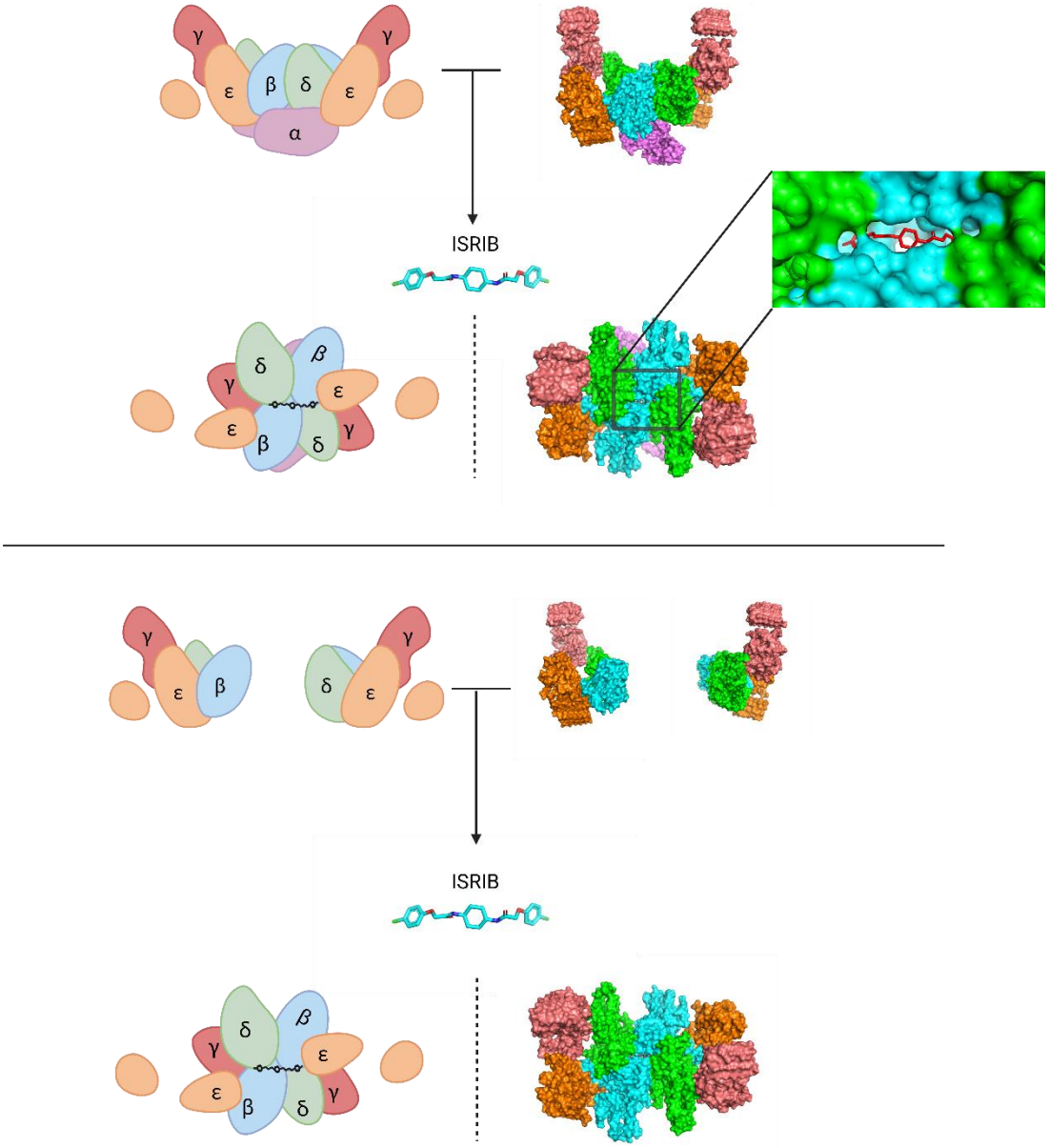

Figure 1.6. ISRIB stabilizes the eIF2B decamer and eIF2B octamer structure.

ISRIB binds to the eIF2Bβ and eIF2Bδ interface of the eIF2B structure, stabilising the eIF2B decamer (top panel). ISRIB is also capable of joining two eIF2B tetramers, forming eIF2B octamers, without the presence of eIF2Bα. (PDB: 6O81, in PyMOL). Image designed in BioRender.

1.5. Subcellular organisation of translation

Following the export of a newly synthesized mRNA to the cytosol, the cell needs to ensure the precise transport to specific intracellular locations before translation initiation occurs. Thus, organisms exhibit the ability to localise mRNAs within subcellular compartments, strategically establishing translation hotspots that grant cells with the exceptional capacity to fine-tune gene expression in distinct locales. When the cellular environment encounters stress, an interaction between 4E-BPs and/or eIF2α kinases leads to the inhibition of protein synthesis, triggering the translocation of transcripts to distinct cytoplasmic granules. Notably, SGs and processing bodies (P-bodies) emerge as potential repositories for specific subsets of mRNA transcripts, involved in either storage or degradation processes, respectively. The discerning localisation of the translation initiation factor, eIF2B, to specific cytoplasmic foci further exemplifies the elaborate control and regulation governing its function. In unison, these observations collectively unveil the highly organized panorama of translation processes within the cellular cytoplasm, both during periods of steady state growth and, more importantly, during episodes of regulatory adaptation in response to cellular stress.

1.5.1. eIF2B localisation

The precise subcellular localisation of proteins plays a pivotal role in determining their functional impact, and cells have evolved intricate mechanisms to finely control protein localisation, thereby exerting precise regulation over various biological processes. eIF2B plays a dual role in translation initiation, not only acting as a crucial recycling factor for eIF2-GDP, but also serving as a key regulatory hub, particularly in response to cellular stress. Using the *Saccharomyces cerevisiae* model, Campbell *et al.,* observed a specific cytoplasmic focus known as the eIF2B body, which serves as a distinctive site of eIF2B localisation (Campbell *et al*., 2005). Under normal conditions, the G-protein eIF2 exhibited co-localisation with eIF2B bodies with dynamic behaviour. The substrate was observed to undergo shuttling within eIF2B bodies, and this movement correlated with the cellular level of eIF2B GEF activity, which was able to be measured through FRAP analysis. Consequently, eIF2B bodies were identified as localised active sites facilitating GDP-GTP exchange processes. eIF2B bodies were not found to be sites for TC, MFC, or 43S PIC, as eIF2B bodies did not co-localise with Met-tRNA$_i$ or other translation initiation factor

(Campbell *et al*., 2005). Whether the eIF2B body contains mRNA transcripts is unknown.

The intriguing aspect of yeast eIF2B bodies lies in their filamentous structure. It is speculated that this structure is energy-independent, not relying on ATP for its formation. Instead, filamentation is induced by cytosolic acidification and spontaneously occurs in cells experiencing starvation conditions (Nüske *et al*., 2020; Taylor *et al*., 2010). Additionally, it is thought that the localisation of eIF2B in specific compartments during energy depletion may serve as a sophisticated mechanism aimed at safeguarding the enzyme from potential denaturation, disassembly, or degradation within the assembly. Moreover, this compartmentalization could play a role in the fine-tuning of eIF2B's enzymatic activity, potentially contributing to its downregulation under conditions of limited energy availability (Marini *et al*., 2020; Moon & Parker, 2018; Petrovska *et al*., 2014). By sequestering eIF2B in these specialized compartments, the cell may strategically control its function and protect it from potential detrimental effects, ensuring its availability for translation initiation when energy resources are restored.

Moreover, these dynamic bodies were observed to exhibit motility throughout the cytoplasm, indicating their active involvement in regulating effective translation initiation. Notably, when the movement of eIF2B bodies was inhibited, there was a corresponding inhibition of translation initiation (Taylor *et al*., 2010), underscoring the crucial role these motile structures play in this fundamental cellular process.

However, localisation of eIF2B bodies has had contradictory results. Studies have suggested that eIF2B bodies are absent in *Saccharomyces cerevisiae* during regular growth conditions, only manifesting under conditions of glucose limitation (Moon & Parker, 2018). Paradoxically, another study points out that eIF2B bodies are not induced during acute glucose starvation, but rather during energy depletion, specifically in the stationary phase. This implies that eIF2B bodies serve as inhibition of activity in response to energy depletion (Marini *et al*., 2020; Nüske *et al*., 2020). While others have found that eIF2B localisation is present in steady-state conditions in yeast (Campbell *et al*., 2005; Norris *et al*., 2021) and mammalian cells (Hanson *et al*., 2023; Hodgson *et al*., 2019). It is of note that Norris *et al.,* found that eIF2B localisation to bodies in *Saccharomyces cerevisiae* varies based on the specific strain under normal growth conditions, however

when subjected to nutritional stress, similar trends in terms of eIF2B body responses are observed across different strains (Norris *et al*., 2021). Furthermore, it raises intriguing speculation to consider that the observed differences in eIF2B body formation among the various yeast strains could potentially stem from variations in the molar concentrations of eIF2 and eIF2B protein complexes (von der Haar & McCarthy, 2002). Such disparities in protein concentrations may exert an influence on the dynamic interplay that governs the assembly and regulation of eIF2B bodies.

One prominent distinction between yeast and mammalian eIF2B localisation lies in their respective compositions. In yeast, the eIF2B body appears as a singular aggregate encompassing all five subunits of eIF2B, strongly indicating the presence of decameric complexes within the eIF2B body. This notion gains further support from the observation that deletion of eIF2Bα results in the dispersal of eIF2B bodies, suggesting that the stable formation of eIF2B bodies in yeast hinges upon the decameric conformation of eIF2B (Norris *et al*., 2021). Furthermore, Marini *et al.,* have proposed that eIF2B bodies in yeast consist of repeated decameric units, arranged in a stacked fashion facilitated by contacts between eIF2Bε subunits of adjacent decamers (Marini *et al*., 2020).

Mammalian cells, in contrast to yeast, exhibit a diverse array of eIF2B bodies, which display variations in size, correlating with its eIF2B subunit composition. Notably, larger eIF2B bodies demonstrate co-localisation of all five eIF2B subunits, suggesting that these bodies contain decameric complexes. The co-localisation of regulatory eIF2B subunits with smaller eIF2B bodies was found to be infrequent or minimal, being mainly composed of eIF2Bγ and eIF2Bε (Hanson *et al*., 2023; Hodgson *et al*., 2019). Previous studies employing native mass spectrometry (MS) have demonstrated the existence of subcomplexes of eIF2B in mammalian cells (Wortham *et al*., 2014), with eIF2B(βδγε) tetramers, eIF2B(γε) heterodimers and eIF2B(α_2) homodimers being identified. Thus, the formation of smaller eIF2B bodies seems to involve stable eIF2B subcomplexes. The organization of eIF2B into subcomplexes within these smaller bodies could provide a means for localised and specialized regulation of translation in response to different stress stimuli. This spatial compartmentalization of eIF2B subunits may facilitate their interaction with specific binding partners or substrates, influencing the efficiency and specificity of translation initiation.

Additionally, the activity of bodies can be modulated through stress induction. Upon acute activation of the ISR, there is an observed increase in the association of p-eIF2α with large bodies, indicating a potential impairment of the GEF activity of eIF2B. Conversely, the movement of eIF2 through smaller bodies was found to be enhanced upon ISR stimulation (Hanson *et al*., 2023; Hodgson *et al*., 2019) (**Figure 1.7**). This implies that the smaller bodies are actively involved in the regulation of translation initiation during cellular stress, and their dynamic movement allows for efficient recycling of eIF2-GDP, facilitating the re-initiation of translation following stress alleviation.

In yeast, the eIF2B body accounts for approximately 40 % of the total eIF2B in the cell, indicating that GDP and GTP exchange, as well as regulation, may also occur in other regions of the cytoplasm (Campbell *et al*., 2005). This suggests that the eIF2B body may serve as a specialized site for specific functions, while other regions of the cytoplasm may participate in more general translation initiation processes.

Furthermore, the presence and distribution of eIF2B bodies appear to be cell-type specific in mammalian models, with different cell lines exhibiting varying percentages of cells with eIF2B bodies. For instance, neuronal cell lines approximately display 20 % of cells with eIF2B bodies, while astrocytic cell lines have approximately 54 % of cells with eIF2B bodies (Hanson *et al*., 2023).

Interestingly, some cells may not show visibly observable eIF2B bodies under microscopic examination, which could imply that eIF2B function is independent of highly assembled states. However, eIF2B complex and subcomplex composition has been shown to alter regulation and activity of this protein, as stated above. It is plausible that eIF2B bodies represent localised hubs of high translation initiation rates for local translation, or they may be indicative of cells that are undergoing elevated translation initiation rates, possibly linked to their cell cycle or other cellular processes, and it could also have implications for diseased pathology in which eIF2B structure and/or body formation is impacted.

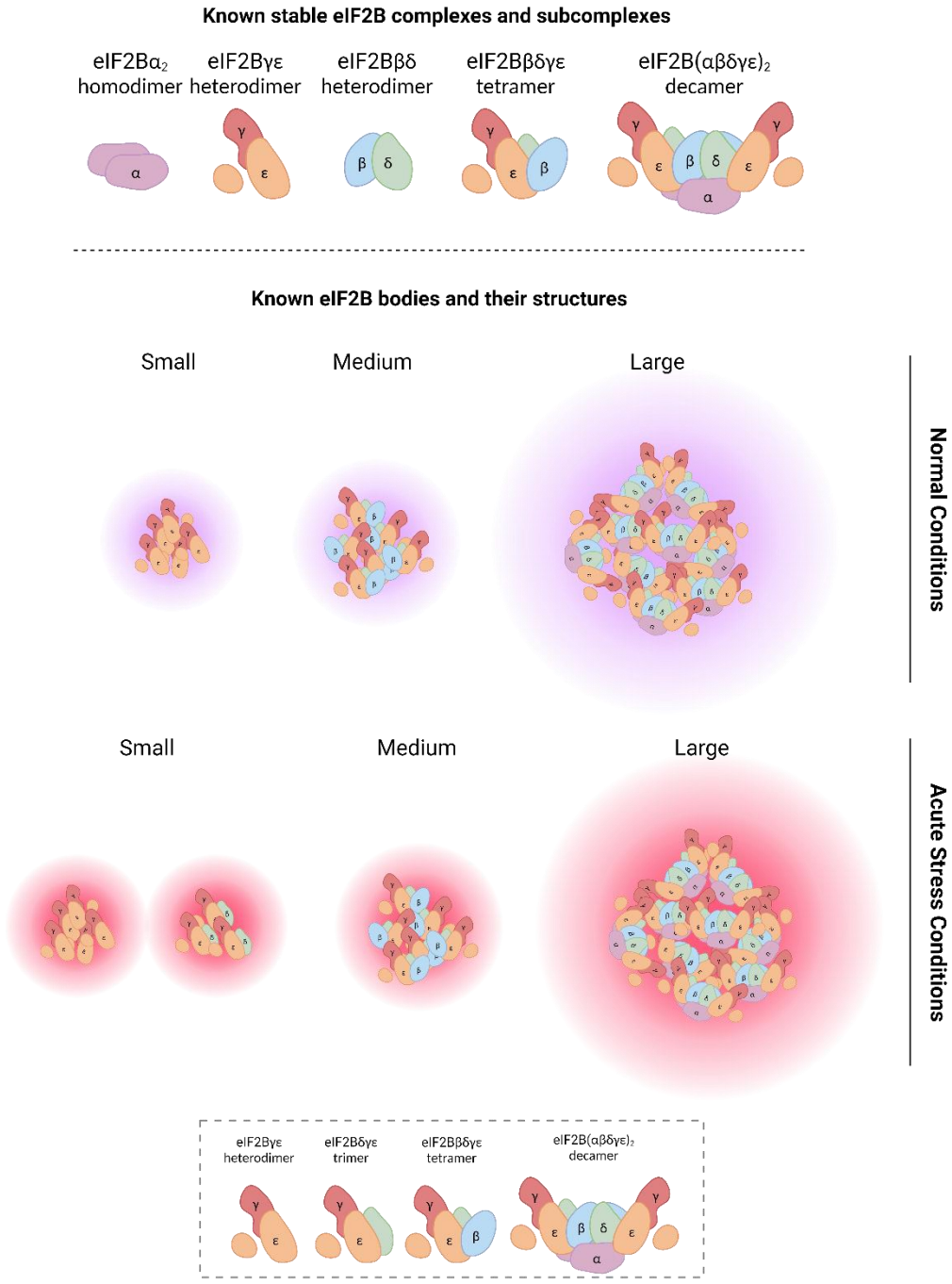

Figure 1.7. eIF2B stable structures and bodies.

eIF2B in its native form assembles to eIF2B decamers, but it is also known to form stable eIF2B subcomplexes – eIF2Bα_2 homodimers, eIF2Bγε heterodimers, eIF2Bβδ heterodimers, eIF2Bβδγε tetramers and eIF2B$(\alpha\beta\gamma\delta\varepsilon)_2$ decamers. In a proposed model by Hodgson *et al.,* (2019) and Hanson *et al.,* (2023), eIF2B subcomplexes localise to different sized eIF2B bodies – small and medium bodies are mainly comprised of eIF2Bγε heterodimers and eIF2Bβδγε tetramers; large bodies are mainly comprised of eIF2B$(\alpha\beta\gamma\delta\varepsilon)_2$ decamers. Following stress induction, remodelling of these bodies occurs, with an increase of the eIF2Bδ subunit presence in small eIF2B bodies – small and medium bodies mainly composed of eIF2Bγε heterodimers, eIF2Bδγε trimers, and eIF2Bβδγε tetramers; large bodies mainly composed of eIF2B$(\alpha\beta\gamma\delta\varepsilon)_2$ decamers. Image designed in BioRender.

1.5.2. Formation of stress granules

An assortment of non-membrane-bound cellular compartments – RNP granule – contain concentrations of protein and RNA. These RNP granules, known for their dynamic nature, rely heavily on RNA for their assembly (Tauber *et al*., 2020) (**Figure 1.8**). The repression of translation initiation conserves precious energy and vital nutrients that are extensively consumed during the intricate process of protein synthesis. Moreover, this deliberate reduction in general translation grants cells the opportunity to strategically reconfigure their gene expression and signalling pathways, thus facilitating an optimised stress alleviation response. SGs are phase-separated, membraneless RNP assemblies, and have been elucidated as intricate triage centres for mRNA during periods of cellular stress. In this process, SGs play a pivotal role in sorting and managing mRNA transcripts, executing one of three essential functions: (1) storing translationally silenced mRNA to conserve cellular resources, (2) transporting mRNA transcripts to P-bodies for degradation, or (3) facilitating the transfer of mRNA back into polysomes, thus reinitiating translation when conditions permit (Bley *et al*., 2015; Campos-Melo *et al*., 2021; Kedersha *et al*., 2013).

Activation of the ISR, which hinges on the phosphorylation of eIF2α, impedes the formation of eIF2-GTP-Met-tRNA$_i$ TCs, thereby inhibiting ribosome loading onto mRNA (detailed in **section 1.3**) (Jennings *et al*., 2017). Consequently, polysomes, complexes of actively translating ribosomes along a mRNA, undergo widespread disassembly, releasing a substantial pool of unbound mRNAs into the cytosol. This dynamic cytosolic pool of mRNAs plays a pivotal role in the formation and stability of SGs. The incorporation of these mRNAs into SGs is a tightly regulated and indispensable process essential for SG assembly and function (Anderson & Kedersha, 2006). Perturbing the equilibrium of mRNA flux by stabilizing polysomes with chemicals like cycloheximide (CHX) or emetine disrupts the formation of SGs induced by stressors that activate the ISR (Hofmann *et al*., 2021).

Inhibition of the eIF4F complex presents an alternative strategy to impede translation initiation and instigate the formation of SGs. Specific chemicals, such as hippuristanol, can obstruct eIF4A's RNA-binding ability, while others like pateamine A and rocaglamide A (RocA) can induce clamping onto RNA and deplete eIF4A from the eIF4F complex, leading to SG formation through an eIF2α-independent route (Dang *et al*., 2006; Emara *et al*., 2010, 2012; Shen &

Pelletier, 2020). Hydrogen peroxide (H_2O_2) generates reactive oxygen species (ROS) in a p-eIF2α independent manner, via 4EBP1 inhibition. This then leads to a decrease dissociation of eIF4E inhibiting eIF4F complex assembly (Emara *et al*., 2012) (**Figure 1.9**).

Additionally, certain stressors can induce SG assembly by directly altering intracellular conditions to promote phase separation. For instance, molecular crowding triggered by hyperosmotic stress leads to the formation of SGs that resist the influence of polysome-stabilizing agents (Aulas *et al*., 2017).

Hence, the formation of SGs can manifest as either dependent or independent of eIF2α phosphorylation, with distinct protein and mRNA compositions dictated by the specific stress condition. Notably, the presence of HSP27 exclusively characterises SGs induced by heat shock, while it remains absent in those prompted by sodium arsenite (SA) (Kedersha *et al*., 1999). Additionally, HSP90 mRNA transcripts are deliberately excluded from SA-induced SGs, emphasizing the intricate selectivity and regulation of SG composition (Stöhr *et al*., 2006). However, overall SGs exist in equilibrium with polysomes. The incorporation of puromycin intensifies SG formation by triggering the premature disassembly of polysomes, whereas the application of CHX obstructs elongation and prevents polysome disassembly, effectively inhibiting SG formation and provoking the disintegration of pre-existing SGs (Mokas *et al*., 2009).

The formation of SGs is regulated by liquid-liquid phase separation (LLPS), a thermodynamically driven and reversible process that involves the de-mixing of two liquid phases facilitated by intricate protein-protein, protein-RNA, and RNA-RNA interactions (Mathieu *et al*., 2020). In this dynamic and finely process, SGs emerge as distinct liquid-like compartments within the cellular cytoplasm, allowing for the concentration and sequestration of specific components in response to cellular stress. SGs exhibit a rich diversity in their proteome composition. Extensive proteomic analysis of the stable substructures, known as "cores," present within SGs reveals that approximately 50 % of their constituents belong to a specific subset of RNA binding proteins (Jain *et al*., 2016). It is of note that, more than 80 % of the SG proteome comprises proteins with well-established RNA-binding capabilities (Youn *et al*., 2019). Homotypic protein-protein interactions facilitated by the nuclear transport factor-like domain of essential proteins Ras-GTPase-activating protein (SH3 domain) binding protein (G3BP) 1 and 2 play a critical role in driving SG formation (Sanders *et al*., 2020;

P. Yang *et al*., 2020). Accurate levels of G3BP1 are essential for efficient SG assembly, and disruptions or mutations in its upstream regulators have been shown to impair SG formation (Somasekharan *et al*., 2015). Moreover, protein-RNA interactions are indispensable for SG formation. For instance, the removal of the RNA-binding domain of G3BP1 completely abolishes SG assembly (Yang *et al*., 2020). The dynamic exchange of SG components with the cytosol, as observed through fluorescence recovery after photobleaching (FRAP), relies on the transient nature of these weak interactions. Additionally, cores or sub-compartments, which likely result from the affinities of specific interaction networks have been found in SGs, with UBAP2L, G3BP1, and IMP1, localising to distinct subregions within SGs, indicating spatial organization (Cirillo *et al*., 2020; Niewidok *et al*., 2018). The central core structures of SGs are rapidly enveloped by a highly dynamic shell, which arises from interactions involving the intrinsically disordered regions of RNA binding proteins (Jain *et al*., 2016). This outer shell contributes to the fluidity and adaptability of SGs, enabling them to accommodate a diverse array of RNA species and protein components essential for their functional role in cellular stress response and translational regulation. Indeed, research has revealed that SG components display rapid shuttling within these granules, and the dynamic shell is believed to serve as a scaffold facilitating this continuous exchange. Various protein and RNA remodelling complexes are thought to play a pivotal role in orchestrating the transition of components between the central core and the surrounding shell of SGs (Buchan, 2014; Jain *et al*., 2016). Hence, SGs exhibit considerable diversity in their composition, reflecting their dynamic nature. SGs appear to be composed of stalled 48S complexes, encompassing mRNAs derived from disassembling polysomes. These 48S complexes consist of poly(A)+ RNA intricately bound to early initiation factors (including eIF4E, eIF3, eIF4A, and eIFG) and small ribosomal subunits, while the large ribosomal subunits are mostly absent from these granules. Some mRNAs may be directed towards decay pathways (Anderson & Kedersha, 2006; Jain *et al*., 2016). However, reports have showcased that these assemblies may not only provide hubs of non-translating mRNPs, but that mRNA translation might occur in these structures. Firstly, L5 and L37 ribosomal proteins showed signal overlapping with SGs (Kimball *et al*., 2003) and that 60S subunits have been confirmed to gather in SGs (Seguin *et al*., 2014). More interestingly, mRNAs localised to SGs have been shown to be capable of undergoing translation, with

the entire translation cycle taking place on transcripts localised to SGs. Additionally, dynamic transitions of translating mRNAs between the cytosol and SGs without altering their translational status was observed (Mateju *et al*., 2020). It has been observed that the downregulation of eIF2B activity leads to the recruitment of specific transcripts to SGs, facilitated by the action of crucial proteins like T-cell restricted intracellular antigen-1 and the TIA-1 related protein (Gilks *et al*., 2004; Kedersha *et al*., 1999). This intriguing connection highlights the potential influence of eIF2B on SG formation and mRNA sorting. Furthermore, eIF2Bε has been observed to co-localise with SGs (Kimball *et al*., 2003). However, it is essential to acknowledge that findings regarding eIF2Bε localisation and its role in SGs have been met with some inconsistencies in the literature (Hodgson *et al*., 2019; Moon & Parker, 2018). Functional RNAi screen has highlighted that eIF2Bα has an essential role in SG formation (Ohn *et al*., 2008), likely due to its p-eIF2α dependent sensing of stress. Nonetheless, exploring the subcellular localisation of these two structures may shed light on the complex regulation of translation and stress response mechanisms in the cell.

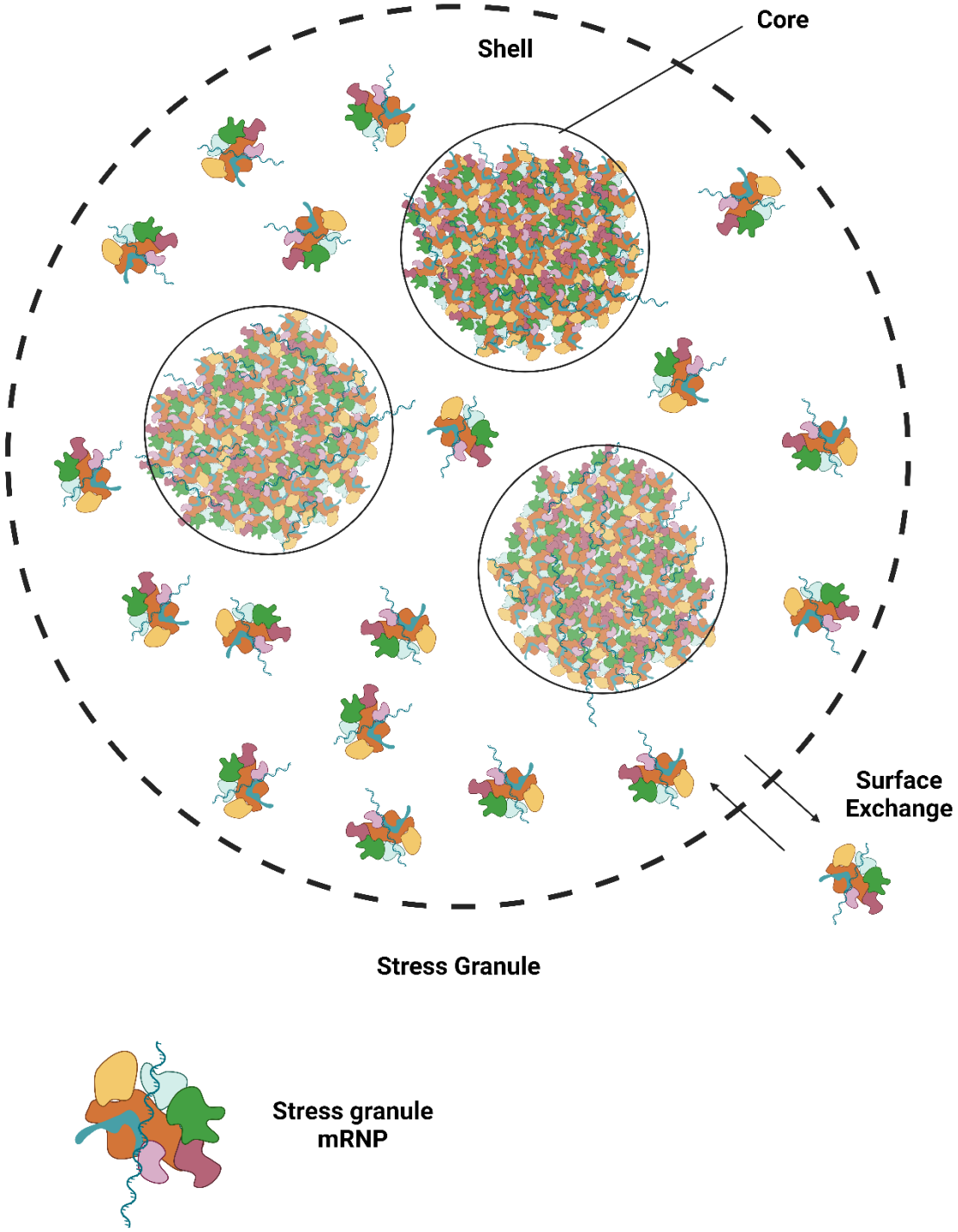

Figure 1.8. Formation of SG.

SG are multimolecular cytoplasmic foci that form following cellular stress. SGs contain an outer shell and core structures, with the composition of these assemblies being dynamic through surface exchange. SG largely contain poly(A)$^+$ mRNAs, 40S ribosomal subunits (orange components), eukaryotic translation initiation factors (dark and light blue components) and other proteins (green, yellow, dark and light purple components), forming SGs mRNP complexes. Image designed in BioRender.

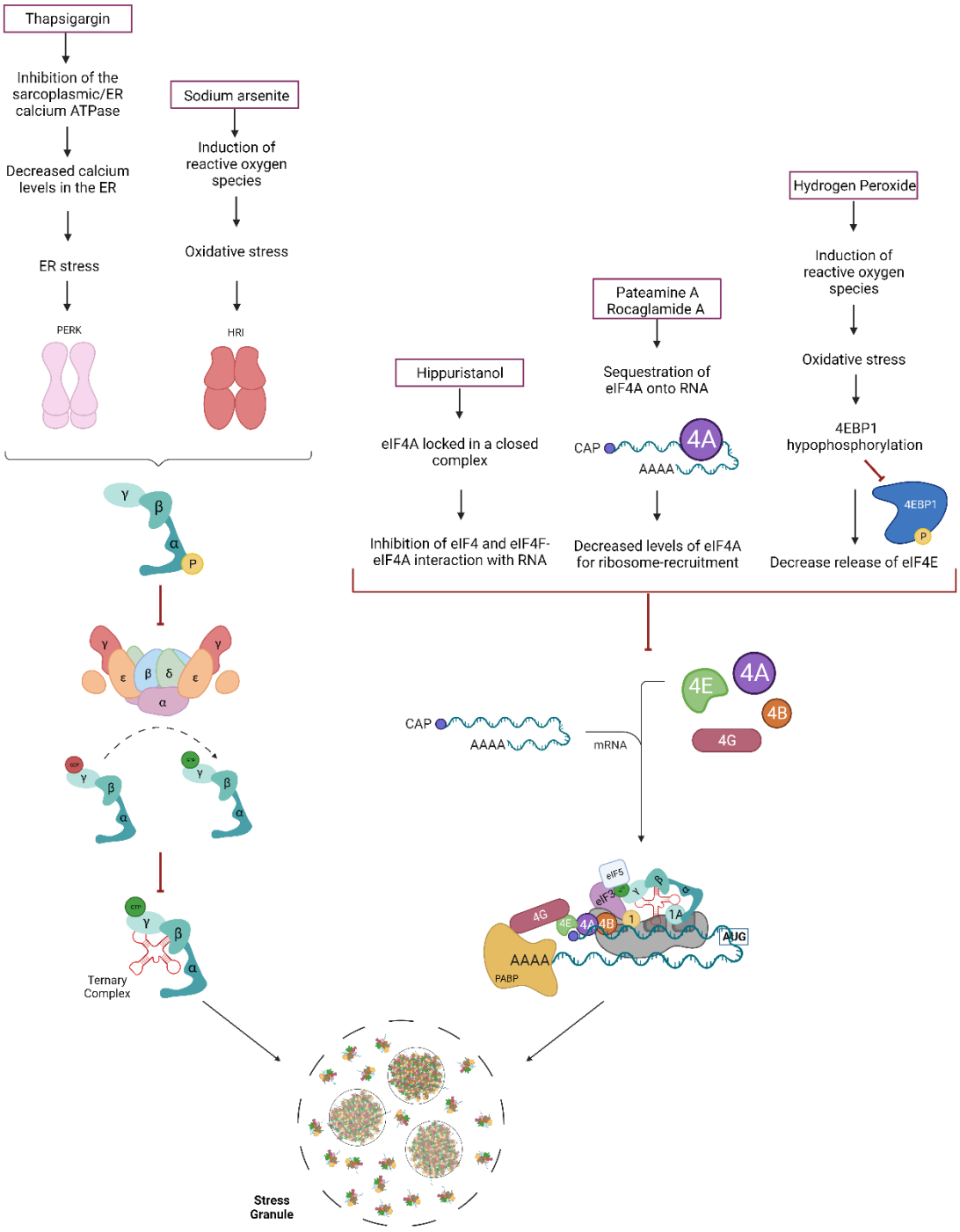

Figure 1.9. Chemical induction of SGs.

Several compounds are capable of modulating translation initiation leading to the formation of SGs. Thapsigargin (Tg) and SA both lead to the phosphorylation of eIF2α through the activation of its kinases, decreasing levels TC. Tg inhibits the sarcoplasmic/ER Ca^{2+} ATPase pump, leading to the increase of intracellular Ca^{2+} levels and depletion of Ca^{2+} in the ER, triggering ER stress activating the PERK kinase. SA causes the formation of ROS leading to oxidative stress. This in turn, leads to the activation of the HRI kinase, which phosphorylates eIF2α. Hippuristanol, pateamine A, RocA and H_2O_2 impact the eIF4F complex formation, which then leads to the inhibition of the activity of 43S PIC, leading to a decrease of protein synthesis. Hippuristanol inhibits the RNA-stimulated ATPase activity of eIF4A, leaving this protein a closed structured

complex, inhibiting its interaction with RNA and the formation of eIF4F complex. Pateamine A and RocA force the interaction between eIF4A and RNA, decreasing levels of available eIF4A to participate in the formation of the eIF4F complex. H_2O_2 also induced the formation of ROS, but the oxidative generated from this compound acts on the mTOR pathway inhibiting the phosphorylation of 4EBP1. The phosphorylation of this protein is required for eIF4E release, thus H_2O_2 subsequently inhibits the formation of eIF4F complex through eIF4E. Image designed in BioRender.

1.5.3. Formation of P-bodies

P-bodies are highly conserved cytoplasmic RNA granules believed to play pivotal roles in the storage and degradation of translationally-repressed mRNAs during cellular stress conditions, albeit phosphorylation of eIF2α is not essential for their formation (Hubstenberger *et al*., 2017; Luo *et al*., 2018). While the complete architecture of P-bodies remains to be fully unveiled, work in yeast models they feature a core ensemble of essential proteins associated with mRNA decay, including decapping-promoting factors such as Lsm1-7p (Tharun & Parker, 2001), the decapping complex Dcp1p/Dcp2p (van Dijk, 2002), and the 5'-3' exoribonuclease Xrn2p (Nagarajan *et al*., 2013). P-bodies were initially hypothesized as sites of mRNA degradation (Kedersha *et al*., 2005; Sheth & Parker, 2003). However, more recent research has challenged this notion, revealing that mRNA molecules present in P-bodies can re-enter the pool of actively translating mRNAs (Brengues *et al*., 2005) and that mRNA decay can proceed independently of P-bodies (Decker *et al*., 2007; Eulalio *et al*., 2007). Consequently, the precise role of P-bodies remains enigmatic, though current hypotheses propose their function as storage granules (Bloch *et al*., 2023; Luo *et al*., 2018). The intricate interchange between SGs and P-bodies, and their dynamic involvement in mRNA fate, adds complexity to the understanding of mRNA regulation and localisation during cellular stress responses.

1.6. Translation dysregulation and disease

1.6.1. VWM

Mutations in all five eIF2B subunits can results in a severe neurological disorder known as VWMD or childhood ataxia with central nervous system hypomyelination (Hamilton *et al*., 2018). Despite its broad influence of eIF2B on translation regulation, glial cells exhibit a particular vulnerability in the

pathophysiology of VWMD (Dooves *et al*., 2016; Herrero *et al*., 2021; Man *et al*., 2023).

VWMD stands prominently as one of the most prevalent inherited leukodystrophies, representing a class of disorders characterised by abnormalities in the white matter of the central nervous system (CNS). This condition predominantly manifests in children, either as a congenital form or an early to late childhood-onset type, with reported incidence rates ranging from 1.2 to 3.01 cases per 100,000 individuals per year (Bugiani *et al*., 2018; Deginet *et al*., 2021). VWMD presents itself as a chronic progressive disorder wherein patients undergo a deterioration of neurological functions that follows episodes of acute physiological distress (Bugiani *et al*., 2018; Pronk *et al*., 2006; van der Knaap *et al*., 2006; Vermeulen *et al*., 2005). The interaction between these acute triggers and the exacerbation of VWMD's clinical course lends complexity to the understanding of the disease's pathophysiology and progression.

Phenotypically, the manifestations of symptoms and disease progression in VWMD exhibit profound variability, likely stemming from the intricate genetic complexity of the condition (Hamilton *et al*., 2018; Slynko *et al*., 2021). Presently, there are approximately 200 identified mutations distributed across the five eIF2B subunits, established as causative factors of VWMD, as documented in the Human Gene Mutation Database.

The fundamental significance of eIF2B in regulating the ISR has prompted a multitude of research endeavours aimed at unravelling its complex engagement in modulating protein synthesis and its ability to react to cellular stress within the brain tissue. Earlier investigations have emphasized the disruptive consequences arising from mutations impacting eIF2B genes, leading to a highly intricate dysregulation of this protein. This disruption significantly impairs the myelination process, through exerting a profound influence on oligodendrocytes and astrocytes, while curiously exhibiting a contrasting tendency to spare neurons from the deleterious effects (Herrero *et al*., 2021; Man *et al*., 2023). The precise reasons for the tissue-specific vulnerability observed in VWMD remain elusive. Furthermore, the genotype-phenotype correlation in VWMD is poor (Liu *et al*., 2011; van der Lei *et al*., 2010), implying that eIF2B harbours puzzling functional characteristics yet to be unveiled. A cure for VWMD remains elusive and understanding the common pathophysiological mechanisms underlying the vast array of causative mutations continues to present significant challenges.

1.6.1.1. Clinical diagnosis and progression

VWMD presents a vast clinical spectrum, encompassing antenatal, early infantile and early childhood onset cases with poor outcomes (van der Knaap *et al*., 2022), as well as adult-onset scenarios with a more gradual progression, with the age at which symptoms manifest playing a pivotal role in predicting the disease's course (Hamilton *et al*., 2018). The archetypal and prevalent manifestation of the disease arises during early childhood, typically between the ages of 2 to 6 years, and is characterised by chronic progressive cerebellar ataxia, and accompanied by epileptic episodes, with relatively less pronounced spasticity. Additionally, mild cognitive decline is also observed (Pronk *et al*., 2006; van der Knaap *et al*., 2006). However, in the context of early-onset and severe variants of this disease, a striking systemic multiorgan involvement becomes evident, giving rise to a myriad of serious complications encompassing encephalopathy, hepatosplenomegaly, pancreatitis, renal dysplasia, cataracts, and impaired growth (Hamilton *et al*., 2018; van der Knaap *et al*., 2006). The prognosis, in general, is grave, as the majority of patients succumb to the condition within a few years. Nonetheless, the disease's course exhibits remarkable heterogeneity, with certain individuals facing an even more accelerated decline, leading to death within several months, while others survive for several decades (van der Knaap *et al*., 2006).

Late-onset VWMD, with the latest reported onset of disease to be 55 years, has been observed in approximately 15 % of all documented cases (Gascon-Bayarri *et al*., 2009; La Piana *et al*., 2012). In adulthood, the spectrum of symptoms encompasses complex migraines, seizures, spasticity, and cerebellar ataxia (van der Knaap *et al*., 2006), with some studies implicating psychiatric manifestations (Accogli *et al*., 2019) and dementia (Prass *et al*., 2001).

Remarkably, individuals affected by VWMD typically demonstrate normal early development, only to undergo neurological deterioration triggered by stress-induced episodes of fast decline. These stressors include fever, head trauma and acute fright. Amidst these episodes, the patient experiences a swift and pronounced deterioration in motor function, with subsequent recovery tending to be partial and frequently insufficient to restore pre-episode levels of functionality (Bugiani *et al*., 2011, 2018; van der Knaap *et al*., 2006; Vermeulen *et al*., 2005). Despite comparable case frequencies between males and females, there exists an intriguing sexual dimorphism in the pathology, with females exhibiting a propensity for milder disease progression compared to their male counterparts

(van der Lei *et al*., 2010). Irrespective of the severity of the disorder, females affected by VWMD may encounter premature ovarian insufficiency, although primary ovarian dysfunction, referred to as ovarioleukodystrophy, is an infrequent association (Fogli *et al*., 2003). The vast array of clinical presentations observed in VWMD poses a significant diagnostic challenge.

The diagnosis of VWMD primarily hinges on the analysis of clinical manifestations and the recognition of pathognomonic patterns revealed by mass resonance imaging (MRI). Subsequently, to establish definitive confirmation, genotyping of potential VWMD patients becomes imperative, as it allows for the precise identification of eIF2B mutations, thus unveiling the underlying genetic basis of the disorder. MRI scans consistently reveal a distinctive pattern, characterised by widespread symmetric anomalies in the cerebral white matter, where degenerative cystic transformations ensue, leading to the replacement of the once functional white matter by fluid-filled regions (Fogli *et al*., 2004; Hanefeld *et al*., 1993). This cascade of structural alterations in the brain's white matter landscape constitutes a critical hallmark of VWMD pathology.

Furthermore, the histopathological hallmarks of VWMD distinctly centre around macroglial cells - astrocytes and oligodendrocytes - where the maturation and functionality of astrocytes seem to play a key role in driving the pathology of oligodendrocytes and axonal abnormalities (Bugiani *et al*., 2018; Dooves *et al*., 2016; Klok *et al*., 2018). Notably, myelin abnormalities have been consistently observed in VWMD patients, exhibiting a spectrum from thin and dispersed sheaths to complete loss, and have been linked to consequent axonal atrophy and/or complete axonal loss (Brück *et al*., 2001; Klok *et al*., 2018). Within VWMD-affected cells, oligodendrocytes exhibit a particularly peculiar and aberrant finely vacuolar-like cytoplasmic morphology, small round nuclei, and fine chromatin, commonly referred to as "foamy" oligodendrocytes. Moreover, early-onset VWMD patients tend to display heightened pro-apoptotic markers in these cells (Francalanci *et al*., 2001; Van Haren *et al*., 2004). In VWMD astrocytes, histological analysis reveals dysmorphic characteristics with large blunt processes, indicative of reduced efficiency in astrogliosis (Dooves *et al*., 2016; Leferink *et al*., 2019). Notably, VWMD astrocytes exhibit an atypical splicing pattern of the glial fibrillary acidic protein (GFAP) isoform GFAPδ, favouring condensed filament networks linked to the presence of arrested immaturity (Huyghe *et al*., 2012; Kamphuis *et al*., 2012). In VWMD, cortical astrocytes

manifest distinct morphological alterations, demonstrating reduced structural complexity. These morphological characteristics suggest that these astrocytes display an immature phenotype and appear to be non-reactive, adding a compelling layer of complexity to the understanding of astrocytic involvement in the disease pathogenesis (Man *et al*., 2023). In VWMD patients, astrocyte dysfunction is the primarily driver of the pathogenesis, classifying the condition as one of the astrocytopathies. This dysfunctional astrocytic influence the impaired maturation of oligodendrocytes and ultimately disrupts the integrity of axonal structures (Bugiani *et al*., 2018; Klok *et al*., 2018), thus unravelling the cellular mechanisms at play in this neurological disorder.

1.6.1.2. Genotype-phenotype link and cellular pathogenesis

VWMD represents a condition of intricate genetic complexity, arising from autosomal recessive mutations predominantly of the missense type, which can manifest in either homozygous or heterozygous states (Nagdev *et al*., 2022). Frameshift and nonsense mutations, though less common (Li *et al*., 2004), carry a profound impact on the disease phenotype, being conspicuously absent in the homozygous state, likely due to their strong association with severe VWM phenotypes (Nagdev *et al*., 2022).

The most prevalent mutations in VWMD are observed in *EIF2B5*, scattered across the gene with a notable sparing of the 3' end, which encodes the crucial catalytic domain of eIF2B. It is hypothesized that mutations occurring in this essential region would likely lead to fatal outcomes. Furthermore, mutations impacting *EIF2B3* tend to cluster around regions sharing sequence homology with *EIF2B5*. A similar clustering pattern is also observed in mutations affecting the regulatory subunits, which display considerable sequence homology in their C-terminal domains. Notably, VWMD-linked mutations in *EIF2B1*, *EIF2B2*, and *EIF2B4* predominantly localise towards the 3' portion of these genes (Pronk *et al*., 2006; Scali *et al*., 2006; Zhang *et al*., 2015), potentially offering crucial insights into the functional significance of these genetic regions and their contribution to the disease phenotype (**Figure 1.10**).

Biochemical studies have been conducted to explore the functional repercussions of VWM mutations on eIF2B. These investigations delve into the intricate molecular interactions and dynamic processes that underlie the disease-causing mutations and their impact on the functionality of eIF2B. In these studies, eIF2B mutations have been shown to affect complex formation, eIF2 binding or

impact GEF activity (Fogli & Boespflug-Tanguy, 2006; Slynko *et al*., 2021). Of particular interest is the observation that the age of onset in VWMD seems to be associated with alterations in the GEF activity. Notably, adult-onset mutations manifest a relatively mild decrease in the GEF activity of eIF2B complexes, typically ranging from around 20 % to 40 %. Conversely, mutations reported in childhood-onset VWMD cases exhibit a more significant reduction in eIF2B activity, falling within the range of approximately 30 % to 80 % (Li *et al*., 2004; Matsukawa *et al*., 2011). This intriguing correlation potentially implies that a pronounced decrease in eIF2B activity might be linked to earlier ages of VWMD onset, hinting at the complex interplay between eIF2B function and disease manifestation in different age groups affected by VWMD. Nevertheless, certain VWMD mutations have shown no discernible effect on the *in vitro* biochemically characterised functions of eIF2B. Paradoxically, these mutations lead to some of the most severe manifestations of the disease (Liu *et al*., 2011; van der Lei *et al*., 2010), indicating that eIF2B harbours *in vivo* functions that are not entirely captured by the *in vitro* studies. This discrepancy highlights the existence of complex and context-dependent regulatory mechanisms governing eIF2B's roles within living organisms, which transcend the limitations of *in vitro* experimental settings.

Although the impact of VMWD mutations on eIF2B structure and function is diverse, one common consequence is the dysregulation of the ISR. In VWMD mouse model homozygous for eIF2Bε^{R191H} (corresponding to R195H in humans), as well as in samples obtained from VWMD patients, an elevation in the expression of the ATF4-driven transcriptome was found (Abbink *et al*., 2019; Wong *et al*., 2019). Despite eIF2B's role as a global regulator of protein synthesis, it exhibits selective vulnerability towards glial cells in the context of VWMD. Certain cell populations appear to be particularly susceptible to acute stress episodes in the presence of VWMD mutations. These cells exhibit a strikingly heightened stress response, characterised by a hyper-induction of ATF4 and an intense suppression of translation (Horzinski *et al*., 2010; Kantor *et al*., 2005; Wong *et al*., 2019). Contradicting results exist when looking at upstream markers of the ISR, with the absence of p-eIF2α in mouse models (Abbink *et al*., 2019; Wong *et al*., 2019), possibly due to enhanced GADD34 expression, whereas lymphoblasts derived from WMD patients exhibited a notable elevation in phosphorylated eIF2α levels that persisted for an extended duration. This

phenomenon was associated with a delayed activation of the GADD34-mediated negative feedback loop, thus allowing an extended recovery period (Moon & Parker, 2018). The complexities surrounding ISR impact in VWMD give rise to two prevailing possibilities: (1) A central role is attributed to the diminished eIF2B GEF activity caused by VWMD mutations, serving as a key driving force behind ISR induction in a manner independent of p-eIF2α. Consequently, the ATF4 transcriptome fails to sufficiently restore homeostatic levels of eIF2B GEF activity, leading to the perpetuation of stress. (2) The activation of the ISR is chronically triggered, subsequently resulting in successive rounds of eIF2α phosphorylation, leading to the gradual elevation of an ISR-inducible GADD34 threshold. Ultimately, this culminates in the establishment of a dysfunctional ISR state.

In an overarching perspective, VWMD cells are in a constant state of stress, significantly impeding cellular differentiation and developmental processes.

1.6.1.3. eIF2B bodies and VWMD

Recently, the link between VWMD mutations and the integrity and functionality of eIF2B bodies has been investigated in yeast. It was found that eIF2B bodies were not able to form in eIF2Bα (*gcn3* in yeast) null strains. Additionally, eIF2Bα^{V184D} point mutation, that does not impact the decameric conformation, led to the disruption of the eIF2B body integrity, forming multiple small punctate foci, termed microbodies (Norris *et al*., 2021). eIF2B bodies emerge as a target for regulation during cellular stress, evident in both yeast and mammalian models (Campbell *et al*., 2005; Hanson *et al*., 2023; Hodgson *et al*., 2019; Taylor *et al*., 2010). In mammalian cells, the heterogeneous subcomplexes of eIF2B bodies exhibit distinctive regulatory patterns concerning stress responses and the rate at which eIF2 is shuttled (Hanson *et al*., 2023; Hodgson *et al*., 2019). These diverse subcomplexes offer intriguing glimpses into the intricacies of cellular stress adaptation, hinting at specialized mechanisms that govern the dynamic interplay between eIF2B complexes and eIF2. Given the established role of the ISR in VWMD cases, the implications of this regulation of eIF2B localisation warrant further investigation in the context of VWMD pathology.

1.6.2. Permanent Neonatal Diabetes Mellitus

An incidence of heterozygous *de novo* missense variants in the *EIF2B1* gene, which encodes eIF2Bα has been identified in patients with PNDM, a disorder resulting in early onset diabetes, typically diagnosed within the first 6 months of life (De Franco *et al*., 2020). *In silico* protein analysis revealed that the eIF2Bα

missense variations identified in PNDM patients were present in either the binding surface occupied by p-eIF2α or altered residues involved in the interaction with eIF2 (Taylor *et al*., 2010). Interestingly two of the mutations identified in PNDM involve residue 44 on eIF2Bα. Mutations in this residue have previously been analysed in yeast and classified as *gcn−* with reduced sensitivity to p-eIF2α (Pavitt *et al*., 1997). This suggests that the PNDM eIF2Bα mutations may hinder or impede the binding between eIF2Bα and p-eIF2α, thus leading to an inadequate sensing and response to cellular stress. Alternatively, these mutations might also operate by enhancing the binding affinity between eIF2Bα and p-eIF2α, consequently entrapping the eIF2B complex within an unproductive or inactive state. This state of the complex could persist even under regular circumstances, rendering it incapable of executing its function.

Additionally, in yeast, mutations in eIF2Bα^{E44} also compromise the formation of eIF2B bodies (Norris *et al*., 2021), either by the decrease of eIF2Bα levels, leading to a decameric instability or by destabilising eIF2B subunit binding. It is known that for the recognition and binding of p-eIF2α, complete eIF2B decamer complex configuration is essential (Bogorad *et al*., 2017; Boone *et al*., 2022; Schoof *et al*., 2021; Zyryanova *et al*., 2021). As such, the faulty sensing of stress in PNDM mutations may be also linked to the incorrect formation of eIF2B bodies, where the assembly of these bodies may play an important role in the regulatory function of this protein.

When juxtaposed with eIF2Bα mutations associated with VWMD, the sites of PNDM eIF2Bα mutations differ greatly. The VWMD mutations are predominantly located in the C-terminal of eIF2Bα and appear to disrupt the formation of the eIF2B decamer, whereas PNDM mutations occur within the N-terminal region and appear to disrupt activation of the ISR (De Franco *et al*., 2020; Schoof *et al*., 2021) (**Figure 1.10**). However, interestingly in a VWMD patient that exhibited diabetic ketoacidosis, the homozygous missense variant was present in the N-terminal (eIF2Bα^{L49R}) (Alamri *et al*., 2016), which would suggest a similar eIF2Bα defect observed in PNDM mutations and could explain the diabetic presentation. While PNDM associated with heterozygous eIF2Bα variants do not exhibit severe neurological features, two reported cases displayed mild learning disability or attention deficit disorder (Alamri *et al*., 2016), highlighting the link between cognitive abilities and eIF2B, which was discussed previously.

The most common monogenic PNDM subtype is Wolcott-Rallison syndrome (WRS; OMIM 226980) and is caused by recessive missense and truncation mutations in the *EIF2AK3* gene, which encodes the eIF2 alpha kinase, PERK (Ozbek *et al*., 2010). The prevailing notion suggests that these mutations impede the activation of the ISR, resulting in a compromised cellular stress response, ultimately culminating in the demise of β-cells. This phenomenon bears an analogy to the consequences observed in eIF2Bα loss-of-function mutations, highlighting the relationship between eIF2B dysfunction and ISR regulation, and their profound implications for cellular viability and function.

ISRIB stabilises the productive conformation of decameric eIF2B, thus concurrently promoting eIF2B GEF activity and attenuating ISR effects (Sekine *et al*., 2015; Tsai *et al*., 2018; Zyryanova *et al*., 2018, 2021). However, its impact on the PNDM-associated eIF2Bα variants in the formation and localisation of eIF2B bodies, and the resulting impact on the GEF activity in mammalian cells is still unknown.

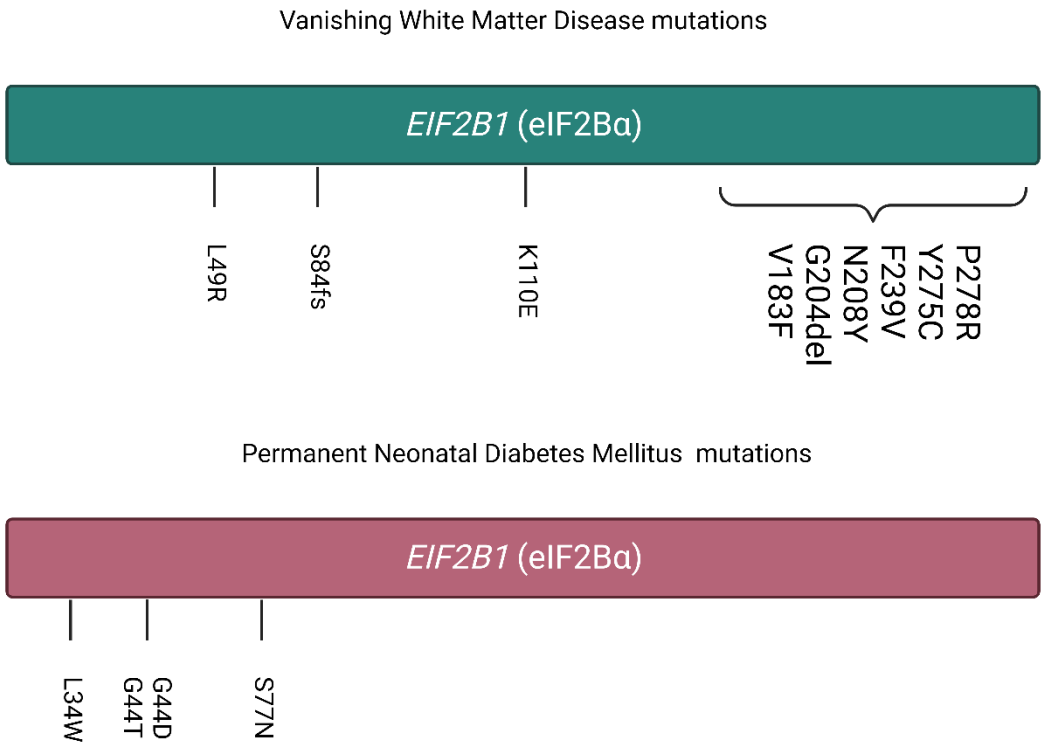

Figure 1.10. The distribution of VWMD and PNDM mutations across the *EIF2B1* gene. VWMD mutations across the eIF2Bα rarely occur within the 5' sequences of the genes and cluster more within the C'-terminal region. PNDM mutations mainly occur within the N-terminal region, with a stop-loss variant p.*306Thrext*12 (not mapped). Variant information gathered from ClinVar database and De Franco *et al.,* (2020). Image designed in BioRender.

1.7. Project overview

The precise subcellular endogenous localisation of eIF2B subunits within mammalian cells has not yet undergone comprehensive investigation. This thesis endeavours to illuminate the intricate patterns of endogenous eIF2B localisation in glial and neuronal cell lines in steady-state and stressed conditions, with particular focus on the eIF2Bα subunit.

In our prior research, our team has successfully exhibited the regulatory modulation of eIF2B cellular localisation during the ISR, and distinct cell-type specific patterns of eIF2B. As mutations affecting eIF2Bα are responsible for triggering the emergence of VWMD and PNDM, we aimed to investigate the role of eIF2Bα, its contribution to the assembly of eIF2B bodies and its interaction with other cellular structures.

Our central hypothesis posits that eIF2Bα plays a pivotal role in orchestrating the formation of eIF2B foci and through p-eIF2α sensing, influencing their role in efficient translation initiation regulation and stress responses within cells.

To address this hypothesis, our aims were the following:

(1) Characterise endogenous eIF2Bα-ε localisation in glial and neuronal cells.
(2) Investigate eIF2B foci formation and ISR modulation in cells depleted of eIF2Bα.
(3) Determine eIF2Bα spatial interaction with other known cytoplasmic aggregates during activation of the ISR.

Chapter 2. Materials and Methods.

2.1. Cell culture.

2.1.1. List of reagents and materials

Table 2.1. List of reagents and materials used in cell culture practices.

Reagents	Supplier	Catalog number	Other information
Minimum Essential Medium (MEM)	Gibco	11095-080	500mL
Dulbecco's modified Eagle's medium:F-12 (1:1) (DMEM:F-12)	Gibco	11574546	500mL
Dulbecco's Modified Eagle Medium (DMEM)	Gibco	11574486	500mL
Rosewell Park Memorial Institute (RPMI) 1640 Medium	Gibco	11875093	500mL
Astrocyte Medium (AM)	ScienCell	1801	500mL
Heat-inactivated fetal bovine serum (FBS)	Gibco	10082-147	500mL
MEM non-essential amino acids (NEAA)	Gibco	11140-035	100x
Sodium pyruvate	Gibco	11360-070	100mM
L-Glutamine	Gibco	25030-081	200mM
Penicillin/streptomycin (P/S)	Gibco	15140-122	10000 U/mL
AM-FBS	ScienCell	0010	10mL
Astrocyte Growth Supplement (AGS)	ScienCell	1852	10mL
AM-P/S	ScienCell	0503	10mL
Trypsin-EDTA solution	Gibco	25300-062	0.05%
Trypan Blue solution	Gibco	15250-061	0.4%
Phosphate-buffered saline (PBS)	Gibco	14190-094	500mL
Dimethyl sulfoxide (DMSO)	VWR	BKC-17	50mL

Materials	Supplier	Catalog number	Other information
Countess™ Cell Counting Chamber Slides	Invitrogen	C10228	-
MycoAlert™ Mycoplasma Detection Kit	Lonza	LT07-318	-
Nalgene® Mr. Frosty	Thermo Scientific	5100-0001	H × diam. 86 mm × 117 mm

2.1.2. Cell lines and maintenance

Human glioblastoma astrocytoma cell line (U373-MG) (purchased from ECACCT, #08061901) were cultured in MEM, supplemented with 10% (v/v) FBS, 1% (w/v) NEAA, 1% (v/v) sodium pyruvate, 1% (v/v) L-glutamine and 1% (v/v) P/S. Human glial oligodendrocytic hybrid cell line (MO3.13) (a kind gift from Prof Nicola Woodroofe, originally derived from Cedarlane, #CLU301) were cultured in high glucose DMEM, supplemented with 10 % (v/v) FBS, 1% (v/v) L-glutamine, and 1% (w/v) P/S. Human adrenergic neuroblastoma cell line (SH-SY5Y) (purchased from ATCC, CRL-2266) were cultured in DMEM:F-12 supplemented with 10% (v/v) FBS, 1% (v/v) L-glutamine and 1% (v/v) P/S. All three cell lines were validated with antibodies against lineage-specific markers (**Figure 2.1**). Human primary astrocytes (HA) were cultured in AM supplemented with 2% (v/v) AM-FBS, 1% (v/v) AGS and 1% (v/v) AM-P/S. Human ovarian adenocarcinoma cell line (SKOV3) and stable derived cell line with a *EIF2B1*$^{L100P/WT}$ mutation (a kind gift from Prof Paul Clarke, originally purchased from ATCC, HTB-77) were cultured in RPMI, supplemented with 10% (v/v) FBS, 1% (v/v) L-glutamine, and 1% (v/v) P/S. All cell lines were maintained at 37°C under 5% CO_2 and were routinely tested for contamination with MycoAlert™ Mycoplasma Detection Kit purchased from.

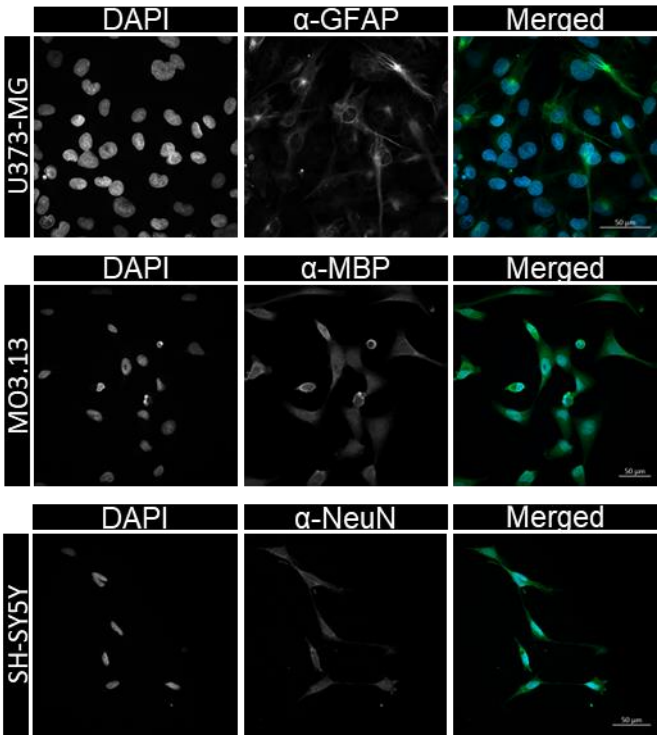

Figure 2.1. Antibodies against selective markers for glial and neuronal cells were used to validate cellular lineage.

Representative confocal images of astrocytoma (U373-MG), hybrid primary oligodendrocytes (MO3.13) and neuroblastoma (SH-SY5Y), immunostained for astrocytic marker GFAP, oligodendrocytic marker myelin basic protein (MBP), and neural marker neuronal nuclei (NeuN), respectively. 4,6-diamidino-2-phenylindole (DAPI) shows nuclei. Scale bar: 50μm.

2.1.3. Cell Passage

Cells were grown in T75 or T175 flasks and sub-cultured upon reaching approximately 70-80 % confluency. All cell lines were sub-cultured no further than passage 27. For cell passage, media was removed, and cells were washed once with PBS. The cells were then incubated with 1 mL (T75) or 3 mL (T175) of trypsin-EDTA at 37ºC for a maximum of 3 min. To inactivate trypsin-EDTA, the cells were resuspended in 9 mL (T75) or 19 mL (T175) of growing media and the suspensions were transferred into 50 mL conical tubes. The cells were centrifuged at 112 x g for 5 min, the supernatant was then discarded, and the pelleted cells were re-suspended in 1 mL of fresh media. Cell counting was carried out by aliquoting 10 μL of suspension with 10 μL of Trypan Blue and loaded into a Countess™ Cell Counting Chamber. The cell suspension was then aliquoted into T75 or T175 flasks containing fresh growing media, depending on the split ratio intended. SH-SY5Y, U373-MG and SKOV3 cells were normally split

in a ratio between 1:3-1:8; MO3.13 and primary astrocytes were usually split between 1:6-1:8.

2.1.4. Thawing and freezing vials

Cell vials stored in liquid nitrogen were thawed in a water bath at 37 ºC until defrosted (approximately 2-3 minutes). The cells were pipetted into T75 flasks containing 15 mL of the corresponding growth media. Media was discarded the following day and replaced with fresh media removing traces of DMSO. To freeze cells, cells were trypsined and centrifuged as described above and the pelleted cells were resuspended in FBS containing 10% (v/v) DMSO and 1 mL was added to cryovials. The tubes were maintained for 24h in a Mr. Frosty™ Freezing Container at -80ºC and moved to liquid nitrogen the following day for long-term storage or maintained at -80ºC for short-term usage.

2.2. DNA manipulation.

2.2.1. List of reagents, materials, and plasmids

Table 2.2. List of reagents, DNA plasmids and materials used.

Reagents	Supplier	Catalog number	Other information
Lysogeny broth (LB)	Sigma-Aldrich	L3022	1 kg
LB agar	Sigma-Aldrich	L2897	1 kg
Carbenicillin disodium salt	Merck	C1389	250 mg
Glycerol	Fischer Scientific	G/0600/17	2.5L
XL Competent Cells	Agilent	200314	5 x 100 uL
Lipofectamine™ 3000 kit	Invitrogen	L3000001	-
3-(N-morpholino)propanesulfonic acid	Sigma-Aldrich	PHG0007	1 kg
Potassium acetate	Sigma-Aldrich	P1190	500 g
Calcium chloride tetrahydrate	Sigma-Aldrich	1.02384	100 g
Plasmids	**Supplier**	**Catalog number**	**Other information**
EIF2B5 (pCMV6-AC-tGFP)	Origene	RG202322	10 µg/uL
EIF2S1 (pCMV6-AC-tGFP)	Origene	RG200368	10 µg/uL
EIF2B1 (pCMV6-AC-tGFP)	Origene	RG210766	10 µg/uL

hEIF2B5-mRFP1, *hEIF2A*-EGFP	VectorBuilder	VB230105-1468qzd	10 µg/uL
pCMV6-AC- monomeric Green Fluorescent Protein (mGFP)	Origene	PS100040	10 µg/uL
pCMV6-AC-RFP	Origene	PS100034	10 µg/uL
Materials	**Supplier**	**Catalog number**	**Other information**
GeneJET™ plasmid Miniprep kit	Thermo Scientific	K0503	-
NanoDrop 1000 spectrophotometer	Thermo Scientific	ND-1000	-
Nunc™ Biobanking and Cell Culture Cryogenic Tubes	Thermo Scientific	377267	-

2.2.2. Plasmid preparation

Commercially bought plasmids upon arrival were centrifuged at 5000 g for 5 min, 100 µL of sterile water was added to dissolve the DNA (final concentration of 0.1 µg/µL) and incubated for 10 min at RT. Plasmid solutions were briefly vortexed followed by 30 second spin (<5000 g) and stored at -20°C.

2.2.3. Plasmid Constructs

pCMV6-AC-tGFP plasmid vector encoding *EIF2B5* (eIF2Bε) and pCMV6-AC-tGFP plasmid vector encoding *EIF2S1* (eIF2α) were purchased from Origene. The coding ORF of *EIF2B5* and *EIF2B1* from the pCMV6-AC-tGFP vector was sub-cloned into a pCMV6-AC-mGFP and pCMV6-AC-RFP vector (performed by Dr Rachel Hodgson, SHU). The constructs were verified by sequencing.

2.2.4. Generating chemically competent *E.coli*

XL 10-Gold ultracompetent cells were inoculated in LB broth and incubated in a shaking incubator at 37°C overnight. Cells were grown to an optical density at 600 nanometre (OD_{600nm}) of approximately 0.5 and incubated for 15 minutes on ice. Cells were pelleted at 1792 x g for 5 minutes at 4°C and then resuspended in transformation buffer (TBF) I buffer (0.03 M potassium acetate, 0.05 M manganese chloride tetrahydrate, 0.01 M potassium chloride, 0.008 M calcium chloride tetrahydrate, 15 % (v/v) glycerol and incubated for 1 hour on ice. Cells were then pelleted at 1792 x g for 5 minutes at 4°C and then resuspended in TBF II buffer (0.001 M 3-(N-morpholino)propanesulfonic acid, 0.001 M potassium

chloride, 0.06 M calcium chloride tetrahydrate, 15 % (v/v) glycerol). Cells were aliquoted, flash frozen in liquid nitrogen and stored at -80°C.

2.2.5. Bacterial Transformation

Plasmid constructs were amplified by bacterial transformation using competent *Escherichia coli* (*E.coli*) cells. Competent DH5α cells were defrosted on ice for 30 minutes prior to transformation. 50 µL of competent *E.coli* were mixed with 0.1 µg of plasmid DNA and incubated on ice for 1 hour. Following incubation, cells were heat shocked at 42°C for 90 seconds and incubated on ice for 2 minutes. Transformations were plated on LB Agar plates containing 50 µg/mL carbenicillin and incubated overnight at 37°C.

2.2.6. Extracting plasmid DNA from transformed *E.coli*

Single colonies were selected and were cultured in LB containing 50µg/mL carbenicillin and incubated overnight at 37°C in a shacking incubator. Plasmid DNA was extracted from cultures using GeneJET plasmid Miniprep kit, according to manufacturer's instructions. The concentration of the purified plasmids was assessed by NanoDrop 1000 spectrophotometer.

2.2.7. Glycerol stocks

For long-term storage, 500 µL of an overnight liquid bacterial culture was mixed with 500 µL of 50 % (v/v) glycerol, mixed and transferred to cryovials. Kept at -80ºC.

2.3. Mammalian cell transfections and cell treatments.

2.3.1. List of reagents and materials

Table 2.3. List of reagents, materials and plasmids/siRNA used for cell transfections and cell treatments.

Reagents	Supplier	Catalog number	Other information
Lipofectamine™ 3000 kit	Invitrogen	L3000001	-
ISRIB	Sigma-Aldrich	SML0843	5 mg
Tg	Sigma-Aldrich	T9033	1 mg
SA	Sigma-Aldrich	S7400	100 g
H_2O_2	Sigma-Aldrich	H1009	30 % (w/w), 100 mL
RocA	MedChemExpress	HY-19356	500 µg

Puromycin dihydrochloride	Gibco	A1113803	10x1 mL
Emetine	Sigma-Aldrich	E2375	50 mg
DMSO	VWR	BKC-17	50mL
CHX	Sigma-Aldrich	203350	25 mg
Silencer™ siRNA Labeling Kit with Cy™3 dye	Thermo Scientific	AM1632	-
Plasmids/siRNA	**Supplier**	**Catalog number**	**Other information**
EIF2B5 (pCMV6-AC-tGFP)	Origene	RG202322	10 µg
EIF2S1 (pCMV6-AC-tGFP)	Origene	RG200368	10 µg
EIF2B1 (pMirTarget-RFP)	Origene	SC209520	10 µg
EIF2B1 (pCMV3-C-Myc)	SinoBiological	HG15825-CM	-
hEIF2B5- mRFP1, *hEIF2A*-EGFP	VectorBuilder	VB230105-1468qzd	10 µg
pCMV6-AC-mGFP	Origene	PS100040	10 µg
pCMV6-AC-RFP	Origene	PS100034	10 µg
ON-TARGETplus Human *EIF2B1* siRNA	Horizon Discovery	L-020180-00-0005	5 nmol
ON-TARGETplus Non-targeting Control siRNAs	Horizon Discovery	D-001810-01-05	5 nmol
Materials	**Supplier**	**Catalog number**	**Other information**
Nunc™ Cell-Culture Treated Multidishes	Thermo Scientific	140675	6-wells
NanoDrop 1000 spectrophotometer	Thermo Scientific	ND-1000	-
Nunc™ Cell-Culture Treated Multidishes	Thermo Scientific	142475	24-wells
Nunc™ MicroWell™ 96-Well, Nunclon Delta-Treated, Flat-Bottom Microplate	Thermo Scientific	167008	96-wells

µ-Slide 8 Well Glass Bottom	Ibidi	80827	-
FluoroDish Cell Culture Dish - 35mm, 23mm well	Wolf Laboratories Limited	FD35-100	-

2.3.2. Transient transfections

For FRAP assays, U373-MG, MO3.13 and SH-SY5Y were seeded at a density of $3x10^5$, $2.5x10^5$ and $2.5x10^5$ cells, respectively, in fluorodishes and cultured for at least 24 hours before transfection. For immunocytochemistry (ICC), U373-MG, MO3.13 and SH-SY5Y were seeded at a density of $1x10^5$, $2.5x10^4$ and $2.5x10^4$, respectively, in a 24-well plate or 8-well glass bottom chamber slide and cultured for at least 24 hours before transfection. Once the cells reached approximately 70% confluency, plasmids were chemically transfected with Lipofectamine 3000 according to manufacturer's instructions. Transfection complexes were prepared in FBS-free media of each cell line (MEM for U373-MG cell line, DMEM for MO3.13 cell line and DMEM:F12 for SH-SY5Y cell line) at a molar ratio of 1.5:1:2 (Lipofectamine [µL] : DNA [µg] : P3000 [µL]) and incubated at RT for 15 minutes. The transfection complexes were added to cells and incubated for 48-96 hours at 37°C under 5% CO2 prior to confocal imaging or protein extraction.

2.3.3. Cy™3 siRNA tag

For siRNA labeling, a Cy3™3 was used. Following siRNA suspension and subsequent quantification through NanoDrop spectrometer, 5µg of SMARTPool of 4 siRNA sequences targeting *EIF2B1* and siRNA negative control were labeled as per the manufacturer's instructions. The labeled siRNA was subsequently stored at -20°C in the dark, before being utilised for siRNA mediated silencing.

2.3.4. siRNA mediated silencing of *EIF2B1*

For protein extraction and FRAP assays, U373-MG, MO3.13 and SH-SY5Y were seeded at a density of $3x10^5$, $2.5x10^5$ and $2.5x10^5$ total cells, respectively, in a 6-well plate or fluorodish and cultured for at least 24 hours before transfection. For ICCs, U373-MG, MO3.13 and SH-SY5Y were seeded at a density of $1x10^5$, $2.5x10^4$ and $2.5x10^4$, respectively, in a 24-well plate or 8-well glass bottom chamber slide and cultured for at least 24 hours before transfection. For cell viability and proliferation assays, U373-MG, MO3.13 and SH-SY5Y cells were seeded at a density of $2x10^4$, $1x10^4$ and $1x10^4$ cells per mL, respectively, in a 96-well plate and cultured for at least 24h before transfection. Once the cells reached approximately 70 % confluency, a SMARTPool of 4 siRNA sequences targeting

EIF2B1 were transfected using Lipofectamine™ 3000 reagent in accordance with manufacturer´s instructions. Transfection complexes were prepared in FBS-free media of each cell line (MEM for U373-MG cell line, DMEM for MO3.13 cell line and DMEM:F12 for SH-SY5Y cell line) at a molar ratio of 1.5:1 (Lipofectamine [µL] : siRNA [µg]) and incubated at RT for 15 minutes. Media was removed and replaced with complete media following 24 hours of transfection. Cells were incubated for an additional 48, 72, 96 or 120h at 37°C under 5 % CO_2. As control, cells transfected with ON-TARGETplus Non-targeting Control siRNAs as described on respective experimental setup.

2.3.5. Cell treatments

For ER stress induction, cells were treated with 1µM Tg (stock solution: 1mg/mL in DMSO stored at -20°C), for 1h and 300 nM Tg for 4 or 6 hours, at 37°C. For oxidative stress induction, cells were treated with 125 µM SA for 30 minutes, 500 µM SA for 1 hour or 0.5 mM, 1 mM or 2 mM H_2O_2 for 1 hour. For eIF4A inhibition, cells were treated with 500 nM RocA for 1 hour. For ISIRB treatments, cells were treated with 200 nM ISRIB for 1h. As control, cells were treated with vehicle solution (DMSO) with the highest volume and treatment duration at 37°C depending on its respective drug experimental setup.

2.3.6. Puromycin incorporation assay

For puromycin integration, 91 µM of puromycin dihydrochloride solution and 208 µM emetine was added to the cells and incubated at 37°C for 5 minutes. Cells were washed twice with ice-cold PBS supplemented with 355 µM CHX, and subsequently harvested, as described in **2.4.2**.

2.4. Immunoblotting.

2.4.1. List of reagents and materials

Table 2.4. List of reagents and materials used in immunoblotting.

Reagents	Supplier	Catalog number	Other information
PBS	Gibco	14190-094	500 mL
CellLytic M	Sigma-Aldrich	C2978	250 mL
Sodium fluoride (NaF)	Sigma-Aldrich	201154	5 g
Phenylmethylsulfonyl fluoride (PMSF)	Sigma-Aldrich	P7626	1 g
β-Glycerophosphate disodium salt hydrate	Sigma-Aldrich	G9422	50 g

Protease inhibitor cocktail I	Sigma-Aldrich	P8340	1 mL
Protease inhibitor cocktail II	Sigma-Aldrich	P5726	1 mL
Protease inhibitor cocktail III	Sigma-Aldrich	P0044	1 mL
4x Laemmli sample buffer	BioRad	1610747	10 mL
2-mercaptoethanol	VWR	BC98	100 mL
Chameleon® Duo Pre-stained Protein Ladder	LiCor	928-60000	500 µL
Revert™ Total Protein Stain	LiCor	926-11011	100 mL
Marvel Original Dried Skimmed Milk	Tesco	n/a	n/a
Bovine serum albumin (BSA)	Merck	A7906	100 g
Tris	Fisher Scientific	T/3710/60	1 kg
Tween-20	Sigma-Aldrich	P1379	500 mL
Sodium dodecyl sulfate (SDS)	VWR	L5750	500 g
Ammonium persulphate (APS)	Sigma-Aldrich	A3678	100 g
N,N,N′,N′-Tetramethyl ethylenediamine (TEMED)	Sigma-Aldrich	T9281	25 mL
Antibodies	**Supplier**	**Catalog number**	**Dilution factor**
Rabbit anti-eIF2Bα	Proteintech	18010-1-AP	1:500
Rabbit anti-eIF2Bβ	Proteintech	11034-1-AP	1:500
Mouse anti-eIF2Bγ	Santa Cruz	sc-137248	1:500
Rabbit anti-eIF2Bδ	Proteintech	11332-1-AP	1:500
Rabbit anti-eIF2Bε	Aviva Systems Biology	ARP61329_P050	1:500
Rabbit anti-eIF2Bε	Sigma-Aldrich	HPA064370	1:500

Rabbit anti-eIF2Bε	Sigma-Aldrich	HPA069303	1:500
Mouse anti-eIF2α	Abcam	ab5369	1:500
Rabbit anti-phosho-eIF2α[ser51] [E90]	Abcam	ab32157	1:500
Rabbit anti-GADD34	Proteintech	10449-1-AP	1:500
Rabbit anti-CHOP	Proteintech	15204-1-AP	1:1000
Rabbit anti-GAPDH	Cell Signalling	#2118	1:5000
Mouse anti-β-actin	Cell Signalling	#3700	1:2500
Mouse anti-puromycin (clone 12D10)	Merck	MABE343	1:500
Goat anti-rabbit IRDye 680RD	LiCor	925-68071	1:10000
Goat anti-mouse IRDye 800CW	LiCor	925-32210	1:10000
Materials	**Supplier**	**Catalog number**	**Other information**
Qubit™ Protein Assay kit	Invitrogen	Q33212	-
Qubit™ tubes	Invitrogen	Q32856	-
4-20% Precast Gels Mini-PROTEAN® TGXTM	BioRad	4561096	**-**
MiniPROTEAN® Handcast System	BioRad	1658000FC	-
Trans-Blot® Turbo™ RTA Mini 0.2 µm Nitrocellulose Transfer Kit	BioRad	1704270	-
Trans-Blot® Turbo™ Transfer System	BioRad	1704150	-
Odyssey Scanner	LiCor	Model 9120	-

2.4.2. Protein extraction from cultured cells

Following the corresponding treatments and transfections, cultured media was removed, and cells were washed with ice-cold PBS. Cells were lysed in Cell Lytic M containing 1% (v/v) protease inhibitor cocktail I, 1% (v/v) protease inhibitor

cocktail II, 1% (v/v) protease inhibitor cocktail III, 17.5 mM β-glycerophosphatase, 1 mM PMSF and 10 mM NaF, for 15 minutes shaking at room temperature. Cell lysates were centrifuged at 18928 x g for 10 minutes at 4°C and protein concentration was quantified by Qubit™ Protein Assay Kit. Lysates were stored at -80°C.

2.4.3. Protein Quantification

Protein extracts were quantified using the Qubit™ Fluorometric Quantification assay. Qubit™ working solution buffer was made up by diluting the Qubit™ reagent in Qubit™ buffer at a ratio of 1:200 (Reagent:Buffer). 200 µL of working solution was prepared for each sample and standards. 1 µL of each extract sample was diluted in 199 µL of Qubit™ working solution in Qubit™ assay tubes. All tubes were incubated for 15 minutes at RT in the dark. The fluorescence intensity calibration of the Qubit™ fluorometer was determined via the standards before every read (automatic standard curve) followed by the readings of each sample (units = µg/mL).

2.4.4. Sample preparation for western blot analysis

After protein quantification, 150 µg of each sample was diluted in 4x Laemmli sample buffer supplemented with 335 mM β-mercaptoethanol and incubated at 95°C for 5 minutes. Working samples were stored at -20°C.

2.4.5. Sodium dodecyl sulphate polyacrylamide gel electrophoresis (SDS-PAGE) and Western blotting

20 µg of total protein lysate were loaded on a 5 % stacking gels and resolved on 12 % polyacrylamide gels or 4-20 % precast gels. For a molecular weight marker, 2 µL of Chameleon® Duo Pre-stained Protein Ladder was used.

Gel electrophoresis was carried out using MiniPROTEAN® Handcast System, in 1x running buffer (25 mM Tris pH 8.3, 250 mM glycine, 0.1 % w/v SDS), at 120 V for approximately 60-75 minutes. Gels were semi-wet transferred using Trans-Blot Turbo Mini-nitrocellulose Transfer packs, utilising a Trans-Blot Turbo system at a 2.5 A and 25 V for 7 minutes. When applicable, membranes were subjected to Revert™ Total Protein Stain according to manufacturer's instructions, imaged and de-stained. Membranes were blocked in 5 % nonfat milk (w/v) or 5 % BSA (w/v) dissolved in Tris-buffered saline (TBS) (20 mM Tris-HCl pH 7.4, 150 mM NaCl) for 1 hour at RT or overnight at 4°C. The membranes were probed with primary antibodies diluted in TBS supplemented with 0.1 % (v/v) Tween-20 (TBST), and 5 % (w/v) milk or 5 % (w/v) BSA, overnight at 4°C under gentle

agitation. The primary antibodies used, and corresponding dilutions can be observed in 2.4.1. Membranes were washed 3 times for 4 minutes/each in TBST and probed with appropriate LiCor secondary antibodies. Membranes were washed 3 times for 4 minutes/each in TBST. Membranes were visualised and quantified using a LiCor Odyssey Scanner with Image Studio Lite software.

2.5. Immunocytochemistry.

2.5.1. List of reagents and materials

Table 2.5. List of reagents and materials used in immunocytochemistry.

Reagents	Supplier	Catalog number	Other information
Industrial Methylated Spirit (IMS)	Fisher Scientific	M/4470/17	2.5L
Methanol	Fisher Scientific	M/3950/17	2.5L
4% Paraformaldehyde in PBS (PFA)	Alfa Aesar	J61899	250mL
PBS	Gibco	14190-094	500mL
Tween-20	Sigma-Aldrich	P1379	500mL
Triton X-100	BDH Laboratories	306324N	500mL
BSA	Merck	A7906	100g
ProLong™ Gold Antifade Mountant with DAPI	Invitrogen	P36935	5x2mL
Antibodies	**Supplier**	**Catalog number**	**Dilution factor**
Rabbit anti-eIF2Bα	Proteintech	18010-1-AP	1:25
Rabbit anti-eIF2Bβ	Proteintech	11034-1-AP	1:25
Mouse anti-eIF2Bγ	Santa Cruz	sc-137248	1:50
Mouse anti-eIF2Bδ	Santa Cruz	sc-271332	1:50
Rabbit anti-eIF2Bε	Abcam	ab32713	1:50
Rabbit anti-eIF2Bε	Sigma-Aldrich	HPA064370	1:100
Rabbit anti-eIF2Bε	Sigma-Aldrich	HPA069303	1:25

Mouse anti-DCP1A (clone: 3G4)	VWR International	12352203	1:100
Mouse anti-Polyubiquitinylated conjugates; FK1	Enzo Life Sciences	BML-PW8805	1:100
Mouse anti-G3BP	Abcam	ab56574	1:100
Mouse anti-puromycin (clone 12D10)	Merck	MABE343	1:50
Mouse anti-eIF2α	Abcam	ab5369	1:100
Rabbit anti-Myc	Cell Signalling	#2272	1:100
Goat anti-Mouse AlexaFluor-488®	Invitrogen	A28175	1:500
Goat anti-Rabbit AlexaFluor-488®	Invitrogen	A-11008	1:500
Goat anti-Rabbit AlexaFluor-568®	Invitrogen	A-11011	1:500
Goat anti-Mouse AlexaFluor-594®	Invitrogen	R37121	1:500
Goat anti-Rabbit AlexaFluor-594®	Invitrogen	A-11012	1:500
Alpaca anti-Rabbit AlexaFluor 488®	Proteintech	srbAF488-1	1:500
Alpaca anti-Mouse AlexaFluor 647®	Proteintech	sms1AF647-1-10	1:500
Materials	**Supplier**	**Catalog number**	**Other information**
Academy squared glass coverslips	Smith Scientific	NPS13/2222	22x22mm

2.5.2. Immunofluorescence assay

U373-MG, SKOV3, MO3.13 and SH-SY5Y cells were seeded on coverslips, previously washed with 70 % IMS, at a cell density of $1x10^5$, $1.5x10^5$, $2.5x10^4$ and $2.5x10^4$, respectively, in 24-well plates and treated as described in **section 2.3**. U373-MG, SH-SY5Y and SKOV3 cells were fixed with ice-cold methanol for 15 minutes at -20°C. MO3.13 cells were fixed with 4 % (w/v) PFA for 20 minutes in RT, washed with PBS supplemented with 0.5 % (v/v) Tween 20 (PBST) 3 times

for 4 minutes each and incubated for 5 minutes at RT with 0.1 % (v/v) X-Triton. Cells were then washed with PBST 3 times for 4 minutes/each and subsequently blocked with PBS supplemented with 1 % (w/v) BSA for 1 hour. Cells were then probed with primary antibodies diluted in blocking solution, overnight at 4°C, under gentle agitation. The primary antibodies used, and corresponding dilutions are listed in Table 2.5. Following primary antibody incubation, cells were washed with PBST and subsequently probed with AlexaFluor conjugated secondary antibodies or Alpaca conjugated secondary antibodies diluted in blocking buffer. The secondary utilised, and corresponding dilutions are listed in Table 2.5. Cells were subsequently washed with PBST 3 times for 4 min/each and mounted with ProLong™ Gold Antifade Mountant with DAPI. Cells were visualised using a Zeiss LSM 800 confocal microscope.

2.6. Confocal Microscopy.

2.6.1. Zeiss LSM 800

Imaging was performed using a Zeiss LSM 800 confocal microscope with Zeiss ZEN 2.3 (blue edition) software for data processing and analysis. 40 X or 63 X plan-apochromat oil objectives were routinely used. For DAPI staining imaging, a 405 nm diode laser with a maximum output of 5 mW was used at 0.2 %. For 488 nm excited fluorophores, a 488 nm diode laser with a maximum output of 10 mW at 5.0 % was used. For 568 and 594 nm excited fluorophores a 561 nm diode laser with a maximum output of 10 mW at 5.0 % was used. For 647 nm excited fluorophores a 640 nm diode laser with maximum output of 10 mW at 5.0 % was used. A 63 x plan-apochromat oil objective, diode lasers with maximum output of at 0.2 % laser transmission and a maximal 0.8 x zoom input was used for Airyscan imaging. Image acquisition was performed by orthogonal projection of a Z-stack of automatically calculated increments for complete single cell imaging and 3D projection. For live imaging, ROI was captured every 3 minutes, for a total of 24 minutes.

2.6.2. FRAP analysis

2.6.2.1. Imaging

FRAP experiments were carried out by live cell imaging in an incubation chamber with 37°C and 5 % CO_2 levels. eIF2α-mGFP foci were manually marked as regions of interest (ROI) for bleaching using 23 iterations at 100 % laser transmission (488 nm diode laser). Pre-bleaching image and intensity of targeted

ROI was captured followed by 44 images captured every 151 milliseconds (ms) for a total of 7.088 seconds (s). In-cell fluorescence intensity was captured to normalise against ROI. Out-of-cell fluorescence, or background intensity, was measured and subtracted from ROI and T values to provide corrected measurements.

2.6.2.2. Analysis of FRAP data

Pre-bleach, bleach and recovery images from each experiment were analysed in accordance with the methodology by (Hodgson *et al*., 2019). Normalised data was fitted to a one-phase association curve using GraphPad Prism to quantify rate of recovery. In the one-phase association model, 'γ_0' is the γ value when x is zero, 'Plateau' is the γ value at infinite values of x and 'K' is the rate constant.

$$\gamma = \gamma_0 + (Plateu - \gamma_0).(1 - e^{(-K.x)})$$

The data was fitted using nonlinear regression. The relative percentage of eIF2 recovery was determined as the mobile phase of recovery curve represented as the plateau of the normalised FRAP curves.

2.7. Analysing populations of eIF2B foci and cells with localisation.

2.7.1. Calculating population of cells with localised eIF2B

Percentages of cells with localised eIF2B foci were observed through the Zeiss ZEN 2.3 (blue edition) software. To determine cells with localised versus dispersed signal, a threshold to authenticate eIF2B foci for each imaging conditions/experiment was analysed using the segment region classes method. It was first set up using the automatic triangle threshold (light regions), with 0 % tolerance, 1 % neighborhood and with holes in segmented objects filled for the appropriate secondary antibodies utilised (488 nm and/or 594 nm). Subsequently, a manual set up was carried out in cases of fluctuations of fluorescence between different captured cells. 0 IDs captured per cell was characterised as a dispersed signal and 1 or more IDs captured were characterised as localised eIF2B signal, *i.e.*, cell with localised foci. The counts of cells were performed by DAPI staining using the images of each region of interest. A population of 100 cells were blindly captured and analysed per replicate. The total number of cells with dispersed or localised signal was converted to percentages (x % of cells = x number of cells *100) and the values were plotted using GraphPad Prism.

2.7.2. Determining co-localisation of antibody staining with eIF2B foci

eIF2B foci were analysed as described in **section 2.7.1**. and assessed on a body-by-body basis of all detected eIF2B foci per cell. eIF2B foci were classed as positive for co-localisation when the two eIF2B antibodies signals overlapped completely as observed in **Figure 2.2**. Additionally, profile and 3D surface profiles were used to create profile/surface plots of protein co-localisation. Following co-localisation efforts, two size categories were determined, large foci: ≥ 1 μm^2 and small foci: < 1 μm^2. The counts were carried out in a population of 30 cells per repeat with at least one foci localised.

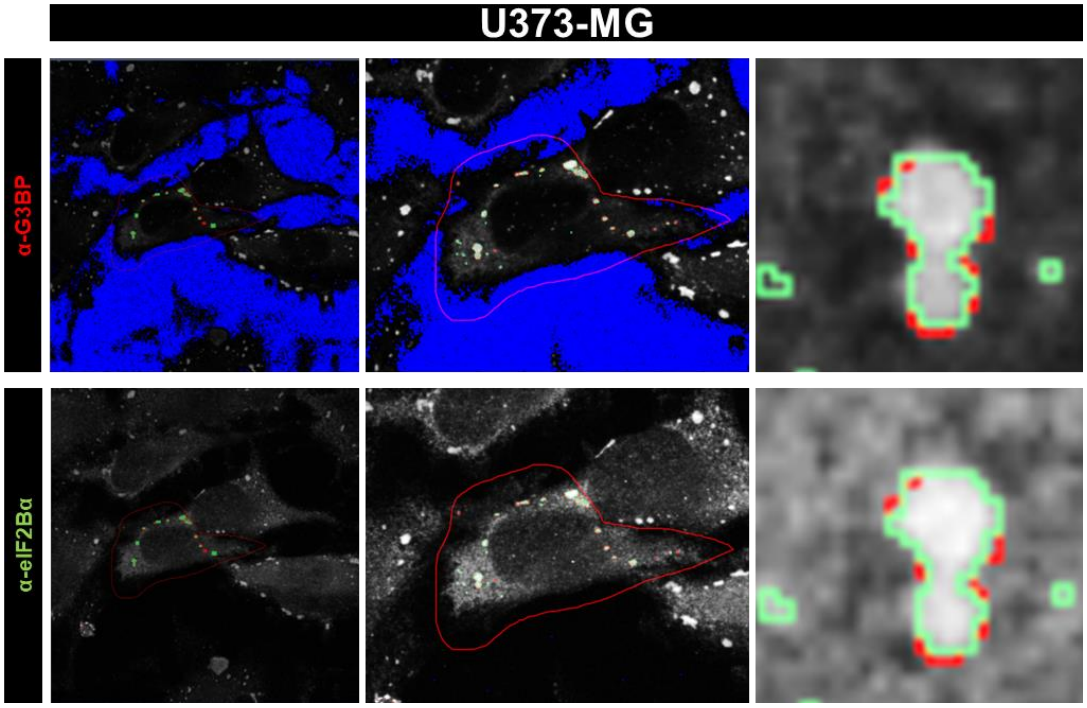

Figure 2.2. Co-localisation determination of antibody staining with eIF2B foci.
Representative images of co-localisation visualisation and determination of spatial interaction. Green lines represent eIF2Bα staining and red lines represent G3BP staining. Overlapping signals were determined as co-localising and non-overlapping signals were determined as not co-localising. Information regarding the area was collected for each eIF2B and G3BP foci. Identical analysis parameters and steps were used for all co-localisation efforts.

2.7.3. Calculating average number of eIF2B foci per cell

To calculate the average number of different sized population of eIF2B foci the Zeiss ZEN 2.3 (blue edition) software was used to determine the number, area and mean intensity of channel of interest through the set-up of the intensity threshold as previously described in 2.7.1. Through the fluorescence intensity

threshold, eIF2B foci were automatically highlighted and subsequently, the number in sequential ID of the objects, area in μm^2 (unit of area of scaling assigned to the image) and/or intensity mean of channel in gray level (the average brightness, *i.e.*, pixel value of the pixels in the object) were analysed for each focus. The average number of foci per cell was determined through the counts of the total number of foci per cell divided by 30 cells (average number per cell = [number of foci per cell 1 + number of foci per cell 2 + number of foci per cell 30]/30). The counts were carried out in a population of 30 cells with at least one foci localisation of the desired target per cell.

2.7.4. Calculating relative percentage of eIF2B foci sub-populations

To calculate the relative percentage of each size category of eIF2B bodies, the number of small bodies and large bodies was divided by the total number of bodies per cell and converted into percentages (% small bodies = [number of bodies with area $<1\mu m^2$/total number of bodies] x 100; (% large bodies = [number of bodies with area $\geq 1\mu m^2$/total number of bodies] x 100). The counts were carried out in a population of 30 cells with at least one foci localisation of the desired target per cell.

2.8. Cell based assays.

2.8.1. List of reagents and materials

Table 2.6. List of reagents and materials for cell based assays.

Reagents	Supplier	Catalog number	Other information
3-(4,5-Dimethylthiazol-2-yl)-2,5-Diphenyltetrazolium Bromide (MTT)	Thermo Scientific	M6494	1 g
NP-40 buffer (50mM Tris-HCl [pH 7.4], 150mM NaCl, 1%NP-40 and 5mM EDTA)	Thermo Scientific	J60766.AP	500 mL
Hydrochloric acid (HCl)	Sigma-Aldrich	258148	100 mL
2-Propanol	Sigma-Aldrich	34863	1L
Phosphate-buffered saline (PBS)	Gibco	14190-094	500mL

Hoechst 33342 Solution	Thermo Scientific	62249	20 mM
Propidium Iodide (PI)	Invitrogen	P1304MP	100 mg
Human ATF4 enzyme-linked immunosorbent assay (ELISA) Kit	Proteintech	KE00147	-
Materials	**Supplier**	**Catalog number**	**Other information**
Nunc™ MicroWell™ 96-Well, Nunclon Delta-Treated, Flat-Bottom Microplate	Thermo Scientific	167008	96-wells
CLARIOstar®	BMG Labtech	*Plus* Model	-
BioTek Cytation 5	Agilent	Cell Imaging Multimode Reader	-

2.8.2. MTT assay following siRNA mediated silencing and cell treatments

Following cell treatments and siRNA mediated silencing of *EIF2B1* described above in **section 2.3**, cells were washed 2 times with fresh media for 3 minutes, and 0.5 mg/mL MTT was added to each well and incubated for 4 hours at 37°C under 5 % CO_2. The formazan product was solubilized with 4 mM HCl, 0.1 % NP40 in isopropanol and incubated for 15 minutes on an orbital shaker at RT. The optical density was measured at 570 nm using a CLARIOstar®Plus plate reader.

2.8.3. Hoechst/PI staining

Following cell treatments and siRNA mediated silencing of *EIF2B1* described above in **section 2.3**, cells were washed twice with PBS, and trypsinised. Cell density was adjusted to $1x10^6$ cells/ml in PBS. Cells were placed in a 96-well plate and labelled with Hoechst 33342 (10 µg/mL) and PI (10 µg/mL) for 20 minutes at 37°C. Fluorescent images and subsequent analysis was carried out using the BioTek Cytation 5 Cell Imaging Multimode Reader and BioTek Gen5 Software, respectively.

2.8.4. ATF4 ELISA

Following cell treatments and siRNA mediated silencing of *EIF2B1* described above in **section 2.3**, and protein extraction described above in **section 2.4.2**, levels of ATF4 were quantified through a Human ATF4 ELISA Kit as per manufacturer's instructions. Each sample and standard were assayed in duplicate, and three replicates were carried out. The absorbance was measured at 450 nm and 630 nm using a CLARIOstar®Plus plate reader. The average of the duplicate reading for each standard and sample was calculated, and the average of the zero standard absorbance was subtracted to these values. A sigmoid four-parameter logistic standard curve was plotted by using the mean absorbance for each standard against the concentration. The samples were interpolated into the standard curves and the levels of ATF4 were plotted using GraphPad Prism.

2.9. Statistical analysis.

In order to determine statistically significant differences within the groups of data presented in this thesis, all data was first subjected to a Shapiro-Wilk test for normality. Data was considered parametric when $p < 0.05$. Depending on the results the groups of data were subjected to: Ordinary one-way ANOVA test followed by a Tukey's multiple comparisons test (three or more groups of parametric data); Kruskal-Wallis test followed by a Dunn's multiple comparisons test (three or more groups of non-parametric data); two-way ANOVA test followed by Tukey's multiple comparisons test (grouped data); Unpaired t-test (two groups of parametric data). Asterisks indicate respective statistical significance as follows: *$p < 0.05$; **$p < 0.01$; ***$p < 0.001$; and ****$p < 0.0001$.

2.10. B-cell epitope prediction software.

PyMOL was used as a visualisation tool of the eIF2B complex and the localisation of epitopes of primary antibodies that bind to such complex (Rigsby & Parker, 2016). B-cell epitope prediction was performed with the use of BepiPred2.0 (Jespersen *et al*., 2017) and DiscoTope2.0 (Kringelum *et al*., 2012) servers.

2.10.1. Bepipred2.0

BepiPred (version 2.0) (*https://services.healthtech.dtu.dk/services/BepiPred-2.0/*) uses epitope information from crystal structures from the Protein Data Bank (PDB) and predicts linear B-cell epitopes by utilising a Random Forest algorithm examining the physico-reagent characteristics based on the protein sequence.

Epitopes were selected according to the threshold selected (0.5) (Jespersen *et al*., 2017).

2.10.2. DiscoTope2.0

DiscoTope (version 2.0) (*http://tools.iedb.org/discotope/*) uses PDB 3D protein structures to predict discontinuous B-cell epitopes, by analysing the contact numbers to determine surface accessibility. Amino acids are highlighted according to -3.7 threshold (Kringelum *et al*., 2012).

2.10.3. Determining of optimal epitopes

From the results of each server, epitopes predicted as optimal by two or more servers were highlighted and used to compare with antibody paratopes. Total number of amino acids and highlighted optimal epitopes were converted into percentages.

Chapter 3. Optimisation of immunocytochemistry methodology for the detection of endogenous eIF2B foci.

3.1. Introduction.

eIF2B bodies are large assemblies that contain the eIF2B protein complex. In mammalian cells different sized bodies are present, which vary in their subunit composition. Small bodies appear to be largely comprised of catalytic subunits, whereas medium and large bodies include the regulatory subunits (Campbell *et al*., 2005; Campbell & Ashe, 2007; Egbe *et al*., 2015; Hanson *et al*., 2023; Hodgson *et al*., 2019; Norris *et al*., 2021; Nüske *et al*., 2020; Taylor *et al*., 2010). In response to stress, eIF2B subunit localisation changes occur, changing the composition of eIF2B bodies (Hanson *et al*., 2023; Hodgson *et al*., 2019).

To investigate the role of eIF2B bodies in the cell response to stress, ICC has been employed to detect and analyse eIF2B bodies in glial cells. In previous studies, green fluorescent protein (GFP) tagged subunits have been utilised to study the localisation of eIF2B bodies (Campbell *et al*., 2005; Campbell & Ashe, 2007; Egbe *et al*., 2015; Hanson *et al*., 2023; Hodgson *et al*., 2019; Norris *et al*., 2021; Nüske *et al*., 2020; Taylor *et al*., 2010). However, the characterisation of endogenous complexes would allow for analysis of eIF2B bodies in patient samples and animal models of disease.

B-cell epitopes are areas of an antigen typically around five to six amino acids, which prompt an activation of immune response, binding precisely to B-cell antigen receptors. Within the structure of the Fv site of antibodies, the paratope region, *i.e.*, the antigen-antibody site, consists of five to ten amino acids. The paratope recognizes and exclusively binds to its corresponding epitope. It is in this domain where the specific characteristics among antibodies arise (Huston *et al*., 1996; Stave & Lindpaintner, 2013). As such, the innate proclivity that antibodies possess to bind to specific molecules allows the identification of a target protein and the observation of its distribution within cells in situ through techniques such as ICC (Burry, 2010; De Matos *et al*., 2010; Im *et al*., 2019; Renshaw, 2016). There are two main types of epitopes within a protein sequence – continuous, which are linear sequences, and discontinuous, which are present in specific complex conformation brought together by the 3D folding pattern of a

protein (Baruah & Bose, 2020). Like the majority of proteins, most epitopes within the eIF2B complex are expected to be discontinuous (Barlow *et al*., 1986).

Reproducibility and specificity of antibodies are prominent concerns when designing and executing a particular ICC experiment. It is essential that inaccuracies concerning steps within the ICC technique are not perpetuated and that standardization is achieved. In fact, several papers have been allocated to the optimisation of immunofluorescence assays, focusing on the fluorescence topic (Huang *et al*., 2018; Hulspas *et al*., 2009; Szabó *et al*., 2018; LZhou *et al*., 2017), others encompassing fixation variability (Danchenko *et al*., 2019; Hagedorn *et al*., n.d.) and others expanding on the antibody labeling (Laberiano-Fernández *et al*., 2021; Piña *et al*., 2022). This highlights that adequate optimisation is crucial for assays reproducibility, correct detection of target and subsequent analysis. These issues are common throughout techniques that employ antibody-antigen recognition, particularly in detection methods that conserve the native 3D structure of targets.

Bioinformatics, particularly immunoinformatic techniques have been developed for design and optimisation of antibodies, for example in reverse vaccinology (V. Sharma *et al*., 2022). These techniques were used recently in evaluating epitope-based vaccine design against SARS-CoV2 (H.-Z. Chen *et al*., 2020; Dong *et al*., 2020). Additionally, these tools can be applied to other methodologies, such as ICC, where we find molecules that are targeted by antibodies in their native form. *In silico* tools which identify optimal epitopes of proteins of interest can be used to compare commercially available antibodies or to produce custom antibodies, for reliable and optimal immunofluorescent assays.

3.1.1. Hypothesis and rationale

To anatomically visualise and characterise these endogenous cytoplasmic aggregates within fixed cells it is necessary to consider the native structure of these proteins. In contrast to immunoblot techniques, where proteins lose their secondary and tertiary structures through the denaturing process, in the ICC method proteins remain with their native form (Burry, 2011; Willingham, 1999). As such, prior knowledge of the 3D structure of proteins might aid in implementing better practices within the ICC methodology employed to characterise eIF2B foci within mammalian cells. Through an immunoinformatic approach of screening the eIF2B subunit sequence and structure for antigenic and exposed areas, we

hypothesise that this will allow for an improved and reliable detection method of eIF2B foci. To do so, the main objectives to this hypothesis are the following:

- Employ continuous and discontinuous B-cell epitope prediction software's to evaluate the eIF2B complex structure.
- Screen primary antibodies which bind to particular exposed areas.
- Determine fluorescence intensity and number of each eIF2B foci according to different primary, secondary antibodies and under normal and stress conditions.

3.2. Results.

3.2.1. ICC detection of endogenous eIF2B subunits in U373-MG cells

In previous studies, transient transfection using fluorescently tagged eIF2B subunits together with ICC methodology, has allowed the detection and analysis of eIF2B bodies in mammalian cells (Hanson *et al*., 2023; Hodgson *et al*., 2019). However, a comprehensive study of the distribution of endogenous subunits has yet to be carried out.

To determine the localisation of the endogenous eIF2B subunits within cells, ICC analysis was carried out in U373-MG cells, utilising formerly established primary antibodies to each eIF2B subunit. Previously published primary antibodies targeting all five eIF2B subunits were validated by western blot analysis (**Figure 3.1A**) (Hodgson *et al*., 2019). Following from this, ICC targeting the five endogenous eIF2B subunits was performed utilising previously published primary and secondary antibodies and it was possible to observe a population of cells with dispersed signal and localised signal for eIF2Bα-ε subunits (**Figure 3.1B**) (Hodgson *et al*., 2019). Initial analysis of 30 cells per repeat with endogenous eIF2B cytoplasmic foci showed that eIF2Bα foci exhibited high fluorescence intensity (quantified through arbitrary units – a.u.) with a mean of 44.33 a.u. (± 10.10), followed by eIF2Bβ and δ foci, with a mean of 16.85 a.u. (± 4.93), 9.74 a.u. (± 2.70), respectively. eIF2Bγ, and particularly eIF2Bε displayed weaker intensity, with a fluorescence mean of 7.88 a.u. (± 2.59) and 4.61 a.u. (± 3.04), respectively (**Figure 3.1C**). Additionally, the number of eIF2B localised foci per cell differed greatly between each subunit (**Figure 3.1D**). In a population of 30 cells per repeat, a mean of 4.61 eIF2Bα foci (± 3.67), 5.19 eIF2Bβ foci (± 3.47), 2.31 eIF2Bγ foci (± 1.32), 3.68 eIF2Bδ foci (± 2.71), and 1.49 eIF2Bε foci (± 0.77) per cell was detected.

Given the discrepancies observed and to ensure that the characterisation of the endogenous proteins was accurate, secondary antibodies with different fluorescent labels and antibody structures were utilised. Alpaca Fc anti-mouse conjugated to AlexaFluor 647 and alpaca Fc anti-rabbit conjugated to AlexaFluor 488 not only failed to enhance the signal of the targeted subunits, but also revealed lower mean fluorescence intensity values than AlexaFluor 488 anti-mouse and AlexaFluor 568 anti-rabbit secondary antibodies, and detected fewer foci within U373-MG cells (**Figure 3.2A**). The mean fluorescence intensity was

studied, with eIF2Bα displaying 16.49 a.u. (± 13.94), eIF2Bβ displaying 18.60 a.u. (± 11.61), eIF2Bγ displaying 7.52 a.u. (± 1.81), eIF2Bδ displaying 14.17 a.u. (± 4.01), and eIF2Bε displaying 10.10 a.u. (± 1.88) (**Figure 3.2B**). The mean number of detected eIF2B foci per cell was the following: eIF2Bα 1.18 (± 0.39), eIF2Bβ 1.06 (± 0.25), eIF2Bγ 1.14 (± 0.35), eIF2Bδ 1.64 (± 0.90), and eIF2Bε 1.88 (± 1.40) (**Figure 3.2C**). It should be noted that a panel of different dilutions of the Alpaca secondary antibodies were tested with the goal of increasing fluorescence intensity, but no changes were seen (data not shown).

Anti-mouse and anti-rabbit AlexaFluor 594 conjugated secondary antibodies were subsequently utilised to eliminate excitation/emission discrepancies in the detection of distinct subunits (**Figure 3.3A**). eIF2Bα and eIF2Bβ showed mean fluorescence intensity of 42.34 a.u. (± 13.33) and 41.40 a.u. (± 11.98), respectively. eIF2Bδ displayed the third highest mean fluorescence intensity with 14.49 a.u. (± 3.90), followed by eIF2Bγ and eIF2Bε which exhibited a mean fluorescence intensity of 8.39 a.u. (± 2.05) and 4.47 a.u. (± 2.09), respectively (**Figure 3.3B**). Additionally, a difference in the number of foci detected per cell was also observed. In U373-MG cells, a mean number per cell of 4.611 (± 3.67) eIF2Bα foci, 5.19 (± 3.47) eIF2Bβ foci, 2.31 (± 1.33) eIF2Bγ foci, 3.68 (± 2.71) eIF2Bδ foci, and 1.49 (± 0.77) eIF2Bε foci (**Figure 3.3C**) was detected.

While Alexa Fluor 594 conjugated secondary antibodies improved overall results, the values of intensity and number of localised foci varied according to the subunit detected. eIF2Bα, β and δ generally appeared to have clear and strong signals with minimal background, while eIF2Bγ and ε displayed low intensity signals with all secondary antibodies used.

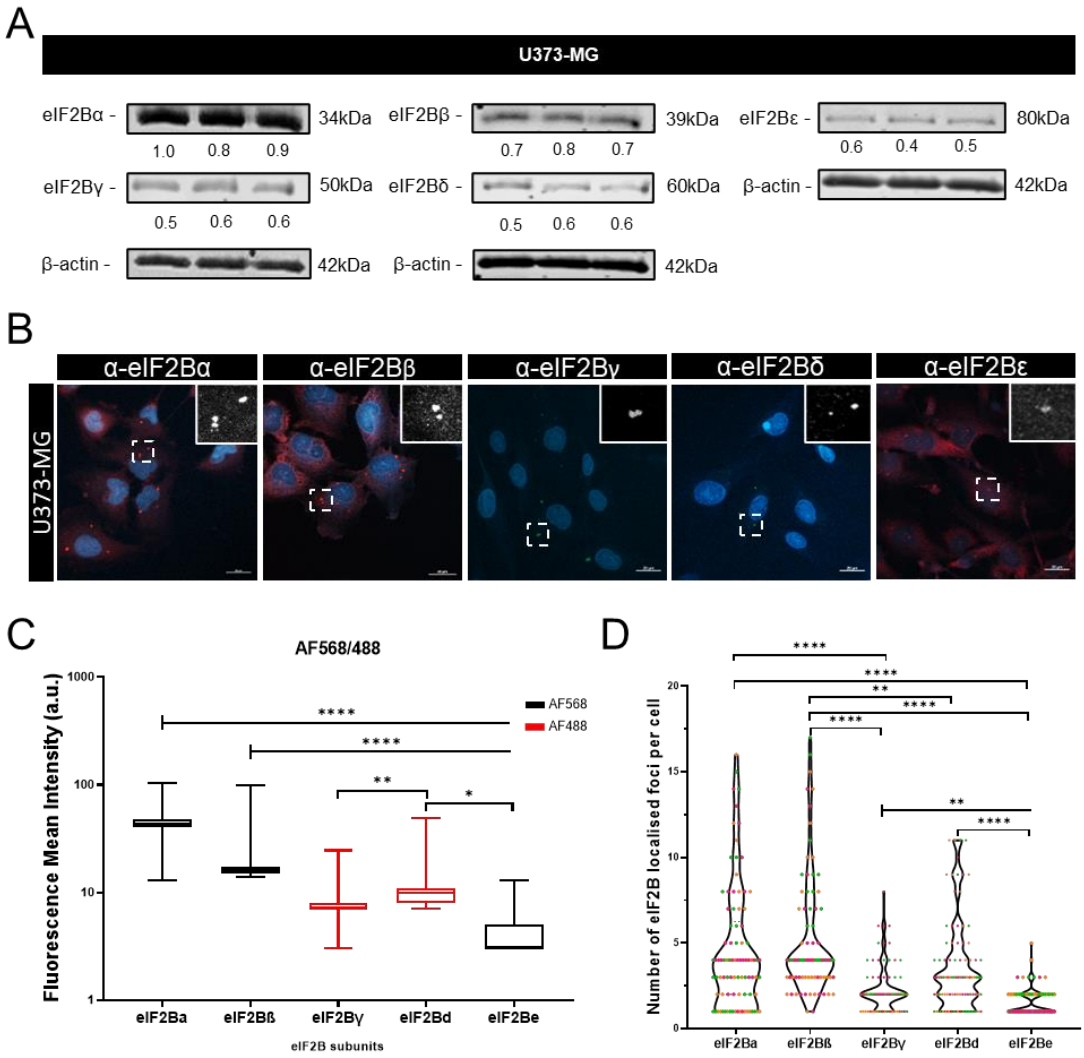

Figure 3.1. eIF2B subunits are detected in U373-MG cells with varying fluorescence intensity.

(A)Western Blot analysis of eIF2Bα-ε utilising previously validated primary antibodies, each lane representing a single biological replicate. Levels of eIF2Bα-ε were normalized to levels of β-actin. (B)Representative images of U373-MG cells fixed in methanol and subject to ICC with primary anti-eIF2Bα, anti-eIF2Bβ, anti-eIF2Bγ, anti-eIF2Bδ and anti-eIF2Bε, and visualised using Alexa Fluor 568 conjugated secondary antibody for eIF2Bα, β and ε subunits and Alexa Fluor 488 conjugated secondary antibody for eIF2Bγ and δ; DAPI stained nuclei. Scale bar = 20 μm. (C)Fluorescence mean intensity of endogenous eIF2B subunits visualised using appropriate Alexa Fluor 568 and 488 conjugated secondary antibodies, in U373-MG cells (n=3 counts of 30 cells), p values were derived from a Kruskal-Wallis test, followed by a Dunn's multiple analysis. *p ≤ 0.05; **p ≤ 0.01; * * * *p ≤ 0.0001. (D) Number of eIF2B localised foci per cell detected in U373-MG cells visualised with appropriate Alexa Fluor 568 and 488 conjugated secondary antibodies (n=3 counts of 30 cells, n=1 in pink, n=2 in orange and n=3 in green), p values were derived from a Kruskal-Wallis test, followed by a Dunn's multiple analysis. **p ≤ 0.01; * * * *p ≤ 0.0001.

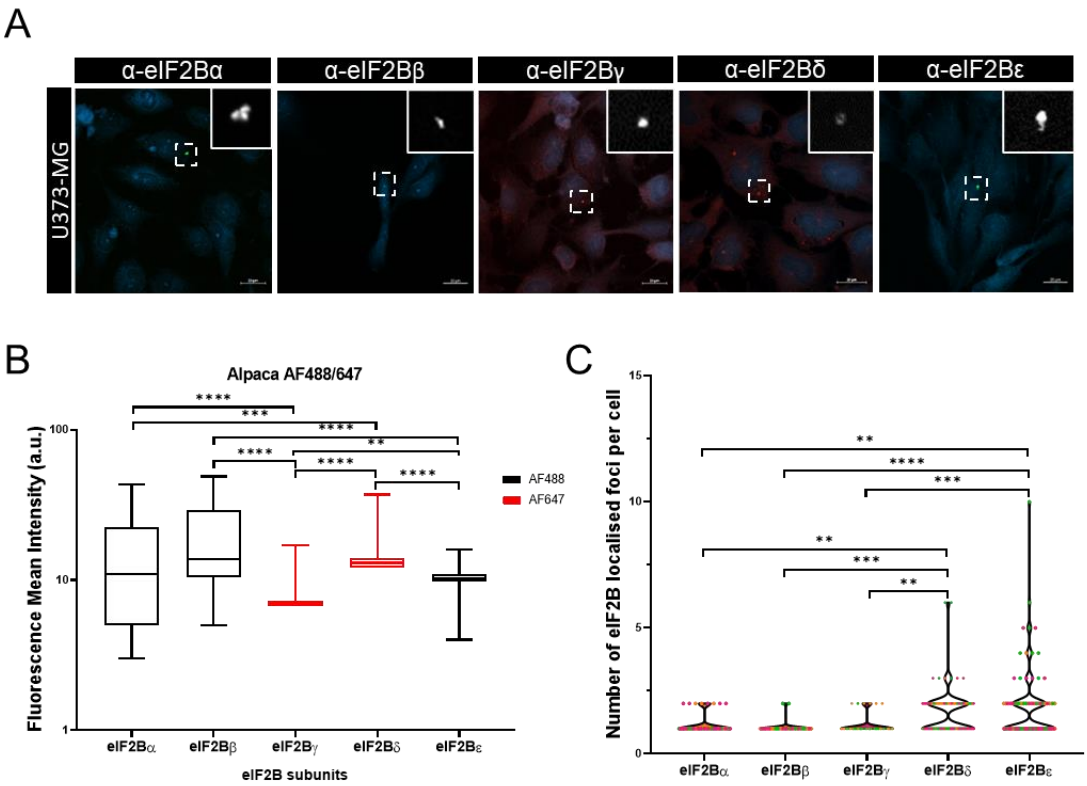

Figure 3.2. Alpaca AlexaFluor antibodies does not increase eIF2B foci fluorescence.
(A)Representative images of U373-MG cells fixed in methanol and subject to ICC with primary anti-eIF2Bα, anti-eIF2Bβ, anti-eIF2Bγ, anti-eIF2Bδ and anti-eIF2Bε, and visualised using Alpaca AlexaFluor 488 conjugated secondary antibody for eIF2Bα, β and ε subunits and Alpaca AlexaFluor 647 conjugated secondary antibody for eIF2Bγ and δ; DAPI stained nuclei. Scale bar = 20 μm. (B)Fluorescence mean intensity of endogenous eIF2B subunits visualised using appropriate Alpaca AlexaFluor 488 and Alpaca AlexaFluor 647 conjugated secondary antibodies, in U373-MG cells (n=3 counts of 30 cells), p values were derived from a Kruskal-Wallis test, followed by a Dunn's multiple analysis. **p ≤ 0.01; ***p ≤ 0.001; * * * *p ≤ 0.0001. (C)Number of eIF2B localised foci per cell detected in U373-MG cells visualised with appropriate Alpaca AlexaFluor 488 and Alpaca AlexaFluor 647 conjugated secondary antibodies (n=3 counts of 30 cells, n=1 in pink, n=2 in orange and n=3 in green), p values were derived from a Kruskal-Wallis test, followed by a Dunn's multiple analysis. **p ≤ 0.01; ***p ≤ 0.001; * * * *p ≤ 0.0001.

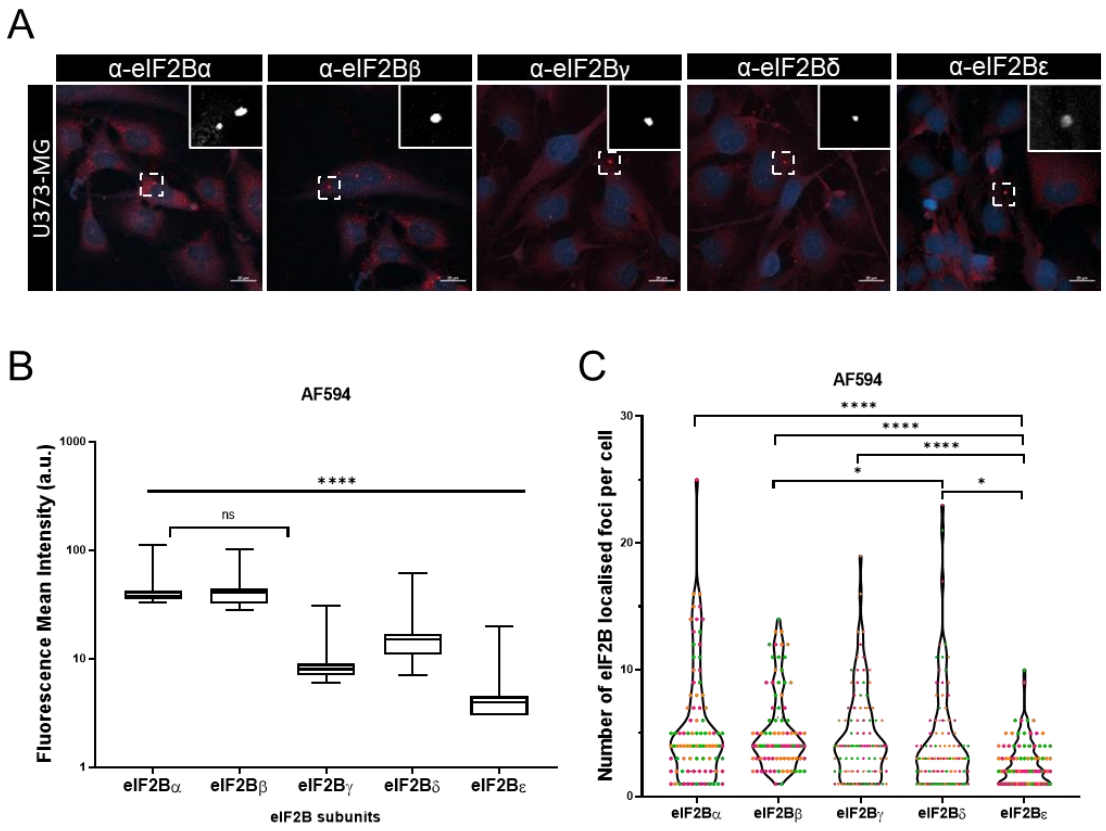

Figure 3.3. AlexaFluor 594 secondary antibodies does not eliminate variability of fluorescence and number of detected eIF2B foci.

(A)Representative images of U373-MG cells fixed in methanol and subject to ICC with primary anti-eIF2Bα, anti-eIF2Bβ, anti-eIF2Bγ, anti-eIF2Bδ and anti-eIF2Bε, and visualised using AlexaFluor 594 conjugated secondary antibody for eIF2Bα-ε subunits; DAPI stained nuclei. Scale bar = 20 μm. (B) Fluorescence mean intensity of endogenous eIF2B subunits visualised using appropriate AlexaFluor 594 conjugated secondary antibodies, in U373-MG cells (n=3 counts of 30 cells), p values were derived from a Kruskal-Wallis test, followed by a Dunn's multiple analysis. * * * *p ≤ 0.0001.(C) Number of eIF2B localised foci per cell detected in U373-MG cells visualised with appropriate AlexaFluor 594 conjugated secondary antibodies (n=3 counts of 30 cells, n=1 in pink, n=2 in orange and n=3 in green), p values were derived from a Kruskal-Wallis test, followed by a Dunn's multiple analysis. *p ≤ 0.05; * * * *p ≤ 0.0001.

3.2.2. Bioinformatic analysis of the eIF2B subunits identifies viable eIF2B epitopes.

As the varying level of fluorescence intensities observed upon ICC analysis of specific eIF2B subunits was not related to the wavelength or structure/subtype of the secondary antibody utilised, we next focused our investigation on improving the specificity of the primary antibodies. In order to select optimal primary antibodies, B-cell epitope prediction of each eIF2B subunit was carried out using BepiPred2.0 (Jespersen *et al*., 2017) and DiscoTope2.0 (Kringelum *et al*., 2012). These B-cell epitope analysis programs were used to predict particularly exposed and optimal antigenic areas for each eIF2B subunit, a methodology already utilised in other fields such as vaccine development (Chen *et al*., 2020). This made it possible to compare these predicted antigenic sites to the epitopes of existing primary antibodies. Exposed and antigenic sites could be altered by different conformations of the eIF2B•eIF2 complex, *i.e.*, productive versus non-productive, or by molecules bound to the eIF2B structure (Kashiwagi *et al*., 2019; Kenner *et al*., 2019; Tsai *et al*., 2018; Zyryanova *et al*., 2018, 2021). As such, various structures with differing configurations of the eIF2B complex were used in each B-cell prediction server (**Table 3.1**).

Antigenic and exposed areas of eIF2B subunits were identified using BepiPred2.0 with a 0.5 threshold configuration (**Figures 3.4**) and DiscoTope2.0 with a ≥ -3.7 threshold configuration (**Figures 3.5**). Amino acids highlighted by the two servers were compiled for each of the five eIF2B subunits (**Figure 3.6**). Single amino acids were considered due to the possibility of being part of a discontinuous epitope area (composed of an arrangement of several isolated amino acids), as illustrated in **Figure 3.7**.

Table 3.1. PDB IDs of eIF2B complex 3D structures.

PDB ID	Species	Small molecules	eIF2α phosphorylation status	Productive/Non-productive	Reference	Notes
6CAJ	Human	ISRIB	eIF2 not present	-	Tsai, *et al.,* 2018	eIF2Bε catalytic domain not included
6K71	Human	-	Unphosphorylated	Productive	Kashiwagi *et al.,* 2019	One molecule of eIF2 bound; eIF2Bε catalytic domain included
6K72	Human	-	Phosphorylated	Non-productive	Kashiwagi *et al.,* 2019	Two molecules eIF2 bound; eIF2Bε catalytic domain not included
6O9Z	Human	ISRIB	Phosphorylated	Non-productive	Kenner *et al.,* 2019	Two molecules of eIF2 bound, eIF2Bε catalytic domain included
6O81	Human	ISRIB	Unphosphorylated	Productive	Kenner *et al.,* 2019	Two molecules of eIF2 bound; eIF2Bε catalytic domain included
6O85	Human	ISRIB	Unphosphorylated	Productive	Kenner *et al.,* 2019	One molecule of eIF2 bound; eIF2Bε catalytic domain included
6EZO	Human	ISRIB	eIF2 not present	-	Zyryanova, *et al.,* 2018	eIF2Bε catalytic domain not included
7D45	Human	PHOSPHONOSERINE	Phosphorylated	Non-productive	Zyryanova, *et al.,* 2021	aP1 complex; eIF2Bε catalytic domain not included
7D44	Human	PHOSPHONOSERINE	Phosphorylated	Non-productive	Zyryanova, *et al.,* 2021	aP2 complex; eIF2Bε catalytic domain not included
7D43	Human	PHOSPHONOSERINE	Phosphorylated	Non-productive	Zyryanova, *et al.,* 2021	αPγ complex, two molecules of eIF2 alpha bound; eIF2Bε catalytic domain not included
7D46	Human	PHOSPHONOSERINE	eIF2 not present	-	Zyryanova, *et al.,* 2021	eIF2Bε catalytic domain not included

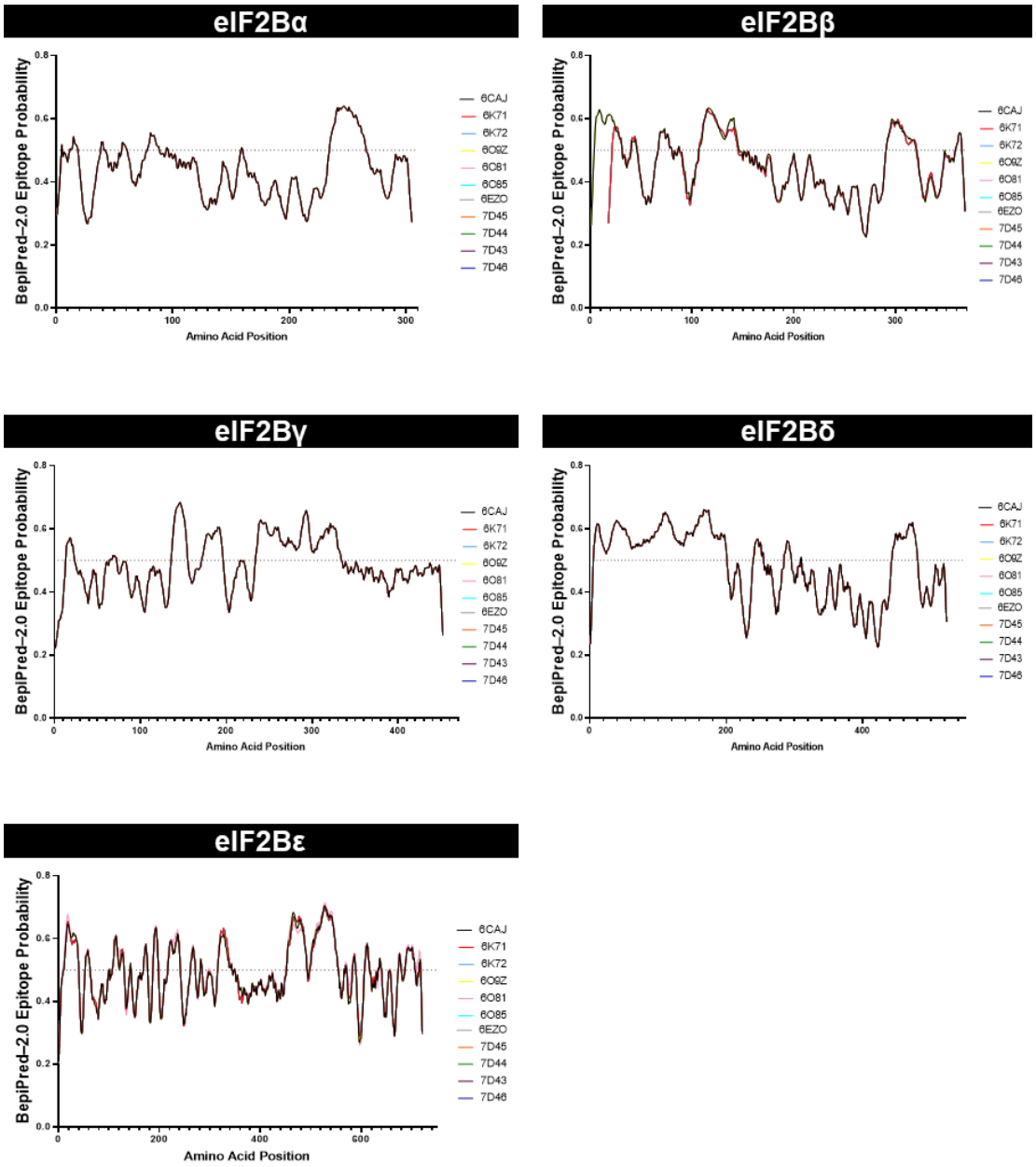

Figure 3.4. eIF2B epitope prediction using BepiPred–2.0.

Epitope probability score with 0.5 threshold of eIF2Bα-ε using PDB FASTA sequence described in table 3.1.

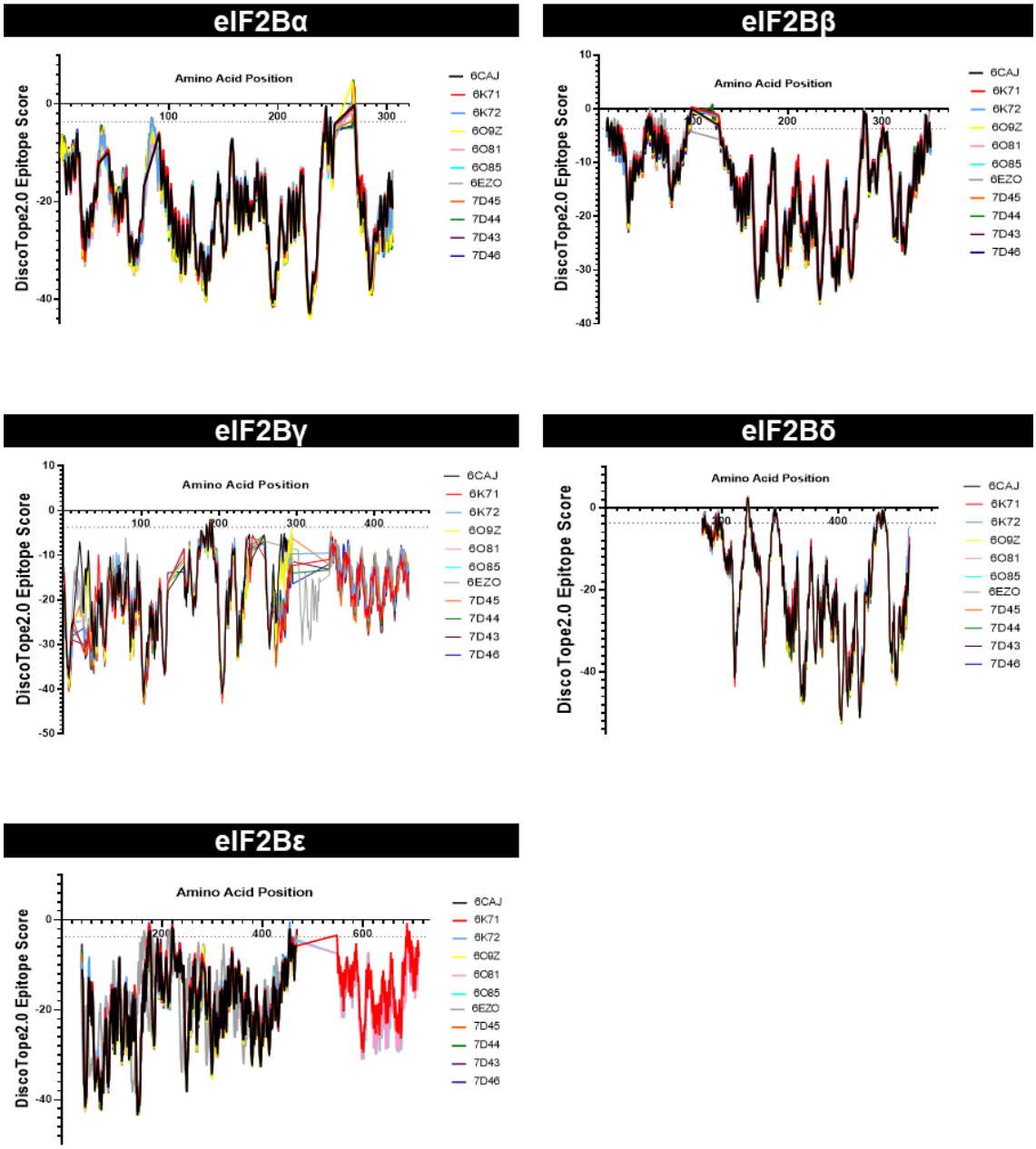

Figure 3.5. eIF2B epitope prediction using DiscoTope2.0.

DiscoTope2.0 Score with a ≥ -3,7 threshold of eIF2Bα-ε using PDB FASTA sequence described in table 3.1.

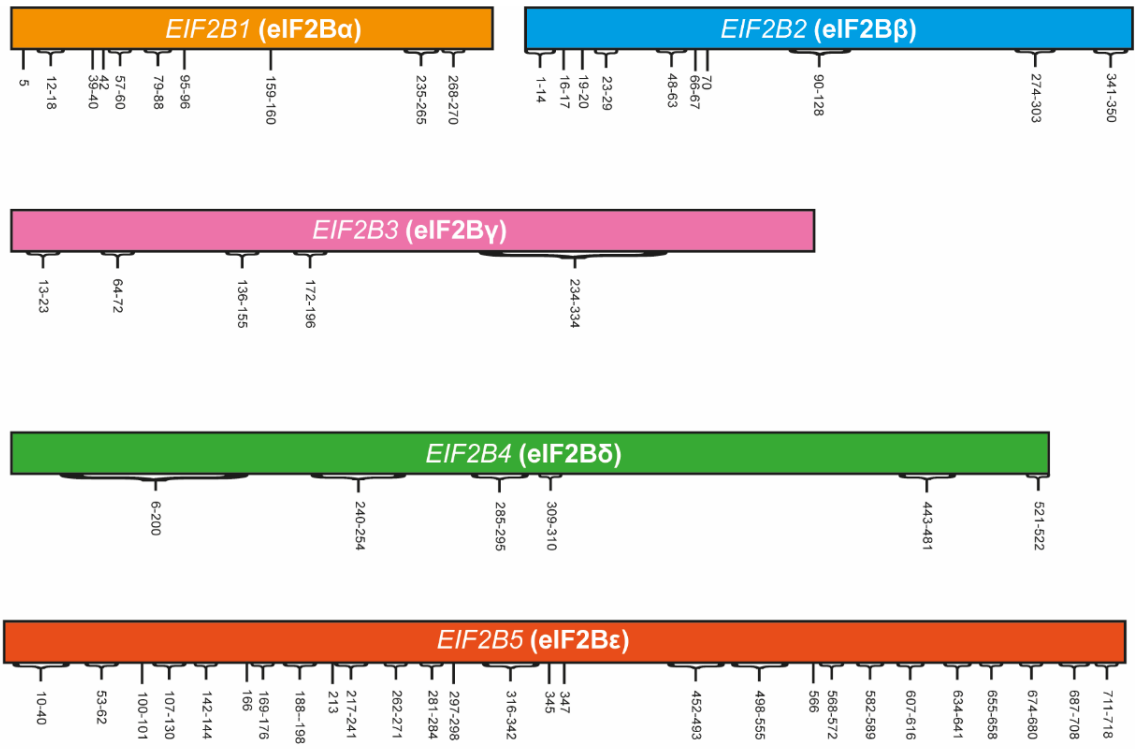

Figure 3.6. eIF2B epitope prediction using BepiPred–2.0 and DiscoTope2.0.

Amino acids highlighted by BepiPred-2.0 and DiscoTope2.0 servers for eIF2Bα-ε mapped.

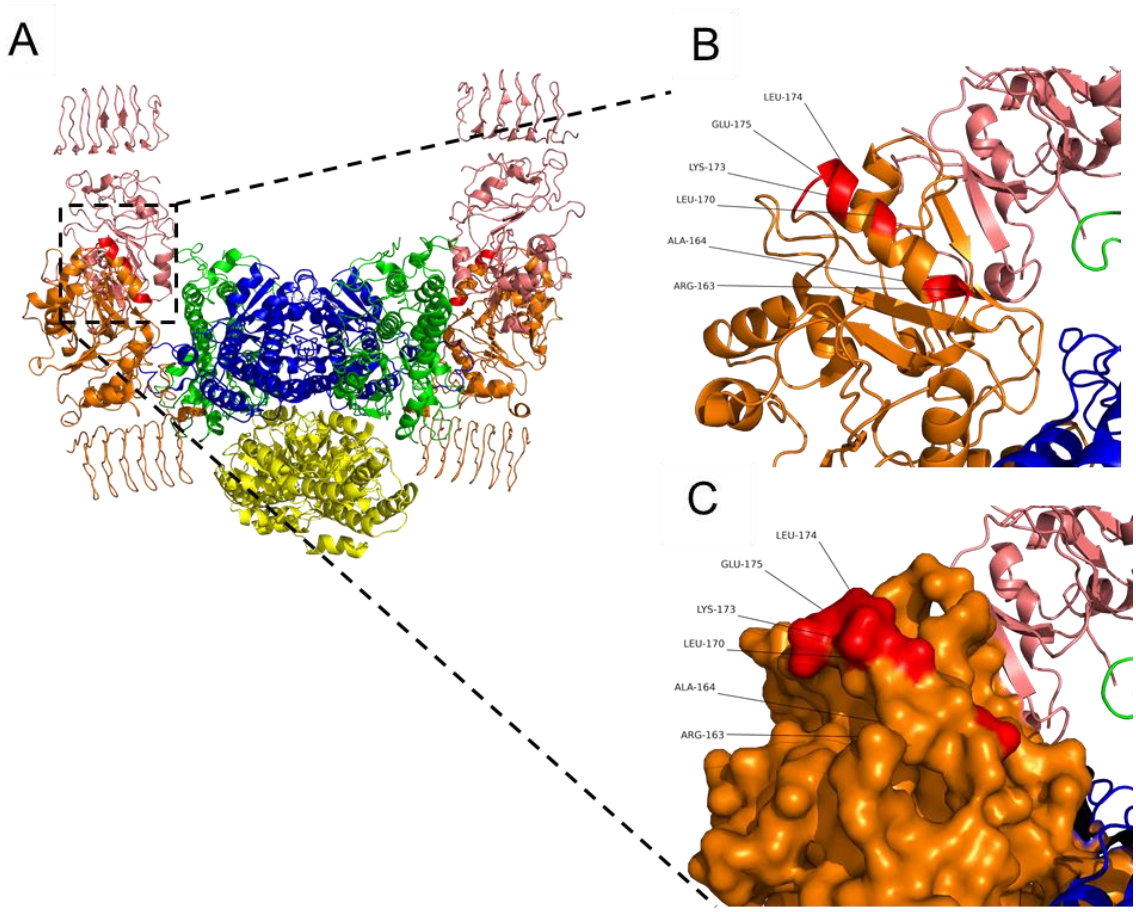

Figure 3.7. Bioinformatic tools are able to identify discontinuous epitopes.
Example of an eIF2Bε discontinuous epitope (PDB code: 6ezo; Zyryanova *et al.,* 2018), from the highlighted epitopes in figure 3.6. In each rendering, the residues that are part of the highlighted epitope are coloured in red, eIF2Bα is coloured yellow, eIF2Bβ is coloured blue, eIF2Bγ is coloured pink, eIF2Bδ is coloured green, and eIF2Bε is coloured orange. (A) eIF2B complex represented as ribbons. (B) Epitope consisted of separate residues represented as ribbons; (C) Surface rendering of the epitope.

3.2.3. Predicted epitope sequences allow selection of commercially available primary antibodies targeting eIF2Bε.

Given the essential function of the eIF2Bε subunit and the predominant number of VWMD mutations within the *EIF2B5* gene and suboptimal results that we obtained detailed in **3.2.1**, we focused our efforts on the optimisation of the detection of this particular subunit. Following epitope analysis, a search was carried out using The Human Protein Atlas (*https://www.proteinatlas.org*), to identify additional commercially available primary antibodies targeting the eIF2Bε subunit. The amino acid sequence of the immunogens for the original primary antibody, ARP61329_P050, and two other commercially available primary antibodies, HPA064370 and HPA069303, were compared with the predicted epitope amino acids highlighted by the two servers (**Figure 3.8**). Subsequently, the number of amino acids and the matching amino acids were converted into percentages (full sequence = 100 %) to cross-compare. Surprisingly, the initially used antibody, ARP61329_P050, displayed the highest percentage of matching amino acids with the predicted epitopes identified by both BepiPred-2.0 and DiscoTope2.0, suggesting that this antibody is optimal for the detection of the eIF2Bε subunit (**Table 3.2**). However, when isolating the epitopes predicted by the DiscoTope2.0 server, only HPA064370 and HPA069303 exhibited a value of matching amino acids, while ARP61329_P050 primary antibody did not (**Table 3.2**). The epitopes identified by Discotope2.0 within the eIF2B decameric structure were illustrated in **Figure 3.9**.

To determine if the HPA064370 and HPA069303 antibodies displayed a higher fluorescence intensity than the previously used antibodies, ICCs using these antibodies were carried out (**Figure 3.10A**). In addition, these ICCs were conducted in the absence or presence of ER stress induction (**Figure 3.11**), to determine whether the detection of eIF2Bε was altered by conformational changes caused by binding of phosphorylated eIF2α. An increase of mean fluorescence intensity was shown for HPA064370 (26.62 a.u. ± 11.18 in normal conditions; 30.15 a.u. ± 12.07 following stress treatment) and HPA069303 (37.47 a.u. ± 12.72 in normal conditions; 31.36 a.u. ± 10.03 following stress treatment) primary antibodies when compared with ARP61329_P050 (6.49 a.u. ± 3.63 in normal conditions; 7.64 a.u. ± 2.91 following stress treatment) (**Figure 3.10B**).

Additionally, both HPA064370 (mean of 3.09 ± 1.63 foci per cell) and HPA069303 (mean of 3.69 ± 2.28 foci per cell) primary antibodies identified a greater number of eIF2Bε localised foci per cell when compared to ARP61329_P050 (mean of 2.16 ± 1.56 foci per cell), closer to the values obtained for the other eIF2B subunits (**Figure 3.10C**). The number of eIF2Bε foci detected with HPA064370 and HPA069303 primary antibodies increased upon Tg treatment, while eIF2Bε detection by ARP61329_P050 did not show similar results (ARP61329_P050 - mean of 2.38 ± 1.34 foci per cell; HPA064370 – mean of 8.17 ± 4.73 foci per cell; and HPA069303 – mean of 7.84 ± 5.49 foci per cell) (**Figure 3.10C**).

The percentage of cells with endogenous eIF2Bε localisation was analysed utilising the different primary antibodies targeting the eIF2Bε subunit in U373-MG cells. The percentage of cells with localised eIF2Bε foci was statistically significant between the three primary antibodies to eIF2Bε, with both HPA064370 and HPA069303 increasing the detection percentage of cells with eIF2Bε foci (eIF2BεARP – 12.00 % ± 2.65; eIF2Bε30 – 29.00 % ± 2.00; eIF2Bε70 – 21.00 % ± 1.00) (**Figure 3.10D**).

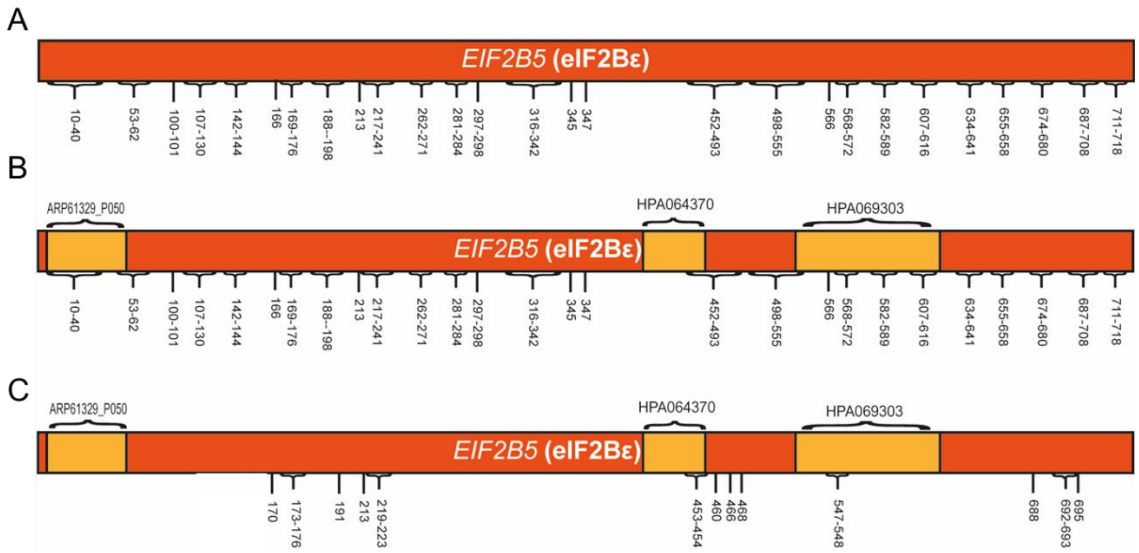

Figure 3.8. eIF2Bε amino acids predicted as viable epitope regions.

(A) Amino acids highlighted by both epitope prediction servers (BepiPred-2.0 and DiscoTope2.0) for the eIF2Bε subunit; (B) Amino acids highlighted by both epitope prediction servers (BepiPred-2.0 and DiscoTope2.0) for the eIF2Bε subunit and the binding sites of primary antibodies that target this protein; (C) Amino acids highlighted by DiscoTope2.0 for the eIF2Bε subunit and the binding sites of primary antibodies that target this protein.

Table 3.2. Percentage of matching amino acids highlighted by B-cell epitope prediction servers with the paratopes of utilised/recommended ICC primary antibodies.

(a) Recommended by Human Protein Atlas.

	Primary antibody ID	% Matching aa with both servers	% Matching aa with DiscoTope2.0
Utilized	ARP61329_P050	76%	0%
Recommended[a]	HPA069303	43%	3%
Recommended[a]	HPA064370	4%	2%

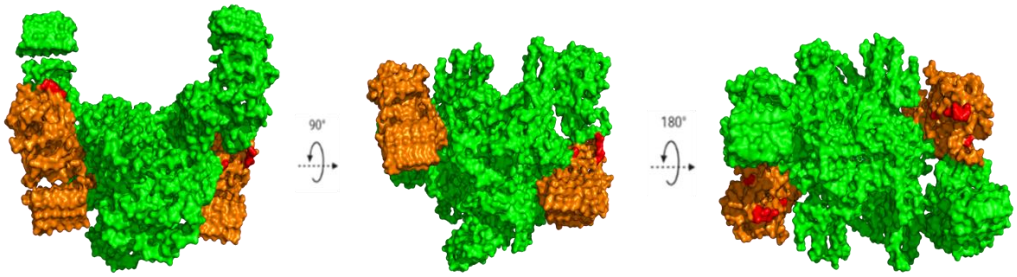

Figure 3.9. PyMOL mapping of DiscoTope2.0 highlighted eIF2Bε epitopes.

Green – eIF2B complex; yellow – eIF2Bε; red – Highlighted epitopes (PDB code: 6EZO, Zyryanova *et al.,* 2018).

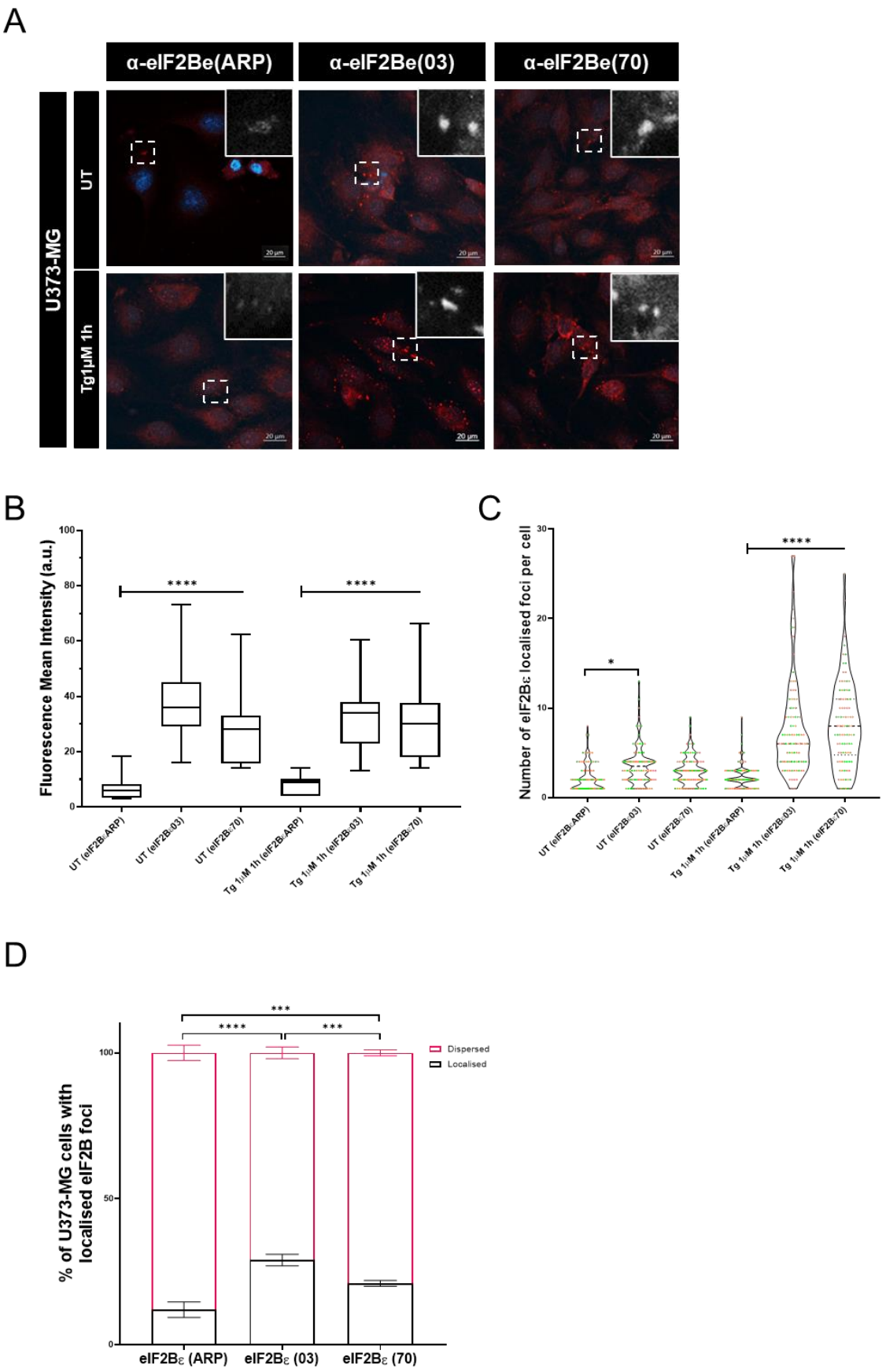

Figure 3.10. Immunoinformatics optimisation of primary antibodies results in an increase in mean fluorescence intensity of eIF2Bε localisation.

(A) Confocal images of endogenous eIF2Bε localised foci in U373-MG cells. Cells were treated with vehicle or 1μM Tg for 1 hour (UT – untreated). Scale bar – 20 μm; (B) Fluorescence mean intensity analysis of U373-MG cells subject to ICC with three primary antibodies to the eIF2Bε subunit. Cells were treated with vehicle or 1μM Tg for 1 hour (n=3, counts of 30 cells). p values were derived from a one-way ANOVA, followed by a Tukey's analysis, ****p ≤0.0001; (C) Number of eIF2Bε localisation detected in a population of U373-MG cells with ARP61329_P050, HPA069303 and HPA064370 primary antibodies targeting eIF2Bε. Cells were treated with vehicle or 1μM Tg for 1 hour (n=3 counts of 30 cells, n=1 in pink, n=2 in orange and n=3 in green). p values were derived from a one-way ANOVA, followed by a Tukey's analysis, **p ≤0.01 and ****p ≤ 0.0001; (D) Percentage of U373-MG cells with eIF2Bε localisation (n=3, counts of 100 cells). p values were derived from a two-way ANOVA test, followed by a Sidak's analysis, ***p ≤ 0.001 and ****p ≤ 0.0001.

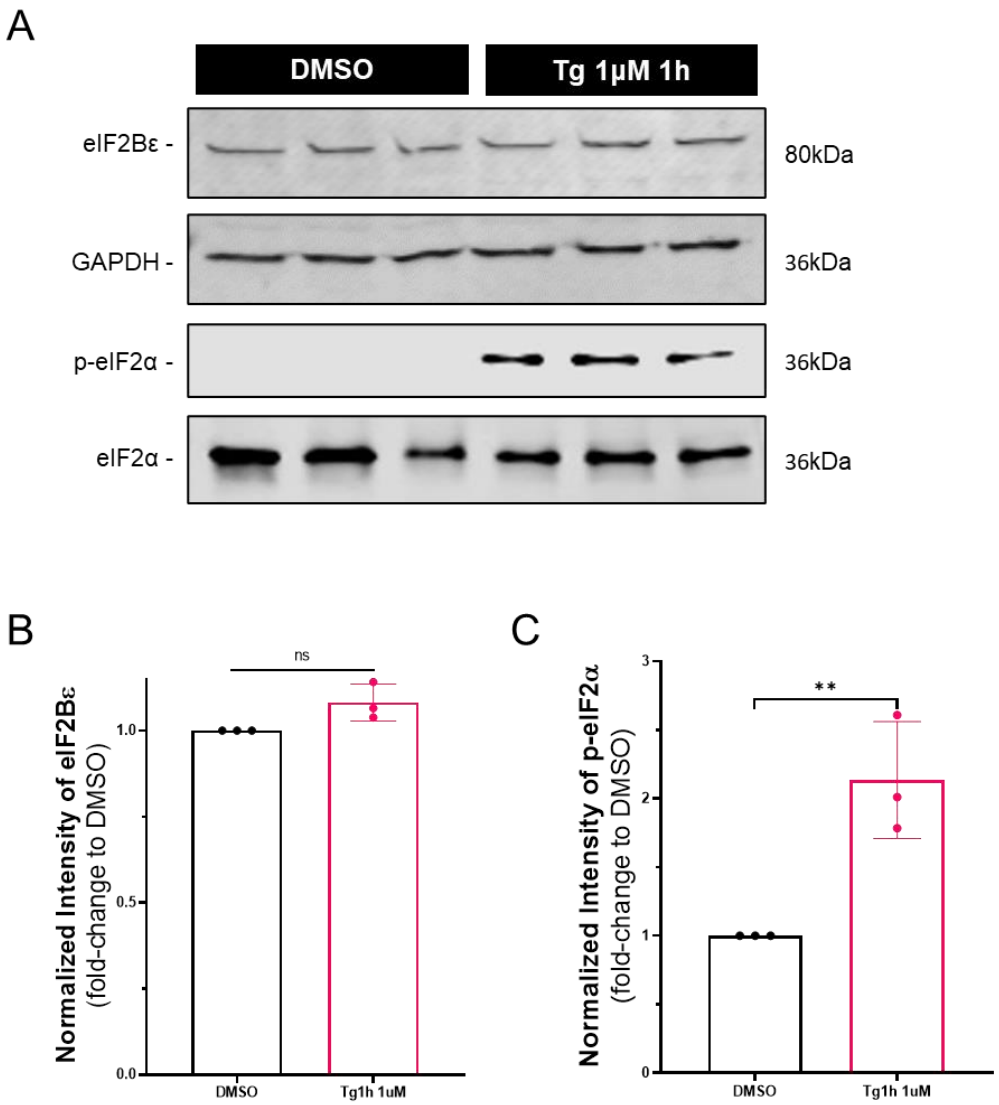

Figure 3.11. Expression levels of eIF2Bε following Tg treatment.

Western blot analysis of the level of eIF2Bε, p-eIF2α and total eIF2α expression in U373-MG cells either treated with DMSO or with 1μM Tg to induce cellular stress. Each lane representing a single biological replicate. Levels of eIF2Bε were normalized to levels of GAPDH (n=3). Levels of p-eIF2α were normalized to levels of total eIF2α (n=3). *p* values were derived from an unpaired t-tes. ***p* ≤0.01.

3.3. Discussion.

3.3.1. Endogenous eIF2B subunit localisation showed to be affected according to primary antibody utilised.

The eIF2B complex is known to localise to cytoplasmic foci, termed eIF2B bodies (Campbell *et al*., 2005; Hanson *et al*., 2023; Hodgson *et al*., 2019; Moon & Parker, 2018; Norris *et al*., 2021). However, the characterisation of these protein complexes was carried out utilising exogenously expressed GFP tagged proteins (Campbell *et al*., 2005; Campbell & Ashe, 2007; Egbe *et al*., 2015; Hodgson *et al*., 2019; Norris *et al*., 2021; Nüske *et al*., 2020). Additionally, due to the potential significance of localisation within a disease context, particularly VWMD and PNDM, the characterisation of endogenous eIF2B localisation would allow the analysis of endogenous mutant proteins within patient cells or animal models. Thus, the aim of this chapter was to optimise the detection and analysis of endogenous eIF2B foci in a glial cell line.

Initially, ICC methodology in U373-MG cells was carried out using previously published primary and secondary antibodies (Hodgson *et al*., 2019) (**Figure 3.1A and 3.1B**). Endogenous eIF2B subunits were found to localise into cytoplasmic foci, as previously observed (**Figure 3.1B**); however, an inconsistency in the detected signal intensity and number of localised foci across the subunits was observed (**Figure 3.1C and 3.1D**).

Currently, there are a wide variety of fluorescent probes for imaging, however, finding the ideal antibody labelled with a fluorescent tag is a critical challenge. Fluorescent proteins are sensitive to methods of conjugation, degree of labelling and nonspecific adsorption of non-target proteins, and an extensive number of papers have been published dedicated to optimising the detection of physiological and pathological markers in immunofluorescent techniques (Huang *et al*., 2018; Hulspas *et al*., 2009; Szabó *et al*., 2018; L. Zhou *et al*., 2017).

To overcome inconsistencies of the signal intensity observed, we utilised Nano-alpaca Fc-conjugated anti-Mouse 647 and Nano-alpaca Fc-conjugated anti-Rabbit 488 secondary antibodies (**Figure 3.2A**). These particular antibodies are smaller compared to conventional secondary antibodies, providing a better epitope access and decreasing any disparity between the fluorescent signal and the target antigen. However, low levels of fluorescence intensity and a decrease

in the number of eIF2B bodies were observed (**Figure 3.2B and 3.2C**). While further optimisation for the use of these antibodies could lead to better results, we proposed that by having different excitation wavelengths for the different five eIF2B subunits could lead to further variability. As such, Alexa Fluor anti-mouse and anti-rabbit 594 were utilised (**Figure 3.3A**). These secondary antibodies displayed improved signals, nonetheless antibodies targeting the eIF2Bγ and ε subunits displayed weaker intensity throughout the range of secondary antibodies (**Figure 3.3B**). Additionally, a lower number of localised eIF2Bε foci was detected when compared to other eIF2B subunits (**Figure 3.3C**). When comparing the different mean fluorescence intensity levels of endogenous eIF2B foci, the results were not dependent on the antibody species, since the subunits with the lower intensity are seen with both anti-mouse and anti-rabbit secondary antibodies. This variability in foci number could be due to the localisation pattern of eIF2B subunits characteristic of U373-MG cells, or due to low intensity signals, which appears to not be only influenced by secondary antibodies, but also primary antibody selection.

3.3.2. Insights into B-cell epitope prediction programs for primary antibody selection

A range of computational methods using machine learning techniques have been developed to accurately predict *in silico* conformational B-cell epitopes (Bukhari *et al*., 2022). These programs are currently being used mainly for epitope-based peptide vaccine design, drug design and disease diagnostics (Galanis *et al*., 2021; Hua *et al*., 2017; Ras-Carmona *et al*., 2022; Schaap-Johansen *et al*., 2021).

Antibodies recognise their antigenic targets through interactions between their binding site (paratope) and a particular portion of the antigen (epitope). Epitopes can be either continuous – linear amino acid sequences – or and discontinuous (Moreau *et al*., 2006). Most B-cell epitopes are discontinuous, *i.e.*, comprised of residues that are separated in the amino acid sequence and brought in spatial proximity by protein folding (Kringelum *et al*., 2012, 2013).

The primary antibodies used for the ICC methodology were examined as a possible cause for the discrepancies in fluorescence intensity and number of foci detected for the individual subunits. When choosing a primary antibody, it is

important to consider the methodology being employed. Western blot analysis utilises antibodies to target the linear structure of unfolded proteins. On the other hand, ICC analysis employs primary antibodies that target proteins with intact native conformation form (Bordeaux *et al*., 2010). As such, the surface accessibility of targeted epitopes is an important topic to consider when choosing primary antibodies for ICC. This is particularly important for the eIF2B complex, which is a complex of five different proteins and has been shown to alter its conformation in response to interaction with molecules such as p-eIF2α or the ISR modulator ISRIB (Marintchev & Ito, 2020; Schoof *et al*., 2021; Zyryanova *et al*., 2021). This conformational change within the eIF2B decamer may in turn change the epitope accessibility. An array of human eIF2B structures were analysed, representing the productive (eIF2B•eIF2) and non-productive (eIF2B•p-eIF2α), structures of the eIF2B complex. Additionally, structures bound to ISRIB have been analysed (**Table 3.1**).

To determine viable and exposed epitopes of the eIF2B subunits, two distinct B-cell epitope programmes were used: BepiPred – 2.0 (linear B-cell epitope prediction programme that uses epitope information obtained from a protein sequence to examine the physico-chemical characteristics utilising a Random Forest algorithm) (**Figure 3.4**); DiscoTope2.0 (discontinuous B-cell epitope prediction server uses the 3D structure information of a protein, such as contact numbers, which is the spatial distance between residue-residue of 3D structures) (Jespersen *et al*., 2017; Kringelum *et al*., 2012) (**Figure 3.5**). Both of these programmes are open sourced and can be easily utilised for B-cell epitope prediction purposes.

Amino acids highlighted by the two servers for each eIF2B subunit were determined (**Figure 3.6**) and single amino acids were not excluded from the analysis due to potential conformational structures of the complex which could then lead to discontinuous epitopes, as observed in **Figure 3.7**. Several potential epitopes were highlighted, which would then provide a template for comparison with commercially available primary antibodies targeting eIF2B subunits with low fluorescence intensity and few detected foci.

3.3.3. Potential B-Cell Epitope Prediction method for optimisation of immunofluorescence techniques and future implications

The evaluation between the results from the B-cell epitope prediction programmes and commercially available primary antibodies requires the immunogen information for the respective targets. We investigated the eIF2Bε subunit in more detail given the low fluorescence intensity and low number of foci detected. The regions of the eIF2Bε protein used to raise the primary antibodies ARP61329_P050, HPA069303 and HPA064370 were compared to the bioinformatic analysis of epitopes within the eIF2Bε subunit (**Table 3.2 and Figure 3.8**). From this, it was found that ARP61329_P050 had the highest percentage match between the region used to raise the antibody and antigenic regions within the eIF2Bε protein (**Table 3.2 and Figure 3.8B**).

As DiscoTope2.0 is the only server utilised that identifies discontinuous epitopes, we evaluated its results alone (**Table 3.2, Figure 3.8C and 3.9**). Whilst DiscoTope2.0 highlighted the lowest number of antigenic amino acids throughout the five eIF2B subunits (**Figure 3.5**), eIF2Bε peptides used to raise HPA064370 and HPA069303 antibodies appeared to match with antigenic regions identified by DiscoTope2.0 analysis, while ARP61329_P050 did not. This suggests that the ARP61329_P050 antibody has antigenic regions on the linear eIF2Bε protein, however within the native eIF2Bε structure this region is not antigenic. It is important to note that the number of highlighted amino acids using DiscoTope2.0 was scarce throughout the subunits, but particularly in eIF2Bε.

Studies have shown that discontinuous based prediction approaches can outperform sequence-based methods (Haste Andersen *et al*., 2006), with structure- or sequence-based programs displaying a limited predictive power (Kringelum *et al*., 2012). The quality of datasets used for structural mapping of B-cell epitopes and the diverse conformation of molecules/complexes of interest could be limitations that are important to consider.

When assessing the cellular localisation of a protein, it is crucial to have specific labelling of the molecules of interest with a fluorescent probe which shows a high fluorescence intensity and photostability. Therefore, experimental approaches to eliminate poor antibody detection as a limiting factor for the reliable detection and characterisation of the targeted molecules is essential. To determine if these bioinformatic results would correlate with experimental ICC detection of eIF2Bε, we analysed the fluorescence intensity and number of localised eIF2Bε foci using ARP61329_P050, HPA064370 and HPA069303 primary anti-eIF2Bε antibodies, visualised with the appropriate secondary antibodies conjugated to Alexa Fluor

594 (**Figure 3.10A**). We found that HPA064370 and HPA069303 antibodies significantly increased the mean fluorescent signal intensity of the endogenous eIF2Bε foci (**Figure 3.10B**). These results support the proposed experimental approach of utilising B-cell epitope servers for optimisation of ICC detection of proteins and indicates that epitopes identified by DiscoTope2.0 are more reliable for ICC methodologies. We suggest that this approach is a useful tool to select commercially available primary antibodies for ICC techniques, which would allow for troubleshooting of suboptimal ICC results. Additionally, immunoinformatics enables the design of custom primary antibodies with optimal antigenicity (Chen *et al*., 2020).

Binding of p-eIF2α alters the conformation of the eIF2B complex (Schoof *et al*., 2021; Zyryanova *et al*., 2021). Our data show that the immunoinformatics analysis does not detect epitope changes between the various 3D structures of the eIF2B•eIF2 complex (**Figure 3.4 and 3.5**). This is unsurprising given the 1-6 Å scale of conformational changes within the eIF2B complex upon binding of p-eIF2α or ISRIB (Schoof *et al*., 2021; Zyryanova *et al*., 2021). Next we analysed the detection of endogenous eIF2Bε in the presence of ER stress, to determine whether the detection of eIF2Bε was altered by conformational changes and if the previously reported modulation of eIF2Bε-GFP bodies upon cellular stress in mammalian cells (Hanson *et al*., 2023; Hodgson *et al*., 2019a) was also observed endogenously. The number of eIF2Bε foci detected was increased following Tg treatment, when employing HPA064370 and HPA069303 primary antibodies, but not with ARP61329_P050 (**Figure 3.10C**). The increase in number of detected foci is comparable for HPA064370 and HPA069303 anti-eIF2Bε primary antibodies, suggesting that it is an increase of eIF2Bε foci formation rather than a change in eIF2Bε conformation. Additionally, both HPA064370 and HPA069303 increased the percentage of detected cells with eIF2Bε localised foci in U373-MG cells (**Figure 3.10D**).

Protein expression levels of eIF2Bε were not impacted by the presence of ER stress, and the fluorescence intensity was similar between normal conditions and Tg treatment in respective of the primary antibody utilised. Thus, we can deduce that the increase in eIF2Bε foci localisation was not due to a change in the protein expression levels of eIF2Bε or due to increase of fluorescence intensity (**Figure 3.11 and 3.10B**). Given these results, we believe that the bioinformatic efforts employed have aided primary antibody selection to observe not only endogenous

localisation of the eIF2B complex, but also detect minute changes of said localisation following stress conditions, which would allow for future experiments to study the implication of stress in the eIF2B subcellular localisation.

3.3.4. Final observations

To conclude, ICC is a powerful methodology to detect the cellular localisation of proteins *in situ*, yet the selection of primary antibodies used is often overlooked. We here describe bioinformatic tools that can aid antibody screening and selection, thus facilitating the study of non-denatured complex structures, such as eIF2B. This allows for inexpensive optimisation, reliable detection and analysis of proteins. However, it is important to consider the types of B-cell epitope prediction servers employed - sequence or structure based - and the protein complex used for analysis – bound to other molecules or not, large portions of unmodeled sections – which could translate into limiting factors for the bioinformatic analysis, impacting the overall results.

Chapter 4. Characterisation of endogenous eIF2B localisation in neuronal and glial cells under stressed and steady-state conditions.

4.1. Introduction.

The cell cytoplasm is comprised of well-defined intracellular compartments focusing on particular roles. Protein synthesis accounts for a large proportion of energy consumption, therefore requiring tight regulation. This membraneless compartmentalisation increases the efficiency of subcellular processes, and it is fundamental for metabolism regulation. eIF2B bodies, are sites eIF2B and eIF2 localisation, key factors in the regulation of translational control. eIF2 has a dynamic interaction with eIF2B bodies, shuttling through the bodies at a rate that correlates to eIF2B GEF activity (Campbell *et al*., 2005; Hanson *et al*., 2023; Hodgson *et al*., 2019; Norris *et al*., 2021).

The eIF2B protein complex exists as a heterodecamer $\alpha_2\beta_2\gamma_2\delta_2\varepsilon_2$ structure (comprised of two eIF2Bβδγε tetramer subcomplexes stabilized by eIF2Bα dimer) (Kuhle *et al*., 2015; Pavitt *et al*., 1998; Wortham *et al*., 2014; Zyryanova *et al*., 2021). In mammalian cells, it was found that different sized eIF2B bodies are present, with varying subunit composition (Hanson *et al*., 2023; Hodgson *et al*., 2019). In response to stress, eIF2B subunit localisation changes occur, changing the composition of eIF2B bodies in what appears to be in a cell-type manner, suggesting that the presence of subcomplexes has an important role in cellular regulation (Hanson *et al*., 2023; Hodgson *et al*., 2019). The increase of small eIF2B bodies was present in astrocytic cells following acute stress induction. Additionally, the increased presence of eIF2Bδ in small eIF2B bodies (containing γ and ε) in glial and neuronal cells, with a concomitant increase of eIF2 shuttling in astrocytic cells, was found following acute ER stress activation (Hanson *et al*., 2023; Hodgson *et al*., 2019). Curiously, this redistribution of the eIF2Bδ subunit to small eIF2B bodies was no longer observed under chronic Tg induced stress conditions (Hanson *et al*., 2023). This suggests that eIF2B subunit reconstruction of small bodies is a transient and dynamic event, possibly linked to recovery or habitual presence of stress.

Mutations in all five eIF2B subunits are linked to VWMD, with the functional impact of eIF2B mutations correlating poorly with the severity of patient phenotype (Leegwater *et al*., 2001; Liu *et al*., 2011; van der Knaap *et al*., 2006;

van der Lei *et al*., 2010). The characterization of endogenous eIF2B foci has yet to be carried out in mammalian cells and given the cell-type specific manner in which these VWMD mutations affect cells, the investigation of eIF2B localisation in glial and neuronal cells will be explored.

4.1.1. Hypothesis and rationale

Given its intrinsic dynamic and perhaps cell-type specific nature of eIF2B localisation, the characterisation of endogenous eIF2B cytoplasmic foci in a range of cell lines, would provide insight into their localisation patterns and possibly correlate it to translation regulation. A further understanding of endogenous eIF2B characteristics within brain cell types might uncover key features of eIF2B localisation functionality. The main aim of this chapter is to investigate the cellular localisation of endogenous eIF2Bα-ε subunits in astrocytic, oligodendrocytic and neuronal cell types. The hypothesis is that the endogenous eIF2B localisation and its different compositions will differ between glial and neuronal cells, which may be an important component to the regulation of eIF2B activity and consequently translation initiation. The selective vulnerability of astrocytes and oligodendrocytes, while sparing neurons, within the pathology of VWMD, adds a particular intriguing dimension to the investigation of eIF2B localisation. The main objectives to test this hypothesis are the following:

- Determine the prevalence of the localisation of each eIF2B subunit in glial and neuronal cells.
- Analyse the composition of different subpopulations of eIF2Bα foci.
- Determine the modulation of eIF2Bα and eIF2Bε subunits localisation upon acute stress induction.

4.2. Results.

4.2.1. eIF2B localisation differs between neuronal and glial cell lines.

Investigating glial and neuronal cells is of particular interest as while astrocytes are primarily targeted and involved in the inhibition of oligodendrocytic maturation there is an obvious neuronal insensitivity to these VWMD mutations (Dooves *et al*., 2016; Leferink *et al*., 2019). It is important to note that secondary consequences from astrocytic dysfunction may be found in neurons, such as axonal atrophy and/or complete axonal loss (Brück *et al*., 2001; Fogli *et al*., 2002; Klok *et al*., 2018). Characterisation of eIF2B foci was conducted in three mammalian cell types – U373-MG-MG (astrocytoma), MO3.13 (hybrid primary oligodendrocytes) and SH-SY5Y (neuroblastoma).

To analyse eIF2B localisation, ICC detection of each endogenous subunit was carried out as described previously in **chapter 3,** with a population of 100 cells per replicate being analysed. In the three cell lines analysed, it was possible to observe heterogenous populations of cells with eIF2Bα, eIF2Bβ, eIF2Bγ, eIF2Bδ, and eIF2Bε cytoplasmic foci (**Figure 4.1A**).

By first analysing the cell lines individually, in U373-MG cells similar localisation of the different five eIF2B subunits was found, with a range of approximately 24-29 % of cells having localised foci, with the majority of cells displaying a dispersed signal. The values of cells with localised foci for each subunit were: eIF2Bα 23.67 % (± 2.08); eIF2Bβ 24.33 % (± 3.06); eIF2Bγ 23.67 % (± 4.93); eIF2Bδ 23.67 % (± 4.04); eIF2Bε 29.67 % (± 2.08) (**Figure 4.1Bi**). These results suggest that U373-MG cells show a similar localisation pattern between all eIF2B subunits, perhaps forming a majority of decameric structures in cells that show eIF2B localisation.

Interestingly, MO3.13 cells showed a different pattern of localisation. Remarkably, 64.33 % (± 4.04) MO3.13 cells showed eIF2Bα foci localisation, significantly higher than the localisation of the other eIF2Bβ-ε subunits. The percentage of cells with eIF2Bβ foci was significantly more prominent when compared to eIF2Bδ and eIF2Bε (eIF2Bβ: 31.00 % ± 2.65; eIF2Bγ: 23.33 % ± 1.53; eIF2Bδ: 20.00 % ± 4.36; eIF2Bε: 16.33 % ± 3.51) (**Figure 4.1Bii**).

SH-SY5Y cells displayed a similar pattern to MO3.13 cells. 69.33 % (± 1.53) of SH-SY5Y cells exhibited eIF2Bα localised foci. eIF2Bβ and eIF2Bε subunits showed significantly different localisation, with 25.67 % (± 1.53) of cells showing

eIF2Bβ foci and 11.67 % (± 1.53) of cells having eIF2Bε in a population of 100 SH-SY5Y cells. eIF2Bγ and δ displayed comparable localisation values, with 20.00 % (± 1.00) and 19.67 % (± 6.51) of SH-SY5Y cells displaying localised foci, respectively (**Figure 4.1Biii**).

When comparing each subunit across the different cell lines an interesting pattern emerges. While eIF2Bβ, γ and δ did not show significant differences between the glial and neuronal cells, eIF2Bα and ε showed contrasting localisation patterns. SH-SY5Y and MO3.13 cells exhibited a significant increase of percentage of cells with eIF2Bα localisation, with a ~2.9 and ~2.7-fold change, respectively, when compared to U373-MG cells. On the other hand, U373-MG cells displayed a significantly higher percentage of cells with eIF2Bε foci when compared to SH-SY5Y and MO3.13, with a ~2.5 and -1.8-fold change, respectively (**Figure 4.2**).

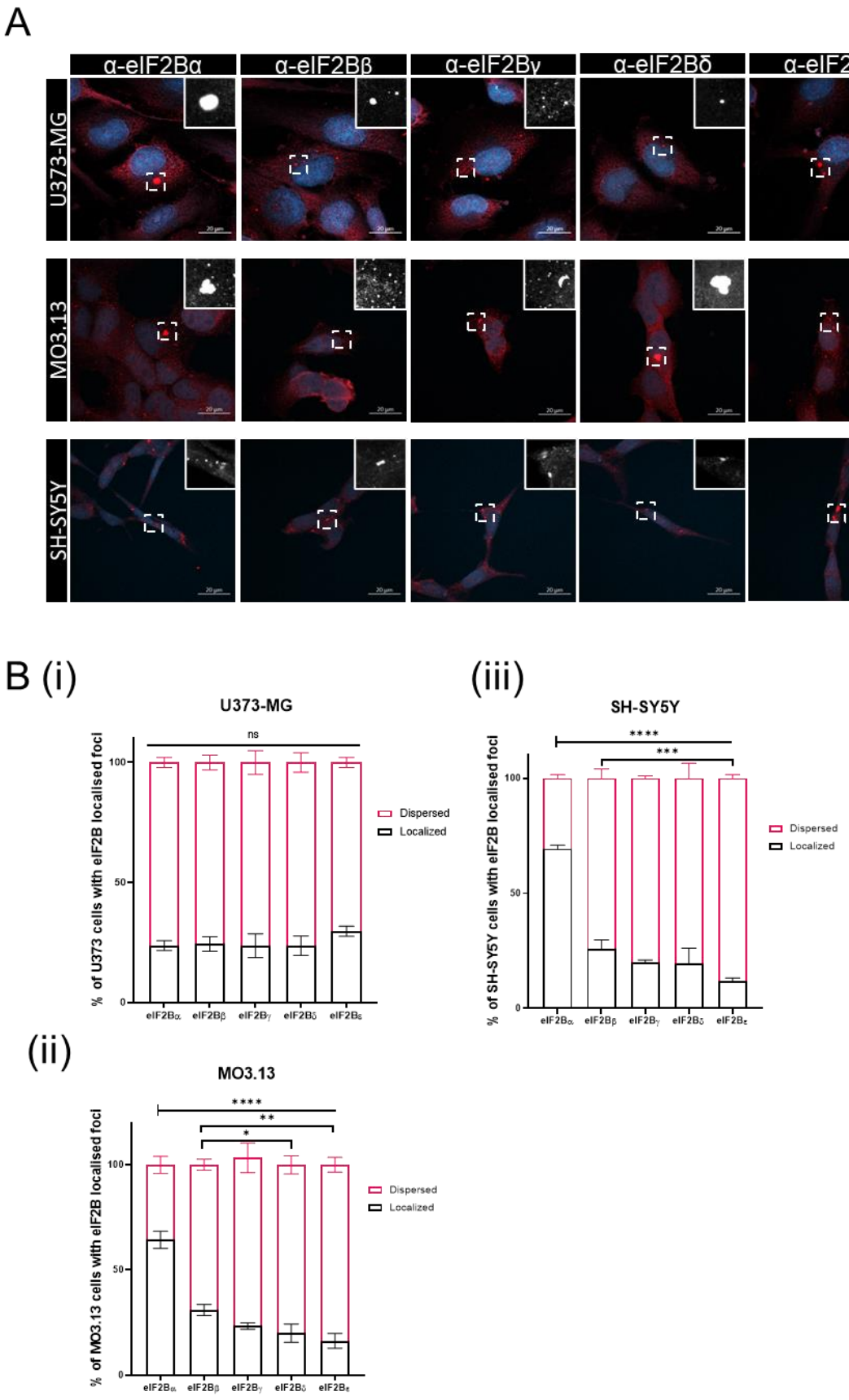

Figure 4.1. eIF2Bα localisation is increased in oligodendrocytic and neuronal cells.

(A) Representative images of (top to bottom) U373-MG, MO3.13 and SH-SY5Y cells immunostained with primary antibodies against (left to right) endogenous α-eIF2Bα, α-eIF2Bβ, α-

eIF2Bγ, α-eIF2Bδ and α-eIF2Bε, and visualized using appropriate secondary antibodies conjugated to Alexa Fluor 594. DAPI stains nuclei. Scale bar: 20μm. (B) Mean percentage of cells displaying dispersed cytoplasmic and localised eIF2Bα-ε foci in a population of 100 cells per replicate, in (i) U373-MG, (ii) MO3.13, and (iii) SH-SY5Y cells. Data was analysed using two-way ANOVA followed by *post-hoc* Tukey's test for multiple comparisons. Error bars: ± s.d. (n=3). *$p \leq 0.05$; **$p \leq 0.01$; ***$p \leq 0.001$; ****$p \leq 0.0001$.

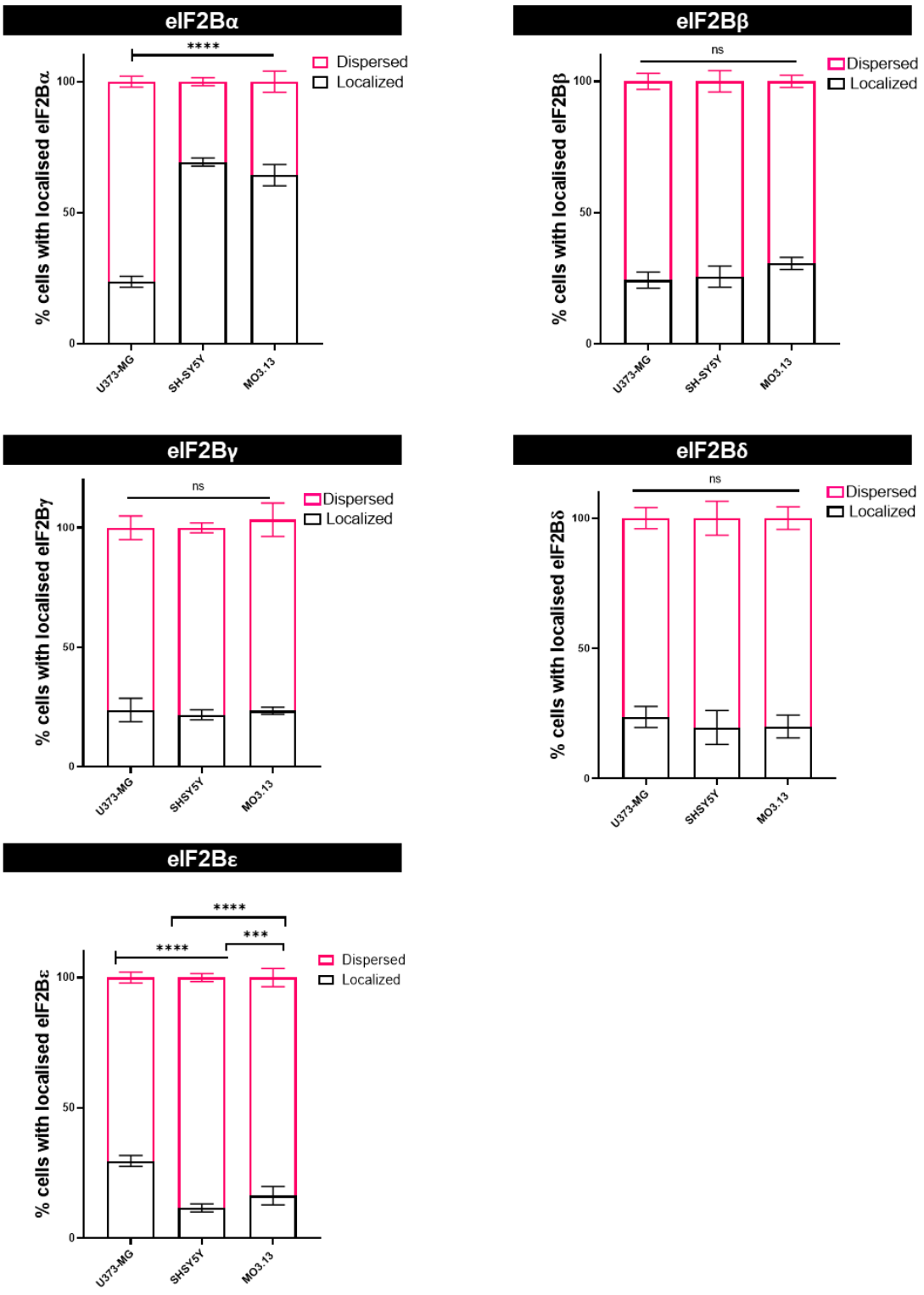

Figure 4.2. eIF2Bα localisation is increased in oligodendrocytic and neuronal cells, and eIF2Bε localisation is increased in astrocytic cells.

Mean percentage of cells displaying dispersed cytoplasmic and localised eIF2Bα-ε foci in a population of 100 cells per replicate, in U373-MG, MO3.13, and SH-SY5Y cells. Data was analysed using two-way ANOVA followed by post-hoc Tukey's test for multiple comparisons. Error bars: ± s.d. (n=3). ***p≤0.001; ****p≤0.0001.

A diverse range of sizes of cytoplasmic foci and abundance per cell was recorded for the five eIF2B subunits. To quantify these heterogenous foci, the area (μm^2) of singular eIF2B foci in 30 cells with localised eIF2B in three biological replicates was carried out for each subunit in all three cell lines. The smaller foci considered had an area of 0.1946 μm^2. The largest foci observed had an area of 13.5275 μm^2 in U373-MG cells (corresponding to the eIF2Bδ subunit), 19.4866 μm^2 in MO3.13 cells (corresponding to the eIF2Bα subunit), and 25.1946 μm^2 in SH-SY5Y cells (corresponding to the eIF2Bα subunit). In U373-MG cells, all subunits exhibited a similar mean value of size (eIF2Bα: 0.91 μm^2 ± 1.45; eIF2Bβ: 0.91 μm^2 ± 1.51; eIF2Bγ: 0.80 μm^2 ± 1.29; eIF2Bδ: 1.02 μm^2 ± 1.66; eIF2Bε: 0.85 μm^2 ± 1.32). In MO3.13 cells, eIF2Bα had a mean of 0.65 (± 1.24), eIF2Bβ 0.67 (± 0.89), eIF2Bγ 0.86 (± 0.98), eIF2Bδ 0.98 (± 0.93) and eIF2Bε 1.02 (± 1.34) μm^2. In SH-SY5Y cells, eIF2Bα had a mean of 0.57 (± 1.23), eIF2Bβ 0.72 (± 1.04), eIF2Bγ 0.92 (± 0.94), eIF2Bδ 0.87 (± 0.88) and eIF2Bε 0.89 (± 0.93) μm^2 (**Figure 4.3A**). In MO3.13 and SH-SY5Y cells, eIF2Bα displayed the smallest mean size value, with the other eIF2B subunits showing similar values.

In U373-MG cells in three biological replicates the number of detected eIF2B localised foci was similar throughout the five eIF2B subunits, while MO3.13 and SH-SY5Y cells showed a larger number of eIF2Bα localised foci when compared to the eIF2Bβ-ε subunits (**Figure 4.3B**). This leads to the idea that the detection method of eIF2B localised foci here presented is sensitive to cell-type specificity. Additionally, we can already observe that according to cell-type, eIF2B foci distribution and arrangement might differ according to subunit, which in turn, might have a significant impact on eIF2B body composition.

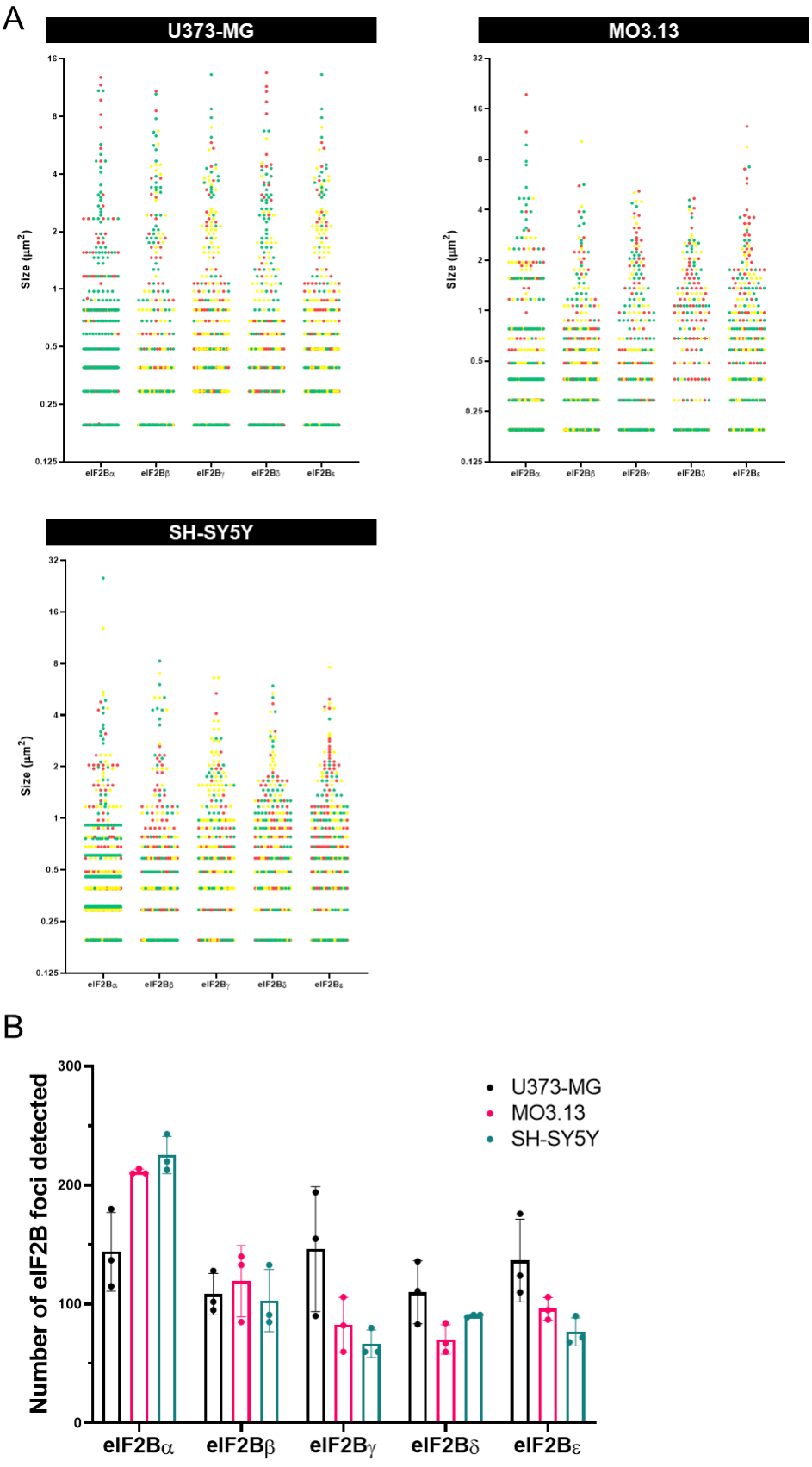

Figure 4.3. A wide range of eIF2Bα-ε foci sizes and numbers were detected in glial and neuronal cell lines.

(A) Size distribution of eIF2Bα-ε foci in 30 cells per repeat with localised eIF2Bα-ε in U373-MG, MO3.13 and SH-SY5Y cells (n=3, each repeat was coloured accordingly, repeat 1 – red; repeat

2 – yellow; repeat 3 – green). (B) Number of eIF2Bα-ε foci in 30 cells with localised eIF2Bα-ε in U373-MG, MO3.13 and SH-SY5Y cells. Error bars: ± s.d. (n=3).

4.2.2. eIF2B(γ, δ) subunits localise to different sized eIF2Bα foci in steady state and stressed conditions

Through the previous analysis of endogenous eIF2B foci localisation (**Figure 4.3A**), all subunits appear to aggregate in foci of varied sizes. This was particularly obvious for the eIF2Bα foci which was significantly different between the glial and neuronal cell lines. It has been shown previously that there is a relationship between eIF2B body composition and size in mammalian cells. From previously published work, eIF2Bα appears to stabilize two eIF2Bβγδε tetramers together, thus being present with the other subunits in the decameric protein complex (Bogorad *et al*., 2014; Marintchev & Ito, 2020; Wortham *et al*., 2014). As such, co-localisation analysis between a catalytic subunit (eIF2Bγ) and a regulatory subunit (eIF2Bα) would allow to distinguish between a decamer structure and other subcomplexes. Detection and co-localisation analysis of endogenous eIF2Bα and eIF2Bγ foci in U373-MG, SH-SY5Y and MO3.13 cells was conducted in 30 cells per biological replicate.

U373-MG cells with eIF2Bα localised foci were analyzed (**Figure 4.4A**). Out of these cells, 61.11 % (± 15.75) of cells showed co-localisation between both subunits in at least one focus (**Figure 4.4B**). eIF2Bα largely co-localised with eIF2Bγ foci at a median of 1.27 μm^2. eIF2Bα foci that did not show co-localisation with eIF2Bγ appeared to be smaller than 1 μm^2, with the median being 0.29 μm^2 (**Figure 4.4C**). Of the total 660 eIF2Bα foci and 265 eIF2Bγ foci detected in all repeats, 19.28 % (± 2.83) co-localised, leaving 65.77 % (± 3.75) of eIF2Bα foci and 14.95 % (± 0.95) of eIF2Bγ foci not co-localising (**Figure 4.4D**).

MO3.13 cells with eIF2Bα localised foci were analyzed (**Figure 4.5A**). Out of these 30 cells, 28.89 % (± 5.09) of cells showed presence of co-localisation between both subunits in at least one focus (**Figure 4.5B**). It was possible to observe that eIF2Bα co-localised with eIF2Bγ foci at a median of 1.50 μm^2. eIF2Bα foci that do not have eIF2Bγ present were smaller than 1 μm^2, with the median being 0.63 μm^2 (± 1.38) (**Figure 4.5C**). Of the total 849 eIF2Bα foci and 109 eIF2Bγ foci in all repeats, 5.31 % (± 1.22) co-localised, leaving 87.90 % (± 3.71) of eIF2Bα foci and 6.78 % (± 2.66) of eIF2Bγ foci not co-localising (**Figure 4.5D**).

SH-SY5Y cells with eIF2Bα localised foci were analysed (**Figure 4.6A**). Out of these cells, 21.11 % (± 10.18) of cells showed presence of co-localisation between both subunits in at least one focus (**Figure 4.6B**). eIF2Bγ largely co-localises with eIF2Bα foci at a median of 0.79 μm^2. eIF2Bα foci that did not spatially interact with eIF2Bγ appeared to favor foci smaller than 0.83 μm^2 (± 2.15) (**Figure 4.6C**). Of the total 884 eIF2Bα foci and 92 eIF2Bγ foci detected in all repeats, 6.79 % (± 2.26) co-localised, leaving 89.90 % (± 2.41) of eIF2Bα foci and 3.31 % (± 0.24) of eIF2Bγ foci not co-localising (**Figure 4.6D**).

eIF2Bα and eIF2Bγ have not been shown to form subcomplexes (Kuhle *et al*., 2015; Pavitt *et al*., 1998; Schoof *et al*., 2021), therefore it is most likely that the co-localisation of eIF2Bα and eIF2Bγ represents eIF2B decamers. As previously determined in Hodgson *et al*., large eIF2B bodies had a greater proportion of all subunits and have been postulated to contain the full decamer. These results build on previous data, and thus we determined that foci < 1 μm^2 represented either subcomplexes or unbound eIF2B subunits, and foci ≥ 1 μm^2 represented the eIF2B decamer. This size discrimination will be used for future analysis in this thesis, with size correlating to subunit composition.

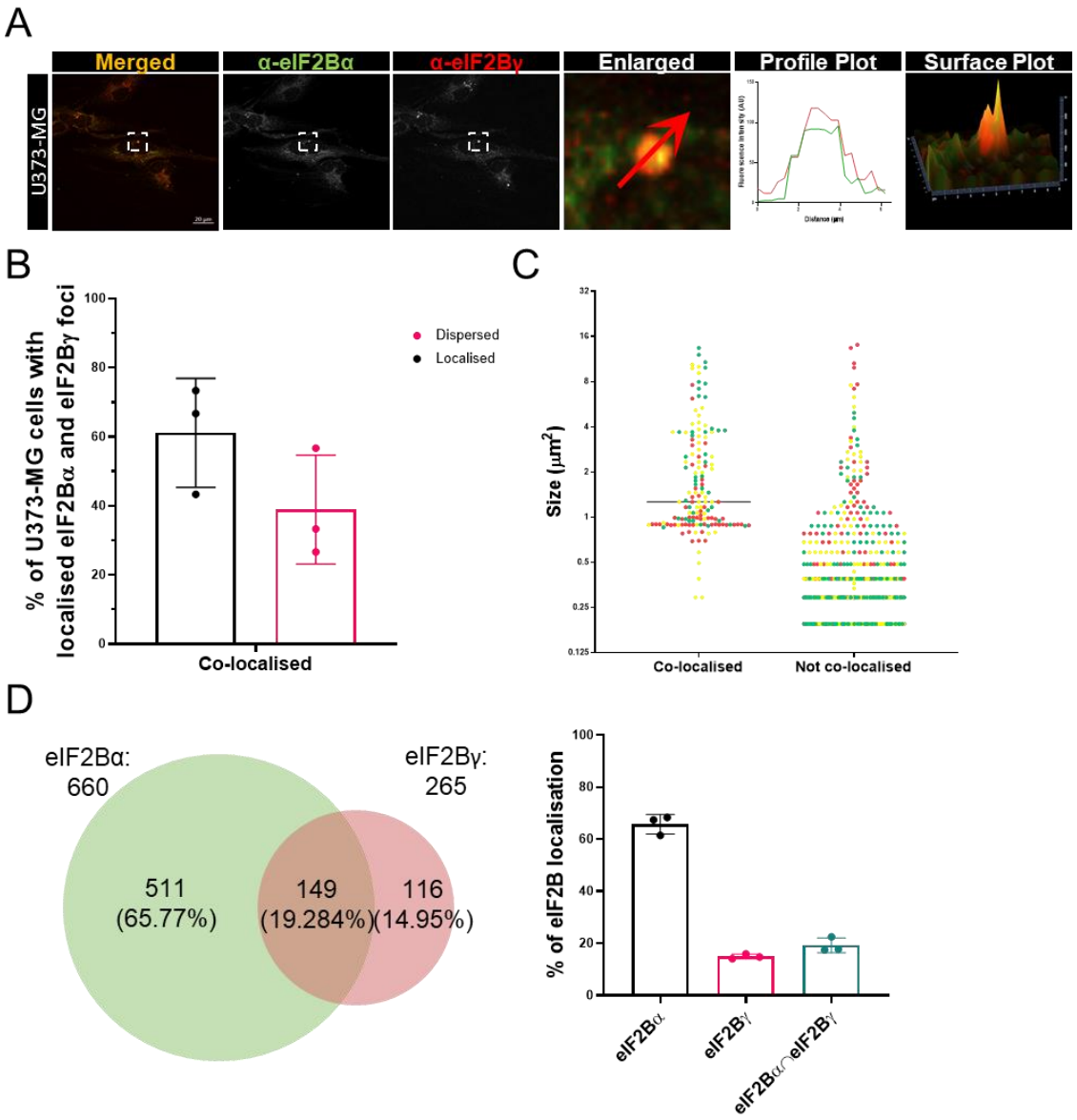

Figure 4.4. eIF2Bα and eIF2Bγ co-localisation in U373-MG cells.

(A) Representative images of U373-MG cells immunostained with primary antibodies against α-eIF2Bα and α-eIF2Bγ and visualized using appropriate secondary antibodies conjugated to AlexaFluor 488 for eIF2Bα and AlexaFluor 594 for eIF2Bγ. DAPI stains nuclei. Scale bar: 20 μm. Area defined was enlarged and the profile plot of the fluorescence intensity of each eIF2B subunit (green line – 488; red line – 594) and surface plot was plotted. (B) Mean percentage of cells displaying dispersed cytoplasmic and localised eIF2Bγ foci in a population of 30 cells per replicate with eIF2Bα localised foci. Error bars: ± s.d. (n=3). (C) Size distribution of eIF2Bα foci in 30 cells with localised eIF2Bα, co-localised or not co-localised with eIF2Bγ foci (n=3, each repeat was coloured accordingly, repeat 1 – red; repeat 2 – yellow; repeat 3 – green). (D) Venn diagram of eIF2Bα and eIF2Bγ foci and co-localisation (n=3 counts in 30 cells with eIF2Bα localisation per repeat). Total number of all three repeats were used to determine percentages of groups. Bar graph of each biological repeat of each group. Error bars: ± s.d.

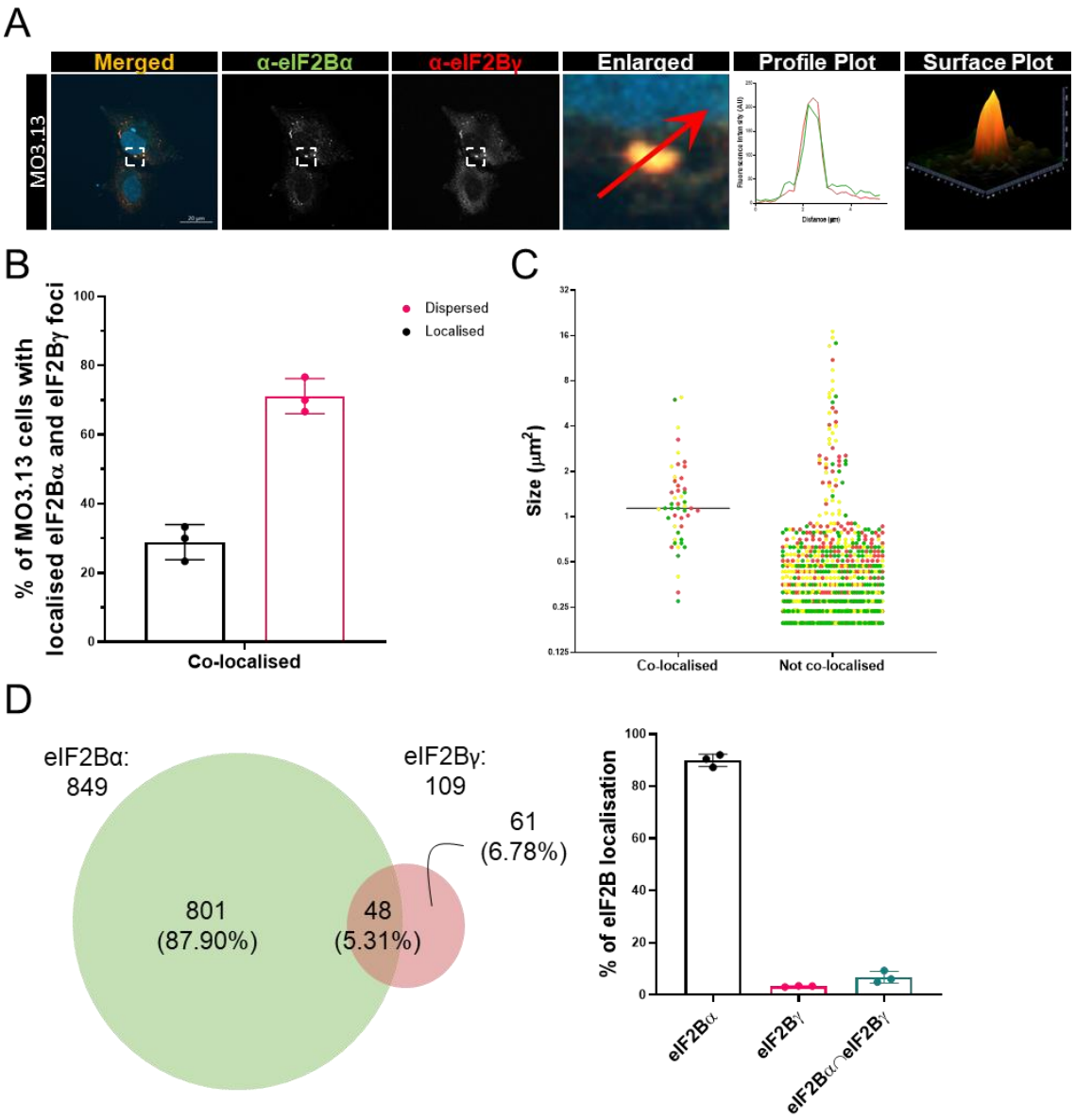

Figure 4.5. eIF2Bα and eIF2Bγ co-localisation in MO3.13 cells.

(A) Representative images of MO3.13 cells immunostained with primary antibodies against α-eIF2Bα and α-eIF2Bγ and visualized using appropriate secondary antibodies conjugated to AlexaFluor 488 for eIF2Bα and AlexaFluor 594 for eIF2Bγ. DAPI stains nuclei. Scale bar: 20 μm. Area defined was enlarged and the profile plot of the fluorescence intensity of each eIF2B subunit (green line – 488; red line – 594) and surface plot was plotted. (B) Mean percentage of cells displaying dispersed cytoplasmic and localised eIF2Bγ foci in a population of 30 cells per replicate with eIF2Bα localised foci. Error bars: ± s.d. (n=3). (C) Size distribution of eIF2Bα foci in 30 cells with localised eIF2Bα, co-localised or not co-localised with eIF2Bγ foci (n=3, each repeat was coloured accordingly, repeat 1 – red; repeat 2 – yellow; repeat 3 – green). (D) Venn diagram of eIF2Bα and eIF2Bγ foci and co-localisation (n=3 counts in 30 cells with eIF2Bα localisation per repeat). Total number of all three repeats were used to determine percentages of groups. Bar graph of each biological repeat of each group. Error bars: ± s.d.

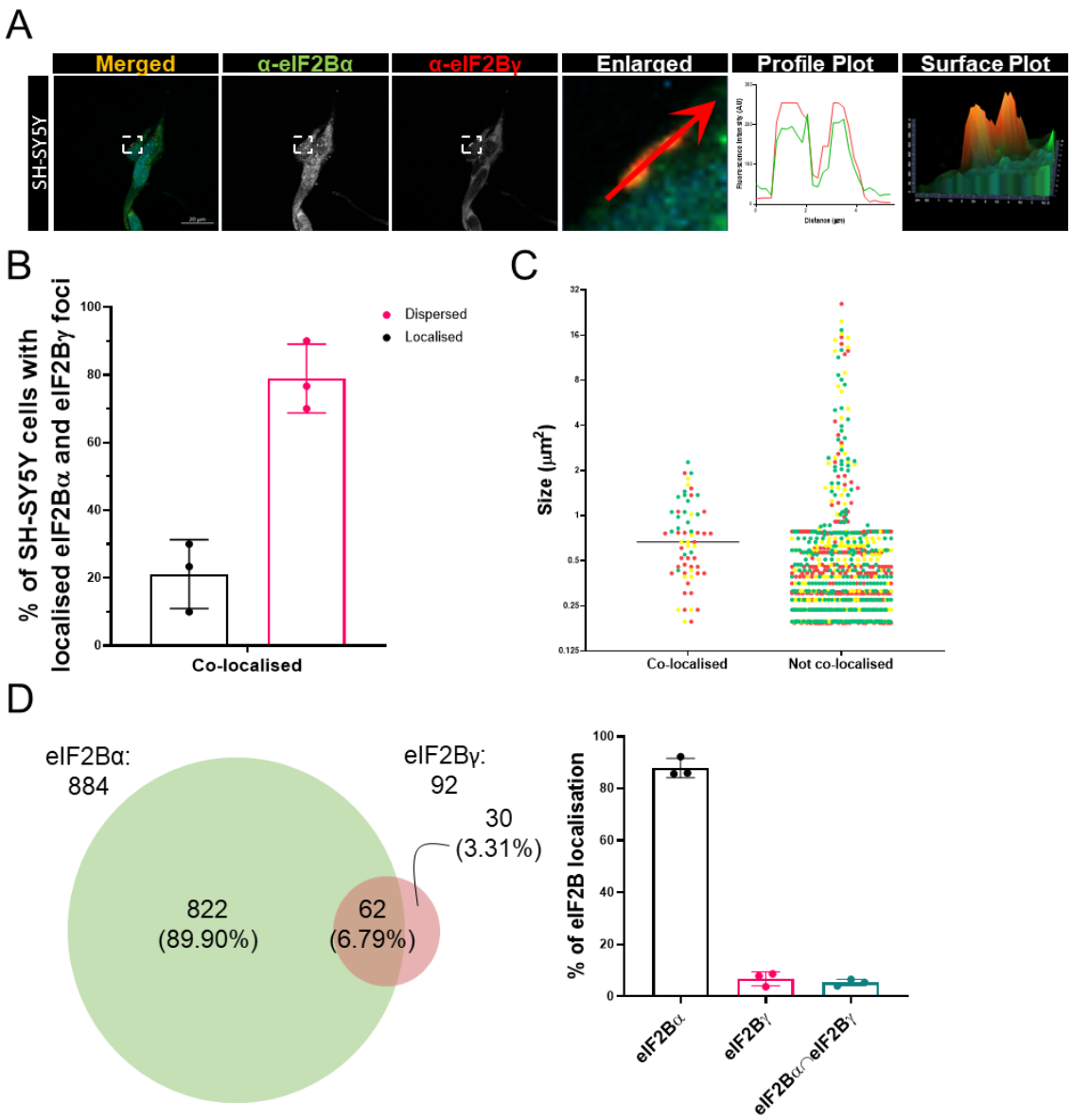

Figure 4.6. eIF2Bα and eIF2Bγ co-localisation in SH-SY5Y cells.

(A) Representative images of SH-SY5Y cells immunostained with primary antibodies against α-eIF2Bα and α-eIF2Bγ and visualized using appropriate secondary antibodies conjugated to AlexaFluor 488 for eIF2Bα and AlexaFluor 594 for eIF2Bγ. DAPI stains nuclei. Scale bar: 20 μm. Area defined was enlarged and the profile plot of the fluorescence intensity of each eIF2B subunit (green line – 488; red line – 594) and surface plot was plotted. (B) Mean percentage of cells displaying dispersed cytoplasmic and localised eIF2Bγ foci in a population of 30 cells per replicate with eIF2Bα localised foci. Error bars: ± s.d. (n=3). (C) Size distribution of eIF2Bα foci in 30 cells with localised eIF2Bα, co-localised or not co-localised with eIF2Bγ foci (n=3, each repeat was coloured accordingly, repeat 1 – red; repeat 2 – yellow; repeat 3 – green). (D) Venn diagram of eIF2Bα and eIF2Bγ foci and co-localisation (n=3 counts in 30 cells with eIF2Bα localisation per repeat). Total number of all three repeats were used to determine percentages of groups. Bar graph of each biological repeat of each group. Error bars: ± s.d.

In U373-MG cells, foci smaller than 1 μm^2, corresponded to a total of 501 eIF2Bα foci and 167 eIF2Bγ foci, with a small percentage co-localising (9.90 % ± 7.58). In MO3.13 cells, of 759 of eIF2Bα and 73 eIF2Bγ foci smaller than 1 μm^2, only 1.95 % (± 0.80) co-localised and in SH-SY5Y cells, of 786 of eIF2Bα and 73 eIF2Bγ foci smaller than 1 μm^2, the same patterned was observed with merely 5.48 % (± 2.97) co-localising (**Figure 4.7**).

In U373-MG cells the majority of eIF2Bα and eIF2Bγ foci larger or equal to 1 μm^2 co-localised (53.08 % ± 13.93). In MO3.13 cells 32.32 % (± 9.90) of large foci co-localised and in SH-SY5Y cells 17.43 % (± 6.38) of large foci co-localised. It is of note that only a small population of large eIF2Bγ foci did not co-localise with eIF2Bα (U373: 4.71 % ± 2.45; MO3.13: 12.62 % ± 10.75; SH-SY5Y: 1.28 % ± 2.22) (**Figure 4.8**), showing that the majority of large eIF2Bγ foci co-localised with eIF2Bα.

The population of the eIF2Bα and eIF2Bγ localised foci in the cells was analysed through the average number of each subunit foci per cell. In a population of 30 U373-MG cells per triplicate repeat, there was an average of 5.57 (± 0.82) and 2.99 (± 0.60) small eIF2Bα and eIF2Bγ foci per cell, respectively, and 1.78 (± 0.17) and 1.81 (± 0.71) large eIF2Bα and eIF2Bγ foci per cell. In MO3.13 cells, there was an average of 8.40 (± 0.58) and 2.51 (± 0.69) small eIF2Bα and eIF2Bγ foci per cell, respectively, and 1.00 (± 0.35) and 1.51 (± 0.18) large eIF2Bα and eIF2Bγ foci per cell, respectively. There was an average of 8.73 (± 2.02) and 3.75 (± 1.43) small eIF2Bα and eIF2Bγ foci per cell, respectively, and 1.09 (± 0.33) and 0.87 (± 0.21) large eIF2Bα and eIF2Bγ foci per cell, respectively, in SH-SY5Y cells (**Figure 4.9**). These results demonstrated that while the average number of large foci is similar, the smaller assemblies of eIF2Bα and eIF2Bγ differ quite dramatically. This suggests that the size discrimination detailed here detects what we propose to be large eIF2B decameric structures and indicates the presence of eIF2B subcomplexes.

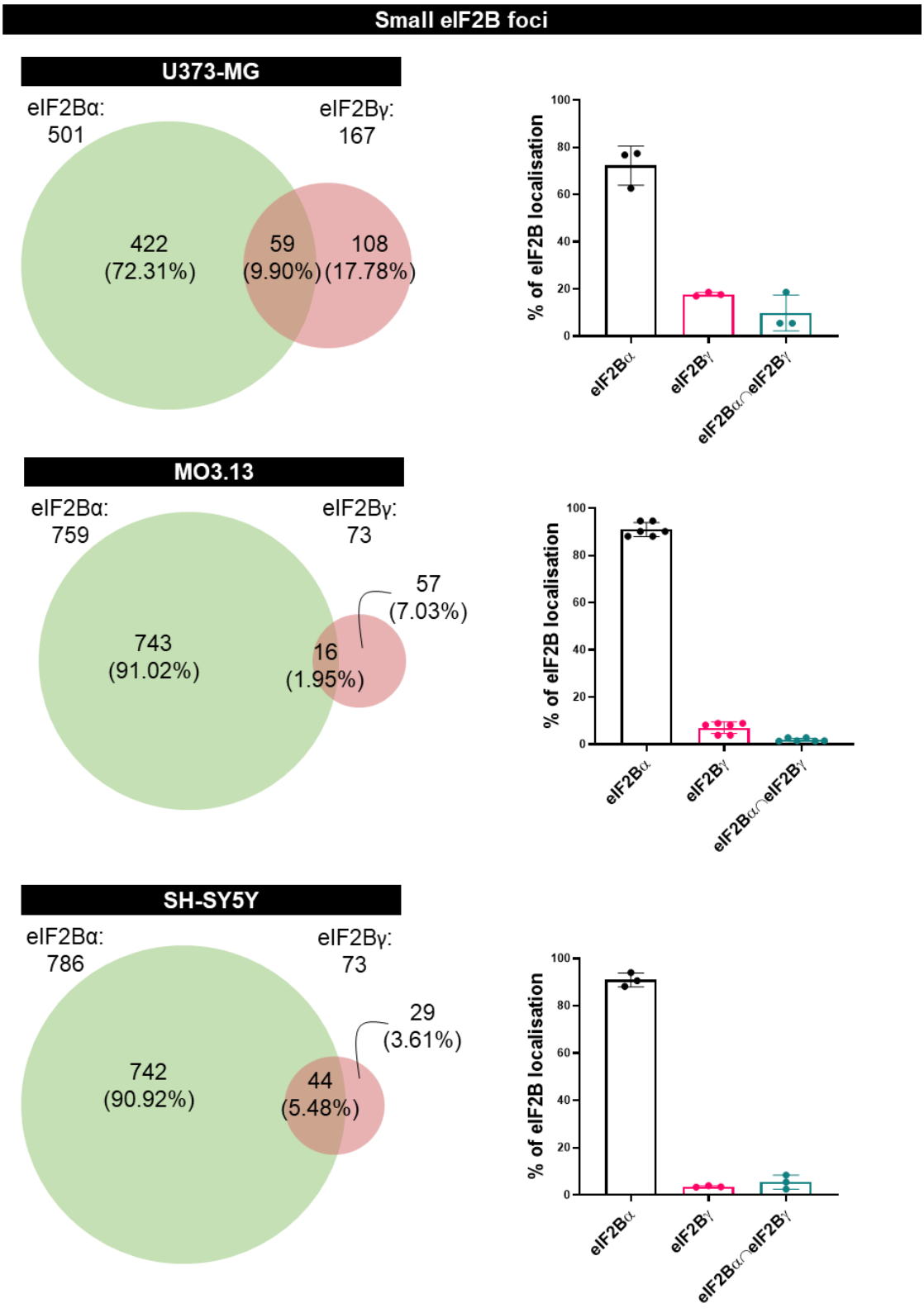

Figure 4.7. eIF2Bα and eIF2Bγ co-localisation of small foci in U373-MG, MO3.13 and SH-SY5Y cells.

Venn diagram of small eIF2Bα and eIF2Bγ foci and co-localisation (n=3 counts in 30 cells with eIF2Bα localisation) (top to bottom) in U373-MG, MO3.13 and SH-SY5Y cells. Total number of all three repeats were used to determine percentages of groups. Bar graph of each biological repeat of each group. Error bars: ± s.d.

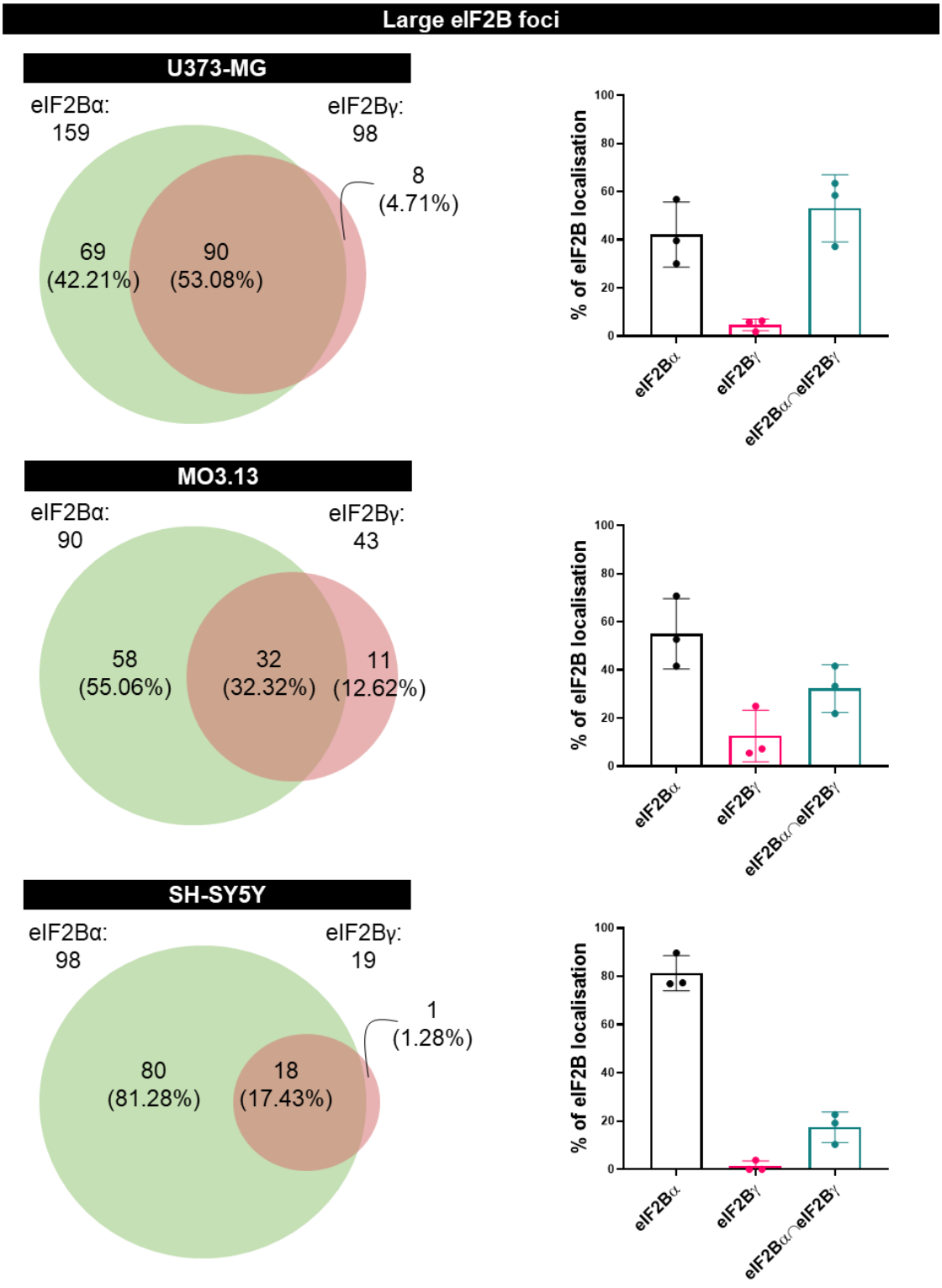

Figure 4.8. eIF2Bα and eIF2Bγ co-localisation of large foci in U373-MG, MO3.13 and SH-SY5Y cells.

Venn diagram of large eIF2Bα and eIF2Bγ foci and co-localisation (n=3 counts in 30 cells with eIF2Bα localisation) (top to bottom) in U373-MG, MO3.13 and SH-SY5Y cells. Total number of all three repeats were used to determine percentages of groups. Bar graph of each biological repeat of each group. Error bars: ± s.d.

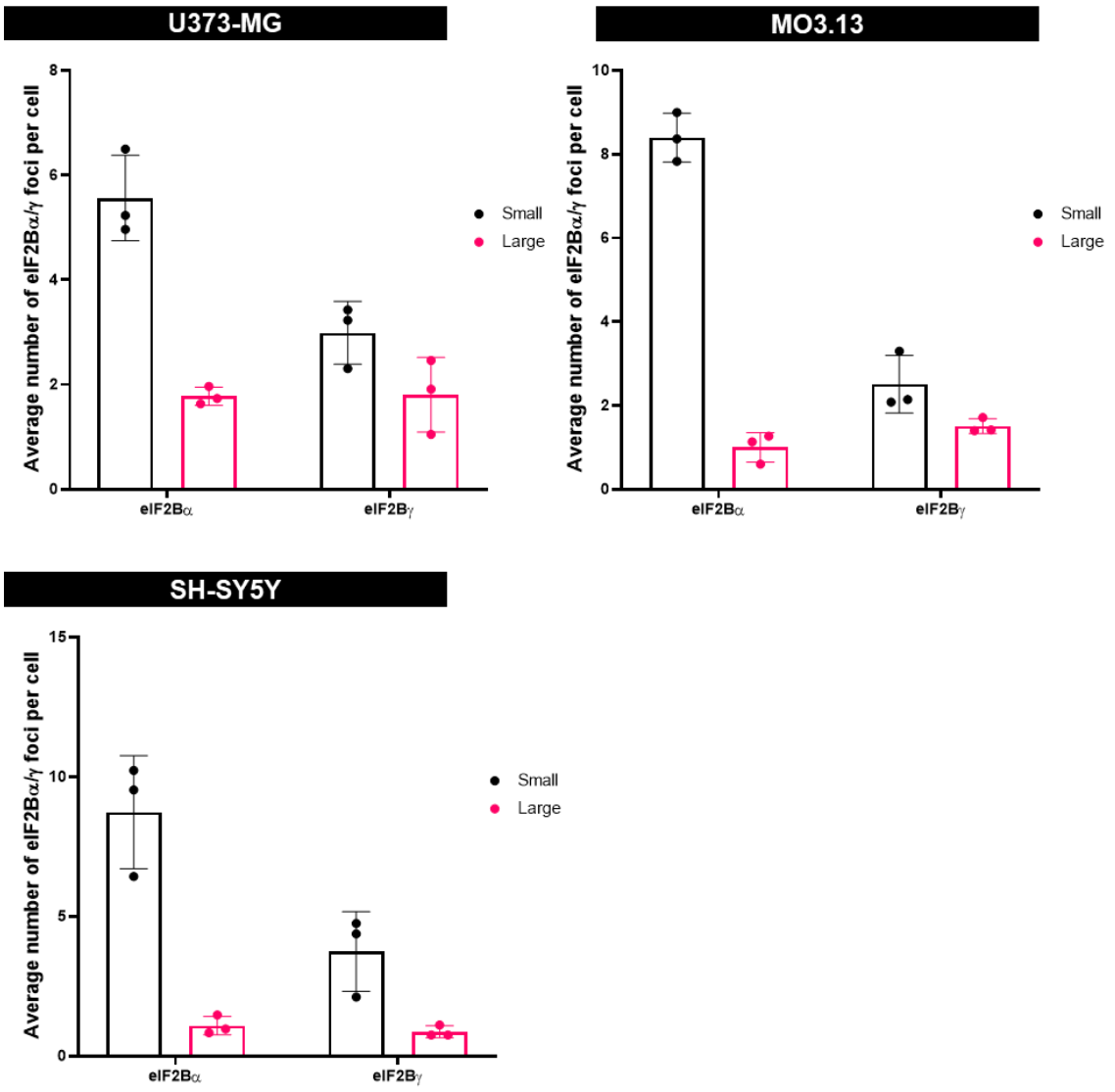

Figure 4.9. Average number of eIF2Bα and eIF2Bγ foci in U373-MG, MO3.13 and SH-SY5Y cells.

Average number of small and large eIF2Bα and eIF2Bγ foci per cell in 30 U373-MG, MO3.13 and SH-SY5Y cells with eIF2Bα localised foci (n=3). Error bars: ± s.d.

Due to the large number of small eIF2Bα foci that appeared to not co-localise with the eIF2Bγ subunit, co-localisation with eIF2Bδ was carried out in order to determine if a subcomplex of eIF2Bα with an additional regulatory subunit was present within cells.

U373-MG cells with eIF2Bα localised foci were analyzed (**Figure 4.10A**). 37.78 % (± 13.47) of cells displayed co-localisation between eIF2Bα and eIF2Bδ (**Figure 4.10B**). The median size of eIF2Bα foci which co-localised with eIF2Bδ was 1.76 μm^2 (± 1.25) and the median size of eIF2Bα foci which did not co-localise with eIF2Bδ was 0.99 μm^2 (± 1.40) (**Figure 4.10C**). Additionally, of the total of 492 eIF2Bα foci and 138 eIF2Bδ foci, 9.27 % (± 3.42) co-localised, while 76.14 % (± 3.53) of eIF2Bα and 14.59 % (± 0.13) of eIF2Bδ did not co-localise (**Figure 4.10D**).

MO3.13 cells with eIF2Bα localised foci were analysed (**Figure 4.11A**). 31.11 % (± 6.94) of cells showed co-localised eIF2Bδ foci with eIF2Bα (**Figure 4.11B**). eIF2Bδ largely co-localised with eIF2Bα in foci larger 1.50 μm^2 (± 0.77). eIF2Bα foci that did not co-localise with eIF2Bγ appeared to favor foci smaller than 1 μm^2, with the median being 0.83 μm^2 (± 1.72) (**Figure 4.11C**). Of the total 686 eIF2Bα foci and 85 eIF2Bδ foci, 6.53 % co-localised, leaving 88.37 % (± 2.75) of eIF2Bα foci and 5.10 % (± 3.16) of eIF2Bδ foci not co-localising (**Figure 4.11D**).

In SH-SY5Y cells with eIF2Bα localised foci (**Figure 4.12A**). 20.00 % (± 3.33) of cells displayed co-localisation between the two eIF2B subunits (**Figure 4.12B**). eIF2Bα foci co-localised with eIF2Bδ had a median size of 0.74 μm^2 (± 0.52) and eIF2Bα foci that did not co-localise had a median size of 0.87 μm^2 (± 1.78) (**Figure 4.12C**). In the population of the 30 cells analysed per repeat, 8.30 % (± 3.20) of the foci co-localised, while 86.79 % (± 4.08) of eIF2Bα foci and 4.91 % (± 1.00) of eIF2Bδ foci did not spatially overlap (**Figure 4.12D**).

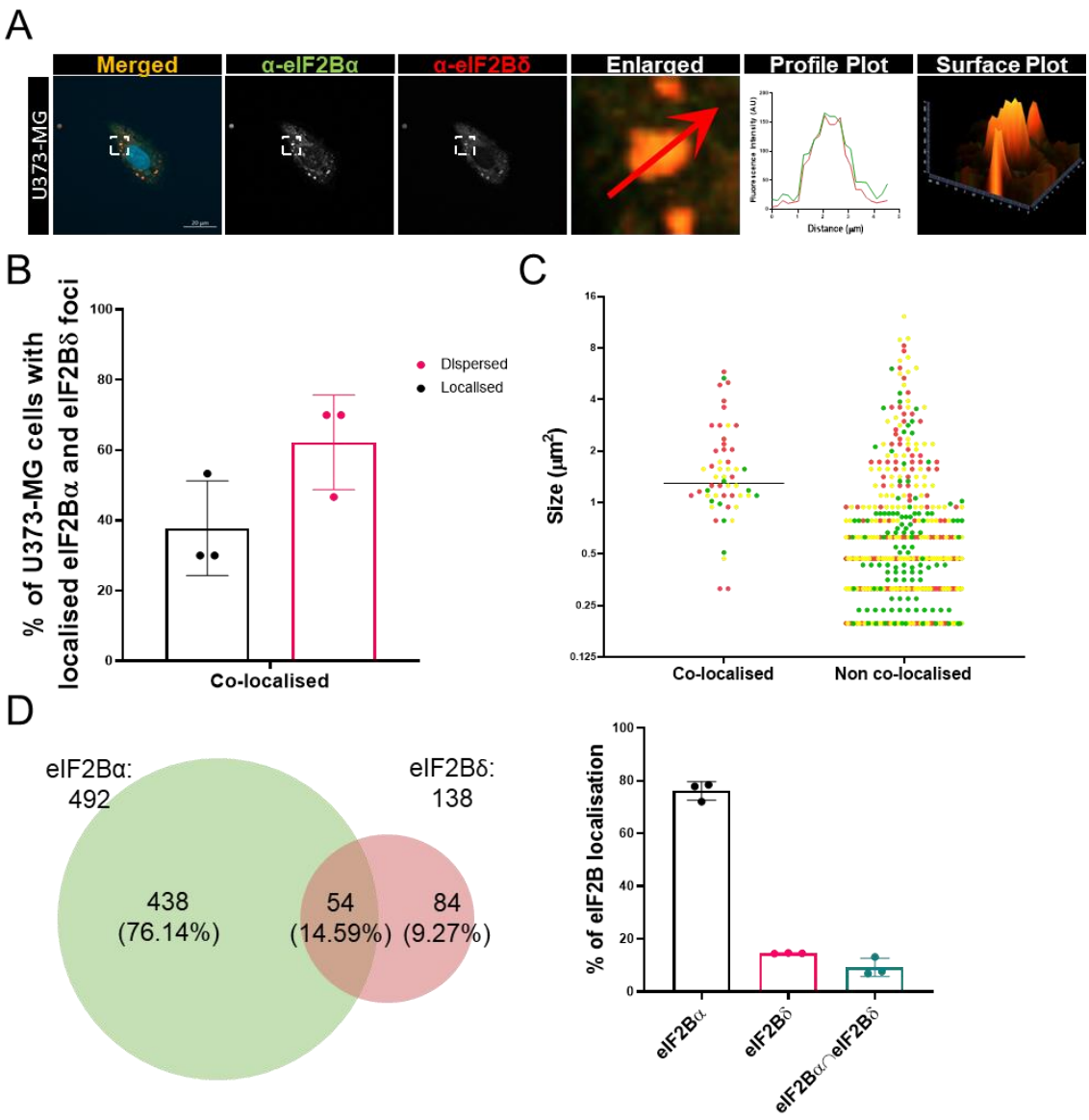

Figure 4.10. eIF2Bα and eIF2Bδ co-localisation in U373-MG cells.

(A) Representative images of U373-MG cells immunostained with primary antibodies against α-eIF2Bα and α-eIF2Bδ and visualized using appropriate secondary antibodies conjugated to AlexaFluor 488 for eIF2Bα and AlexaFluor 594 for eIF2Bδ. DAPI stains nuclei. Scale bar: 20 μm. Area defined was enlarged and the profile plot of the fluorescence intensity of each eIF2B subunit (green line – 488; red line – 594) and surface plot was plotted. (B) Mean percentage of cells displaying dispersed cytoplasmic and localised eIF2Bδ foci in a population of 30 cells per replicate with eIF2Bα localised foci. Error bars: ± s.d. (n=3). (C) Size distribution of eIF2Bα foci in 30 cells with localised eIF2Bα, co-localised or not co-localised with eIF2Bδ foci (n=3, each repeat was coloured accordingly, repeat 1 – red; repeat 2 – yellow; repeat 3 – green). (D) Venn diagram of eIF2Bα and eIF2Bδ foci and co-localisation (n=3 counts in 30 cells with eIF2Bα localisation). Total number of all three repeats were used to determine percentages of groups. Bar graph of each biological repeat of each group. Error bars: ± s.d.

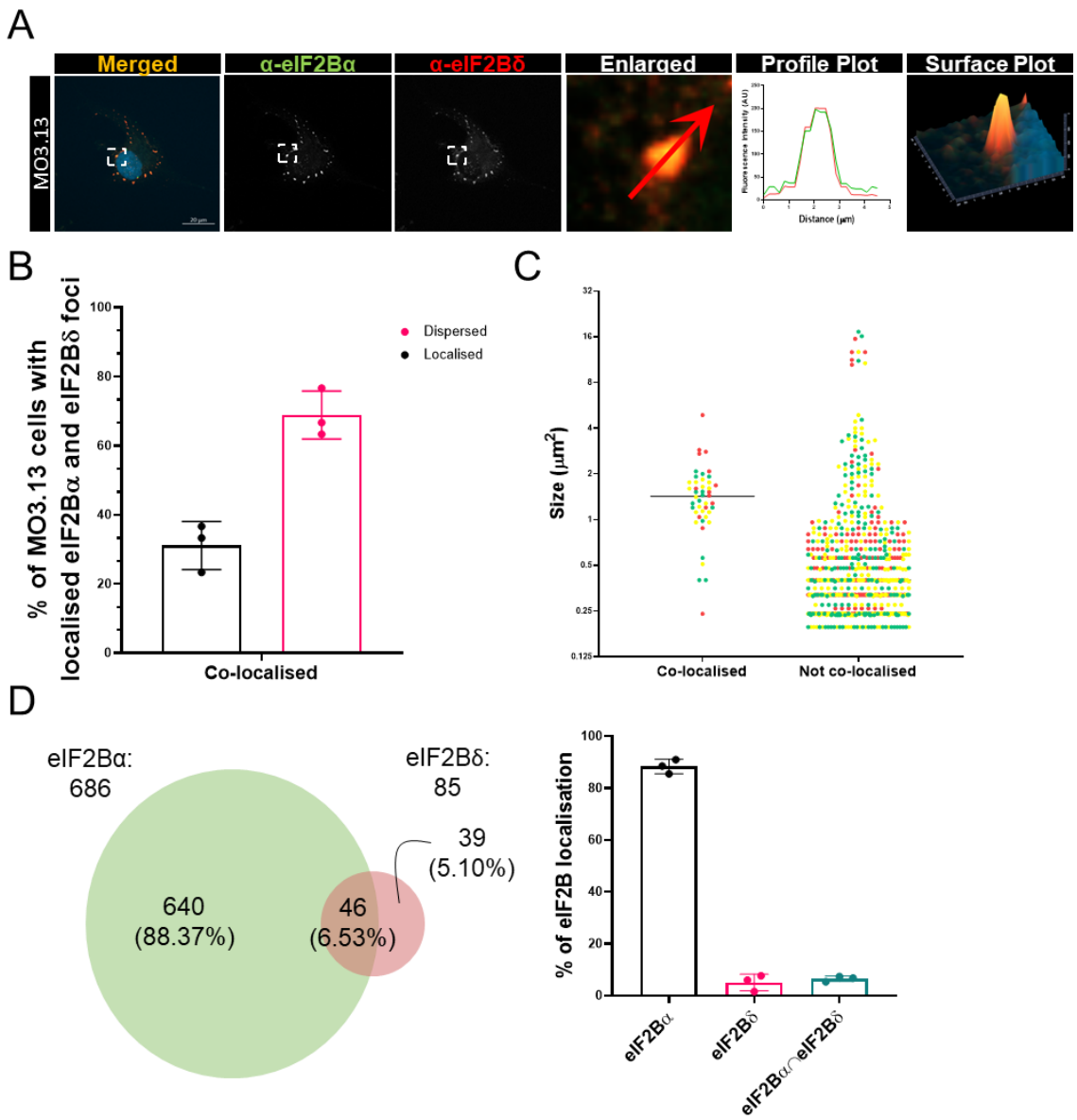

Figure 4.11. eIF2Bα and eIF2Bδ co-localisation in MO3.13 cells.

(A) Representative images of MO3.13 cells immunostained with primary antibodies against α-eIF2Bα and α-eIF2Bδ and visualized using appropriate secondary antibodies conjugated to AlexaFluor 488 for eIF2Bα and AlexaFluor 594 for eIF2Bδ. DAPI stains nuclei. Scale bar: 20 μm. Area defined was enlarged and the profile plot of the fluorescence intensity of each eIF2B subunit (green line – 488; red line – 594) and surface plot was plotted. (B) Mean percentage of cells displaying dispersed cytoplasmic and localised eIF2Bδ foci in a population of 30 cells per replicate with eIF2Bα localised foci. Error bars: ± s.d. (n=3). (C) Size distribution of eIF2Bα foci in 30 cells with localised eIF2Bα, co-localised or not co-localised with eIF2Bδ foci (n=3, each repeat was coloured accordingly, repeat 1 – red; repeat 2 – yellow; repeat 3 – green). (D) Venn diagram of eIF2Bα and eIF2Bδ foci and co-localisation (n=3 counts in 30 cells with eIF2Bα localisation). Total number of all three repeats were used to determine percentages of groups. Bar graph of each biological repeat of each group. Error bars: ± s.d.

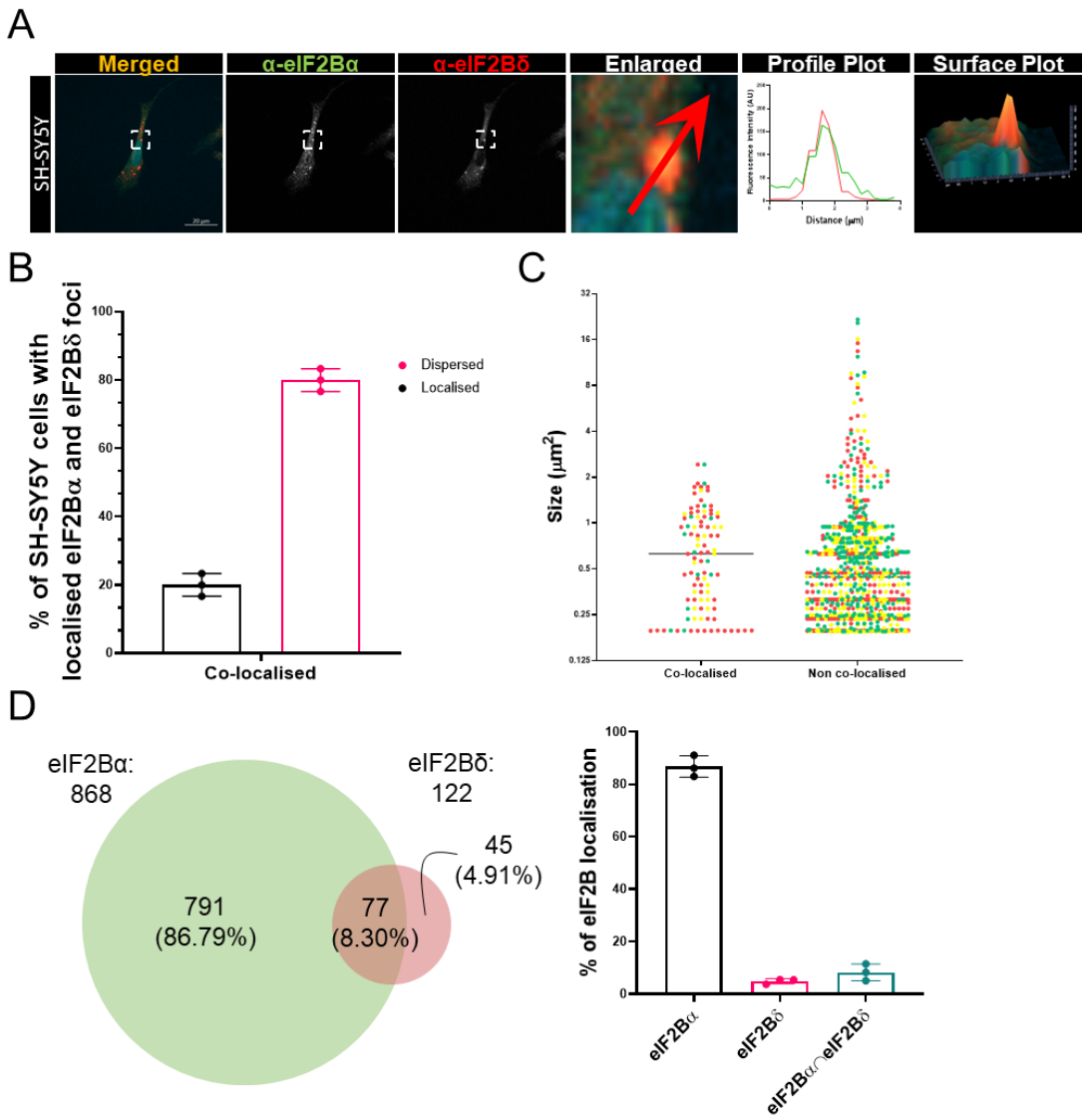

Figure 4.12. eIF2Bα and eIF2Bδ co-localisation in SH-SY5Y cells.

(A) Representative images of SH-SY5Y cells immunostained with primary antibodies against α-eIF2Bα and α-eIF2Bδ and visualized using appropriate secondary antibodies conjugated to AlexaFluor 488 for eIF2Bα and AlexaFluor 594 for eIF2Bδ. DAPI stains nuclei. Scale bar: 20 μm. Area defined was enlarged and the profile plot of the fluorescence intensity of each eIF2B subunit (green line – 488; red line – 594) and surface plot was plotted. (B) Mean percentage of cells displaying dispersed cytoplasmic and localised eIF2Bδ foci in a population of 30 cells per replicate with eIF2Bα localised foci. Error bars: ± s.d. (n=3). (C) Size distribution of eIF2Bα foci in 30 cells with localised eIF2Bα, co-localised or not co-localised with eIF2Bδ foci. (n=3, each repeat was coloured accordingly, repeat 1 – red; repeat 2 – yellow; repeat 3 – green). (D) Venn diagram of eIF2Bα and eIF2Bδ foci and co-localisation (n=3 counts in 30 cells with eIF2Bα localisation). Total number of all three repeats were used to determine percentages of groups. Bar graph of each biological repeat of each group. Error bars: ± s.d.

Only 2.60 % (± 0.35) of small eIF2Bα and eIF2Bδ co-localised in U373-MG cells. In MO3.13 cells, 1.58 % (± 0.65) of small eIF2Bα and eIF2Bδ foci co-localised and in SH-SY5Y cells 7.35 % (± 3.32) of small eIF2Bα and eIF2Bδ foci co-localised (**Figure 4.13**).

Large eIF2Bα and eIF2Bδ foci showed a much higher percentage of co-localisation in all three cell lines (U373-MG: 28.21 % ± 6.32; MO3.13: 28.21 % ± 6.32; SH-SY5Y: 14.08 % ± 2.58). As seen with the pattern of co-localisation between eIF2Bα and eIF2Bγ, the majority of large eIF2Bδ foci co-localised with eIF2Bα (U373-MG: 4.65 % ± 5.50; MO3.13: 4.65 % ± 5.50; SH-SY5Y: 0.74 % ± 1.28) (**Figure 4.14**).

The average number of each subunit foci per cell was investigated. In U373-MG cells there was an average of 3.88 (± 0.79) and 2.08 (± 0.75) small eIF2Bα and eIF2Bδ foci per cell, respectively, and 1.59 (± 0.66) and 1.07 (± 0.35) large eIF2Bα and eIF2Bδ foci per cell. In MO3.13 cells there was an average of 7.18 (± 1.63) and 1.65 (± 1.20) small eIF2Bα and eIF2Bδ foci per cell, respectively, and 1.44 (± 0.49) and 1.48 (± 0.34) large eIF2Bα and eIF2Bδ foci per cell, respectively. In SH-SY5Y cells, an average of 8.16 (± 0.28) and 5.18 (± 2.36) small eIF2Bα and eIF2Bδ foci per cell was recorded, and 1.49 (± 0.43) and 1.04 (± 0.44) large eIF2Bα and eIF2Bδ foci per cell, respectively (**Figure 4.15**).

These results provided evidence that co-localisation between the eIF2Bα and eIF2Bγ allowed for deduction of eIF2B assembly composition. Additionally, co-localisation between eIF2Bα and eIF2Bδ allows us to exclude the possibility that eIF2B regulatory subcomplexes lead to eIF2B localisation in these glial and neuronal cells. As such, we could extract from these results that additional novel populations of localised eIF2Bα assemblies are present in varying amounts, in glial and neuronal cells. This suggests that there may be an additional functional and/or compositional role of eIF2Bα in the formation and regulation of eIF2B bodies, which will be discussed further.

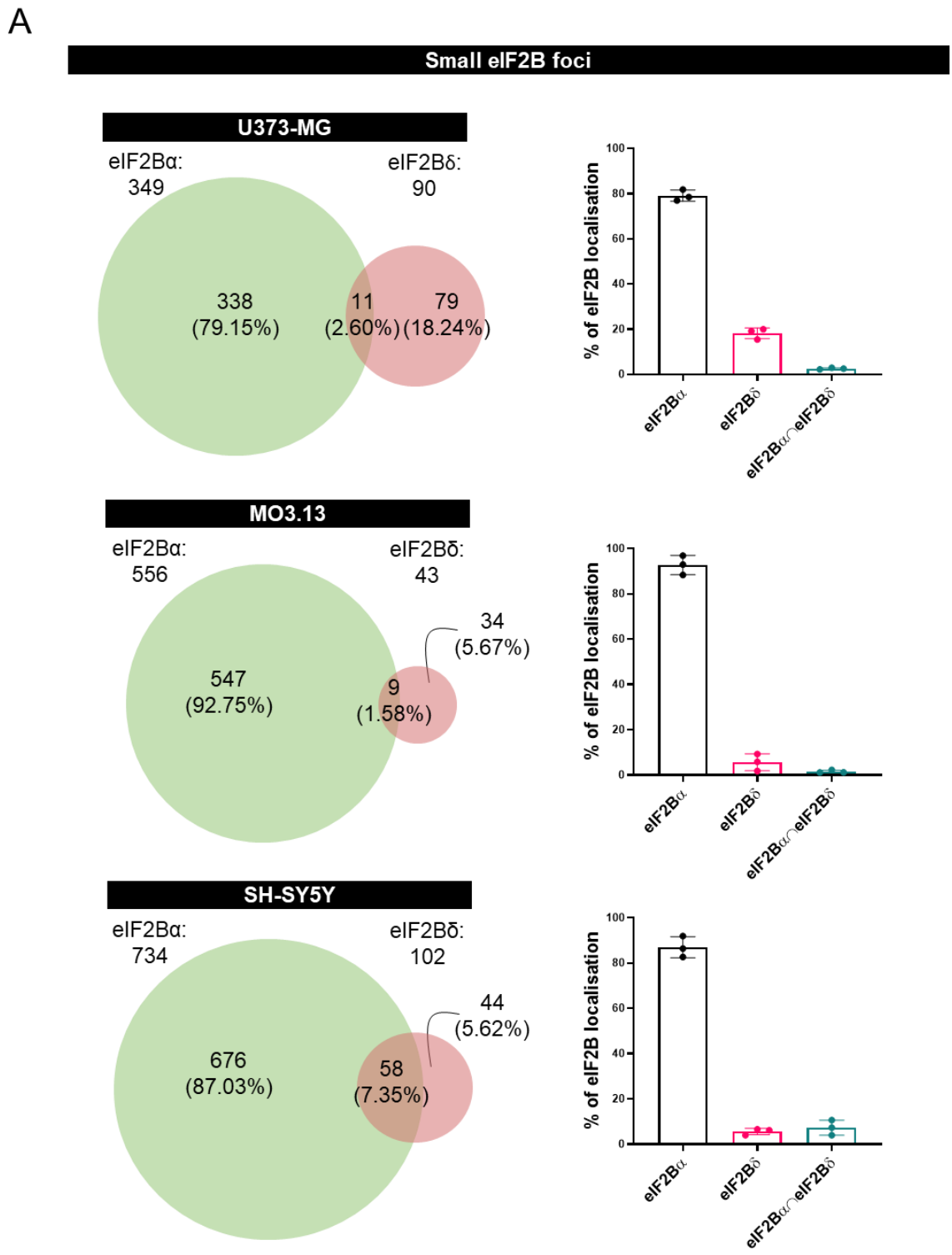

Figure 4.13. eIF2Bα and eIF2Bδ co-localisation of small foci in U373-MG, MO3.13 and SH-SY5Y cells.

Venn diagram of small eIF2Bα and eIF2Bδ foci and co-localisation (n=3 counts in 30 cells with eIF2Bα localisation) (top to bottom) in U373-MG, MO3.13 and SH-SY5Y cells. Total number of all three repeats were used to determine percentages of groups. Bar graph of each biological repeat of each group. Error bars: ± s.d.

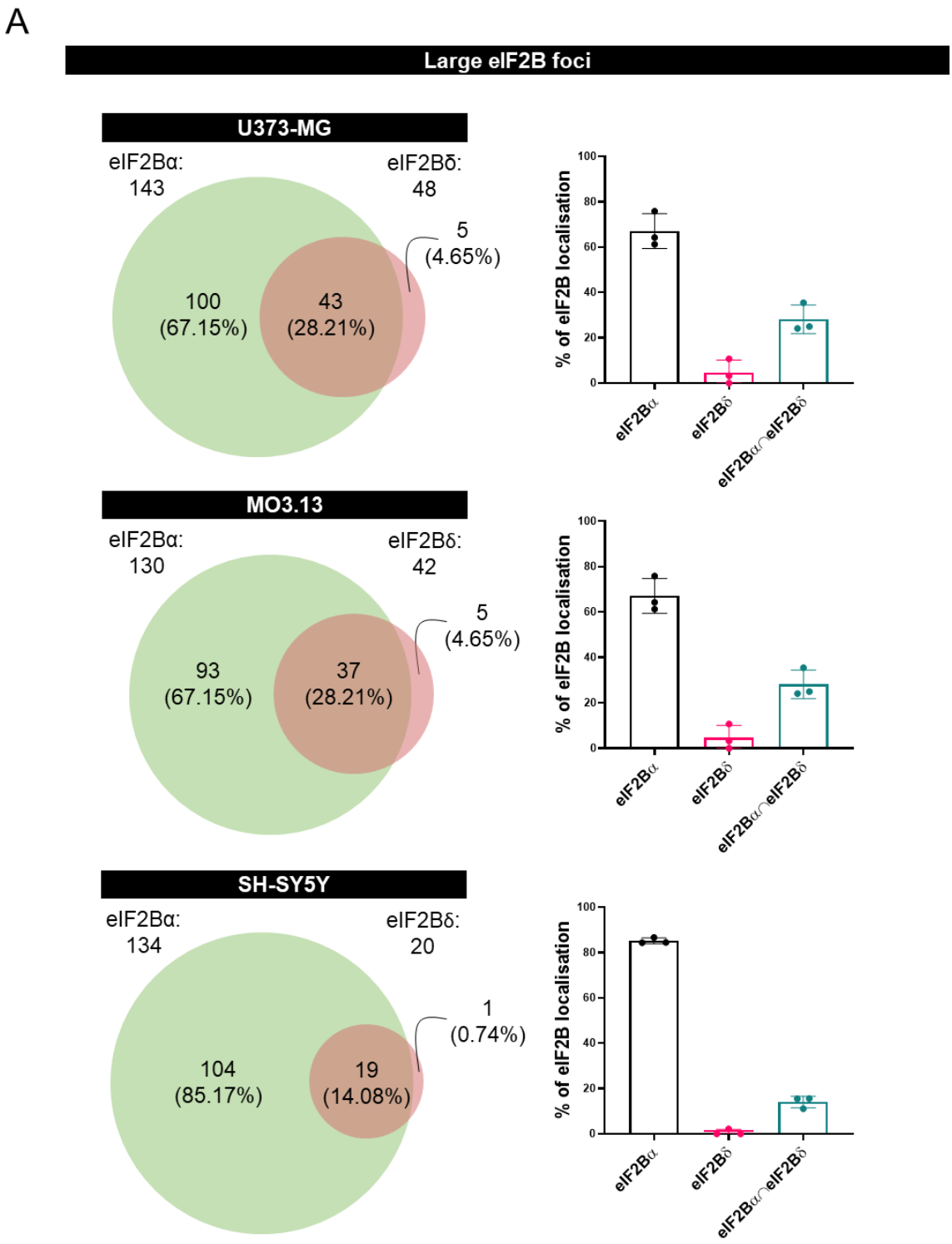

Figure 4.14. eIF2Bα and eIF2Bδ co-localisation of large foci in U373-MG, MO3.13 and SH-SY5Y cells.

Venn diagram of large eIF2Bα and eIF2Bδ foci and co-localisation (n=3 counts in 30 cells with eIF2Bα localisation) (top to bottom) in U373-MG, MO3.13 and SH-SY5Y cells. Total number of all three repeats were used to determine percentages of groups. Bar graph of each biological repeat of each group. Error bars: ± s.d.

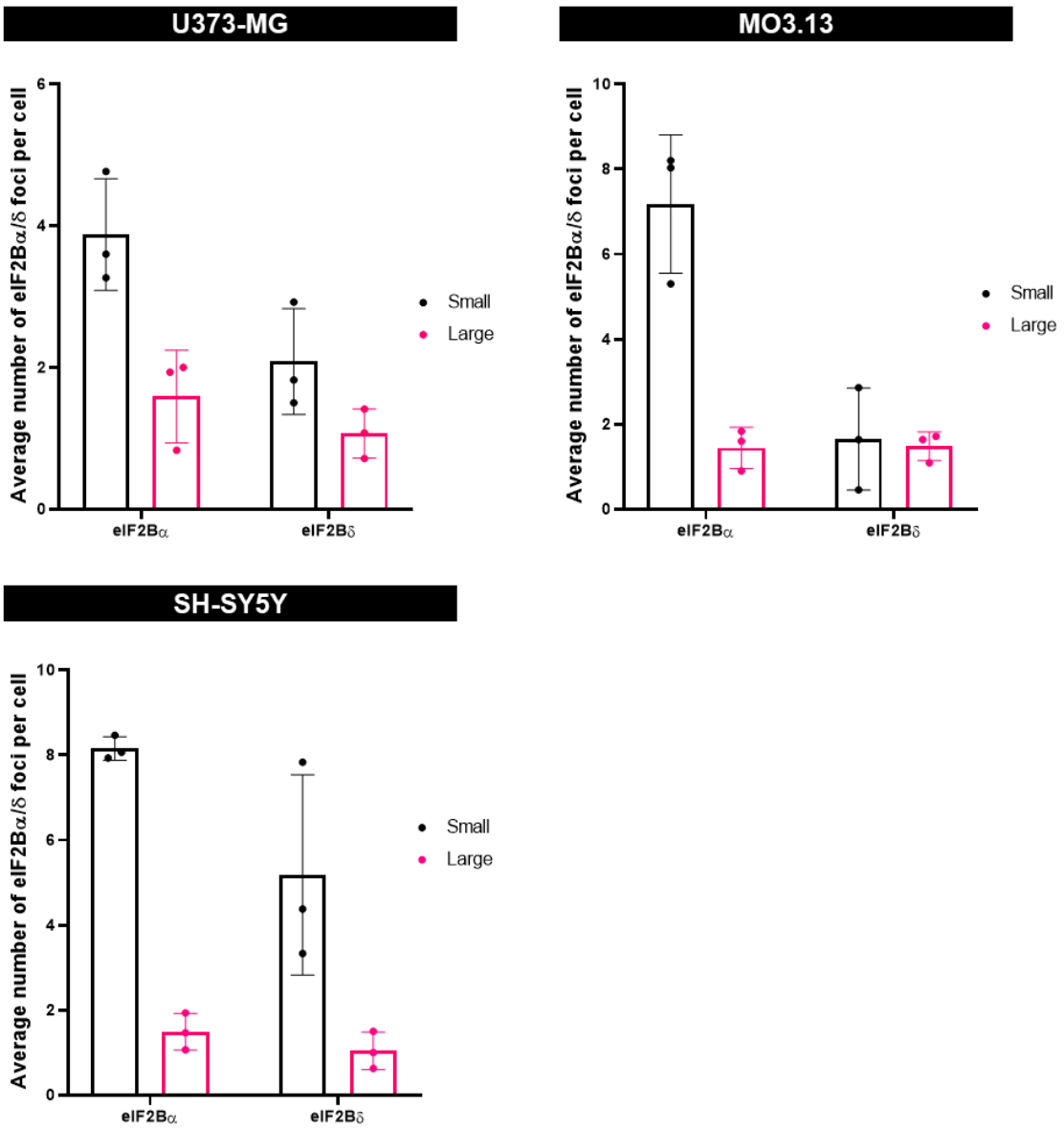

Figure 4.15. Average number of eIF2Bα and eIF2Bδ foci in U373-MG, MO3.13 and SH-SY5Y cells.

Average number of small and large eIF2Bα and eIF2Bδ foci per cell in 30 U373-MG, MO3.13 and SH-SY5Y cells with eIF2Bα localised foci (n=3). Error bars: ± s.d.

4.2.3. Endogenous eIF2B cytoplasmic foci have a distinct localisation pattern between different mammalian cell lines.

Given that it is possible to distinguish the composition of eIF2B foci according to their size, two populations were classified – small foci < 1μm^2, composed of differently arranged subcomplexes, and large foci ≥ 1μm^2, illustrating full eIF2B decamers.

As such, the number of eIF2B foci was analyzed according to the mentioned distinction of sizes/composition. To do so, 30 cells with one or more eIF2B localised foci were evaluated in all three mammalian cell lines in two separate manners – the average number of foci per cell divided between small and large and the proportion between small versus large foci per cell (**Figure 4.16**).

Comparing each subunit within individual cell lines, it was possible to observe that large eIF2Bα-ε foci do not vary significantly in all three cell lines, with an average number ranging from 0.58 (± 0.14) to 0.96 (± 0.21) foci per cell across the glial and neuronal cell lines (**Figure 4.17**).

In U373-MG cells we observed a significant increase in localisation of small foci for eIF2Bε, with an average number of 3.63 foci per cell (± 0.87), compared to eIF2Bβ and δ, with both having an average number of 2.04 foci per cell (± 0.46 and ± 0.70, respectively) (**Figure 4.17**).

In MO3.13 and SH-SY5Y cells a significantly higher average number of small eIF2Bα foci was identified, with 6.21 (± 1.06) and 5.88 (± 0.55) eIF2Bα foci per cell, respectively, when comparing with all the eIF2B subunits (**Figure 4.17**).

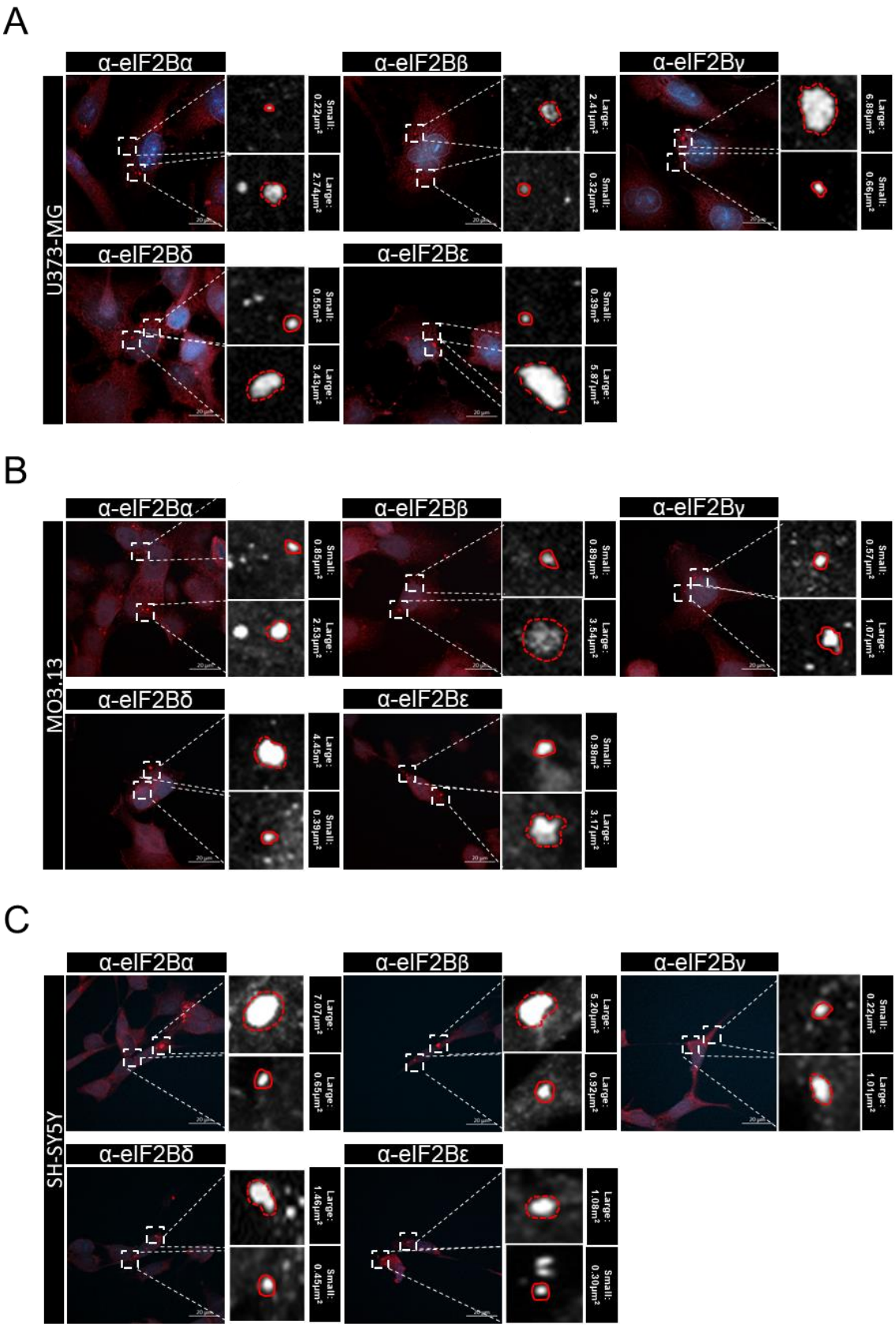

Figure 4.16. U373-MG, MO3.13 and SH-SY5Y show large and small localised foci for all five eIF2B subunits.

(A) Representative images of U373-MG cells immunostained with primary antibodies against endogenous α-eIF2Bα, α-eIF2Bβ, α-eIF2Bγ, α-eIF2Bδ and α-eIF2Bε, and visualized using

appropriate secondary antibodies conjugated to Alexa Fluor 594. DAPI stains nuclei. Scale bar: 20 µm. (B) Representative confocal images of MO3.13 cells immunostained with primary antibodies against endogenous α-eIF2Bα, α-eIF2Bβ, α-eIF2Bγ, α-eIF2Bδ and α-eIF2Bε, and visualized using appropriate secondary antibodies conjugated to Alexa Fluor 594. DAPI stains nuclei. Scale bar: 20 µm. (C) Representative confocal images of SH-SY5Y cells immunostained with primary antibodies against endogenous α-eIF2Bα, α-eIF2Bβ, α-eIF2Bγ, α-eIF2Bδ and α-eIF2Bε, and visualized using appropriate secondary antibodies conjugated to Alexa Fluor 594. DAPI stains nuclei. Scale bar: 20 µm.

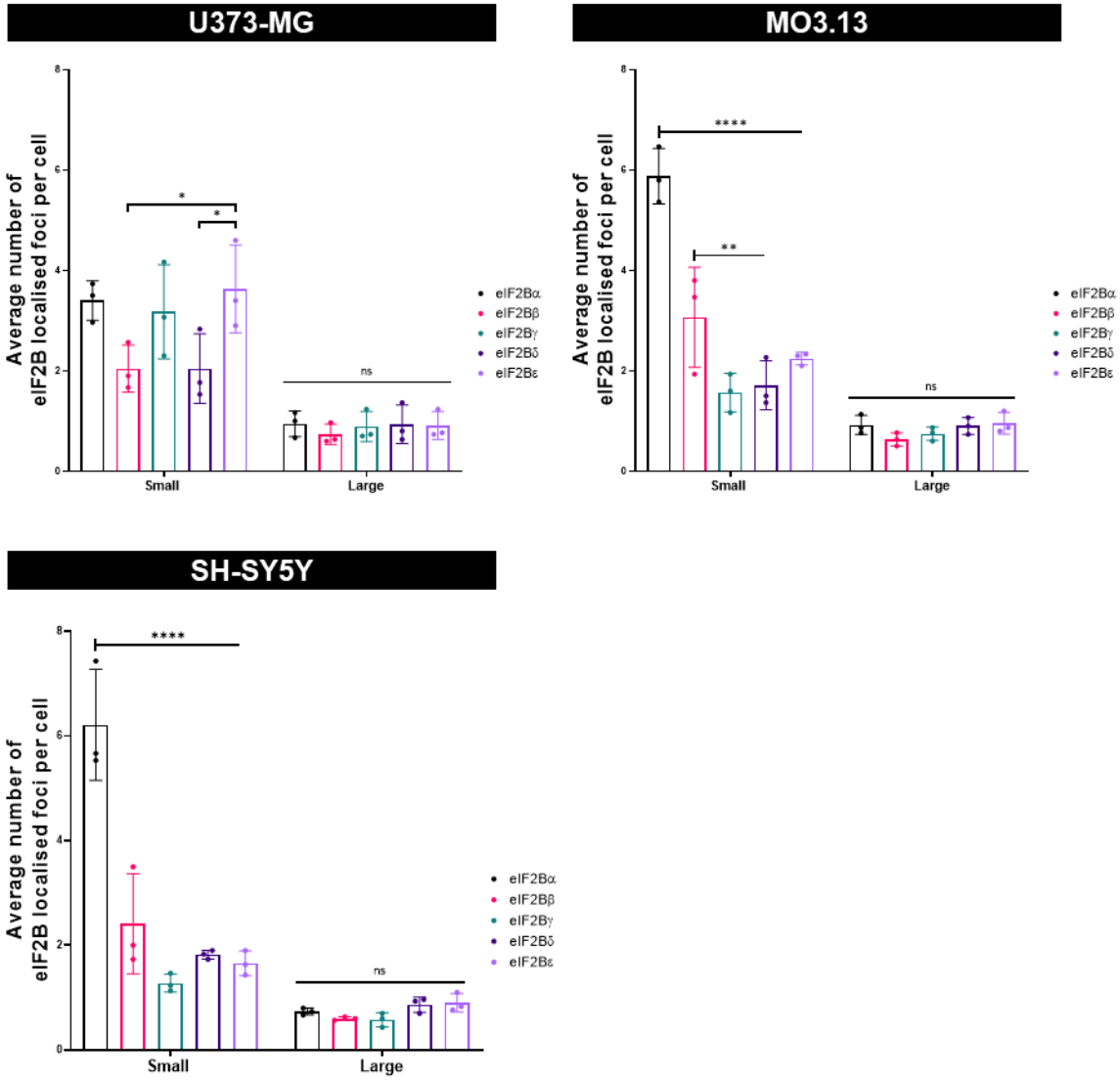

Figure 4.17. Average number of large and small eIF2Bα-ε foci per cell in U373-MG, MO3.13 and SH-SY5Y cells.

Average number of small and large eIF2Bα-ε foci per cell in a population of 30 U373-MG, MO3.13 and SH-SY5Y cells with localised eIF2Bα-ε (n=3). Data was analysed using two-way ANOVA followed by *post-hoc* Tukey's test for multiple comparisons. Error bars: ± s.d. (n=3). *$p \leq 0.05$; **$p \leq 0.01$; ****$p \leq 0.0001$.

We next compared the average localisation patterns across the studied cell lines. Large eIF2B foci of each subunit showed a similar pattern of across the cell lines with no significant variations between the cell lines (**Figure 4.18A**). However, we discovered some intriguing counts of small eIF2B foci.

U373-MG cells showed a significantly higher number of small eIF2Bγ and eIF2Bε localisation per cell, with eIF2Bγ showing ~2.0-fold change and eIF2Bε showing ~1.6-fold change when compared to MO3.13 cells, and eIF2Bγ showing ~2.5-fold change and eIF2Bε showing ~2.2-fold change when compared to SH-SY5Y cells. All three cell lines presented similar number of small eIF2Bβ and eIF2Bδ foci per cell in steady state conditions (**Figure 4.18B**).

Most strikingly, the average number of localised eIF2Bα displayed a large disparity according to cell type. Under steady state conditions, MO3.13 and SH-SY5Y showed a significantly higher number of small eIF2Bα foci per cell, with ~1.7 and ~1.8-fold change, respectively, compared to the U373-MG cells (3.40 ± 0.39) (**Figure 4.18B**).

These data suggest that eIF2B localisation may exist in a cell-type specific manner. While large eIF2B foci, which we can speculate to demonstrate eIF2B decameric localisation, were constant throughout the glial and neuronal cell lines, a higher presence of small eIF2Bγ and eIF2Bε localised foci was present U373-MG cells. More strikingly, a higher population of small eIF2Bα localised foci per cell were present in MO3.13 and SH-SY5Y cells. From the analysis of percentage of cells with eIF2B foci (detailed in **section 4.2.1**) and the co-localisation work (detailed in **section 4.2.2**), a large proportion of eIF2Bα assemblies appear to be independent of the localisation of the other eIF2B subunits, reinforcing our hypothesis that eIF2Bα structures, such as the homodimer structure, can localise to discrete cytoplasmic foci in mammalian cells.

To observe whether there was any correlation between protein expression and changes in localisation western blot analysis was carried out. In all three cell types similar trends of protein expression was observed for each subunit (**Figure 4.19**). Thus, the cell-type specific subunit composition of eIF2B foci was independent of its expression levels. However, it's worth noting that

following overexpression of eIF2Bα, eIF2Bα localised foci appeared to no longer being able to form (**Figure 4.20**). This aberrant localisation of eIF2Bα was able to be corrected through co-transfection of eIF2Bα-RFP and siRNA-mediated silencing of *EIF2B1* (**Figure 4.21**). Additionally, through live imaging of these eIF2Bα-RFP foci, it was possible to observe that these assemblies were highly dynamic structures and appeared to share LLPS characteristics (**Figure 4.22**).

A

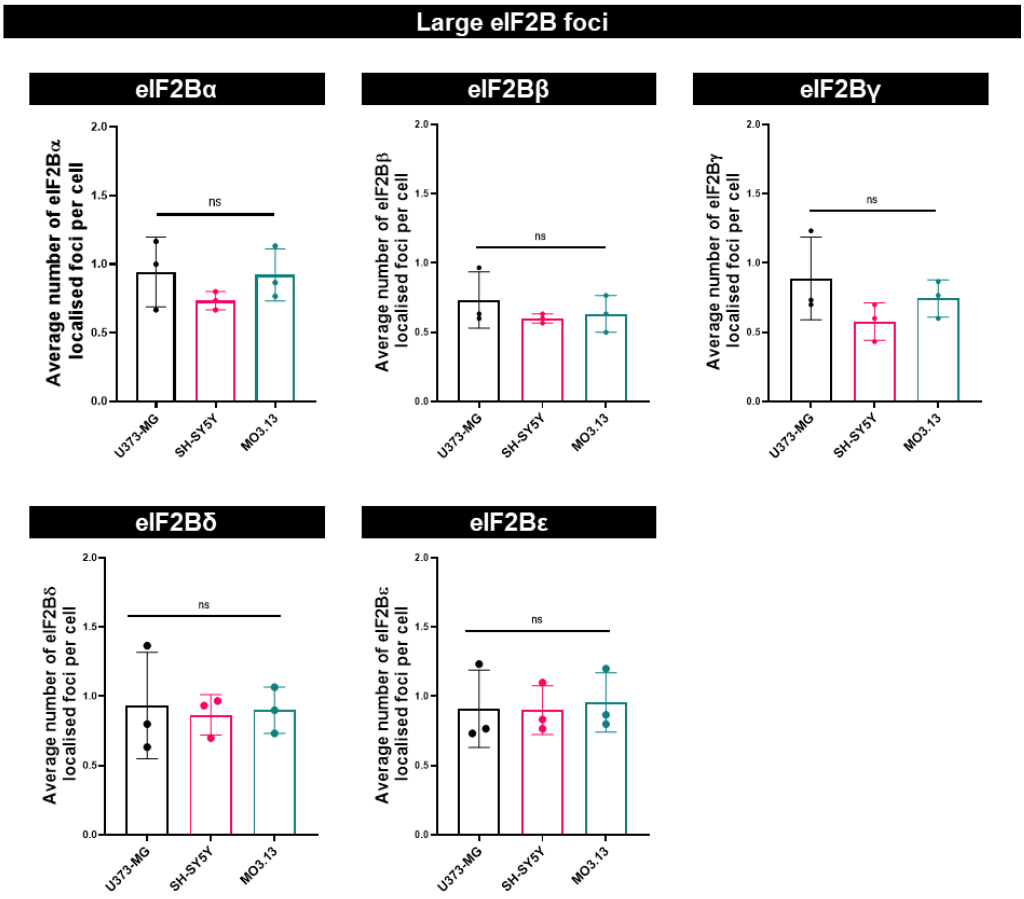
Large eIF2B foci
eIF2Bα
eIF2Bβ
eIF2Bγ
eIF2Bδ
eIF2Bε
Average number of eIF2Bα localised foci per cell
Average number of eIF2Bβ localised foci per cell
Average number of eIF2Bγ localised foci per cell
Average number of eIF2Bδ localised foci per cell
Average number of eIF2Bε localised foci per cell
ns
U373-MG
SH-SY5Y
MO3.13

B

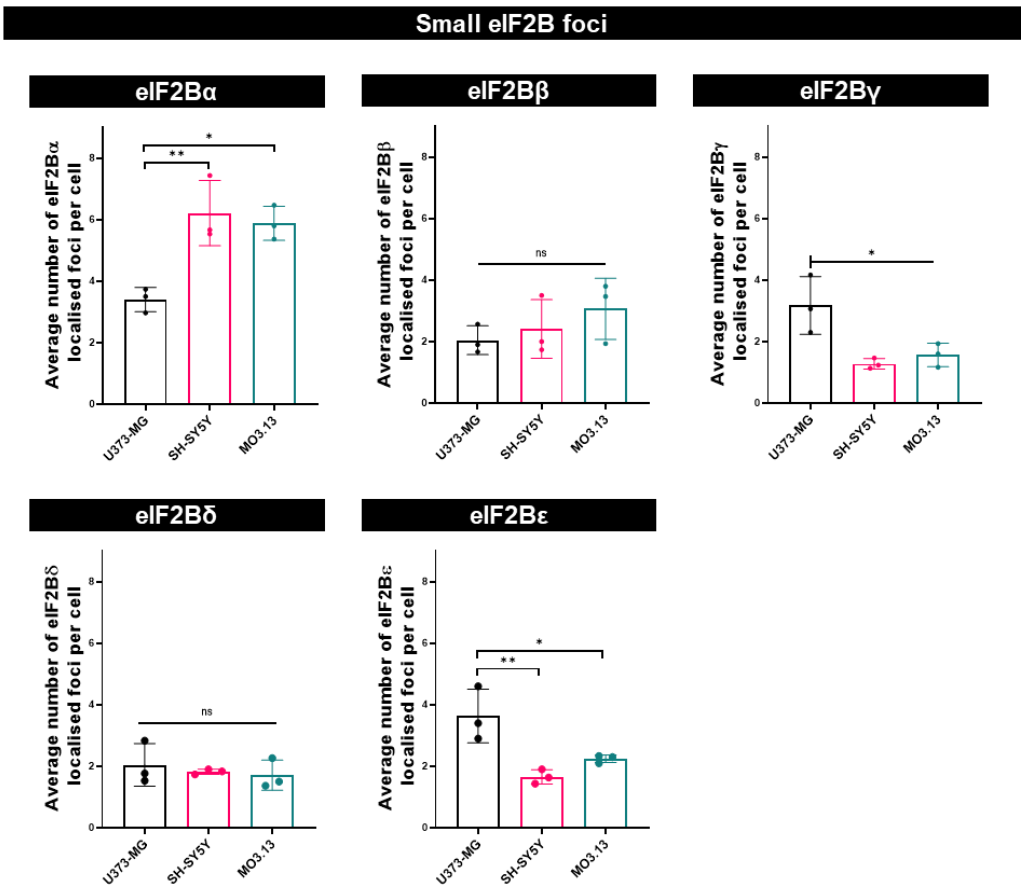
Small eIF2B foci
eIF2Bα
eIF2Bβ
eIF2Bγ
eIF2Bδ
eIF2Bε
Average number of eIF2Bα localised foci per cell
Average number of eIF2Bβ localised foci per cell
Average number of eIF2Bγ localised foci per cell
Average number of eIF2Bδ localised foci per cell
Average number of eIF2Bε localised foci per cell
ns
*
**
U373-MG
SH-SY5Y
MO3.13

Figure 4.18. Oligodendrocytic and neuronal cells display a higher average number of small eIF2Bα foci per cell and astrocytic cells display a higher average number of small eIF2Bγ and eIF2Bε foci per cell.

(A) Average number of large eIF2Bα-ε foci per cell in a population of 30 U373-MG, MO3.13 and SH-SY5Y cells with localised eIF2Bα-ε (n=3). Data was analysed using one-way ANOVA followed by *post-hoc* Tukey's test for multiple comparisons. Error bars: ± s.d. (n=3). (B) Average number of small eIF2Bα-ε foci per cell in a population of 30 U373-MG, MO3.13 and SH-SY5Y cells with localised eIF2Bα-ε (n=3). Data was analysed using one-way ANOVA followed by *post-hoc* Tukey's test for multiple comparisons. Error bars: ± s.d. (n=3). *$p \leq 0.05$; **$p \leq 0.01$.

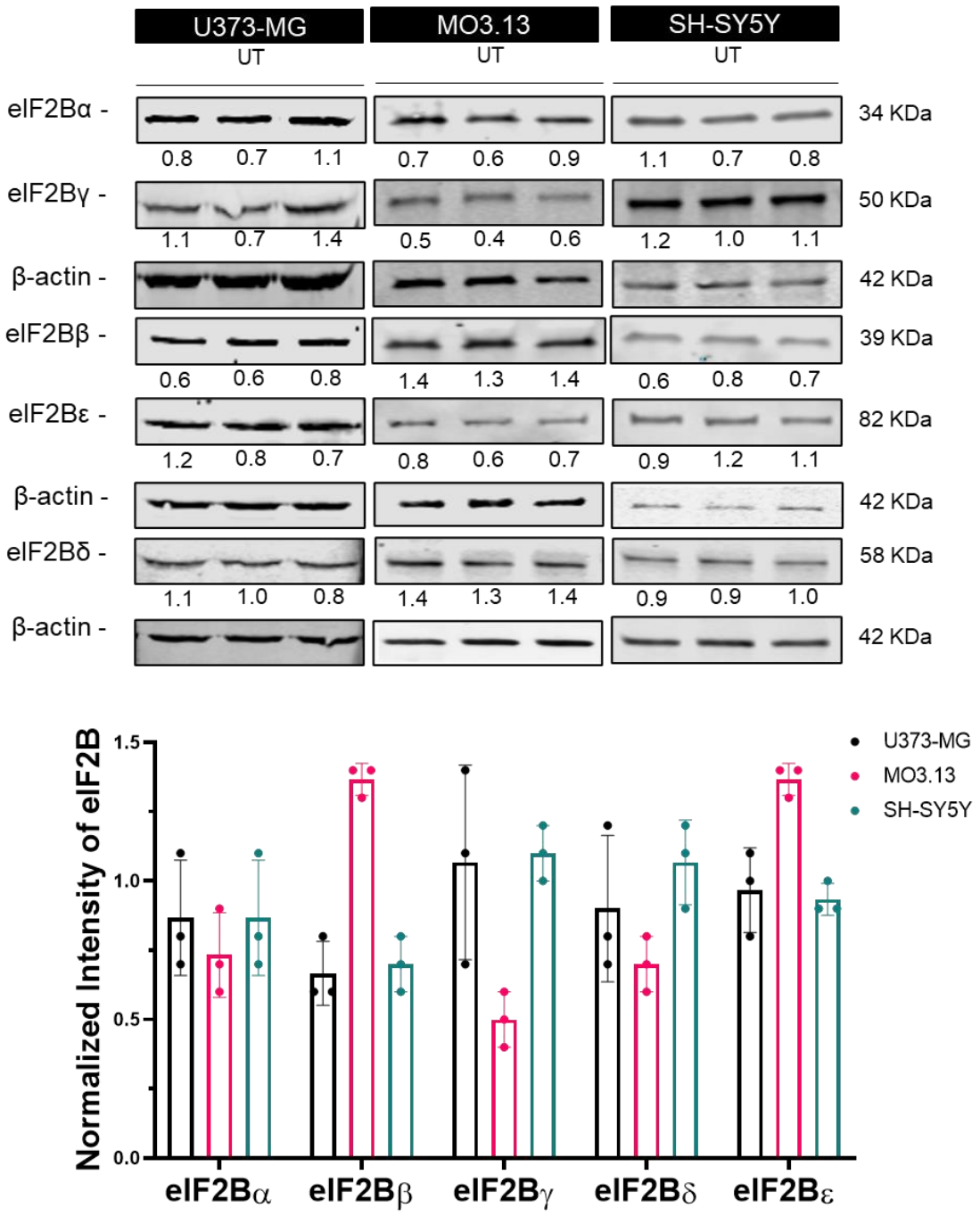

Figure 4.19. eIF2B expression levels do not correlate with eIF2B localisation patterns in U373-MG, MO3.13 and SH-SY5Y cells.

Western Blot analysis of the levels of eIF2Bα-ε expression in U373-MG, MO3.13 and SH-SY5Y cells under untreated conditions. Levels of eIF2Bα-ε were normalized to levels of β-actin. Each lane represents a single biological replicate (UT – untreated).

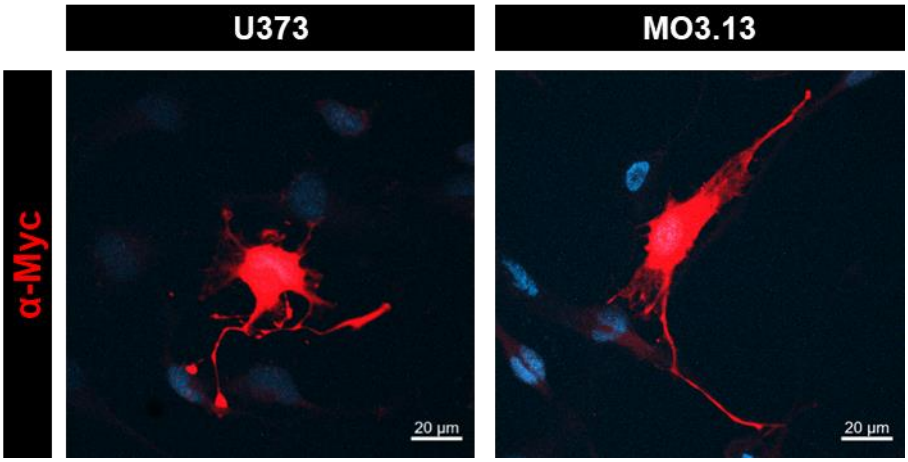

Figure 4.20. Overexpression of eIF2Bα leads to dispersed localisation.

U373-MG and MO3.13 cells were transiently transfected with eIF2Bα-Myc for 48 hours. They were subsequently subjected to ICC with anti-eIF2Bα primary antibodies and visualized using appropriate secondary antibodies conjugated to Alexa Fluor 594. Scale bar: 20 µm.

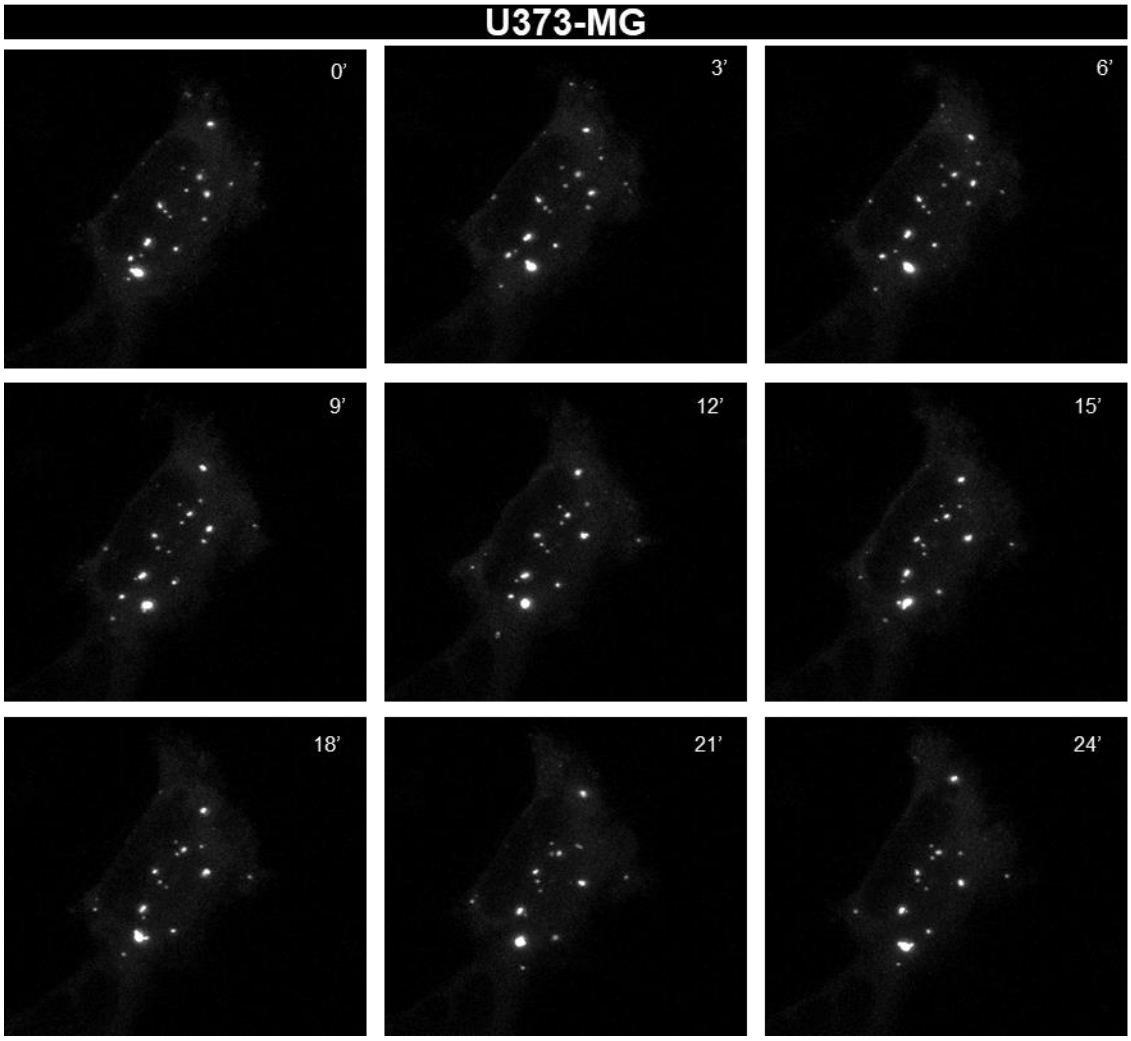

Figure 4.21. eIF2Bα foci are dynamic structures.

Representative live-images of a U373-MG cell transfected with eIF2Bα-RFP and captured over 24 minutes. Scale bar: 5 μm.

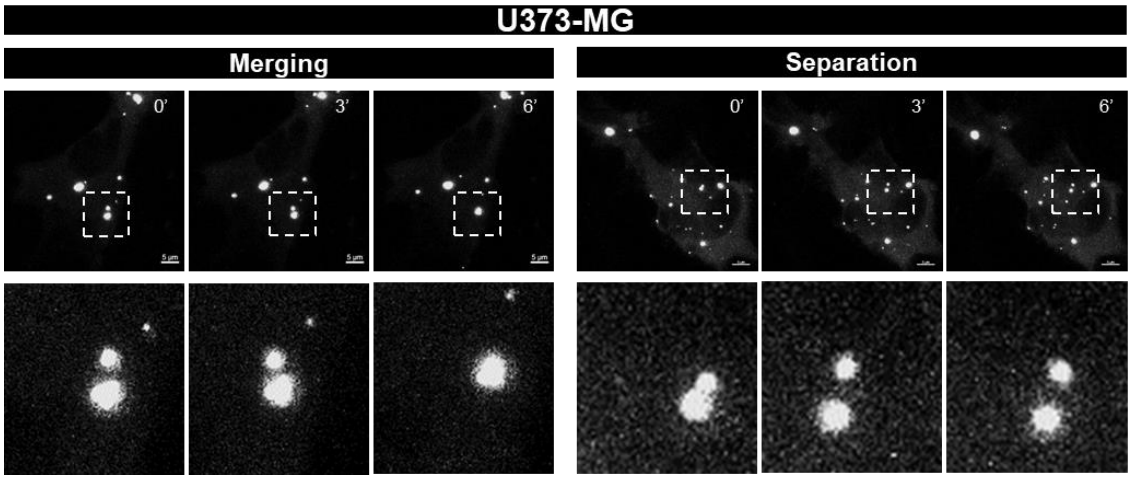

Figure 4.22. eIF2B foci share resemblance to LLPS granules.

Representative live-imaging of a U373-MG cell transfected with eIF2Bα-RFP and captured over 6 minutes showing merging and segregation of eIF2Bα-RFP foci. Scale bar: 5 μm.

4.2.4. eIF2Bα and eIF2Bε foci localise and modulate upon ER stress in a cell type-specific manner.

Given that regulatory subunits, but particularly eIF2Bα, are necessary for the sensing of eIF2α phosphorylation, which subsequently inhibits eIF2B activity (Kashiwagi *et al*., 2019), it was of interest to determine the localisation of eIF2Bα in the presence of cellular stress in the glial and neuronal cell lines. PERK-mediated phosphorylation of eIF2α was induced through Tg. This agent causes depletion of ER calcium levels, thus triggering the UPR/ISR (Liang *et al*., 2006). ICC targeting eIF2Bα in untreated cells as a control and cells treated with DMSO (as vehicle) and Tg for 1h (1μM) was carried out.

Firstly, the population of cells with eIF2Bα localisation, *i.e.*, with one or more foci per cell, was determined in all three mammalian cell lines (**Figure 4.23A**).

There was a significant increase in percentage of U373-MG cells with eIF2Bα localisation upon treatment with Tg (UT: 23.67 % ± 2.08; DMSO: 29.00 % ± 3.61; Tg: 59.00 % ± 5.29). This increase was not observed for SH-SY5Y and MO3.13 cells which appeared to have similar localisation between steady state and stressed conditions. 65.67 % (± 3.79) and 66.33 % (± 5.03) of MO3.13 cells displayed eIF2Bα localisation in untreated and DMSO treated environments, with a slight increase of 75.67 % (± 3.51) cells with eIF2Bα foci followed acute stress. SH-SY5Y cells showed 71.67 % (± 2.52), 71.33 % (± 3.51) and 76.67 % (± 2.08) cells with eIF2Bα foci under untreated, DMSO and Tg treatment conditions, respectively (**Figure 4.23B**).

The median size of these foci was comparable throughout in U373 cells (UT: 0.97 μm^2 ± 1.44; DMSO: 1.06 μm^2 ± 1.55; Tg: 0.89 μm^2 ± 1.26). The median size of eIF2Bα under these conditions in MO3.13 was 0.57 μm^2 (UT ± 0.65), 0.52 μm^2 (DMSO ± 0.67), and 0.63 μm^2 (Tg ± 0.85). The mean size of eIF2Bα was 0.94 μm^2 (UT ± 1.65), 0.70 μm^2 (DMSO ± 0.85), and 0.79 μm^2 (Tg ± 0.96) in SH-SY5Y cells (**Figure 4.24**).

Following this, the average number of eIF2Bα cytoplasmic foci per cell, classified by size, was investigated. eIF2Bα localisation significantly increased following ER stress induction in all three cell lines.

Large and small eIF2Bα foci showed a significant increase of average number of foci following stress treatments. In U373-MG cells, untreated and cells treated with DMSO, showed a 0.93 (± 0.13) and 1.26 (± 0.43) average number of large foci, respectively. Tg treatment for 1h lead to an increase of the average number

of large foci to 3.14 (± 0.72). In MO3.13 cells, untreated and cells treated with DMSO, showed a 0.86 (± 0.05) and 0.82 (± 0.25) average number of large foci, respectively. Tg treatment for 1h lead to an increase of the average number of large foci of 1.80 (± 0.48). In SH-SY5Y cells, untreated and cells treated with DMSO, showed a 1.01 (± 0.14) and 1.10 (± 0.19) average number of large foci, respectively. Tg treatment for 1h lead to an increase of the average number of large foci of 2.54 (± 0.63) (**Figure 4.25A**). In U373-MG cells, an average of 3.08 (± 0.62) and 2.91 (± 0.95) eIF2Bα foci per cell were detected in steady state conditions, while an average of 10.07 (± 1.12) eIF2Bα foci per cell was observed following Tg treatment. In MO3.13, untreated and cells treated with DMSO appeared to showcase an average of 5.83 (± 1.05) and 6.56 (± 0.38) of eIF2Bα foci per cell, respectively. Tg treated showed a significant increase in eIF2Bα localisation, with an average of 10.26 (± 2.22) foci per cell being identified. Finally, SH-SY5Y cells showed an average of 5.94 (± 0.24) and 5.97 (± 1.65) of eIF2Bα foci per cell in untreated and DMSO treated cells. A significant increase of these foci was identified following Tg treatment, with a 9.26 (± 0.98) average of eIF2Bα foci per cell being detected (**Figure 4.25B**). This increase in localisation did not correlate with the increase of protein levels, as observed in **Figure 4.26**.

A

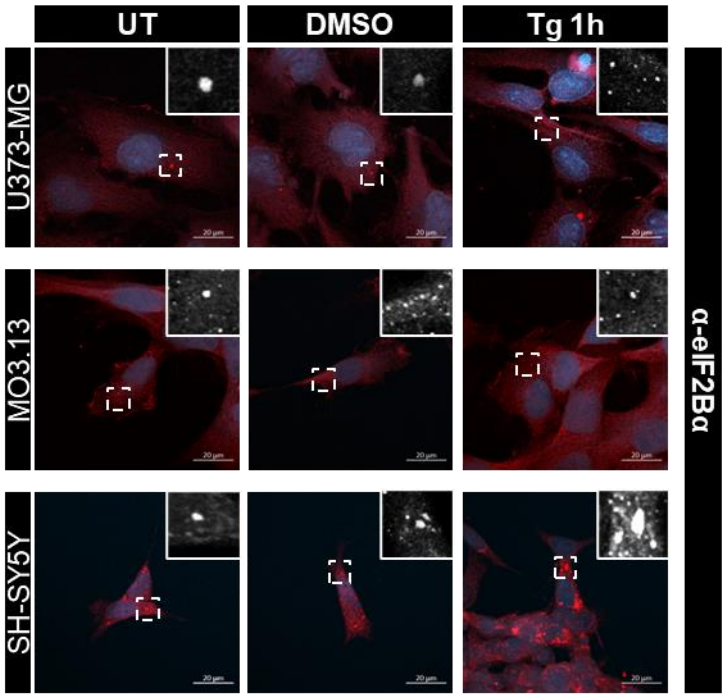
UT
DMSO
Tg 1h
U373-MG
MO3.13
SH-SY5Y
α-eIF2Bα

B

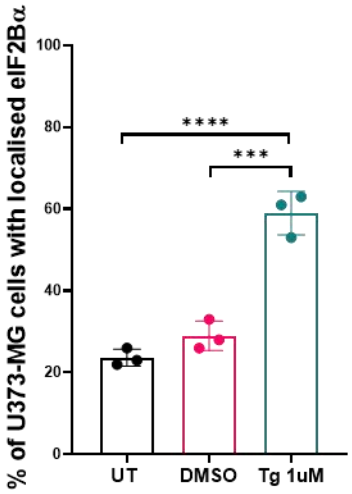
% of U373-MG cells with localised eIF2Bα
100
80
60
40
20
0
****
***
UT
DMSO
Tg 1uM

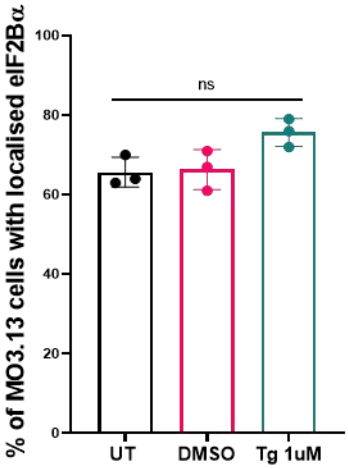
% of MO3.13 cells with localised eIF2Bα
100
80
60
40
20
0
ns
UT
DMSO
Tg 1uM

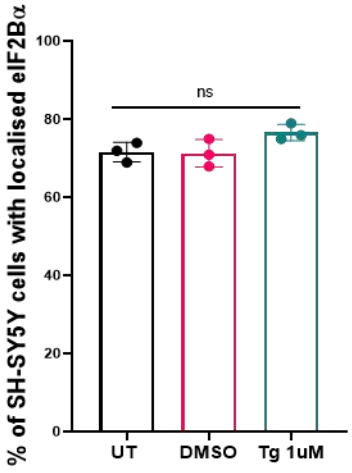
% of SH-SY5Y cells with localised eIF2Bα
100
80
60
40
20
0
ns
UT
DMSO
Tg 1uM

Figure 4.23. eIF2Bα localisation increases in astrocytic cells following acute ER stress.
(A) Representative images of (top to bottom) U373-MG, MO3.13 and SH-SY5Y cells immunostained with primary antibodies against endogenous α-eIF2Bα and visualized using appropriate secondary antibodies conjugated to Alexa Fluor 594, following untreated, DMSO and Tg 1μM 1h treatment (UT – untreated). DAPI stains nuclei. Scale bar: 20 μm. (B) Mean percentage of cells displaying dispersed cytoplasmic and localised eIF2Bα foci in a population of 100 cells per replicate, in U373-MG, MO3.13, and SH-SY5Y cells, following untreated, DMSO and Tg 1μM 1h treatment. Data was analysed using one-way ANOVA followed by post-hoc Tukey's test for multiple comparisons. Error bars: ± s.d. (n=3). ***p≤0.001; ****p≤0.0001.

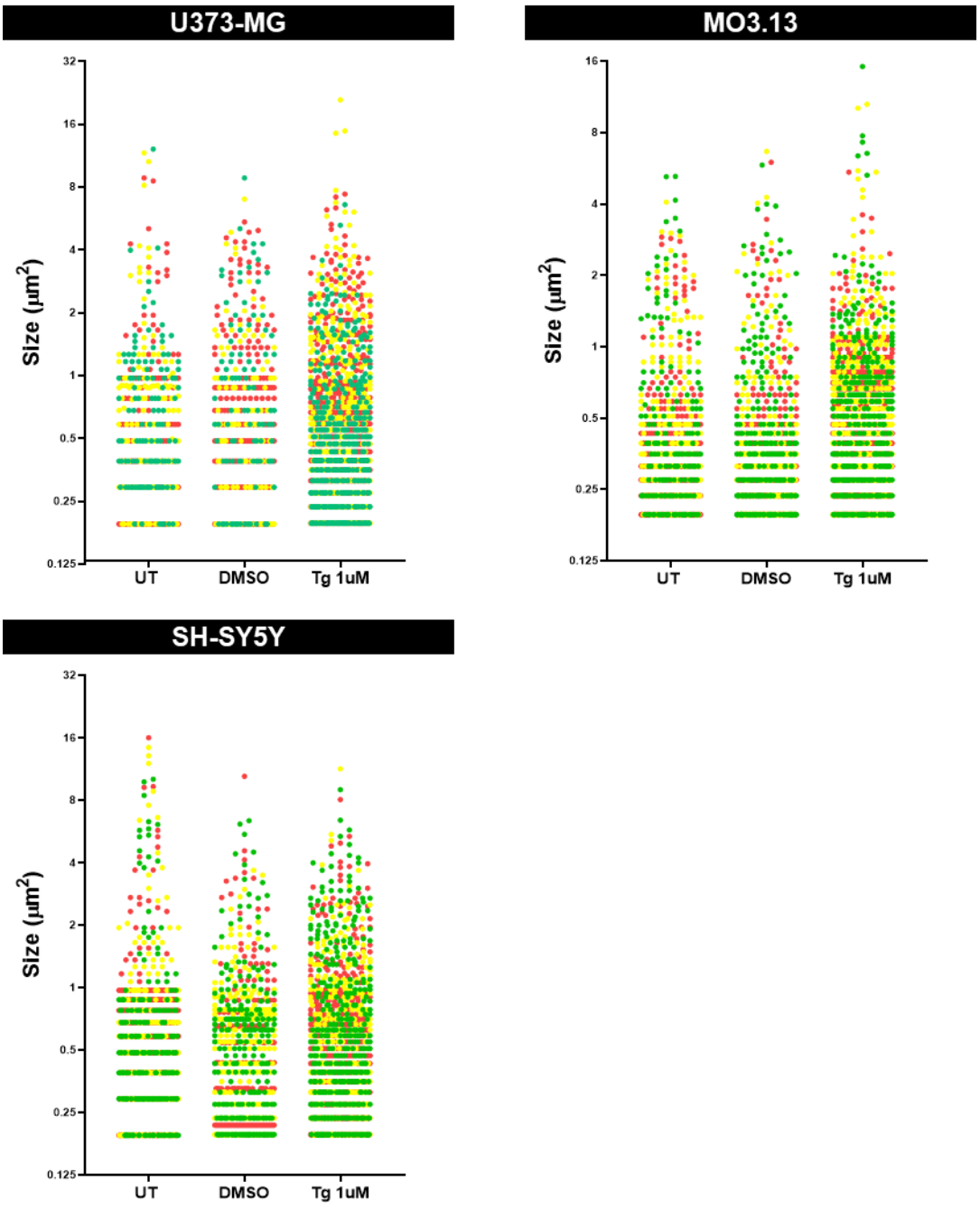

Figure 4.24. The size distribution of eIF2Bα has similar values to untreated conditions, following acute ER stress, in U373-MG, MO3.13 and SH-SY5Y.

Size distribution of eIF2Bα foci in 30 cells with localised eIF2Bα in U373-MG, MO3.13 and SH-SY5Y cells, following untreated, DMSO and Tg 1 µM 1h treatment (UT – untreated; n=3, each repeat was coloured accordingly, repeat 1 – red; repeat 2 – yellow; repeat 3 – green).

A

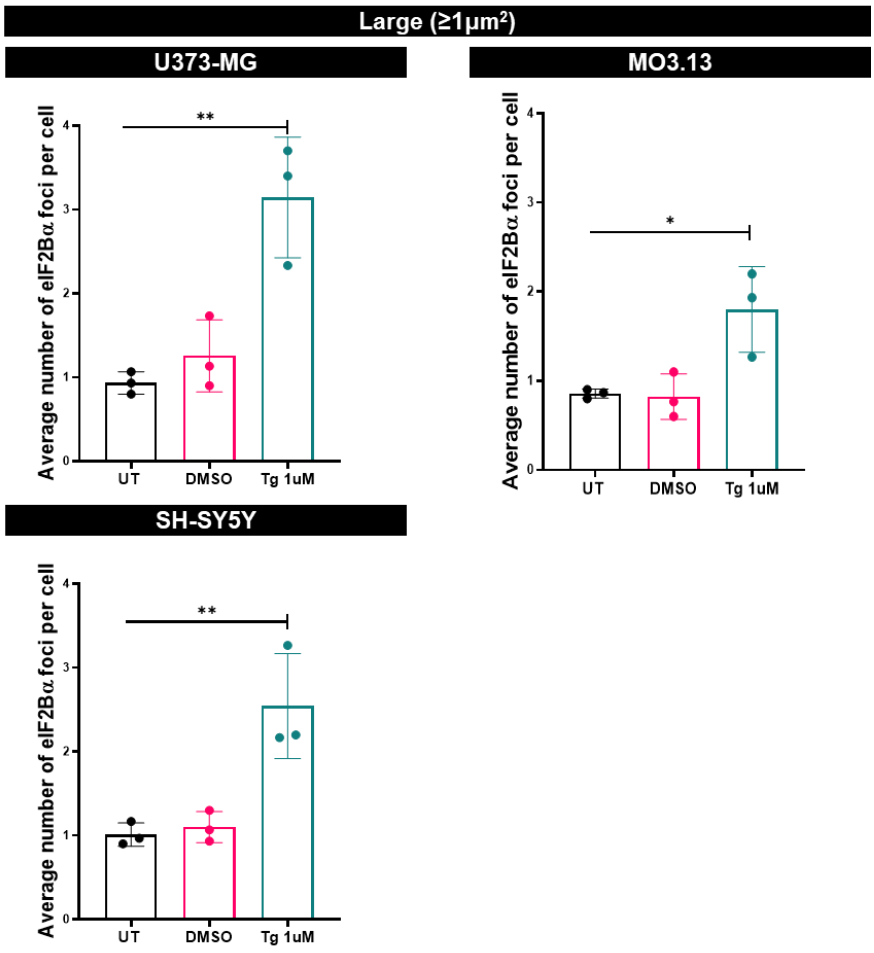
Large (≥1µm²)
U373-MG
MO3.13
SH-SY5Y
Average number of eIF2Bα foci per cell
UT
DMSO
Tg 1uM
**
*
**

B

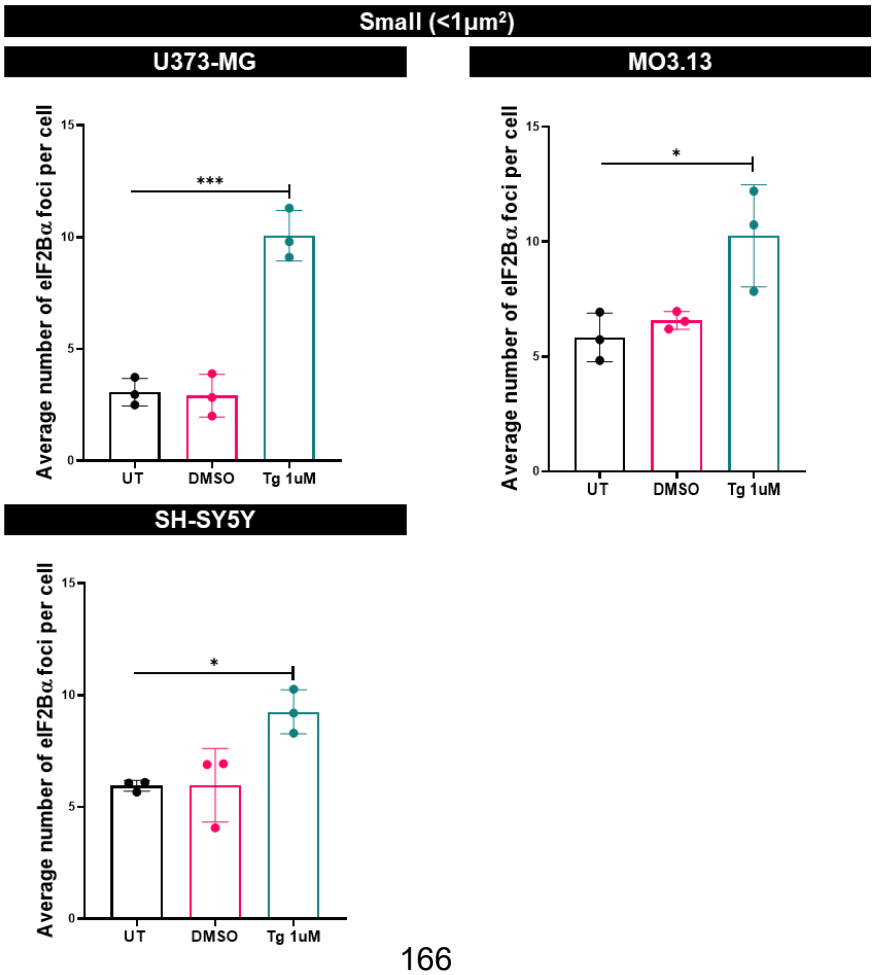
Small (<1µm²)
U373-MG
MO3.13
SH-SY5Y
Average number of eIF2Bα foci per cell
UT
DMSO
Tg 1uM
***
*
*

Figure 4.25. Large and small eIF2Bα foci increase following ER stress in U373-MG, MO3.13 and SH-SY5Y cells.

(A) Average number of large eIF2Bα foci per cell in a population of 30 U373-MG, MO3.13 and SH-SY5Y cells with localised eIF2Bα, following untreated, DMSO and Tg 1 μM 1h treatment (UT – untreated; n=3). Data was analysed using one-way ANOVA followed by *post-hoc* Tukey's test for multiple comparisons. Error bars: ± s.d. (n=3). *$p \leq 0.05$; **$p \leq 0.01$. (B) Average number of small eIF2Bα foci per cell in a population of 30 U373-MG, MO3.13 and SH-SY5Y cells with localised eIF2Bα, following untreated, DMSO and Tg 1 μM 1h treatment (n=3). Data was analysed using one-way ANOVA followed by *post-hoc* Tukey's test for multiple comparisons. Error bars: ± s.d. (UT – untreated; n=3). *$p \leq 0.05$; ***$p \leq 0.001$.

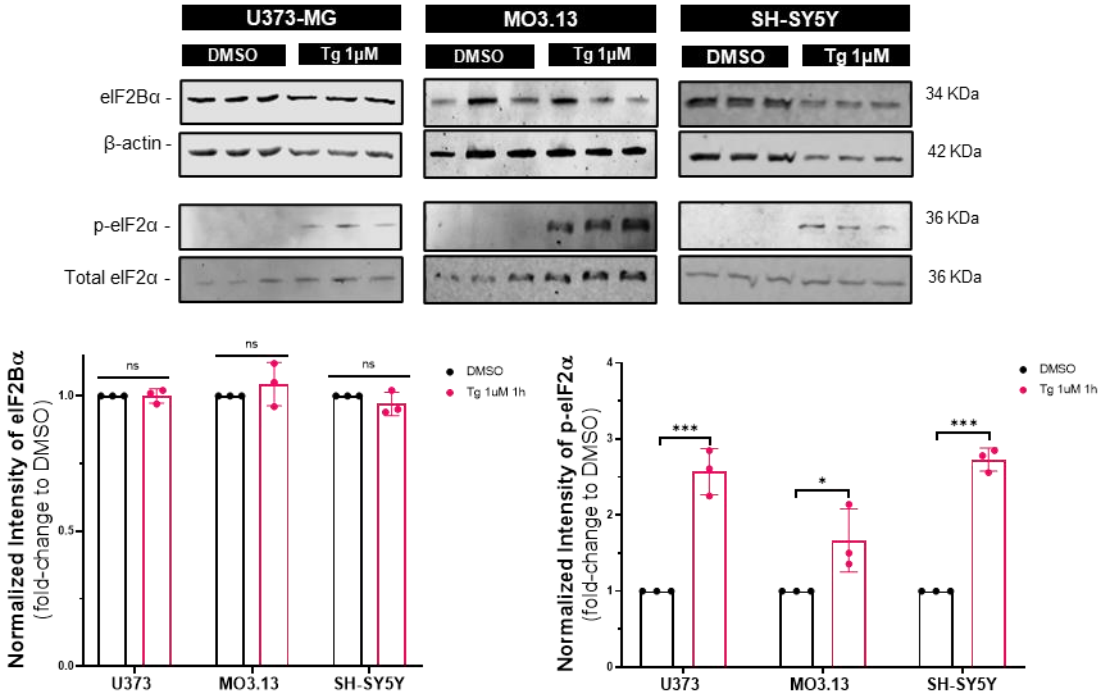

Figure 4.26. Expression levels of eIF2Bα were not increased following acute ER stress. Western Blot analysis of the levels of eIF2Bα, p-eIF2α and total eIF2α expression in U373-MG, MO3.13 and SH-SY5Y cells, following untreated, DMSO and Tg 1 μM 1h treatment. Levels of eIF2Bα were normalized to levels of β-actin (n=3). Levels of p-eIF2α were normalized to levels of total eIF2α (n=3). Data was analysed using two-way ANOVA followed by *post-hoc* Tukey's test for multiple comparisons. Error bars: ± s.d. (n=3). **p*≤0.05; ****p*≤0.001. Each lane represented a single biological replicate.

From previous studies which discussed and investigated eIF2Bε localisation and role following stress through the transient expression of GFP tagged eIF2Bε, the increase of small eIF2Bε foci, hypothesized as being composed of catalytic subunits (*i.e.*, eIF2Bγ and eIF2Bε subunits), was observed following Tg treatment (Hodgson *et al*., 2019). We next determined the localisation of endogenous eIF2Bε localisation under the same conditions described earlier. The population of cells with eIF2Bε foci, *i.e.*, cells with one or more eIF2Bε foci was first detected (**Figure 4.27A**) and subsequently converted into percentages (**Figure 4.27B**).

In U373-MG cells a significant increase of cells with eIF2Bε localisation was observed following stress. Under normal conditions, 30.67 % (± 2.08, UT) and 28.67 % (± 3.22, DMSO) of cells showed eIF2Bε foci and following stress induction 49.67 % (± 1.53, Tg) of cells displayed eIF2Bε localisation. 14.00 % (± 2.00) and 13.67 % (± 3.22) of MO3.13 cells displayed eIF2Bε localisation in untreated and DMSO treated conditions. A significant increase was observed following Tg treatment, with 44.00 % (Tg ± 6.08) of MO3.13 displaying eIF2Bε foci. Finally, SH-SY5Y cells showed a similar pattern, with 10.00 % (± 2.00) of untreated cells, 11.33 % (± 1.53) of DMSO treated cells and 58.00 % (± 4.58) of Tg treated cells showed one or more eIF2Bε foci (**Figure 4.27B**).

Additionally, the size distribution of the eIF2Bε localisation was determined under previously stated conditions. In U373-MG cells similar median values were observed in all conditions (UT: 0.77 μm^2 ± 0.91; DMSO: 0.82 μm^2 ± 0.94; Tg: 0.63 μm^2 ± 0.58). In MO3.13 a slightly smaller size of eIF2Bε foci was detected following stress induction (UT: 0.83 μm^2 ± 0.85; DMSO: 0.93 μm^2 ± 1.17; Tg: 0.64 μm^2 ± 0.72).In SH-SY5Y cells, a similar trend to MO3.13 was observed regarding size distribution, with a smaller median size observed in stress condition (UT: 0.87 μm^2 ± 0.95; DMSO: 1.14 μm^2 ± 1.50; Tg: 0.76 μm^2 ± 1.18) (**Figure 4.28**).

Following this analysis, the eIF2Bε localisation was classified into large and small foci. There was no significant increase in the number of large eIF2Bε localisation per cell in all three cell lines analysed (**Figure 4.29A**). An average of 3.91 (± 0.85, UT) and 3.00 (± 0.21, DMSO) of small eIF2Bε foci was detected under steady state conditions in U373-MG cells. Following stress induction, a significant increase of the number of small eIF2Bε foci was observed, with an average number of 7.19 (± 0.17) of eIF2Bε foci being detected. In MO3.13 cells, 2.41 (± 0.18), 2.13 (± 0.26) and 4.38 (± 0.23) of small eIF2Bε foci per cell was detected in UT, DMSO and Tg conditions, respectively. In SH-SY5Y cells, steady state

conditions presented an average of 2.01 (± 0.32, UT) and 1.47 (± 0.34, DMSO) foci per cell, and following Tg treatment, a significant increase was identified, with an average of 4.21 (± 0.17) small eIF2Bε foci per cell (**Figure 4.29B**). This increase in localisation did not correlate with the increase of protein levels, as observed in **Figure 4.30**.

In these results we report that eIF2B localisation was influenced by cellular stress induction. The percentage of cells with localised eIF2Bε subunits was increased in all cell types analysed, and eIF2Bα was selectively increased in U373-MG cells following stress. It is of note that eIF2Bα preexisting assemblies in SH-SY5Y and MO3.13 were present in larger percentages than U373-MG cells in normal conditions.

Most importantly, we observed an overall increase of small eIF2Bα and eIF2Bε foci in all cell lines following Tg treatment. We can speculate that these eIF2Bα might be homodimer structures created from disassembly of eIF2B decamers, which could be corroborated by *in vitro* works, that found eIF2Bα to readily dissociate from eIF2B decamer (Wortham *et al*., 2014). Additionally, the increased number of eIF2Bα structures might interact with other proteins or act as an isolated stress responsive function, given eIF2Bα known function of sensing cellular stress. The increased number of small eIF2B bodies, mainly containing catalytic subunits following stress in astrocytic cells (Hodgson *et al*., 2019a), corroborates the results that we observed with the increase of localised small eIF2Bε foci. Hodgson *et al*, reported that eIF2B large bodies following stress have a downregulated GEF activity upon induction of eIF2α phosphorylation.

A

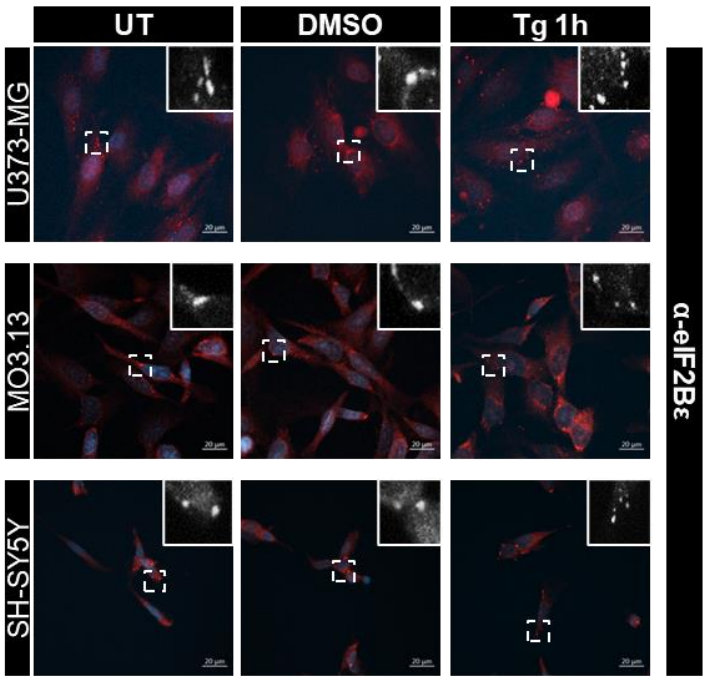
UT
DMSO
Tg 1h
U373-MG
MO3.13
SH-SY5Y
α-eIF2Bε

B

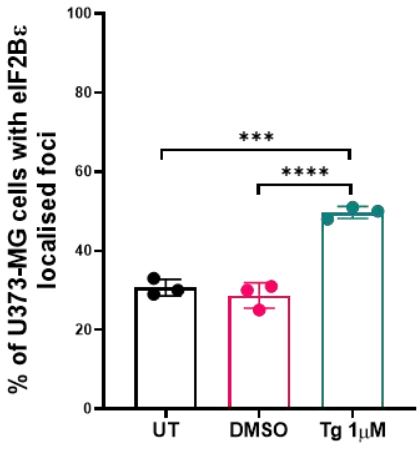
% of U373-MG cells with eIF2Bε localised foci
100
80
60
40
20
0
***
****
UT
DMSO
Tg 1μM

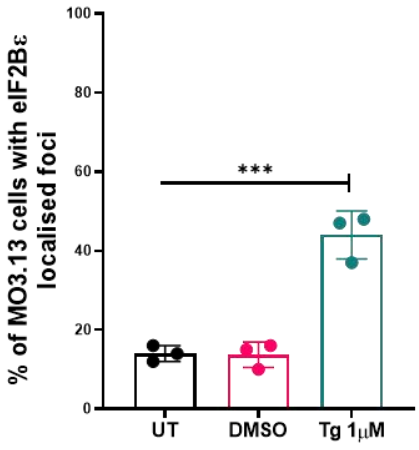
% of MO3.13 cells with eIF2Bε localised foci
100
80
60
40
20
0
***
UT
DMSO
Tg 1μM

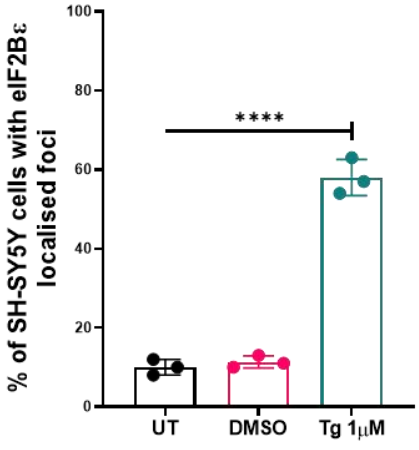
% of SH-SY5Y cells with eIF2Bε localised foci
100
80
60
40
20
0
****
UT
DMSO
Tg 1μM

Figure 4.27. eIF2Bε localisation increases in astrocytic cells following acute ER stress.
(A) Representative images of (top to bottom) U373-MG, MO3.13 and SH-SY5Y cells immunostained with primary antibodies against endogenous α-eIF2Bε and visualized using appropriate secondary antibodies conjugated to Alexa Fluor 594, following untreated, DMSO and Tg 1 μM 1h treatment (UT – untreated). DAPI stains nuclei. Scale bar: 20 μm. (B) Mean percentage of cells displaying dispersed cytoplasmic and localised eIF2Bε foci in a population of 100 cells per replicate, in U373-MG, MO3.13, and SH-SY5Y cells, following untreated, DMSO and Tg 1 μM 1h treatment. Data was analysed using one-way ANOVA followed by *post-hoc* Tukey's test for multiple comparisons. Error bars: ± s.d. (n=3). ***$p \leq 0.001$; ****$p \leq 0.0001$.

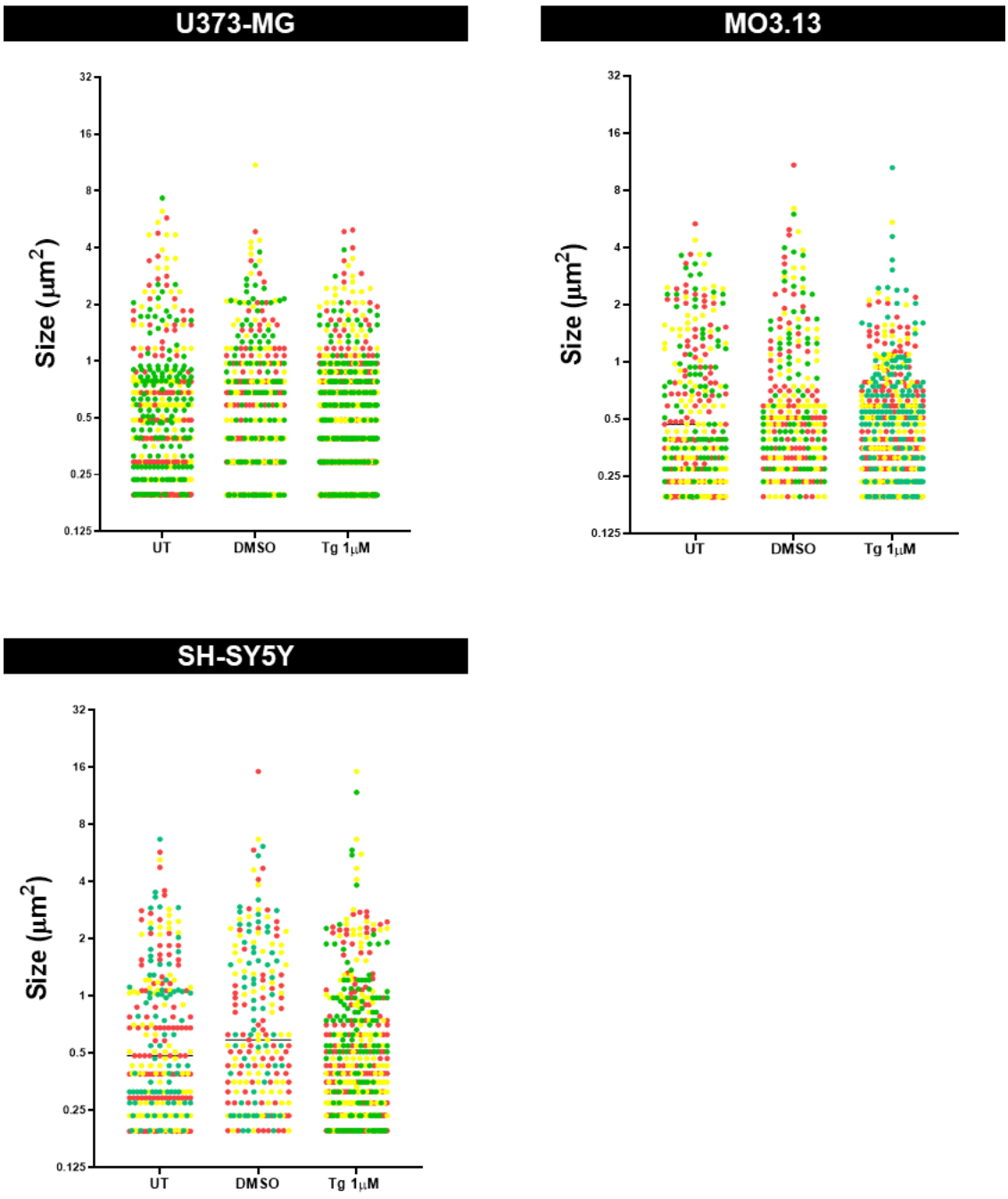

Figure 4.28. The size distribution of eIF2Bε has similar values to untreated conditions, following acute ER stress, in U373-MG, MO3.13 and SH-SY5Y.

Size distribution of eIF2Bε foci in 30 cells with localised eIF2Bε in U373-MG, MO3.13 and SH-SY5Y cells, following untreated, DMSO and Tg 1 µM 1h treatment (UT – untreated; n=3, each repeat was coloured accordingly, repeat 1 – red; repeat 2 – yellow; repeat 3 – green).

A

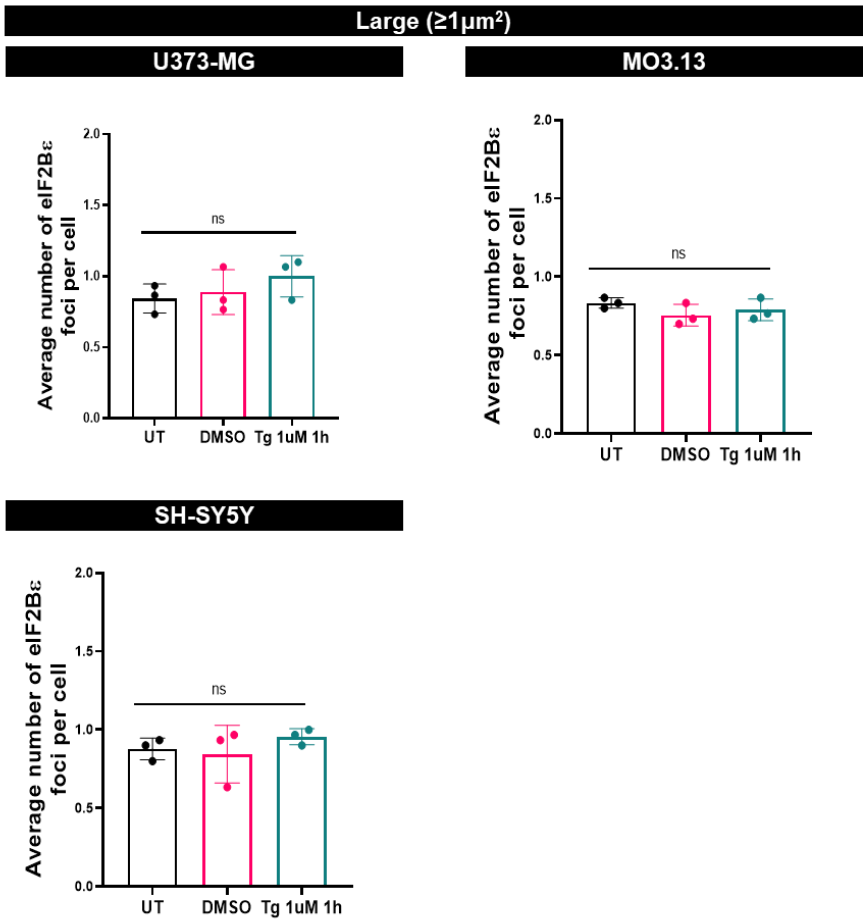
Large (≥1µm²)
U373-MG
MO3.13
SH-SY5Y
Average number of eIF2Bε foci per cell
ns
UT
DMSO
Tg 1uM 1h

B

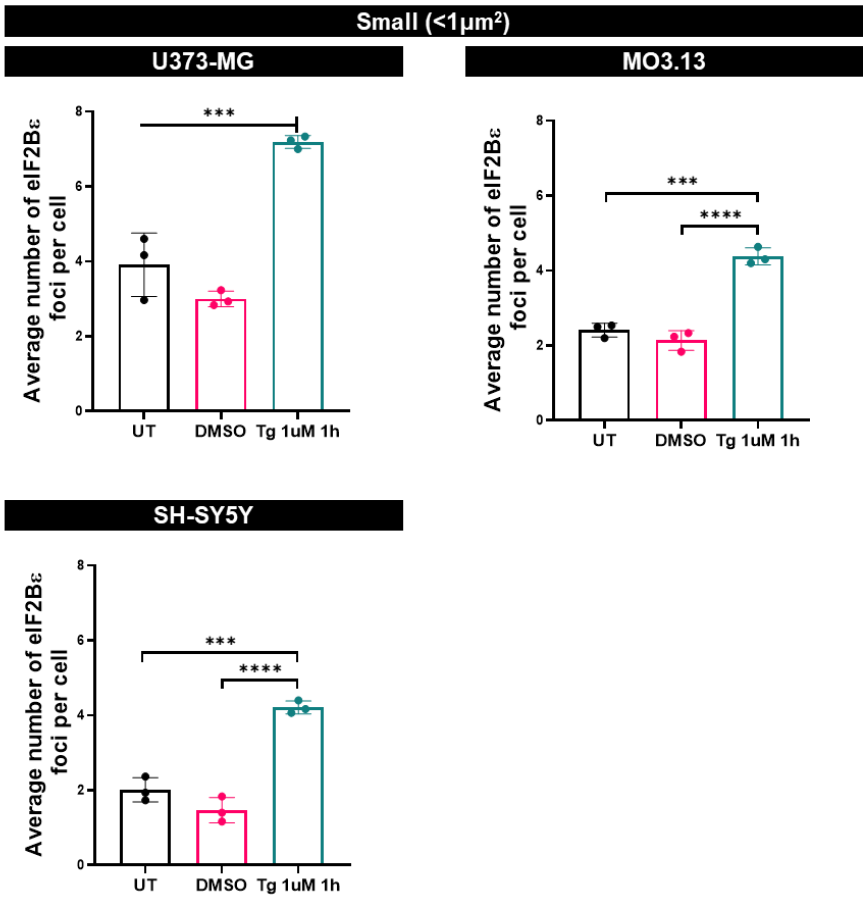
Small (<1µm²)
U373-MG
MO3.13
SH-SY5Y
Average number of eIF2Bε foci per cell
***
****
UT
DMSO
Tg 1uM 1h

Figure 4.29. Small eIF2Bε foci increase following ER stress in U373-MG, MO3.13 and SH-SY5Y cells.

(A) Average number of large eIF2Bε foci per cell in a population of 30 U373-MG, MO3.13 and SH-SY5Y cells with localised eIF2Bε, following untreated, DMSO and Tg 1 μM 1h treatment (n=3). Data was analysed using one-way ANOVA followed by *post-hoc* Tukey's test for multiple comparisons. Error bars: ± s.d. (UT – untreated; n=3). **p*≤0.05; ***p*≤0.01. (B) Average number of small eIF2Bε foci per cell in a population of 30 U373-MG, MO3.13 and SH-SY5Y cells with localised eIF2Bε, following untreated, DMSO and Tg 1 μM 1h treatment (n=3). Data was analysed using one-way ANOVA followed by *post-hoc* Tukey's test for multiple comparisons. Error bars: ± s.d. (UT – untreated; n=3). **p*≤0.05; ****p*≤0.001.

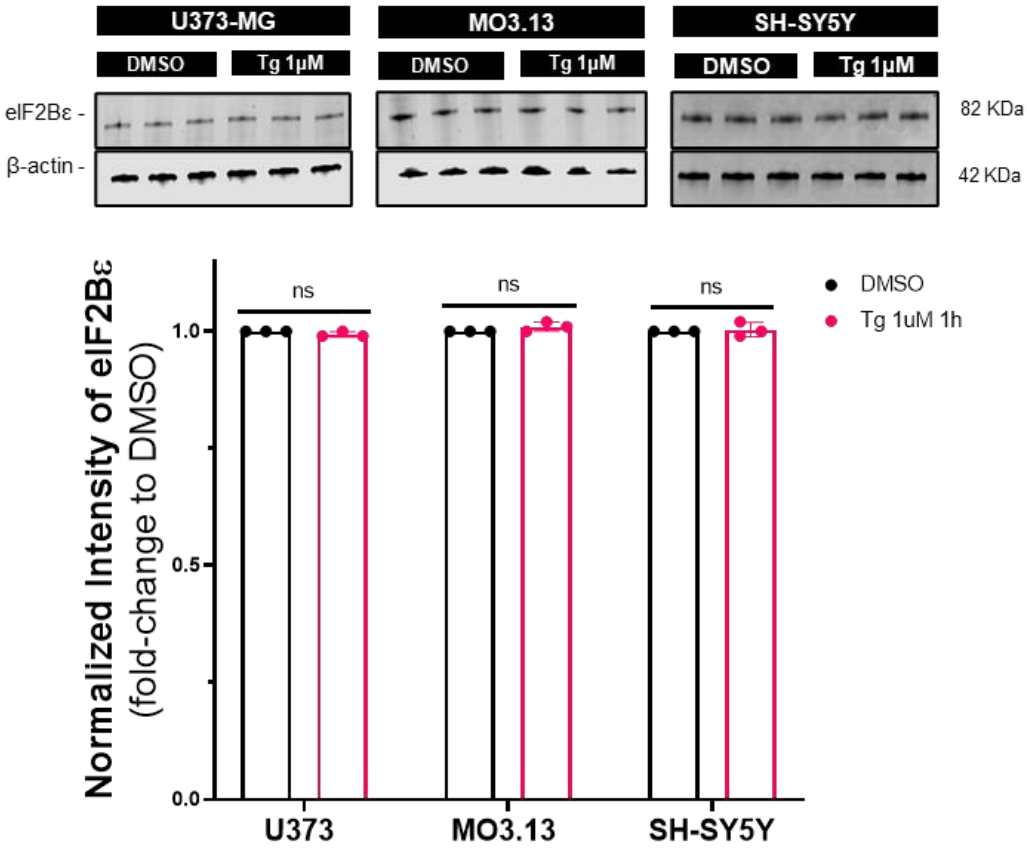

Figure 4. 30. Expression levels of eIF2Bε were not increased following acute ER stress. Western Blot analysis of the levels of eIF2Bε expression in U373-MG, MO3.13 and SH-SY5Y cells, following untreated, DMSO and Tg 1 µM 1h treatment. Levels of eIF2Bε were normalized to levels of β-actin (n=3). Protein lysates used in figure 4.26. Data was analysed using two-way ANOVA followed by *post-hoc* Tukey's test for multiple comparisons. Error bars: ± s.d. Each lane represented a single biological replicate.

4.2.5. Endogenous eIF2B localisation pattern in primary human astrocytes is similar to U373-MG cells.

The cellular localisation of eIF2B and its characterisation in glial and neuronal cells shown previously, may elucidate the functional impact that VWMD mutations have on eIF2B mutations, a topic expanded further in this thesis. Due to astrocytes being one of the main cell types affected by VWMD and having determined the endogenous localisation patterns of eIF2B subunits in the human astrocytoma cell line U373-MG, the cellular localisation of these subunits in primary human astrocytes was investigated.

The percentage of cells with eIF2Bα-ε appeared to mimic the pattern shown by U373-MG cells (**Figure 4.31A**). Primary astrocytes had a mean of 30.67 % (± 3.22), 23.00 % (± 4.36), 24.00 % (± 3.61), 20.00 % (± 4.00), 26.00 % (± 2.65) localisation of eIF2Bα, eIF2Bβ, eIF2Bγ, eIF2Bδ and eIF2Bε, respectively (**Figure 4.31B**). The average number of small foci of primary astrocytes appeared to emulate U373-MG localisation seen in **4.2.3.** (eIF2Bα – 3.91 ± 0.68; eIF2Bβ – 3.66 ± 0.40; eIF2Bγ – 2.77 ± 0.23; eIF2Bδ – 2.53 ± 0.94; and eIF2Bε – 3.67 ± 1.07) with a slight significant increase being present between eIF2Bα and eIF2Bγ (**Figure 4.31C**). When comparing with the results obtained in **4.2.1**., while a significant difference between the percentage of cells with eIF2Bα foci between U373-MG cells and primary astrocytes was present, it was still possible to observe that the pattern of the astrocytic lineages having a smaller percentage of cells with eIF2Bα localisation continues, when compared with MO3.13 and SH-SY5Y cell lines, a display replicated by U373-MG cells. Additionally, there is a similar pattern of eIF2Bε localisation between U373-MG and primary astrocytes, with a significant increase of primary astrocytes percentage with eIF2Bε localised foci, when compared to MO3.13 and SH-SY5Y cells (**Figure 4.32**).

When comparing the results observed in **4.2.3.**, eIF2Bβ and eIF2Bδ small and large localised foci showed similar values in all cells analysed. eIF2Bα, eIF2Bγ and eIF2Bε small and large localised foci, showed similar patterns between U373-MG cell line and primary astrocytes (**Figure 4.33A and Figure 4.33B**), with SH-SY5Y and MO3.13 having a significant higher average number of small eIF2Bα, and U373-MG and primary astrocytes displaying a significant higher average number of small eIF2Bγ and eIF2Bε localised foci (**Figure 4.33B**).

The average number large foci in primary astrocytes appeared to be consistent throughout all five eIF2B subunits under steady state conditions, (eIF2Bα – 1.24

± 0.41; eIF2Bβ – 1.06 ± 0.42; eIF2Bγ – 0.74 ± 0.38; eIF2Bδ – 1.68 ± 0.70; and eIF2Bε – 1.10 ± 0.34) (**Figure 4.33A**). Overall, U373-MG and primary astrocytes did not show major differences (**Figure 4.32 and Figure 4.33**), displaying similar patterns for all eIF2B localised subunits.

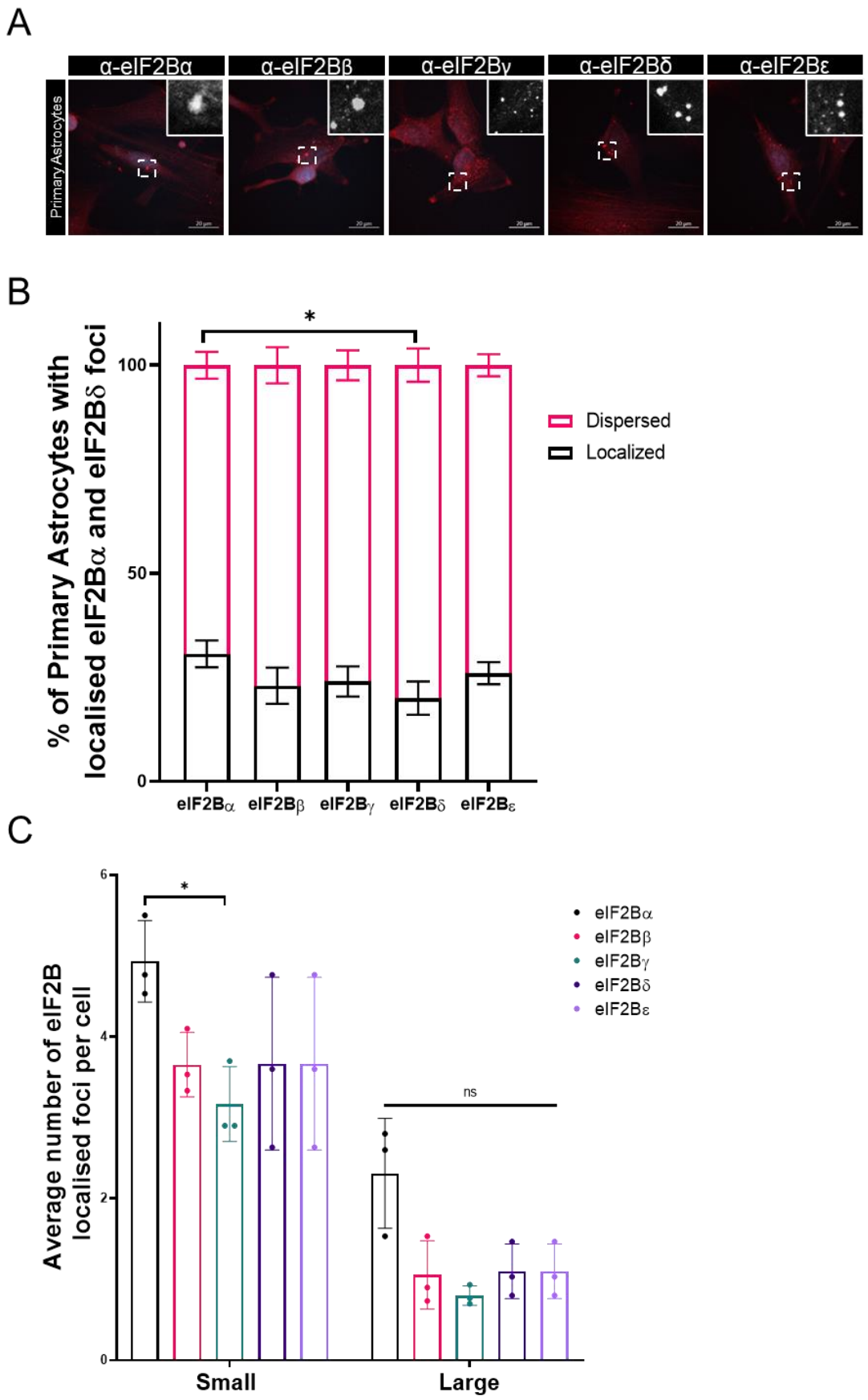

Figure 4.31. eIF2Bα-ε localisation in primary astrocytes.

(A) Representative images of primary astrocytes immunostained with primary antibodies against endogenous α-eIF2Bα, α-eIF2Bβ, α-eIF2Bγ, α-eIF2Bδ and α-eIF2Bε, and visualized using

appropriate secondary antibodies conjugated to Alexa Fluor 594. DAPI stains nuclei. Scale bar: 20 µm. (B) Mean percentage of cells displaying dispersed cytoplasmic and localised eIF2Bα-ε foci in a population of 100 cells per replicate in primary astrocytes. Data was analysed using two-way ANOVA followed by *post-hoc* Tukey's test for multiple comparisons. Error bars: ± s.d. (n=3). *$p \leq 0.05$. (C) Average number of small and large eIF2Bα-ε foci per cell in a population of 30 primary astrocytes with localised eIF2Bα-ε (n=3). Data was analysed using two-way ANOVA followed by *post-hoc* Tukey's test for multiple comparisons. Error bars: ± s.d. (n=3). *$p \leq 0.05$.

eIF2Bα

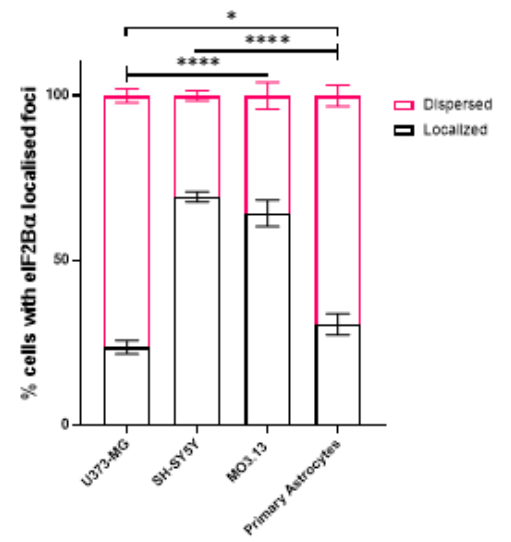

eIF2Bβ

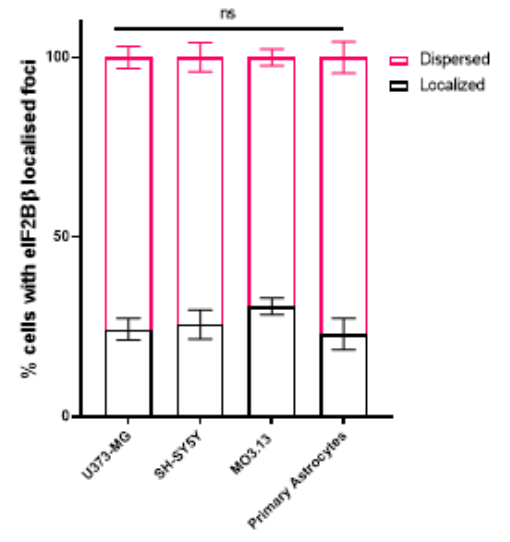

eIF2Bγ

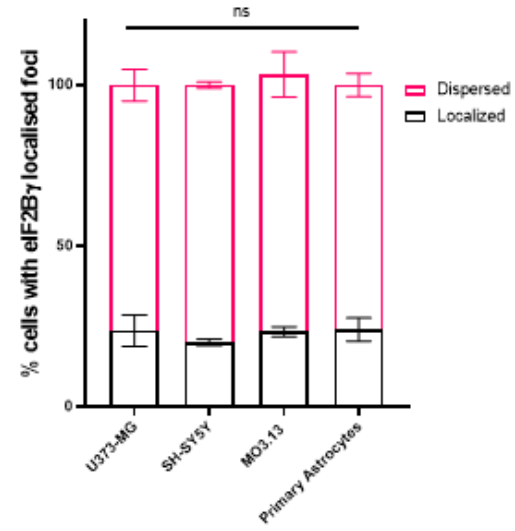

eIF2Bδ

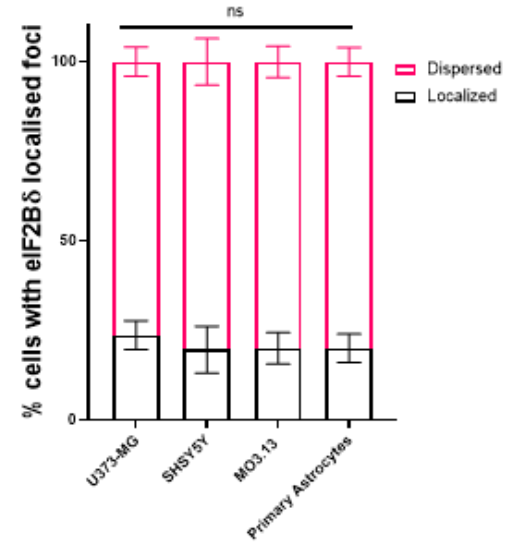

eIF2Bε

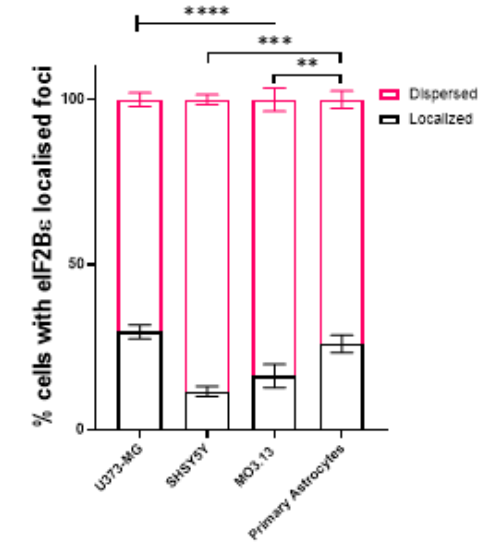

Figure 4.32. Primary astrocytes display similar eIF2Bα-ε localisation patterns to U373-MG cells.

Mean percentage of cells displaying dispersed cytoplasmic and localised eIF2Bα-ε foci in a population of 100 cells per replicate in U373-MG, MO3.13, SH-SY5Y cells and primary astrocytes. Data was analysed using two-way ANOVA followed by *post-hoc* Tukey's test for multiple comparisons. Error bars: ± s.d. (n=3). *$p \leq 0.05$; *$p \leq 0.0001$.

A

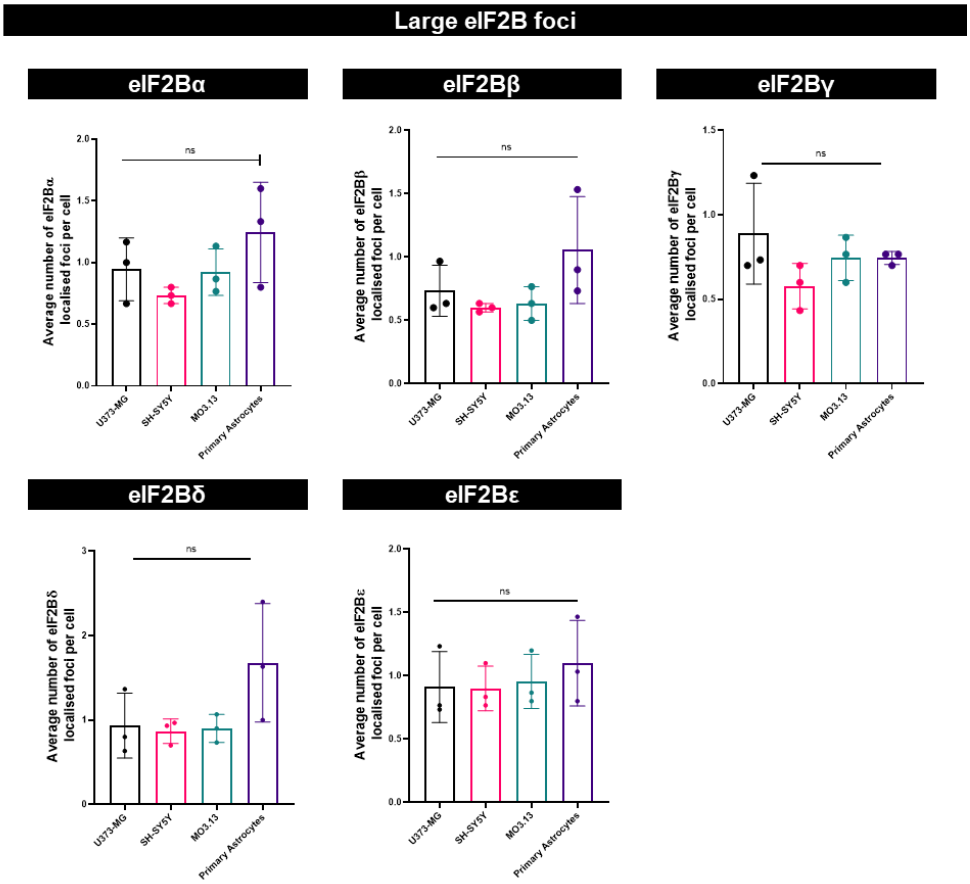
Large eIF2B foci
eIF2Bα
eIF2Bβ
eIF2Bγ
eIF2Bδ
eIF2Bε
Average number of eIF2Bα localised foci per cell
Average number of eIF2Bβ localised foci per cell
Average number of eIF2Bγ localised foci per cell
Average number of eIF2Bδ localised foci per cell
Average number of eIF2Bε localised foci per cell
ns
U373-MG
SH-SY5Y
MO3.13
Primary Astrocytes

B

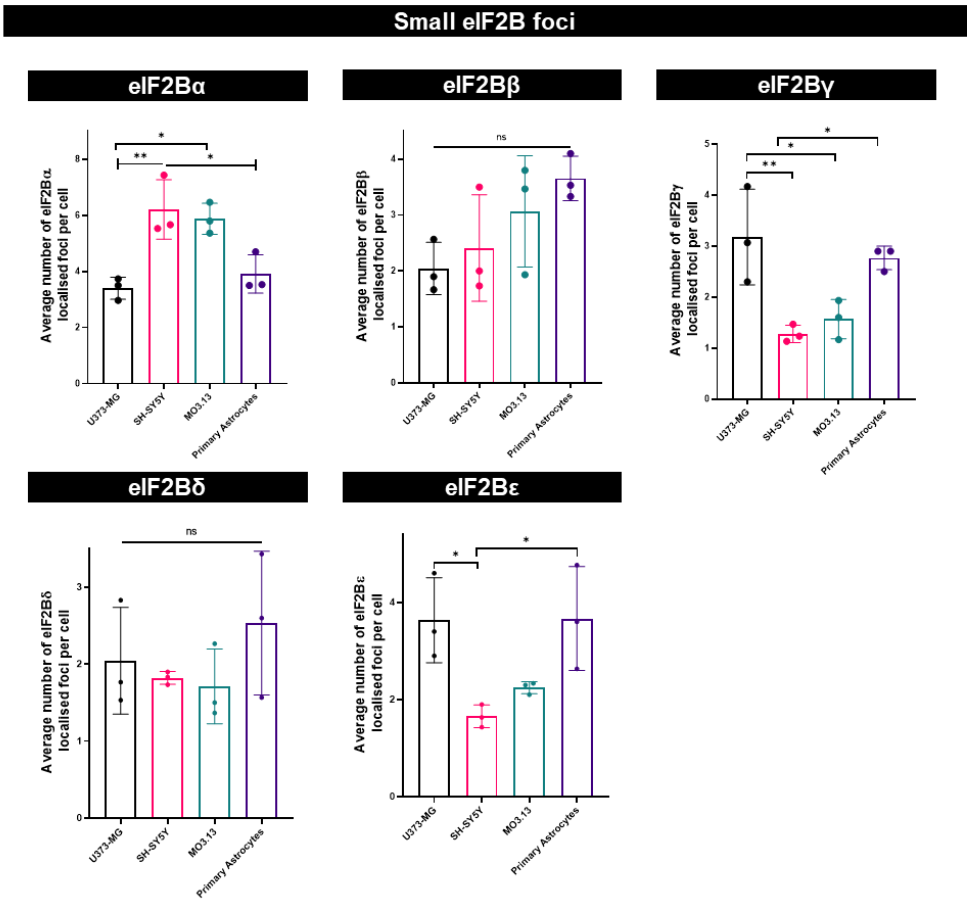
Small eIF2B foci
eIF2Bα
eIF2Bβ
eIF2Bγ
eIF2Bδ
eIF2Bε
Average number of eIF2Bα localised foci per cell
Average number of eIF2Bβ localised foci per cell
Average number of eIF2Bγ localised foci per cell
Average number of eIF2Bδ localised foci per cell
Average number of eIF2Bε localised foci per cell
ns
*
**
U373-MG
SH-SY5Y
MO3.13
Primary Astrocytes

Figure 4.33. Primary astrocytes display a lower average number of small eIF2B when compared to oligodendrocytic and neuronal cells and displays a higher average number of small eIF2Bγ and eIF2Bε foci per cell, similar to U373-MG cells.

(A) Average number of large eIF2Bα-ε foci per cell in a population of 30 U373-MG, MO3.13, SH-SY5Y cells and primary astrocytes with localised eIF2Bα-ε (n=3). Data was analysed using one-way ANOVA followed by *post-hoc* Tukey's test for multiple comparisons. Error bars: ± s.d. (n=3). (B) Average number of small eIF2Bα-ε foci per cell in a population of 30 U373-MG, MO3.13, SH-SY5Y cells and primary astrocytes with localised eIF2Bα-ε (n=3). Data was analysed using one-way ANOVA followed by *post-hoc* Tukey's test for multiple comparisons. Error bars: ± s.d. (n=3). *$p \leq 0.05$; **$p \leq 0.01$.

4.3. Discussion.

Our lab has previously shown that eIF2B localise in cytoplasmic foci, termed eIF2B bodies. Additionally, it was shown that the composition and abundance of these bodies can be modulated upon induction of stress, suggesting that eIF2B localisation plays a role during adverse conditions (Hodgson *et al*., 2019). It is of note that eIF2B activity not only plays an essential role in protein synthesis under normal condition, following stress it reveals itself as a key regulator of cellular fate (Marintchev & Ito, 2020). Moreover, while eIF2B is a housekeeping protein, mutations in any of the five subunits of eIF2B are causative of the neurological disorder VWMD, impacting specifically astrocytes and oligodendrocytes, sparing neurons. As such, we aimed to characterise the endogenous localisation of each eIF2B subunit in glial and neuronal cells with the VWMD backdrop, possibly uncovering a cell type-specific localisation.

4.3.1. eIF2B localisation is cell-type specific amongst glial and neuronal cell lines.

Following optimisation efforts detailed in chapter 3, the characterisation of endogenous eIF2B localisation in astrocytic (U373-MG), oligodendrocytic (MO3.13) and neuronal (SH-SY5Y) cells was carried out. eIF2B bodies operate as steady-state clusters of eIF2B complexes and sites of localised GEF activity, as reported by (Campbell *et al*., 2005; Hanson *et al*., 2023; Hodgson *et al*., 2019; Norris *et al*., 2021). In this initial analysis detailed in **chapter 4** will only discuss the localisation of individual eIF2B subunits. Whilst biochemical analysis of the eIF2B complex has examined the activity of fully formed decamers, which contain all five eIF2B subunits (Bogorad *et al*., 2014; Kuhle *et al*., 2015; Marintchev & Ito, 2020; Wortham *et al*., 2014), the presence of foci of individual eIF2B subunits could be independent of the co-localisation of other eIF2B subunits, and that individual eIF2B subunit foci could form during the assembly/disassembly of eIF2B bodies or exist to perform an additional unknown function.

From previous studies three distinctive eIF2B complexes with different percentages of GEF activity were identified – decameric (eIF2B$\alpha_2\beta_2\gamma_2\delta_2\varepsilon_2$) – 100 %, tetrameric (eIF2B$\beta\gamma\delta\varepsilon$) – 50 % and heterodimeric (eIF2B$\gamma\varepsilon$) – 20 % (Bogorad *et al*., 2014; Hodgson *et al*., 2019; Kuhle *et al*., 2015; Wortham *et al*., 2016). As

such, perhaps small eIF2B localised foci, which may or may not interact with other eIF2B subunits, are formed from these known stable eIF2B structures.

Additionally, localised eIF2B foci only account for a particular portion of total eIF2B, possibly representing hotspots of GEF activity. We therefore hypothesize that the localisation may differ according to cellular requirement of its eIF2B activity during steady-state and stress conditions.

While the presence of eIF2B foci in U373-MG cells was similar throughout all five eIF2B subunits (**Fig 4.1B**), a significantly higher prevalence of eIF2Bα foci was present in MO3.13 (~64 %) and SH-SY5Y cells (~69 %), when compared to the other subunits. Additionally, the percentage of cells with eIF2Bβ appeared to be increased in MO3.13 (~31 %) and SH-SY5Y (~25 %) cells when compared with the other eIF2B subunits within the same cell line (**Figure 4.1B**). This initial result can give us insight into the populations of eIF2B foci and possibly the subcomplexes present in steady-state conditions in these cells lines.

We could speculate that the fact that U373-MG cells show an equivalent proportion of cells with localisation of all eIF2B subunits (**Figure 4.1B**) suggests that the cells have a larger proportion of decameric eIF2B complexes in bodies compared to other cell types. However, we observed as well that the number of eIF2B localised foci differs between subunits with a higher population of small eIF2Bγ and eIF2Bε foci (**Figure 4.18B**), suggesting that while these cells tend to have a more constant abundance of cells with eIF2Bα-ε localisation, the eIF2B body and eIF2B localised subcomplexes composition may vary within these cells. On the other hand, MO3.13 and SH-SY5Y cells, may have a higher proportion of possibly stable eIF2Bα homodimerized molecules (**Figure 4.1B**), as observed previously *in vitro* (Bogorad *et al*., 2014; Wortham *et al*., 2014). These cells show a similar percentage of localised eIF2Bβ-ε subunits (approximately 25 % in MO3.13 cells and 20 % in SH-SY5Y cells), which could indicate that approximately 20 % of cells may contain localisation of eIF2Bβ-ε subunits simultaneously. Expanding on this idea, in the approximately 65 % of MO3.13 cells that show eIF2Bα and in the approximately 70 % of SH-SY5Y cells that show eIF2Bα, 40 % and 50 % of these cells will not display eIF2Bβ-ε foci, thus only containing eIF2Bα localised foci.

It is of note that in higher concentrations than physiological, eIF2Bα has been found to form a mixture of tetramers, hexamers, and octamers (Bogorad *et al*.,

2014). These additional structures could reveal a potential unidentified function or regulation of eIF2Bα in MO3.13 and SH-SY5Y cells.

An additional interesting pattern emerges when comparing each cell line according to subunit. eIF2Bβ, eIF2Bγ and eIF2Bδ subunits showed a consistent degree of localisation in all cell lines analysed. As stated previously, a higher population of MO3.13 and SH-SY5Y cells with eIF2Bα localisation was observed. More intriguingly, an opposite pattern of localisation was observed for eIF2Bε foci, with U373-MG showing a significantly higher percentage of cells with localised eIF2Bε (~30 %) when compared to MO3.13 (~16 %) and SH-SY5Y (~11 %) cells (**Figure 4.34**), highlighting a more varied range of eIF2B subcomplexes structures in oligodendrocytic and neuronal cells (**Figure 4.2**), which will be further explored in **4.2.2**.

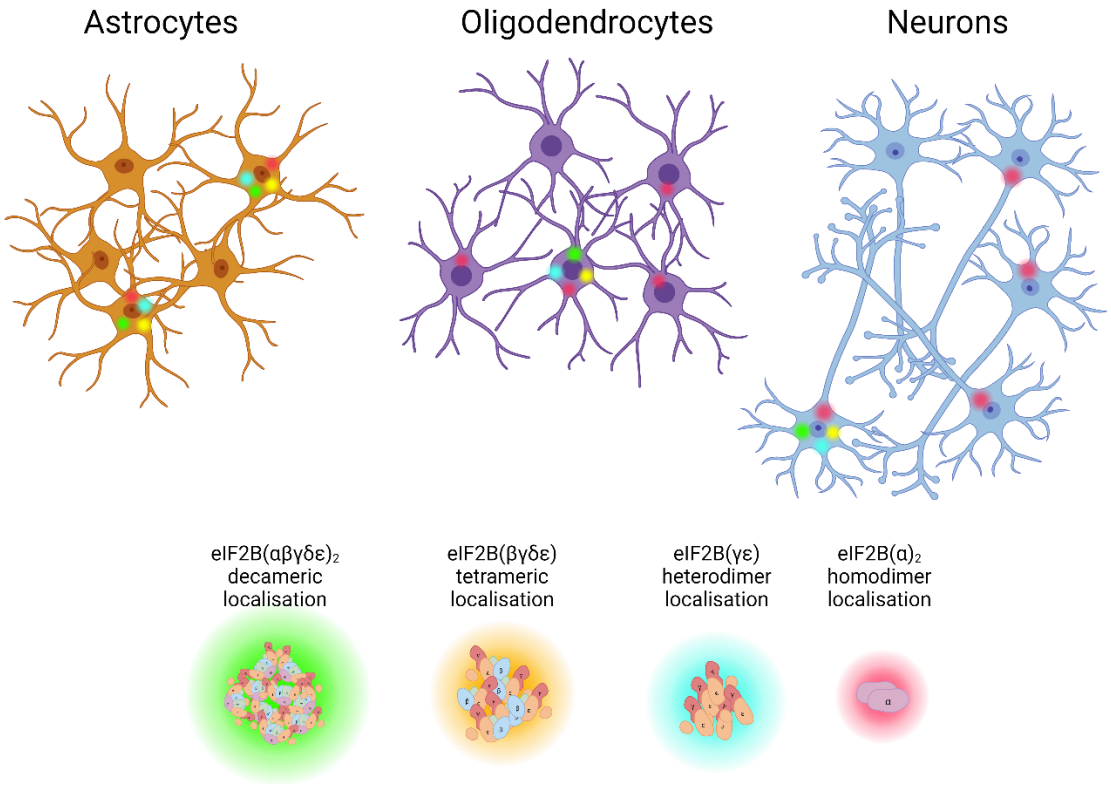

Figure 4.34. Abundance of cells with eIF2Bα-ε localisation is cell-type and eIF2B subunit specific.

eIF2B subunits localise to cytoplasmic foci, with specific subunit composition. eIF2B bodies, functional aggregates of eIF2B, have been shown to have varying size correlated with subunit in mammalian cells (Hodgson *et al.,* 2019; Hanson *et al.,* 2023). The abundance of cells with eIF2B localisation is diverse according to subunit and cell line. Astrocytes show approximately 20-25 % cells with eIF2Bα-ε localisation, which imply these cells have all eIF2B subunits localisation, even with diverse degrees of abundance per cell. Oligodendrocytes and neurons show approximately 65 and 75 % cells with eIF2Bα localisation, respectively, with approximately 25-20 % of cells displaying eIF2Bβ-ε. This suggests that a large population of cells only have eIF2Bα foci. This proposed model is a combination of the results described in **chapter 4** and known stable eIF2B structures. Image designed in BioRender.

4.3.2. eIF2B foci size correlates with eIF2B subunit composition in a cell-type specific manner.

Our lab has previously shown that all five eIF2B subunits localised to large eIF2B bodies in astrocytic cells, proposing the presence of the eIF2B decamer in large bodies, while small eIF2B bodies mostly comprised of eIF2Bγε heterodimers (Hodgson *et al*., 2019). However, these findings were carried out through the co-localisation with transiently expressed GFP tagged eIF2Bε subunit. As such, this chapter explores the classification of subcomplexes according to eIF2Bα co-localisation. From *in vitro* and *in vivo* research, eIF2Bα assembly to two sets of eIF2Bβγδε tetramers is the last stage of the formation of the eIF2B decamer (Schoof *et al*., 2021; Tsai *et al*., 2018; Wortham *et al*., 2014, 2016). Additionally, previous modelling and structural work has projected that the regulatory subunits form an $eIF2B\alpha_2\beta_2\delta_2$ hexamer (Bogorad *et al*., 2014; Kuhle *et al*., 2015).

Through size distribution analysis, small eIF2Bα localised foci were present in all cell lines (**Figure 4.3A**). Previous reports only showed eIF2Bα to co-localise in large eIF2B bodies (Hodgson *et al*., 2019), which did not explain these additional small eIF2Bα foci. Thus, in order to clarify the correlation of foci size to subunit composition, we analysed co-localisation between eIF2Bα and eIF2Bγ, which should clarify size standards for the decameric eIF2B structure, and between eIF2Bα and eIF2Bδ, which should identify regulatory subcomplexes, observed *in vitro*.

From the population of cells with eIF2Bα foci, it was possible to observe that U373-MG cells showed a higher percentage of cells that also displayed eIF2Bγ localisation (~63 %), when compared to MO3.13 (~32 %) and SH-SY5Y (~23 %) cells (**Figure 4.4B, 4.5B and 4.6B**), and a higher percentage of eIF2Bα foci co-localised with eIF2Bγ (~19 %), when compared to MO3.13 (~5 %) and SH-SY5Y (~7 %) cells (**Figure 4.4D, 4.5D and 4.6D**). This indicates that in MO3.13 and SH-SY5Y cells, a higher population of eIF2Bα foci does not spatially interact with eIF2Bγ subunit, when compared to U373-MG cells.

Importantly, a size discrimination emerges, classifying large foci, *i.e.*, containing all five eIF2B subunits, as ≥ 1μm^2, and small foci, *i.e.*, containing varied subunit composition forming subcomplexes, as < 1μm^2 (**Figure 4.4C, 4.5C and 4.6C**).

Utilising this discrimination tool, it was possible to then apply it to the population of eIF2Bα localised cells and determine co-localisation patterns between eIF2Bγ according to size. eIF2Bα foci smaller than 1 μm^2 showed a low percentage of

co-localisation throughout all three cell lines analysed (**Figure 4.7**). Not surprisingly, when analysing the eIF2Bα foci larger or equal to 1 μm^2, a higher population of eIF2Bγ co-localises. It is of note, that the majority of large eIF2Bγ foci co-localised with eIF2Bα, corroborating our hypothesis that large eIF2Bβγδε foci contain all five eIF2B subunits (**Figure 4.8**). However, it was possible to observe a considerable population of large eIF2Bα foci that do not co-localise to what is thought to be the full decamer.

Given the previously reported regulatory subcomplex structures, co-localisation analysis of eIF2Bα and eIF2Bδ were carried out. U373-MG cells showed a similar pattern as stated previously, displaying a higher percentage of cells with co-localised foci (~49 %), when compared to MO3.13 (~32 %) and SH-SY5Y (~22 %) cells (**Figure 4.10B, 4.11B and 4.12B)**, and a higher percentage of eIF2Bα foci co-localised with eIF2Bδ (~15 %), when compared to MO3.13 (~7 %) and SH-SY5Y (~8 %) cells (**Figure 4.10D, 4.11D and 4.12D**). Co-localised foci showed a size distribution similar to eIF2Bγ, with only a slight decrease observed in SH-SY5Y cells (~0.73 μm^2) (**Figure 4.12C**). Applying the same discrimination standards as used previously, the majority of large eIF2Bδ foci co-localised with eIF2Bα in all cell lines investigated (**Figure 4.14**). However, no considerable population of small eIF2Bα foci co-localising with eIF2Bδ foci in all three cell lines was detected (**Figure 4.13 and Figure 4.15**). This could indicate that regulatory subcomplexes composed of eIF2Bα, eIF2Bβ and eIF2Bδ, while stable and formed *in vitro*, do not translate to localised eIF2B foci in mammalian cells. Additionally, a high degree of large eIF2Bα foci with no apparent co-localisation with the other eIF2B subunits continues to be observed (**Figure 4.13 and Figure 4.14**). This suggests that the tetrameric, hexameric, and octameric eIF2Bα structures observed in higher than physiological *in vitro* concentrations (Bogorad *et al*., 2014), could also be observed in a cellular context.

To better characterise the localisation of endogenous eIF2B foci, the foci detected were then classified and distinguished by the size previously determined to correlate with subunit composition. Thus, the average number of eIF2B foci according to size was analysed in glial and neuronal cells. Most strikingly, we observe that within MO3.13 and SH-SY5Y cells, a higher number of small eIF2Bα foci per cell was detected when compared to the other subunits (MO3.13: eIF2Bα – 5.88 ± 0.55; SH-SY5Y: eIF2Bα – 6.21 ± 1.06) (**Figure 4.17**). Moreover, while the average number of large eIF2B foci per cell was consistent throughout subunit

and cell line, small eIF2Bα foci are more prevalent in MO3.13 and SH-SY5Y per cell than U373-MG (**Figure 4.18A**), with a paradoxical result observed in small eIF2Bγ and eIF2Bε foci (**Figure 4.19B**). As previously reported *in vitro* biochemical assays, stable subcomplexes composed solely of catalytic eIF2B subunits are able to form and to localise in mammalian cells, termed small eIF2B bodies. Additionally, these small eIF2B bodies have been found to still contain, albeit lower, GEF activity (Bogorad *et al*., 2014; Hanson *et al*., 2023; Hodgson *et al*., 2019; Kuhle *et al*., 2015; X. Wang *et al*., 2012; Wortham *et al*., 2016). Thus, these small but active catalytic hubs of GEF activity, also appear to localise endogenously.

Immortalisation of cells can alter cell metabolism, thus not behaving as primary cells. Particurlaly, impairing cell-cycle checkpoint pathways and cell-cycle regulators (Irfan Maqsood *et al*., 2013; Kaur & Dufour, 2012). As such, the study of primary astrocytic localisation was carried out, and similar patterns to U373-MG cells of endogenous localisation were displayed in human primary astrocytes (**Figure 4.31, Figure 4.32 and Figure 4.33**), showing that the endogenous pattern of eIF2B localisation between immortalised cells and primary cells appears to be similar according to cell-type.

While we have not reported on the functionality of these endogenous foci, thus not labelling the detected cytoplasmic foci as eIF2B bodies, and while we did not investigated the entire eIF2B localisation composition, we speculate that these eIF2B foci are composed of stable subcomplexes and complexes, which in turn have functional activities. It is important to note, that these structures are dynamic and that the pre-assembly of smaller eIF2B structures could be a stepwise process.

In this chapter, a compelling observation emerges as astrocytic cells exhibit a more consistent eIF2B localisation pattern, with a similar value of cells exhibiting eIF2Bα-ε subunit localisation. This, however, coincides with a higher prevalence of small eIF2Bγ and eIF2Bε foci likely constituted of simply catalytic subunits, due to a higher average number of small eIF2Bγ and eIF2Bε of foci when compared to the other subunits. This distinguishing characteristic sets astrocytes apart from oligodendrocytes and neuronal cells (**Figure 4.35**). Notably, these assemblies not only fulfill their well-established function, providing low basal GEF activity through small catalytic bodies in tandem with 100 % activity facilitated by larger complexes, but they also possess the potential to drive the assembly of even

larger eIF2B assemblies. Remarkably, particular yeast models corroborate this notion, wherein the filamentous eIF2B body assembly is proposed to be dependent of eIF2B decamer formation and subsequent eIF2Bε (Gcd6p) interaction stabilised by eIF2Bγ (Gcd1p) with other eIF2B decamers (Marini *et al*., 2020). Astrocytes play a major role in the CNS homeostasis (Ishibashi *et al*., 2006). These cells have diverse interactions with neurons and oligodendrocytes. For oligodendrocytes to mature from endogenous glial progenitor cells and myelination to commence, normal astrocytic function is necessary (Bugiani *et al*., 2011). Additionally, astrocytes require rapid and constant translation rates and have high energetic requirements for astrocytic activity and oligodendrocyte support (Bugiani *et al*., 2011; Dooves *et al*., 2016). The heterogenous population of eIF2B localisation, specifically the presence of small catalytic eIF2B bodies, may bypass p-eIF2α stress induction via the absence of eIF2B regulatory subunits, allowing for a subsection of constant basal level GEF activity under steady state conditions in astrocytic cells.

While small catalytic bodies have been reported to be localised in oligodendrocytes and neuronal cells (Hanson *et al*., 2023), it was noteworthy that in MO3.13 and SH-SY5Y cells there is the high population of seemingly independent eIF2Bα homodimers. The stoichiometric expression of eIF2B subunits and their regulation is essential for the complexes' correct function (Wortham *et al*., 2016). However, eIF2Bα expression and perhaps localisation, is not under this control. Additionally, the eIF2Bα subunit has shown to dissociate most readily from the eIF2B decameric structure (Wortham *et al*., 2014). While eIF2B localisation of all subunits was visible, the prominently population present in MO3.13 and SH-SY5Y cels were eIF2Bα localised foci. These assemblies could be due to a higher expression of the eIF2Bα protein, thus mimicking *in vitro* assays with high concentration eIF2B levels, leading to the assembly of several homodimers, however, western blot analysis did not show changes in protein expression (**Figure 4.19 and Figure 4.35**). It was noted, however, that the overexpression of eIF2Bα lead to the inhibition of eIF2Bα foci formation, with a dispersed signal being observed (**Figure 4.20**). eIF2Bα localised foci was able to be reinstated when co-transfection of eIF2Bα-RFP and siRNA-mediated silencing of *EIF2B1* was performed (**Figure 4.21**). Thus, while the expression levels in physiological levels appear to not regulate eIF2Bα localising among glial and neuronal cells, the increase of eIF2Bα concentration above physiological levels

has a significant impact on its localisation. Furthermore, these eIF2Bα foci appeared to share LLPS characteristics (**Figure 4.22**). LLPS granules are usually driven by environmental triggers, which supports the increase in eIF2Bα foci upon stress induction. Further investigation and experimental validation regarding LLPS-driven features of eIF2Bα and the other eIF2B subunits should be carried out, such as the investigation of presence of RNA in these eIF2B assemblies (a key feature of LLPS structures, (Roden & Gladfelter, 2021), through RNA immunoprecipitation or incPRINT, and the investigation of disordered domains, low sequence complexity and repeat motifs of these eIF2B subunits (Martin & Mittag, 2018), through bioinformatic tools like LPS-annotate (Harbi *et al*., 2011), SPOT-Disorder2 (J. Hanson *et al*., 2019) and/or IU/Pred (Mészáros *et al*., 2018). eIF2Bα has a key role within the ISR. Under cellular stress, phosphorylated eIF2α binds directly to eIF2Bα, subsequently changing the conformation of the eIF2B decamer, which attenuates the catalytic activity of eIF2B, reducing levels of TCs and consequently inhibiting global protein production (Bogorad *et al*., 2017; Zyryanova *et al*., 2018). The additional foci observed in oligodendritic and neuronal cells consisting solely of eIF2Bα could provide an preliminary pre-assembled eIF2Bα dimer configuration, priming the cells to sense and respond to stress in a highly sensitive and regulated manner. It is of note, that structural studies regarding a eIF2Bα•p-eIF2α complex have not been carried out, thus it is not possible to conclude that eIF2Bα structures would be able to bind to p-eIF2α without being in a eIF2B decamer formation beforehand.

Insights gleaned from investigations of human hypomyelinating disorders and dysmyelinating animal models offer compelling evidence that underscores the remarkable sensitivity of oligodendrocytes to disturbances in protein translation and protein secretory pathways (Bellato & Hajj, 2016; Costa-Mattioli *et al*., 2007; Cristobal *et al*., 2022; Geva *et al*., 2010; Z. Jiang *et al*., 2010; Spaas *et al*., 2021). Among the diverse cellular constituents, oligodendrocytes stand out as highly susceptible entities, acutely affected by translational regulation and the delicate organisation of protein secretion processes. Moreover, a growing notion suggests that the translational shift instigated by p-eIF2α is imperative for maintaining optimal neuronal function in the absence of stress. This underscores the pivotal role of eIF2 as a crucial regulator of synaptic plasticity. The dependence on p-eIF2α-mediated translation regulation enables neurons to swiftly modify their protein composition in direct response to activity/enviorment. This mechanism

plays a vital role in facilitating both the formation of long-term potentiation and long-term depression crucial for synaptic plasticity (Bellato & Hajj, 2016; Costa-Mattioli *et al*., 2007; Z. Jiang *et al*., 2010). Taking this together, the observed eIF2Bα foci, seemingly operating autonomously from other eIF2B subunits, hold the potential to yield significant regulatory functions within these specific cell types, thereby fulfilling particular roles accordint to cell-type.

Further analysis with pulldown assays, size-exclusion chromoatography and native MS analysis of the additional eIF2Bα assemblies under steady-state conditions would be able to provide insight into the eIF2Bα_2 homodimer conformation, more complex structures, and perhaps, a novel interaction with other proteins. A previous study has identified specific binding between eIF2Bα and a subset of G protein-coupled receptors (α_2A-, α_2B-, α_2C-, and β_2-adrenergic receptors) and co-localisation between β_2-adrenergic receptors and eIF2Bα was shown in cells (Klein *et al*., 1997). Additional research regarding this interaction might elucidate on a potential novel role of eIF2Bα, possibly enhancing receptor-mediated singling or it could have an effect on the eIF2Bα role in regulation of translation.

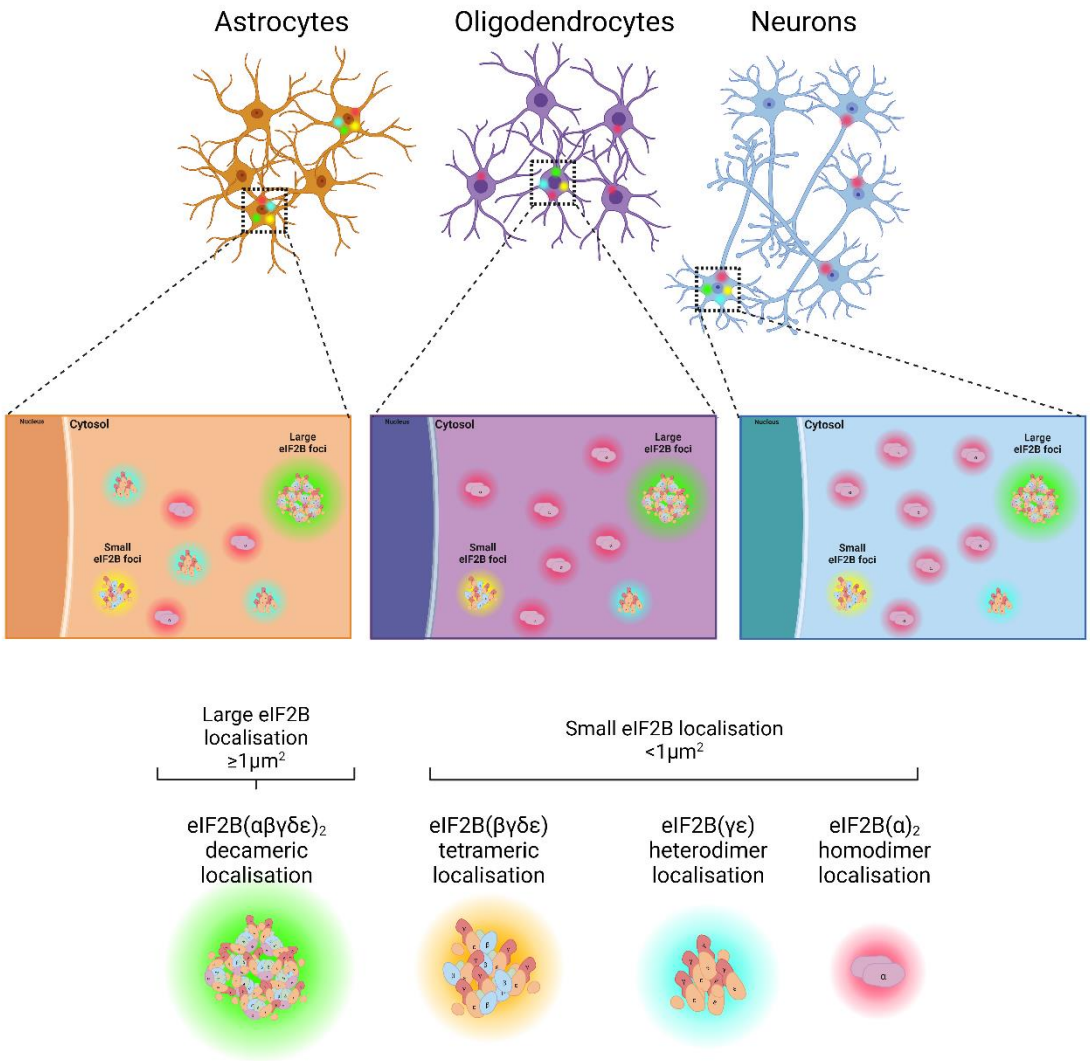

Figure 4.35. eIF2Bα-ε localisation per cell is cell-type specific.

In mammalian cells with eIF2B localisation, the number of eIF2Bα-ε foci varies according to cell-type in steady state conditions. Through co-localisation efforts between eIF2Bα and eIF2B catalytic (eIF2Bγ) and regulatory (eIF2Bδ) subunits, large eIF2B localised foci, ≥ 1 μm^2, are proposed to be composed of all eIF2B subunits, potentially eIF2B decamers, and small eIF2B localised foci, < 1 μm^2, have varying eIF2B structure (here modelled according to results described in chapter 4 and known stable eIF2B subcomplexes). Astrocytes show a higher number of eIF2Bγ and eIF2Bε foci per cell, when compared with oligodendrocytes and neurons, potentially displaying eIF2B catalytic localisation. Oligodendrocytes and neurons reveal a substantial number of eIF2Bα foci per cell, which we propose to be composed of eIF2Bα homodimers, thus independent of other eIF2B subunits. Image designed in BioRender.

4.3.3. Acute ISR induction alters eIF2B localisation in a cell-type specific manner.

In previous work, composition and distribution of eIF2B bodies have been shown to be altered during cellular stress (Hanson *et al*., 2023; Hodgson *et al*., 2019). In these studies, which encompased astrocytic, oligodendritic and neuronal cells, it was found that small catalytic bodies increased in number following ISR stimulation. The data presented here aimed to determine the modulation of endogenous eIF2Bα and eIF2Bε localisation upon acute ISR induction.

While the percentage of cells with eIF2Bα foci following Tg treatment was increased in U373-MG cells, a similar pattern was not observed in MO3.13 and SH-SY5Y cells (**Figure 4.23**), which could be explained by the preexisting high percentage of cells with eIF2Bα cytoplasmic localisation (**Figure 4.2**). However, an increase in the number of large and small eIF2Bα foci per cell was observed throughout all cell lines studied (**Figure 4.25 and Figure 4.36**). It is important to note that the exact composition of these assemblies are unknown and co-localisation efforts with other eIF2B subunits and other proteins should be carried out. U373-MG, MO3.13 and SH-SY5Y cells displayed an overall increase of small eIF2Bε localised foci following acute stress induction (**Figure 4.27**). In contrast with the results observed when analysing eIF2Bα localisation, Tg treatment did not lead to the increase of large eIF2Bε foci. Acute ISR induction led however, to an overall increase of small eIF2Bε foci (**Figure 4.29 and Figure 4.36**), mimicking results observed previously (Hodgson *et al*., 2019). Additionally, alteration of composition of small eIF2B bodies have been found following ER stress (Hanson *et al*., 2023). It is possible that the increased levels of the small eIF2Bα and eIF2Bε bodies serve distinct purposes within a cellular stress context. eIF2Bε does not require the assembly of eIF2B regulatory subunits to carry out its GEF function, with eIF2Bγ enhancing the activity of the ε subunit (Li *et al*., 2004). Thus, these small eIF2Bε foci, could represent the assembly of eIF2B catalytic bodies, carrying out basal levels of GEF activity during stress. eIF2Bα on the other hand, is necessary for sensing of stress, thus these assemblies may present a key point for regulation and recovery of adverse conditions.

Conversely, small eIF2Bα foci could be formed following the disassembly of eIF2B bodies with decamer structures in stressed conditions. These would in turn allow for the formation of eIF2B bodies insensitive to p-eIF2α inhibition, thus still

capable of having GEF activity. Given that eIF2B decameric structure is stable and that large eIF2B foci appear to be formed from these assemblies, the formation of small eIF2B foci with eIF2B subcomplexes might not be an preliminary assembly that then leads to the formation of large decameric eIF2B foci. It couls be that these small localised foci are formed from large eIF2B foci dismantling.

Further co-localision efforts between endogenous eIF2Bα and other subunits under these conditions should be carried out to determine possible remodeling of eIF2Bα localisation composition.

While the study of the composition of these eIF2Bα foci could elucidate their particular function and the reason for their modulation following stress, certain conclusions can be taken from these results: (1) eIF2Bα and eIF2Bε endogenous localisation distribution and prevalence is modulated upon cellular stress; (2) increased localisation is not correlated with the increase of protein expression; (3) increased number of large eIF2Bα foci is not accompanied by the increased number of large eIF2Bε foci, suggesting that these eIF2Bα structures are eIF2B independent, perhaps binding to other partners.

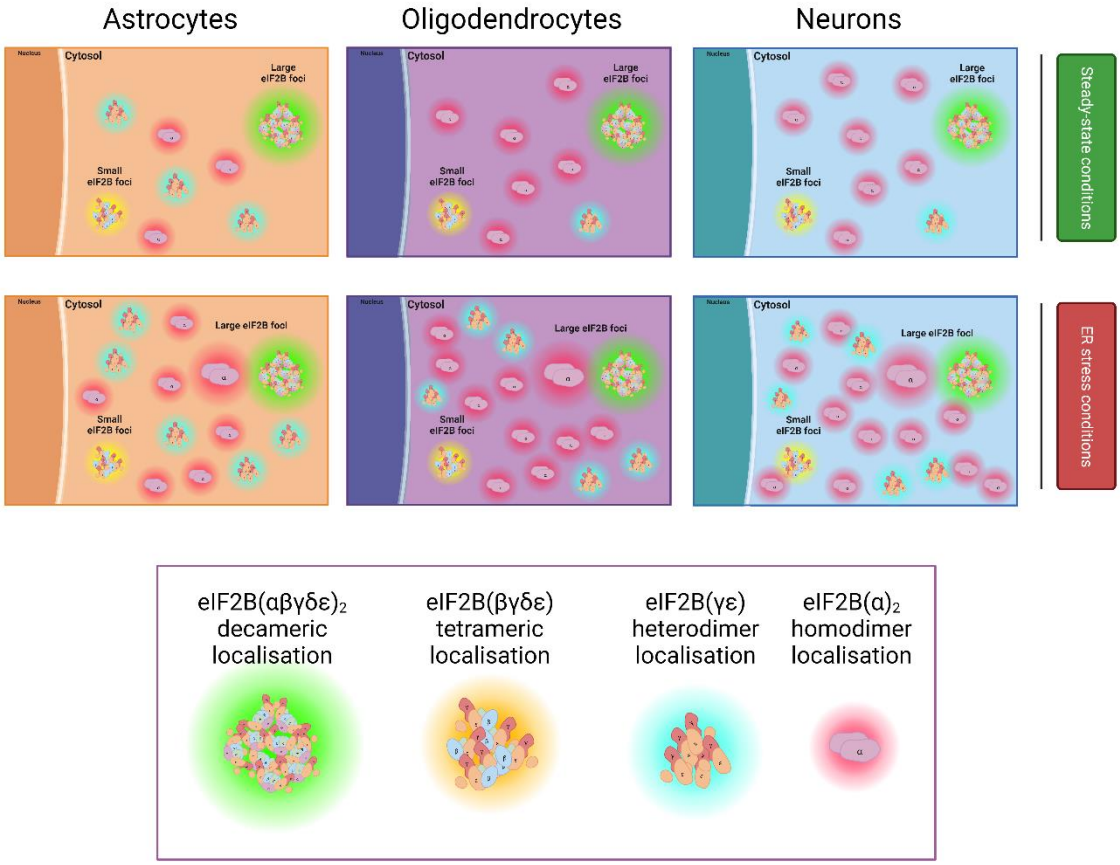

Figure 4.36. eIF2Bα and eIF2Bε localisation is modulated following ER stress induction. Following acute ER stress induction induces an increase of the number of small eIF2Bα and eIF2Bε foci per cell and an increase of large eIF2Bα foci per cell in glial and neuronal cell types, thus a general feature of acute ISR induction. These small eIF2Bε foci are proposed to be eIF2B catalytic subcomplexes and small/large eIF2Bα are proposed to be independent of spatial interaction of other eIF2B subunits, perhaps interacting with other proteins. Image designed in BioRender.

4.3.4. Final observations

In this chapter, we conlude that endogenous eIF2B subunits localise to spatially distinct cytoplasmic foci in a cell-type specific manner amongst glial and neuronal cells. The results showcase that cell types possess a specialised, dynamic, subcellular localisation of eIF2B subunits. eIF2B bodies represent sites of GEF activity, which thus have a direct impact on translation initation rates. Thus, the presence of cell-type specific localisation patterns suggests a tailored regulation of translation initiation and subsequently protein production. Furthermore, the modulation of eIF2B localisation upon acute stress appears to be shared across the glial and neuronal cells, with localisation of eIF2Bα and eIF2Bε being altered, perhaps organised according to function, complex stability, assembly/dissassembly rates, or pre-made structures present in steady-state conditions. Additionally, the presence of eIF2B subcomplexes, particularly the assembly of proposed eIF2B independent eIF2Bα structures, may play a key role in cellular stress sensing and/or large eIF2B foci formation.

Chapter 5. The role of eIF2Bα in eIF2B body formation in neuronal and glial cells.

5.1. Introduction.

Previous studies have shed light on the existence of distinct subcomplexes within eIF2B bodies in mammalian cells, with a correlation between their size and subunit composition (Hanson *et al*., 2023; Hodgson *et al*., 2019). As previously mentioned, investigations in yeast and mammalian cells have confirmed the presence of eIF2B as a decamer with additional tetrameric structure comprising eIF2Bβ, eIF2Bγ, eIF2Bδ, and eIF2Bε, alongside the catalytic subcomplexes composed of eIF2Bγ and eIF2Bε, with stable eIF2Bα homodimers also being present (Kashiwagi *et al*., 2016; Wortham *et al*., 2016). These stable structures may possibly account for the localisation and composition distinctions observed in assemblies observed within mammalian cells (Hanson *et al*., 2023; Hodgson *et al*., 2019).

The intricacies of eIF2B decameric assembly and its pivotal role in driving the formation of eIF2B bodies have been elucidated through yeast models. This process is susceptible to disruption, as missense mutations in the eIF2Bα subunit have been found to impede both decamer formation and the subsequent assembly of eIF2B bodies (Norris *et al*., 2021; Taylor *et al*., 2010). The impact of missense mutations, either within the eIF2Bα and p-eIF2α interface, or in the interface between eIF2Bα and eIF2Bβ as well as eIF2Bδ are of great interest (De Franco *et al*., 2020; Norris *et al*., 2021; Wortham & Proud, 2015). Gcn- mutations are thought to prevent p-eIF2α from binding to the eIF2B complex in response to cellular stress, preventing the cell from producing a stress response, thus being mainly thought to be in mutations that impact eIF2Bα and p-eIF2α interface. Gcd- mutations have been shown to decrease eIF2Bs GEF activity, reducing global protein synthesis and subsequently leading to the constitutive expression of Gcn4p (ATF4), being mainly thought to be caused by issues with eIF2Bα binding to eIF2Bβ and eIF2Bδ (Hannig *et al*., 1990; Pavitt *et al*., 1997).

These findings suggest that the establishment of stable interactions involving eIF2B subunits and eIF2Bα stands as a prerequisite for the particular eIF2B localisation patterns to form.

Moreover, recent publications have revealed that the absence of eIF2Bα leads to the accumulation of unassembled eIF2Bβγδε tetramers within cells. Intriguingly,

the introduction of ISRIB promotes the binding of these free tetramers, resulting in the formation of functionally active octamers. In the absence of eIF2Bα, the ISR is triggered. However, the introduction of ISRIB proves to be a restorative measure, effectively rescuing the induced ISR (Schoof *et al*., 2021; Sekine *et al*., 2015; Sidrauski *et al*., 2015; Tsai *et al*., 2018; Zyryanova *et al*., 2018). In **chapter 4** we have demonstrated that in glial and neuronal cell lines a large percentage of cells with localised eIF2Bα and a high number of eIF2Bα foci per cells without co-localising with catalytic or regulatory eIF2B subunits.

While published studies have provided valuable insights into the structural aspects of eIF2B complexes and how individual subunits interact to form the full eIF2B decamer, a crucial aspect that remains unexplored is the native localisation of the eIF2B subunits as the decamer assembles and the specific role played by eIF2Bα in the formation of eIF2B bodies within mammalian cells. Previous studies (Schoof *et al*., 2021; Tsai *et al*., 2018; Zyryanova *et al*., 2018) show the potential significance of eIF2Bα homodimers as stable subcomplexes essential for the assembly of the eIF2B decameric structure, and possibly crucial for the formation of the eIF2B body.

5.1.1. Hypothesis and rational

The significance of eIF2B localisation is exhibited by the fact that subcellular bodies of eIF2B co-localise with eIF2 and exhibit high levels of eIF2 shuttling, with this shuttling correlating with GEF activity. Additionally, eIF2B bodies, with varying eIF2B subunit composition, have shown to display different rates of eIF2 shuttling and therefore varying GEF activity (Campbell *et al*., 2005; Hanson *et al*., 2023; Hodgson *et al*., 2019). By unraveling the mechanisms underpinning eIF2B assembly and disassembly and relating them to the formation of eIF2B bodies we may gain insights into the highly regulated process of translation in different cell types. In yeast models, the absence of eIF2Bα results in a dispersed eIF2B body localisation, whereas the presence of Gcd- missense mutations leads to the formation of microbodies, which exhibit diminished levels of eIF2 shuttling (Norris *et al*., 2021). These observations offer compelling evidence that the spatial organization of eIF2B plays a pivotal role in orchestrating the precise regulation of translation, thus highlighting the intricate nature of this crucial cellular process. Within this chapter, we aim to explore the impact of decreased expression of eIF2Bα in the formation of eIF2B bodies in mammalian cells.

We hypothesise that eIF2Bα is required for the stabilization of eIF2B subunits to form large eIF2B bodies. To test this hypothesis, the main objectives were to:

- Decrease expression levels of eIF2Bα and determine its impact on eIF2B subunit localisation in glial and neuronal cells.
- Analyse the impact of modulation/activation of stress on eIF2B foci formation and cell viability in the absence of eIF2Bα.
- Determine the impact of decreased expression of eIF2Bα on the GEF activity of eIF2B bodies.
- Determine how the small molecule ISRIB impacts the modulation of the ISR and eIF2B localisation in the absence of eIF2Bα expression.

5.2. Results.

5.2.1. siRNA mediated silencing of *EIF2B1* leads to the altered eIF2B localisation in neuronal and glial cells.

In order to determine the role of eIF2Bα in the localisation of cytoplasmic foci of eIF2B in mammalian cells, we utilised siRNA to decrease expression of *EIF2B1*. To determine optimal time of siRNA transfection to obtain maximum *EIF2B1* silencing cells were harvested at 72h, 96h and 120h post siRNA^{EIF2B1} transfection in U373-MG cells (**Figure 5.1A**). A significant decrease in expression levels was observed in all time periods (72h: 0.35-fold ± 0.05; 96h: 0.15-fold ± 0.02; 120h: 0.17-fold ± 0.01), with the highest fold change present at 96h. It is of note, that following 120h of incubation, an increase in cell death was observed (data not shown), and as such, this time point was dismissed. Western blot analysis of eIF2Bα expression levels revealed that the optimal incubation period was 96h, which was used for future mediated gene silencing, unless stated otherwise.

U373-MG, SH-SY5Y and MO3.13 cells were then subjected to siRNA targeting the *EIF2B1* gene (sieIF2Bα). Expression levels of eIF2Bα were significantly reduced following knockdown of eIF2Bα in all cell lines utilised (U373: 0.25-fold ± 0.13; SH-SY5Y: 0.22-fold ± 0.08; MO3.13: 0.18-fold ± 0.03) (**Figure 5.1B**). A negative scrambled control siRNA highlighted the specificity of *EIF2B1* silencing as no significant difference to the eIF2Bα expression levels were observed for this scrambled siRNA (**Figure 5.1B**). Given that the expression of the eIF2B subunits, other than eIF2Bα, are stoichiometrically regulated and that regulation of eIF2B subunit expression is necessary for correct complexes/subcomplexes function (Wortham *et al*., 2016), the expression levels of eIF2Bβ-ε were analysed following knockdown of eIF2Bα to confirm that the decrease expression of eIF2Bα would not impact the expression of the other eIF2B subunits (**Figure 5.2**). We observed that no significant differences of eIF2Bβ-ε expression levels between untreated and siRNA mediated silencing of *EIF2B1*, illustrating that while eIF2Bβ-ε subunits are stoichiometrically regulated, the modulation of expression of eIF2Bα does not impact the expression of the other eIF2B subunits in mammalian cells (**Figure 5.2**).

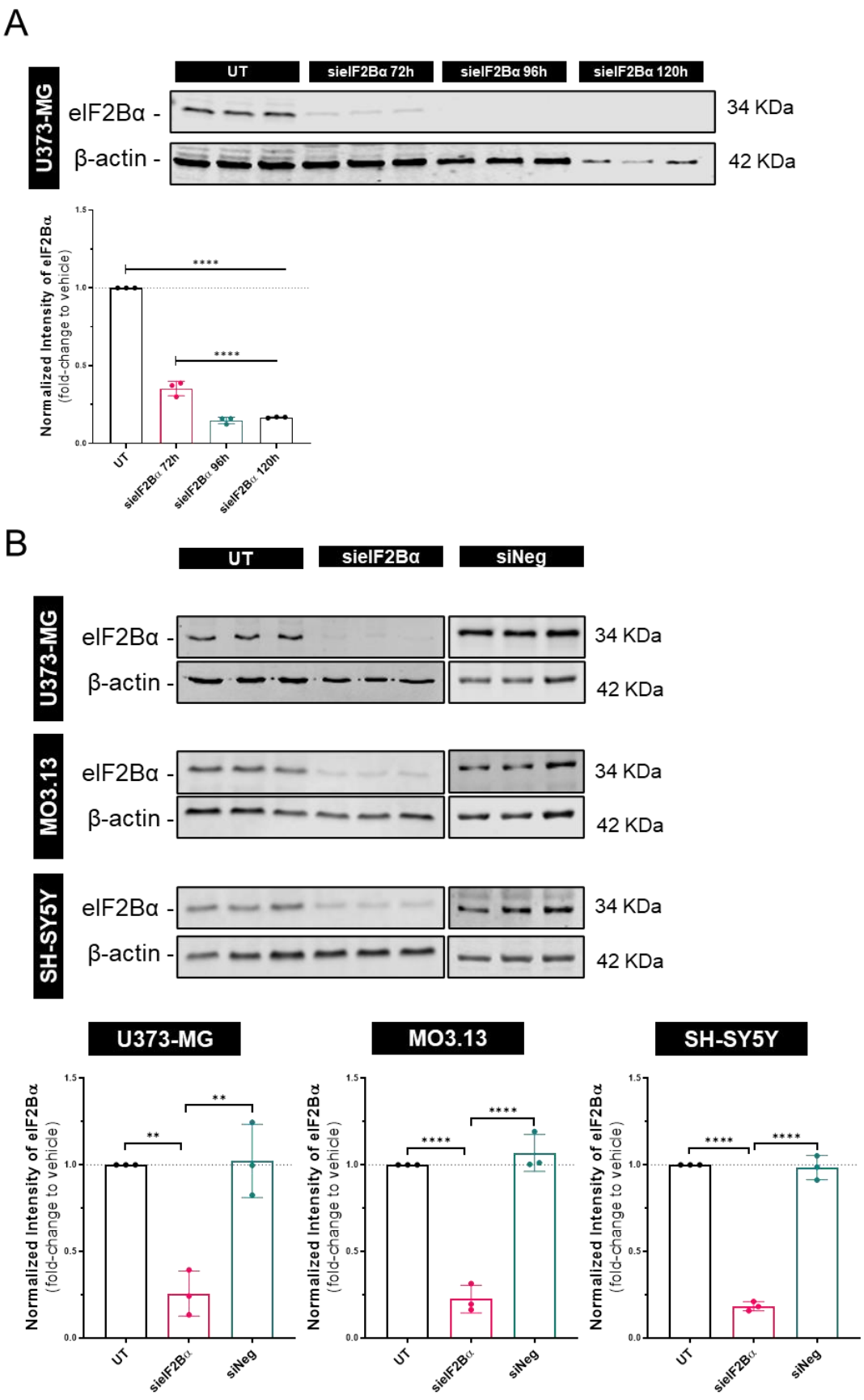

Figure 5.1. siRNA mediated silencing of *EIF2B1* leads to significant decrease of eIF2Bα expression levels following 96h of transfection.

(A) Western Blot analysis of the level of eIF2Bα expression in U373-MG cells following untreated and siRNA mediated silencing of eIF2Bα for 72h, 96h and 120h. Levels of eIF2Bα were normalized to levels of β-actin and presented as mean ± SD (UT – untreated; n=3). Data was analysed by one-way ANOVA test, followed by a Tukey's multiple analysis. ****$p \leq 0.0001$. (B) Western Blot analysis of the level of eIF2Bα expression in U373-MG, MO3.13 and SH-SY5Y cells following untreated and siRNA mediated silencing of eIF2Bα and siRNA negative control for 96h. Levels of eIF2Bα were normalized to levels of β-actin and presented as mean ± SD (UT – untreated; n=3). Data was analysed by one-way ANOVA test, followed by a Tukey's multiple analysis. **$p \leq 0.01$; ****$p \leq 0.0001$.

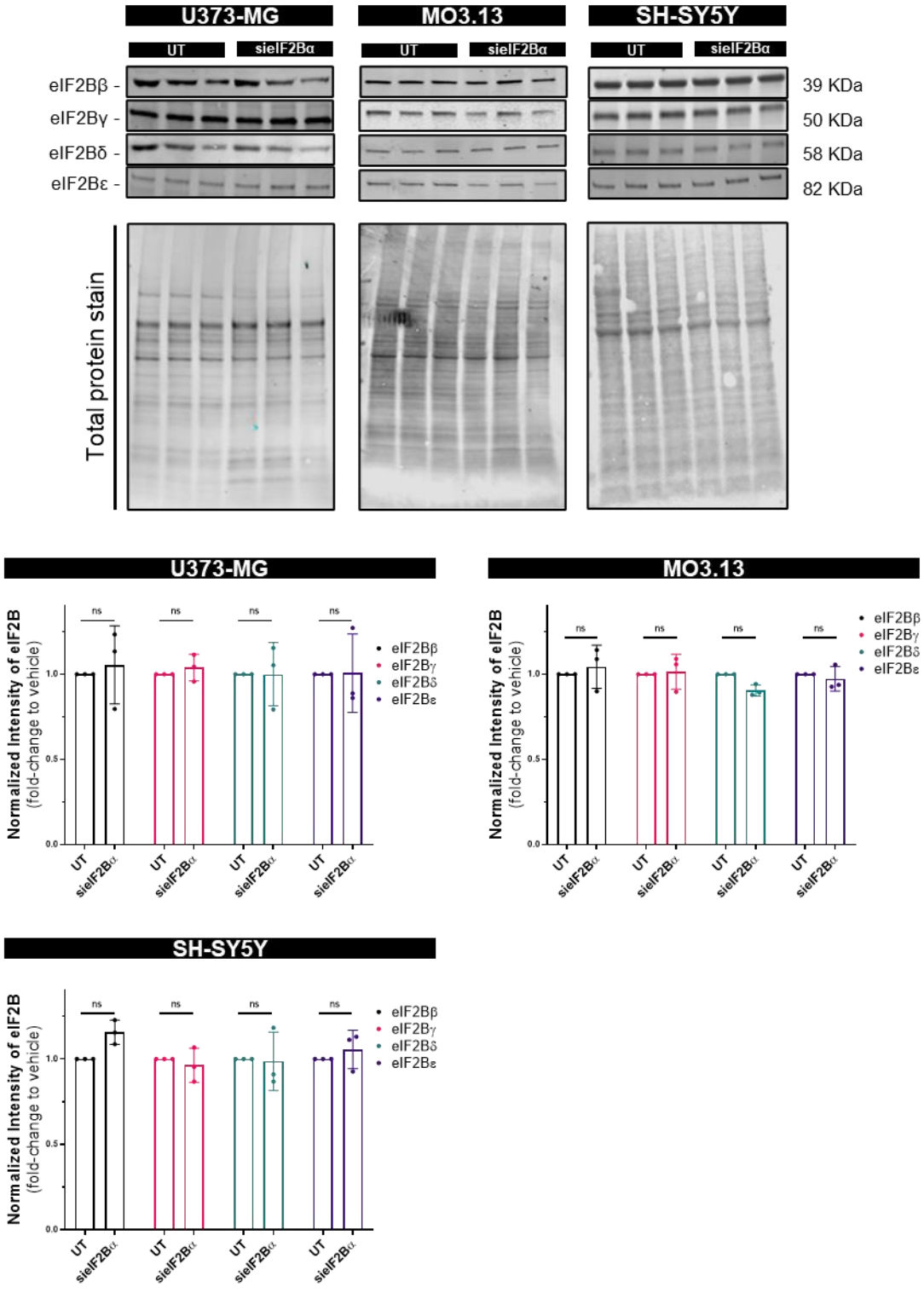

Figure 5.2. siRNA mediated silencing of *EIF2B1* does not alter eIF2Bβ-ε expression levels. Western Blot analysis of the level of eIF2Bβ-ε expression in U373-MG, MO3.13 and SH-SY5Y cells following untreated and siRNA mediated silencing of eIF2Bα for 96h. Levels of eIF2Bβ-ε were normalized to levels of total protein stain and presented as mean ± SD (UT – untreated; n=3); n.s. = non-significant. Data was analysed by two-way ANOVA test, followed by a Tukey's multiple analysis.

Following eIF2Bα knockdown, as expected a significant decrease in percentage of cells with eIF2Bα localisation was observed in a population of 100 U373-MG, MO3.13 and SH-SY5Y cells per replicate (U373: UT – 28.00 % ± 6.08, sieIF2Bα – 10.00 % ± 1.00; MO3.13: UT – 62.33 % ± 5.86, sieIF2Bα – 16.00 % ± 3.61; SH-SY5Y: UT – 66.67 % ± 4.73, sieIF2Bα – 24.67 % ± 4.73) (**Figure 5.3**). In addition, the average number of small and large foci per cell was also studied to ascertain if the impact of reduced expression of eIF2Bα affected small and large foci equally. In all three cell lines subjected to knockdown of eIF2Bα, the average number of small and large foci per cell was significantly decreased when compared to untreated cells and cells transfected with a siRNA control (siNeg) (**Figure 5.4**).

These results show that the decreased localisation of eIF2Bα was a consequence of decreased expression. This adds to the results observed in **chapter 4**, indicating that cell-type specificity of proportion and abundance of eIF2Bα foci are not entirely governed by expression levels. However, near-absent protein expression leads to near-absent localisation, confirming that these additional aggregates of eIF2Bα seen in **4.2.** are in fact eIF2Bα structures and that they are not artifacts.

While a decrease in expression and localisation of eIF2Bα was observed, the ICC images displayed some cells with eIF2Bα localisation potentially caused by un-transfected cells without any modulation of eIF2Bα expression levels. To test this, siRNAs targeting *EIF2B1* gene and siRNA negative control were labeled with a fluorescent dye. ICC detection and subsequent analysis of cells, which had been transfected was carried out to ensure we could determine which cells have decreased eIF2Bα levels (**Figure 5.5**). Through this, we were able to observe that cells transfected with siRNAs targeting *EIF2B1* gene did not display eIF2Bα localised foci, while cells transfected with siRNA negative control still exhibited eIF2Bα localised foci (**Figure 5.5**). Firstly, transfection rate was determined through the analysis of 100 cells per triplicate repeat with or without the incorporation of labeled siRNA (**Figure 5.6A**). Following 96h incubation period, labeled siRNA targeting eIF2Bα was incorporated into 69.00 % (± 8.18) of U373-MG cells, 79.67 % (± 3.05) of MO3.13 cells, and 86.00 % (± 7.00) of SH-SY5Y cells. Therefore, a large population of cells have undergone some level of modulation of eIF2Bα protein expression, which has a direct consequence in its localisation, demonstrating transfection rate correlation with decrease eIF2Bα

expression and localisation, as seen in **figure 5.3 and 5.4**. Subsequently, similar levels of cells showing eIF2Bα localisation were observed when compared with results in **Figure 5.3** (U373: sieIF2Bα – 8.33 % ± 2.08, siNeg – 27.00 % ± 2.00; MO3.13: sieIF2Bα – 16.67 % ± 1.53, siNeg – 63.33 % ± 3.51; SH-SY5Y: sieIF2Bα – 12.00 % ± 2.00, siNeg – 68.67 % ± 1.53) (**Figure 5.6B**).

Two main conclusions can be drawn from these results: (1) a large proportion of cells were transfected with the siRNA, and transfected cells had decreased eIF2Bα expression following siRNA mediated silencing of *EIF2B1*; (2) the study of a population of cells per replicate allows for a sensitive and reliable method to observe changes in localisation patterns which correlate with expression levels of eIF2Bα.

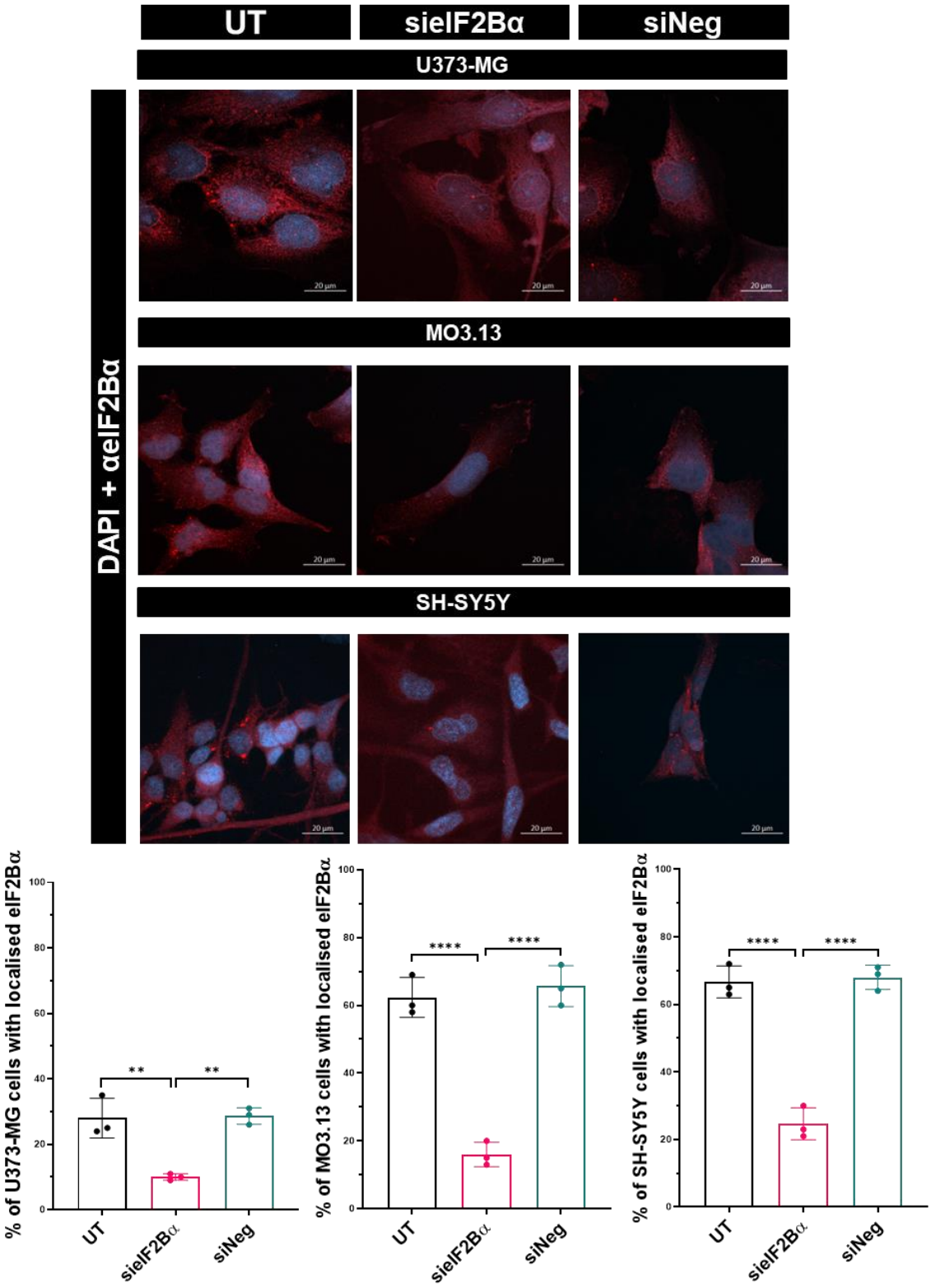

Figure 5.3. siRNA mediated silencing of *EIF2B1* leads to significant decrease of eIF2Bα localisation in glial and neuronal cells.

Representative images of endogenous eIF2Bα localising to cytoplasmic foci following untreated, siRNA mediated silencing of eIF2Bα and siRNA negative control, for 96h. U373-MGand SH-SY5Y cells were fixed in methanol, MO3.13 cells were fixed in 4%PFA and subjected to ICC with anti-eIF2Bα primary antibodies and visualized using appropriate secondary antibodies conjugated to Alexa Fluor 594. Mean percentages of cells that showed localisation, *i.e.*, one or more foci of

eIF2Bα (UT – untreated; n=3 counts of 100 cells per repeat) presented as mean ± SD. *p* Values derived from one-way ANOVA test, followed by a Tukey's multiple analysis. $^{**}p \leq 0.01$; $^{****}p \leq 0.0001$. Scale bar: 20 μm. DAPI stains nuclei.

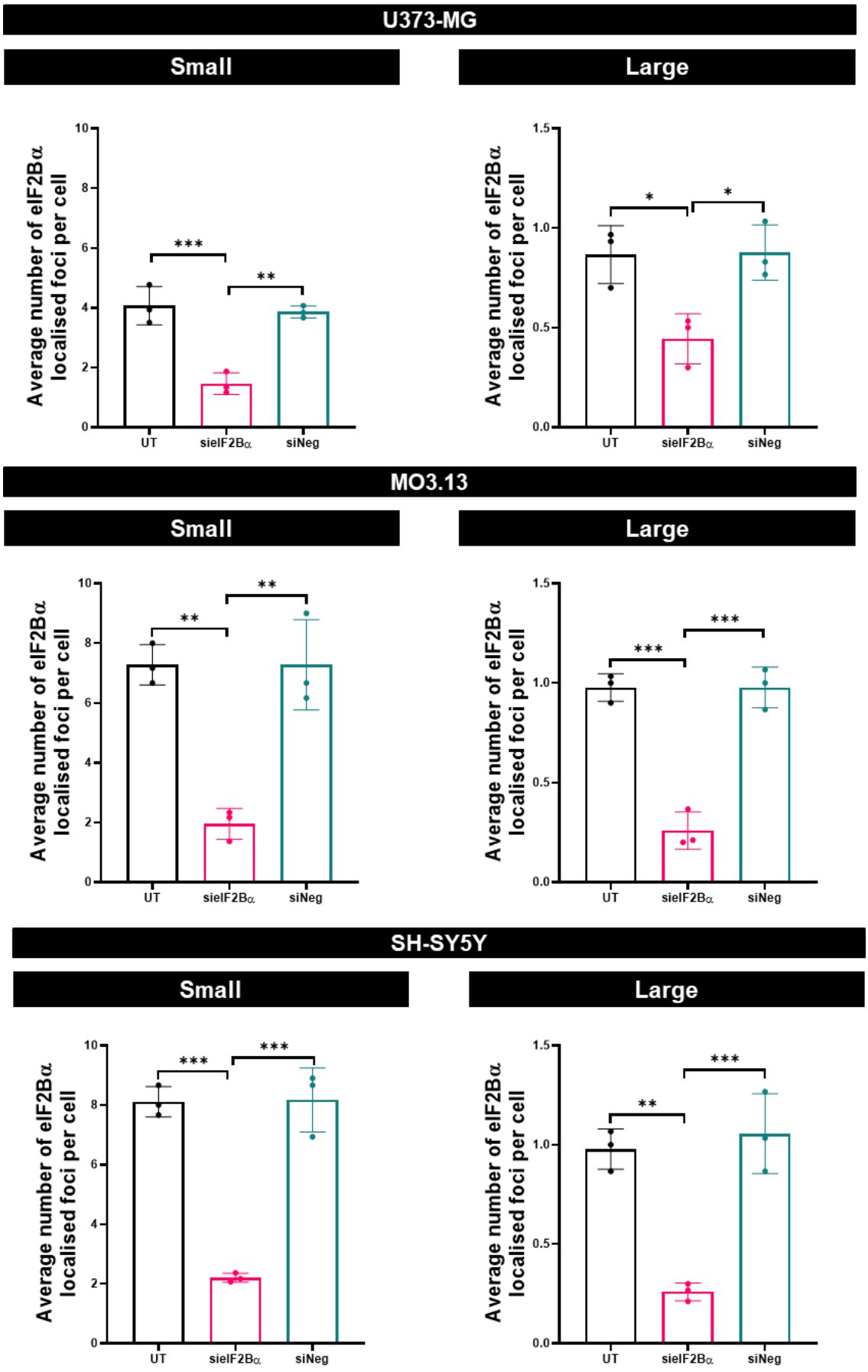

Figure 5.4. siRNA mediated silencing of *EIF2B1* leads to significant decrease of eIF2Bα small and large foci in glial and neuronal cells.

Average number of small and large eIF2Bα foci per cell in 30 U373-MG, MO3.13 and SH-SY5Y cells with eIF2Bα localised foci (UT – untreated; n=3). Average number of Error bars: ± s.d. *p* Values derived from one-way ANOVA test, followed by a Tukey's multiple analysis. *$p \leq 0.05$; **$p \leq 0.01$; ***$p \leq 0.001$.

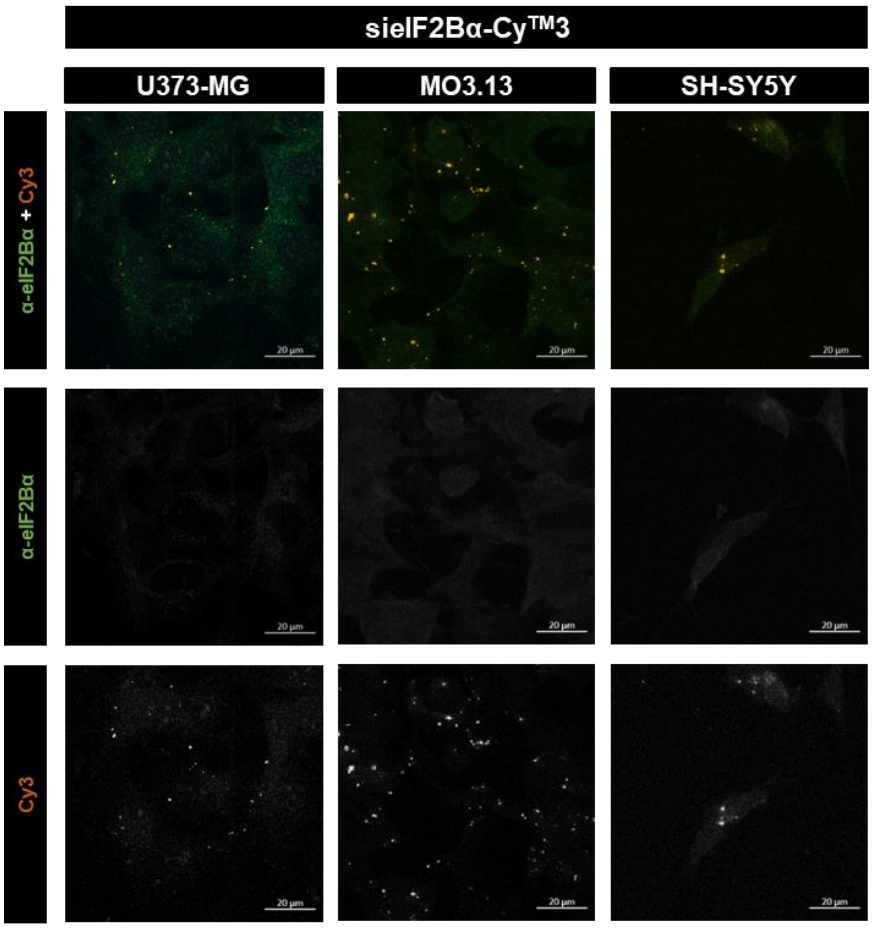
sielF2Bα-Cy™3
U373-MG
MO3.13
SH-SY5Y
α-eIF2Bα + Cy3
α-eIF2Bα
Cy3
20 µm

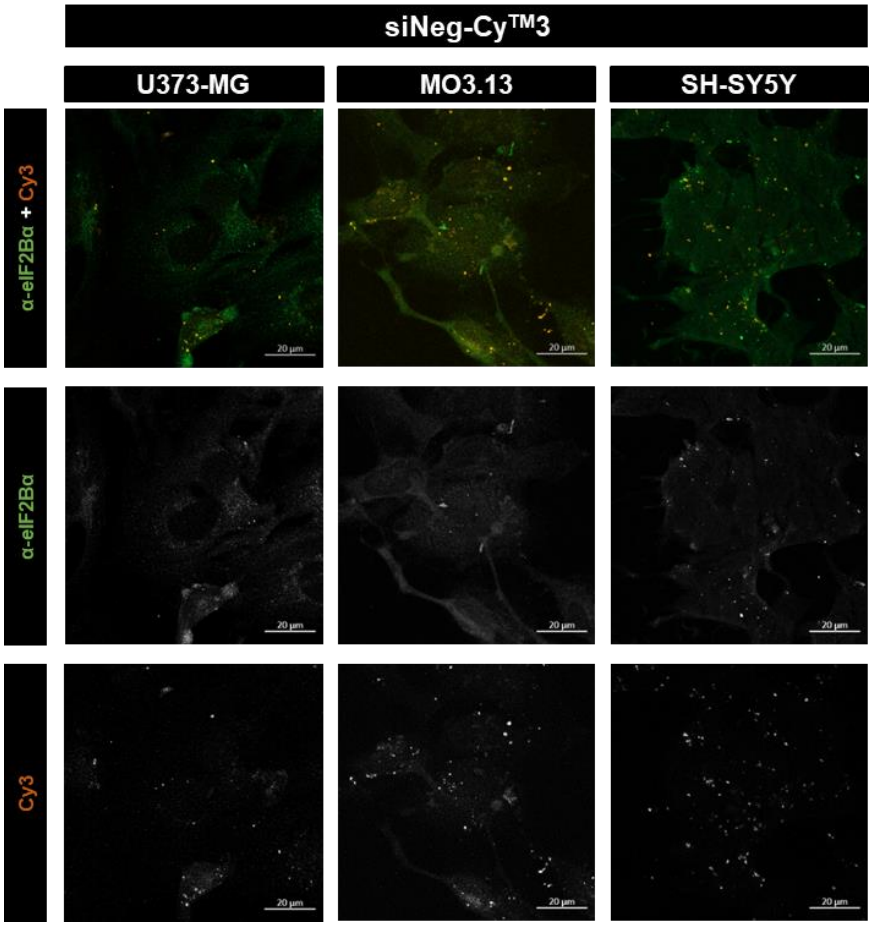
siNeg-Cy™3
U373-MG
MO3.13
SH-SY5Y
α-eIF2Bα + Cy3
α-eIF2Bα
Cy3
20 µm

Figure 5.5. Labelled siRNA targeting *EIFB1,* and siRNA negative control allow to observe transfected cells.

Representative images of Cy3 siRNA labelling and endogenous eIF2Bα localising to cytoplasmic foci following Cy3 tagged siRNA mediated silencing of *EIF2B1* (top panel) and Cy3 tagged siRNA negative control (bottom panel), for 96h. U373-MG and SH-SY5Y cells were fixed in methanol, MO3.13 cells were fixed in 4 % PFA and subjected to ICC with anti-eIF2Bα primary antibodies and visualized using appropriate secondary antibodies conjugated to Alexa Fluor 488. Scale bar: 20 μm.

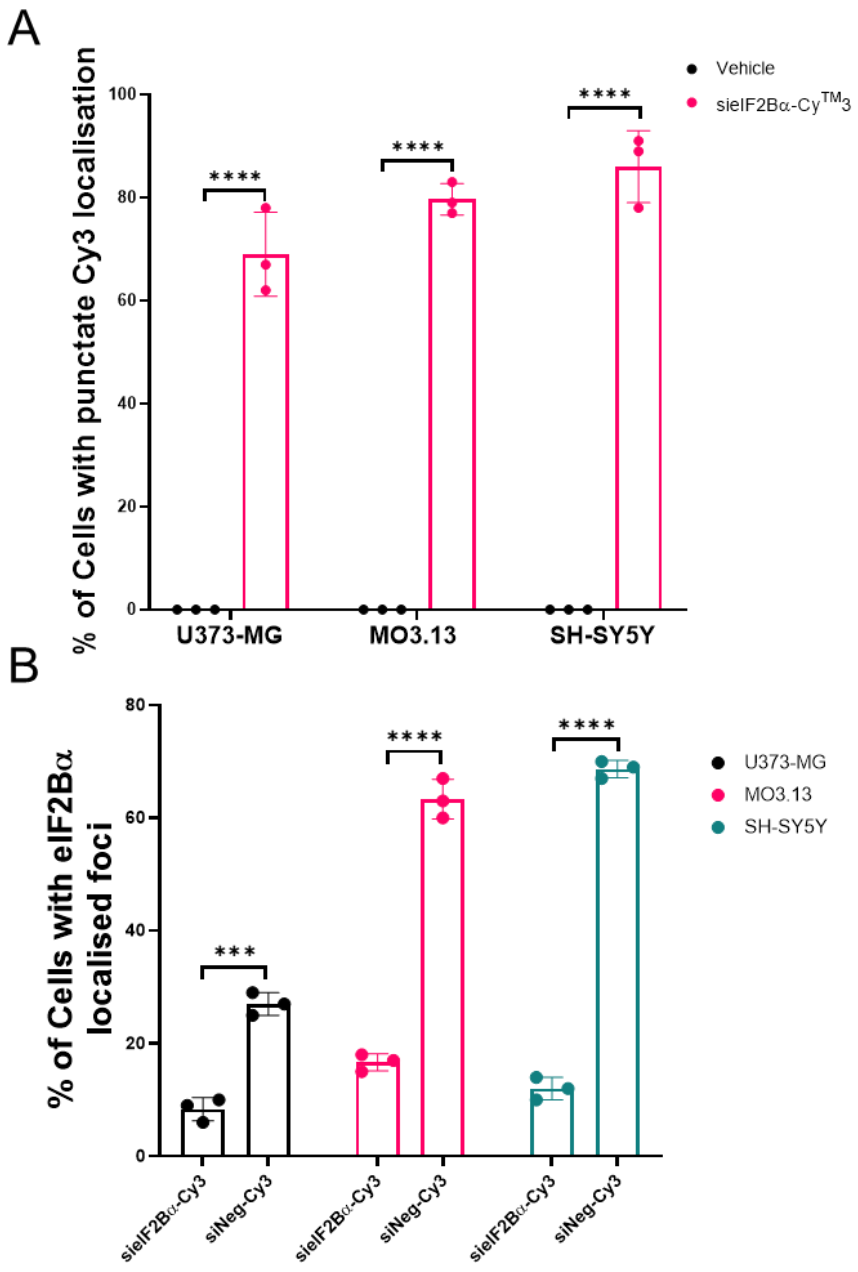

Figure 5.6. Glial and neuronal cells display high transfection rate of labelled siRNA targeting *EIF2B1* and siRNA negative control does not impact eIF2Bα localisation.

(A) Mean percentages of U373-MG, MO3.13 and SH-SY5Y cells that showed punctate Cy3 localisation, *i.e.*, one or more puncti, following vehicle (Cy3 label) and Cy3 tagged siRNA mediated silencing of eIF2Bα, for 96h (n=3 counts of 100 cells per repeat) presented as mean ± SD. *p* Values derived from two-way ANOVA test, followed by a Tukey's multiple analysis. ****$p \leq 0.0001$. (B) Mean percentages of U373-MG, MO3.13 and SH-SY5Y cells that showed endogenous eIF2Bα localising to cytoplasmic foci, *i.e.*, one or more foci, following Cy3 tagged siRNA mediated silencing of eIF2Bα and Cy3 tagged siRNA negative control, for 96h (n=3 counts of 100 cells per repeat) presented as mean ± SD. *p* Values derived from two-way ANOVA test, followed by a Tukey's multiple analysis. ***$p \leq 0.001$; ****$p \leq 0.0001$.

5.2.2. siRNA mediated silencing of *EIF2B1* leads to the disruption of foci formation of eIF2Bβ-ε and ISRIB rescues the formation of large foci.

The eIF2Bα subunit has two major known functions – sensing of stress and stabilizing the eIF2B decameric structure (Kenner *et al*., 2019; Schoof *et al*., 2021). While there have been reports which correlate eIF2B decamer formation to eIF2B localisation in cells, the investigation on how eIF2Bα may play a role in both has yet to be fully understood.

A significant decrease in eIF2Bα expression led to a significant decrease in eIF2Bα localisation. However, this did not affect eIF2Bβ-ε expression levels. Given the previous published work where eIF2Bα has been highlighted as a subunit necessary to assemble the eIF2B decamer (Schoof *et al*., 2021; Tsai *et al*., 2018; Zyryanova *et al*., 2018), this leads to the following question: In the cellular context with decreased expression and localisation levels of eIF2Bα, how does this impact on eIF2Bβ-ε localisation?

Therefore, following siRNA mediated silencing of *EIF2B1*, U373-MG (**Figure 5.7**), MO3.13 (**Figure 5.8**) and SH-SY5Y (**Figure 5.9**) cells were then subjected to ICC targeting the endogenous eIF2Bβ-ε subunits.

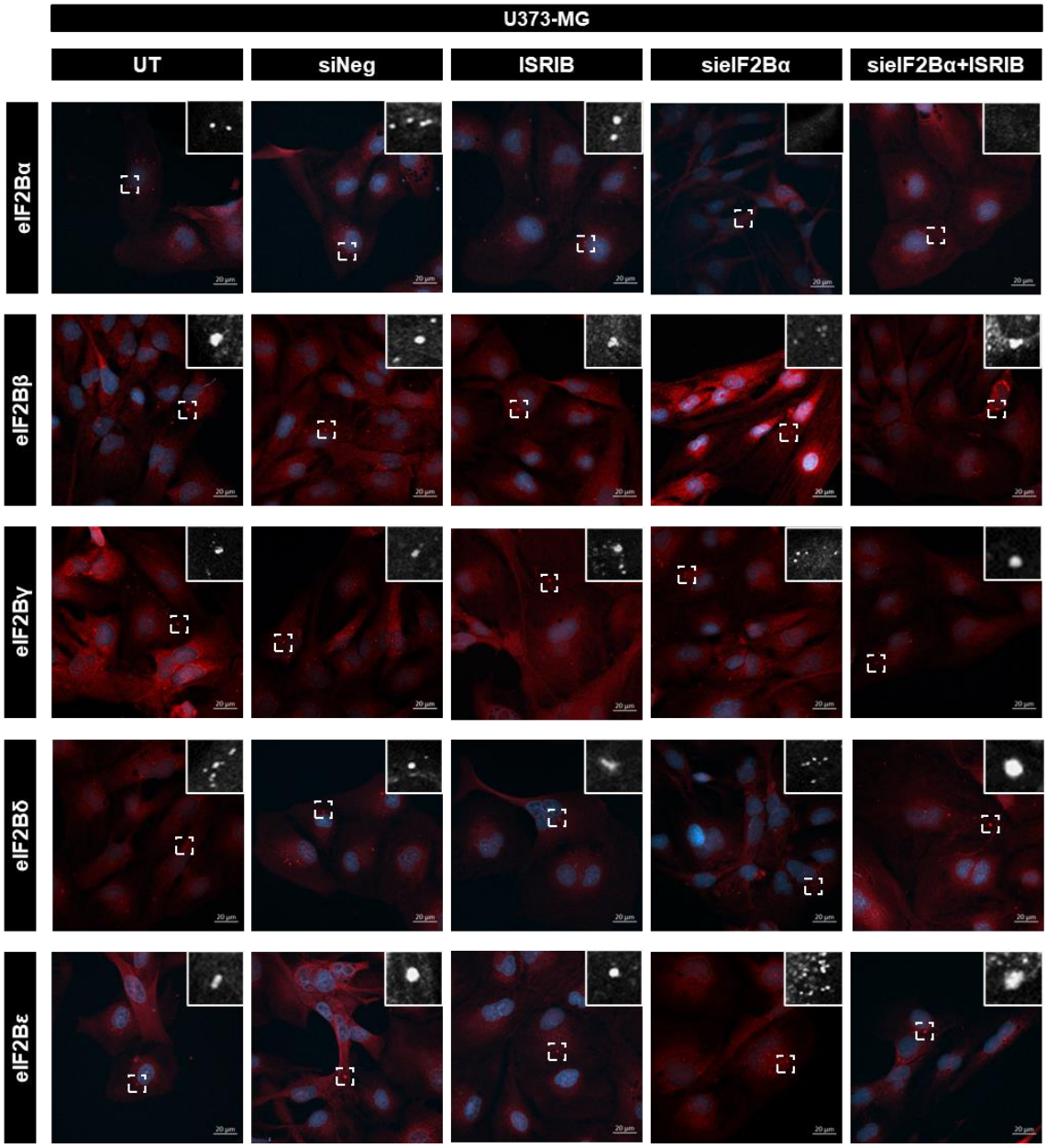

Figure 5.7. siRNA mediated silencing of *EIF2B1* with/without ISRIB treatment leads to altered eIF2Bβ-ε localisation in U373-MG cells.

Representative confocal images of U373-MG cells immunostained with primary antibodies against (top to bottom) endogenous α-eIF2Bα, α-eIF2Bβ, α-eIF2Bγ, α-eIF2Bδ and α-eIF2Bε foci with diverse sizes, and visualized using appropriate secondary antibodies conjugated to Alexa Fluor 594 following siRNA negative control transfection for 96h, ISRIB 200 nM 1h treatment, siRNA mediated silencing of *EIF2B1* transfection for 96h and siRNA mediated silencing of *EIF2B1* transfection for 96h coupled with ISRIB 200 nM 1h treatment (UT – untreated). DAPI stains nuclei. Scale bar: 20 μm.

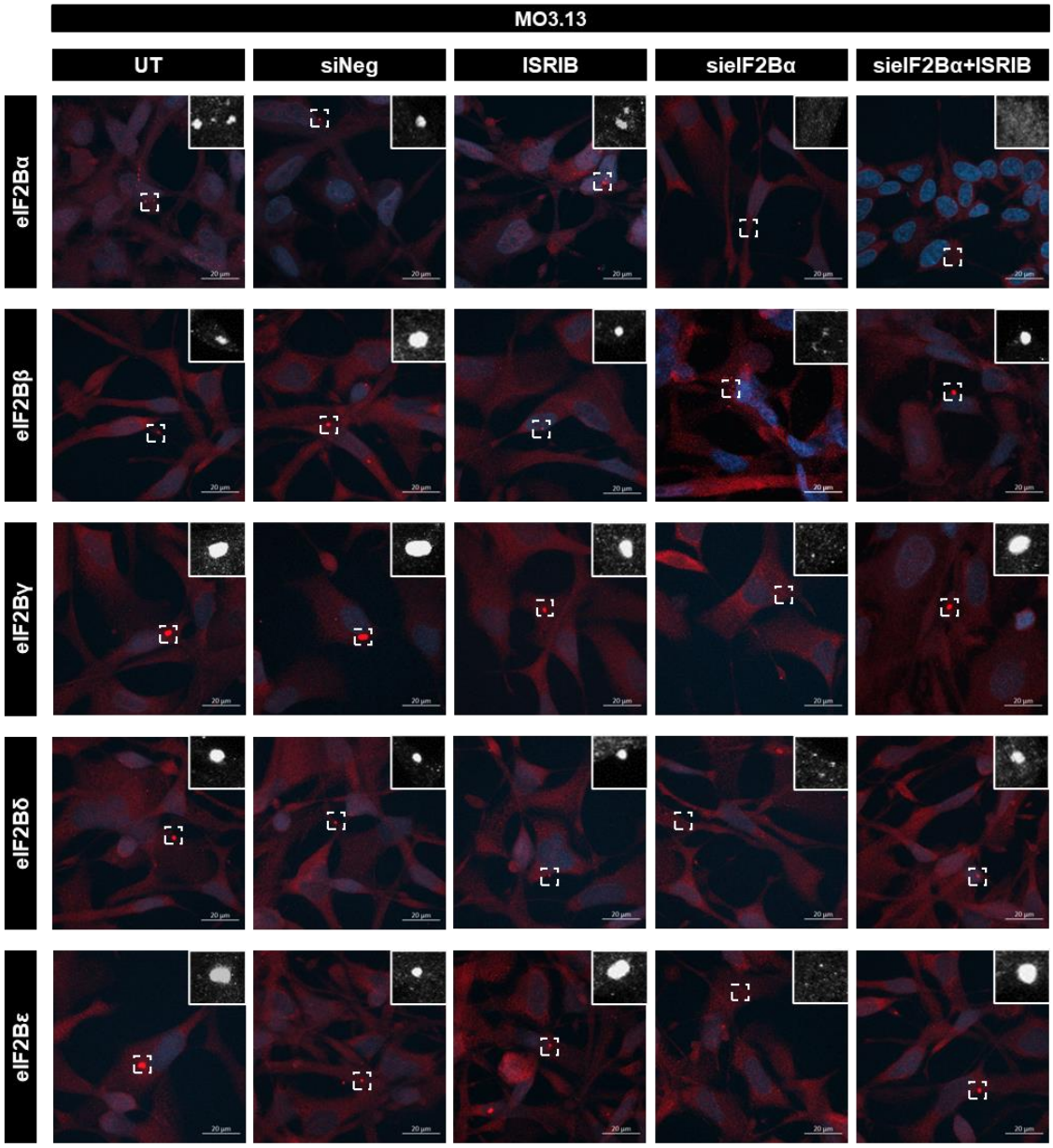

Figure 5.8. siRNA mediated silencing of *EIF2B1* with/without ISRIB treatment leads to altered eIF2Bβ-ε localisation in MO3.13 cells.

Representative confocal images of MO3.13 cells immunostained with primary antibodies against (top to bottom) endogenous α-eIF2Bα, α-eIF2Bβ, α-eIF2Bγ, α-eIF2Bδ and α-eIF2Bε foci with diverse sizes, and visualized using appropriate secondary antibodies conjugated to Alexa Fluor 594 following siRNA negative control transfection for 96h, ISRIB 200 nM 1h treatment, siRNA mediated silencing of *EIF2B1* transfection for 96h and siRNA mediated silencing of *EIF2B1* transfection for 96h coupled with ISRIB 200 nM 1h treatment (UT – untreated). DAPI stains nuclei. Scale bar: 20 μm.

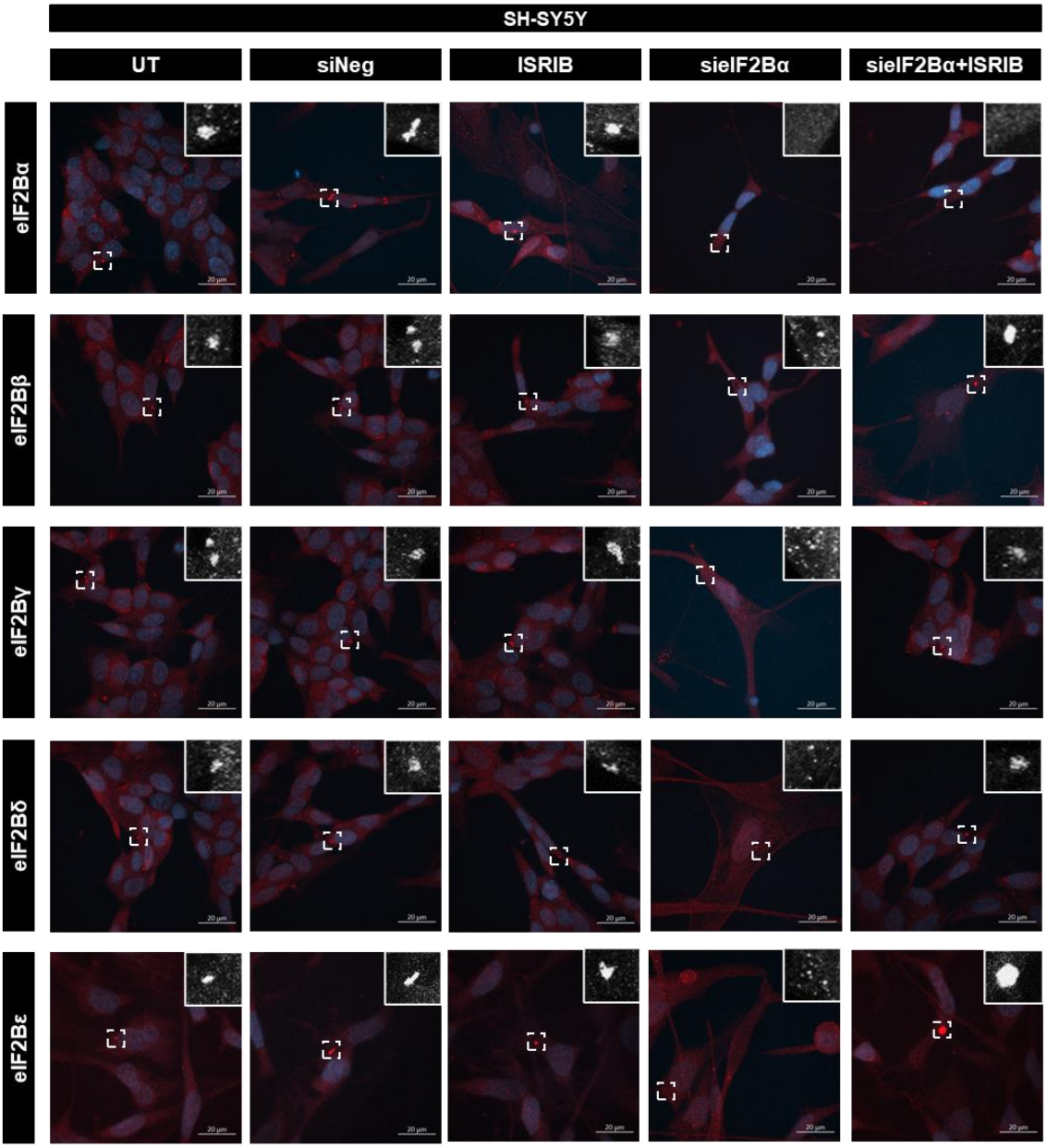

Figure 5.9. siRNA mediated silencing of *EIF2B1* with/without ISRIB treatment leads to altered eIF2Bβ-ε localisation in SH-SY5Y cells.

Representative confocal images of SH-SY5Y cells immunostained with primary antibodies against (top to bottom) endogenous α-eIF2Bα, α-eIF2Bβ, α-eIF2Bγ, α-eIF2Bδ and α-eIF2Bε foci with diverse sizes, and visualized using appropriate secondary antibodies conjugated to Alexa Fluor 594 following siRNA negative control transfection for 96h, ISRIB 200 nM 1h treatment, siRNA mediated silencing of *EIF2B1* transfection for 96h and siRNA mediated silencing of *EIF2B1* transfection for 96h coupled with ISRIB 200 nM 1h treatment (UT – untreated). DAPI stains nuclei. Scale bar: 20 μm.

The percentage of 100 cells per replicate U373-MG, MO3.13 and SH-SY5Y cells with localised eIF2Bβ-ε subunits, *i.e.,* one or more foci, were analysed following knockdown of eIF2Bα or control conditions (**Figure 5.10A, Figure 5.11A and Figure 5.12A)**. The knockdown of eIF2Bα and control conditions did not alter the percentage of cells with eIF2Bβ-ε localised foci in glial (**Figure 5.10A and Figure 5.11A**) and neuronal (**Figure 5.12A**) cell lines analysed.

Interestingly, when the average number of small and large eIF2Bβ-ε localised foci per cell was analysed, the decreased expression of eIF2Bα led to significant effects. In 30 U373-MG cells with localised eIF2B foci per repeat, we observed an overall significant increase of small eIF2Bβ-ε foci following knockdown of eIF2Bα. Additionally, treatment with ISRIB during inhibition of eIF2Bα expression led to the decrease in small foci back to untreated to levels (**Figure 5.10B**).

In 30 MO3.13 cells with localised foci per repeat, a similar result was present, with a significant increase in the average number of small eIF2Bβ-ε localised foci per cell following knockdown of eIF2Bα. This increase was restored to normal values when cells depleted of eIF2Bα were treated with ISRIB for 1 hour (**Figure 5.11B**). In 30 SH-SY5Y cells with localised foci per repeat, the average number of small eIF2Bβ-ε was significantly increased in the absence of eIF2Bα, with ISRIB treatment in the absence of eIF2Bα restoring normal values (**Figure 5.12B**). Therefore, while the percentage of cells with eIF2Bβ-ε foci remained unchanged following siRNA mediated eIF2Bα silencing, the overall increase of smaller eIF2B foci represented the presence of unassembled eIF2Bβ-ε subcomplexes.

More strikingly, we observed that the formation of large eIF2Bβ-ε foci was significantly reduced by eIF2Bα knockdown in glial and neuronal cells, which was then restored to untreated values when coupled with ISRIB treatment. In 30 U373-MG cells with localised foci per repeat, an average of 0.39 (± 0.11), 0.27 (± 0.09), 0.28 (± 0.07) and 0.26 (± 0.02) large eIF2Bβ-ε foci per cell, respectively, was observed in the absence of eIF2Bα. Knockdown of eIF2Bα coupled with ISRIB treatment lead to an increase of these large assemblies (eIF2Bβ: 0.99 ± 0.07; eIF2Bγ: 0.80 ± 0.03; eIF2Bδ: 1.18 ± 0.40; eIF2Bε: 0.78 ± 0.18) (**Figure 5.10C**).

In 30 MO3.13 cells with localised foci per repeat, similar results were observed, with a significant decrease in large eIF2Bβ-ε foci present following eIF2Bα knockdown (eIF2Bβ: 0.26 ± 0.05; eIF2Bγ: 0.23 ± 0.09; eIF2Bδ: 0.27 ± 0.07; eIF2Bε: 0.30 ± 0.03), values which were then restored by ISRIB treatment in cells

depleted of eIF2Bα (eIF2Bβ: 1.04 ± 0.18; eIF2Bγ: 0.83 ± 0.13; eIF2Bδ: 0.88 ± 0.07; eIF2Bε: 0.80 ± 0.09) (**Figure 5.11C**).

A comparable effect was obtained in 30 SH-SY5Y cells with localised foci per repeat following siRNA^{EIF2B1}, with significant decreased formation of large eIF2Bβ-ε foci (eIF2Bβ: 0.44 ± 0.11; eIF2Bγ: 0.27 ± 0.03; eIF2Bδ: 0.23 ± 0.03; eIF2Bε: 0.46 ± 0.14), and ISRIB being able to restore the formation of large eIF2Bβ-ε foci in cells depleted of eIF2Bα (eIF2Bβ: 1.38 ± 0.32; eIF2Bγ: 0.94 ± 0.16; eIF2Bδ: 0.90 ± 0.15; eIF2Bε: 0.95 ± 0.18) (**Figure 5.12C**).

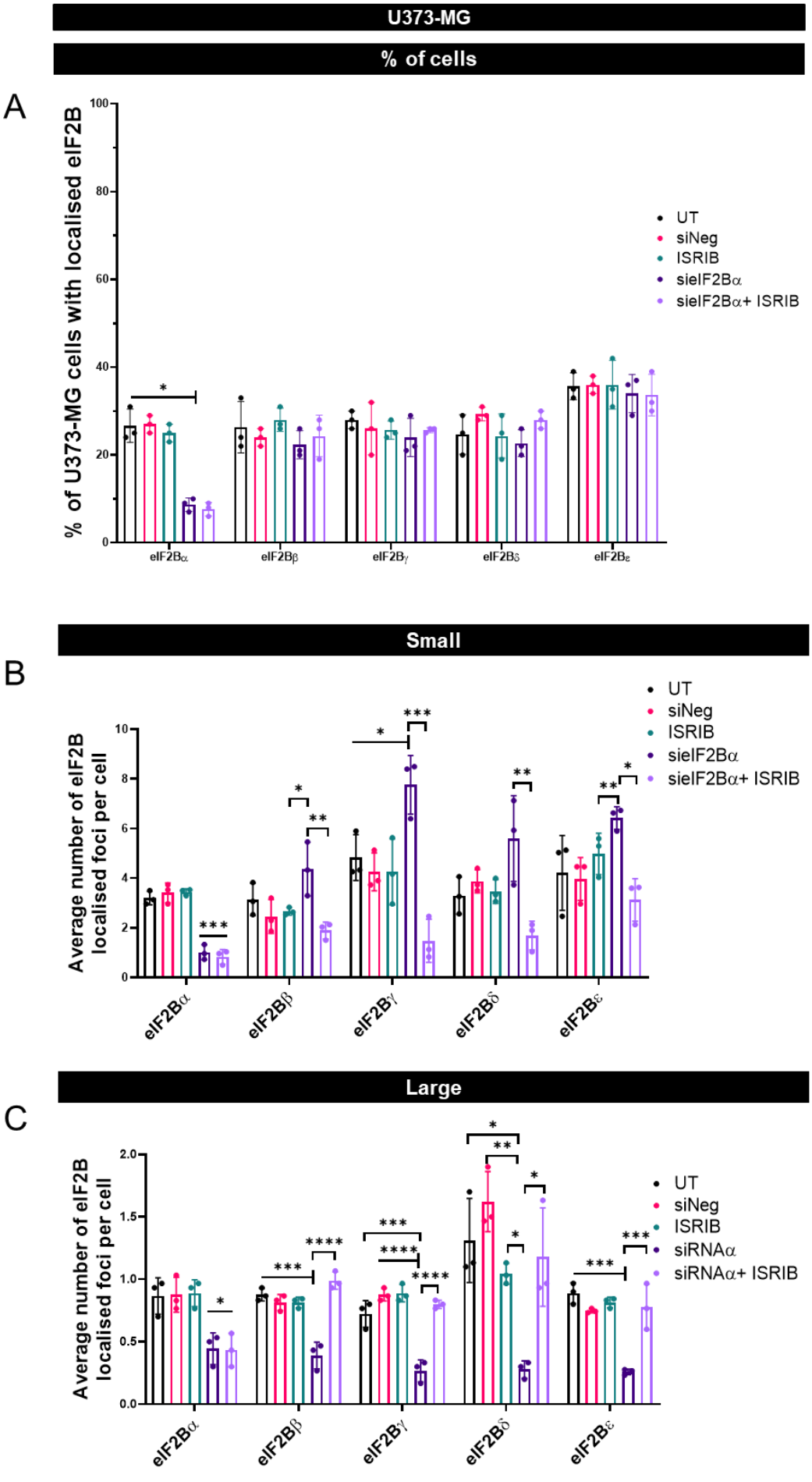
U373-MG
% of cells
A
% of U373-MG cells with localised eIF2B
100
80
60
40
20
0
*
UT
siNeg
ISRIB
sieIF2Bα
sieIF2Bα+ ISRIB
eIF2Bα
eIF2Bβ
eIF2Bγ
eIF2Bδ
eIF2Bε
Small
B
Average number of eIF2B localised foci per cell
10
8
6
4
2
0
*
**
***
UT
siNeg
ISRIB
sieIF2Bα
sieIF2Bα+ ISRIB
eIF2Bα
eIF2Bβ
eIF2Bγ
eIF2Bδ
eIF2Bε
Large
C
Average number of eIF2B localised foci per cell
2.0
1.5
1.0
0.5
0.0
*
**
***
****
UT
siNeg
ISRIB
siRNAα
siRNAα+ ISRIB
eIF2Bα
eIF2Bβ
eIF2Bγ
eIF2Bδ
eIF2Bε

Figure 5.10. siRNA mediated silencing of *EIF2B1* leads to an increase of eIF2Bβ-ε foci and decrease of large eIF2Bβ-ε foci, and ISRIB treatment rescue large eIF2B foci formation in U373-MG cells.

(A) Mean percentages of U373-MG cells with eIF2Bα-ε localised foci, in untreated cells and following siRNA negative control transfection for 96h, ISRIB 200 nM 1h treatment, siRNA mediated silencing of *EIF2B1* transfection for 96h and siRNA mediated silencing of *EIF2B1* transfection for 96h coupled with ISRIB 200 nM 1h treatment (UT – untreated; n=3 counts of 100 cells per repeat) presented as mean ± SD. *p* Values derived from one-way ANOVA test, followed by a Tukey's multiple analysis. *$p \leq 0.05$. (B) Average number of small eIF2Bα foci per cell in U373-MG cells with eIF2Bα-ε localised foci in untreated cells and following siRNA negative control transfection for 96h, ISRIB 200 nM 1h treatment, siRNA mediated silencing of *EIF2B1* transfection for 96h and siRNA mediated silencing of *EIF2B1* transfection for 96h coupled with ISRIB 200 nM 1h treatment (UT – untreated; n=3, counts of 30 cells with localised eIF2B foci per repeat). Average number of Error bars: ± s.d. *p* Values derived from one-way ANOVA test, followed by a Tukey's multiple analysis. *$p \leq 0.05$; **$p \leq 0.01$; ***$p \leq 0.001$. (C) Average number of large eIF2Bα foci per cell in U373-MG cells with eIF2Bα-ε localised foci in untreated cells and following siRNA negative control transfection for 96h, ISRIB 200 nM 1h treatment, siRNA mediated silencing of *EIF2B1* transfection for 96h and siRNA mediated silencing of *EIF2B1* transfection for 96h coupled with ISRIB 200 nM 1h treatment (UT – untreated; n=3, counts of 30 cells with localised eIF2B foci per repeat). Average number of Error bars: ± s.d. *p* Values derived from one-way ANOVA test, followed by a Tukey's multiple analysis. *$p \leq 0.05$; **$p \leq 0.01$; ***$p \leq 0.001$; ****$p \leq 0.0001$.

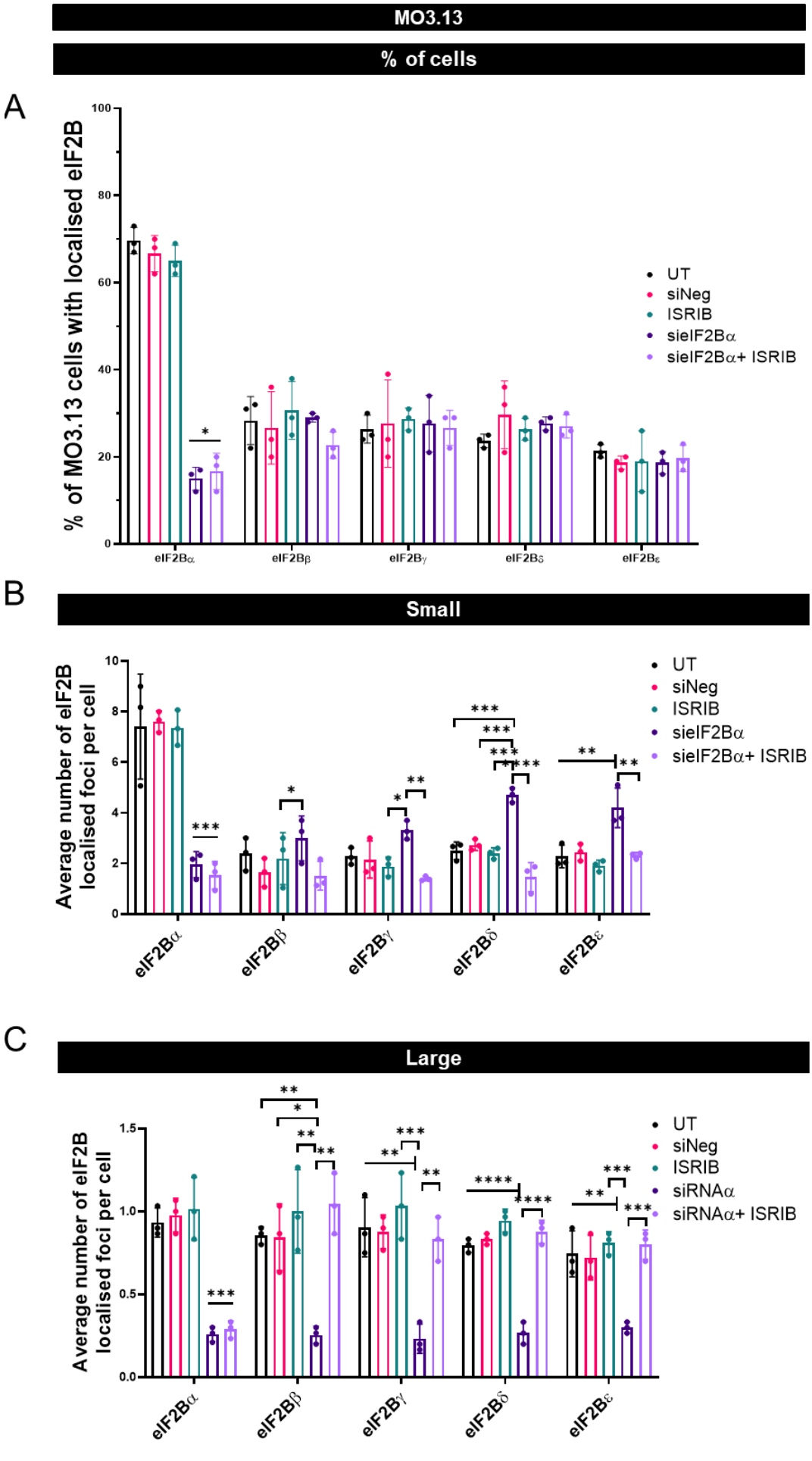
MO3.13
% of cells
A
% of MO3.13 cells with localised eIF2B
100
80
60
40
20
0
*
eIF2Bα
eIF2Bβ
eIF2Bγ
eIF2Bδ
eIF2Bε
UT
siNeg
ISRIB
sieIF2Bα
sieIF2Bα+ ISRIB
B
Small
Average number of eIF2B localised foci per cell
10
8
6
4
2
0
***
*
**
***
***
***
**
**
eIF2Bα
eIF2Bβ
eIF2Bγ
eIF2Bδ
eIF2Bε
UT
siNeg
ISRIB
sieIF2Bα
sieIF2Bα+ ISRIB
C
Large
Average number of eIF2B localised foci per cell
1.5
1.0
0.5
0.0
**
*
**
**
***
**
**
****
****
**
***
***
eIF2Bα
eIF2Bβ
eIF2Bγ
eIF2Bδ
eIF2Bε
UT
siNeg
ISRIB
siRNAα
siRNAα+ ISRIB

Figure 5.11. siRNA mediated silencing of *EIF2B1* leads to an increase of eIF2Bβ-ε foci and decrease of large eIF2Bβ-ε foci, and ISRIB treatment rescue large eIF2B foci formation in MO3.13 cells.

(A) Mean percentages of MO3.13 cells with eIF2Bα-ε localised foci, in untreated cells and following siRNA negative control transfection for 96h, ISRIB 200 nM 1h treatment, siRNA mediated silencing of *EIF2B1* transfection for 96h and siRNA mediated silencing of *EIF2B1* transfection for 96h coupled with ISRIB 200 nM 1h treatment (UT – untreated; n=3 counts of 100 cells per repeat) presented as mean ± SD. *p* Values derived from one-way ANOVA test, followed by a Tukey's multiple analysis. *$p \leq 0.05$. (B) Average number of small eIF2Bα foci per cell in MO3.13 cells with eIF2Bα-ε localised foci in untreated cells and following siRNA negative control transfection for 96h, ISRIB 200 nM 1h treatment, siRNA mediated silencing of *EIF2B1* transfection for 96h and siRNA mediated silencing of *EIF2B1* transfection for 96h coupled with ISRIB 200 nM 1h treatment (UT – untreated; n=3, counts of 30 cells with localised eIF2B foci per repeat). Average number of Error bars: ± s.d. *p* Values derived from one-way ANOVA test, followed by a Tukey's multiple analysis. *$p \leq 0.05$; **$p \leq 0.01$; ***$p \leq 0.001$; ****$p \leq 0.0001$. (C) Average number of large eIF2Bα foci per cell in MO3.13 cells with eIF2Bα-ε localised foci in untreated cells and following siRNA negative control transfection for 96h, ISRIB 200 nM 1h treatment, siRNA mediated silencing of *EIF2B1* transfection for 96h and siRNA mediated silencing of *EIF2B1* transfection for 96h coupled with ISRIB 200 nM 1h treatment (UT – untreated; n=3, counts of 30 cells with localised eIF2B foci per repeat). Average number of Error bars: ± s.d. *p* Values derived from one-way ANOVA test, followed by a Tukey's multiple analysis. *$p \leq 0.05$; **$p \leq 0.01$; ***$p \leq 0.001$; ****$p \leq 0.0001$.

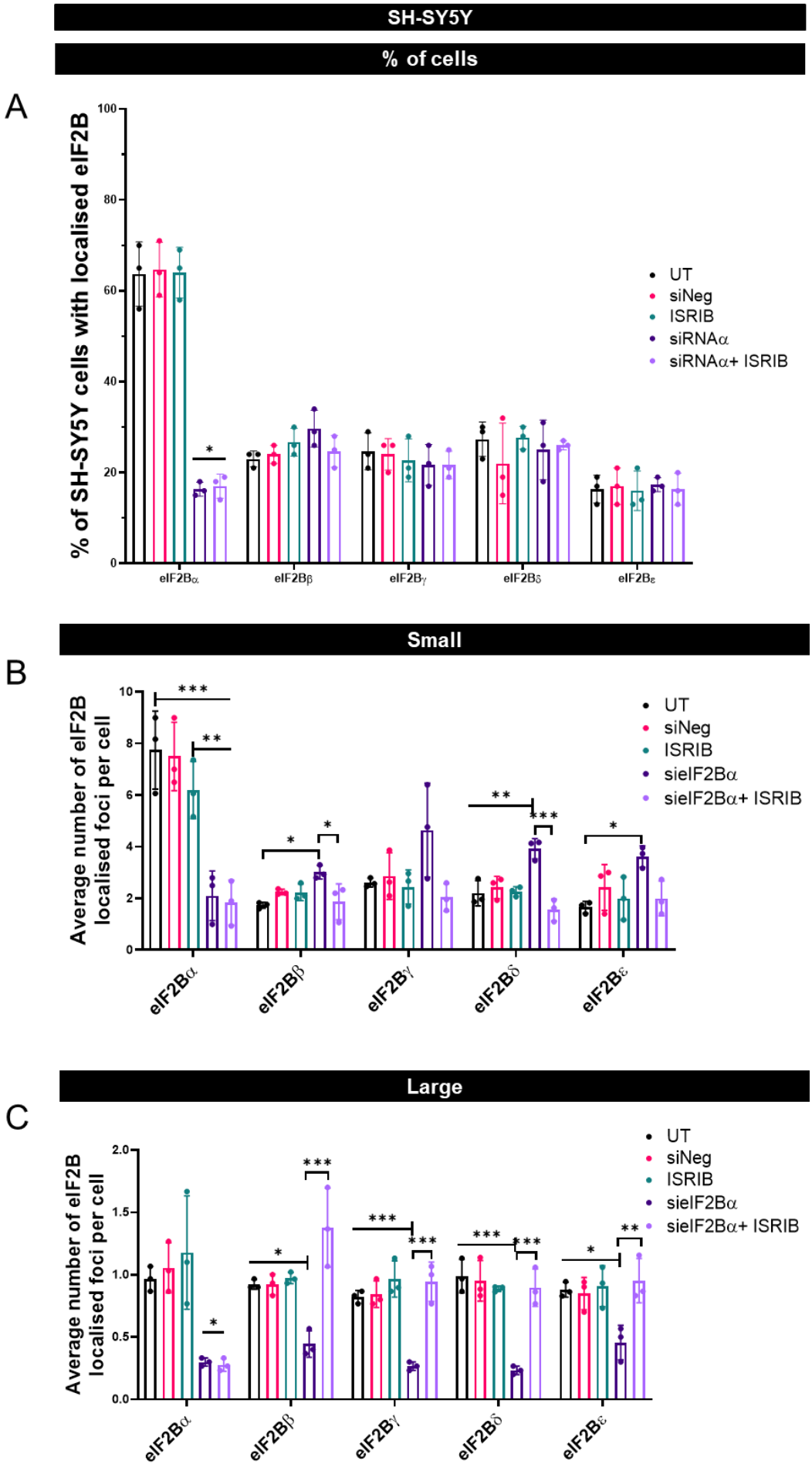
SH-SY5Y
% of cells
A
% of SH-SY5Y cells with localised eIF2B
100
80
60
40
20
0
*
eIF2Bα
eIF2Bβ
eIF2Bγ
eIF2Bδ
eIF2Bε
UT
siNeg
ISRIB
siRNAα
siRNAα+ ISRIB
Small
B
Average number of eIF2B localised foci per cell
10
8
6
4
2
0
***
**
*
**
***
*
eIF2Bα
eIF2Bβ
eIF2Bγ
eIF2Bδ
eIF2Bε
UT
siNeg
ISRIB
sieIF2Bα
sieIF2Bα+ ISRIB
Large
C
Average number of eIF2B localised foci per cell
2.0
1.5
1.0
0.5
0.0
*
***
*
***
***
***
***
*
**
eIF2Bα
eIF2Bβ
eIF2Bγ
eIF2Bδ
eIF2Bε
UT
siNeg
ISRIB
sieIF2Bα
sieIF2Bα+ ISRIB

Figure 5.12. siRNA mediated silencing of *EIF2B1* leads to an increase of eIF2Bβ-ε foci and decrease of large eIF2Bβ-ε foci, and ISRIB treatment rescue large eIF2B foci formation in SH-SY5Y cells.

(A) Mean percentages of SH-SY5Y cells with eIF2Bα-ε localised foci, in untreated cells and following siRNA negative control transfection for 96h, ISRIB 200 nM 1h treatment, siRNA mediated silencing of *EIF2B1* transfection for 96h and siRNA mediated silencing of *EIF2B1* transfection for 96h coupled with ISRIB 200 nM 1h treatment (UT – untreated; n=3 counts of 100 cells per repeat) presented as mean ± SD. *p* Values derived from one-way ANOVA test, followed by a Tukey's multiple analysis. *$p \leq 0.05$. (B) Average number of small eIF2Bα foci per cell in SH-SY5Y cells with eIF2Bα-ε localised foci in untreated cells and following siRNA negative control transfection for 96h, ISRIB 200 nM 1h treatment, siRNA mediated silencing of *EIF2B1* transfection for 96h and siRNA mediated silencing of *EIF2B1* transfection for 96h coupled with ISRIB 200 nM 1h treatment (UT – untreated; n=3, counts of 30 cells with localised eIF2B foci per repeat). Average number of Error bars: ± s.d. *p* Values derived from one-way ANOVA test, followed by a Tukey's multiple analysis. *$p \leq 0.05$; **$p \leq 0.01$; ***$p \leq 0.001$. (C) Average number of large eIF2Bα foci per cell in SH-SY5Y cells with eIF2Bα-ε localised foci in untreated cells and following siRNA negative control transfection for 96h, ISRIB 200 nM 1h treatment, siRNA mediated silencing of *EIF2B1* transfection for 96h and siRNA mediated silencing of *EIF2B1* transfection for 96h coupled with ISRIB 200 nM 1h treatment (UT – untreated; n=3, counts of 30 cells with localised eIF2B foci per repeat). Average number of Error bars: ± s.d. *p* Values derived from one-way ANOVA test, followed by a Tukey's multiple analysis. *$p \leq 0.05$; **$p \leq 0.01$; ***$p \leq 0.001$.

While the transfection rates of the cells analysed were elevated, the detection of eIF2Bα-ε localisation following eIF2Bα knockdown was repeated in cells with labeled sieIF2Bα-Cy^{TM}3 to ensure that the cells that were analysed have decreased eIF2Bα expression (**Figure 5.13**). As such, only cells with sieIF2Bα-Cy^{TM}3 incorporated were analysed. As seen previously in the non-labelled sieIF2Bα transfected cells, no apparent modulation of percentage of cells with eIF2Bβ-ε was present following transfection or in control conditions in a population of 100 U373-MG, MO3.13 and SH-SY5Y cells (**Figure 5.14A, Figure 5.15A and Figure 5.16A**).

While biological repeats would allow to categorically ascertain if identical changes to small and large eIF2Bβ-ε foci were observed in cells with labelled sieIF2Bα, similar values were detected in all three cell lines analysed. Additionally, ISRIB treatment following transfection showed to restore the formation of large eIF2Bβ-ε foci in these cells (**Figure 5.14B, Figure 5.14C, Figure 5.15B, Figure 5.16B, Figure 5.15C and Figure 5.16C**).

Transfection of untagged siRNA may lead to the analysis of cells which have not been transfected, thus not completely reliably studying the impact of reduced eIF2Bα on the formation of eIF2B foci. However, transfection rate percentages and analysis of cells transfected with labeled siRNA targeting the *EIF2B1* gene, displayed a majority of cells being transfected with siRNA. These cells also exhibited comparable results of decreased expression and localisation of eIF2Bα, as seen in untagged siRNA^{EIF2B1}. Therefore, the outcomes obtained in **figures 5.10, 5.11 and 5.12** appeared to be due to changes in eIF2Bα expression/localisation. Additionally, the restoration of large eIF2Bβ-ε foci following ISRIB treatment in eIF2Bα depleted cells was also observed in cells transfected with labelled siRNA^{EIF2B1}. We could then conclude, that these large eIF2Bβ-ε localised foci are present in cells with decreased eIF2Bα expression and formed through ISRIB action.

Thus, from our investigations, two pivotal conclusions emerge, each shedding light on distinct facets of the role of eIF2Bα in the assembly of eIF2B foci. Firstly, reduction in the expression of eIF2Bα leads to a loss in its endogenous localisation. Secondly, our findings reveal an essential role of eIF2Bα in the formation of eIF2B foci in mammalian cells. While expression of eIF2Bα does not appear to be essential for the assembly of eIF2Bβ-ε foci, it is notably pivotal in the formation of large eIF2B foci.

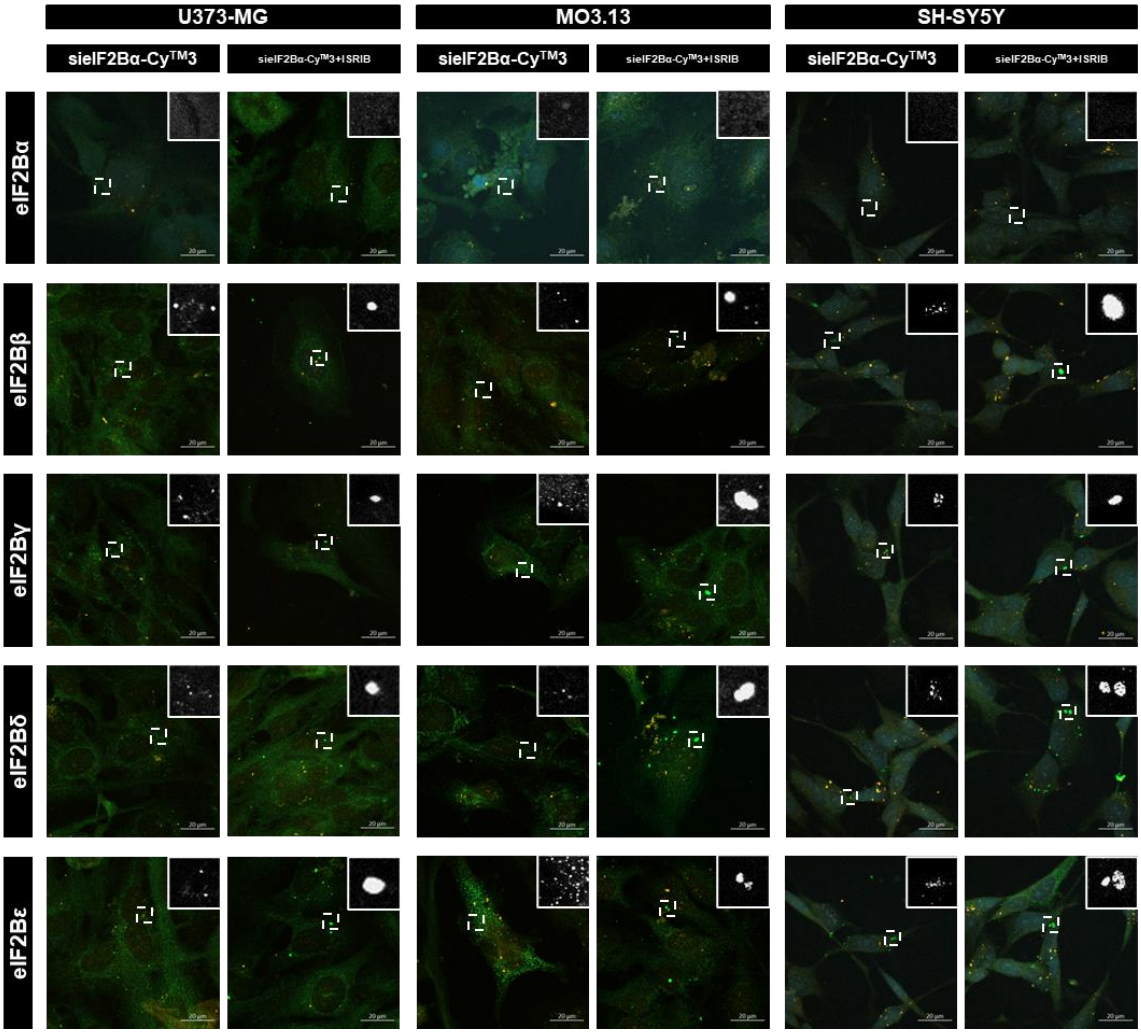

Figure 5.13. Glial and neuronal cells with labelled Cy3 siRNA mediated silencing of *EIF2B1* displays altered localisation of eIF2Bα-ε with/without ISRIB treatment.

Representative images of Cy3 and endogenous eIF2Bα-ε localising to cytoplasmic foci following Cy3 tagged siRNA mediated silencing of *EIF2B1* for 96h and Cy3 tagged siRNA mediated silencing of *EIF2B1* for 96h coupled with ISRIB 200nM 1h treatment. U373-MG and SH-SY5Y cells were fixed in methanol, MO3.13 cells were fixed in 4 % PFA and subjected to ICC with anti-eIF2Bα-ε primary antibodies and visualized using appropriate secondary antibodies conjugated to Alexa Fluor 488. Scale bar: 20 μm. Enlarged areas represent AlexaFluor 488 staining.

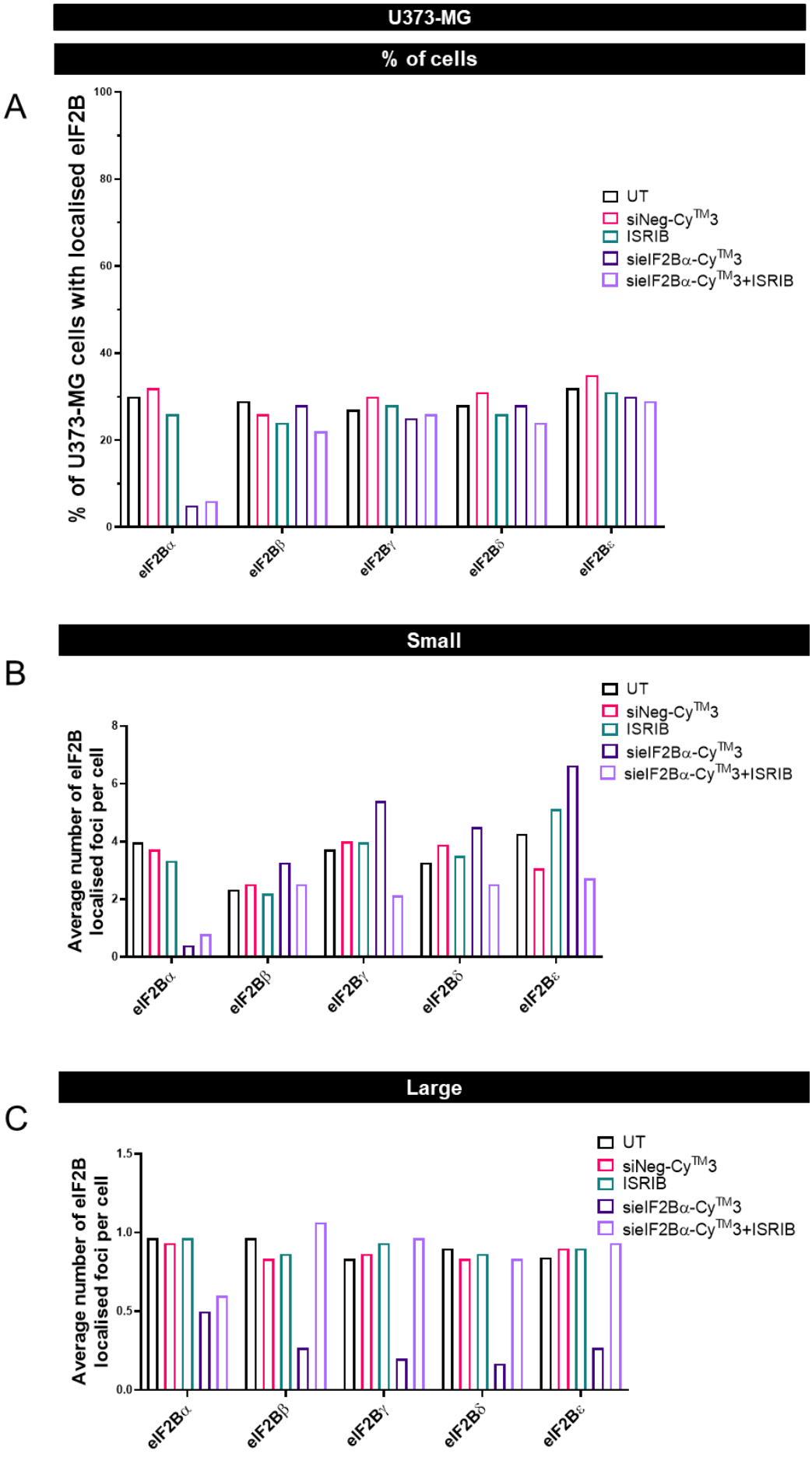
U373-MG
% of cells
A
% of U373-MG cells with localised eIF2B
100
80
60
40
20
0
UT
siNeg-Cy™3
ISRIB
sieIF2Bα-Cy™3
sieIF2Bα-Cy™3+ISRIB
eIF2Bα
eIF2Bβ
eIF2Bγ
eIF2Bδ
eIF2Bε
Small
B
Average number of eIF2B localised foci per cell
8
6
4
2
0
UT
siNeg-Cy™3
ISRIB
sieIF2Bα-Cy™3
sieIF2Bα-Cy™3+ISRIB
eIF2Bα
eIF2Bβ
eIF2Bγ
eIF2Bδ
eIF2Bε
Large
C
Average number of eIF2B localised foci per cell
1.5
1.0
0.5
0.0
UT
siNeg-Cy™3
ISRIB
sieIF2Bα-Cy™3
sieIF2Bα-Cy™3+ISRIB
eIF2Bα
eIF2Bβ
eIF2Bγ
eIF2Bδ
eIF2Bε

Figure 5.14. Cy3 labelled siRNA mediated silencing of *EIF2B1* leads to an increase of eIF2Bβ-ε foci and decrease of large eIF2Bβ-ε foci, and ISRIB treatment rescue large eIF2B foci formation in U373-MG cells.

(A) Mean percentages of U373-MG cells with eIF2Bα-ε localised foci and Cy3 puncti, in untreated cells and following Cy3 labelled siRNA negative control transfection for 96h, ISRIB 200 nM 1h treatment, Cy3 labelled siRNA mediated silencing of *EIF2B1* transfection for 96h and Cy3 labelled siRNA mediated silencing of *EIF2B1* transfection for 96h coupled with ISRIB 200 nM 1h treatment (UT – untreated; n=1 counts of 100 cells) presented as mean. (B) Average number of small eIF2Bα foci per cell in U373-MG cells with eIF2Bα-ε localised in untreated cells and following Cy3 labelled siRNA negative control transfection for 96h, ISRIB 200 nM 1h treatment, Cy3 labelled siRNA mediated silencing of *EIF2B1* transfection for 96h and Cy3 labelled siRNA mediated silencing of *EIF2B1* transfection for 96h coupled with ISRIB 200 nM 1h treatment (UT – untreated; n=1, counts of 30 cells with localised eIF2B foci). (C) Average number of large eIF2Bα foci per cell in U373-MG cells with eIF2Bα-ε localised foci in untreated cells and following Cy3 labelled siRNA negative control transfection for 96h, ISRIB 200 nM 1h treatment, Cy3 labelled siRNA mediated silencing of *EIF2B1* transfection for 96h and Cy3 labelled siRNA mediated silencing of *EIF2B1* transfection for 96h coupled with ISRIB 200 nM 1h treatment (UT – untreated; n=1, counts of 30 cells with localised eIF2B foci).

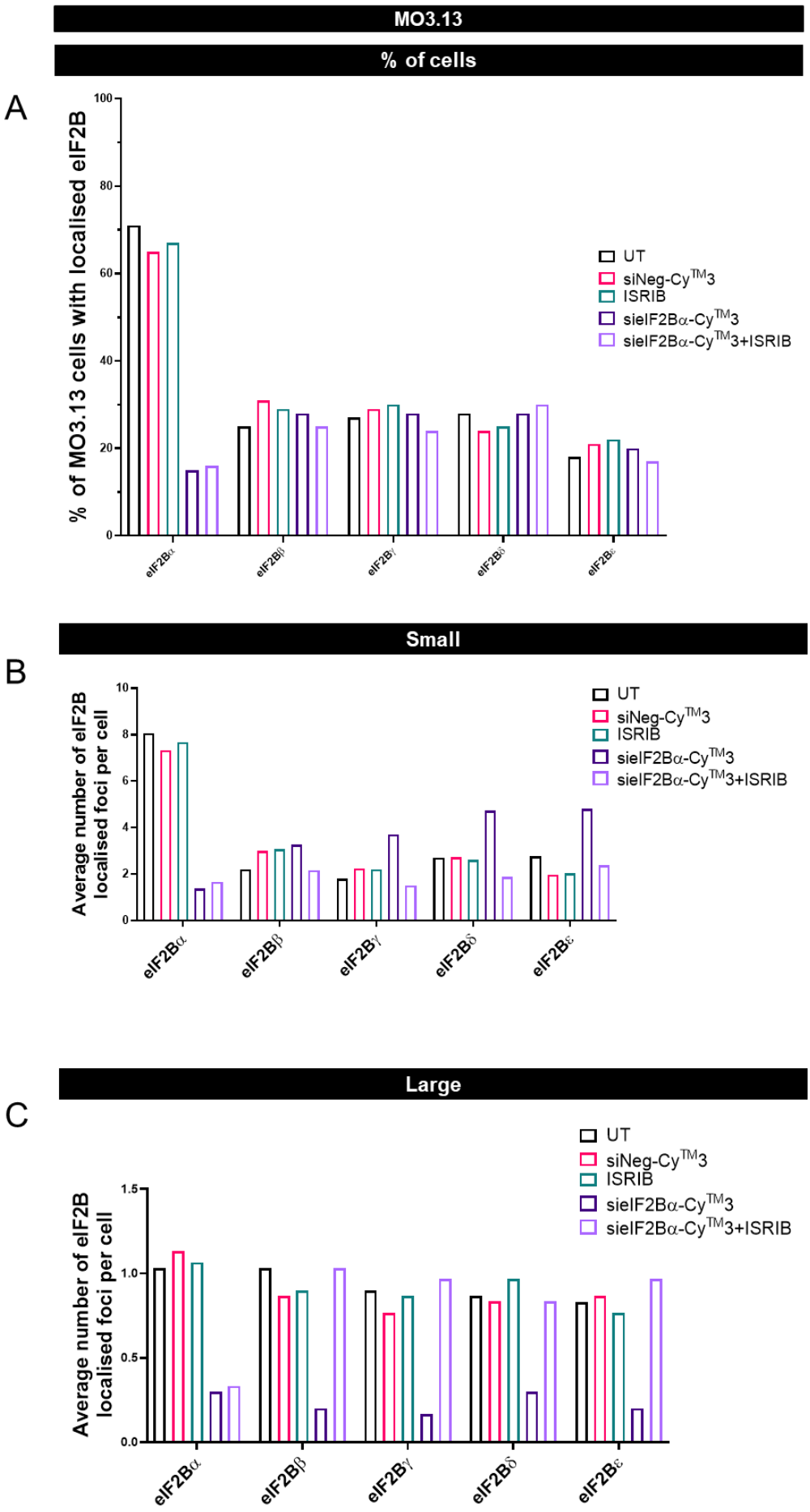
MO3.13
% of cells
A
% of MO3.13 cells with localised eIF2B
100
80
60
40
20
0
UT
siNeg-Cy™3
ISRIB
sieIF2Bα-Cy™3
sieIF2Bα-Cy™3+ISRIB
eIF2Bα
eIF2Bβ
eIF2Bγ
eIF2Bδ
eIF2Bε
Small
B
Average number of eIF2B localised foci per cell
10
8
6
4
2
0
UT
siNeg-Cy™3
ISRIB
sieIF2Bα-Cy™3
sieIF2Bα-Cy™3+ISRIB
eIF2Bα
eIF2Bβ
eIF2Bγ
eIF2Bδ
eIF2Bε
Large
C
Average number of eIF2B localised foci per cell
1.5
1.0
0.5
0.0
UT
siNeg-Cy™3
ISRIB
sieIF2Bα-Cy™3
sieIF2Bα-Cy™3+ISRIB
eIF2Bα
eIF2Bβ
eIF2Bγ
eIF2Bδ
eIF2Bε

Figure 5.15. Cy3 labelled siRNA mediated silencing of *EIF2B1* leads to an increase of eIF2Bβ-ε foci and decrease of large eIF2Bβ-ε foci, and ISRIB treatment rescue large eIF2B foci formation in MO3.13 cells.

(A) Mean percentages of MO3.13 cells with eIF2Bα-ε localised foci and Cy3 puncti, in untreated cells and following Cy3 labelled siRNA negative control transfection for 96h, ISRIB 200 nM 1h treatment, Cy3 labelled siRNA mediated silencing of *EIF2B1* transfection for 96h and Cy3 labelled siRNA mediated silencing of *EIF2B1* transfection for 96h coupled with ISRIB 200 nM 1h treatment (UT – untreated; n=1 counts of 100 cells) presented as mean. (B) Average number of small eIF2Bα foci per cell in MO3.13 cells with eIF2Bα-ε localised in untreated cells and following Cy3 labelled siRNA negative control transfection for 96h, ISRIB 200 nM 1h treatment, Cy3 labelled siRNA mediated silencing of *EIF2B1* transfection for 96h and Cy3 labelled siRNA mediated silencing of *EIF2B1* transfection for 96h coupled with ISRIB 200 nM 1h treatment (UT – untreated; n=1, counts of 30 cells with localised eIF2B foci). (C) Average number of large eIF2Bα foci per cell in MO3.13 cells with eIF2Bα-ε localised foci in untreated cells and following Cy3 labelled siRNA negative control transfection for 96h, ISRIB 200 nM 1h treatment, Cy3 labelled siRNA mediated silencing of *EIF2B1* transfection for 96h and Cy3 labelled siRNA mediated silencing of *EIF2B1* transfection for 96h coupled with ISRIB 200 nM 1h treatment (UT – untreated; n=1, counts of 30 cells with localised eIF2B foci).

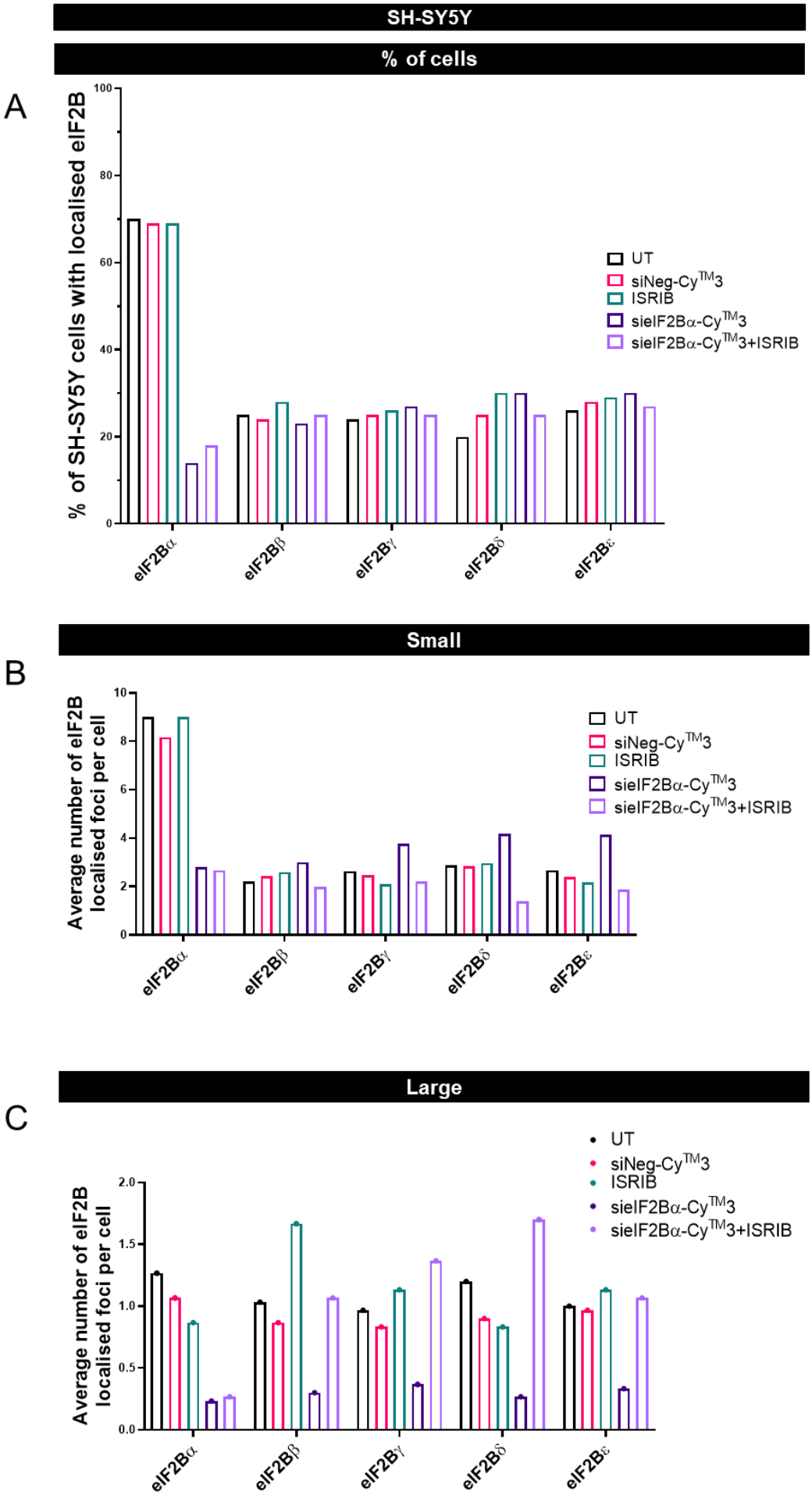
SH-SY5Y
% of cells
A
% of SH-SY5Y cells with localised eIF2B
100
80
60
40
20
0
UT
siNeg-Cy™3
ISRIB
sieIF2Bα-Cy™3
sieIF2Bα-Cy™3+ISRIB
eIF2Bα
eIF2Bβ
eIF2Bγ
eIF2Bδ
eIF2Bε
Small
B
Average number of eIF2B localised foci per cell
10
8
6
4
2
0
UT
siNeg-Cy™3
ISRIB
sieIF2Bα-Cy™3
sieIF2Bα-Cy™3+ISRIB
eIF2Bα
eIF2Bβ
eIF2Bγ
eIF2Bδ
eIF2Bε
Large
C
Average number of eIF2B localised foci per cell
2.0
1.5
1.0
0.5
0.0
UT
siNeg-Cy™3
ISRIB
sieIF2Bα-Cy™3
sieIF2Bα-Cy™3+ISRIB
eIF2Bα
eIF2Bβ
eIF2Bγ
eIF2Bδ
eIF2Bε

Figure 5.16. Cy3 labelled siRNA mediated silencing of *EIF2B1* leads to an increase of eIF2Bβ-ε foci and decrease of large eIF2Bβ-ε foci, and ISRIB treatment rescue large eIF2B foci formation in SH-SY5Y cells.

(A) Mean percentages of SH-SY5Y cells with eIF2Bα-ε localised foci and Cy3 puncti, in untreated cells and following Cy3 labelled siRNA negative control transfection for 96h, ISRIB 200 nM 1h treatment, Cy3 labelled siRNA mediated silencing of *EIF2B1* transfection for 96h and Cy3 labelled siRNA mediated silencing of *EIF2B1* transfection for 96h coupled with ISRIB 200 nM 1h treatment (UT – untreated; n=1 counts of 100 cells) presented as mean. (B) Average number of small eIF2Bα foci per cell in SH-SY5Y cells with eIF2Bα-ε localised in untreated cells and following Cy3 labelled siRNA negative control transfection for 96h, ISRIB 200 nM 1h treatment, Cy3 labelled siRNA mediated silencing of *EIF2B1* transfection for 96h and Cy3 labelled siRNA mediated silencing of *EIF2B1* transfection for 96h coupled with ISRIB 200 nM 1h treatment (UT – untreated; n=1, counts of 30 cells with localised eIF2B foci). (C) Average number of large eIF2Bα foci per cell in SH-SY5Y cells with eIF2Bα-ε localised foci in untreated cells and following Cy3 labelled siRNA negative control transfection for 96h, ISRIB 200 nM 1h treatment, Cy3 labelled siRNA mediated silencing of *EIF2B1* transfection for 96h and Cy3 labelled siRNA mediated silencing of *EIF2B1* transfection for 96h coupled with ISRIB 200 nM 1h treatment (UT – untreated; n=1, counts of 30 cells with localised eIF2B foci).

5.2.3. siRNA mediated silencing of *EIF2B1* leads to the activation of the ISR independently of eIF2α phosphorylation, which can be attenuated by ISRIB.

Previous studies have shown that eIF2B(βδγε) and eIF2B(γε) sub-complexes display a progressive reduction in GEF activity compared to the full holocomplex. Specifically, the eIF2B(βδγε) sub-complex illustrates an approximate 50 % reduction in GEF activity, while the eIF2B(γε) sub-complex exhibits a GEF activity of approximately 20 % (Liu *et al*., 2011; Wortham *et al*., 2014). Our working hypothesis was that the absence of eIF2Bα impedes the formation of decamer complexes, resulting in the inhibition of the formation of large eIF2B foci with complete GEF activity. Consequently, although subcomplexes can still assemble, as observed in **section 5.2.2**, their expected GEF activity rate is anticipated to be lower. This interplay between subcomplexes and altered GEF activity would alter the levels of TC formation, ultimately impacting the overall rate of protein production within a cell.

In light of these considerations, puromycin incorporation assays were conducted subsequent to siRNA-mediated silencing of *EIF2B1*, to ascertain whether the absence of eIF2Bα leads to reduced levels of global protein synthesis. In addition, cells with reduced eIF2Bα expression were treated with ISRIB for 1 hour, to determine the potential translational recovery in the absence of eIF2Bα through this drug.

The reduction in eIF2Bα levels exhibited a consistent decrease in global protein synthesis across all cell lines. Under steady state conditions, ISRIB treatment alone failed to induce any discernible increase in protein translation. When combined with the absence of eIF2Bα expression, ISRIB fully restored translation levels, to the same level as the untreated state (U373: sieIF2Bα – ~3.1-fold change, sieIF2Bα+ISRIB – ~0.9-fold change; MO3.13: sieIF2Bα – ~1.9-fold change, sieIF2Bα+ISRIB – ~0.9 fold change; SH-SY5Y: sieIF2Bα – ~2.4- fold change, sieIF2Bα+ISRIB – ~0.8 fold change) (**Figure 5.17**).

Given the decrease of global translation in cells depleted of eIF2Bα we aimed to detect changes in expression levels of ISR markers, including p-eIF2α and total eIF2α, CHOP, and GADD34, through western blot analysis. Additionally, ATF4 levels were studied through an ELISA.

We found that decreased expression levels of eIF2Bα did not induce the phosphorylation of eIF2α (**Figure 5.17**), thereby failing to activate any p-eIF2α kinase, as expected. However, downstream ISR markers were present (GADD34, CHOP – **Figure 5.18A**, and ATF4- **Figure 5.18B**), presumably stemming from the reduced protein synthesis under siRNA mediated *EIF2B1* silencing. Furthermore, we found a subtle yet discernible decrease of these markers, upon coupling the *EIF2B1* silencing with ISRIB treatment (**Figure 5.18**).

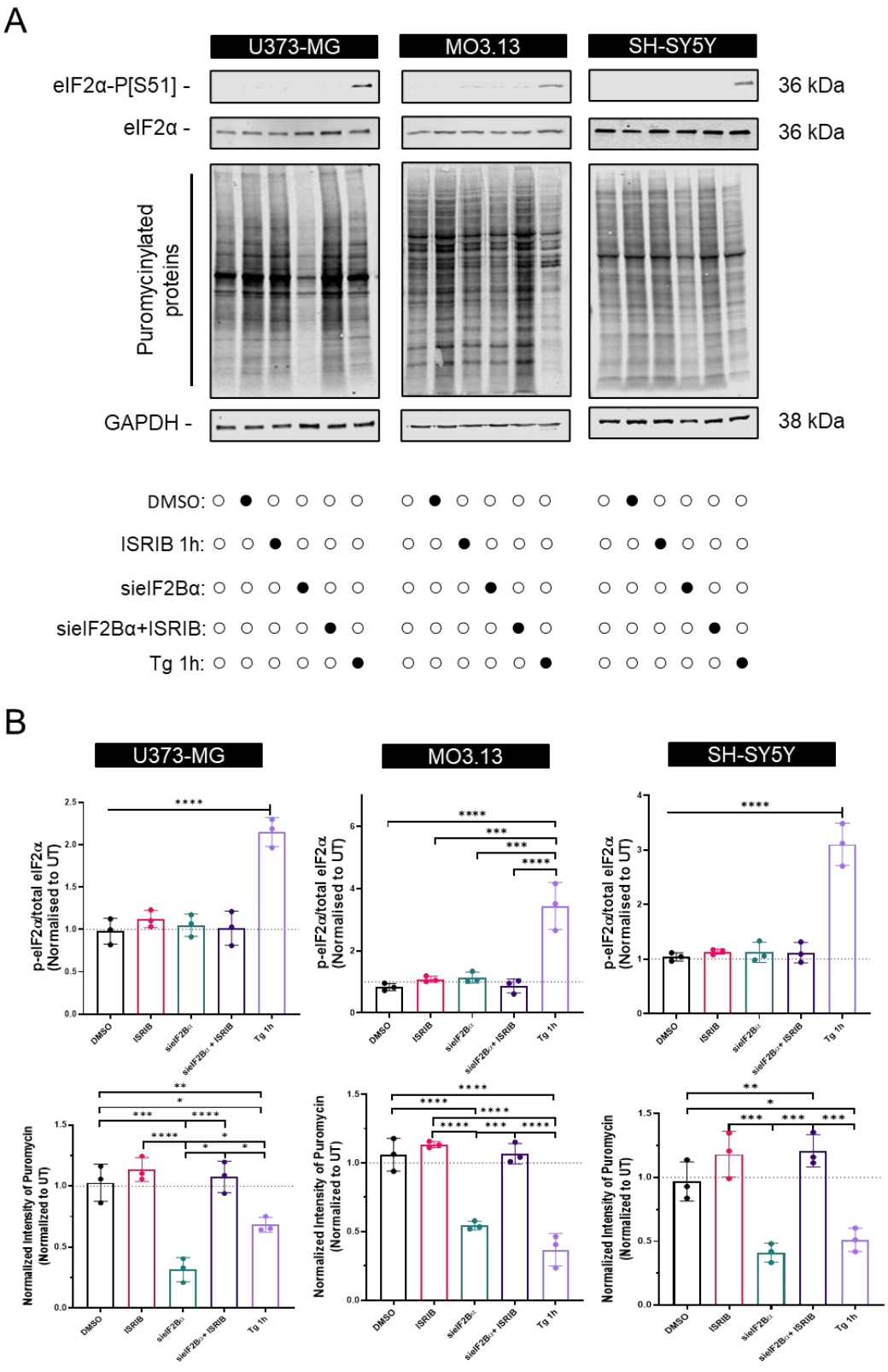

Figure 5.17. siRNA mediated silencing of *EIF2B1* leads to a decrease in protein synthesis levels, with coupled ISRIB treatment rescuing it.

U373-MG, MO3.13 and SH-SY5Y cells were treated with DMSO for 1h, ISRIB 1h (200 nM) and Tg for 1h (1 μM), and cells were subjected to siRNA mediated silencing of *EIF2B1* with/without ISRIB 1h treatment. (A) Western blot analysis of U373-MG, MO3.13, and SH-SY5Y cells immunoblotted against p-eIF2α and total eIF2α, and puromycin incorporation levels. GAPDH

levels were used as loading control. (B) Quantification of intensity levels of p-eIF2α normalised against total levels of eIF2α and analysed using one-way ANOVA followed by a Tukey's multiple analysis. ****$p \leq 0.0001$. Data is presented as fold-change levels of p-eIF2α:total-eIF2α ratio in comparison to untreated levels. Error bars: ± s.d. (n=3). Quantification of intensity levels of puromycinylated proteins normalised against GAPDH levels and analysed using one-way ANOVA followed by a Tukey's multiple analysis. *$p \leq 0.05$, **$p \leq 0.01$, ***$p \leq 0.001$, ****$p \leq 0.0001$. Data is presented as fold-change levels of puromycin:GAPDH ratio in comparison to untreated levels. Error bars:±s.d. (n=3).

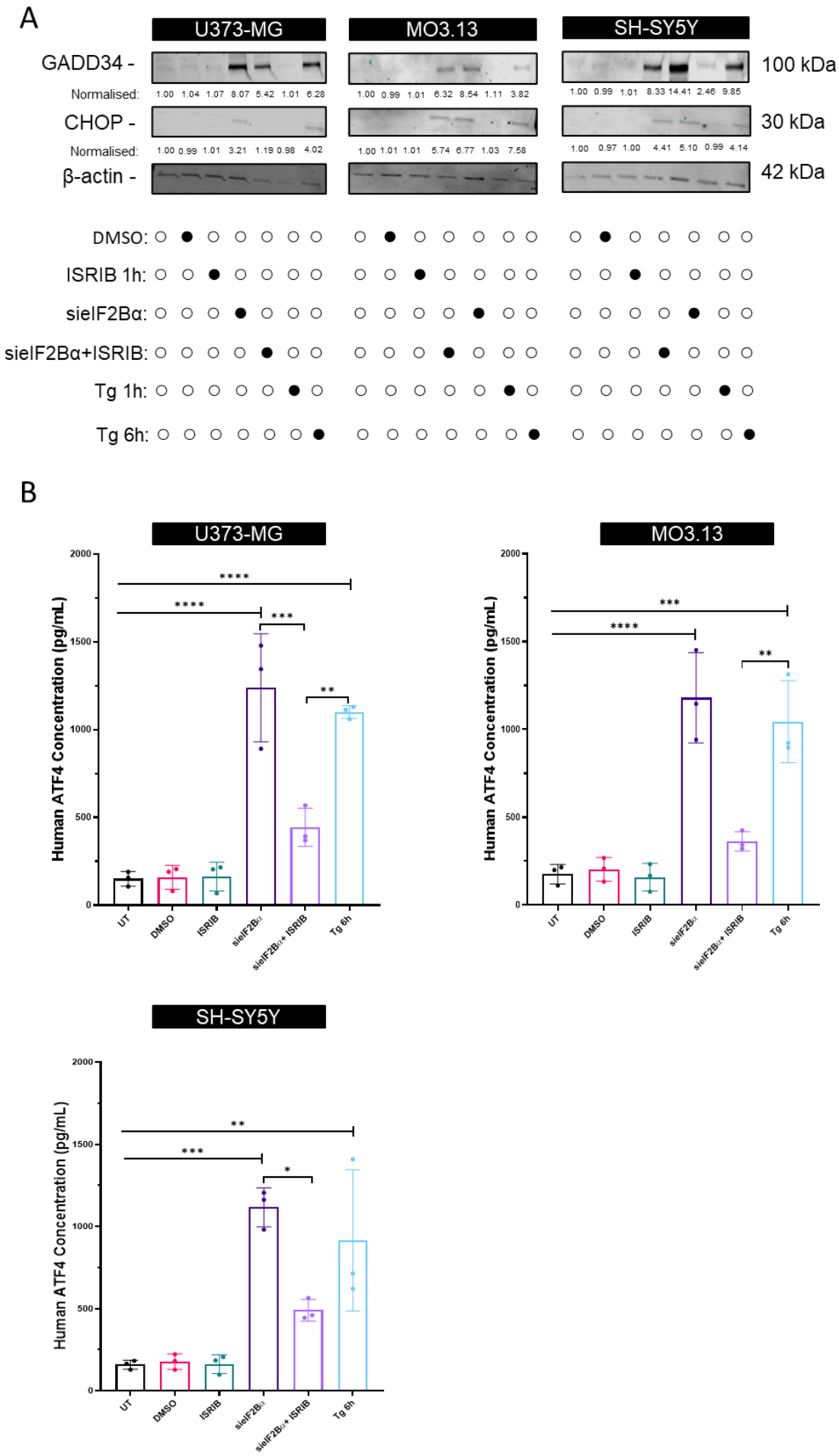
A
U373-MG
MO3.13
SH-SY5Y
GADD34 -
100 kDa
Normalised:
1.00 1.04 1.07 8.07 5.42 1.01 6.28
1.00 0.99 1.01 6.32 8.54 1.11 3.82
1.00 0.99 1.01 8.33 14.41 2.46 9.85
CHOP -
30 kDa
Normalised:
1.00 0.99 1.01 3.21 1.19 0.98 4.02
1.00 1.01 1.01 5.74 6.77 1.03 7.58
1.00 0.97 1.00 4.41 5.10 0.99 4.14
β-actin -
42 kDa
DMSO:
ISRIB 1h:
sieIF2Bα:
sieIF2Bα+ISRIB:
Tg 1h:
Tg 6h:
B
U373-MG
MO3.13
SH-SY5Y
Human ATF4 Concentration (pg/mL)
2000
1500
1000
500
0
UT
DMSO
ISRIB
sieIF2Bα
sieIF2Bα+ ISRIB
Tg 6h

Figure 5.18. siRNA mediated silencing of *EIF2B1* leads to ISR activation, with ISRIB attenuating it.

U373-MG, MO3.13 and SH-SY5Y cells were treated with DMSO for 1h, ISRIB 1h (200 nM) and Tg for 6h (300 nM), and cells were subjected to siRNA mediated silencing of *EIF2B1* with/without ISRIB 1h treatment. (A) Western blot analysis of U373-MG, MO3.13, and SH-SY5Y cells immunoblotted against GADD34 and CHOP. β-actin levels were used as loading control. Fold-enrichment of GADD34:β-actin and CHOP:β-actin ratios in comparison to untreated levels are labelled below respective blots. (B) ATF4 levels were measured by ELISA (n=3). Error bars: ± s.d. and analysed using one-way ANOVA followed by a Tukey's multiple analysis. *$p \leq 0.05$, **$p \leq 0.01$, ***$p \leq 0.001$, ****$p \leq 0.0001$.

5.2.4. siRNA mediated silencing of *EIF2B1* leads to the formation of SGs

The process of assembling the TC is governed by a rate-limiting step, the recycling of the eIF2α-GDP to eIF2α-GTP by the GEF eIF2B (Gebauer & Hentze, 2004). It is widely recognized that the phosphorylation of eIF2α leads to the inhibition of formation of the TC and therefore instigates the formation of SGs. Contrary to the traditional focus on eIF2α phosphorylation status alone, further studies have unveiled that the pivotal factor governing SG formation is the levels of the TC, rather than the phosphorylation status of eIF2α per se (Emara *et al*., 2012; Mokas *et al*., 2009; Panas *et al*., 2016). In light of our existing hypothesis, which posits that the absence of eIF2Bα precipitates a decline in eIF2B activity, leading to reduced global protein synthesis without the induction of p-eIF2α (**section 5.3.3)**, we set forth to investigate whether the decreased expression of eIF2Bα also results in the formation of SGs.

Following siRNA mediated silencing of *EIF2B1*, there was a striking increase in the percentage of cells exhibiting SGs, with ISRIB 1 hour treatment in cells depleted of eIF2Bα reducing SG formation (U373: sieIF2Bα – 15.33 % ± 5.51, sieIF2Bα+ISRIB – 5.00 % ± 2.00; MO3.13: sieIF2Bα – 18.00 % ± 5.57, sieIF2Bα+ISRIB – 5.67 % ± 4.04; SH-SY5Y: sieIF2Bα – 14.67 % ± 2.52, sieIF2Bα+ISRIB – 5.00 % ± 2.00 – 100 cells per repeat) (**Figure 5.19**). We propose that the assembly of these SGs results from decreased levels of eIF2B activity. Treatment with ISRIB stabilizes what we surmise to be active eIF2B$(\beta\gamma\delta\varepsilon)_2$ structures and therefore increases eIF2B activity, thus reducing SG formation.

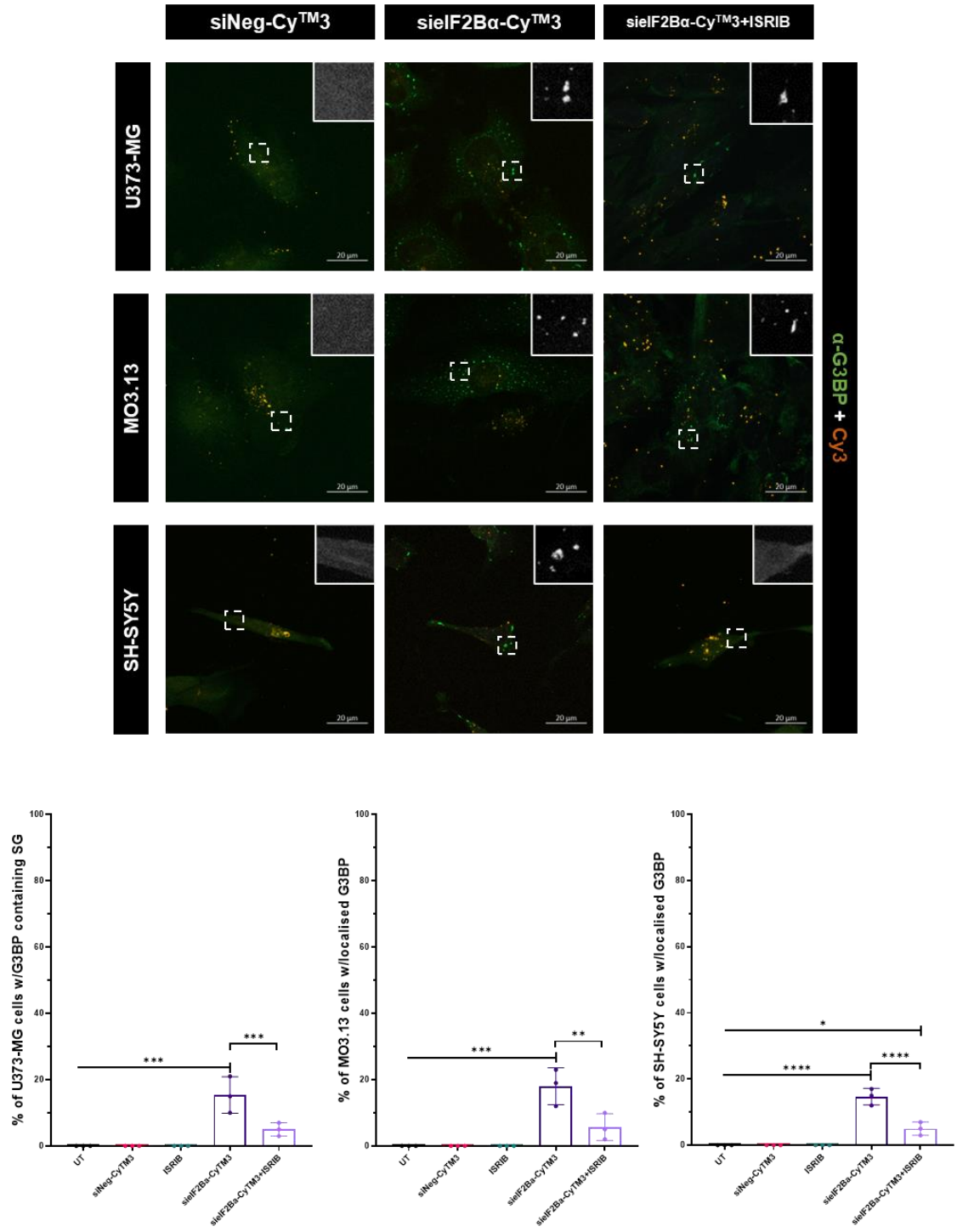

Figure 5.19. siRNA mediated silencing of *EIF2B1* leads to the formation of SGs.

Representative images of cells transfected with Cy3 labelled siRNA negative control, Cy3 labelled siRNA targeting *EIF2B1*, and Cy3 labelled siRNA targeting *EIF2B1* coupled with ISRIB 1h (200 nM) treatment. U373-MG and SH-SY5Y cells were fixed in methanol, MO3.13 cells were fixed in 4%PFA and subjected to ICC with anti-G3BP primary antibody and visualized using appropriate secondary antibodies conjugated to Alexa Fluor 488. Scale bar: 20 µm. Enlarged areas represent AlexaFluor 488 staining. Mean percentages of U373-MG, MO3.13 and SH-SY5Y cells with G3BP-containing SGs. Error bars: ±s.d. Data was analysed using one-way ANOVA followed by a Tukey's multiple analysis. *$p \leq 0.05$, **$p \leq 0.01$, ***$p \leq 0.001$, ****$p \leq 0.0001$.

5.2.5. GEF activity is impacted by siRNA mediated silencing of *EIF2B1*

Following the observation that reduction of eIF2Bα expression induces downstream ISR markers (**section 5.2.3.**) and modulation of the formation of eIF2B foci (**section 5.2.2.**), we next investigated whether the level of GEF activity was altered when eIF2Bα was not present.

Campbell and Ashe (2007) established a protocol of FRAP to monitor the movement of eIF2 within eIF2B bodies. This technique capitalizes on the irreversibility of photobleaching, a process that entails the photon-induced loss of fluorescence within a specific region of interest. Following photobleaching, recovery of fluorescence in the region of interest is only possible through the movement of neighboring fluorophore-bound constructs. The movement of eIF2 through eIF2B bodies in live cells has been shown to correlate with eIF2B GEF activity (Campbell & Ashe, 2007; Hanson *et al*., 2023; Hodgson *et al*., 2019).

U373-MG cells were transiently transfected with eIF2α-GFP/eIF2Bε-RFP. Live cell imaging confirmed the co-localisation of eIF2α-GFP foci and eIF2Bε-RFP foci. FRAP analysis was performed by quantifying the rate of recovery of fluorescence intensity of an individual region of interest containing a large eIF2α-GFP foci, *i.e.*, ≥ 1μm^2 (**Figure 5.20A**).

Preliminary results obtained showed that, as seen previously (Hanson *et al*., 2023; Hodgson *et al*., 2019), in U373-MG cells, following Tg stress for 1 hour the activity of eIF2B large bodies was slightly affected with slower T1/2 (measured by its half-time) (Tg 1h: 0.88 s) and by the decreased eIF2α-GFP recovery (28.35 %). Vehicle and ISRIB treated cells did not impact the T1/2 (Vehicle: 0.70 s; ISRIB: 0.56 s) or the percentage of eIF2α-GFP recovery (vehicle: 50.03 % s; ISRIB: 50.1 %). However, Tg 1 hour treatment coupled with ISRIB treatment rescued recovery rate to the level of UT cells (Tg+ISRIB: T1/2 0.63 s; recovery 48.84 %) (**Figure 5.20B**). Collectively, these results established that acute ER stress decreases the movement of eIF2 within large eIF2B bodies in astrocytic cells. ISRIB, however reverses this effect, as seen previously (Hanson *et al*., 2023; Hodgson *et al*., 2019).

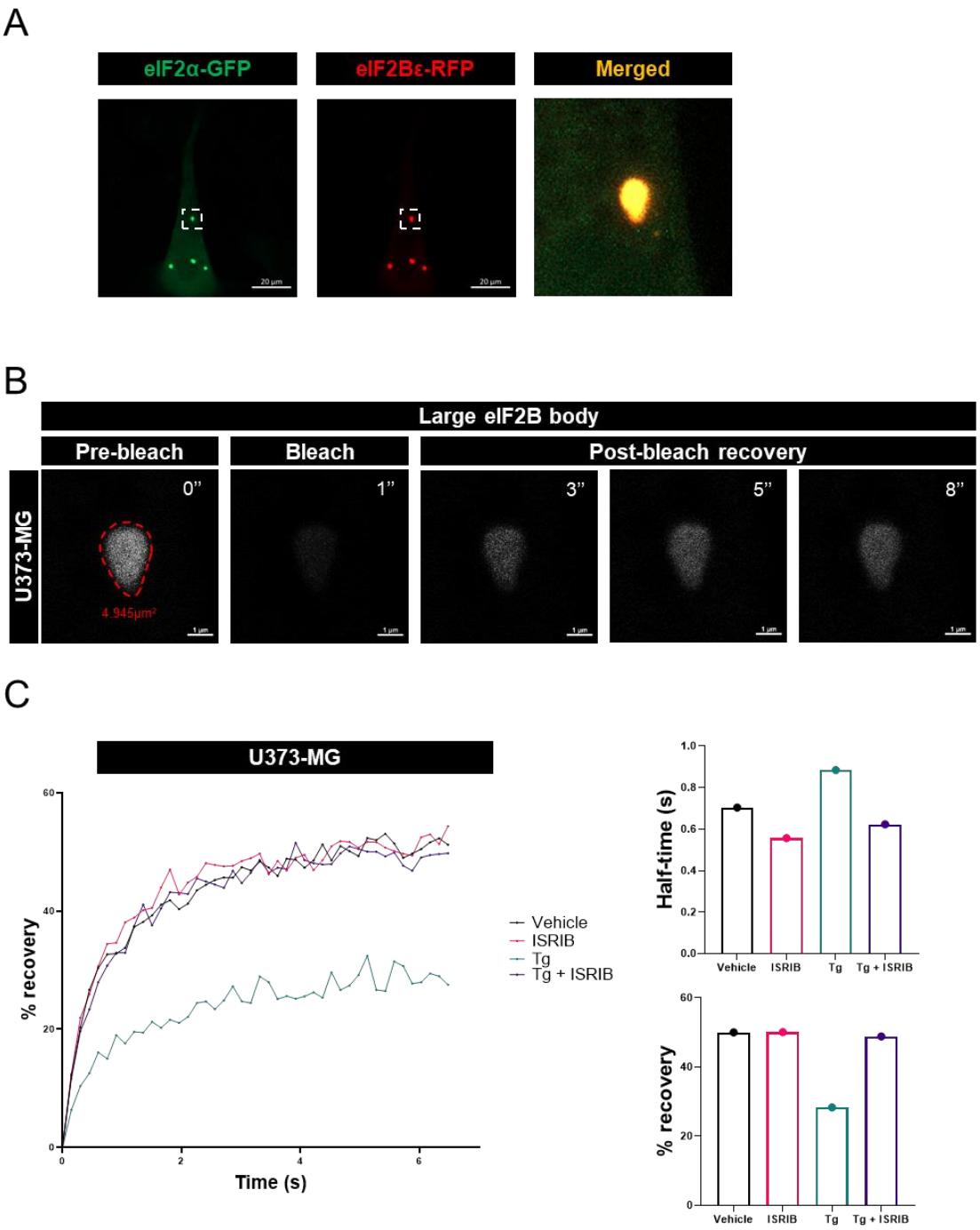

Figure 5.20. Shuttling of eIF2α-GFP through large eIF2Bε-RFP bodies is decreased following acute ER stress in U373-MG cells.

U373-MG cells were transiently transfected with eIF2α-GFP/eIF2Bε-RFP. eIF2α-GFP foci fluorescence was quantified to carry out FRAP. eIF2Bε-RFP foci mark the eIF2B body. Cells were subjected to DMSO 1h (vehicle), ISRIB 1h (200 nM), Tg 1h (1 µM), and ISRIB 1h (200 nM) coupled with Tg 1h (1 µM). (A) Representative live cell imaging of a U373-MG cell co-expressing eIF2α-GFP and eIF2Bε-RFP; Scale bar – 20 µm. (B) FRAP was performed in single large (≥1 µm^2) eI2FB bodies; Scale bar – 1 µm. (C) Quantification of normalised FRAP curves for eIF2α-GFP of 10 large eIF2Bε-RFP (≥1 µm^2) bodies of U373-MG cells. The data were graphed and shown as the mean (n=1). Quantification of the half time need for post-bleach full recovery of eIF2α-GFP. Mean percentage of eIF2α-GFP recovery determined from normalised FRAP curve.

We next explored the activity of large eIF2B bodies in the context of decreased eIF2Bα expression in cells with sieIF2Bα-Cy^{TM}3 transfection.

U373-MG, MO3.13 and SH-SY5Y cells were transiently transfected with eIF2α-GFP/eIF2Bε-RFP. Live cell imaging confirmed the co-localisation of eIF2α-GFP foci and eIF2Bε-RFP foci and the presence of tagged-siRNA. FRAP analysis was performed by quantifying the rate of recovery of fluorescence intensity of an individual region of interest containing a large eIF2α-GFP foci, *i.e.*, ≥ 1 μm^2 (**Figure 5.21A**).

The collection of sufficient data was hindered by two technical factors. Firstly, the number of large eIF2B bodies observed in cells transfected with siRNA-*EIF2B1* was low, as also shown in **section 5.2.2**, and secondly, a high incidence of cell death was noted upon co-transfection of eIF2α-GFP/eIF2Bε-RFP with siRNA-*EIF2B1* (data not shown). We hypothesize that the small number of large eIF2B bodies retained following siRNA-mediated silencing of *EIF2B1* may still harbor residual eIF2Bα subunits, as eIF2Bα expression has been reduced but not eliminated (**Figure 5.1B**). Thus, we measured the modulation of eIF2 shuttling dynamics within large eIF2B bodies in cells with decreased eIF2Bα expression coupled with a 1-hour ISRIB treatment.

In U373-MG cells, ISRIB alone demonstrated no significant effect on the T1/2 or % recovery of eIF2α-GTP in large eIF2B bodies (Vehicle: 48.20 % and 0.59 s; ISRIB: 46.30 % and 0.59 s) (**Figure 5.21B**). In contrast, Tg treatment reduced the percentage of eIF2α-GTP recovery and increased the T1/2 value (Tg: 28.64 % and 0.83 s). Of particular significance, the coupling of ISRIB treatment with cells exhibiting decreased eIF2Bα led to a T1/2 value (sieIF2Bα-CyTM3+ISRIB: 0.79 s) and percentage recovery rate of eIF2-GTP (sieIF2Bα-CyTM3+ISRIB: 34.89 %) at a point between the control and Tg treated cells (**Figure 5.21B**).

Interestingly in MO3.13 cells, eIF2α-GTP shuttling remain largely unaffected with the various treatments (Vehicle: 29.48 % and 0.65 s; ISRIB: 30.12 % and 0.77 s; Tg: 28.03 % and 0.97 s; sieIF2Bα-CyTM3+ISRIB: 28.93 % and 0.92 s). In SH-SY5Y cells similar results to U373-MG cells were found. As seen previously, ISRIB alone did not impact eIF2α-GFP shuttling (Vehicle: 44.52 % and 0.77 s; ISRIB: 43.21 % and 0.89 s) and Tg lead to a decrease in percentage of recovery (Tg: 25.14 % and 0.91 s). Interestingly, we observed that ISRIB treatment coupled with siRNA mediated silencing of *EIF2B1*, lead to an increase in rate of recovery

and the percentage of eIF2α-GFP to a level midway between controls and stressed cells (sieIF2Bα-CyTM3+ISRIB: 35.32 % and 1.56 s) (**Figure 5.21B)**.

This preliminary dataset (n=1) offers a glimpse into the dynamics governing eIF2B assembly and GEF activity in various cell types. In the context of astrocytes and neuronal cells, the rescue of large assemblies upon ISRIB treatment in the absence of eIF2Bα was seen (**section 5.2.2),** however GEF activity was not entirely restored in these cells. In contrast, oligodendrocytic cells were seemingly unaffected by acute ER stress, ISRIB treatment, or the absence of eIF2Bα coupled with ISRIB treatment.

A

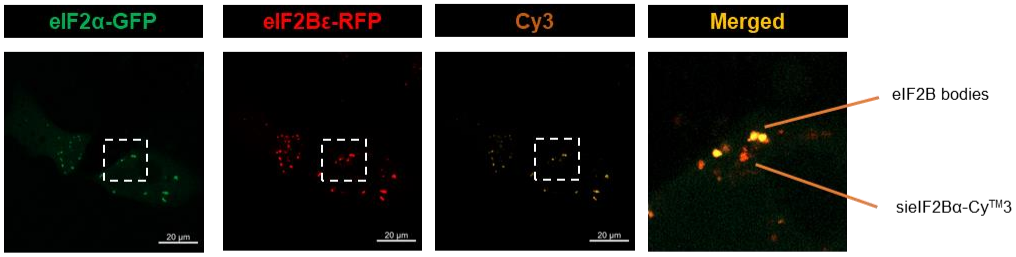

B

U373

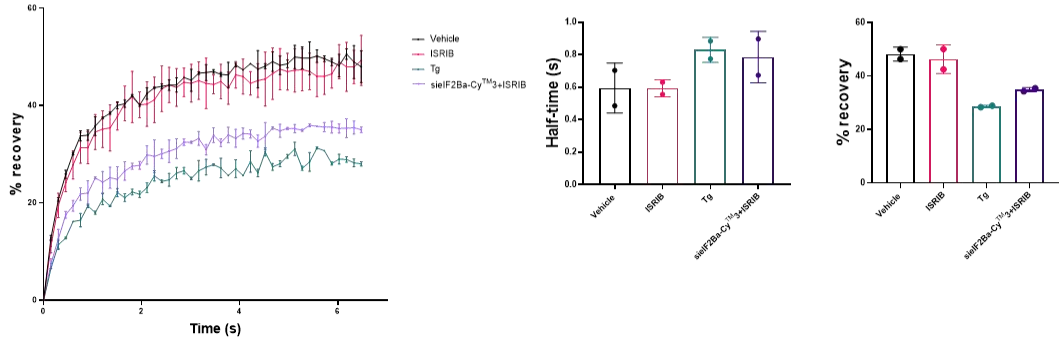

MO3.13

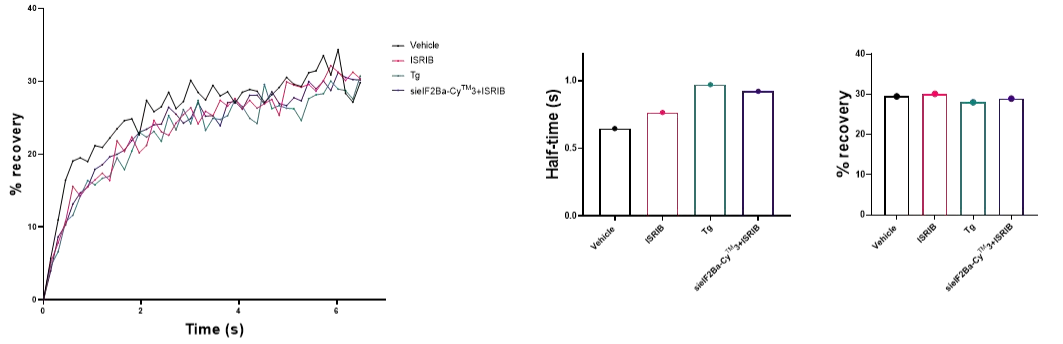

SH-SY5Y

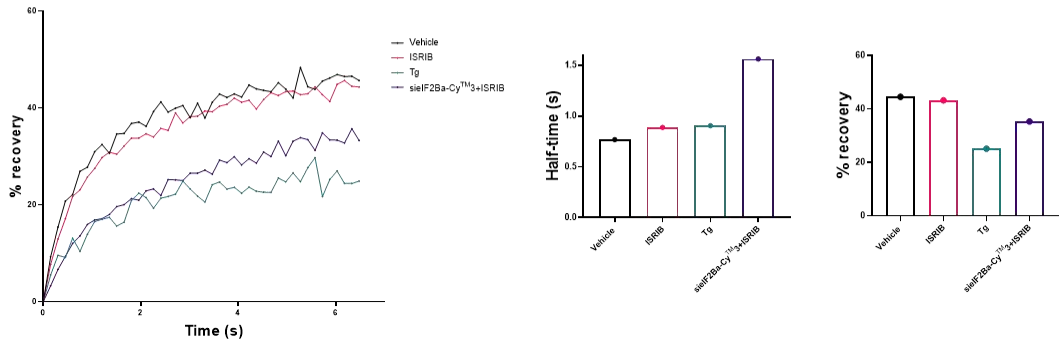

Figure 5.21. ISRIB treatment does not completely rescue large eIF2-GTP shuttling in cells with depleted eIF2Bα expression.

U373-MG cells were transiently co-transfected with eIF2α-GFP/eIF2Bε-RFP and Cy3 labelled siRNA targeting *EIF2B1*. eIF2α-GFP foci fluorescence was quantified to carry out FRAP. eIF2Bε-RFP foci mark the eIF2B body. Cells were subjected to DMSO 1h (vehicle), ISRIB 1h (200 nM), Tg 1h (1 μM), and siRNA mediated silencing of *EIF2B1* coupled with ISRIB 1h (200 nM).

(A) Representative live cell imaging of a U373-MG cell co-expressing eIF2α-GFP and eIF2Bε-RFP with Cy3 cytoplasmic puncti; Scale bar – 20 μm. (B) Quantification of normalised FRAP curves for eIF2α-GFP of 10 large eIF2Bε-RFP (≥ 1 μm^2) bodies of (top to bottom) U373-MG, MO3.13 and SH-SY5Y cells. The data were graphed and shown as the mean and error as ±s.d. for U373-MG (n=2). The data were graphed and shown as the mean for MO3.13 and SH-SY5Y (n=1). Quantification of the half time need for post-bleach full recovery of eIF2α-GFP. Mean percentage of eIF2α-GFP recovery determined from normalised FRAP curve.

5.2.6. siRNA mediated silencing of *EIF2B1* leads to the decrease of cell proliferation and insensitivity to stress

Although, eIF2Bα/Gcn3p has been shown to be necessary for regulatory function of eIF2B, it is not essential for cellular growth in yeast and HeLa cells (Elsby *et al*., 2011; Hannig & Hinnebusch, 1988; Norris *et al*., 2021). Protein synthesis stands as a fundamental measure of cell growth (Wittrup & Lieberman, 2015). Given the pivotal role of protein synthesis in cellular growth & expansion, together with the observation of reduced global protein synthesis in **section 5.2.3**, resulting from reduced expression of eIF2Bα, we next investigated the impact of reduced eIF2Bα expression on cell viability and proliferation.

To discern the effects on cell viability, Hoechst/PI staining was carried out on cells subjected to siRNA mediated silencing of *EIF2B1* in combination with either Tg and/or ISRIB. Representative images of U373-MG, MO3.13 and SH-SY5Y cells stained with Hoechst/PI following siRNA^{EIF2B1} transfection and following siRNA^{EIF2B1} transfection with Tg 1 hour treatment are shown (**Figure 5.22**).

In comparison with cells treated with vehicle, DMSO, ISRIB and Tg, decreased expression of eIF2Bα exhibited no significant impact on cellular viability. Cells with decreased eIF2Bα expression and treated with Tg exhibited a significant increase in cell death. While the presence of cell death was still evident, the co-treatment of cells with ISRIB in cells with decreased eIF2Bα levels and treated with Tg appeared to mitigate this decreased viability albeit subtly (**Figure 5.23**).

We carried out an MTT assay to measure cellular metabolic activity, which is known to correlate with cell proliferation, and observed that cells with decreased expression of eIF2Bα showed a significant decrease in cell proliferation (**Figure 5.24**). Thus, while ISRIB treatment of 1 hour following siRNA^{EIF2B1} was able to rescue induction of cell death, the same was not observed for cell proliferation.

From our analysis, cell viability remains unaffected by the knockdown of eIF2Bα. However, our results show that cells where eIF2Bα is absent exhibit compromised responsiveness to stress, ultimately culminating in cell death. ISRIB administration displayed a capacity to alleviate this response, yet significant cell death persisted, potentially implicating the intricate interplay of p-eIF2α and the eIF2B•eIF2α complex. Furthermore, our observations unveiled a noteworthy finding: in the absence of eIF2Bα, cell proliferation of U373-MG, MO3.13 and SH-SY5Y cells experienced a significant decline.

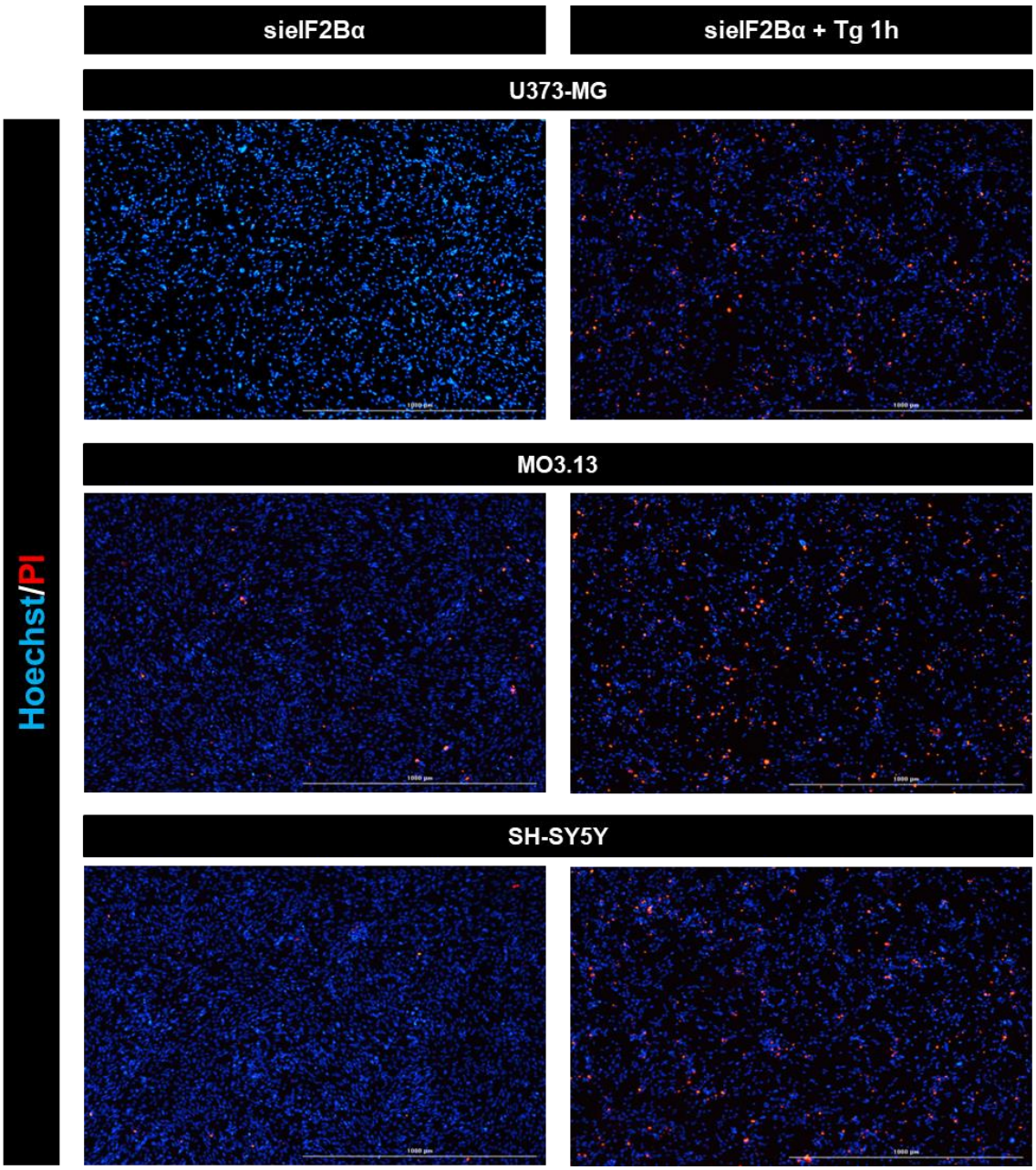

Figure 5.22. Acute ER stress displays a decrease in cell viability in eIF2Bα depleted cells. Representative fluorescence images of Hoechst and PI double staining in (top to bottom) U373-MG, MO3.13 and SH-SY5Y cells following siRNA mediated silencing of *EIF2B1* and siRNA mediated silencing of *EIF2B1* coupled with Tg 1h (1 μM) treatment. Scale bar – 1000 μm.

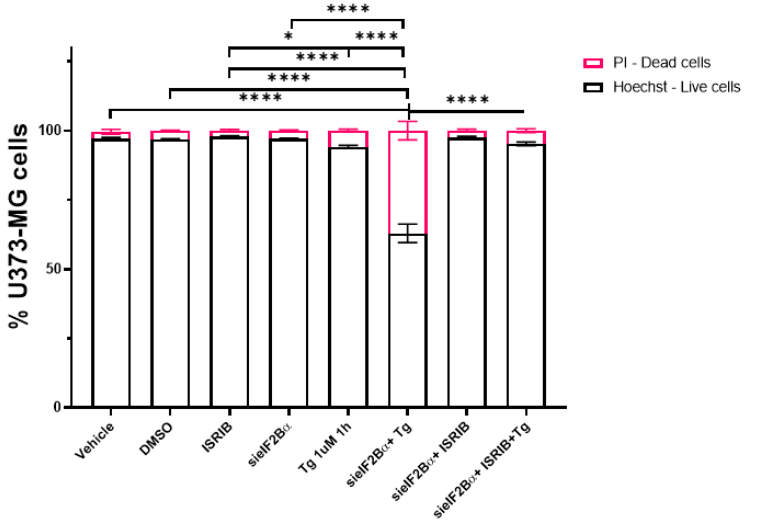
% U373-MG cells
PI - Dead cells
Hoechst - Live cells
Vehicle
DMSO
ISRIB
sielF2Bα
Tg 1uM 1h
sielF2Bα+ Tg
sielF2Bα+ ISRIB
sielF2Bα+ ISRIB+Tg

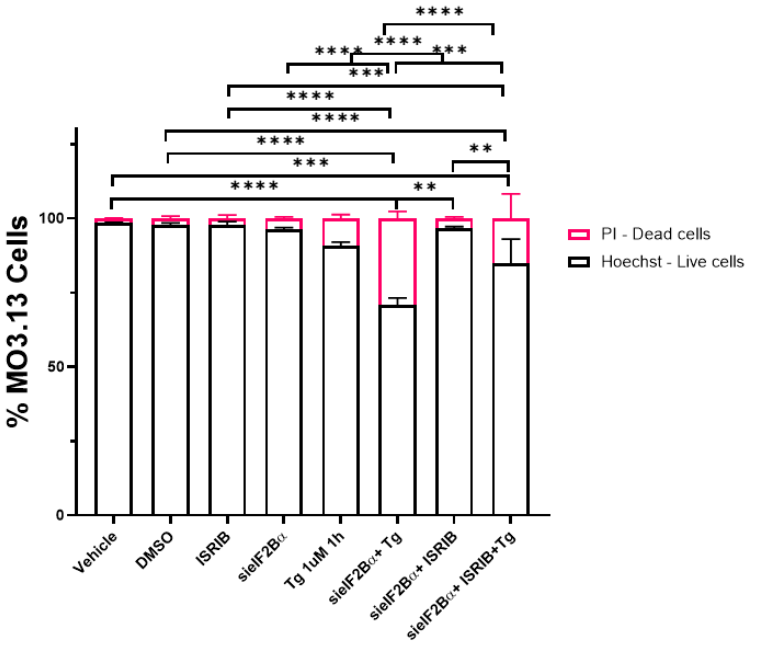
% MO3.13 Cells
PI - Dead cells
Hoechst - Live cells
Vehicle
DMSO
ISRIB
sielF2Bα
Tg 1uM 1h
sielF2Bα+ Tg
sielF2Bα+ ISRIB
sielF2Bα+ ISRIB+Tg

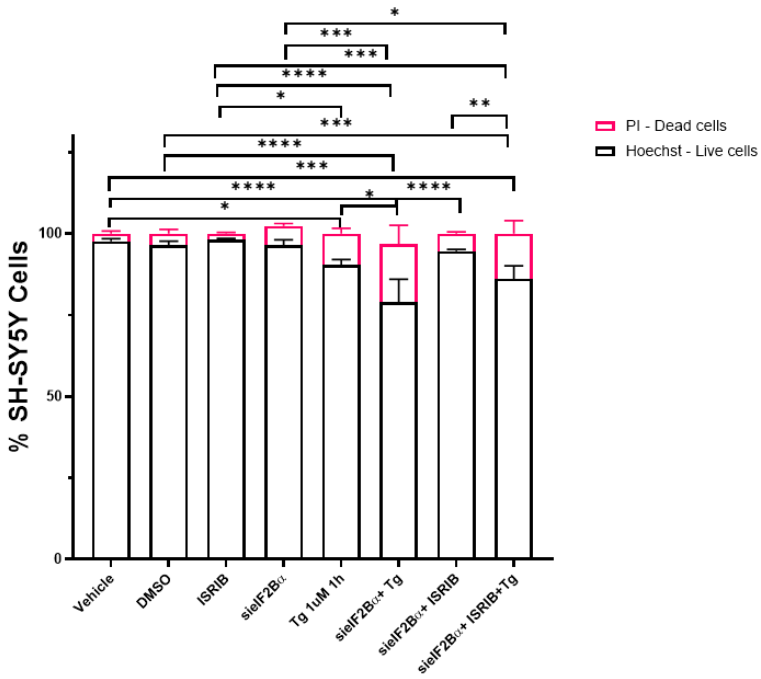
% SH-SY5Y Cells
PI - Dead cells
Hoechst - Live cells
Vehicle
DMSO
ISRIB
sielF2Bα
Tg 1uM 1h
sielF2Bα+ Tg
sielF2Bα+ ISRIB
sielF2Bα+ ISRIB+Tg

Figure 5.23. Acute ER stress displays a decrease in cell viability in eIF2Bα depleted cells, which ISRIB is able to mitigate.

Percentage of dead (PI) and live (Hoechst) in (top to bottom) U373-MG, MO3.13 and SH-SY5Y cells following untreated conditions (vehicle), DMSO 1h treatment, ISRIB 1h (200 nM) treatment, siRNA mediated silencing of *EIF2B1*, Tg 1h (1 μM) treatment, siRNA mediated silencing of *EIF2B1* coupled with Tg 1h (1 μM) treatment, siRNA mediated silencing of *EIF2B1* coupled with ISRIB 1h (200 nM) treatment, and siRNA mediated silencing of *EIF2B1* coupled with ISRIB 1h (200 nM) and Tg 1h (1 μM) treatment (n=3). Error bars: ± s.d. Data was analysed using two-way ANOVA followed by a Tukey's multiple analysis. **p* ≤0.05, ***p* ≤0.01, ****p* ≤0.001, *****p* ≤ 0.0001.

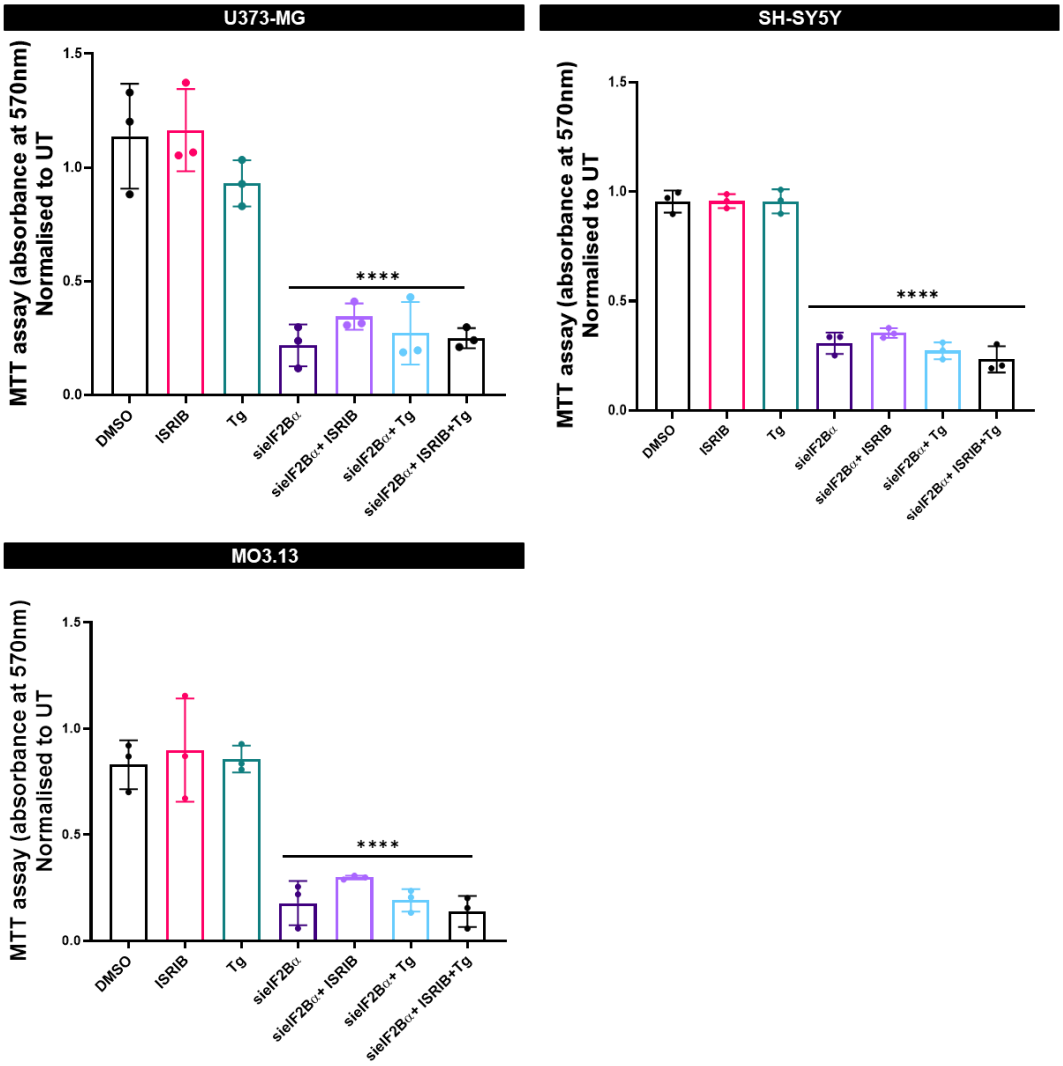

Figure 5.24. Cell proliferation is decreased in eIF2Bα depleted cells.

Relative absorbance at 570nm in (top to bottom) U373-MG, MO3.13 and SH-SY5Y cells following untreated conditions (vehicle), DMSO 1h treatment, ISRIB 1h (200 nM) treatment, siRNA mediated silencing of *EIF2B1*, Tg 1h (1 μM) treatment, siRNA mediated silencing of *EIF2B1* coupled with Tg 1h (1 μM) treatment, siRNA mediated silencing of *EIF2B1* coupled with ISRIB 1h (200 nM) treatment, and siRNA mediated silencing of *EIF2B1* coupled with ISRIB 1h (200 nM) and Tg 1h (1 μM) treatment (n=3). Error bars: ± s.d. Data was analysed using one-way ANOVA followed by a Tukey's multiple analysis. ****$p \leq 0.0001$.

5.3. Discussion.

5.3.1. eIF2B localisation is impacted by eIF2Bα subunit modulation

Despite the significant strides made in understanding eIF2B decamer formation (Gordiyenko *et al*., 2014; Kashiwagi *et al*., 2016; Schoof *et al*., 2021; Tsai *et al*., 2018; Wortham *et al*., 2014), the precise mechanism of eIF2B complex assembly remains a subject of ongoing debate. A growing body of evidence suggests a compelling and specific assembly pathway. The assembly process of the eIF2B decamer is orchestrated through precursors of sub-complexes (Wortham *et al*., 2016). This process begins with the initial formation of eIF2Bγε heterodimers, governed by their dimerization capacity. Subsequently, the dynamic interplay continues with the formation of heterodimers of eIF2Bβ and δ, which then bind to the existing eIF2Bγε heterodimers, culminating in the emergence of an intermediate eIF2Bβδγε tetramer. MS and crystallography results showed that interactions between eIF2Bε-β and γ-δ subunits primarily stabilize the tetrameric subcomplex (Kashiwagi *et al*., 2016; Wortham *et al*., 2014). Intriguingly, eIF2Bα exhibits the capacity to form homodimers, representing a pivotal actor in the final stage of eIF2B assembly. It facilitates the integration of two tetramers, acting as a requirement to generate the fully mature eIF2B$(\alpha\beta\delta\gamma\varepsilon)_2$ holocomplex (Wortham *et al*., 2016).

In this chapter we demonstrate compelling evidence pointing towards a crucial necessity of eIF2Bα for the stabilization of the decamer or its subcomplexes in the process of localisation of eIF2B foci in mammalian cells.

In our investigation, we observed that the expression levels of eIF2B subunits did not exhibit a direct correlation with their localisation pattern, as evidenced in **Chapter 4**. However, an approximately 90 % reduction in eIF2Bα expression resulted in a significant decrease in localisation (**5.2.1 section**). This indicates that while overall protein expression of the eIF2B subunits might not serve as the primary determinant of localisation, the precise regulation of expression levels for individual eIF2B subunits could significantly influence the observed localisation patterns discussed in **Chapter 4**.

To ensure that the decreased expression and localisation of eIF2Bα was due to the siRNA specificity, a non-targeting control siRNA was used. Any changes observed in protein levels or localisation in cells transfected with this negative control would reflect a baseline cellular response that can be compared to the

levels in cells treated with target-specific siRNA. Expression levels of eIF2Bα and the percentage of cells eIF2Bα localisation were not impacted by non-targeting control siRNA.

Following siRNA-mediated silencing of *EIF2B1*, our observations revealed an increase of small eIF2Bβ-ε foci concomitant with the reduction of large eIF2Bβ-ε foci (**5.2.2 section**). We hypothesise that these small foci may be stable subcomplexes of eIF2Bβδγε tetramers (Kashiwagi *et al*., 2016; Wortham *et al*., 2014) that localise within cells in the absence of eIF2Bα (**Figure 5.25**). Similar results were obtained by Schoof *et al.,* (2021), with fluorescence resonance energy transfer assays showing that the disassembly of eIF2B decamers upon eIF2Bα degradation, form eIF2Bβδγε tetramers.

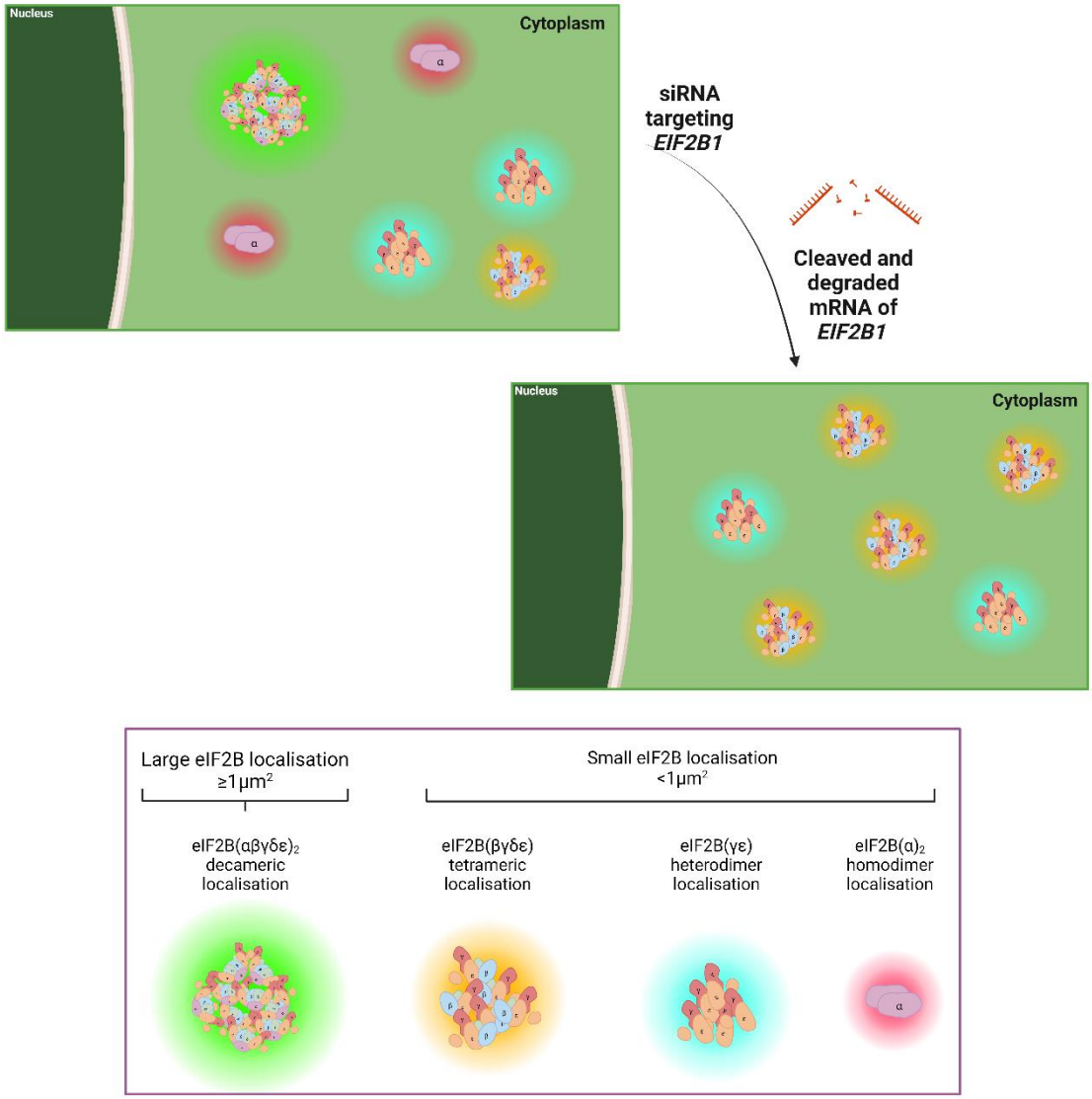

Figure 5.25. Large eIF2B foci do not form in eIF2Bα depleted cells.

Following siRNA mediated silencing of *EIF2B1*, the presence of large eIF2Bβ-ε foci was considerably decreased, while an increase of small eIF2Bβ-ε foci was displayed. We propose that these smaller foci are free eIF2B(βγδε) tetramers, as these subcomplexes are known to be joined by eIF2B(α)$_2$ homodimers, subsequently forming eIF2B decamer. Thus, we hypothesise that the formation of large eIF2B foci, which are thought to be composed by eIF2B decamers, is inhibited in cells depleted of eIF2Bα. Image designed in BioRender.

5.3.2. The ISR is modulated by eIF2B assembly state

The significance of eIF2Bα in the regulatory function of eIF2B is notable; however, in yeast Gcn3p/eIF2Bα appears to be dispensable for growth (Norris *et al*., 2021; Pavitt *et al*., 1997). This observation suggests the existence of compensatory mechanisms or redundant factors that can partially complement the absence of eIF2Bα in supporting essential cellular functions.

In our study, we observed that the depletion of eIF2Bα in mammalian cells exerted a profound impact on global protein production (**Figure 5.17**). Similar findings had been reported in prior studies, where experimental depletion of eIF2Bα led to the activation of ISR signaling, even in the absence of eIF2 phosphorylation (Schoof *et al.,* 2021). These earlier studies attributed this ISR activation to the accumulation of unassembled eIF2B tetramers in cells. We speculate that stress induction stems from the presence of localised subcomplexes and the functional implications of changes in eIF2B foci formation. Known stable eIF2B subcomplexes, such as eIF2Bγε and eIF2Bβγδε, present in normal conditions, are in dynamic relationship with the eIF2B decamer. When the decameric structure is no longer possible to form due to the absence of eIF2Bα, a decline in GEF activity is to be expected. Notably, eIF2B sub-complexes exhibit a progressive decline in GEF activity compared to the full decamer, manifesting GEF activities of approximately 50 % and 20 %, respectively (Liu *et al*., 2011; Wortham *et al*., 2014, 2016). We hypothesise that the observed decline in protein synthesis arises from decreased levels of TC, a direct outcome of reduced eIF2B GEF activity attributed to the diminished expression of eIF2Bα. This impacts the process of translation initiation and, subsequently, triggers downstream ISR signaling, which was observed with the induction of GADD34, CHOP and ATF4 (**Figure 5.18 and Figure 5.26**).

Intriguingly, despite the observed unaltered cell viability upon eIF2Bα depletion (**Figure 5.23**), a striking impact was seen on cell proliferation. Cells subjected to reduced expression of eIF2Bα displayed a substantial decrease in their proliferation rate (**Figure 5.24**). siRNA mediated silencing yielded a substantial reduction in eIF2Bα expression; however, it remains plausible that residual levels of eIF2Bα persist, potentially serving as an adequate reservoir to sustain eIF2B activity under steady-state conditions and subsequently not trigger cell death. This observation raises the possibility of a regulatory threshold, where even

subtle changes in eIF2Bα might exert a profound impact on eIF2B functionality within the context of normal cellular physiology.

These findings deviate from the outcomes of other studies, particularly in yeast and insect models, where null or mutated eIF2Bα/Gcnp3 strains were observed to leave cellular growth unaffected (Fabian *et al*., 1997; Kimball *et al*., 1998; Norris *et al*., 2021; Pavitt *et al*., 1997). This disparity may be indicative of a requirement for eIF2Bα presence in governing cellular function within mammalian cells. Additional observations, such as in HeLa cells, where knockdown of eIF2Bα did not manifest any discernible impact on cell proliferation, protein synthesis rates, or stress response (Elsby *et al*., 2011) suggests that the impact of changes in eIF2Bα expression are cell type specific. Nevertheless, it is noteworthy that this seemingly divergent result in HeLa cells could be potentially attributed to an underlying defect in eIF2B activity in this cell-type. It has been reported that the GEF function of eIF2B downstream of eIF2 is frequently aberrant in transformed cells, with eIF2B-mediated guanine nucleotide exchange rates being greatly enhanced and eIF2Bε levels being increased in these cells, thus neutralizing p-eIF2α (Balachandran & Barber, 2004). These contrasting outcomes across different cell types hint at cell-type specific requirements and potential functions of eIF2Bα.

Furthermore, our investigation revealed that cells with depleted eIF2Bα expression experienced a substantial increase in cell death when exposed to acute ER stress (**Figure 5.23**). This finding aligns with earlier studies that have implicated the absence of eIF2Bα in the lack of stress response (Elsby *et al*., 2011; Wortham *et al*., 2014). The underlying mechanism behind this observation likely arises from the absence of p-eIF2α-mediated inhibition, which is a pivotal regulatory mechanism governing eIF2B function. In normal physiological conditions, eIF2 does not interact significantly with eIF2Bα. However, under cellular stress, the phosphorylated form of eIF2α undergoes tight binding with both eIF2Bα and eIF2Bδ, conformational changing the eIF2•eIF2B complex, effectively inhibiting GEF activity (Adomavicius *et al*., 2019; Schoof *et al*., 2021; Zyryanova *et al*., 2021). This relationship between eIF2Bα and p-eIF2α serves as a key regulatory nexus, allowing cells to fine-tune their stress response and survival strategies in the face of adverse conditions. Thus, in cells depleted of eIF2Bα expression when exposed to stress conditions, correct activation and downstream response is not present, leading cell death.

These findings emphasize the significance of eIF2Bα and p-eIF2α in governing cellular stress responses, cell survival, and cell death pathways, as it has been discussed previously (Marintchev & Ito, 2020).

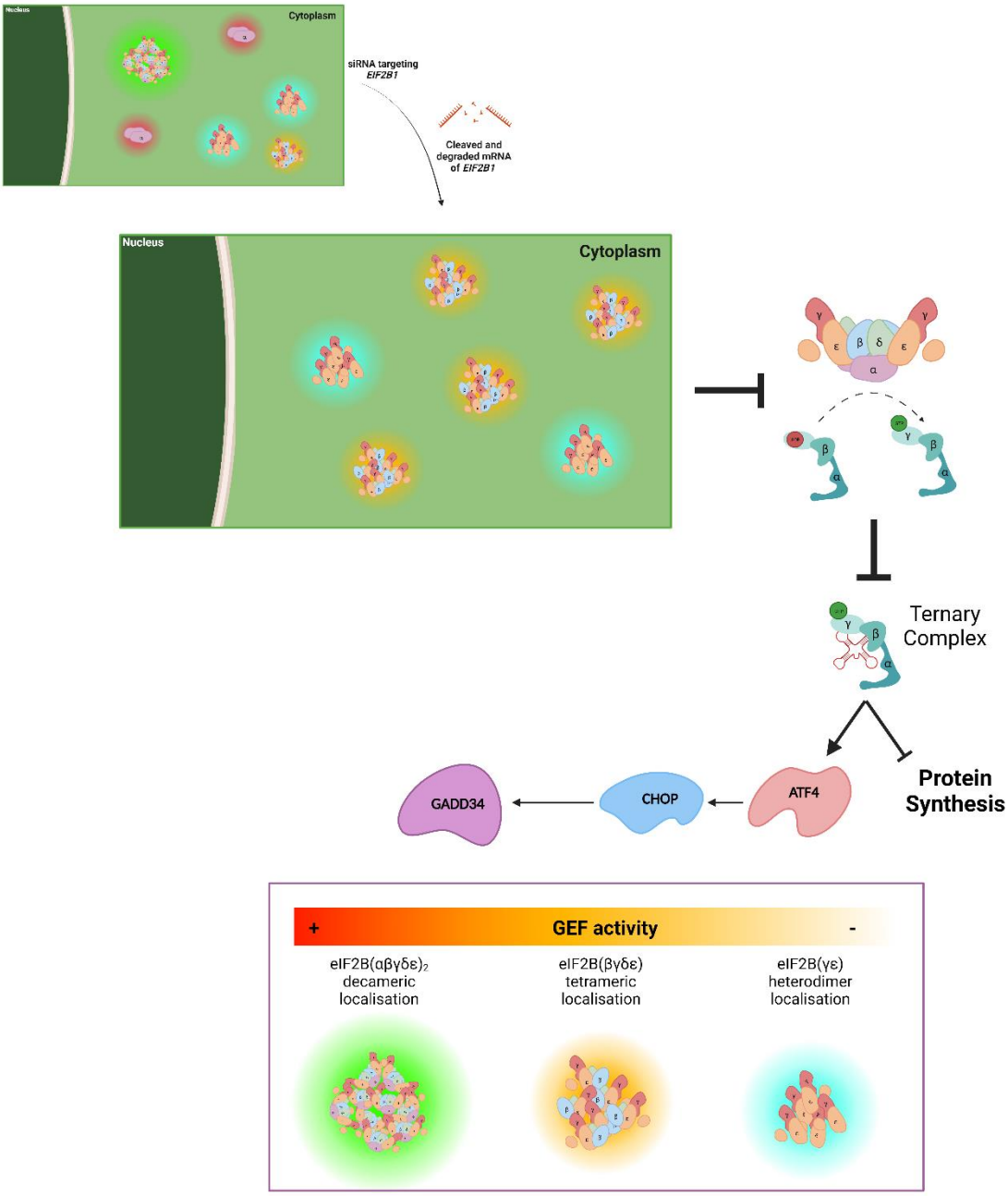

Figure 5.26. Cells with depleted eIF2Bα leads to the induction of the ISR downstream of p-eIF2α.

The depletion of eIF2Bα, in the absence of eIF2 phosphorylation, still activates downstream ISR. We propose that the disassembly/inhibition of large eIF2B foci, GEF activity is decreased. This in turn leads to decreased levels of TC, which limits protein synthesis, seen in **figure 5.17** through the puromycin incorporation assay, and subsequently activation of ATF4, CHOP and GADD34, seen in **figure 5.18**. Image designed in BioRender.

5.3.3. ISRIB influences eIF2B localisation and ISR response in the absence of eIF2Bα

In response to adverse cellular conditions, it is crucial to have a tight regulation of translation, where a balance between energy conservation and the synthesis of stress responsive proteins is required. While there are different stress responsive pathways, one of the most diverse mechanisms of translational control is the ISR (Brostrom & Brostrom, 1997; Dever *et al*., 1992). In a recent publication, ISRIB was shown to functionally replace eIF2Bα in its role of decamer stabilization (Schoof *et al*., 2021). Thus, in eIF2Bα depleted cells, ISRIB is able to join eIF2Bβγδε tetramers and form functional eIF2B octamers.

In our investigation, we revealed that large eIF2Bβ-ε foci following siRNA-mediated silencing of *EIF2B1* were not formed. Strikingly, the introduction of ISRIB treatment displayed a rescue effect, reinstating the formation of these large eIF2Bβ-ε foci. Building upon insights from Schoof *et al*., (2021), we posit that these localised structures represent stable eIF2B octamers that lack eIF2Bα and are stabilized by the action of ISRIB, as elaborated in **section 5.2.2**. This showcases the interaction between ISRIB and eIF2B, where ISRIB serves as a critical modulator that facilitates the stabilization of these large eIF2B structures.

We hypothesise that two mechanisms may lead to this rearrangement of eIF2B foci: (1) the preassembled large eIF2B complexes present in large eIF2B bodies, inherently dynamic in composition, undergo disassembly and lose their ability to reassemble in the absence of eIF2Bα; (2) the stepwise assembly of eIF2B commences with the formation of heterodimers of eIF2Bβ and δ, which subsequently bind to eIF2Bγε heterodimers, culminating in an intermediate eIF2Bβδγε tetramer. In the absence of eIF2Bα_2, this tetrameric structure is rendered incapable of progressing to larger decameric structures.

The increased formation of smaller eIF2Bβ-ε foci and the concomitant inhibition of large eIF2Bβ-ε foci assembly reinforces the significance of eIF2Bα in orchestrating the stable formation of large eIF2B foci within cells. It is, however, essential to highlight the potential involvement of post-translational modifications in the modulation of eIF2B subunit localisation across different cell types. These modifications could potentially serve as dynamic regulatory mechanisms that govern the localisation dynamics of eIF2B.

Notably, we have found that the percentage of cells with eIF2B localisation and average number of foci per cell exhibited a distinct cell-type specificity according

to eIF2B subunit (as explored in **4.2.1** and **4.2.3**), revealing the fascinating diversity of eIF2B regulation in different cell types. However, amidst this diversity, a striking universal trait emerges—the indispensable requirement of eIF2Bα for the formation of larger foci, observed consistently across all the cell lines analyzed – astrocytes, oligodendrocytes, and neuronal cells. This underscores the fundamental significance of eIF2Bα in orchestrating the assembly dynamics of eIF2B complexes, suggesting its pivotal role in shaping the overall regulatory landscape governing eIF2B function in various cell types. Therefore, the frequency of large eIF2B foci, which remain unformed in the context of decreased eIF2Bα expression, could potentially vary in the presence of eIF2Bα mutations or result from cell-type specific variations in the abundance of eIF2Bα.

Interestingly, while ISRIB treatment alone was insufficient to rescue cell proliferation (**Figure 5.24**), the combination of ISRIB and Tg proved to mitigate cell death in cells depleted of eIF2Bα (**Figure 5.23**). It is of note that ISRIB's presence and action are only sensed in the presence of p-eIF2α ((Hodgson *et al*., 2019; Rabouw *et al*., 2019; Zyryanova *et al*., 2021). Global protein synthesis was inhibited in the absence of eIF2Bα, culminating in the activation of the downstream ISR. ISRIB emerged as a potent agent capable of restoring formation of large eIF2B foci in cells depleted of eIF2Bα, leading to the rescue of protein synthesis to normal levels, as evidenced by **Figure 5.17 and Figure 5.18**. Additionally, in cells with depleted levels of eIF2Bα, the formation of SGs was observed (**Figure 5.19**). While the phosphorylation of eIF2α was not present, the decreased levels of global protein synthesis seen (**Figure 5.17**), might suggest that the absence of eIF2Bα reduces levels of TC, which subsequently stalls translation initiation leading to the formation of SGs (**Figure 5.19**).

ISRIB was able to form large eIF2Bβ-ε cytoplasmic foci even in the absence of eIF2Bα. Intriguingly, despite the restoration of large eIF2B bodies by treatment with ISRIB in the absence of eIF2Bα, the full 100 % restoration of GEF activity is not achieved (**Figure 5.21**). There are two plausible explanations for this observation. Firstly, it is conceivable that the incomplete rescue of GEF activity may be attributed to the relatively short duration of ISRIB treatment, warranting further exploration to identify the optimal treatment conditions for maximal restorative effects. Secondly, the arrangement of the eIF2B structure, in the absence of eIF2Bα, could impinge on eIF2 binding dynamics, a facet that ISRIB alone may be insufficient to resolve (**Figure 5.27**).

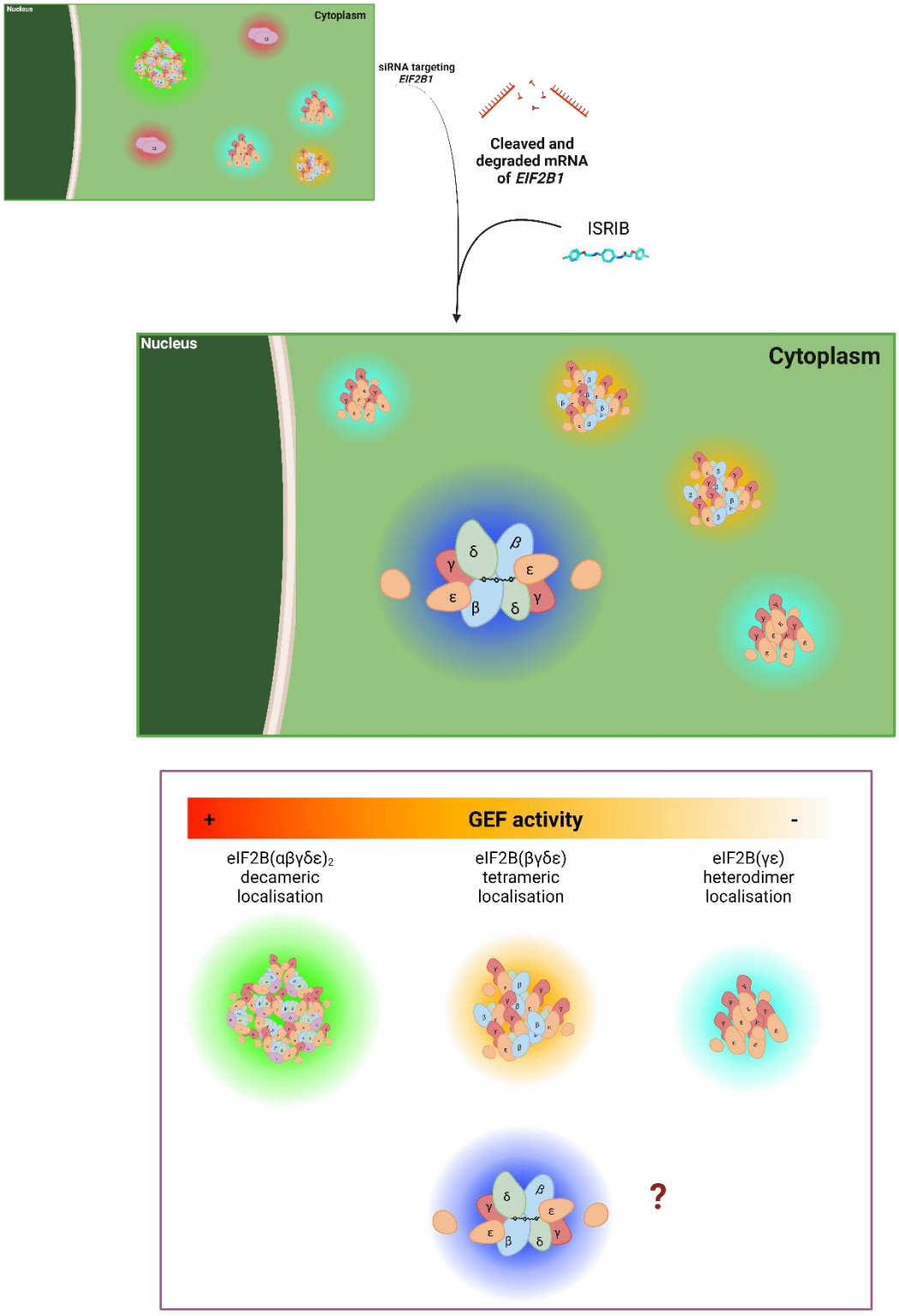

Figure 5.27. ISRIB is able to functionally replace eIF2Bα in the formation of large eIF2Bβ-ε foci.

In cells depleted of eIF2Bα, ISRIB 1 hour treatment is able to rescue large eIF2Bβ-ε foci formation. We propose that these large assemblies are a result of joining free eIF2Bβγδε tetramers, created in the absence of eIF2Bα, through the binding of ISRIB in the eIF2Bβ and eIF2Bδ symmetrical interface pocket. While these larger foci are able to be rescued by ISRIB's action, the analysis of

GEF activity, while preliminary, indicates that is not fully recovered in the absence of eIF2Bα. Image designed in BioRender.

5.3.4. Final observations

The analysis presented in this chapter culminates in two noteworthy outcomes: Firstly, ISRIB's assembly-promoting activity is contingent upon the absence of eIF2Bα_2, given that no increase in large eIF2Bβ-ε foci was present when cells were treated solely with ISRIB. This observation bears implications, particularly in the context of eIF2Bα mutations, wherein aberrant binding of eIF2Bα to other eIF2B subunits impairs the correct formation of eIF2B decamers. The analysis of eIF2B bodies formation in the presence of such mutations may offer valuable insights into the etiology of diverse disease conditions where dysregulated eIF2Bα plays a pivotal role, potentially paving the way for targeted therapeutic interventions aimed at restoring proper eIF2B assembly and function, which has been initially investigated in yeast models (Norris *et al*., 2021). Secondly, as p-eIF2α binds at the eIF2Bα/eIF2Bδ interface to mediate inhibition, this specific binding site does not exist in complexes lacking eIF2Bα, thus being inert to inhibition by p-eIF2α. This finding may have significance in disease conditions characterised by either persistent eIF2B inhibition or activation of the ISR, both of which have been implicated in the pathogenesis and progression of various disorders (Moortgat *et al*., 2016; Pakos-Zebrucka *et al*., 2016; Stanik *et al*., 2018; Szewczyk *et al*., 2023)

We have observed in our work, that cells depleted of eIF2Bα are not able to properly respond to acute ER stress induction, leading to an increase of cellular death (**Figure 5.23**). It is of note that mice harboring homozygous mutations at the eIF2α phosphorylation site (Ser51Ala) are required for cellular survival in response to ER stress. It was shown that mice died within 18h following birth due to hypoglycemia and displayed a deficiency in pancreatic β-cells (Scheuner *et al*., 2001). This work highlights how essential proper cellular response to stress is to cell viability.

It is of note that, eIF2Bα localisation pattern could be modulated through diverse regulatory mechanisms, such as fine-tuned biosynthesis, targeted degradation, or post-translational modifications. Additionally, eIF2Bα might be sequestered into specialized compartments, such as SG, a compelling line of inquiry that we shall explore in the forthcoming chapter. eIF2Bα has been shown to have binding

of various sugar phosphate metabolites to conserved regions, which is thought to enhance decamer formation (Hao *et al*., 2021). We postulate that endogenous eIF2B$(\beta\delta\gamma\varepsilon)_2$ octamers could potentially be stabilized by putative alternate assembly factors, which might encompass a diverse range of metabolites or proteins that, akin to ISRIB, have the unique capacity to substitute for eIF2Bα_2 in facilitating eIF2B assembly.

Chapter 6. The role of eIF2Bα in stress granules.

6.1. Introduction.

The precise regulation of translation and mRNA degradation constitutes a fundamental aspect of normal cell function. This regulation plays a pivotal role in countering adverse conditions, wherein biological responses are triggered to restore cellular homeostasis. Key to this process is the establishment of subcellular compartmentalisation, which enables the spatiotemporal control of these responses, ensuring a finely coordinated and context-specific cellular defense mechanism. Understanding the underlying mechanisms governing this interplay between translation, mRNA degradation, and subcellular compartmentalisation is of paramount importance for unraveling the intricacies of cellular stress response and adaptation (Donato *et al*., 2019; Ismail *et al*., 2021; Velázquez-Cruz *et al*., 2021).

Aberrant proteins have been found to accumulate as toxic aggregated in cases where the proteostasis machineries become comprised (Hipp *et al*., 2014; Klaips *et al*., 2018). This sustained aggregation has been linked to several neurodegenerative disorders (Bäuerlein *et al*., 2020; Hipp *et al*., 2014; Klaips *et al*., 2018). On the other hand, control of protein aggregation in a reversible manner aids the management of a wide range of cellular processes such as stress response, gene expression, memory, cell development and differentiation (Monsellier *et al*., 2008; Naskar & Gour, 2023; Stefani & Dobson, 2003). Protein aggregation, formerly thought to be merely pathological, can be necessary for vital biological processes (Cox *et al*., 2020; Fassler *et al*., 2021; Wen *et al*., 2023). One example of this is eIF2B bodies, which have been found to be highly active sites facilitating GDP-GTP exchange processes during steady-state conditions and stress conditions (Campbell *et al*., 2005; Hanson *et al*., 2023; Hodgson *et al*., 2019; Norris *et al*., 2021). Additionally, given the increase of eIF2Bα that appear to not interact with other eIF2B subunits following ER stress described in **section 4.2**, the investigation of eIF2B foci, known stress responsive clusters and how these interact is of great significance.

Proteotoxic stress results in organized sequestration of misfolded proteins at cytosolic quality control deposition sites, such as ubiquitin-mediated protein degradation (Dudek *et al*., 2010; Zeng *et al*., 2006). Ubiquitin-mediated protein

degradation may play a crucial role in orchestrating cellular responses to misfolding events, thereby shaping the fate and dynamics of protein aggregation. The intricate regulation of gene expression in eukaryotic cells involves precise control over mRNA translation, stability, and subcellular localisation. Cytosolic mRNAs, in response to these regulatory mechanisms, undergo dynamic transitions between distinct functional states and subcellular compartments. Polysomes scattered throughout the cytoplasm house translating mRNAs, while under stress, non-translating mRNAs tend to aggregate in specialized cytoplasmic RNA-protein (ribonucleoprotein) granules, such as P-bodies and SG. P-bodies are predominantly characterised by their association with mRNA decay components(Anderson & Kedersha, 2006; Protter & Parker, 2016). Despite their distinct characteristics, both granules share specific mRNAs and some common proteins, exhibiting dynamic docking and overlapping interactions (Buchan *et al*., 2011; Hoyle *et al*., 2007; Kedersha *et al*., 2005; Moon *et al*., 2019; Moon & Namkoong, 2023; van Leeuwen *et al*., 2022). This suggests a potential interface where mRNP particles might be remodeled, and individual mRNAs exchanged between the two granules, although direct evidence for this phenomenon remains to be established (Moon & Namkoong, 2023).

eIF2Bα has emerged as a critical eIF2B subunit, required for stress perception and SG formation (Ohn *et al*., 2008). Notably, the phosphorylated state of eIF2α binds with eIF2Bα within the non-productive model of eIF2•eIF2B interaction. This binding recognition serves as a fundamental checkpoint, leading to downstream effects in translation initiation and stress-induced translational repression within the cellular landscape (Kashiwagi *et al*., 2019; Ohn *et al*., 2008; Schoof *et al*., 2021; Zyryanova *et al*., 2021).

Investigating the role of eIF2Bα in stress sensing and its impact on the assembly of these dynamic cytoplasmic organelles is of significant interest not only for delving into the intricacies of translation regulation but also for elucidating the pathophysiological mechanisms underlying disorders that directly impinge upon eIF2B and SGs.

6.1.1. Hypothesis and rationale

Our next endeavor was to explore the potential interaction of eIF2B foci with stress-responsive condensates. Our hypothesis posits that, while eIF2B foci serve as biologically relevant structures in normal physiological states,

functioning as pivotal hubs of GEF activity for translation initiation, their composition is dynamic under stress conditions. Additionally, we have shown that in the absence of eIF2Bα, an increase in cells with SG was observed (seen in **section 5.2.5**). Accordingly, we propose that eIF2B foci may engage in direct interactions with stress-responsive complexes or influence their formation in adverse conditions, thus uncovering novel dimensions of the regulatory landscape governing cellular stress response mechanisms. By investigating these interrelationships, we aim to shed light on the sophisticated network of molecular events orchestrating cellular adaptation and SG dynamics in the face of diverse challenges.

To test these theories, the following objectives were employed:

- Determine co-localisation patterns between eIF2Bα and poly-ubiquitin, p-bodies and SGs.
- Determine co-localisation patterns between eIF2Bε and SGs.
- Analyse the impact of eIF2Bα in the formation of SGs in p-eIF2α dependent and independent conditions.

6.2. Results.

6.2.1. eIF2Bα foci do not co-localise with polyubiquitin.

Misfolded proteins, which tend to form intracellular aggregates, can pose significant toxicity to cellular health. One pivotal component of these aggregates' clearance mechanism is the UPS. To mitigate this, multiple ubiquitin molecules are strategically attached to these aberrant proteins, facilitating their selective recognition and subsequent delivery to the 26S proteasome for targeted degradation (Kleiger & Mayor, 2014; Nguyen *et al*., 2014; Reyes-Turcu *et al*., 2009). Due to the presence of eIF2Bα aggregates which appear to be independent of regulatory or catalytic eIF2B subunits shown in glial and neuronal cells, but particularly in MO3.13 and SH-SY5Y cell lines (seen in **4.2.1.** and **4.2.3.**), it was essential to ensure that these foci were not aggregates of protein which have been targeted for degradation. To do so, co-localisation between endogenous eIF2Bα and poly-ubiquitin FK1 was analysed (Danielson & Hope, 2013). Across all three cell lines examined, a conspicuous absence of co-localisation between eIF2Bα and poly-ubiquitin was observed, implying that these eIF2Bα cytoplasmic foci do not represent targeted substrates for proteolytic degradation (**Figure 6.1, Figure 6.2, and Figure 6.3**).

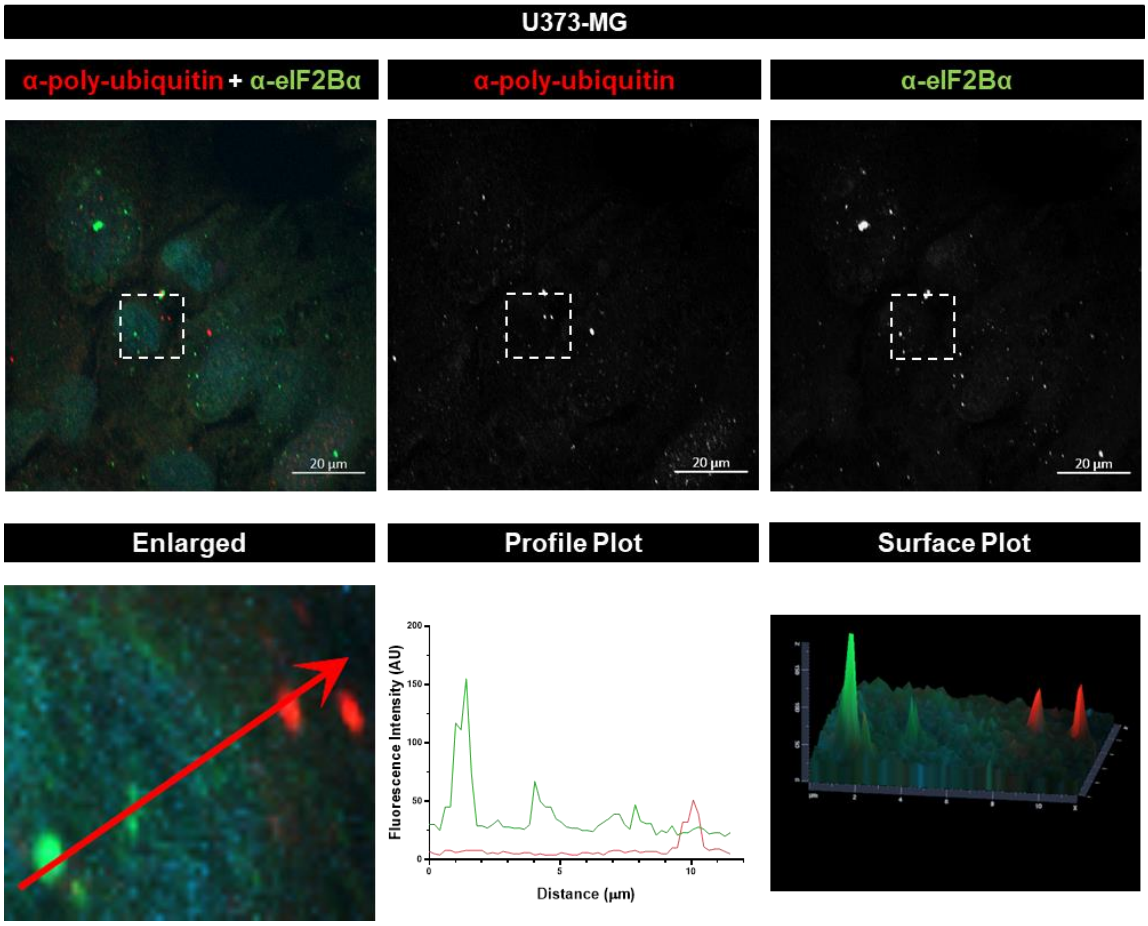

Figure 6.1. eIF2Bα foci do not co-localise with polyubiquitin in U373-MG cells.

Representative images of U373-MG cells subjected to ICC with anti-eIF2Bα, visualised using secondary antibodies conjugated to AlexaFluor 488 and anti-polyubiquitin primary antibodies, visualized using secondary antibodies conjugated to AlexaFluor 594. DAPI stained nuclei. Scale bar: 20 µm. The boxed region is enlarged, profile and surface plots were used to not show co-localisation (separate colours shown on graphics), (n=1).

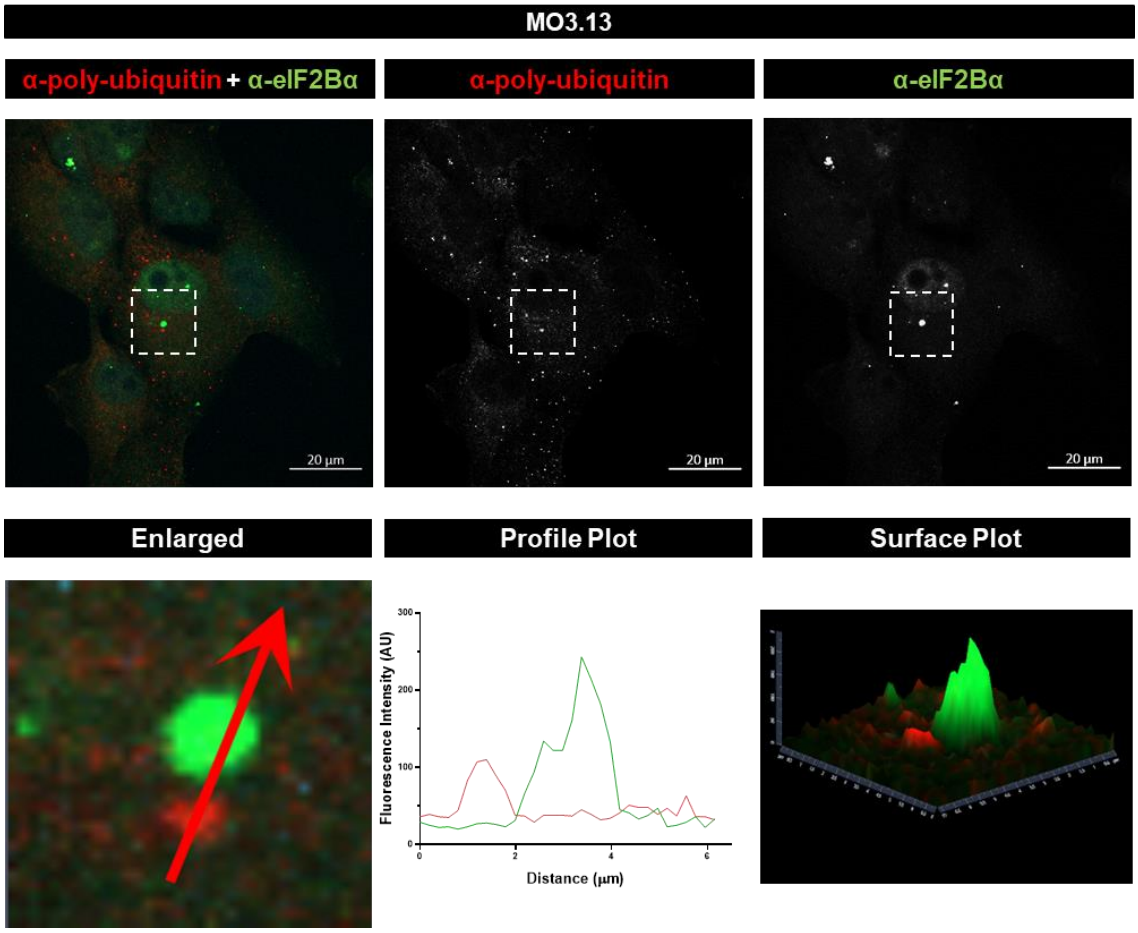

Figure 6.2. eIF2Bα foci do not co-localise with polyubiquitin in MO3.13 cells.

Representative images of MO3.13 cells subjected to ICC with anti-eIF2Bα, visualised using secondary antibodies conjugated to AlexaFluor 488 and anti-polyubiquitin primary antibodies, visualized using secondary antibodies conjugated to AlexaFluor 594. DAPI stained nuclei. Scale bar: 20 µm. The boxed region is enlarged, profile and surface plots were used to not show co-localisation (separate colours shown on graphics), (n =1).

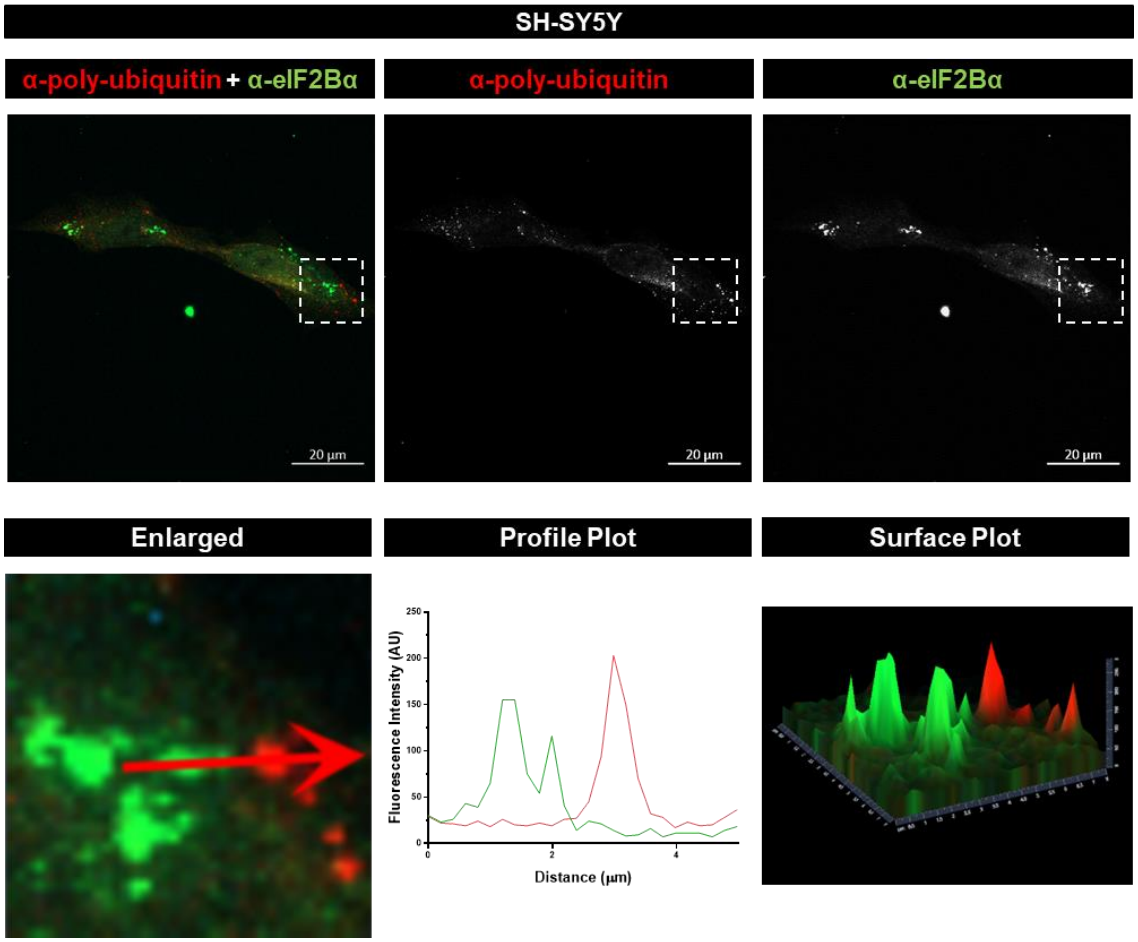

Figure 6. 3. eIF2Bα foci do not co-localise with polyubiquitin in SH-SY5Y cells.

Representative images of SH-SY5Y cells subjected to ICC with anti-eIF2Bα, visualised using secondary antibodies conjugated to AlexaFluor 488 and anti-polyubiquitin primary antibodies, visualized using secondary antibodies conjugated to AlexaFluor 594. DAPI stained nuclei. Scale bar: 20 µm. The boxed region is enlarged, profile and surface plots were used to not show co-localisation (separate colours shown on graphics), (n =1).

6.2.2. eIF2Bα foci do not co-localise with P-bodies.

P-bodies are cytosolic dynamic compartments comprised of primarily mRNAs in complex with mRNA degradation machinery proteins (Ivanov *et al*., 2019). Their formation is intrinsically dependent on protein-RNA interactions, low-complexity sequences and LLPS, highlighting the similarity with other RNP granules (Banani *et al*., 2017). However, their composition and function distinguish them from other RNP granules.

As mentioned earlier, under conditions of cellular stress, cytoplasmic granules emerge, harboring translationally repressed mRNAs. Given the intriguing resemblance between eIF2B bodies and other translation-associated cytoplasmic granules, it becomes paramount to explore potential associations between these eIF2B structures and P-bodies. For this purpose, we subjected cells to acute stress induction, using ER stress treatment with Tg for 1 hour and oxidative stress with SA for 1 hour, followed by fixation and probing for eIF2Bα and DCP1A.

Confocal microscopy confirmed that eIF2Bα foci were spatially distinct from DCP1A containing P-bodies (**Figure 6.4**). Thus, these results suggest that eIF2Bα foci and P-bodies are independent molecular assemblies.

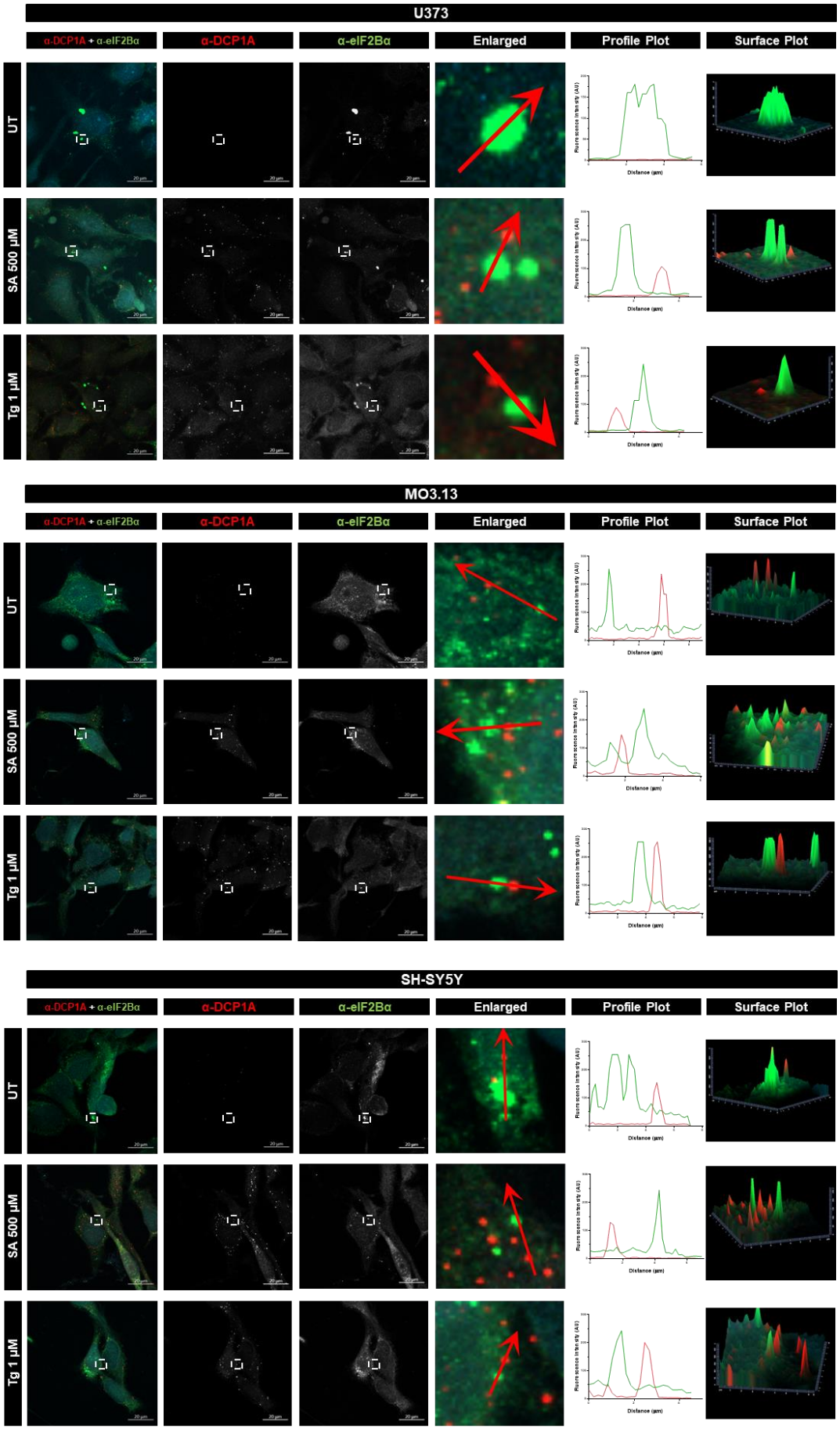

Figure 6. 4. eIF2Bα foci does not co-localise with DCP1A containing P-bodies.

Representative images of eIF2Bα and DCP1A, in untreated conditions, following SA 1h (500 μM) and Tg 1h (1 μM) treatments (UT – untreated). (Top to bottom) U373-MG, MO3.13 and SH-SY5Y cells were subjected to ICC with anti-eIF2Bα, visualised using secondary antibodies conjugated to AlexaFluor 488 and anti-DCP1A primary antibodies, visualized using secondary antibodies conjugated to AlexaFluor 594. DAPI stained nuclei. Scale bar: 20 μm. The boxed region is enlarged, profile and surface plots were used to not show co-localisation (separate colours shown on graphics), (n=1).

6.2.3. eIF2Bα co-localised with G3BP-containing stress granules following oxidative and ER stress

In a previous study, the eIF2Bε subunit has been shown to co-localise SG in mammalian cells (Kimball *et al*., 2003), while conflicting research in yeast and mammalian models have found that the eIF2B body formation is independent to SG (Hodgson *et al*., 2019; Moon & Parker, 2018). Additionally, *EIF2B1* has been shown to be an indispensable gene for SG assembly, highlighting its role within stress responsive pathways (Ohn *et al*., 2008). Thus, to observe if eIF2Bα foci interacted with SGs, cells were subjected to ER stress through Tg 1 hour treatment (1 μM) and oxidative stress through SA 30 minutes (125 μM) and 1 hour treatment (500 μM).

Cells were then probed with G3BP1, a SG core marker, and eIF2Bα, and co-localisation efforts were carried out in glial and neuronal cell lines (**Figure 6.5**).

In a population of 100 cells per biological repeat, a large percentage of cells formed SG following ER, through Tg treatment for 1 hour, and oxidative stress treatments, through SA treatment for 30 minutes and 1 hour (**Figure 6.6**).

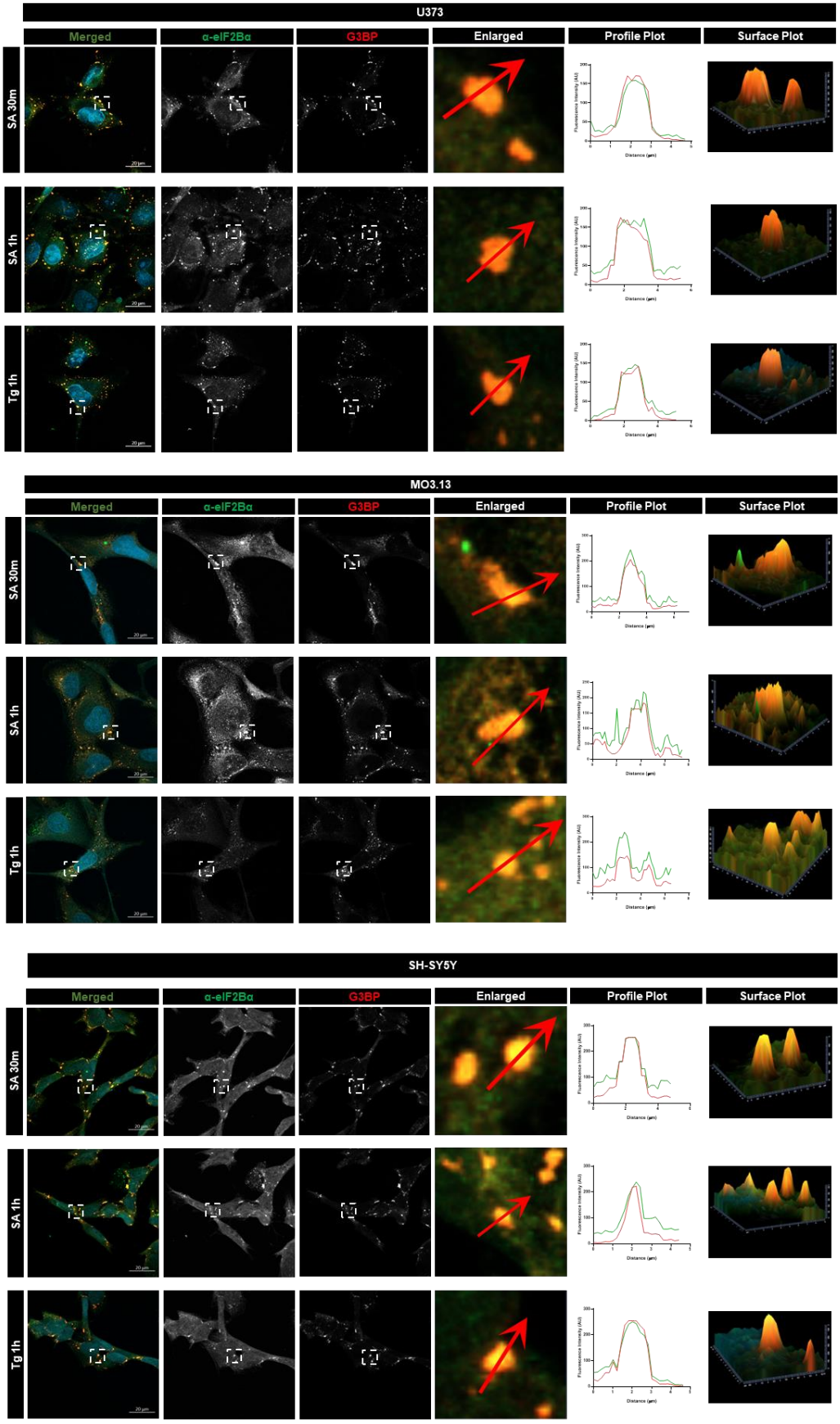

Figure 6.5. eIF2Bα foci displays co-localisation with G3BP-containing SGs.

Representative images of eIF2Bα and G3BP, in untreated conditions, following SA 30 minutes (125 μM), SA 1h (500 μM) and Tg 1h (1 μM) treatments. (Top to bottom) U373-MG, MO3.13 and

SH-SY5Y cells were subjected to ICC with anti-eIF2Bα, visualised using secondary antibodies conjugated to AlexaFluor 488 and anti-G3BP primary antibodies, visualized using secondary antibodies conjugated to AlexaFluor 594. DAPI stained nuclei. Scale bar: 20 μm. The boxed region is enlarged, profile and surface plots were used to not show co-localisation (separate colours shown on graphics).

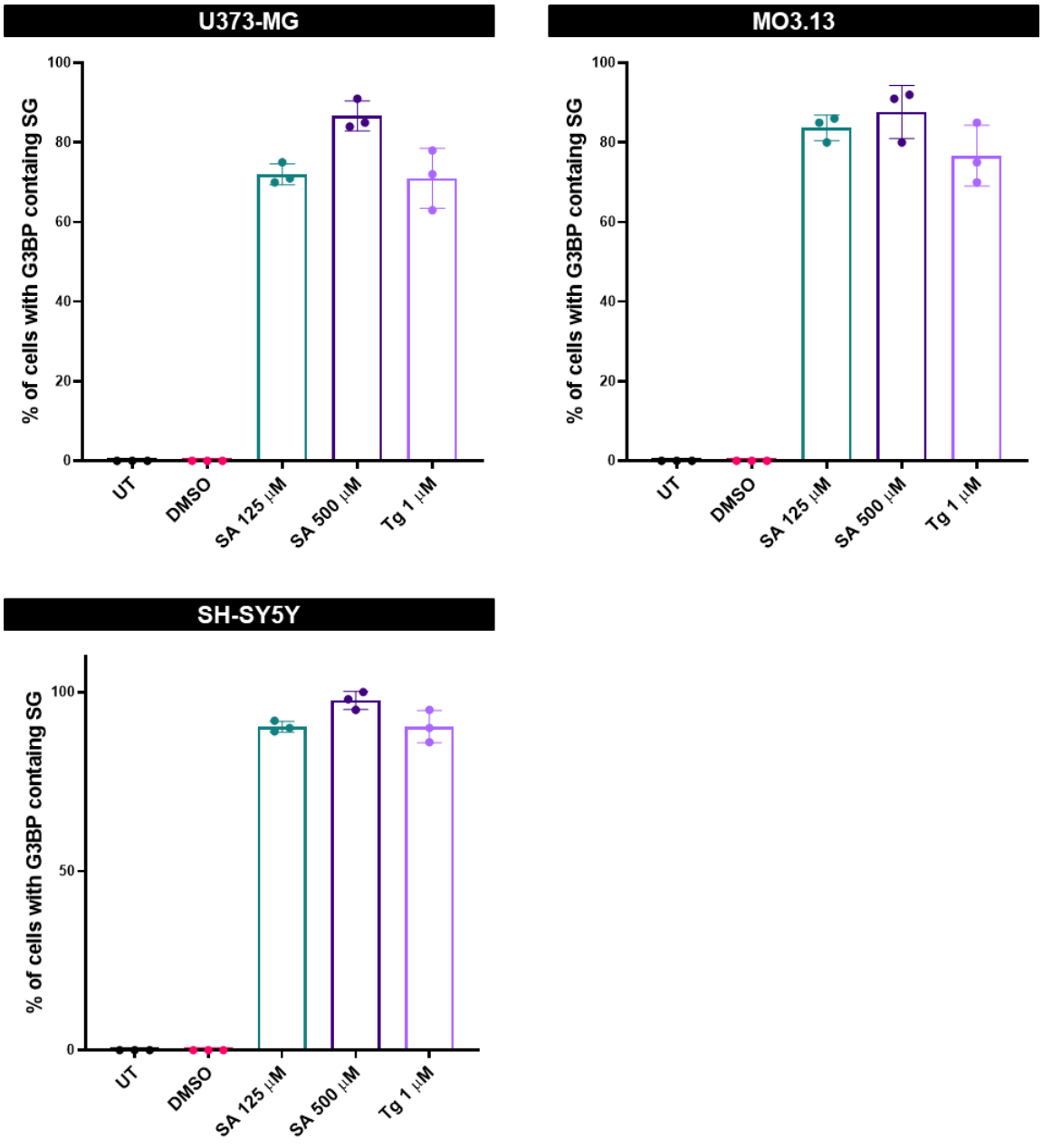

Figure 6.6. Oxidative and ER stress conditions lead to SG formation in glial and neuronal cells.

Mean percentage of U373-MG, MO3.13 and SH-SY5Y cells displaying G3BP-containing SGs in untreated conditions, DMSO 1h, SA 30 minutes (125 μM), SA 1h (500 μM) and Tg 1h (1 μM) treated cells (UT – untreated; n=3, counts of 100 cells per replicate). Error bars: ± s.d. (n=3).

In a population of 100 U373-MG cells per biological repeat, a significant increase of percentage of cells with localised eIF2Bα was observed after oxidative and ER stress induction (UT: 31.33 % ± 3.22; DMSO: 33.33 % ± 2.52; SA 125 μM: 84.33 % ± 3.22; SA 500 μM: 85.67 % ± 4.04; Tg 1 μM: 73.67 % ± 4.16) (**Figure 6.7A**). As seen previously in chapter 4, the number of small and large eIF2Bα foci increased after SA and Tg stress treatments (Small: UT – 3.73 ± 0.12; DMSO – 3.50 ± 0.74, SA 125 μM – 10.39 ± 2.26, SA 500 μM – 12.14 ± 2.10, Tg 1 μM – 8.63 ± 1.50; Large: UT – 1.10 ± 0.15, DMSO – 1.12 ± 0.36, SA 125 μM – 2.27 ± 0.90, SA 500 μM – 2.64 ± 1.48, Tg 1 μM – 2.26 ± 0.58) (**Figure 6.7B**). Interestingly, in U373-MG cells following SA treatment for 30 minutes, 41.09 % (816) foci of eIF2Bα and G3BP co-localised; SA treatment for 1 hour increased co-localisation to 46.00 % (983); and Tg treatment for 1h showed 48.70 % (655) of co-localisation (**Figure 6.7C**).

In a population of 100 MO3.13 cells per repeat, induction of acute stress led to a slight increase of percentages of cells with eIF2Bα foci (**Figure 6.8A**), which could be explained by the already prevalence presence of cells with eIF2Bα localisation in normal conditions. The number of small and large eIF2Bα foci per cell increased after SA and Tg stress treatments (Small: UT – 8.01 ± 0.54; DMSO – 7.12 ± 1.17; SA 125 μM – 18.17 ± 3.32, SA 500 μM – 19.47 ± 4.22, Tg 1 μM – 11.28 ± 1.56; Large: UT – 1.46 ± 0.37; DMSO – 1.26 ± 0.35; SA 125 μM – 2.84 ± 1.21 SA 500 μM – 3.32 ± 1.45, Tg 1 μM – 2.23 ± 0.38) (**Figure 6.8B**). When examining all eIF2Bα and G3BP foci detected in the three biological replicates following stress treatments described above, a large percentage co-localised, particularly following acute oxidate stress (SA 125 μM: 37.97 % foci co-localised – 919 total foci; SA 500 μM: 41.55 % foci co-localised – 1364 total foci; Tg 1 μM: 23.70 % foci co-localised – 682 total foci) (**Figure 6.8C**).

A slight, yet significant, increase of percentage of SH-SY5Y cells with eIF2Bα was found following oxidative stress (**Figure 6.9A**). It is of note, that the increase of percentage of cells with eIF2Bα after stress conditions, was coupled with a visible increase of the average number of small and large eIF2Bα foci (Small: UT – 5.16 ± 0.61, DMSO – 5.08 ± 0.65, SA 125 μM – 6.74 ± 1.78, SA 500 μM – 12.07 ± 4.20, Tg 1 μM – 6.01 ± 2.35; Large: UT – 1.17 ± 0.17, DMSO – 1.00 ± 0.03, SA 125 μM – 1.88 ± 0.98 SA 500 μM – 2.00 ± 0.84, Tg 1 μM – 2.52 ± 0.41) (**Figure 6.9B**). Considerable percentages of co-localisation between eIF2Bα and G3BP containing SG were found throughout all three stress conditions in SH-SY5Y

cells, with the majority of G3BP detected assemblies co-localising with eIF2Bα (SA 125 µM: 38.57 % foci co-localised – 444 total foci; SA 500 µM: 34.25 % foci co-localised – 572 total foci; Tg 1 µM: 51.79 % foci co-localised – 491 total foci) (**Figure 6.9C**).

Generally, a high degree of co-localisation was observed between eIF2Bα foci and SGs in glial and neuronal cells, particularly in response to oxidative stress. However, the outcomes following ER stress induction displayed some variability, with glial cells exhibiting a higher prevalence of independent molecular assemblies of eIF2Bα and SG compared to neuronal cells (**Figure 6.7C, Figure 6.8C, and Figure 6.9C**). This observation may potentially be linked to the total number of G3BP and eIF2Bα foci detected, particularly in glial cells, where a substantial increase in foci was discerned.

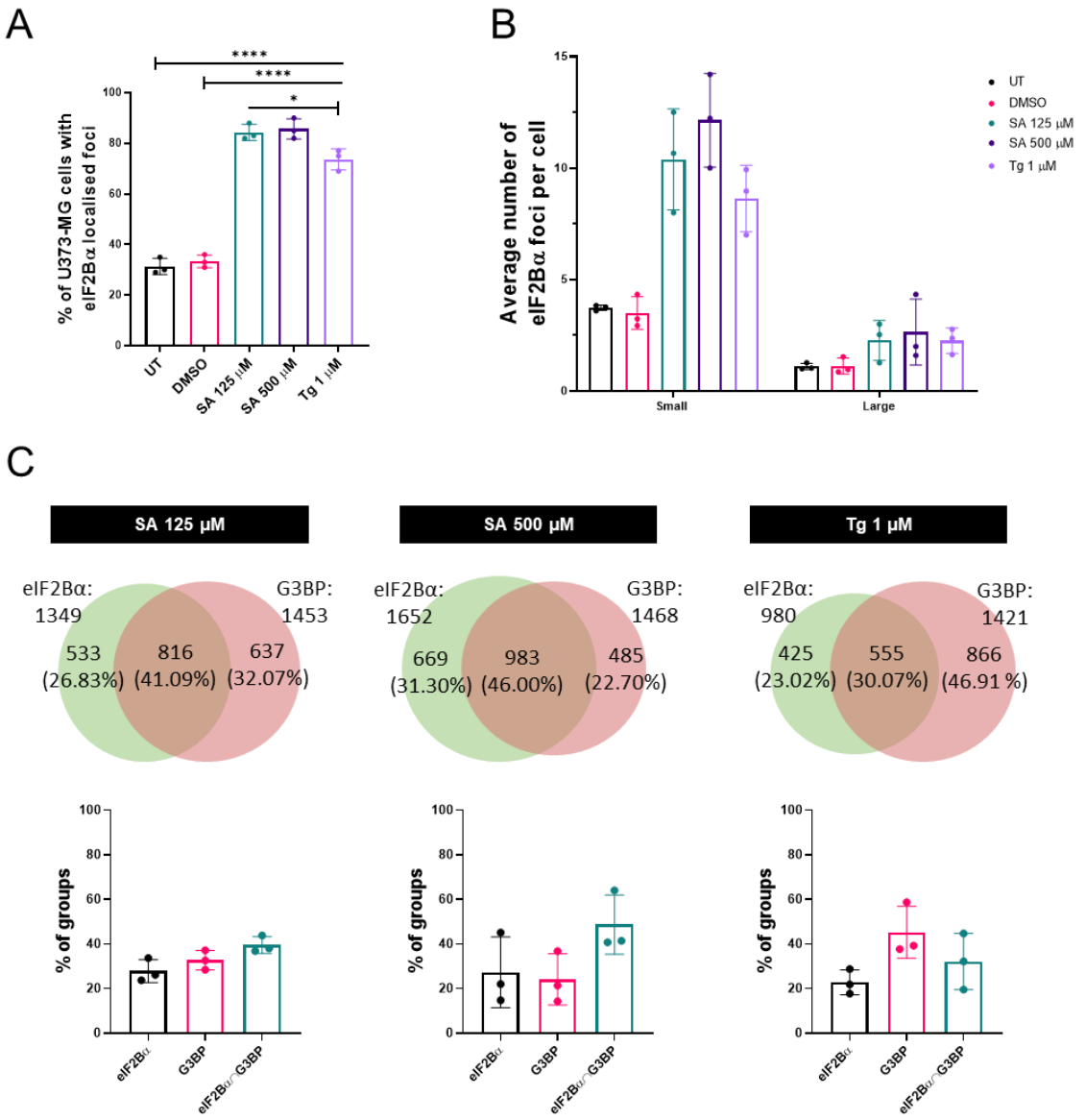

Figure 6.7. eIF2Bα co-localises with G3BP-containing SGs in U373-MG cells.

U373-MG cells were under untreated conditions, DMSO 1h, SA 30 minutes (125 μM), SA 1h (500 μM) and Tg 1h (1 μM) treatments (UT – untreated). (A) Mean percentage of U373-MG cells displaying one or more eIF2Bα foci in a population of 100 cells per repeat. Error bars: ± s.d. (n=3). Data was analysed using one-way ANOVA followed by a Tukey's multiple analysis. *$p \leq 0.05$, ****$p \leq 0.0001$. (B) Average number of small and large eIF2Bα foci per cell in a population of 30 cells per repeat with localised eIF2Bα foci (n=3). Error bars: ± s.d. (C) Venn diagram of eIF2Bα and G3BP foci and co-localisation (n=3 counts in 30 cells with eIF2Bα localisation). Total number of all three repeats were used to determine percentages of groups. Bar graph of each biological repeat of each group. Error bars: ± s.d.

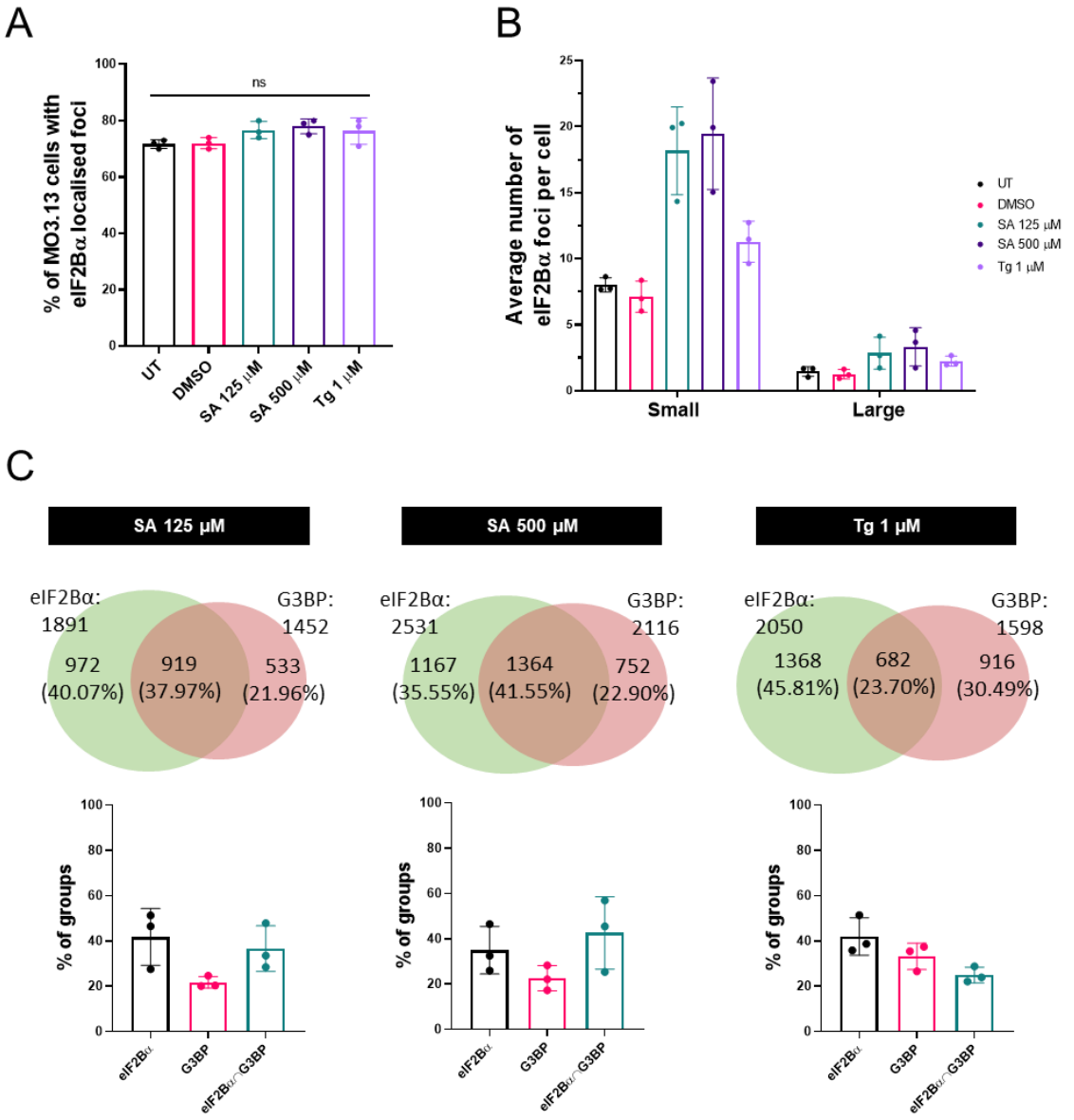

Figure 6.8. eIF2Bα co-localises with G3BP-containing SGs in MO3.13 cells.

MO3.13 cells were under untreated conditions, DMSO 1h, SA 30 minutes (125 μM), SA 1h (500 μM) and Tg 1h (1 μM) treatments (UT – untreated). (A) Mean percentage of MO3.13 cells displaying one or more eIF2Bα foci in a population of 100 cells per repeat. Error bars: ± s.d. (n=3). Data was analysed using one-way ANOVA followed by a Tukey's multiple analysis. (B) Average number of small and large eIF2Bα foci per cell in a population of 30 cells per repeat with localised eIF2Bα foci (n=3). Error bars: ± s.d. (C) Venn diagram of eIF2Bα and G3BP foci and co-localisation (n=3 counts in 30 cells with eIF2Bα localisation). Total number of all three repeats were used to determine percentages of groups. Bar graph of each biological repeat of each group. Error bars: ± s.d.

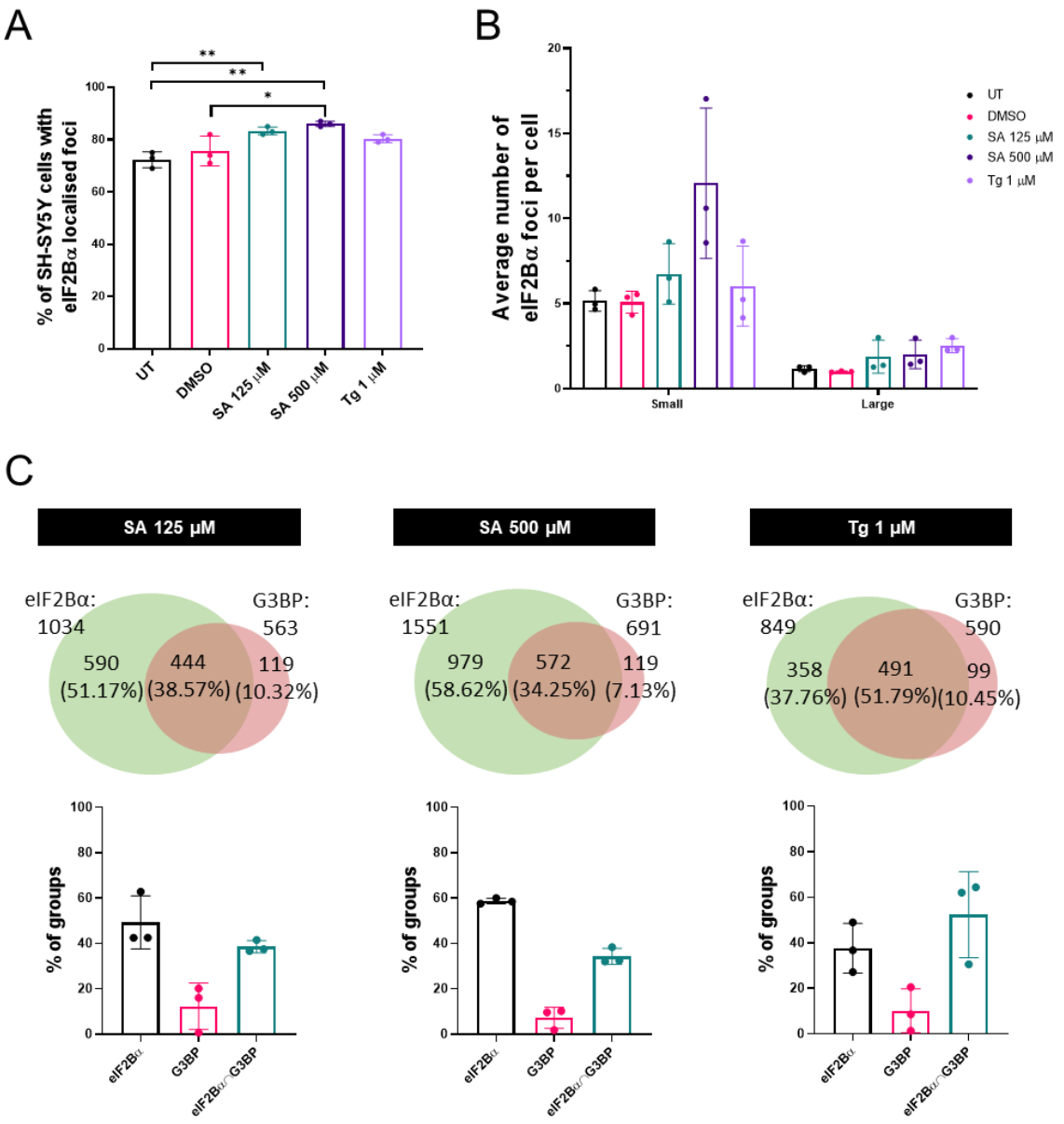

Figure 6. 9. eIF2Bα co-localises with G3BP-containing SGs in SH-SY5Y cells.

SH-SY5Y cells were under untreated conditions, DMSO 1h, SA 30 minutes (125 μM), SA 1h (500 μM) and Tg 1h (1 μM) treatments (UT – untreated). (A) Mean percentage of SH-SY5Y cells displaying one or more eIF2Bα foci in a population of 100 cells per repeat. Error bars: ± s.d. (n=3). Data was analysed using one-way ANOVA followed by a Tukey's multiple analysis. *$p \leq 0.05$, **$p \leq 0.01$. (B) Average number of small and large eIF2Bα foci per cell in a population of 30 cells per repeat with localised eIF2Bα foci (n=3). Error bars: ± s.d. (C) Venn diagram of eIF2Bα and G3BP foci and co-localisation (n=3 counts in 30 cells with eIF2Bα localisation). Total number of all three repeats were used to determine percentages of groups. Bar graph of each biological repeat of each group. Error bars: ± s.d.

6.2.4. eIF2Bε largely does not co-localised with G3BP containing stress granules following oxidative stress.

As previously mentioned, the existing literature presents conflicting findings concerning the interaction of eIF2Bε with SGs. Furthermore, the emerging evidence highlighting the recruitment of translating mRNA to SGs (Mateju *et al*., 2020) suggests a potential role for SGs beyond mere translation repression, possibly serving as hubs for translation initiation. Additionally, given the high percentage of eIF2Bα co-localising with SGs, as described in **section 6.2.3**, we aimed to investigate the potential spatial interaction between eIF2Bε and SGs in glial and neuronal cell lines.

We carried out co-localisation investigations between G3BP and eIF2Bε in SH-SY5Y cells (**Figure 6.10A**).

In a population of 100 SH-SY5Y cells per repeat, induction of acute stress led to a significant increase of percentage of cells with localised eIF2Bε (Vehicle: 14.33 % ± 1.53; SA 500 µM: 64.00 % ± 5.57) (**Figure 6.10B**). The number of small eIF2Bε foci increased under stress conditions (Small: Vehicle – 2.89 ± 0.64, SA 500 µM – 10.54 ± 2.21; Large: Vehicle – 1.64 ± 0.16, SA 500 µM – 1.36 ± 0.74) (**Figure 6.10C**). When analyzing the total detected foci of eIF2Bε and G3BP in the three biological replicates following SA 500 µM stress and how these two groups interacted, a small percentage of eIF2Bε and G3BP co-localised (1.07 % foci co-localised – 19 total foci), with the majority of eIF2Bε foci and G3BP-containing SGs not spatially interacting (**Figure 6.10D**). Additionally, Airyscan imaging was performed in eIF2Bε, eIF2Bα and G3BP foci (**Figure 6.11**). Considering co-localisation parameters discussed in **section 2.7.2** and **figure 2.2**, it was possible to observe that while a proximity between eIF2Bε and G3BP foci was present, co-localisation was not observed. It is of note, the targets were on different Z-stack planes, thus creating the appearance of close proximity (data not shown). Conversely, eIF2Bα and G3BP-containing SG entirely spatially overlapped (**Figure 6.11**).

These results indicate that eIF2Bε foci and G3BP-containing SGs are distinct molecular assemblies.

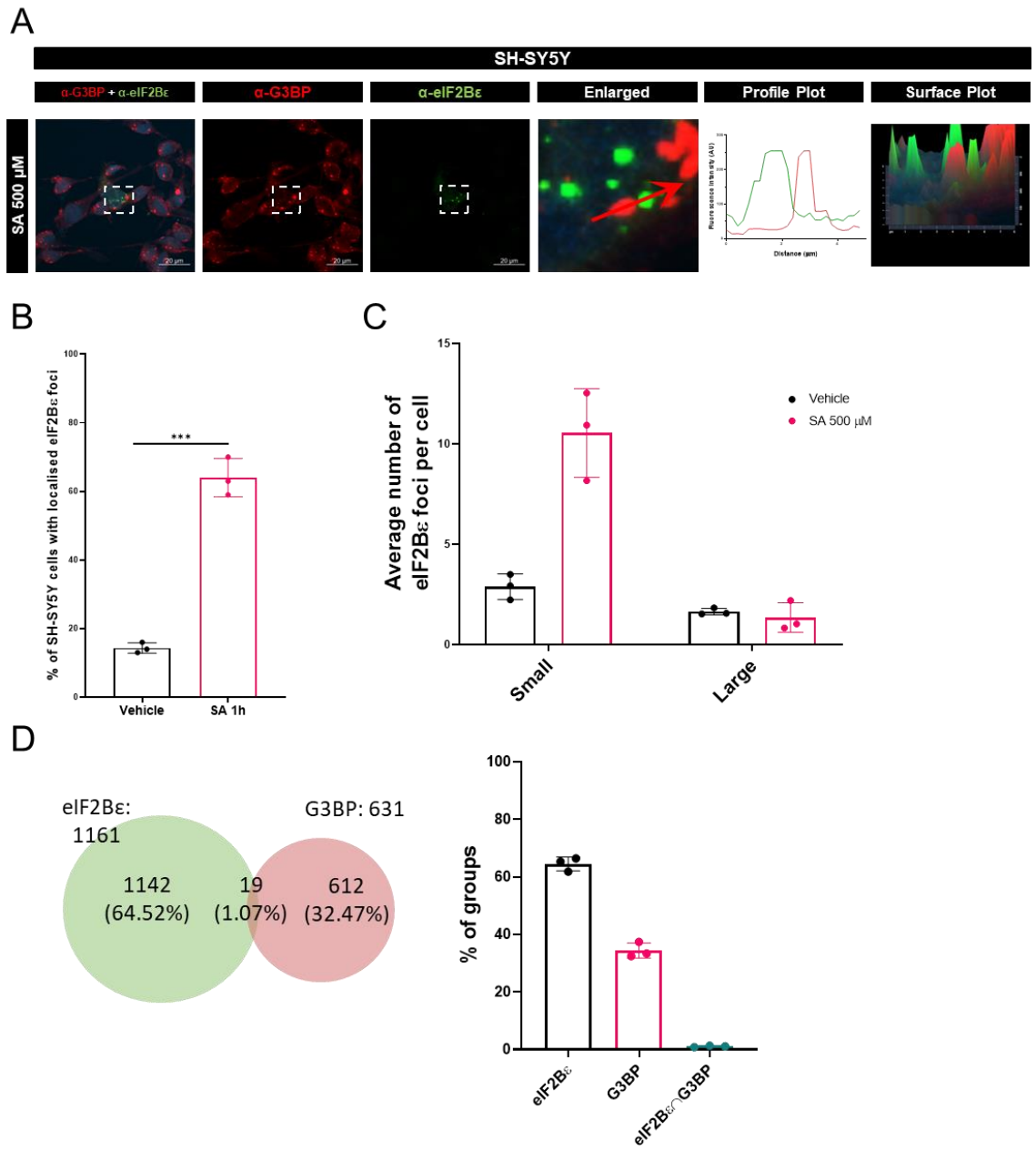

Figure 6.10. eIF2Bε does not co-localise with G3BP-containing SGs in SH-SY5Y cells. SH-SY5Y cells were under DMSO 1h (vehicle) and SA 1h (500 μM) treatments. (A) Representative images of eIF2Bε and G3BP SA 1h (500 μM) treatments. SH-SY5Y cells were subjected to ICC with anti-eIF2Bε, visualised using secondary antibodies conjugated to AlexaFluor 488 and anti-G3BP primary antibodies, visualized using secondary antibodies conjugated to AlexaFluor 594. DAPI stained nuclei. Scale bar: 20 μm. The boxed region is enlarged, profile and surface plots were used to not show co-localisation (separate colours shown on graphics). (B) Mean percentage of SH-SY5Y cells displaying one or more eIF2Bα foci in a population of 100 cells per repeat. Error bars: ± s.d. (n=3). Data was analysed using one-way ANOVA followed by a Tukey's multiple analysis. ***$p \leq 0.001$. (C) Average number of small and large eIF2Bε foci per cell in a population of 30 cells per repeat with localised eIF2Bε foci (n=3). Error bars: ± s.d. (D) Venn diagram of eIF2Bε and G3BP foci and co-localisation (n=3 counts in 30 cells with eIF2Bε localisation). Total number of all three repeats were used to determine percentages of groups. Bar graph of each biological repeat of each group. Error bars: ± s.d.

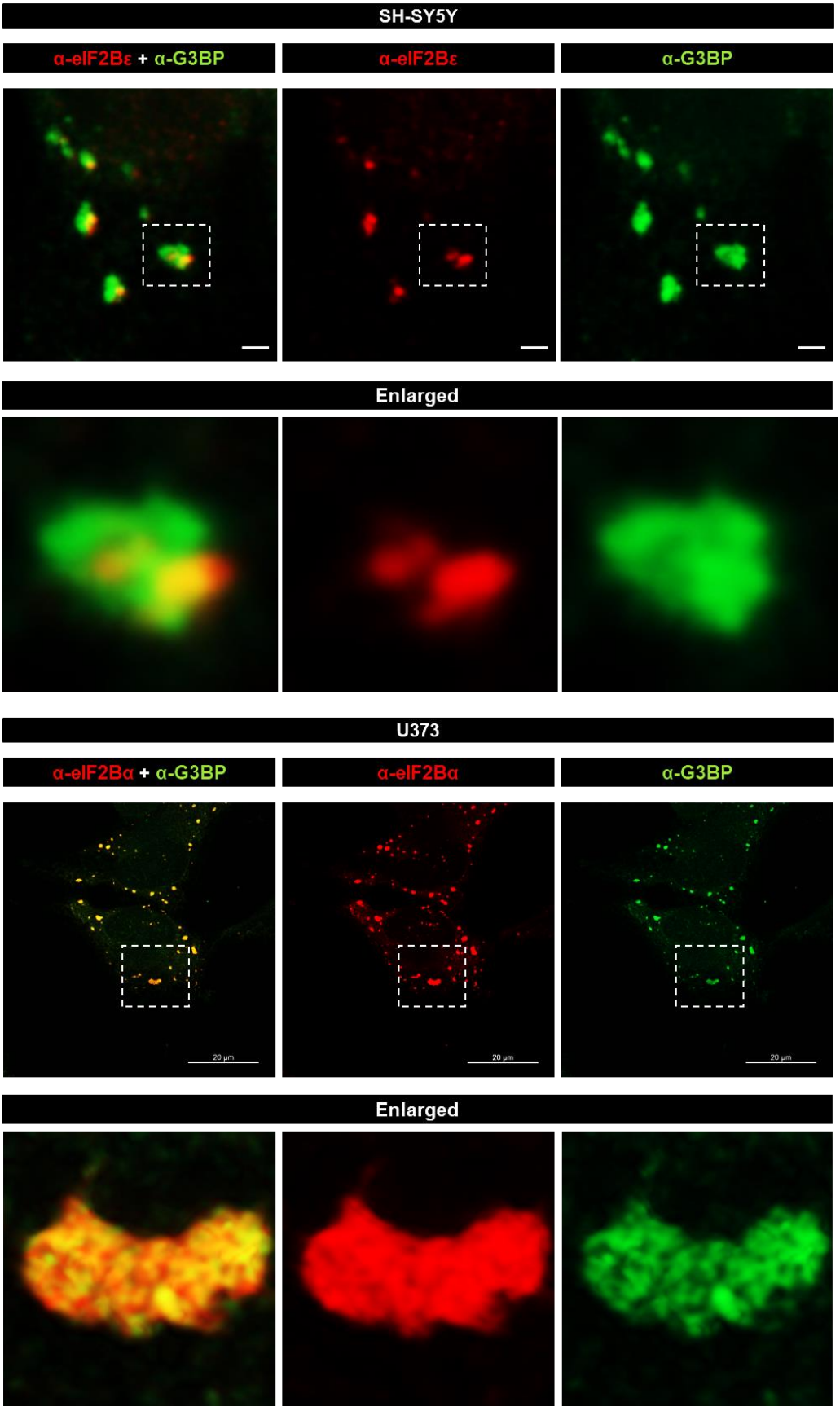

Figure 6.11. Airyscan imaging of eIF2Bε and eIF2Bα co-localisation with G3BP.

Representative Airyscan images following orthogonal projection of Z-stacks of eIF2Bε and G3BP (top panel) and eIF2Bα and G3BP (bottom panel) following SA 1h (500 µM) treatments in SH-SY5Y and U373 cells. Top panel scale bar: 1 µM. Bottom panel scale bar: 20 µM.

6.2.5. Mutations in the eIF2Bα subunit appear to alter SG formation.

We next investigated the assembly dynamics of SGs in response to the induction of phosphorylated eIF2α in a *EIF2B1*$^{L100P/WT}$ variant context (**Figure 6.12**). We utilised an ovarian adenocarcinoma SKOV3 stable cell line bearing a heterozygous *EIF2B1*$^{L100P/WT}$ Gcn- mutation, which is unresponsive to ISR activation, and its wild-type counterpart (Powers, *et al*., – unpublished data). A population of 100 SKOV3 cells were analysed per repeat. WT SKOV3 cells showed a significant increase of cells with eIF2Bα localised foci upon stress induction (Vehicle: 23.67 % ± 1.53; SA 500 μM: 64.00 % ± 7.00), while the mutant *EIF2B1*$^{L100P/WT}$ SKOV3 showed a similar percentage throughout the different conditions (Vehicle: 22.67 % ± 4.73; SA 500 μM: 32.00 % ± 2.65) (**Figure 6.13A**). Additionally, while there was an increase of the average number of small and large eIF2Bα in wild-type SKOV3 cells following SA 500 μM treatment (Small: vehicle – 2.36 ± 0.29, SA 500 μM – 5.09 ± 0.37; Large: vehicle – 1.60 ± 0.15, SA 500 μM – 2.87 ± 0.09), the same was not present in the mutant cells (Small: vehicle – 2.93 ± 0.29, SA 500 μM – 2.72 ± 0.05; Large: vehicle – 1.22 ± 0.25, SA 500 μM – 1.07 ± 0.23) (**Figure 6.13B**). When examining the percentage of total localised foci, the wild-type SKOV3 cells displayed 31.01 % of foci co-localised, whereas the mutant cell line exhibited only 3.97 % of foci co-localised (**Figure 6.13C**). In the context of mutant SKOV3 cells, the heterozygous presence of the *EIF2B1*^{L100P} mutation poses a potential hindrance to the interaction between the eIF2Bα subunit and p-eIF2α during the ISR. This disruption in the interaction interface may engender an insensitivity of the eIF2B structure to p-eIF2α, thereby impeding the sequestration of translation initiation. This was further revealed by Powers *et al*., (unpublished data) through the lack of ISR markers in mutant *EIF2B1*$^{L100P/WT}$ SKOV3 cells upon stress conditions. Upon subjecting the mutant cells to stress conditions, a notable reduction in SG formation was observed, aligning with a reduction in the increase of cells exhibiting eIF2Bα localisation and an absence of increased numbers of both small and large eIF2Bα foci. These cumulative results strongly suggest an inability of these *EIF2B1*$^{L100P/WT}$ mutant cells to mount an eIF2B-dependent regulatory response to oxidative stress.

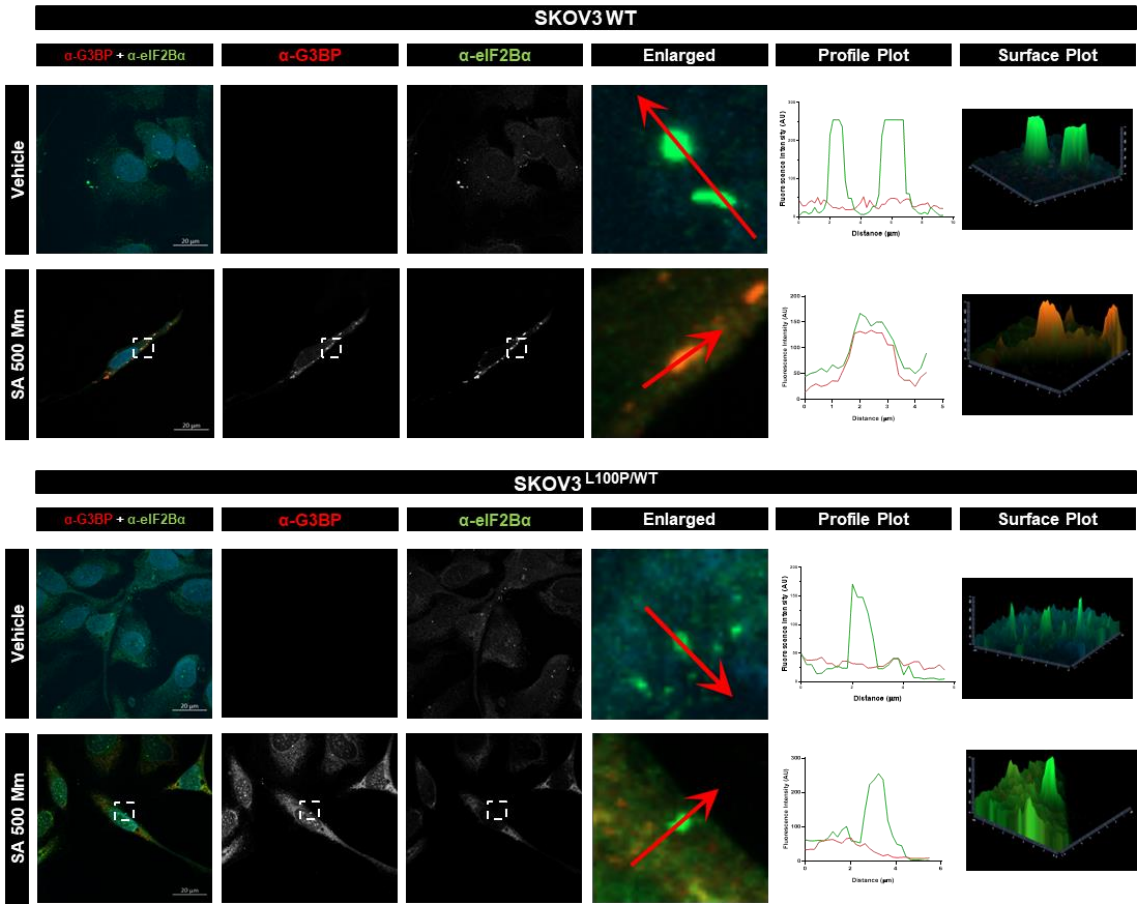

Figure 6.12. eIF2Bα shows co-localisation with G3BP-containing SGs in SKOV3 WT cells, while *EIF2B1*$^{L100P/WT}$ led to impaired SG formation.

Representative images of eIF2Bα and G3BP SA 1h (500 μM) treatments in SKOV3 WT and *EIF2B1*$^{L100P/WT}$ cells were subjected to ICC with anti-eIF2Bα, visualised using secondary antibodies conjugated to AlexaFluor 488 and anti-G3BP primary antibodies, visualized using secondary antibodies conjugated to AlexaFluor 594. DAPI stained nuclei. Scale bar: 20 μm. The boxed region is enlarged, profile and surface plots were used to not show co-localisation (separate colours shown on graphics).

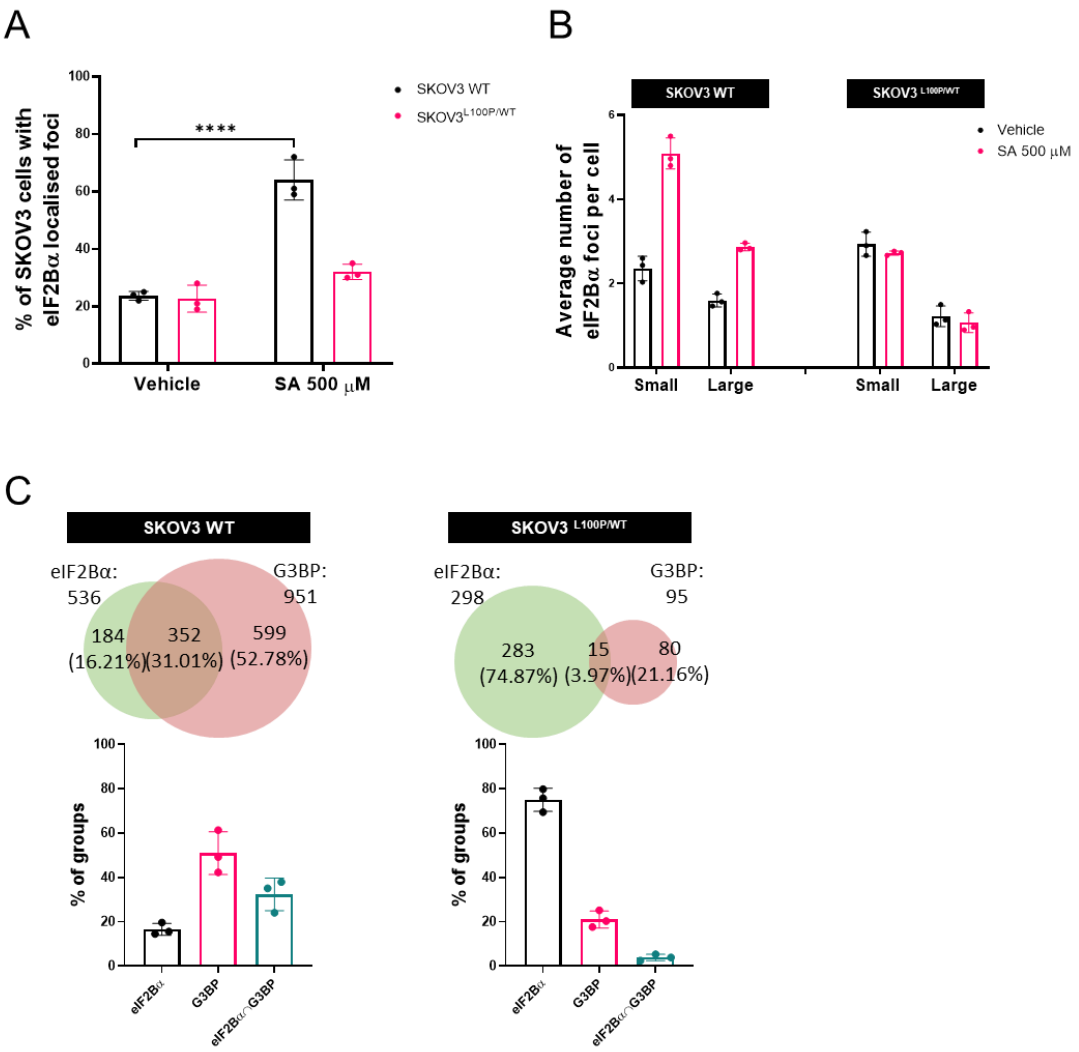

Figure 6.13. eIF2Bα co-localises with G3BP-containing SGs in SKOV3 WT cells, while *EIF2B1*$^{L100P/WT}$ led to impaired SG formation.

SKOV3 WT and *EIF2B1*$^{L100P/WT}$ cells were under DMSO 1h (vehicle) and SA 1h (500 μM) treatments. (A) Mean percentage of cells displaying one or more eIF2Bα foci in a population of 100 cells per repeat. Error bars: ± s.d. (n=3). Data was analysed using one-way ANOVA followed by a Tukey's multiple analysis. *$p \leq 0.05$, **$p \leq 0.01$. (B) Average number of small and large eIF2Bα foci per cell in a population of 30 cells per repeat with localised eIF2Bα foci (n=3). Error bars: ± s.d. (C) Venn diagram of eIF2Bα and G3BP foci and co-localisation (n=3 counts in 30 cells with eIF2Bα localisation). Total number of all three repeats were used to determine percentages of groups. Bar graph of each biological repeat of each group. Error bars: ± s.d.

6.2.6. eIF2Bα relocation to SG is dependent on p-eIF2α

Having confirmed the essential role of eIF2Bα in sensing stress and facilitating the formation of SGs under p-eIF2α dependent conditions, and observing its interaction and co-localisation with SGs, we sought to delve deeper into the relationship between eIF2Bα and eIF2α in this stress pathway.

While some stresses are strictly dependent on eIF2α phosphorylation for SG formation, others are not. H_2O_2 is an agent which induces ROS, leading to oxidative stress. While H_2O_2 may induce some degree of p-eIF2α, it is noteworthy that p-eIF2α itself is not necessary for the formation of H_2O_2-induced SGs, unlike the case with SA-induced SGs (Emara *et al*., 2012; Palangi *et al*., 2017). H_2O_2, through its indirect influence, facilitates the binding of 4E-BP1 to eIF4E by promoting a state of hypo-phosphorylation in 4E-BP1 (Emara *et al*., 2012; Palangi *et al*., 2017). Additionally, RocA, an agent known for its translation inhibitory effects in an eIF2α-independent manner by targeting the RNA helicase eIF4A, triggers the formation of SGs. Notably, these foci exhibit positive staining for core SG markers, yet intriguingly, they display a negative signal for poly(A) mRNAs, indicating a selective impact on specific mRNA populations within these RocA-induced foci (Aulas *et al*., 2017; M. Chen *et al*., 2021). Accordingly, we utilised these stressors in U373-MG cells, along with both WT and mutant SKOV3 cells, in order to scrutinize the eIF2B-dependent and independent stress response and its multifaceted implications on SG formation. Moreover, we sought to gain deeper insights into the interaction of eIF2Bα with SGs under the influence of p-eIF2α-dependent and independent pathways by examining U373-MG, SKOV3 WT and *EIF2B1*$^{L100P/WT}$ following stress conditions (**Figure 6.14**).

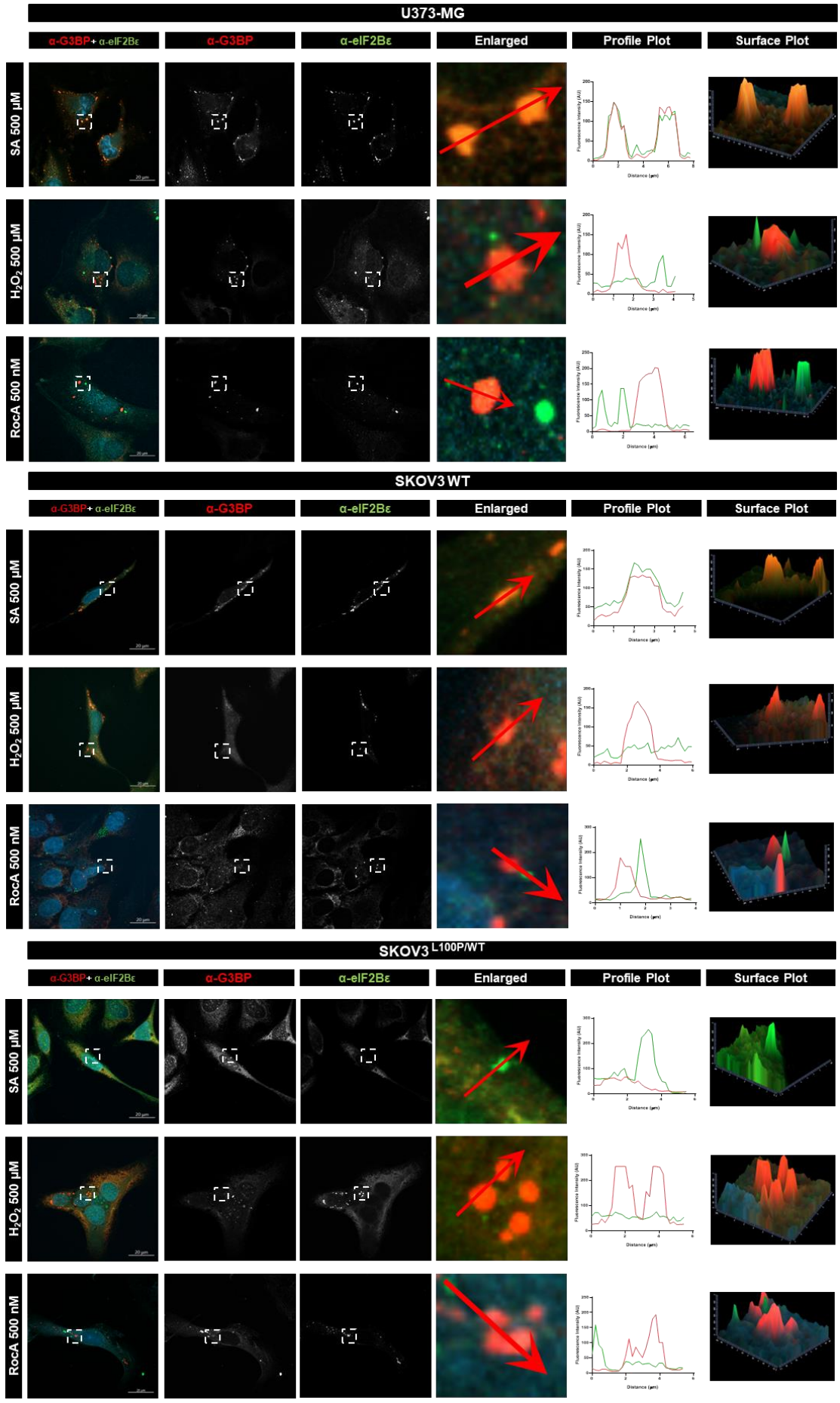

Figure 6.14. eIF2Bα shows co-localisation with G3BP in a p-eIF2α dependent manner.

U373-MG, SKOV3 WT and *EIF2B1*$^{L100P/WT}$ cells were under H_2O_2 1h (500 µM) and RocA 1h (500 nm) treatments. Data from SA 1h (500µM) treatments in **6.5** and **6.12** was used in this figure. Representative images of eIF2Bα and G3BP in U373-MG, SKOV3 WT and *EIF2B1*$^{L100P/WT}$ cells were subjected to ICC with anti-eIF2Bα, visualised using secondary antibodies conjugated to AlexaFluor 488 and anti-G3BP primary antibodies, visualized using secondary antibodies conjugated to AlexaFluor 594. DAPI stained nuclei. Scale bar: 20 µm. The boxed region is enlarged, profile and surface plots were used to not show co-localisation (separate colours shown on graphics).

The percentage of U373-MG and WT SKOV3 cells exhibiting eIF2Bα localisation displayed a notable increase in response to SA 500 µM treatment, while the mutant cells did not exhibit such a response. Our investigations revealed that both H_2O_2 and RocA treatments failed to induce as a significant increase in cells with eIF2Bα localisation across all three cell lines under examination (**Figure 6.15A**).

Additionally, when looking at the average number of eIF2Bα foci following stress conditions, the increase of small and large foci was not present following H_2O_2 and RocA treatments in all cell lines analysed, a distinct contrast from the results observed with SA stress (**Figure 6.15B**). This marked disparity underscores the distinct responses elicited by these stressors compared to the SA-induced stress, elucidating the variations in eIF2Bα foci dynamics in the face of different cellular challenges.

Upon analyzing the percentages of cells exhibiting SG assembly in response to H_2O_2 and RocA, important distinctions emerge. It is of note that H_2O_2 induces a higher percentage of U373-MG cells to assemble SGs when compared to SKOV3 cells (U373: 72.00 % ± 8.88; SKOV3 WT: 25.00 % ± 5.57; SKOV3$^{L100P/WT}$ 32.00 % ± 6.25). However, this discrepancy could potentially be attributed to the fact that SKOV3 cells displayed cell death following exposure to these stress conditions, necessitating further optimisation for more precise evaluation (data not shown). RocA also induces SG assembly in all examined cell lines at a higher percentage in U373-MG (U373: 65.33 % ± 3.22; SKOV3 WT: 48.67 % ± 3.06; SKOV3$^{L100P/WT}$ 51.67 % ± 9.45). From these observations, we can deduce that the p-eIF2α dependent stress response is profoundly influenced by *EIF2B1* mutations which have been known to not respond to stress induction. p-eIF2α independent stresses bypass this, thereby making SG assembly feasible even in the presence of Gcn- eIF2Bα mutations (**Figure 6.16**). While the SA and Tg treatments, as observed in **section 6.2.3**, led to a substantial percentage of co-localisation between eIF2Bα and SG, the H_2O_2 and RocA conditions displayed a notably reduced overall interaction across all examined cell lines (U373: H_2O_2 – 4.25 % of foci, RocA 5.28 % of foci; SKOV3 WT: H_2O_2 – 3.15 % of foci, RocA 10.50 % of foci; SKOV3$^{L100P/WT}$: H_2O_2 – 3.47 % of foci, RocA 4.93 % of foci) (**Figure 6.16**). These conditions in turn show did not induce phosphorylation of eIF2α in glial and neuronal cell lines (**Figure 6.17**).

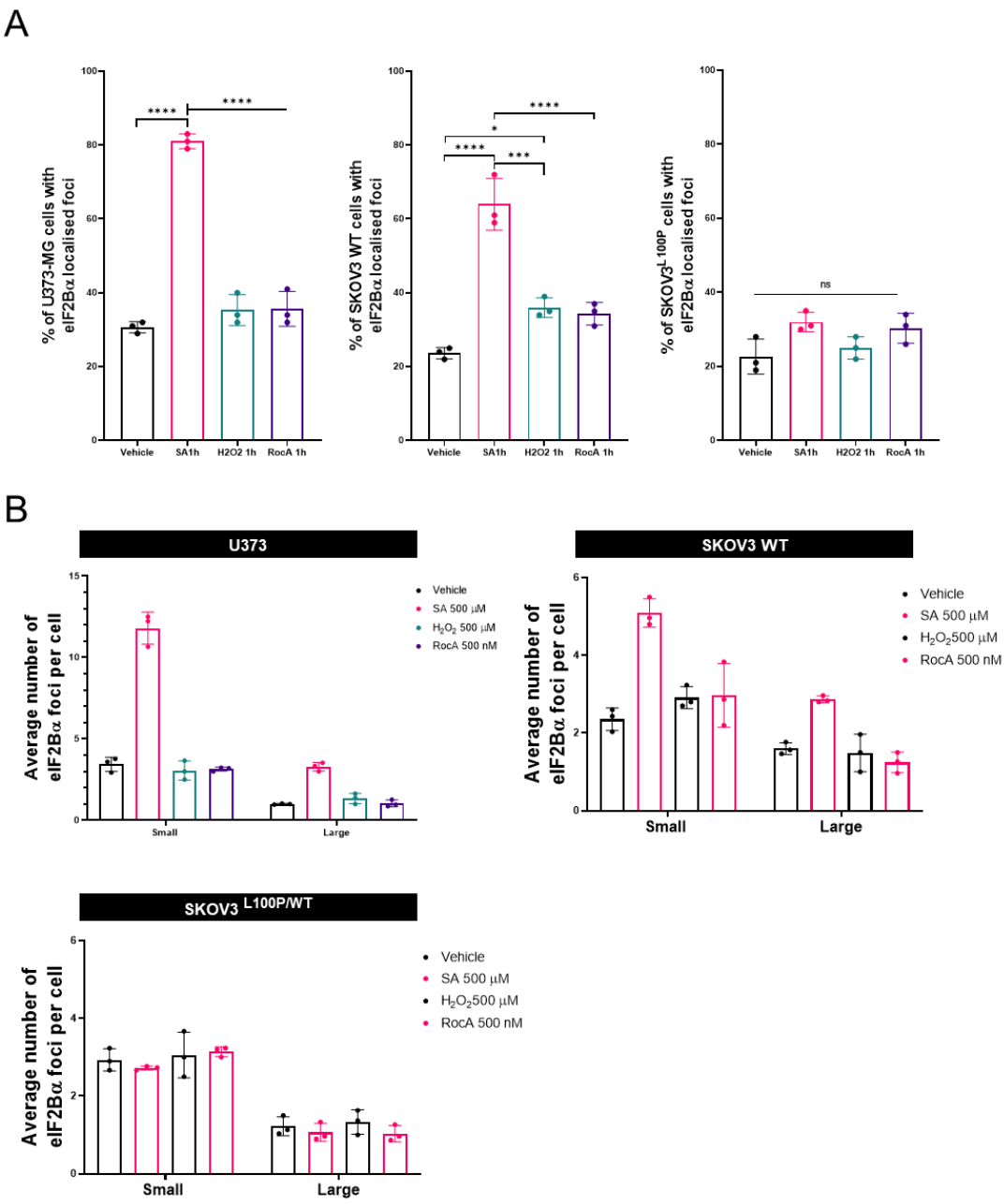

Figure 6.15. Formation eIF2Bα foci is not impacted by stress in *EIF2B1*$^{L100P/WT}$ cells. U373-MG, SKOV3 WT and *EIF2B1*$^{L100P/WT}$ cells were under untreated conditions, and H_2O_2 1h (500 µM) and RocA 1h (500 nm) treatments. Data from SA 1h (500 µM) treatments in **6.5** and **6.12** was used in this figure. (A) Mean percentage of cells displaying one or more eIF2Bα foci in a population of 100 cells per repeat. Error bars: ± s.d. (n=3). Data was analysed using one-way ANOVA followed by a Tukey's multiple analysis. *$p \leq 0.05$, ***$p \leq 0.001$, ****$p \leq 0.0001$. (B) Average number of small and large eIF2Bα foci per cell in a population of 30 cells per repeat with localised eIF2Bα foci (n=3). Error bars: ± s.d.

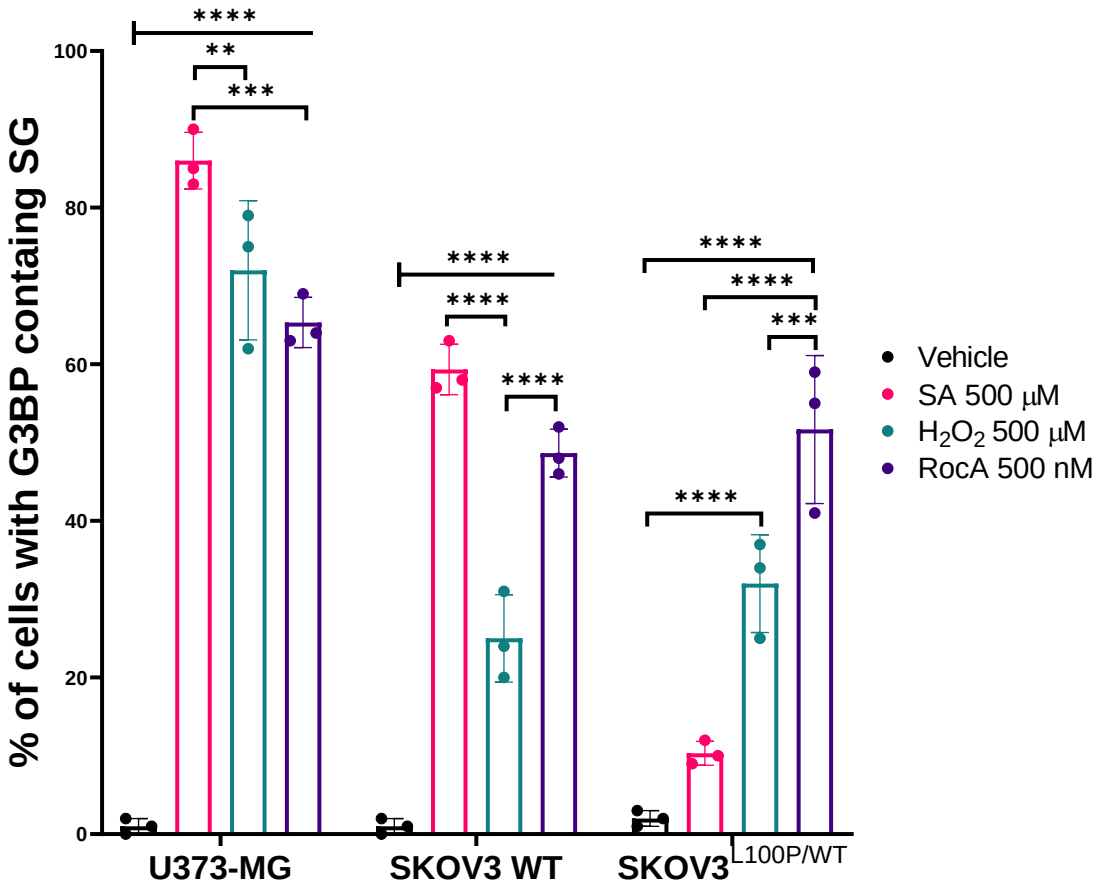

Figure 6.16. SG formation is impacted by heterozygous *EIF2B1*$^{L100P/WT}$ mutations.
U373-MG, SKOV3 WT and *EIF2B1*$^{L100P/WT}$ cells were under untreated conditions, and H_2O_2 1h (500 µM) and RocA 1h (500 nm) treatments. Data from SA 1h (500 µM) treatments in **6.5** and **6.12** was used in this figure. Mean percentage of cells displaying G3BP-containing SGs in a population of 100 cells per repeat. Error bars: ± s.d. (n=3). Data was analysed using one-way ANOVA followed by a Tukey's multiple analysis. $^{**}p \leq 0.01$, $^{***}p \leq 0.001$, $^{****}p \leq 0.0001$.

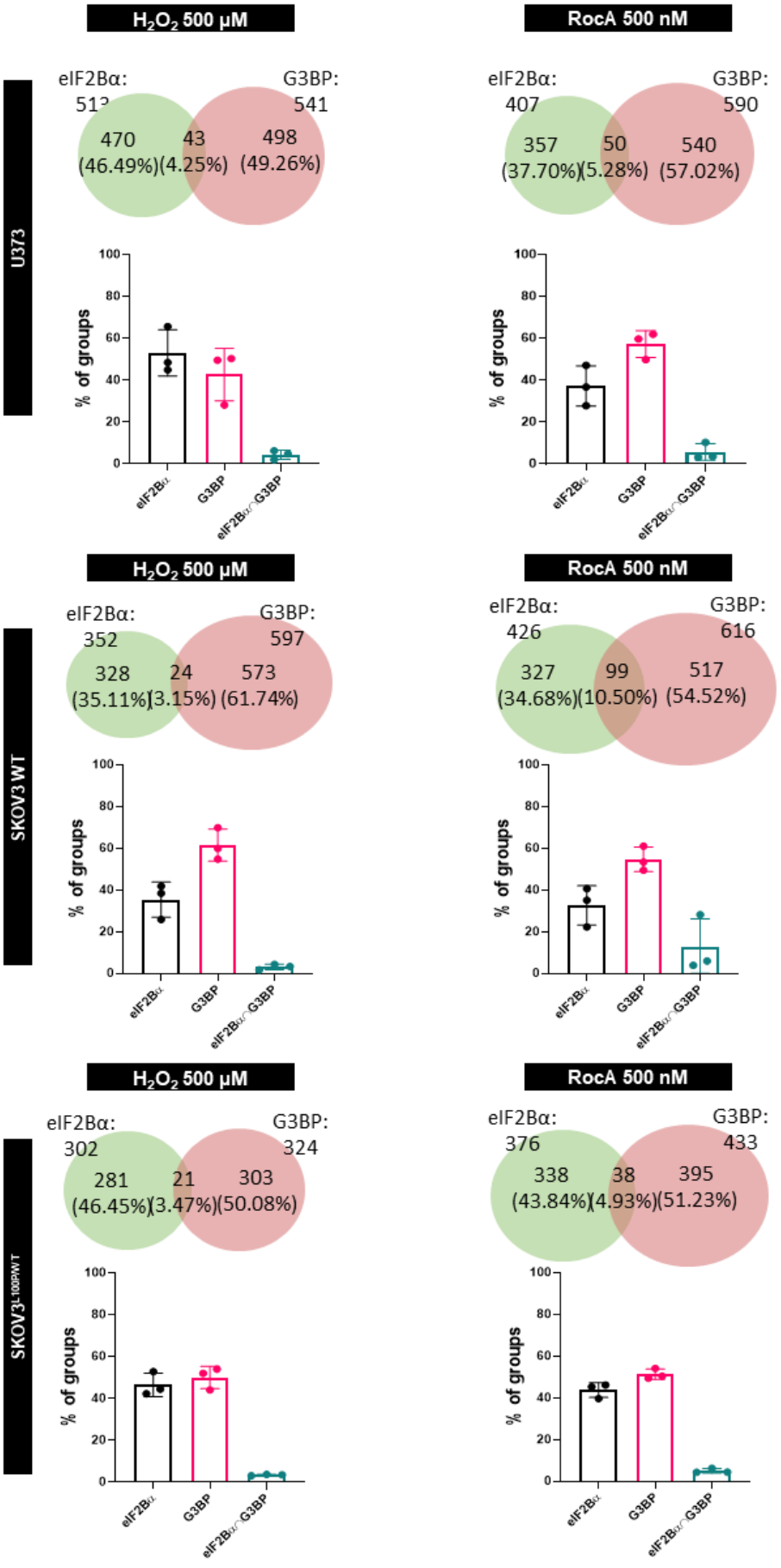

Figure 6.17. SG co-localisation with eIF2Bα is impacted by heterozygous *EIF2B1*$^{L100P/WT}$ mutations.

U373-MG, SKOV3 WT and *EIF2B1*$^{L100P/WT}$ cells under H_2O_2 1h (500 μM) and RocA 1h (500 nm) treatments. Venn diagram of eIF2Bα and G3BP foci and co-localisation (n=3 counts in 30 cells with eIF2Bα localisation). Total number of all three repeats were used to determine percentages of groups. Bar graph of each biological repeat of each group. Error bars: ± s.d.

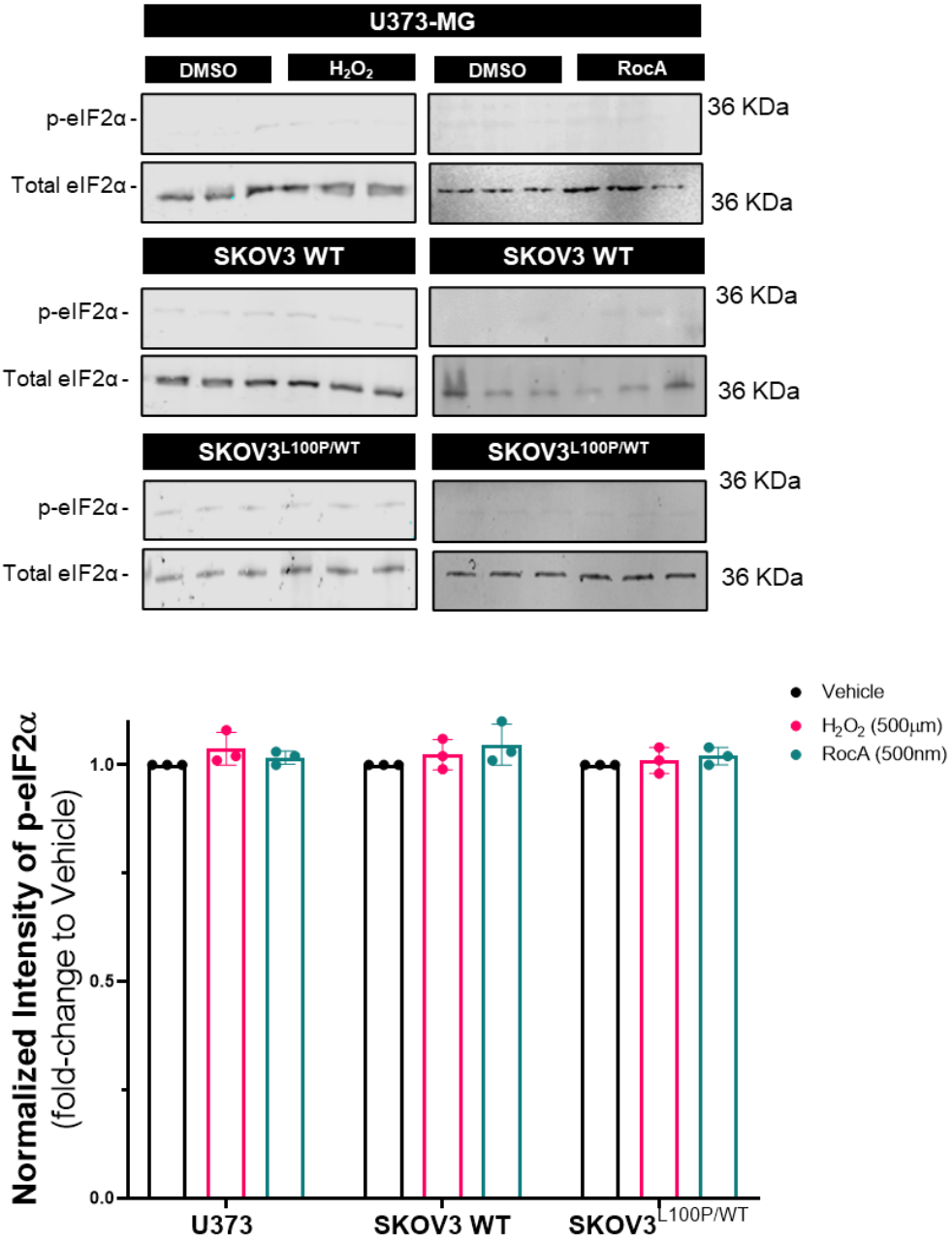

Figure 6.18. H_20_2 and RocA do not induce p-eIF2α in glial and neuronal cells.

Western Blot analysis of the levels of p-eIF2α and total eIF2α expression. Levels of p-eIF2α were normalized to levels of total eIF2α, each lane representing a single biological replicate (n=3). Data was analysed using two-way ANOVA followed by *post-hoc* Tukey's test for multiple comparisons. Error bars: ± s.d.

6.3. Discussion.

6.3.1. Oxidative and ER stress promote eIF2Bα accumulation in SGs.

When the delicate equilibrium of functional proteins within living cells is disturbed, a cascade of protective quality control systems is triggered to counteract the impact. These intricate mechanisms aim to either repair damaged proteins or sequester misfolded proteins, which have the potential to exert cytotoxic effects, into protective aggregates. In response to cellular stressors or pathological conditions, these quality control systems spring into action, orchestrating a sophisticated interplay of molecular processes that safeguard cellular integrity and promote adaptive responses. The timely activation of these systems reflects the intricate and finely tuned cellular defense mechanisms that constantly strive to maintain protein homeostasis and uphold cellular functionality even under challenging conditions (M. P. Jackson & Hewitt, 2016; Moreno-Gonzalez & Soto, 2011).

The interaction between poly-ubiquitin and protein aggregates exemplifies cellular attempts to degrade unfolded polypeptides (Pohl & Dikic, 2019). The conspicuous abundance of eIF2Bα-localised foci in both glial and neural cells, seen in **chapter 4**, sparked contemplation on whether these assemblies might represent protein aggregates earmarked for subsequent protein degradation processes. This highlighted the potential involvement of cellular quality control mechanisms in the recognition and clearance of these eIF2Bα foci. Consequently, to investigate the potential interaction between eIF2Bα and poly-ubiquitin, we conducted co-localisation experiments. Our findings revealed that, under steady-state conditions, eIF2Bα is not subject to poly-ubiquitination, implying that it is not targeted for subsequent degradation via the ubiquitin-proteasome system (**Figure 6.1, Figure 6.2 and Figure 6.3**).

P-bodies have been detected at different developmental stages and under diverse stress conditions (Luo *et al*., 2018; Sheth & Parker, 2003). Traditionally regarded as sites for mRNA decay, P-bodies are closely associated with de-capping complexes, implicating their involvement in mRNA turnover processes (Sheth & Parker, 2003). However, emerging evidence challenges this simplistic view and points to an additional function of P-bodies. Specifically, these dynamic cytoplasmic granules have been shown to transiently store translationally silenced mRNAs, suggesting a potential role as reservoirs for mRNAs that might

later reenter the translation process. Given the high likelihood of translation initiation factors being associated with these dynamic complexes, we embarked on investigating the co-localisation of eIF2Bα with P-bodies. However, our findings reveal that these two structures do not exhibit any discernible interaction, either under steady-state conditions nor during periods of cellular stress (**Figure 6.4**).

eIF2α, eIF3, eIF4E, eIF4G, and small ribosomal subunits are prominently present within SGs, containing most of the components of the 48S PIC (Anderson & Kedersha, 2002; Kimball *et al*., 2003). However, in previous studies, large ribosomal subunits are notably absent from these granules, suggesting that SGs may selectively concentrate on assembling and regulating specific stages of translation initiation.

The presence of eIF2Bε within SGs has been a subject of debate, as conflicting results have emerged from various studies. While some studies have reported the association of eIF2Bε with SGs (Kimball *et al*., 2003), others have not observed this interaction (Hodgson *et al*., 2019; Kedersha *et al*., 2002; Moon & Parker, 2018). In alignment with the previous findings indicating a limited co-localisation of eIF2Bε with G3BP-containing SGs (**Figure 6.10**), our study also yielded similar results.

However, it is noteworthy that a strikingly different trend emerged with eIF2Bα foci, where a substantial proportion displayed spatial interaction with SGs, as seen in **chapter 6.2.3** (**Figure 6.9**). Recent investigations have revealed that mRNAs localised to SGs still retain the capacity to undergo translation. Astonishingly, SG-associated translation is not an uncommon phenomenon, as the entire translation cycle, encompassing initiation, elongation, and termination, has been observed to occur on transcripts within SGs (Mateju *et al*., 2020). Emerging evidence suggests that SGs may harbor a more dynamic landscape than previously thought, with the presence of actively translating mRNA transcripts within these granules. This paradigm-shifting discovery prompts a reevaluation of the traditional view and raises intriguing questions about the functional diversity of SGs and their potential role in shaping the intricate landscape of mRNA metabolism and translation control. Indeed, the regulatory function of eIF2Bα in translation initiation and its close association with phosphorylated eIF2α provide a compelling rationale for the observed co-localisation of eIF2Bα with SGs. As a key component of the eIF2B complex,

eIF2Bα plays a pivotal role in modulating the activity of eIF2, a critical translation initiation factor. The connection between p-eIF2α and eIF2Bα could enable a fine-tuned regulatory mechanism that governs SG assembly and activity, ensuring an appropriate translational response to cellular stress (**Figure 6.19**).

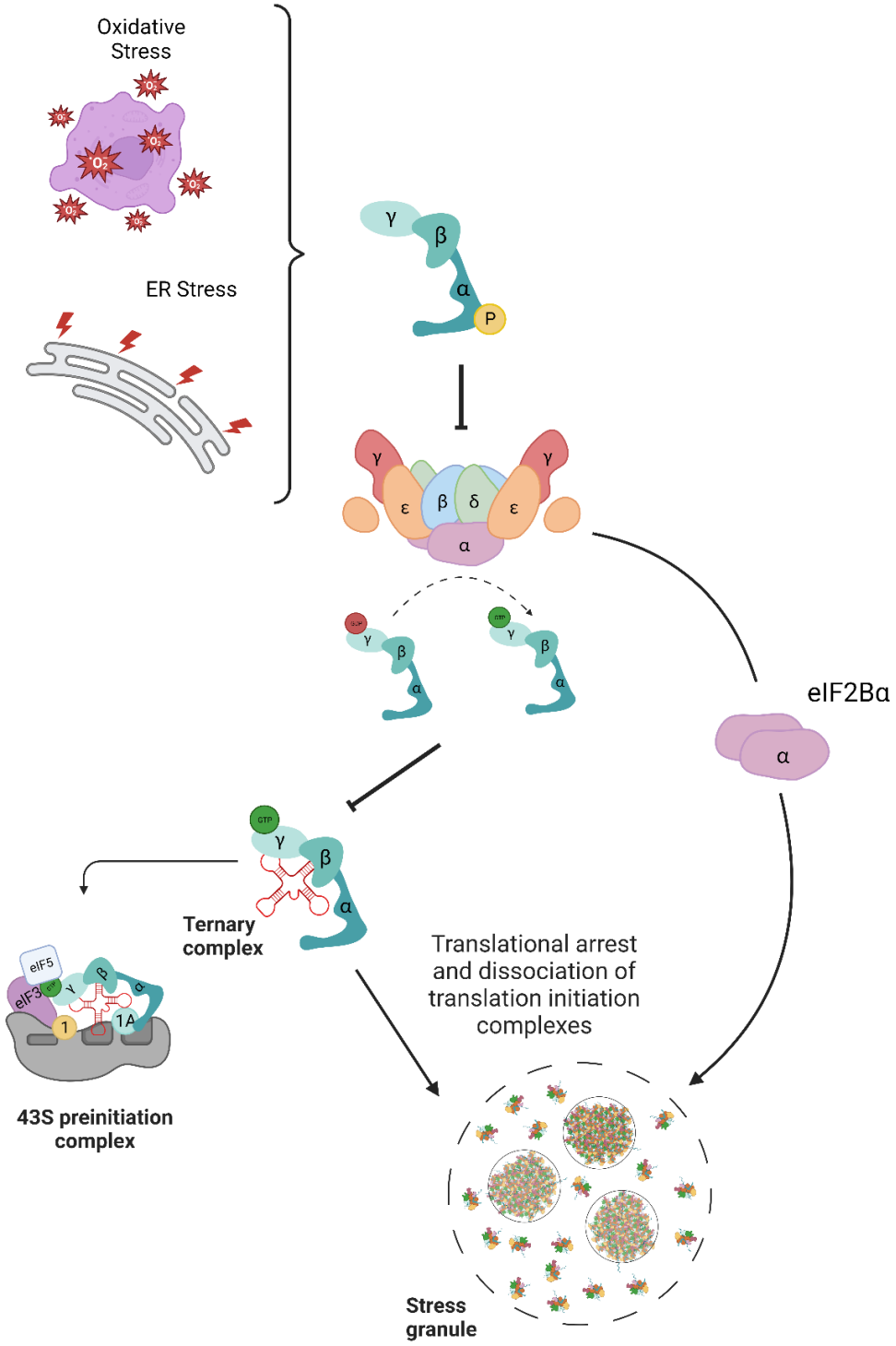

Figure 6.19. eIF2Bα spatially interacts with G3BP-containing SGs following phosphorylation of eIF2α.

The formation of SGs can be caused by various cell-damaging conditions, and in our work, we utilised Tg and SA agents to induce ER and oxidative stress, respectively. Both lead to the phosphorylation of eIF2α. This in turn leads to translational arrest and the formation of translation initiation complexes is inhibited. Subsequently, mRNAs and RNA-binding proteins accumulate and assemble forming SGs. Following co-localisation analysis of a known SG core element, G3BP, and eIF2Bα, it was possible to observe that eIF2Bα spatially interacts with SGs. Image designed in BioRender.

6.3.2. eIF2Bα (Gcn-) mutations renders cells insensitive to stress.

Analysis in a mammalian cell context revealed that the significant decrease in eIF2Bα expression not only affected cell proliferation but also had a profound impact on cell viability when exposed to stress conditions (as shown in **Chapter 5**).

In this study, we present compelling evidence that mutations which disrupt the interface between eIF2Bα and p-eIF2α exert a significant influence on stress sensing mechanisms and the formation of SGs. Through our investigation, we made a noteworthy discovery pertaining to SKOV3 *EIF2B1*$^{L100P/WT}$ cells exposed to oxidative stress induced by SA treatment. Specifically, these cells exhibited a remarkable reduction in SG assembly, when compared to their wild-type counterpart, as depicted in **Figure 6.13**. This observation was accompanied by a notable absence of an increase of the number of eIF2Bα foci. It is worth noting that in a prior chapter, we had established the occurrence of an increase in eIF2Bα foci following stress. The confluence of these findings highlights the intricate and dynamic interaction between sensing of stress, SG formation, and eIF2Bα foci dynamics.

The insensitivity observed in response to stress-induced conditions in *EIF2B1*$^{L100P/WT}$ cells can be attributed to two plausible causes, giving rise to a multifaceted regulatory landscape: (1) Firstly, it is conceivable that p-eIF2α may encounter difficulties in effectively binding and interacting with eIF2Bα. Such an impaired interaction could severely disrupt the regulation of translation initiation, thereby hindering the cell's capacity to mount a proper response to stress. (2) Secondly, given its unresponsive nature and subsequent inept activation of the ISR in these *EIF2B1*$^{L100P/WT}$ cells (Powers, *et al*., unpublished data), levels of TC are in turn not reduced, with active translating polysome. This in turn impairs the formation of SGs even in a heterozygous model. Cumulatively, our data lends strong support to the notion that eIF2Bα plays a pivotal role as a critical regulator of translation precisely at the juncture of eIF2α phosphorylation.

6.3.3. eIF2Bα interaction with SGs is p-eIF2α dependent

As demonstrated in **section 6.3.3**, the formation of SGs in response to oxidative and ER stress exhibited a compelling association with the spatial interaction of eIF2Bα foci populations with these structures. Notably, this interaction was conspicuously absent upon stress induction in a manner independent of p-eIF2α.

Furthermore, the loss of stress sensing observed in *EIF2B1*$^{L100P/WT}$ cells (**Figure 6.13 and Figure 6.15**) was distinctly absent when subjected to stress conditions devoid of p-eIF2α involvement.

Based on these findings, two primary conclusions can be drawn, each contributing to a deeper understanding of the underlying complexities: (1) The spatial interaction between eIF2Bα and SG structures appears to be contingent on eIF2α phosphorylation, which might be attributed to the tight binding to eIF2Bα to p-eIF2α and known presence of eIF2 within SGs. This interaction could be linked to the lack of increase of eIF2Bα foci following RocA and H_2O_2 stress induction. (2) The insensitivity to stress observed in cells harbouring *EIF2B1*$^{L100P/WT}$ mutations, is solely manifested under p-eIF2α-dependent stress conditions. Consequently, the implications of the absence of stress sensing in *EIF2B1*$^{L100P/WT}$ cells may be limited to specific stressors, while other stress-sensing pathways may continue to function effectively, as we observed when utilising H_20_2 and RocA (**Figure 6.17**).

Additionally, in the preceding chapter, our investigation led to the observation of SG formation in response to the absence of eIF2Bα. As we delve into future studies, a crucial avenue of exploration entails deciphering the composition of these structures, with a particular focus on differentiating between p-eIF2α-dependent and p-eIF2α-independent SG assemblies. Given the lack of p-eIF2α induction in the absence of eIF2Bα, we postulate that SGs which form when eIF2Bα expression is silenced, are induced as a direct consequence of TC depletion.

These contrasting outcomes suggest that diverse stress conditions intricately modulate the spatial relationship between eIF2Bα and SG and point to the existence of distinct regulatory mechanisms that dictate the assembly dynamics of SGs under varied cellular stressors.

6.3.4. Final observations

The work presented in this chapter culminates in two noteworthy outcomes: Firstly, spatial interaction between eIF2Bα and G3BP-containing SGs was observed in U373-MG, MO3.13, SH-SY5Y and SKOV3 cells. This in turn suggests that, while with varying degrees of interaction between eIF2Bα and SGs according to cell line, is conserved amongst cell types. Additionally, the co-localisation between eIF2Bα and SGs was only observed under p-eIF2α-dependent stress conditions. As stated previously, there are stress-specific

differences in assembly and composition of SGs, thus the absence of eIF2Bα in SGs following RocA and H_2O_2 treatments could be explained by the tight binding between p-eIF2α and eIF2Bα and subsequent relocation of eIF2 in SGs during ISR activating stressors, which is not observed in p-eIF2α-independent stresses. Secondly, *EIF2B1*$^{L100P/WT}$ heterozygous mutation, which has been shown to be unresponsive to ISR activation, displayed decrease formation of SGs under p-eIF2α-inducing treatments, thus bypassing p-eIF2α translation initiation regulation.

Chapter 7. General discussion.

The work and analysis presented in this thesis emphasizes the capability of bioinformatic tools to enhance immunostaining techniques that preserve the integrity of native protein structures. Moreover, this study has unveiled the cell-type specificity of eIF2B localisation, particularly focusing on eIF2Bα localisation. The eIF2Bα-ε foci exhibit a diverse range of sizes, demonstrating possible diverse eIF2B structures that localise in cells. Notably, a considerable number of eIF2Bα foci were evident in oligodendrocytes and neurons, with most of these foci existing independently from spatial interactions with other eIF2B subunits. Consequently, our proposal posits that eIF2Bα subcomplexes manifest separate localisation within cells, distinct from the eIF2B complex. Upon induction of the ISR, a discernible shift in eIF2Bα and eIF2Bε localisation was observable, characterised by an overall increase in numbers of localised foci per cell. In addition, our investigation exposed the central role of eIF2Bα in the formation of large eIF2Bβ-ε localised foci, emphasizing its function within the eIF2B decamer in steady state conditions. ISRIB emerged as a functional substitute for eIF2Bα in generating these large foci; however, its ability to fully reinstate GEF activity appeared limited. Conclusively, we have established the spatial interaction between eIF2Bα and G3BP-containing SGs in a manner contingent upon p-eIF2α, while variants of *EIF2B1* displayed compromised stress response. This study culminates in providing compelling evidence that eIF2Bα localisation contributes to translation regulation through its involvement in eIF2B complex assemblies and interactions with other proteins, thus delineating a pivotal avenue for future research endeavors.

7.1. eIF2Bα localisation is cell-type specific.

In Chapter 4, we delved deeper into a previously established concept regarding distinct eIF2B cytoplasmic bodies of varying sizes within mammalian cells, as discussed in Hodgson *et al.,* (2019) and Hanson *et al.,* (2023). Our investigation revealed a compelling landscape: all eIF2B subunits exhibited diverse patterns of localisation in glial and neuronal cell lines, resulting in foci of differing sizes, possibly with diverse eIF2B composition. Our findings emphasized the correlation between the size of these cytoplasmic foci and the composition of subunits. Larger structures notably encompassed regulatory and catalytic subunits, hinting at their formation through eIF2B decamer interactions.

However, the prevalence and constitution of eIF2B foci exhibited an intriguing cell-type specificity. Particularly noteworthy was the revelation that a substantial percentage of oligodendrocytic and neuronal cells exclusively manifested eIF2Bα localisation independent of other eIF2B subunits (**Figure 4.2**). Moreover, the number of smaller eIF2Bα foci per cell was notably increased within these two cell lines (**Figure 4.18**). This observation shows that the formation of these eIF2Bα foci diverges based on the cell type, potentially under the sway of physiological regulation. In essence, the availability of eIF2Bα could potentially be modulated by multifaceted regulatory mechanisms. These could encompass the modulation of biosynthesis or degradation rates (Sha *et al*., 2018), post-translational modifications (Schaffert & Carter, 2020), or confinement within an inaccessible cellular pool. Additionally, due to eIF2B bodies representing hubs of highlight active GEF activity, eIF2B localisation can also be modulated by cell cycle, which is tightly regulated by protein synthesis (Polymenis & Aramayo, 2015). Thus, investigation of the possible correlation between cell cycle and eIF2B localisation should be carried out, either through live imaging tracking of cell cycle and fluorescently tagged eIF2B plasmids, and/or through cell cycle arrest and subsequent immunofluorescence detection of eIF2B foci.

It is important to note that VWMD mutations mainly affect astrocytes and subsequently oligodendrocytes, sparing neurons (Dooves *et al*., 2016; Herrero *et al*., 2021). Given that the percentage of cells with eIF2Bα localisation and the number of eIF2Bα per cell is enhanced in oligodendrocytes and neuronal cells, but not in astrocytes, perhaps reveals an important role for eIF2Bα localisation in this astrocytic-driven disorder.

It's worth noting that when eIF2Bα is overexpressed, cells fail to generate eIF2Bα foci and instead display a dispersed signal (**Figure 4.20**). Co-transfecting eIF2Bα-RFP with siRNA-mediated silencing of *EIF2B1*, led to the formation of eIF2Bα foci, and it was then possible to observe that these foci are dynamic in movement and perhaps in composition (**Figure 4.21**). Thus, the assembly of these localised eIF2Bα foci requires further investigation (**Figure 7.4**). Consequently, although expression levels seemingly do not exhibit a straightforward correlation with eIF2Bα abundance within oligodendrocytes and neuronal cells, the control of eIF2Bα expression levels does indeed exert an influence on the localisation of eIF2Bα, particularly under extreme circumstances. Through live imaging it was possible to observe that these eIF2Bα foci appeared

to have LLPS characteristics (**Figure 4.22**). LLPS aggregates are condensates of proteins and RNA-binding proteins, which are dynamic assemblies resembling liquid droplets. These granules are dynamically assembled, maintained, segregated and fully dissolved (Brownsword & Locker, 2023; B. Wang *et al*., 2021), as hinted in **figure 4.22**.

We provided compelling evidence that, while certain foci of eIF2Bα co-localise with other regulatory and catalytic subunits of eIF2B in **section 4.2.3**, a significant portion appears to operate independently from these eIF2Bβ-ε proteins. While the involvement of additional assembly factors remains plausible, we propose that the smaller and larger eIF2Bα foci might indeed represent autonomous eIF2Bα homodimers. Isolation of these assemblies followed by size-exclusion chromatography would be able to elucidate this idea.

Within this framework, it becomes conceivable that through dynamic assembly and disassembly mechanisms, these eIF2Bα foci could function as pre-formed entities, poised for rapid decamer arrangement, thus giving rise to larger eIF2B bodies. Alternatively, they could emerge due to the disintegration of large eIF2B bodies, ultimately manifesting as distinct cytoplasmic foci from the other eIF2B subunits. Notably, the broader landscape should encompass the recognition that eIF2Bα's functional roles might extend beyond its association with the other eIF2B subunits and sensing of stress conditions (**Figure 7.4**), as proposed formerly (Hao *et al*., 2021; Klein *et al*., 1997). Lastly, it remains vital to underline that, in the context of steady-state conditions, other assembly factors might indeed interact with localised eIF2Bα. To understand potential interactions, pulldown assays with subsequent western blot detection, sequence analysis or MS identification, could be utilised.

Collectively, our results demonstrate that under normal conditions cells display a cell-type specific localisation of eIF2Bα. The existence of different eIF2Bα subcomplexes may allow for unique rates of eIF2B assembly or caused by different rates of eIF2B disassembly and may allow for a more a more efficient and/or more easily regulated translation initiation.

(A) Formation of eIF2Bα foci following disassembly of larger eIF2B foci

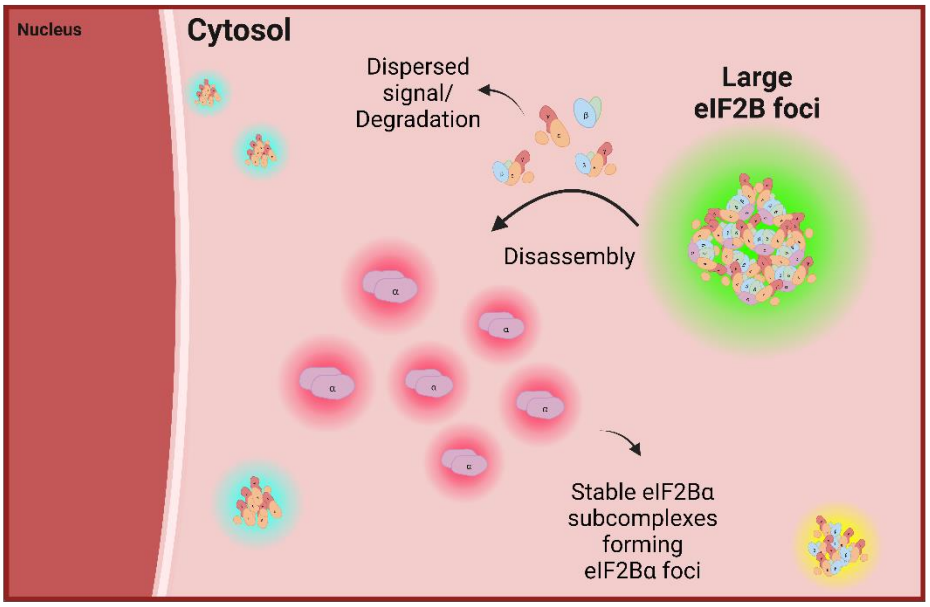

(B) Pre-existing eIF2Bα foci essential for large eIF2B foci assembly

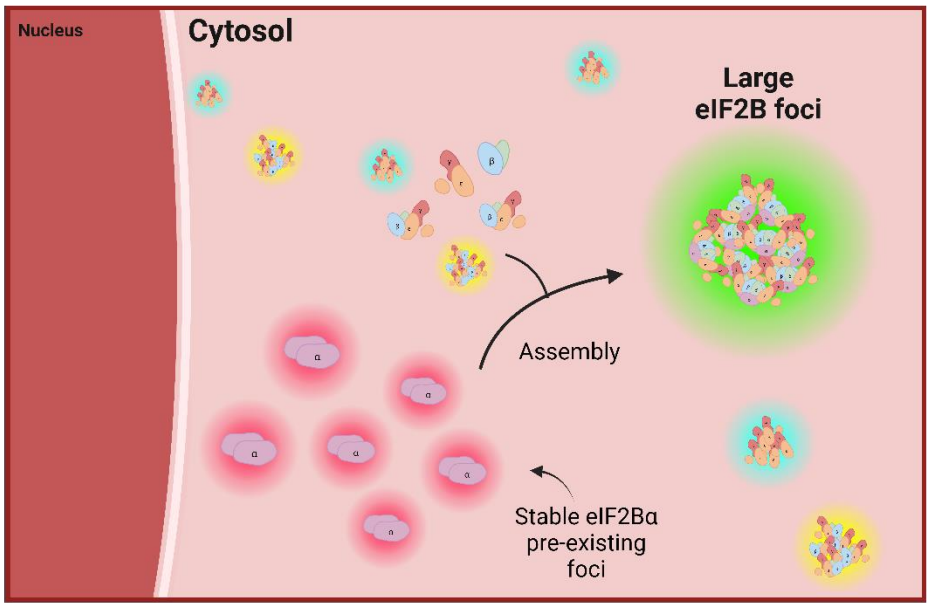

Figure 7.1. eIF2Bα localised cytoplasmic foci and its formation in mammalian cells. Abundant seemingly eIF2Bβγδε-independent eIF2Bα localised foci are present in glial and neuronal cells in steady-state conditions. (A) The eIF2Bα localised foci could be formed through the disassembly of large eIF2B foci which contain all five eIF2B subunits. While the subcomplexes of eIF2Bβγδε could be formed, they could also be targeted for degradation or give way to dispersed signal, while stable eIF2Bα structures form eIF2Bα foci. (B) The observed eIF2Bα foci could also be pre-formed assemblies, readily available for large eIF2B foci assembly, through eIF2B decamer formation. It is also possible that the formation of these eIF2Bα foci are assembled through both dynamic assembly and disassembly mechanisms according to cell's translation activity/regulation requirements. Image designed in BioRender.

7.2. eIF2Bα and ISRIB share functional roles in large eIF2Bβ-ε foci formation.

In **chapter 5** we explored the role of eIF2Bα in the formation of large eIF2Bβ-ε foci. Building upon recent work from the Walter lab (Schoof *et al.*, 2021) and previous structural investigations, the significance of eIF2Bα in the orchestration of eIF2B decamer assembly, effectively bridging eIF2Bβγδε tetramers, comes into sharp focus. This context served as the impetus for our investigation into whether the localisation of eIF2Bβ-ε foci could be impacted in the absence of eIF2Bα. Given that large eIF2B bodies contain all eIF2B subunits, these assemblies are thought to be formed through the aggregation of eIF2B decamers. Guided by this rationale, we postulated that the formation of large eIF2Bβ-ε foci might be impeded in cells where eIF2Bα was depleted. To investigate this, we employed siRNA-mediated silencing of *EIF2B1* and, as anticipated, discovered a significant decrease in the formation of large eIF2Bβ-ε foci. This was accompanied by a surge in the number of smaller eIF2Bβ-ε foci. We hypothesize that these smaller assemblies potentially house eIF2Bβγδε tetramers or other stable eIF2B structures that lack eIF2Bα. ISRIB treatment in cells depleted of eIF2Bα demonstrated its capacity to reinstate the presence of large eIF2Bβ-ε foci while concurrently diminishing the prevalence of smaller ones. This restoration process reinforces our hypothesis that the presence of these large eIF2Bβ-ε foci were through the amalgamation of localised, free eIF2Bβγδε tetramers and/or other stable eIF2B structures. We also show that cells depleted of eIF2Bα exhibit a decrease in global protein synthesis and an increase in ISR markers downstream of p-eIF2α and SGs, due to decreased levels of GEF activity, which ISRIB treatment is able to restore. A more comprehensive exploration of this aspect warrants further investigation, with polysome profiling of cells depleted of eIF2Bα elucidating the impact on translation initiation.

Additionally, while cell viability is not affected solely by the decreased expression of eIF2Bα, when coupled with acute stress, cells show significant decrease in cell viability. This in turn highlights the importance of eIF2Bα in correct sensing of stress through p-eIF2α. To explore this further SKOV3 cells with a *EIF2B1*$^{I100P/WT}$ variant were subjected to p-eIF2α-dependent and independent stress, and these cells showed that while p-eIF2α-independent stress conditions lead to the formation of SGs, p-eIF2α-dependent stress did not. Showing that the absence

of eIF2Bα and/or mutations in this subunit impact cellular response to stress, which could particularly impact PNDM eIF2Bα causative (**Figure 7.5**).

It has been shown in yeast models, where eIF2B bodies are thought to only contain localised eIF2B decamers and not other subcomplexes, that *EIF2B1* variants have an impact on localisation, with some showing a dispersed signal of eIF2B bodies and other forming microfoci, which display reduced GEF activity (Norris *et al*., 2021). This emphasizes that in cells lacking eIF2Bα or in the presence of *EIF2B1* mutations, eIF2B localisation is greatly impacted, which could be a key to understanding the pathogenesis of VWMD and PNDM *EIF2B1* causative mutations (**Figure 7.5**). Thus, the investigation of VWMD and PNDM *EIF2B1* causative variants in mammalian cells and its impact on eIF2B localisation should be carried out. This could be accomplished by homologous direct repair via CRISPR-Cas9 and subsequent immunofluorescence detection of eIF2B subunits.

Taking a different perspective, disorders characterised by the persistent onset of stress, such as diabetes, neurodegenerative conditions, obesity, and cancer (M. Wang & Kaufman, 2016), present an intriguing context for exploration. In this scenario, a combined strategy targeting eIF2Bα for degradation or reduced expression, coupled with ISRIB treatment, could potentially offer a novel therapeutic avenue. The deliberate reduction or absence of eIF2Bα could hold the key to rendering cells less responsive to the ongoing activation of eIF2α phosphorylation, a hallmark of chronic stress conditions. Meanwhile, the administration of ISRIB could restore large eIF2B bodies and, potentially, restore full GEF activity (**Figure 7.5**).

In conclusion, we have demonstrated the influence of eIF2Bα on the localisation of eIF2B, emphasizing its substantial role in this regulatory process. Moreover, our research highlights the intriguing potential of ISRIB to effectively restore the presence of large eIF2B bodies.

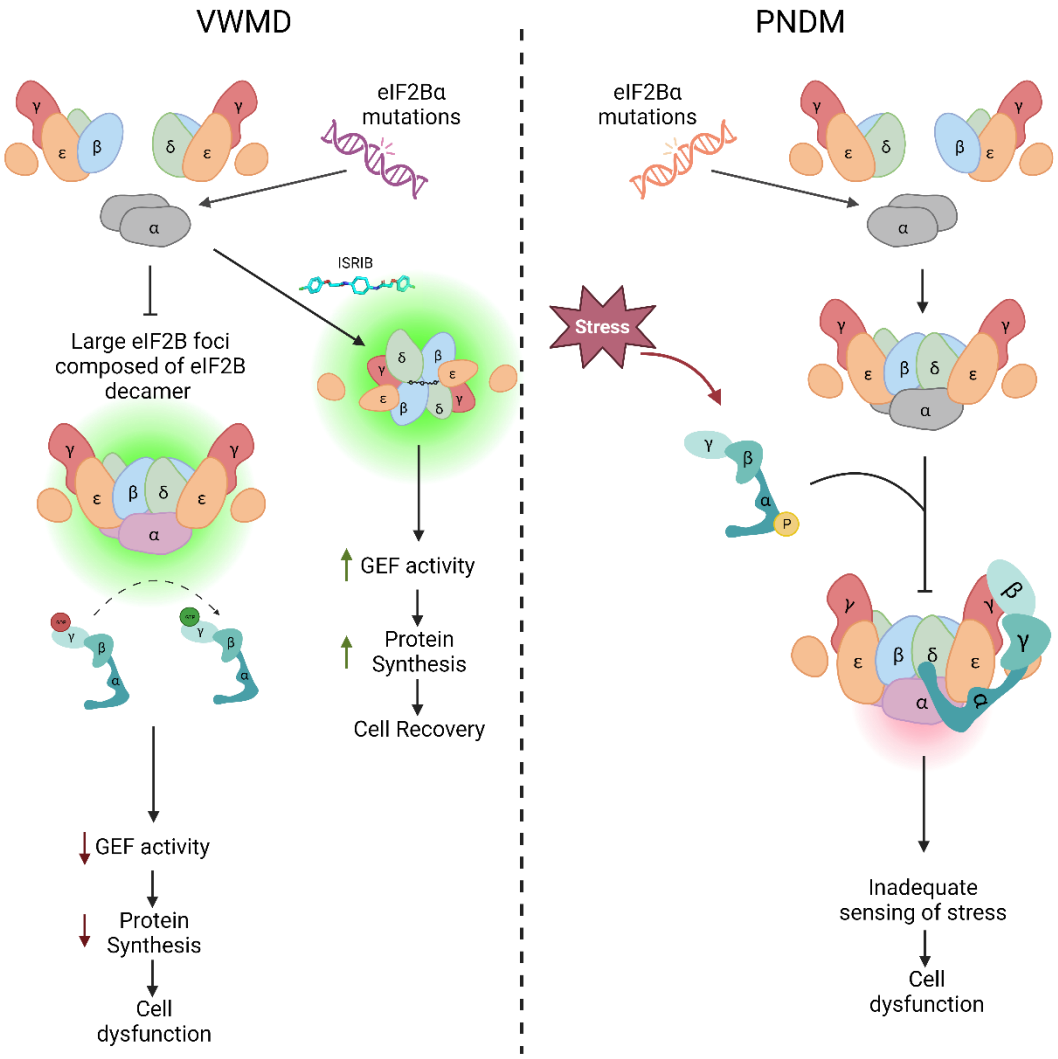

Figure 7. 2. Proposed model of VWMD and PNDM eIF2Bα causative mutations.
While features of eIF2Bα variants that cause VWMD and PNDM may overlap, with both disorders presenting an impact on eIF2B foci formation and hindrance in stress-sensing, we propose a simplistic model to explain the mutations effects. VWMD eIF2Bα mutations are majorly in binding surfaces with other eIF2B subunits, thus suggesting that the final stage of eIF2B decameric formation, which is mediated by eIF2Bα, is impacted. Large eIF2B foci, which it is thought to be composed of eIF2B decamers, are in turn not able to form. These assemblies have been shown to have 100 % GEF activity. By inhibiting its formation, GEF activity could be decreased, which could lead to a decrease in global protein synthesis, consequently leading to cell dysfunction. It is of note that through siRNA mediated silencing of *EIF2B1*, we found that ISRIB treatment in cells depleted of eIF2Bα rescued the formation of large eIF2B foci. This hints that GEF activity might be somewhat rescued, leading to an increase in protein synthesis and cellular homeostasis. Conversely, PNDM eIF2Bα mutations are mainly in binding sites with p-eIF2α, indicating that during cellular stress, cells may not be able to respond correctly due to a lack of eIF2Bα sensing of p-eIF2α. This in turn, could lead to cell dysfunction and possibly cell death. Image designed in BioRender.

7.3. Insights into eIF2Bα localisation in stress conditions.

In Chapter 4, a notable observation emerged: post-stress conditions led to an augmentation in the localisation of eIF2Bα, manifested through the increase of both small and large foci within cells. A similar trend manifested in the localisation pattern of eIF2Bε, as seen previously (Hanson *et al*., 2023; Hodgson *et al*., 2019a), wherein the increase of small eIF2Bε foci occurred in both glial and neuronal cells. Thus, we aimed to investigate if these assemblies could interact with other cytoplasmic foci in the presence of stress. While eIF2Bα did not co-localise with P-bodies, a large population of eIF2Bα foci and G3BP-containing SG spatially interacted following ER and oxidative stress in glial and neuronal cells, as further explored through Airyscan imaging (**Figure 6.11**). When co-localisation was carried out, only a few eIF2Bε foci co-localised with SGs under oxidative stress in neuronal cells. It is of note that through Airyscan imaging of these assemblies, proximity between SGs and eIF2Bε, while no complete co-localisation, was possible to observe. Thus, whilst eIF2Bε might not spatially interact with SGs core components, such as G3BP, it might dynamically exist within SGs shell. Further work regarding eIF2Bε interaction with SGs should be carried out (**Figure 6.11**).

Consequently, we speculate that a substantial fraction of eIF2Bα undergoes relocation towards SGs subsequent to stress induction. This phenomenon, in turn, could trigger disassembly and/or hinder the formation of eIF2B decameric large foci, thereby giving rise to the surge in smaller eIF2Bβ-ε foci (**Figure 7.7**). While additional investigations remain imperative to fully unravel this, eIF2Bα holds the potential to function as reservoirs for binding with p-eIF2α, which subsequently undergo translocation to SGs.

While the significance of these results is yet to be fully understood, our current hypotheses stand as follows: In response to cellular stress, the inhibition posed by p-eIF2α on eIF2B prompts the generation of small eIF2B assemblies, aimed at reestablishing cellular equilibrium. Among these, the smaller foci, possibly containing eIF2Bε and eIF2Bγ, could serve as hubs for p-eIF2α-insensitive GEF activity, while both small and large eIF2Bα foci might exist within eIF2B decameric assemblies (large foci). Stress conditions would in turn still require a baseline of eIF2B activity in order to reinstate homoeostasis. Consequently, while larger

eIF2B decameric formations encounter inhibition, the need for less susceptible smaller eIF2B foci becomes apparent. This leads to the disassembly of large eIF2B assemblies leading to the emergence of catalytic eIF2B foci and independent eIF2Bα foci. The diversity within the populations of eIF2Bα foci could potentially confer distinct rates of adaptability to stress, culminating in enhanced translational efficiency and/or more facile regulatory mechanisms.

Furthermore, the increase of eIF2Bα localised foci per cell and co-localisation with SGs was only observed in stress conditions that activate the phosphorylation of eIF2α. While H_2O_2 and RocA still assembled SGs, the number of eIF2Bα foci per cell was not increased and the co-localisation with SGs was not present. Thus, this interaction between p-eIF2α and the eIF2B complex, but particularly eIF2Bα, drives the modulation and spatial interaction of eIF2B foci. It would be of interest to study the localisation patterns of the other eIF2B subunits, following the induction of these stressors.

It is interesting to speculate, if this reallocation of eIF2Bα is observed in neurodegenerative disorders that are characterised by pathological SG formation, such as amyotrophic lateral sclerosis, frontotemporal degeneration, and Alzheimer's diseases (Asadi *et al*., 2021). Considering the potential sequestration of eIF2Bα foci within SGs, a fascinating hypothesis arises: could these assemblies represent reservoirs of functionally inaccessible eIF2Bα? Our research indicates a dual role for eIF2Bα: not only is it pivotal for stress sensing, but it's also essential for the formation of large eIF2B foci. In the scenario where eIF2Bα becomes sequestered and thus unavailable for these crucial functions, a plausible connection could be drawn to the drivers of dysregulation observed in these neurodegenerative disorders.

Additionally, SGs have been found to not only be hub of non-translating mRNPs, but also sites of active translation (Mateju *et al*., 2020). Thus, while eIF2Bε was not shown to largely co-localise with SGs, there is the possibility eIF2B subunits dynamically shuttle to SGs to carry out its GEF activity. Further work needs to be carried out, which will be further expanded on in the next section.

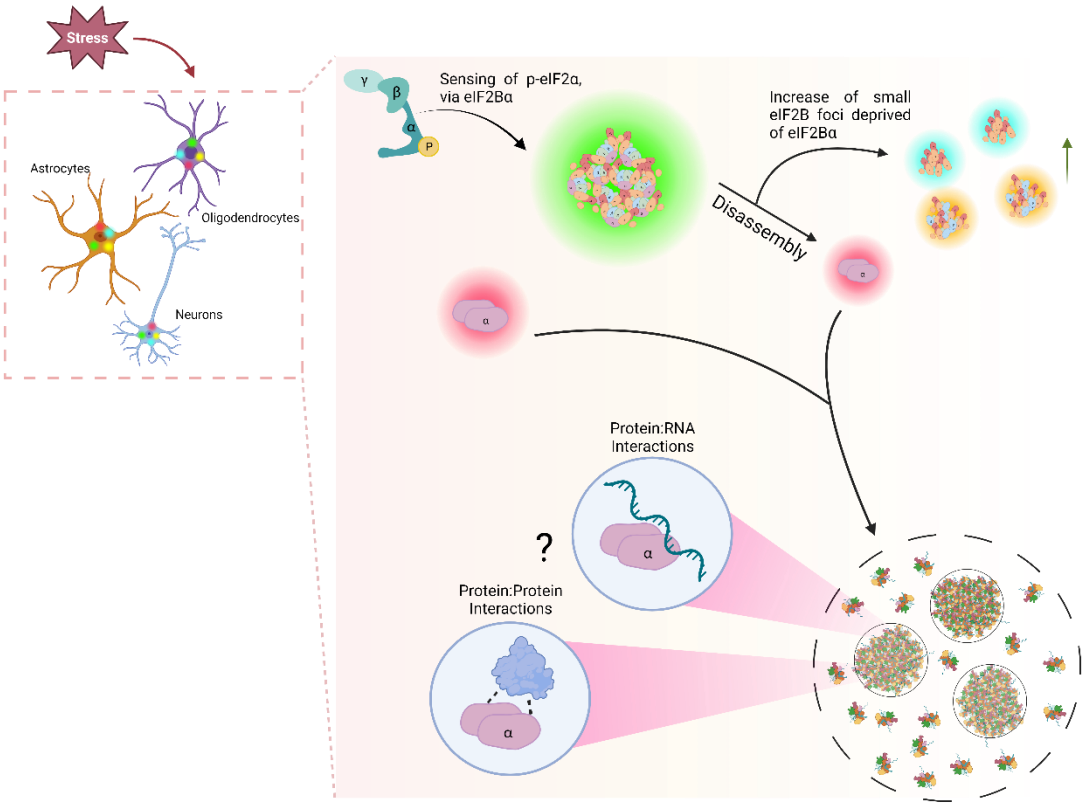

Figure 7.3. eIF2Bα relocation to SGs, which is p-eIF2α dependent, may lead to an increase of small eIF2B foci deprived of eIF2Bα.

Following the induction of p-eIF2α through cellular stress conditions, the sensing of stress, which is mediated by the binding of p-eIF2α and eIF2Bα, may cause the disassembly of large eIF2B foci composed of all five eIF2B subunits, leading to the observed increase of small eIF2Bε foci. This in turn frees eIF2Bα foci to relocate to SGs through protein:RNA and/or protein:protein interactions. Image designed in BioRender.

7.4. Limitations and future research.

While in the work presented here, we were able to characterise endogenous eIF2B localisation, investigate the role of eIF2Bα and study potential binding proteins of eIF2Bα, the experimental model detailed in this thesis holds important limitations that need to be considered in this study and for future work.

1) Characterisation of eIF2B foci and not bodies: In the work presented here, the detection of eIF2Bα-ε subunits was mainly carried out singularly in glial and neuronal cells. While co-localisation efforts between eIF2Bα and eIF2Bγ/δ were carried out, establishing correlation between the presence of eIF2B regulatory/catalytic subunits in the detected eIF2Bα foci, the full scope of eIF2B foci composition was not able to be carried out. Additionally, these eIF2B localised foci, but particularly eIF2Bα foci, cannot be termed eIF2B bodies, due to the lack of investigation regarding their GEF activity. Thus, further investigation regarding the characterisation of endogenous eIF2B bodies should be carried out. Through a well-planned multichannel immunofluorescence, fluorescently labeled primary antibodies targeting the five eIF2B subunits would allow for the endogenous detection of localised complexes and subcomplexes. Additionally, FRAP analysis allows for the study of eIF2 shuttling through eIF2B bodies. As such, the analysis of eIF2Bα localised foci and their GEF activity should also be carried out, to establish them as eIF2B bodies.
2) Co-localisation assay: As stated above the verification of eIF2B subunits in eIF2B foci/bodies would allow for a better understanding regarding eIF2B complex and subcomplex localisation in mammalian cells. As such, isolation of the localised eIF2B foci/bodes through size exclusion chromatography and/or pulldown assays with subsequent proteomic analysis would aid to resolve this issue.
3) Size distribution analysis: Size discrimination analysis was notably influenced by the limited count of eIF2Bα foci that exhibited co-localisation compared to the substantial number of foci that did not co-localise with other eIF2B subunits. The disparity in co-localisation patterns presented challenges in precisely assessing and distinguishing foci based on their sizes, contributing to the intricacies of interpreting the data and necessitating a comprehensive investigation to discern underlying patterns and significance. A larger and more proportional population of both co-localised and non-co-localised foci

would allow for a more comprehensive study of size distribution.

4) eIF2Bα binding to eIF2α: Currently, there are no published works that elucidate if eIF2Bα is capable of binding to eIF2α in the absence of other eIF2B subunits. Further co-localisation work between eIF2Bα and eIF2α would allow for the study of potential size/composition differences were binding between these two proteins occur. Subsequently, investigation of the presence of absence of eIF2Bβ-ε subunits in foci where eIF2Bα and eIF2α co-localise would, would allow to answer this question.
5) Characterisation of eIF2B foci and bodies in *EIF2B1* mutated cells: The *EIF2B1*$^{L100P/WT}$ cell model allowed us to investigate the cellular response to stress in cells with mutated eIF2Bα. Given the results presented, the characterisation of endogenous eIF2Bα-ε foci and study of eIF2B body activity would allow us to understand eIF2B localisation/function impact in mutated cells. This study would be expanded to other eIF2Bα mutations, encompassing VWMD and PNDM causative mutations allowing for a disease context implication of localisation and function of eIF2B. Furthermore, *EIF2B1*$^{L100P/WT}$ cell model should be further explored regarding cellular response to stress. Cell viability assays to chronic and acute stress, coupled with cell proliferation assays could expand on the insights gathered in this thesis regarding the role of eIF2Bα in translation initiation and stress regulation.
6) eIF2Bα co-localisation with SGs: While we were able to discern that eIF2Bα reallocates to SGs following p-eIF2α-dependent stress induction, co-localisation efforts between components of independent-p-eIF2α SGs would allow for a more comprehensive study of the different SGs assemblies and the spatial interaction between then and eIF2Bα.
7) Molecular composition of eIF2B foci: In this study we were able to find a size to subunit composition correlation. However, we do not know the molecular composition of these foci. As such, the combination of immunofluorescence and electron microscopy, such as correlative light and electron microscopy, would allow for further understanding regarding the molecular composition of these eIF2B assemblies. Additionally, isolation and size-exclusion chromatography of eIF2Bα foci would allow to understand the structural assembly necessary to form the foci.
8) Potential other binding partners of eIF2Bα: In this thesis we have focused our

co-localisation work to known eIF2Bα binding proteins, such as eIF2Bγ and δ and SGs. However, given the large number of eIF2Bα foci which appear to not interact spatially with other eIF2B in steady-state conditions, it suggests that other possible proteins might interact with eIF2Bα. Previous work has suggested that adrenergic receptors interact with eIF2Bα (Klein *et al*., 1997). Additionally, sugar phosphatases have been found to bind to the ancestral catalytic pocket of the eIF2Bα subunit (Hao *et al*., 2021). Isolation of eIF2Bα foci and subsequent proteomic profiling of binding partners in an array of cell lines would allow for a deeper investigation of the localised foci. Additionally, RNA fluorescence *in situ* hybridization coupled with immunofluorescence staining of eIF2Bα and the other eIF2B subunits would allow the analysis of the composition of these foci with RNA molecules.

9) Cell models: The choice of cell models in this study, while convenient for experimental purposes, also presents a limitation, especially when examining the intricacies of translation initiation regulation. U373-MG (astrocytoma) and SH-SY5Y (neuroblastoma) cell lines stem from cancer origins and consequently fail to replicate the metabolic demands observed in non-cancerous astrocytes and neurons (Ikari *et al.,* 2021; Vander Heiden & DeBerardinis, 2017). To overcome these challenges, future work should be directed towards induced pluripotent stem cell (iPSC)-derived neural progenitor cells that have been systematically differentiated into neurons, astrocytes, and oligodendrocyte (Ladran *et al*., 2013). Furthermore, the use of developed of 3D organoid with VWMD patient-derived iPSCs (Deng *et al*., 2023), would allow for a more profound comprehension of VWMD pathology and the role of eIF2B localisation in a more complex model.

References

Abbink, T. E. M., Wisse, L. E., Jaku, E., Thiecke, M. J., Voltolini-González, D., Fritsen, H., Bobeldijk, S., Braak, T. J., Polder, E., Postma, N. L., Bugiani, M., Struijs, E. A., Verheijen, M., Straat, N., Sluis, S., Thomas, A. A. M., Molenaar, D., & Knaap, M. S. (2019). Vanishing white matter: deregulated integrated stress response as therapy target. *Annals of Clinical and Translational Neurology*, *6*(8), 1407–1422.

Accogli, A., Brais, B., Tampieri, D., & La Piana, R. (2019). Long-Standing Psychiatric Features as the Only Clinical Presentation of Vanishing White Matter Disease. *The Journal of Neuropsychiatry and Clinical Neurosciences*, *31*(3), 276–279.

Adomavicius, T., Guaita, M., Zhou, Y., Jennings, M. D., Latif, Z., Roseman, A. M., & Pavitt, G. D. (2019). The structural basis of translational control by eIF2 phosphorylation. *Nature Communications*, *10*(1), 2136.

Agirrezabala, X., Liao, H. Y., Schreiner, E., Fu, J., Ortiz-Meoz, R. F., Schulten, K., Green, R., & Frank, J. (2012). Structural characterization of mRNA-tRNA translocation intermediates. *Proceedings of the National Academy of Sciences*, *109*(16), 6094–6099.

Ait Ghezala, H., Jolles, B., Salhi, S., Castrillo, K., Carpentier, W., Cagnard, N., Bruhat, A., Fafournoux, P., & Jean-Jean, O. (2012). Translation termination efficiency modulates ATF4 response by regulating ATF4 mRNA translation at 5′ short ORFs. *Nucleic Acids Research*, *40*(19), 9557–9570.

Alamri, H., Al Mutairi, F., Alothman, J., Alothaim, A., Alfadhel, M., & Alfares, A. (2016). Diabetic ketoacidosis in vanishing white matter. *Clinical Case Reports*, *4*(8), 717–720.

Algire, M. A., Maag, D., & Lorsch, J. R. (2005). Pi Release from eIF2, Not GTP Hydrolysis, Is the Step Controlled by Start-Site Selection during Eukaryotic Translation Initiation. *Molecular Cell*, *20*(2), 251–262.

Alkalaeva, E. Z., Pisarev, A. V., Frolova, L. Y., Kisselev, L. L., & Pestova, T. V. (2006). In Vitro Reconstitution of Eukaryotic Translation Reveals Cooperativity between Release Factors eRF1 and eRF3. *Cell*, *125*(6), 1125–1136.

Amesz, H., Goumans, H., Haubrich-Morree, T., Voorma, H. O., & Benne, R. (1979). Purification and Characterization of a Protein Factor that Reverses

the Inhibition of Protein Synthesis by the Heme-Regulated Translational Inhibitor in Rabbit Reticulocyte Lysates. *European Journal of Biochemistry*, *98*(2), 513–520.

Anand, A. A., & Walter, P. (2020). Structural insights into ISRIB, a memory-enhancing inhibitor of the integrated stress response. *The FEBS Journal*, *287*(2), 239–245.

Anderson, P., & Kedersha, N. (2002). Visibly stressed: the role of eIF2, TIA-1, and stress granules in protein translation. *Cell Stress & Chaperones*, *7*(2), 213.

Anderson, P., & Kedersha, N. (2006). RNA granules. *The Journal of Cell Biology*, *172*(6), 803–808.

Asadi, M. R., Sadat Moslehian, M., Sabaie, H., Jalaiei, A., Ghafouri-Fard, S., Taheri, M., & Rezazadeh, M. (2021). Stress Granules and Neurodegenerative Disorders: A Scoping Review. *Frontiers in Aging Neuroscience*, *13*.

Asano, K. (1999). Conserved bipartite motifs in yeast eIF5 and eIF2Bepsilon , GTPase-activating and GDP-GTP exchange factors in translation initiation, mediate binding to their common substrate eIF2. *The EMBO Journal*, *18*(6), 1673–1688.

Aulas, A., Fay, M. M., Lyons, S. M., Achorn, C. A., Kedersha, N., Anderson, P., & Ivanov, P. (2017). Stress-specific differences in assembly and composition of stress granules and related foci. *Journal of Cell Science*.

Balachandran, S., & Barber, G. N. (2004). Defective translational control facilitates vesicular stomatitis virus oncolysis. *Cancer Cell*, *5*(1), 51–65.

Banani, S. F., Lee, H. O., Hyman, A. A., & Rosen, M. K. (2017). Biomolecular condensates: organizers of cellular biochemistry. *Nature Reviews Molecular Cell Biology*, *18*(5), 285–298.

Barlow, D. J., Edwards, M. S., & Thornton, J. M. (1986). Continuous and discontinuous protein antigenic determinants. *Nature*, *322*(6081), 747–748.

Baruah, V., & Bose, S. (2020). Immunoinformatics-aided identification of T cell and B cell epitopes in the surface glycoprotein of 2019-nCoV. *Journal of Medical Virology*, *92*(5), 495–500.

Bäuerlein, F. J. B., Fernández-Busnadiego, R., & Baumeister, W. (2020). Investigating the Structure of Neurotoxic Protein Aggregates Inside Cells. *Trends in Cell Biology*, *30*(12), 951–966.

Bellato, H. M., & Hajj, G. N. M. (2016). Translational control by eIF2α in neurons: Beyond the stress response. *Cytoskeleton*, *73*(10), 551–565.

Ben-Shem, A., Jenner, L., Yusupova, G., & Yusupov, M. (2010). Crystal Structure of the Eukaryotic Ribosome. *Science*, *330*(6008), 1203–1209.

Beringer, M., & Rodnina, M. V. (2007). The Ribosomal Peptidyl Transferase. *Molecular Cell*, *26*(3), 311–321.

Berlanga, J. J., Ventoso, I., Harding, H. P., Deng, J., Ron, D., Sonenberg, N., Carrasco, L., & de Haro, C. (2006). Antiviral effect of the mammalian translation initiation factor 2α kinase GCN2 against RNA viruses. *The EMBO Journal*, *25*(8), 1730–1740.

Bley, N., Lederer, M., Pfalz, B., Reinke, C., Fuchs, T., Glaß, M., Möller, B., & Hüttelmaier, S. (2015). Stress granules are dispensable for mRNA stabilization during cellular stress. *Nucleic Acids Research*, *43*(4), e26–e26.

Bloch, D. B., Sinow, C. O., Sauer, A. J., & Corman, B. H. P. (2023). Assembly and regulation of the mammalian mRNA processing body. *PLOS ONE*, *18*(3), e0282496.

Boesen, T., Mohammad, S. S., Pavitt, G. D., & Andersen, G. R. (2004). Structure of the Catalytic Fragment of Translation Initiation Factor 2B and Identification of a Critically Important Catalytic Residue. *Journal of Biological Chemistry*, *279*(11), 10584–10592.

Bogorad, A. M., Lin, K. Y., & Marintchev, A. (2017). Novel mechanisms of eIF2B action and regulation by eIF2α phosphorylation. *Nucleic Acids Research*, *45*(20), 11962–11979.

Bogorad, A. M., Xia, B., Sandor, D. G., Mamonov, A. B., Cafarella, T. R., Jehle, S., Vajda, S., Kozakov, D., & Marintchev, A. (2014). Insights into the Architecture of the eIF2Bα/β/δ Regulatory Subcomplex. *Biochemistry*, *53*(21), 3432–3445.

Boone, M., Wang, L., Lawrence, R. E., Frost, A., Walter, P., & Schoof, M. (2022). A point mutation in the nucleotide exchange factor eIF2B constitutively activates the integrated stress response by allosteric modulation. *ELife*, *11*.

Bordeaux, J., Welsh, A. W., Agarwal, S., Killiam, E., Baquero, M. T., Hanna, J. A., Anagnostou, V. K., & Rimm, D. L. (2010). Antibody validation. *BioTechniques*, *48*(3), 197–209.

Brengues, M., Teixeira, D., & Parker, R. (2005). Movement of Eukaryotic mRNAs Between Polysomes and Cytoplasmic Processing Bodies. *Science*, *310*(5747), 486–489.

Brostrom, C. O., & Brostrom, M. A. (1997). *Regulation of Translational Initiation during Cellular Responses to Stress* (pp. 79–125).

Browning, K. S., & Bailey-Serres, J. (2015). Mechanism of Cytoplasmic mRNA Translation. *The Arabidopsis Book*, *13*, e0176.

Brownsword, M. J., & Locker, N. (2023). A little less aggregation a little more replication: Viral manipulation of stress granules. *WIREs RNA*, *14*(1).

Brück, W., Herms, J., Brockmann, K., Schulz-Schaeffer, W., & Hanefeld, F. (2001). Myelinopathia centralis diffusa (vanishing white matter disease): Evidence of apoptotic oligodendrocyte degeneration in early lesion development. *Annals of Neurology*, *50*(4), 532–536.

Buchan, J. R. (2014). mRNP granules. *RNA Biology*, *11*(8), 1019–1030.

Buchan, J. R., Yoon, J.-H., & Parker, R. (2011). Stress-specific composition, assembly and kinetics of stress granules in *Saccharomyces cerevisiae*. *Journal of Cell Science*, *124*(2), 228–239.

Bugiani, M., Boor, I., van Kollenburg, B., Postma, N., Polder, E., van Berkel, C., van Kesteren, R. E., Windrem, M. S., Hol, E. M., Scheper, G. C., Goldman, S. A., & van der Knaap, M. S. (2011). Defective Glial Maturation in Vanishing White Matter Disease. *Journal of Neuropathology & Experimental Neurology*, *70*(1), 69–82.

Bugiani, M., Vuong, C., Breur, M., & van der Knaap, M. S. (2018). Vanishing white matter: a leukodystrophy due to astrocytic dysfunction. *Brain Pathology*, *28*(3), 408–421.

Bukhari, S. N. H., Webber, J., & Mehbodniya, A. (2022). Decision tree based ensemble machine learning model for the prediction of Zika virus T-cell epitopes as potential vaccine candidates. *Scientific Reports*, *12*(1), 7810.

Burry, R. W. (2010). *Immunocytochemistry*. Springer New York.

Burry, R. W. (2011). Controls for Immunocytochemistry. *Journal of Histochemistry & Cytochemistry*, *59*(1), 6–12.

Bushman, J. L., Foiani, M., Cigan, A. M., Paddon, C. J., & Hinnebusch, A. G. (1993). Guanine Nucleotide Exchange Factor for Eukaryotic Translation Initiation Factor 2 in *Saccharomyces cerevisiae* : Interactions between the

Essential Subunits GCD2, GCD6, and GCD7 and the Regulatory Subunit GCN3. *Molecular and Cellular Biology*, *13*(8), 4618–4631.

Campbell, S. G., & Ashe, M. P. (2007). *An Approach to Studying the Localization and Dynamics of Eukaryotic Translation Factors in Live Yeast Cells* (pp. 33–45).

Campbell, S. G., Hoyle, N. P., & Ashe, M. P. (2005). Dynamic cycling of eIF2 through a large eIF2B-containing cytoplasmic body: Implications for translation control. *Journal of Cell Biology*, *170*(6), 925–934.

Campos-Melo, D., Hawley, Z. C. E., Droppelmann, C. A., & Strong, M. J. (2021). The Integral Role of RNA in Stress Granule Formation and Function. *Frontiers in Cell and Developmental Biology*, *9*.

Castilho, B. A., Shanmugam, R., Silva, R. C., Ramesh, R., Himme, B. M., & Sattlegger, E. (2014). Keeping the eIF2 alpha kinase Gcn2 in check. *Biochimica et Biophysica Acta (BBA) - Molecular Cell Research*, *1843*(9), 1948–1968.

Chen, H.-Z., Tang, L.-L., Yu, X.-L., Zhou, J., Chang, Y.-F., & Wu, X. (2020). Bioinformatics analysis of epitope-based vaccine design against the novel SARS-CoV-2. *Infectious Diseases of Poverty*, *9*(1), 88.

Chen, M., Asanuma, M., Takahashi, M., Shichino, Y., Mito, M., Fujiwara, K., Saito, H., Floor, S. N., Ingolia, N. T., Sodeoka, M., Dodo, K., Ito, T., & Iwasaki, S. (2021). Dual targeting of DDX3 and eIF4A by the translation inhibitor rocaglamide A. *Cell Chemical Biology*, *28*(4), 475-486.e8.

Cheung, Y.-N., Maag, D., Mitchell, S. F., Fekete, C. A., Algire, M. A., Takacs, J. E., Shirokikh, N., Pestova, T., Lorsch, J. R., & Hinnebusch, A. G. (2007). Dissociation of eIF1 from the 40S ribosomal subunit is a key step in start codon selection in vivo. *Genes & Development*, *21*(10), 1217–1230.

Chowdhury, A., & Tharun, S. (2009). Activation of decapping involves binding of the mRNA and facilitation of the post-binding steps by the Lsm1-7-Pat1 complex. *RNA (New York, N.Y.)*, *15*(10), 1837–1848.

Choy, M. S., Yusoff, P., Lee, I. C., Newton, J. C., Goh, C. W., Page, R., Shenolikar, S., & Peti, W. (2015). Structural and Functional Analysis of the GADD34:PP1 eIF2α Phosphatase. *Cell Reports*, *11*(12), 1885–1891.

Chukka, P. A. R., Wetmore, S. D., & Thakor, N. (2021). Established and Emerging Regulatory Roles of Eukaryotic Translation Initiation Factor 5B (eIF5B). *Frontiers in Genetics*, *12*.

Circir, A., Koksal Bicakci, G., Savas, B., Doken, D. N., Henden, Ş. O., Can, T., Karaca, E., & Erson-Bensan, A. E. (2022). A C-term truncated EIF2Bγ protein encoded by an intronically polyadenylated isoform introduces unfavorable EIF2Bγ–EIF2γ interactions. *Proteins: Structure, Function, and Bioinformatics*, *90*(3), 889–897.

Cirillo, L., Cieren, A., Barbieri, S., Khong, A., Schwager, F., Parker, R., & Gotta, M. (2020). UBAP2L Forms Distinct Cores that Act in Nucleating Stress Granules Upstream of G3BP1. *Current Biology*, *30*(4), 698-707.e6.

Colgan, D. F., & Manley, J. L. (1997). Mechanism and regulation of mRNA polyadenylation. *Genes & Development*, *11*(21), 2755–2766.

Coots, R. A., Liu, X.-M., Mao, Y., Dong, L., Zhou, J., Wan, J., Zhang, X., & Qian, S.-B. (2017). m6A Facilitates eIF4F-Independent mRNA Translation. *Molecular Cell*, *68*(3), 504-514.e7.

Costa-Mattioli, M., Gobert, D., Stern, E., Gamache, K., Colina, R., Cuello, C., Sossin, W., Kaufman, R., Pelletier, J., Rosenblum, K., Krnjević, K., Lacaille, J.-C., Nader, K., & Sonenberg, N. (2007). eIF2α Phosphorylation Bidirectionally Regulates the Switch from Short- to Long-Term Synaptic Plasticity and Memory. *Cell*, *129*(1), 195–206.

Cox, D., Raeburn, C., Sui, X., & Hatters, D. M. (2020). Protein aggregation in cell biology: An aggregomics perspective of health and disease. *Seminars in Cell & Developmental Biology*, *99*, 40–54.

Cristobal, C. D., Wang, C.-Y., Zuo, Z., Smith, J. A., Lindeke-Myers, A., Bellen, H. J., & Lee, H. K. (2022). Daam2 Regulates Myelin Structure and the Oligodendrocyte Actin Cytoskeleton through Rac1 and Gelsolin. *The Journal of Neuroscience*, *42*(9), 1679–1691.

Cui, W., Li, J., Ron, D., & Sha, B. (2011). The structure of the PERK kinase domain suggests the mechanism for its activation. *Acta Crystallographica Section D Biological Crystallography*, *67*(5), 423–428. h

Danchenko, M., Csaderova, L., Fournier, P. E., & Sekeyova, Z. (2019). Optimized fixation of actin filaments for improved indirect immunofluorescence staining of rickettsiae. *BMC Research Notes*, *12*(1), 657.

Dang, Y., Kedersha, N., Low, W.-K., Romo, D., Gorospe, M., Kaufman, R., Anderson, P., & Liu, J. O. (2006). Eukaryotic Initiation Factor 2α-

independent Pathway of Stress Granule Induction by the Natural Product Pateamine A. *Journal of Biological Chemistry*, *281*(43), 32870–32878.

Danielson, C. M., & Hope, T. J. (2013). Using Antiubiquitin Antibodies to Probe the Ubiquitination State Within rhTRIM5α Cytoplasmic Bodies. *AIDS Research and Human Retroviruses*, *29*(10), 1373–1385.

De Franco, E., Caswell, R., Johnson, M. B., Wakeling, M. N., Zung, A., Dũng, V. C., Bích Ngọc, C. T., Goonetilleke, R., Vivanco Jury, M., El-Khateeb, M., Ellard, S., Flanagan, S. E., Ron, D., & Hattersley, A. T. (2020). De Novo Mutations in *EIF2B1* Affecting eIF2 Signaling Cause Neonatal/Early-Onset Diabetes and Transient Hepatic Dysfunction. *Diabetes*, *69*(3), 477–483.

de Haro, C., & Ochoa, S. (1978). Mode of action of the hemin-controlled inhibitor of protein synthesis: studies with factors from rabbit reticulocytes. *Proceedings of the National Academy of Sciences*, *75*(6), 2713–2716.

De Matos, L. L., Trufelli, D. C., De Matos, M. G. L., & Da Silva Pinhal, M. A. (2010). Immunohistochemistry as an Important Tool in Biomarkers Detection and Clinical Practice. *Biomarker Insights*, *5*, BMI.S2185.

Decker, C. J., Teixeira, D., & Parker, R. (2007). Edc3p and a glutamine/asparagine-rich domain of Lsm4p function in processing body assembly in *Saccharomyces cerevisiae*. *The Journal of Cell Biology*, *179*(3), 437–449.

Deginet, E., Tilahun, R., Bishaw, S., Eshetu, K., & Moges, A. (2021). Probable Vanishing White Matter Disease: A Case Report and Literature Review. *Ethiopian Journal of Health Sciences*, *31*(6), 1307–1310.

Demeshkina, N., Jenner, L., Westhof, E., Yusupov, M., & Yusupova, G. (2012). A new understanding of the decoding principle on the ribosome. *Nature*, *484*(7393), 256–259.

Deng, J., Zhang, J., Gao, K., Zhou, L., Jiang, Y., Wang, J., & Wu, Y. (2023). Human-induced pluripotent stem cell-derived cerebral organoid of leukoencephalopathy with vanishing white matter. *CNS Neuroscience & Therapeutics*, *29*(4), 1049–1066.

Dever, T. E., Feng, L., Wek, R. C., Cigan, A. M., Donahue, T. F., & Hinnebusch, A. G. (1992). Phosphorylation of initiation factor 2α by protein kinase GCN2 mediates gene-specific translational control of GCN4 in yeast. *Cell*, *68*(3), 585–596.

Dever, T. E., & Green, R. (2012). The Elongation, Termination, and Recycling Phases of Translation in Eukaryotes. *Cold Spring Harbor Perspectives in Biology*, *4*(7), a013706–a013706.

Dever, T. E., Kinzy, T. G., & Pavitt, G. D. (2016). Mechanism and Regulation of Protein Synthesis in *Saccharomyces cerevisiae*. *Genetics*, *203*(1), 65–107.

Dey, M., Cao, C., Sicheri, F., & Dever, T. E. (2007). Conserved Intermolecular Salt Bridge Required for Activation of Protein Kinases PKR, GCN2, and PERK. *Journal of Biological Chemistry*, *282*(9), 6653–6660.

Dholakia, J. N., & Wahba, A. J. (1989). Mechanism of the nucleotide exchange reaction in eukaryotic polypeptide chain initiation. Characterization of the guanine nucleotide exchange factor as a GTP-binding protein. *The Journal of Biological Chemistry*, *264*(1), 546–550.

Donato, A., Kagias, K., Zhang, Y., & Hilliard, M. A. (2019). Neuronal sub-compartmentalization: a strategy to optimize neuronal function. *Biological Reviews*, *94*(3), 1023–1037.

Dong, R., Chu, Z., Yu, F., & Zha, Y. (2020). Contriving Multi-Epitope Subunit of Vaccine for COVID-19: Immunoinformatics Approaches. *Frontiers in Immunology*, *11*.

Dooves, S., Bugiani, M., Postma, N. L., Polder, E., Land, N., Horan, S. T., van Deijk, A.-L. F., van de Kreeke, A., Jacobs, G., Vuong, C., Klooster, J., Kamermans, M., Wortel, J., Loos, M., Wisse, L. E., Scheper, G. C., Abbink, T. E. M., Heine, V. M., & van der Knaap, M. S. (2016). Astrocytes are central in the pathomechanisms of vanishing white matter. *Journal of Clinical Investigation*, *126*(4), 1512–1524.

Dudek, E. J., Lampi, K. J., Lampi, J. A., Shang, F., King, J., Wang, Y., & Taylor, A. (2010). Ubiquitin Proteasome Pathway–Mediated Degradation of Proteins: Effects Due to Site-Specific Substrate Deamidation. *Investigative Opthalmology & Visual Science*, *51*(8), 4164.

Egbe, N. E., Paget, C. M., Wang, H., & Ashe, M. P. (2015). Alcohols inhibit translation to regulate morphogenesis in C. albicans. *Fungal Genetics and Biology*, *77*, 50–60.

Elia, A., Henry-Grant, R., Adiseshiah, C., Marboeuf, C., Buckley, R. J., Clemens, M. J., Mudan, S., & Pyronnet, S. (2017). Implication of 4E-BP1 protein dephosphorylation and accumulation in pancreatic cancer cell death

induced by combined gemcitabine and TRAIL. *Cell Death & Disease*, *8*(12), 3204.

Eliseev, B., Kryuchkova, P., Alkalaeva, E., & Frolova, L. (2011). A single amino acid change of translation termination factor eRF1 switches between bipotent and omnipotent stop-codon specificity †. *Nucleic Acids Research*, *39*(2), 599–608.

Elsby, R., Heiber, J. F., Reid, P., Kimball, S. R., Pavitt, G. D., & Barber, G. N. (2011). The Alpha Subunit of Eukaryotic Initiation Factor 2B (eIF2B) Is Required for eIF2-Mediated Translational Suppression of Vesicular Stomatitis Virus. *Journal of Virology*, *85*(19), 9716–9725.

Emara, M. M., Fujimura, K., Sciaranghella, D., Ivanova, V., Ivanov, P., & Anderson, P. (2012). Hydrogen peroxide induces stress granule formation independent of eIF2α phosphorylation. *Biochemical and Biophysical Research Communications*, *423*(4), 763–769.

Emara, M. M., Ivanov, P., Hickman, T., Dawra, N., Tisdale, S., Kedersha, N., Hu, G.-F., & Anderson, P. (2010). Angiogenin-induced tRNA-derived Stress-induced RNAs Promote Stress-induced Stress Granule Assembly. *Journal of Biological Chemistry*, *285*(14), 10959–10968.

Erickson, F. L., & Hannig, E. M. (1996). Ligand interactions with eukaryotic translation initiation factor 2: role of the gamma-subunit. *The EMBO Journal*, *15*(22), 6311–6320.

Eulalio, A., Behm-Ansmant, I., Schweizer, D., & Izaurralde, E. (2007). P-Body Formation Is a Consequence, Not the Cause, of RNA-Mediated Gene Silencing. *Molecular and Cellular Biology*, *27*(11), 3970–3981.

Fabian, J. R., Kimball, S. R., Heinzinger, N. K., & Jefferson, L. S. (1997). Subunit Assembly and Guanine Nucleotide Exchange Activity of Eukaryotic Initiation Factor-2B Expressed in Sf9 Cells. *Journal of Biological Chemistry*, *272*(19), 12359–12365.

Fan-Minogue, H., Du, M., Pisarev, A. V., Kallmeyer, A. K., Salas-Marco, J., Keeling, K. M., Thompson, S. R., Pestova, T. V., & Bedwell, D. M. (2008). Distinct eRF3 Requirements Suggest Alternate eRF1 Conformations Mediate Peptide Release during Eukaryotic Translation Termination. *Molecular Cell*, *30*(5), 599–609.

Fassler, J. S., Skuodas, S., Weeks, D. L., & Phillips, B. T. (2021). Protein Aggregation and Disaggregation in Cells and Development. *Journal of Molecular Biology*, *433*(21), 167215.

Ferreira, J. P., Noderer, W. L., Diaz de Arce, A. J., & Wang, C. L. (2014). Engineering ribosomal leaky scanning and upstream open reading frames for precise control of protein translation. *Bioengineered*, *5*(3), 186–192.

Fogli, A., & Boespflug-Tanguy, O. (2006). The large spectrum of eIF2B-related diseases. *Biochemical Society Transactions*, *34*(1), 22.

Fogli, A., Dionisi-Vici, C., Deodato, F., Bartuli, A., Boespflug-Tanguy, O., & Bertini, E. (2002). A severe variant of childhood ataxia with central hypomyelination/vanishing white matter leukoencephalopathy related to EIF21B5 mutation. *Neurology*, *59*(12), 1966–1968.

Fogli, A., Rodriguez, D., Eymard-Pierre, E., Bouhour, F., Labauge, P., Meaney, B. F., Zeesman, S., Kaneski, C. R., Schiffmann, R., & Boespflug-Tanguy, O. (2003). Ovarian Failure Related to Eukaryotic Initiation Factor 2B Mutations. *The American Journal of Human Genetics*, *72*(6), 1544–1550.

Fogli, A., Schiffmann, R., Bertini, E., Ughetto, S., Combes, P., Eymard-Pierre, E., Kaneski, C. R., Pineda, M., Troncoso, M., Uziel, G., Surtees, R., Pugin, D., Chaunu, M.-P., Rodriguez, D., & Boespflug-Tanguy, O. (2004). The effect of genotype on the natural history of eIF2B-related leukodystrophies. *Neurology*, *62*(9), 1509–1517.

Francalanci, P., Eymard-Pierre, E., Dionisi-Vici, C., Boldrini, R., Piemonte, F., Virgili, R., Fariello, G., Bosman, C., Santorelli, F. M., Boespflug-Tanguy, O., & Bertini, E. (2001). Fatal infantile leukodystrophy: A severe variant of CACH/VWM syndrome, allelic to chromosome 3q27. *Neurology*, *57*(2), 265–270.

Frank, C. L., Ge, X., Xie, Z., Zhou, Y., & Tsai, L.-H. (2010). Control of Activating Transcription Factor 4 (ATF4) Persistence by Multisite Phosphorylation Impacts Cell Cycle Progression and Neurogenesis*. *Journal of Biological Chemistry*, *285*(43), 33324–33337.

Fringer, J. M., Acker, M. G., Fekete, C. A., Lorsch, J. R., & Dever, T. E. (2007). Coupled Release of Eukaryotic Translation Initiation Factors 5B and 1A from 80S Ribosomes following Subunit Joining. *Molecular and Cellular Biology*, *27*(6), 2384–2397.

Galanis, K. A., Nastou, K. C., Papandreou, N. C., Petichakis, G. N., Pigis, D. G., & Iconomidou, V. A. (2021). Linear B-Cell Epitope Prediction for In Silico Vaccine Design: A Performance Review of Methods Available via Command-Line Interface. *International Journal of Molecular Sciences*, *22*(6), 3210.

García, M. A., Gil, J., Ventoso, I., Guerra, S., Domingo, E., Rivas, C., & Esteban, M. (2006). Impact of Protein Kinase PKR in Cell Biology: from Antiviral to Antiproliferative Action. *Microbiology and Molecular Biology Reviews*, *70*(4), 1032–1060.

Gascon-Bayarri, J., Campdelacreu, J., Sanchez-Castaneda, C., Martinez-Yelamos, S., Moragas, M., Scheper, G. C., Van der Knaap, M. S., & Rene, R. (2009). Leukoencephalopathy with vanishing white matter presenting with presenile dementia. *Journal of Neurology, Neurosurgery & Psychiatry*, *80*(7), 810–811.

Gebauer, F., & Hentze, M. W. (2004). Molecular mechanisms of translational control. *Nature Reviews Molecular Cell Biology*, *5*(10), 827–835.

Geva, M., Cabilly, Y., Assaf, Y., Mindroul, N., Marom, L., Raini, G., Pinchasi, D., & Elroy-Stein, O. (2010). A mouse model for eukaryotic translation initiation factor 2B-leucodystrophy reveals abnormal development of brain white matter. *Brain*, *133*(8), 2448–2461.

Gilbert, W. V., Zhou, K., Butler, T. K., & Doudna, J. A. (2007). Cap-Independent Translation Is Required for Starvation-Induced Differentiation in Yeast. *Science*, *317*(5842), 1224–1227.

Gilks, N., Kedersha, N., Ayodele, M., Shen, L., Stoecklin, G., Dember, L. M., & Anderson, P. (2004). Stress Granule Assembly Is Mediated by Prion-like Aggregation of TIA-1. *Molecular Biology of the Cell*, *15*(12), 5383–5398.

Goh, K. C. (2000). The protein kinase PKR is required for p38 MAPK activation and the innate immune response to bacterial endotoxin. *The EMBO Journal*, *19*(16), 4292–4297.

Gomez, E., Mohammad, S. S., & Pavitt, G. D. (2002). Characterization of the minimal catalytic domain within eIF2B: the guanine-nucleotide exchange factor for translation initiation. *The EMBO Journal*, *21*(19), 5292–5301.

Gordiyenko, Y., Llácer, J. L., & Ramakrishnan, V. (2019). Structural basis for the inhibition of translation through eIF2α phosphorylation. *Nature Communications*, *10*(1), 1–11.

Gordiyenko, Y., Schmidt, C., Jennings, M. D., Matak-Vinkovic, D., Pavitt, G. D., & Robinson, C. V. (2014). eIF2B is a decameric guanine nucleotide exchange factor with a γ2ε2 tetrameric core. *Nature Communications*, *5*(1), 3902.

Goss, D. J., Parkhurst, L. J., Mehta, H. B., Woodley, C. L., & Wahba, A. J. (1984). Studies on the role of eukaryotic nucleotide exchange factor in polypeptide chain initiation. *The Journal of Biological Chemistry*, *259*(12), 7374–7377.

Gromadski, K. B., Schümmer, T., Strømgaard, A., Knudsen, C. R., Kinzy, T. G., & Rodnina, M. V. (2007). Kinetics of the Interactions between Yeast Elongation Factors 1A and 1Bα, Guanine Nucleotides, and Aminoacyl-tRNA. *Journal of Biological Chemistry*, *282*(49), 35629–35637.

Gross, J. D., Moerke, N. J., von der Haar, T., Lugovskoy, A. A., Sachs, A. B., McCarthy, J. E. G., & Wagner, G. (2003). Ribosome Loading onto the mRNA Cap Is Driven by Conformational Coupling between eIF4G and eIF4E. *Cell*, *115*(6), 739–750.

Hagedorn, M., Neuhaus, E. M., & Soldati, T. (n.d.). Optimized Fixation and Immunofluorescence Staining Methods for <i>Dictyostelium</i> Cells. In *Dictyostelium discoideum Protocols* (pp. 327–338). Humana Press.

Halliday, M., Radford, H., Sekine, Y., Moreno, J., Verity, N., le Quesne, J., Ortori, C. A., Barrett, D. A., Fromont, C., Fischer, P. M., Harding, H. P., Ron, D., & Mallucci, G. R. (2015). Partial restoration of protein synthesis rates by the small molecule ISRIB prevents neurodegeneration without pancreatic toxicity. *Cell Death & Disease*, *6*(3), e1672–e1672.

Hamilton, E. M. C., van der Lei, H. D. W., Vermeulen, G., Gerver, J. A. M., Lourenço, C. M., Naidu, S., Mierzewska, H., Gemke, R. J. B. J., de Vet, H. C. W., Uitdehaag, B. M. J., Lissenberg-Witte, B. I., & van der Knaap, M. S. (2018). Natural History of Vanishing White Matter. *Annals of Neurology*, *84*(2), 274–288.

Han, A.-P. (2001). Heme-regulated eIF2alpha kinase (HRI) is required for translational regulation and survival of erythroid precursors in iron deficiency. *The EMBO Journal*, *20*(23), 6909–6918.

Han, J., Back, S. H., Hur, J., Lin, Y.-H., Gildersleeve, R., Shan, J., Yuan, C. L., Krokowski, D., Wang, S., Hatzoglou, M., Kilberg, M. S., Sartor, M. A., &

Kaufman, R. J. (2013). ER-stress-induced transcriptional regulation increases protein synthesis leading to cell death. *Nature Cell Biology*, *15*(5), 481–490.

Hanefeld, F., Holzbach, U., Kruse, B., Wilichowski, E., Christen, H., & Frahm, J. (1993). Diffuse White Matter Disease in Three Children: An Encephalopathy with Unique Features on Magnetic Resonance Imaging and Proton Magnetic Resonance Spectroscopy. *Neuropediatrics*, *24*(05), 244–248.

Hannig, E. M., & Hinnebusch, A. G. (1988). Molecular analysis of GCN3, a translational activator of GCN4: evidence for posttranslational control of GCN3 regulatory function. *Molecular and Cellular Biology*, *8*(11), 4808–4820.

Hannig, E. M., Williams, N. P., Wek, R. C., & Hinnebusch, A. G. (1990). The translational activator GCN3 functions downstream from GCN1 and GCN2 in the regulatory pathway that couples GCN4 expression to amino acid availability in Saccharomyces cerevisiae. *Genetics*, *126*(3), 549–562.

Hanson, F. M., de Oliveira, M. I. R., Cross, A. K., Allen, K. E., & Campbell, S. G. (2023). eIF2B localisation and its regulation during the integrated stress response is cell type specific. *BioRxiv*.

Hanson, J., Paliwal, K. K., Litfin, T., & Zhou, Y. (2019). SPOT-Disorder2: Improved Protein Intrinsic Disorder Prediction by Ensembled Deep Learning. *Genomics, Proteomics & Bioinformatics*, *17*(6), 645–656.

Hao, Q., Heo, J.-M., Nocek, B. P., Hicks, K. G., Stoll, V. S., Remarcik, C., Hackett, S., LeBon, L., Jain, R., Eaton, D., Rutter, J., Wong, Y. L., & Sidrauski, C. (2021). Sugar phosphate activation of the stress sensor eIF2B. *Nature Communications*, *12*(1), 3440.

Harbi, D., Kumar, M., & Harrison, P. M. (2011). LPS-annotate: complete annotation of compositionally biased regions in the protein knowledgebase. *Database*, *2011*(0), baq031–baq031.

Haste Andersen, P., Nielsen, M., & Lund, O. (2006). Prediction of residues in discontinuous B-cell epitopes using protein 3D structures. *Protein Science*, *15*(11), 2558–2567.

Hellen, C. U. T. (2018). Translation Termination and Ribosome Recycling in Eukaryotes. *Cold Spring Harbor Perspectives in Biology*, *10*(10), a032656.

Herrero, M., Daw, M., Atzmon, A., & Elroy-Stein, O. (2021). The Energy Status of Astrocytes Is the Achilles' Heel of eIF2B-Leukodystrophy. *Cells*, *10*(8), 1858.

Hershey, J. W. B., Sonenberg, N., & Mathews, M. B. (2019). Principles of Translational Control. *Cold Spring Harbor Perspectives in Biology*, *11*(9), a032607.

Hilbert, M., Kebbel, F., Gubaev, A., & Klostermeier, D. (2011). eIF4G stimulates the activity of the DEAD box protein eIF4A by a conformational guidance mechanism. *Nucleic Acids Research*, *39*(6), 2260–2270.

Hinnebusch, A. G. (2014). The Scanning Mechanism of Eukaryotic Translation Initiation. *Annual Review of Biochemistry*, *83*(1), 779–812.

Hinnebusch, A. G., & Lorsch, J. R. (2012). The Mechanism of Eukaryotic Translation Initiation: New Insights and Challenges. *Cold Spring Harbor Perspectives in Biology*, *4*(10), a011544–a011544.

Hipp, M. S., Park, S.-H., & Hartl, F. U. (2014). Proteostasis impairment in protein-misfolding and -aggregation diseases. *Trends in Cell Biology*, *24*(9), 506–514.

Hodgson, R. E., Varanda, B. A., Ashe, M. P., Allen, K. E., & Campbell, S. G. (2019). Cellular eIF2B subunit localization: implications for the integrated stress response and its control by small molecule drugs. *Molecular Biology of the Cell*, *30*(8), 942–958.

Hofmann, S., Kedersha, N., Anderson, P., & Ivanov, P. (2021). Molecular mechanisms of stress granule assembly and disassembly. *Biochimica et Biophysica Acta (BBA) - Molecular Cell Research*, *1868*(1), 118876.

Horzinski, L., Kantor, L., Huyghe, A., Schiffmann, R., Elroy-Stein, O., Boespflug-Tanguy, O., & Fogli, A. (2010). Evaluation of the endoplasmic reticulum-stress response in eIF2B-mutated lymphocytes and lymphoblasts from CACH/VWM patients. *BMC Neurology*, *10*(1), 94.

Hoyle, N. P., Castelli, L. M., Campbell, S. G., Holmes, L. E. A., & Ashe, M. P. (2007). Stress-dependent relocalization of translationally primed mRNPs to cytoplasmic granules that are kinetically and spatially distinct from P-bodies. *The Journal of Cell Biology*, *179*(1), 65–74.

Hua, C. K., Gacerez, A. T., Sentman, C. L., Ackerman, M. E., Choi, Y., & Bailey-Kellogg, C. (2017). Computationally-driven identification of antibody epitopes. *ELife*, *6*.

Huang, T., Phelps, C., Wang, J., Lin, L.-J., Bittel, A., Scott, Z., Jacques, S., Gibbs, S. L., Gray, J. W., & Nan, X. (2018). Simultaneous Multicolor Single-Molecule Tracking with Single-Laser Excitation via Spectral Imaging. *Biophysical Journal*, *114*(2), 301–310.

Hubstenberger, A., Courel, M., Bénard, M., Souquere, S., Ernoult-Lange, M., Chouaib, R., Yi, Z., Morlot, J.-B., Munier, A., Fradet, M., Daunesse, M., Bertrand, E., Pierron, G., Mozziconacci, J., Kress, M., & Weil, D. (2017). P-Body Purification Reveals the Condensation of Repressed mRNA Regulons. *Molecular Cell*, *68*(1), 144-157.e5.

Hulspas, R., O'Gorman, M. R. G., Wood, B. L., Gratama, J. W., & Sutherland, D. R. (2009). Considerations for the control of background fluorescence in clinical flow cytometry. *Cytometry Part B: Clinical Cytometry*, *76B*(6), 355–364.

Huston, J. S., Margolies, M. N., & Haber, E. (1996). *Antibody Binding Sites* (pp. 329–450).

Huyghe, A., Horzinski, L., Hénaut, A., Gaillard, M., Bertini, E., Schiffmann, R., Rodriguez, D., Dantal, Y., Boespflug-Tanguy, O., & Fogli, A. (2012). Developmental Splicing Deregulation in Leukodystrophies Related to EIF2B Mutations. *PLoS ONE*, *7*(6), e38264.

Ikari, R., Mukaisho, K., Kageyama, S., Nagasawa, M., Kubota, S., Nakayama, T., Murakami, S., Taniura, N., Tanaka, H., Kushima, R. P., & Kawauchi, A. (2021). Differences in the Central Energy Metabolism of Cancer Cells between Conventional 2D and Novel 3D Culture Systems. *International Journal of Molecular Sciences*, *22*(4), 1805.

Im, K., Mareninov, S., Diaz, M. F. P., & Yong, W. H. (2019). *An Introduction to Performing Immunofluorescence Staining* (pp. 299–311).

Irfan Maqsood, M., Matin, M. M., Bahrami, A. R., & Ghasroldasht, M. M. (2013). Immortality of cell lines: challenges and advantages of establishment. *Cell Biology International*, *37*(10), 1038–1045.

Ishibashi, T., Dakin, K. A., Stevens, B., Lee, P. R., Kozlov, S. V., Stewart, C. L., & Fields, R. D. (2006). Astrocytes Promote Myelination in Response to Electrical Impulses. *Neuron*, *49*(6), 823–832.

Ismail, H., Liu, X., Yang, F., Li, J., Zahid, A., Dou, Z., Liu, X., & Yao, X. (2021). Mechanisms and regulation underlying membraneless organelle plasticity control. *Journal of Molecular Cell Biology*, *13*(4), 239–258.

Ivanov, P., Kedersha, N., & Anderson, P. (2019). Stress Granules and Processing Bodies in Translational Control. *Cold Spring Harbor Perspectives in Biology*, *11*(5), a032813.

Jackson, M. P., & Hewitt, E. W. (2016). Cellular proteostasis: degradation of misfolded proteins by lysosomes. *Essays in Biochemistry*, *60*(2), 173–180.

Jackson, R. J., Hellen, C. U. T., & Pestova, T. V. (2010). The mechanism of eukaryotic translation initiation and principles of its regulation. *Nature Reviews Molecular Cell Biology*, *11*(2), 113–127.

Jain, S., Wheeler, J. R., Walters, R. W., Agrawal, A., Barsic, A., & Parker, R. (2016). ATPase-Modulated Stress Granules Contain a Diverse Proteome and Substructure. *Cell*, *164*(3), 487–498.

Jennings, M. D., Kershaw, C. J., Adomavicius, T., & Pavitt, G. D. (2017). Fail-safe control of translation initiation by dissociation of eIF2α phosphorylated ternary complexes. *ELife*, *6*.

Jennings, M. D., & Pavitt, G. D. (2010). eIF5 has GDI activity necessary for translational control by eIF2 phosphorylation. *Nature*, *465*(7296), 378–381.

Jennings, M. D., & Pavitt, G. D. (2014). A new function and complexity for protein translation initiation factor eIF2B. *Cell Cycle*, *13*(17), 2660–2665.

Jennings, M. D., Zhou, Y., Mohammad-Qureshi, S. S., Bennett, D., & Pavitt, G. D. (2013). eIF2B promotes eIF5 dissociation from eIF2•GDP to facilitate guanine nucleotide exchange for translation initiation. *Genes & Development*, *27*(24), 2696–2707.

Jespersen, M. C., Peters, B., Nielsen, M., & Marcatili, P. (2017). BepiPred-2.0: improving sequence-based B-cell epitope prediction using conformational epitopes. *Nucleic Acids Research*, *45*(W1), W24–W29.

Jiang, H.-Y., & Wek, R. C. (2005). Phosphorylation of the α-Subunit of the Eukaryotic Initiation Factor-2 (eIF2α) Reduces Protein Synthesis and Enhances Apoptosis in Response to Proteasome Inhibition. *Journal of Biological Chemistry*, *280*(14), 14189–14202.

Jiang, Z., Belforte, J. E., Lu, Y., Yabe, Y., Pickel, J., Smith, C. B., Je, H.-S., Lu, B., & Nakazawa, K. (2010). eIF2α Phosphorylation-Dependent Translation in CA1 Pyramidal Cells Impairs Hippocampal Memory Consolidation without Affecting General Translation. *The Journal of Neuroscience*, *30*(7), 2582–2594.

Kamphuis, W., Mamber, C., Moeton, M., Kooijman, L., Sluijs, J. A., Jansen, A. H. P., Verveer, M., de Groot, L. R., Smith, V. D., Rangarajan, S., Rodríguez, J. J., Orre, M., & Hol, E. M. (2012). GFAP Isoforms in Adult Mouse Brain with a Focus on Neurogenic Astrocytes and Reactive Astrogliosis in Mouse Models of Alzheimer Disease. *PLoS ONE*, *7*(8), e42823.

Kantor, L., Harding, H. P., Ron, D., Schiffmann, R., Kaneski, C. R., Kimball, S. R., & Elroy-Stein, O. (2005). Heightened stress response in primary fibroblasts expressing mutant eIF2B genes from CACH/VWM leukodystrophy patients. *Human Genetics*, *118*(1), 99–106.

Kärblane, K., Gerassimenko, J., Nigul, L., Piirsoo, A., Smialowska, A., Vinkel, K., Kylsten, P., Ekwall, K., Swoboda, P., Truve, E., & Sarmiento, C. (2015). ABCE1 Is a Highly Conserved RNA Silencing Suppressor. *PLOS ONE*, *10*(2), e0116702.

Kashiwagi, K., Shichino, Y., Osaki, T., Sakamoto, A., Nishimoto, M., Takahashi, M., Mito, M., Weber, F., Ikeuchi, Y., Iwasaki, S., & Ito, T. (2021). eIF2B-capturing viral protein NSs suppresses the integrated stress response. *Nature Communications*, *12*(1), 7102.

Kashiwagi, K., Takahashi, M., Nishimoto, M., Hiyama, T. B., Higo, T., Umehara, T., Sakamoto, K., Ito, T., & Yokoyama, S. (2016). Crystal structure of eukaryotic translation initiation factor 2B. *Nature*, *531*(7592), 122–125.

Kashiwagi, K., Yokoyama, T., Nishimoto, M., Takahashi, M., Sakamoto, A., Yonemochi, M., Shirouzu, M., & Ito, T. (2019). Structural basis for eIF2B inhibition in integrated stress response. *Science*, *364*(6439), 495–499.

Kaufman, R. J. (1999). Stress signaling from the lumen of the endoplasmic reticulum: coordination of gene transcriptional and translational controls. *Genes & Development*, *13*(10), 1211–1233.

Kaur, G., & Dufour, J. M. (2012). Cell lines. *Spermatogenesis*, *2*(1), 1–5.

Kedersha, N., Chen, S., Gilks, N., Li, W., Miller, I. J., Stahl, J., & Anderson, P. (2002). Evidence That Ternary Complex (eIF2-GTP-tRNA$_i^{Met}$)–Deficient Preinitiation Complexes Are Core Constituents of Mammalian Stress Granules. *Molecular Biology of the Cell*, *13*(1), 195–210.

Kedersha, N., Ivanov, P., & Anderson, P. (2013). Stress granules and cell signaling: more than just a passing phase? *Trends in Biochemical Sciences*, *38*(10), 494–506.

Kedersha, N. L., Gupta, M., Li, W., Miller, I., & Anderson, P. (1999). RNA-Binding Proteins Tia-1 and Tiar Link the Phosphorylation of Eif-2α to the Assembly of Mammalian Stress Granules. *The Journal of Cell Biology*, *147*(7), 1431–1442.

Kedersha, N., Stoecklin, G., Ayodele, M., Yacono, P., Lykke-Andersen, J., Fritzler, M. J., Scheuner, D., Kaufman, R. J., Golan, D. E., & Anderson, P. (2005). Stress granules and processing bodies are dynamically linked sites of mRNP remodeling. *The Journal of Cell Biology*, *169*(6), 871–884.

Kenner, L. R., Anand, A. A., Nguyen, H. C., Myasnikov, A. G., Klose, C. J., McGeever, L. A., Tsai, J. C., Miller-Vedam, L. E., Walter, P., & Frost, A. (2019). eIF2B-catalyzed nucleotide exchange and phosphoregulation by the integrated stress response. *Science*, *364*(6439), 491–495.

Kershaw, C. J., Jennings, M. D., Cortopassi, F., Guaita, M., Al-Ghafli, H., & Pavitt, G. D. (2021). GTP binding to translation factor eIF2B stimulates its guanine nucleotide exchange activity. *IScience*, *24*(12), 103454.

Kimball, S. R., Horetsky, R. L., & Jefferson, L. S. (1998). Implication of eIF2B Rather Than eIF4E in the Regulation of Global Protein Synthesis by Amino Acids in L6 Myoblasts. *Journal of Biological Chemistry*, *273*(47), 30945–30953.

Kimball, S. R., Horetsky, R. L., Ron, D., Jefferson, L. S., & Harding, H. P. (2003). Mammalian stress granules represent sites of accumulation of stalled translation initiation complexes. *American Journal of Physiology-Cell Physiology*, *284*(2), C273–C284.

Klaips, C. L., Jayaraj, G. G., & Hartl, F. U. (2018). Pathways of cellular proteostasis in aging and disease. *Journal of Cell Biology*, *217*(1), 51–63.

Kleiger, G., & Mayor, T. (2014). Perilous journey: a tour of the ubiquitin–proteasome system. *Trends in Cell Biology*, *24*(6), 352–359.

Klein, U., Ramirez, M. T., Kobilka, B. K., & von Zastrow, M. (1997). A Novel Interaction between Adrenergic Receptors and the α-Subunit of Eukaryotic Initiation Factor 2B. *Journal of Biological Chemistry*, *272*(31), 19099–19102.

Klok, M. D., Bugiani, M., de Vries, S. I., Gerritsen, W., Breur, M., van der Sluis, S., Heine, V. M., Kole, M. H. P., Baron, W., & van der Knaap, M. S. (2018). Axonal abnormalities in vanishing white matter. *Annals of Clinical and Translational Neurology*, *5*(4), 429–444.

Korneeva, N.L. (2022) ‘Integrated stress response in neuronal pathology and in health’, *Biochemistry (Moscow)*, 87(S1). doi:10.1134/s0006297922140103.

Konieczny, A., & Safer, B. (1983). Purification of the eukaryotic initiation factor 2-eukaryotic initiation factor 2B complex and characterization of its guanine nucleotide exchange activity during protein synthesis initiation. *Journal of Biological Chemistry*, *258*(5), 3402–3408.

Koonin, E. V. (1995). Multidomain organization of eukaryotic guanine nucleotide exchange translation initiation factor eIF-2B subunits revealed by analysis of conserved sequence motifs. *Protein Science*, *4*(8), 1608–1617.

Kringelum, J. V., Lundegaard, C., Lund, O., & Nielsen, M. (2012). Reliable B Cell Epitope Predictions: Impacts of Method Development and Improved Benchmarking. *PLoS Computational Biology*, *8*(12), e1002829.

Kringelum, J. V., Nielsen, M., Padkjær, S. B., & Lund, O. (2013). Structural analysis of B-cell epitopes in antibody:protein complexes. *Molecular Immunology*, *53*(1–2), 24–34.

Kuhle, B., Eulig, N. K., & Ficner, R. (2015). Architecture of the eIF2B regulatory subcomplex and its implications for the regulation of guanine nucleotide exchange on eIF2. *Nucleic Acids Research*, gkv930.

Kwan, T., & Thompson, S. R. (2019). Noncanonical Translation Initiation in Eukaryotes. *Cold Spring Harbor Perspectives in Biology*, *11*(4), a032672.

La Piana, R., Vanderver, A., van der Knaap, M., Roux, L., Tampieri, D., Brais, B., & Bernard, G. (2012). Adult-Onset Vanishing White Matter Disease Due to a Novel EIF2B3 Mutation. *Archives of Neurology*, *69*(6).

Laberiano-Fernández, C., Hernández-Ruiz, S., Rojas, F., & Parra, E. R. (2021). Best Practices for Technical Reproducibility Assessment of Multiplex Immunofluorescence. *Frontiers in Molecular Biosciences*, *8*.

Ladran, I., Tran, N., Topol, A., & Brennand, K. J. (2013). Neural stem and progenitor cells in health and disease. *WIREs Systems Biology and Medicine*, *5*(6), 701–715.

Lavoie, H., Li, J. J., Thevakumaran, N., Therrien, M., & Sicheri, F. (2014). Dimerization-induced allostery in protein kinase regulation. *Trends in Biochemical Sciences*, *39*(10), 475–486.

Lee, J. H., Pestova, T. V., Shin, B.-S., Cao, C., Choi, S. K., & Dever, T. E. (2002). Initiation factor eIF5B catalyzes second GTP-dependent step in

eukaryotic translation initiation. *Proceedings of the National Academy of Sciences*, *99*(26), 16689–16694.

Leegwater, P. A. J., Vermeulen, G., Könst, A. A. M., Naidu, S., Mulders, J., Visser, A., Kersbergen, P., Mobach, D., Fonds, D., van Berkel, C. G. M., Lemmers, R. J. L. F., Frants, R. R., Oudejans, C. B. M., Schutgens, R. B. H., Pronk, J. C., & van der Knaap, M. S. (2001). Subunits of the translation initiation factor eIF2B are mutant in leukoencephalopathy with vanishing white matter. *Nature Genetics*, *29*(4), 383–388.

Leferink, P. S., Dooves, S., Hillen, A. E. J., Watanabe, K., Jacobs, G., Gasparotto, L., Cornelissen-Steijger, P., Knaap, M. S., & Heine, V. M. (2019). Astrocyte Subtype Vulnerability in Stem Cell Models of Vanishing White Matter. *Annals of Neurology*, *86*(5), 780–792.

Li, W., Wang, X., van der Knaap, M. S., & Proud, C. G. (2004). Mutations Linked to Leukoencephalopathy with Vanishing White Matter Impair the Function of the Eukaryotic Initiation Factor 2B Complex in Diverse Ways. *Molecular and Cellular Biology*, *24*(8), 3295–3306.

Liang, S.-H., Zhang, W., Mcgrath, B. C., Zhang, P., & Cavener, D. R. (2006). PERK (eIF2α kinase) is required to activate the stress-activated MAPKs and induce the expression of immediate-early genes upon disruption of ER calcium homoeostasis. *Biochemical Journal*, *393*(1), 201–209.

Liberman, N., Gandin, V., Svitkin, Y. V., David, M., Virgili, G., Jaramillo, M., Holcik, M., Nagar, B., Kimchi, A., & Sonenberg, N. (2015). DAP5 associates with eIF2β and eIF4AI to promote Internal Ribosome Entry Site driven translation. *Nucleic Acids Research*, *43*(7), 3764–3775.

Lin, H.-K., Chen, Z., Wang, G., Nardella, C., Lee, S.-W., Chan, C.-H., Yang, W.-L., Wang, J., Egia, A., Nakayama, K. I., Cordon-Cardo, C., Teruya-Feldstein, J., & Pandolfi, P. P. (2010). Skp2 targeting suppresses tumorigenesis by Arf-p53-independent cellular senescence. *Nature*, *464*(7287), 374–379.

Liu, R., van der Lei, H. D. W., Wang, X., Wortham, N. C., Tang, H., van Berkel, C. G. M., Mufunde, T. A., Huang, W., van der Knaap, M. S., Scheper, G. C., & Proud, C. G. (2011). Severity of vanishing white matter disease does not correlate with deficits in eIF2B activity or the integrity of eIF2B complexes. *Human Mutation*, *32*(9), 1036–1045.

Llácer, J. L., Hussain, T., Saini, A. K., Nanda, J. S., Kaur, S., Gordiyenko, Y., Kumar, R., Hinnebusch, A. G., Lorsch, J. R., & Ramakrishnan, V. (2018). Translational initiation factor eIF5 replaces eIF1 on the 40S ribosomal subunit to promote start-codon recognition. *ELife*, *7*.

Loveland, A. B., Demo, G., Grigorieff, N., & Korostelev, A. A. (2017). Ensemble cryo-EM elucidates the mechanism of translation fidelity. *Nature*, *546*(7656), 113–117.

Lozano, G., Francisco-Velilla, R., & Martinez-Salas, E. (2018). Deconstructing internal ribosome entry site elements: an update of structural motifs and functional divergences. *Open Biology*, *8*(11), 180155.

Lu, L., Han, A.-P., & Chen, J.-J. (2001). Translation Initiation Control by Heme-Regulated Eukaryotic Initiation Factor 2α Kinase in Erythroid Cells under Cytoplasmic Stresses. *Molecular and Cellular Biology*, *21*(23), 7971–7980.

Lu, P. D., Harding, H. P., & Ron, D. (2004). Translation reinitiation at alternative open reading frames regulates gene expression in an integrated stress response. *The Journal of Cell Biology*, *167*(1), 27–33.

Luna, R. E., Arthanari, H., Hiraishi, H., Nanda, J., Martin-Marcos, P., Markus, M. A., Akabayov, B., Milbradt, A. G., Luna, L. E., Seo, H.-C., Hyberts, S. G., Fahmy, A., Reibarkh, M., Miles, D., Hagner, P. R., O'Day, E. M., Yi, T., Marintchev, A., Hinnebusch, A. G., … Wagner, G. (2012). The C-Terminal Domain of Eukaryotic Initiation Factor 5 Promotes Start Codon Recognition by Its Dynamic Interplay with eIF1 and eIF2β. *Cell Reports*, *1*(6), 689–702.

Luo, Y., Na, Z., & Slavoff, S. A. (2018). P-Bodies: Composition, Properties, and Functions. *Biochemistry*, *57*(17), 2424–2431.

Maag, D., & Lorsch, J. R. (2003). Communication Between Eukaryotic Translation Initiation Factors 1 and 1A on the Yeast Small Ribosomal Subunit. *Journal of Molecular Biology*, *330*(5), 917–924.

Majumdar, R., Bandyopadhyay, A., & Maitra, U. (2003). Mammalian Translation Initiation Factor eIF1 Functions with eIF1A and eIF3 in the Formation of a Stable 40 S Preinitiation Complex. *Journal of Biological Chemistry*, *278*(8), 6580–6587.

Man, J. H. K., van Gelder, C. A. G. H., Breur, M., Molenaar, D., Abbink, T., Altelaar, M., Bugiani, M., & van der Knaap, M. S. (2023). Regional vulnerability of brain white matter in vanishing white matter. *Acta Neuropathologica Communications*, *11*(1), 103.

Manchester, K. L. (2001). Catalysis of Guanine Nucleotide Exchange on eIF2 by eIF2B: Can It Be both a Substituted Enzyme and a Sequential Mechanism? *Biochemical and Biophysical Research Communications*, *289*(3), 643–646.

Marasco, O. N. J. M., Roussel, M. R., & Thakor, N. (2022). Probabilistic models of uORF-mediated ATF4 translation control. *Mathematical Biosciences*, *343*, 108762.

Marini, G., Nüske, E., Leng, W., Alberti, S., & Pigino, G. (2020). Reorganization of budding yeast cytoplasm upon energy depletion. *Molecular Biology of the Cell*, *31*(12), 1232–1245.

Marintchev, A., & Ito, T. (2020). eIF2B and the Integrated Stress Response: A Structural and Mechanistic View. *Biochemistry*, *59*(13), 1299–1308.

Martin, E. W., & Mittag, T. (2018). Relationship of Sequence and Phase Separation in Protein Low-Complexity Regions. *Biochemistry*, *57*(17), 2478–2487.

Mateju, D., Eichenberger, B., Voigt, F., Eglinger, J., Roth, G., & Chao, J. A. (2020). Single-Molecule Imaging Reveals Translation of mRNAs Localized to Stress Granules. *Cell*, *183*(7), 1801-1812.e13.

Mathieu, C., Pappu, R. V., & Taylor, J. P. (2020). Beyond aggregation: Pathological phase transitions in neurodegenerative disease. *Science*, *370*(6512), 56–60.

Matsukawa, T., Wang, X., Liu, R., Wortham, N. C., Onuki, Y., Kubota, A., Hida, A., Kowa, H., Fukuda, Y., Ishiura, H., Mitsui, J., Takahashi, Y., Aoki, S., Takizawa, S., Shimizu, J., Goto, J., Proud, C. G., & Tsuji, S. (2011). Adult-onset leukoencephalopathies with vanishing white matter with novel missense mutations in EIF2B2, EIF2B3, and EIF2B5. *Neurogenetics*, *12*(3), 259–261.

Mayberry, L. K., Allen, M. L., Dennis, M. D., & Browning, K. S. (2009). Evidence for Variation in the Optimal Translation Initiation Complex: Plant eIF4B, eIF4F, and eIF(iso)4F Differentially Promote Translation of mRNAs. *Plant Physiology*, *150*(4), 1844–1854.

McEwen, E., Kedersha, N., Song, B., Scheuner, D., Gilks, N., Han, A., Chen, J.-J., Anderson, P., & Kaufman, R. J. (2005). Heme-regulated Inhibitor Kinase-mediated Phosphorylation of Eukaryotic Translation Initiation Factor 2 Inhibits Translation, Induces Stress Granule Formation, and Mediates

Survival upon Arsenite Exposure. *Journal of Biological Chemistry*, *280*(17), 16925–16933.

Mercado, G., Castillo, V., Soto, P., López, N., Axten, J. M., Sardi, S. P., Hoozemans, J. J. M., & Hetz, C. (2018). Targeting PERK signaling with the small molecule GSK2606414 prevents neurodegeneration in a model of Parkinson's disease. *Neurobiology of Disease*, *112*, 136–148.

Merrick, W. C., & Pavitt, G. D. (2018). Protein Synthesis Initiation in Eukaryotic Cells. *Cold Spring Harbor Perspectives in Biology*, *10*(12), a033092.

Mészáros, B., Erdős, G., & Dosztányi, Z. (2018). IUPred2A: context-dependent prediction of protein disorder as a function of redox state and protein binding. *Nucleic Acids Research*, *46*(W1), W329–W337.

Meyer, K. D., Patil, D. P., Zhou, J., Zinoviev, A., Skabkin, M. A., Elemento, O., Pestova, T. V., Qian, S.-B., & Jaffrey, S. R. (2015). 5′ UTR m6A Promotes Cap-Independent Translation. *Cell*, *163*(4), 999–1010.

Mohammad-Qureshi, S. S., Haddad, R., Hemingway, E. J., Richardson, J. P., & Pavitt, G. D. (2007). Critical Contacts between the Eukaryotic Initiation Factor 2B (eIF2B) Catalytic Domain and both eIF2β and -2γ Mediate Guanine Nucleotide Exchange. *Molecular and Cellular Biology*, *27*(14), 5225–5234.

Mokas, S., Mills, J. R., Garreau, C., Fournier, M.-J., Robert, F., Arya, P., Kaufman, R. J., Pelletier, J., & Mazroui, R. (2009). Uncoupling Stress Granule Assembly and Translation Initiation Inhibition. *Molecular Biology of the Cell*, *20*(11), 2673–2683.

Monsellier, E., Ramazzotti, M., Taddei, N., & Chiti, F. (2008). Aggregation Propensity of the Human Proteome. *PLoS Computational Biology*, *4*(10), e1000199.

Moon, S. L., Morisaki, T., Khong, A., Lyon, K., Parker, R., & Stasevich, T. J. (2019). Multicolour single-molecule tracking of mRNA interactions with RNP granules. *Nature Cell Biology*, *21*(2), 162–168.

Moon, S. L., & Parker, R. (2018a). Analysis of eIF2B bodies and their relationships with stress granules and P-bodies. *Scientific Reports*, *8*(1), 12264.

Moon, S. L., & Parker, R. (2018b). EIF2B2 mutations in vanishing white matter disease hypersuppress translation and delay recovery during the integrated stress response. *RNA*, *24*(6), 841–852.

Moon, S., & Namkoong, S. (2023). Ribonucleoprotein Granules: Between Stress and Transposable Elements. *Biomolecules*, *13*(7), 1027.

Moortgat, S., Désir, J., Benoit, V., Boulanger, S., Pendeville, H., Nassogne, M.-C., Lederer, D., & Maystadt, I. (2016). Two novel *EIF2S3* mutations associated with syndromic intellectual disability with severe microcephaly, growth retardation, and epilepsy. *American Journal of Medical Genetics Part A*, *170*(11), 2927–2933.

Moreau, V., Granier, C., Villard, S., Laune, D., & Molina, F. (2006). Discontinuous epitope prediction based on mimotope analysis. *Bioinformatics*, *22*(9), 1088–1095.

Moreno-Gonzalez, I., & Soto, C. (2011). Misfolded protein aggregates: Mechanisms, structures and potential for disease transmission. *Seminars in Cell & Developmental Biology*, *22*(5), 482–487.

Muaddi, H., Majumder, M., Peidis, P., Papadakis, A. I., Holcik, M., Scheuner, D., Kaufman, R. J., Hatzoglou, M., & Koromilas, A. E. (2010). Phosphorylation of eIF2α at Serine 51 Is an Important Determinant of Cell Survival and Adaptation to Glucose Deficiency. *Molecular Biology of the Cell*, *21*(18), 3220–3231.

Nagarajan, V. K., Jones, C. I., Newbury, S. F., & Green, P. J. (2013). XRN 5′→3′ exoribonucleases: Structure, mechanisms and functions. *Biochimica et Biophysica Acta (BBA) - Gene Regulatory Mechanisms*, *1829*(6–7), 590–603.

Nagdev, G., Vhora, R. S., Chavan, G., & Sahu, G. (2022). Adult Onset Vanishing White Matter Disease: A Rare Case Report. *Cureus*.

Nakamura, A., Fujihashi, M., Aono, R., Sato, T., Nishiba, Y., Yoshida, S., Yano, A., Atomi, H., Imanaka, T., & Miki, K. (2012). Dynamic, Ligand-dependent Conformational Change Triggers Reaction of Ribose-1,5-bisphosphate Isomerase from Thermococcus kodakarensis KOD1. *Journal of Biological Chemistry*, *287*(25), 20784–20796.

Nanduri, S. (2000). A dynamically tuned double-stranded RNA binding mechanism for the activation of antiviral kinase PKR. *The EMBO Journal*, *19*(20), 5567–5574.

Naskar, S., & Gour, N. (2023). Realization of Amyloid-like Aggregation as a Common Cause for Pathogenesis in Diseases. *Life*, *13*(7), 1523.

Naveau, M., Lazennec-Schurdevin, C., Panvert, M., Dubiez, E., Mechulam, Y., & Schmitt, E. (2013). Roles of yeast eIF2α and eIF2β subunits in the binding of the initiator methionyl-tRNA. *Nucleic Acids Research*, *41*(2), 1047–1057.

Neill, G., & Masson, G. R. (2023). A stay of execution: ATF4 regulation and potential outcomes for the integrated stress response. *Frontiers in Molecular Neuroscience*, *16*.

Nguyen, L. K., Zhao, Q., Varusai, T. M., & Kholodenko, B. N. (2014). Ubiquitin chain specific auto-ubiquitination triggers sustained oscillation, bistable switches and excitable firing. *IET Systems Biology*, *8*(6), 282–292.

Niewidok, B., Igaev, M., Pereira da Graca, A., Strassner, A., Lenzen, C., Richter, C. P., Piehler, J., Kurre, R., & Brandt, R. (2018). Single-molecule imaging reveals dynamic biphasic partition of RNA-binding proteins in stress granules. *Journal of Cell Biology*, *217*(4), 1303–1318.

Noeske, J., & Cate, J. H. (2012). Structural basis for protein synthesis: snapshots of the ribosome in motion. *Current Opinion in Structural Biology*, *22*(6), 743–749.

Norris, K., Hodgson, R. E., Dornelles, T., Allen, K. E., Abell, B. M., Ashe, M. P., & Campbell, S. G. (2021). Mutational analysis of the alpha subunit of eIF2B provides insights into the role of eIF2B bodies in translational control and VWM disease. *Journal of Biological Chemistry*, *296*, 100207.

Nüske, E., Marini, G., Richter, D., Leng, W., Bogdanova, A., Franzmann, T. M., Pigino, G., & Alberti, S. (2020). Filament formation by the translation factor eIF2B regulates protein synthesis in starved cells. *Biology Open*.

Ohn, T., Kedersha, N., Hickman, T., Tisdale, S., & Anderson, P. (2008). A functional RNAi screen links O-GlcNAc modification of ribosomal proteins to stress granule and processing body assembly. *Nature Cell Biology*, *10*(10), 1224–1231.

Onuki, R., Bando, Y., Suyama, E., Katayama, T., Kawasaki, H., Baba, T., Tohyama, M., & Taira, K. (2004). An RNA-dependent protein kinase is involved in tunicamycin-induced apoptosis and Alzheimer's disease. *The EMBO Journal*, *23*(4), 959–968.

Ozbek, M. N., Senée, V., Aydemir, S., Kotan, L. D., Mungan, N. O., Yuksel, B., Julier, C., & Topaloglu, A. K. (2010). Wolcott-Rallison syndrome due to the

same mutation (W522X) in EIF2AK3 in two unrelated families and review of the literature*. *Pediatric Diabetes*, *11*(4), 279–285.

Paddon, C. J., & Hinnebusch, A. G. (1989). gcd12 mutations are gcn3-dependent alleles of GCD2, a negative regulator of GCN4 in the general amino acid control of Saccharomyces cerevisiae. *Genetics*, *122*(3), 543–550.

Pakos-Zebrucka, K., Koryga, I., Mnich, K., Ljujic, M., Samali, A., & Gorman, A. M. (2016). The integrated stress response. *EMBO Reports*, *17*(10), 1374–1395.

Palam, L. R., Baird, T. D., & Wek, R. C. (2011). Phosphorylation of eIF2 Facilitates Ribosomal Bypass of an Inhibitory Upstream ORF to Enhance CHOP Translation. *Journal of Biological Chemistry*, *286*(13), 10939–10949.

Palangi, F., Samuel, S. M., Thompson, I. R., Triggle, C. R., & Emara, M. M. (2017). Effects of oxidative and thermal stresses on stress granule formation in human induced pluripotent stem cells. *PLOS ONE*, *12*(7), e0182059.

Panas, M. D., Ivanov, P., & Anderson, P. (2016). Mechanistic insights into mammalian stress granule dynamics. *Journal of Cell Biology*, *215*(3), 313–323.

Passmore, L. A., Schmeing, T. M., Maag, D., Applefield, D. J., Acker, M. G., Algire, M. A., Lorsch, J. R., & Ramakrishnan, V. (2007). The Eukaryotic Translation Initiation Factors eIF1 and eIF1A Induce an Open Conformation of the 40S Ribosome. *Molecular Cell*, *26*(1), 41–50.

Pavitt, G. D., Ramaiah, K. V. A., Kimball, S. R., & Hinnebusch, A. G. (1998). eIF2 independently binds two distinct eIF2B subcomplexes that catalyze and regulate guanine-nucleotide exchange. *Genes & Development*, *12*(4), 514–526.

Pavitt, G. D., Yang, W., & Hinnebusch, A. G. (1997). Homologous Segments in Three Subunits of the Guanine Nucleotide Exchange Factor eIF2B Mediate Translational Regulation by Phosphorylation of eIF2. *Molecular and Cellular Biology*, *17*(3), 1298–1313.

Petrovska, I., Nüske, E., Munder, M. C., Kulasegaran, G., Malinovska, L., Kroschwald, S., Richter, D., Fahmy, K., Gibson, K., Verbavatz, J.-M., & Alberti, S. (2014). Filament formation by metabolic enzymes is a specific adaptation to an advanced state of cellular starvation. *ELife*, *3*.

Piña, R., Santos-Díaz, A. I., Orta-Salazar, E., Aguilar-Vazquez, A. R., Mantellero, C. A., Acosta-Galeana, I., Estrada-Mondragon, A., Prior-Gonzalez, M., Martinez-Cruz, J. I., & Rosas-Arellano, A. (2022). Ten Approaches That Improve Immunostaining: A Review of the Latest Advances for the Optimization of Immunofluorescence. *International Journal of Molecular Sciences*, *23*(3), 1426.

Pisarev, A. V., Kolupaeva, V. G., Pisareva, V. P., Merrick, W. C., Hellen, C. U. T., & Pestova, T. V. (2006). Specific functional interactions of nucleotides at key - 3 and + 4 positions flanking the initiation codon with components of the mammalian 48S translation initiation complex. *Genes & Development*, *20*(5), 624–636.

Pisarev, A. V., Skabkin, M. A., Pisareva, V. P., Skabkina, O. V., Rakotondrafara, A. M., Hentze, M. W., Hellen, C. U. T., & Pestova, T. V. (2010). The Role of ABCE1 in Eukaryotic Posttermination Ribosomal Recycling. *Molecular Cell*, *37*(2), 196–210.

Pisareva, V. P., Skabkin, M. A., Hellen, C. U. T., Pestova, T. V, & Pisarev, A. V. (2011). Dissociation by Pelota, Hbs1 and ABCE1 of mammalian vacant 80S ribosomes and stalled elongation complexes. *The EMBO Journal*, *30*(9), 1804–1817.

Pohl, C., & Dikic, I. (2019). Cellular quality control by the ubiquitin-proteasome system and autophagy. *Science*, *366*(6467), 818–822.

Polymenis, M., & Aramayo, R. (2015). Translate to divide: control of the cell cycle by protein synthesis. *Microbial Cell*, *2*(4), 94–104.

Powers, M., Hodgson, R, & Clarke, P. *Personal Communication.*

Prass, K., Brück, W., Schröder, N. W. J., Bender, A., Prass, M., Wolf, T., Van Der Knaap, M. S., & Zschenderlein, R. (2001). Adult-onset leukoencephalopathy with vanishing white matter presenting with dementia. *Annals of Neurology*, *50*(5), 665–668.

Pronk, J. C., van Kollenburg, B., Scheper, G. C., & van der Knaap, M. S. (2006). Vanishing white matter disease: A review with focus on its genetics. *Mental Retardation and Developmental Disabilities Research Reviews*, *12*(2), 123–128.

Protter, D. S. W., & Parker, R. (2016). Principles and Properties of Stress Granules. *Trends in Cell Biology*, *26*(9), 668–679.

Proudfoot, N. J., Furger, A., & Dye, M. J. (2002). Integrating mRNA Processing with Transcription. *Cell*, *108*(4), 501–512.

Rabouw, H. H., Langereis, M. A., Anand, A. A., Visser, L. J., de Groot, R. J., Walter, P., & van Kuppeveld, F. J. M. (2019). Small molecule ISRIB suppresses the integrated stress response within a defined window of activation. *Proceedings of the National Academy of Sciences*, *116*(6), 2097–2102.

Ras-Carmona, A., Lehmann, A. A., Lehmann, P. V., & Reche, P. A. (2022). Prediction of B cell epitopes in proteins using a novel sequence similarity-based method. *Scientific Reports*, *12*(1), 13739.

Ratje, A. H., Loerke, J., Mikolajka, A., Brünner, M., Hildebrand, P. W., Starosta, A. L., Dönhöfer, A., Connell, S. R., Fucini, P., Mielke, T., Whitford, P. C., Onuchic, J. N., Yu, Y., Sanbonmatsu, K. Y., Hartmann, R. K., Penczek, P. A., Wilson, D. N., & Spahn, C. M. T. (2010). Head swivel on the ribosome facilitates translocation by means of intra-subunit tRNA hybrid sites. *Nature*, *468*(7324), 713–716.

Renshaw, S. (2016). Immunohistochemistry and Immunocytochemistry. In *Immunohistochemistry and Immunocytochemistry: Essential Methods* (pp. 35–102). John Wiley & Sons, Ltd.

Reyes-Turcu, F. E., Ventii, K. H., & Wilkinson, K. D. (2009). Regulation and Cellular Roles of Ubiquitin-Specific Deubiquitinating Enzymes. *Annual Review of Biochemistry*, *78*(1), 363–397.

Rigsby, R. E., & Parker, A. B. (2016). Using the PyMOL application to reinforce visual understanding of protein structure. *Biochemistry and Molecular Biology Education*, *44*(5), 433–437.

Roden, C., & Gladfelter, A. S. (2021). RNA contributions to the form and function of biomolecular condensates. *Nature Reviews Molecular Cell Biology*, *22*(3), 183–195.

Roll-Mecak, A., Alone, P., Cao, C., Dever, T. E., & Burley, S. K. (2004). X-ray Structure of Translation Initiation Factor eIF2γ. *Journal of Biological Chemistry*, *279*(11), 10634–10642.

SALIMANS, M., GOUMANS, H., AMESZ, H., BENNE, R., & VOORMA, H. O. (1984). Regulation of protein synthesis in eukaryotes. Mode of action of eRF, an eIF-2-recycling factor from rabbit reticulocytes involved in GDP/GTP exchange. *European Journal of Biochemistry*, *145*(1), 91–98.

Sanders, D. W., Kedersha, N., Lee, D. S. W., Strom, A. R., Drake, V., Riback, J. A., Bracha, D., Eeftens, J. M., Iwanicki, A., Wang, A., Wei, M.-T., Whitney, G., Lyons, S. M., Anderson, P., Jacobs, W. M., Ivanov, P., & Brangwynne, C. P. (2020). Competing Protein-RNA Interaction Networks Control Multiphase Intracellular Organization. *Cell*, *181*(2), 306-324.e28.

Scali, O., Di Perri, C., & Federico, A. (2006). The spectrum of mutations for the diagnosis of vanishing white matter disease. *Neurological Sciences*, *27*(4), 271–277.

Schaap-Johansen, A.-L., Vujović, M., Borch, A., Hadrup, S. R., & Marcatili, P. (2021). T Cell Epitope Prediction and Its Application to Immunotherapy. *Frontiers in Immunology*, *12*.

Schaffert, L.-N., & Carter, W. G. (2020). Do Post-Translational Modifications Influence Protein Aggregation in Neurodegenerative Diseases: A Systematic Review. *Brain Sciences*, *10*(4), 232.

Scheuner, D., Song, B., McEwen, E., Liu, C., Laybutt, R., Gillespie, P., Saunders, T., Bonner-Weir, S., & Kaufman, R. J. (2001). Translational Control Is Required for the Unfolded Protein Response and In Vivo Glucose Homeostasis. *Molecular Cell*, *7*(6), 1165–1176.

Schmitt, E., Naveau, M., & Mechulam, Y. (2010). Eukaryotic and archaeal translation initiation factor 2: A heterotrimeric tRNA carrier. *FEBS Letters*, *584*(2), 405–412.

Schmitt, E., Panvert, M., Lazennec-Schurdevin, C., Coureux, P. D., Perez, J., Thompson, A., & Mechulam, Y. (2012). Structure of the ternary initiation complex aIF2-GDPNP-methionylated initiator tRNA. *Nature Structural and Molecular Biology*, *19*(4), 450–454.

Schoof, M., Boone, M., Wang, L., Lawrence, R., Frost, A., & Walter, P. (2021). eIF2B conformation and assembly state regulate the integrated stress response. *ELife*, *10*.

Schütz, P., Bumann, M., Oberholzer, A. E., Bieniossek, C., Trachsel, H., Altmann, M., & Baumann, U. (2008). Crystal structure of the yeast eIF4A-eIF4G complex: An RNA-helicase controlled by protein–protein interactions. *Proceedings of the National Academy of Sciences*, *105*(28), 9564–9569.

Seguin, S. J., Morelli, F. F., Vinet, J., Amore, D., De Biasi, S., Poletti, A., Rubinsztein, D. C., & Carra, S. (2014). Inhibition of autophagy, lysosome

and VCP function impairs stress granule assembly. *Cell Death & Differentiation*, *21*(12), 1838–1851.

Sekine, Y., Zyryanova, A., Crespillo-Casado, A., Fischer, P. M., Harding, H. P., & Ron, D. (2015). Mutations in a translation initiation factor identify the target of a memory-enhancing compound. *Science*, *348*(6238), 1027–1030.

Sha, Z., Zhao, J., & Goldberg, A. L. (2018). *Measuring the Overall Rate of Protein Breakdown in Cells and the Contributions of the Ubiquitin-Proteasome and Autophagy-Lysosomal Pathways* (pp. 261–276).

Sharma, D. K., Bressler, K., Patel, H., Balasingam, N., & Thakor, N. (2016). Role of Eukaryotic Initiation Factors during Cellular Stress and Cancer Progression. *Journal of Nucleic Acids*, *2016*, 1–19.

Sharma, V., Rai, H., Gautam, D. N. S., Prajapati, P. K., & Sharma, R. (2022). Emerging evidence on Omicron (B.1.1.529) SARS-CoV-2 variant. *Journal of Medical Virology*, *94*(5), 1876–1885.

Shatkin, A. J., & Manley, J. L. (2000). The ends of the affair: capping and polyadenylation. *Nature Structural Biology*, *7*(10), 838–842.

Shatsky, I. N., Terenin, I. M., Smirnova, V. V., & Andreev, D. E. (2018). Cap-Independent Translation: What's in a Name? *Trends in Biochemical Sciences*, *43*(11), 882–895.

Shen, L., & Pelletier, J. (2020). Selective targeting of the DEAD-box RNA helicase eukaryotic initiation factor (eIF) 4A by natural products. *Natural Product Reports*, *37*(5), 609–616.

Sheth, U., & Parker, R. (2003). Decapping and Decay of Messenger RNA Occur in Cytoplasmic Processing Bodies. *Science*, *300*(5620), 805–808.

Shi, Y., Yang, Y., Hoang, B., Bardeleben, C., Holmes, B., Gera, J., & Lichtenstein, A. (2016). Therapeutic potential of targeting IRES-dependent c-myc translation in multiple myeloma cells during ER stress. *Oncogene*, *35*(8), 1015–1024.

Shin, B.-S., Kim, J.-R., Walker, S. E., Dong, J., Lorsch, J. R., & Dever, T. E. (2011). Initiation factor eIF2γ promotes eIF2–GTP–Met-tRNAiMet ternary complex binding to the 40S ribosome. *Nature Structural & Molecular Biology*, *18*(11), 1227–1234.

Shoemaker, C. J., Eyler, D. E., & Green, R. (2010). Dom34:Hbs1 Promotes Subunit Dissociation and Peptidyl-tRNA Drop-Off to Initiate No-Go Decay. *Science*, *330*(6002), 369–372.

Sidrauski, C., Acosta-Alvear, D., Khoutorsky, A., Vedantham, P., Hearn, B. R., Li, H., Gamache, K., Gallagher, C. M., Ang, K. K.-H., Wilson, C., Okreglak, V., Ashkenazi, A., Hann, B., Nader, K., Arkin, M. R., Renslo, A. R., Sonenberg, N., & Walter, P. (2013). Pharmacological brake-release of mRNA translation enhances cognitive memory. *ELife*, *2*.

Sidrauski, C., McGeachy, A. M., Ingolia, N. T., & Walter, P. (2015). The small molecule ISRIB reverses the effects of eIF2α phosphorylation on translation and stress granule assembly. *ELife*, *4*.

Siekierka, J., Mitsui, K. I., & Ochoa, S. (1981). Mode of action of the heme-controlled translational inhibitor: relationship of eukaryotic initiation factor 2-stimulating protein to translation restoring factor. *Proceedings of the National Academy of Sciences*, *78*(1), 220–223.

Singh, C. R., Lee, B., Udagawa, T., Mohammad-Qureshi, S. S., Yamamoto, Y., Pavitt, G. D., & Asano, K. (2006). An eIF5/eIF2 complex antagonizes guanine nucleotide exchange by eIF2B during translation initiation. *The EMBO Journal*, *25*(19), 4537–4546.

Slynko, I., Nguyen, S., Hamilton, E. M. C., Wisse, L. E., Esch, I. J. P., Graaf, C., Bruning, J. B., Proud, C. G., Abbink, T. E. M., & Knaap, M. S. (2021). Vanishing white matter: Eukaryotic initiation factor 2B model and the impact of missense mutations. *Molecular Genetics & Genomic Medicine*, *9*(3).

Sokabe, M., Fraser, C. S., & Hershey, J. W. B. (2012). The human translation initiation multi-factor complex promotes methionyl-tRNA i binding to the 40S ribosomal subunit. *Nucleic Acids Research*, *40*(2), 905–913.

Somasekharan, S. P., El-Naggar, A., Leprivier, G., Cheng, H., Hajee, S., Grunewald, T. G. P., Zhang, F., Ng, T., Delattre, O., Evdokimova, V., Wang, Y., Gleave, M., & Sorensen, P. H. (2015). YB-1 regulates stress granule formation and tumor progression by translationally activating G3BP1. *Journal of Cell Biology*, *208*(7), 913–929.

Spaas, J., van Veggel, L., Schepers, M., Tiane, A., van Horssen, J., Wilson, D. M., Moya, P. R., Piccart, E., Hellings, N., Eijnde, B. O., Derave, W., Schreiber, R., & Vanmierlo, T. (2021). Oxidative stress and impaired oligodendrocyte precursor cell differentiation in neurological disorders. *Cellular and Molecular Life Sciences*, *78*(10), 4615–4637.

Stanik, J., Skopkova, M., Stanikova, D., Brennerova, K., Barak, L., Ticha, L., Hornova, J., Klimes, I., & Gasperikova, D. (2018). Neonatal Hypoglycemia,

Early-Onset Diabetes and Hypopituitarism Due to the Mutation in EIF2S3 Gene Causing MEHMO Syndrome. *Physiological Research*, 331–337.

Stave, J. W., & Lindpaintner, K. (2013). Antibody and Antigen Contact Residues Define Epitope and Paratope Size and Structure. *The Journal of Immunology*, *191*(3), 1428–1435.

Stefani, M., & Dobson, C. M. (2003). Protein aggregation and aggregate toxicity: new insights into protein folding, misfolding diseases and biological evolution. *Journal of Molecular Medicine*, *81*(11), 678–699.

Stöhr, N., Lederer, M., Reinke, C., Meyer, S., Hatzfeld, M., Singer, R. H., & Hüttelmaier, S. (2006). ZBP1 regulates mRNA stability during cellular stress. *The Journal of Cell Biology*, *175*(4), 527–534.

Svitkin, Y. V., Pause, A., Haghighat, A., Pyronnet, S., Witherell, G., Belsham, G. J., & Sonenberg, N. (2001). The requirement for eukaryotic initiation factor 4A (eIF4A) in translation is in direct proportion to the degree of mRNA 5′ secondary structure. *RNA*, *7*(3), S135583820100108X.

Szabó, E., Türk, D., Telbisz, Á., Kucsma, N., Horváth, T., Szakács, G., Homolya, L., Sarkadi, B., & Várady, G. (2018). A new fluorescent dye accumulation assay for parallel measurements of the ABCG2, ABCB1 and ABCC1 multidrug transporter functions. *PLOS ONE*, *13*(1), e0190629.

Szewczyk, B., Günther, R., Japtok, J., Frech, M. J., Naumann, M., Lee, H. O., & Hermann, A. (2023). FUS ALS neurons activate major stress pathways and reduce translation as an early protective mechanism against neurodegeneration. *Cell Reports*, *42*(2), 112025.

Talukdar, G., Orr, H. T., & Lei, Z. (2023). The PERK pathway: beneficial or detrimental for neurodegenerative diseases and tumor growth and cancer. *Human Molecular Genetics*, *32*(16), 2545–2557.

Tauber, D., Tauber, G., Khong, A., Van Treeck, B., Pelletier, J., & Parker, R. (2020). Modulation of RNA Condensation by the DEAD-Box Protein eIF4A. *Cell*, *180*(3), 411-426.e16.

Taylor, E. J., Campbell, S. G., Griffiths, C. D., Reid, P. J., Slaven, J. W., Harrison, R. J., Sims, P. F. G., Pavitt, G. D., Delneri, D., & Ashe, M. P. (2010). Fusel Alcohols Regulate Translation Initiation by Inhibiting eIF2B to Reduce Ternary Complex in a Mechanism That May Involve Altering the Integrity and Dynamics of the eIF2B Body. *Molecular Biology of the Cell*, *21*(13), 2202–2216.

Teske, B. F., Fusakio, M. E., Zhou, D., Shan, J., McClintick, J. N., Kilberg, M. S., & Wek, R. C. (2013). CHOP induces activating transcription factor 5 (ATF5) to trigger apoptosis in response to perturbations in protein homeostasis. *Molecular Biology of the Cell*, *24*(15), 2477–2490.

Tharun, S., & Parker, R. (1999). Analysis of Mutations in the Yeast mRNA Decapping Enzyme. *Genetics*, *151*(4), 1273–1285.

Tharun, S., & Parker, R. (2001). Targeting an mRNA for Decapping. *Molecular Cell*, *8*(5), 1075–1083.

Tsai, J. C., Miller-Vedam, L. E., Anand, A. A., Jaishankar, P., Nguyen, H. C., Renslo, A. R., Frost, A., & Walter, P. (2018). Structure of the nucleotide exchange factor eIF2B reveals mechanism of memory-enhancing molecule. *Science*, *359*(6383).

Unbehaun, A., Borukhov, S. I., Hellen, C. U. T., & Pestova, T. V. (2004). Release of initiation factors from 48S complexes during ribosomal subunit joining and the link between establishment of codon-anticodon base-pairing and hydrolysis of eIF2-bound GTP. *Genes & Development*, *18*(24), 3078–3093.

Uppala, J. K., Ghosh, C., Sathe, L., & Dey, M. (2018). Phosphorylation of translation initiation factor eIF 2α at Ser51 depends on site- and context-specific information. *FEBS Letters*, *592*(18), 3116–3125.

Vaklavas, C., Grizzle, W. E., Choi, H., Meng, Z., Zinn, K. R., Shrestha, K., & Blume, S. W. (2016). IRES inhibition induces terminal differentiation and synchronized death in triple-negative breast cancer and glioblastoma cells. *Tumor Biology*, *37*(10), 13247–13264.

Valadkhan, S., & Manley, J. L. (2001). Splicing-related catalysis by protein-free snRNAs. *Nature*, *413*(6857), 701–707.

van der Knaap, M. S., Bonkowsky, J. L., Vanderver, A., Schiffmann, R., Krägeloh-Mann, I., Bertini, E., Bernard, G., Fatemi, S. A., Wolf, N. I., Saunier-Vivar, E., Rauner, R., Dekker, H., van Bokhoven, P., van de Ven, P., & Leferink, P. S. (2022). Therapy Trial Design in Vanishing White Matter. *Neurology Genetics*, *8*(2), e657.

van der Knaap, M. S., Pronk, J. C., & Scheper, G. C. (2006). Vanishing white matter disease. *The Lancet Neurology*, *5*(5), 413–423.

van der Lei, H. D. W., van Berkel, C. G. M., van Wieringen, W. N., Brenner, C., Feigenbaum, A., Mercimek-Mahmutoglu, S., Philippart, M., Tatli, B., Wassmer, E., Scheper, G. C., & van der Knaap, M. S. (2010). Genotype-

phenotype correlation in vanishing white matter disease. *Neurology*, *75*(17), 1555–1559.

van Dijk, E. (2002). Human Dcp2: a catalytically active mRNA decapping enzyme located in specific cytoplasmic structures. *The EMBO Journal*, *21*(24), 6915–6924.

Van Eden, M. E., Byrd, M. P., Sherrill, K. W., & Lloyd, R. E. (2004). Demonstrating internal ribosome entry sites in eukaryotic mRNAs using stringent RNA test procedures. *RNA (New York, N.Y.)*, *10*(4), 720–730.

Van Haren, K., Van Der Voorn, J. P., Peterson, D. R., Van Der Knaap, M. S., & Powers, J. M. (2004). The Life and Death of Oligodendrocytes in Vanishing White Matter Disease. *Journal of Neuropathology & Experimental Neurology*, *63*(6), 618–630.

van Leeuwen, W., VanInsberghe, M., Battich, N., Salmén, F., van Oudenaarden, A., & Rabouille, C. (2022). Identification of the stress granule transcriptome via RNA-editing in single cells and in vivo. *Cell Reports Methods*, *2*(6), 100235.

Vander Heiden, M. G., & DeBerardinis, R. J. (2017). Understanding the Intersections between Metabolism and Cancer Biology. *Cell*, *168*(4), 657–669.

Vanselow, S., Neumann-Arnold, L., Wojciech-Moock, F., & Seufert, W. (2022). Stepwise assembly of the eukaryotic translation initiation factor 2 complex. *Journal of Biological Chemistry*, *298*(2), 101583.

Vattem, K. M., & Wek, R. C. (2004). Reinitiation involving upstream ORFs regulates *ATF4* mRNA translation in mammalian cells. *Proceedings of the National Academy of Sciences*, *101*(31), 11269–11274.

Vazquez De Aldana, C. R., Wek, R. C., Segundo, P. S., Truesdell, A. G., & Hinnebusch, A. G. (1994). Multicopy tRNA Genes Functionally Suppress Mutations in Yeast eIF-2α Kinase GCN2: Evidence for Separate Pathways Coupling *GCN4* Expression to Uncharged tRNA. *Molecular and Cellular Biology*, *14*(12), 7920–7932.

Velázquez-Cruz, A., Baños-Jaime, B., Díaz-Quintana, A., De la Rosa, M. A., & Díaz-Moreno, I. (2021). Post-translational Control of RNA-Binding Proteins and Disease-Related Dysregulation. *Frontiers in Molecular Biosciences*, *8*.

Vermeulen, G., Seidl, R., Mercimek-Mahmutoglu, S., Rotteveel, J. J., Scheper, G. C., & van der Knaap, M. S. (2005). Fright is a provoking factor in vanishing white matter disease. *Annals of Neurology*, *57*(4), 560–563.

Vicens, Q., Kieft, J. S., & Rissland, O. S. (2018). Revisiting the Closed-Loop Model and the Nature of mRNA 5′–3′ Communication. *Molecular Cell*, *72*(5), 805–812.

Villa, N., Do, A., Hershey, J. W. B., & Fraser, C. S. (2013). Human Eukaryotic Initiation Factor 4G (eIF4G) Protein Binds to eIF3c, -d, and -e to Promote mRNA Recruitment to the Ribosome. *Journal of Biological Chemistry*, *288*(46), 32932–32940.

von der Haar, T., & McCarthy, J. E. G. (2002). Intracellular translation initiation factor levels in *Saccharomyces cerevisiae* and their role in cap-complex function. *Molecular Microbiology*, *46*(2), 531–544.

Walton, G. M., & Gill, G. N. (1975). Nucleotide regulation of a eukaryotic protein synthesis initiation complex. *Biochimica et Biophysica Acta (BBA) - Nucleic Acids and Protein Synthesis*, *390*(2), 231–245.

Wang, B., Zhang, L., Dai, T., Qin, Z., Lu, H., Zhang, L., & Zhou, F. (2021). Liquid–liquid phase separation in human health and diseases. *Signal Transduction and Targeted Therapy*, *6*(1), 290.

Wang, M., & Kaufman, R. J. (2016). Protein misfolding in the endoplasmic reticulum as a conduit to human disease. *Nature*, *529*(7586), 326–335.

Wang, P., Li, J., Tao, J., & Sha, B. (2018). The luminal domain of the ER stress sensor protein PERK binds misfolded proteins and thereby triggers PERK oligomerization. *Journal of Biological Chemistry*, *293*(11), 4110–4121.

Wang, X., & Proud, C. G. (2008). A Novel Mechanism for the Control of Translation Initiation by Amino Acids, Mediated by Phosphorylation of Eukaryotic Initiation Factor 2B. *Molecular and Cellular Biology*, *28*(5), 1429–1442.

Wang, X., Wortham, N. C., Liu, R., & Proud, C. G. (2012). Identification of Residues That Underpin Interactions within the Eukaryotic Initiation Factor (eIF2) 2B Complex. *Journal of Biological Chemistry*, *287*(11), 8263–8274.

Wek, R. C., Jiang, H.-Y., & Anthony, T. G. (2006). Coping with stress: eIF2 kinases and translational control. *Biochemical Society Transactions*, *34*(1), 7.

Wen, J.-H., He, X.-H., Feng, Z.-S., Li, D.-Y., Tang, J.-X., & Liu, H.-F. (2023). Cellular Protein Aggregates: Formation, Biological Effects, and Ways of Elimination. *International Journal of Molecular Sciences*, *24*(10), 8593.

Will, C. L., & Luhrmann, R. (2011). Spliceosome Structure and Function. *Cold Spring Harbor Perspectives in Biology*, *3*(7), a003707–a003707.

Willcocks, M. M., Carter, M. J., & Roberts, L. O. (2004). Cleavage of eukaryotic initiation factor eIF4G and inhibition of host-cell protein synthesis during feline calicivirus infection. *Journal of General Virology*, *85*(5), 1125–1130.

Williams, D. D., Price, N. T., Loughlin, A. J., & Proud, C. G. (2001). Characterization of the Mammalian Initiation Factor eIF2B Complex as a GDP Dissociation Stimulator Protein. *Journal of Biological Chemistry*, *276*(27), 24697–24703.

Willingham, M. C. (1999). Conditional Epitopes: Is Your Antibody Always Specific? *Journal of Histochemistry & Cytochemistry*, *47*(10), 1233–1235.

Wittrup, A., & Lieberman, J. (2015). Knocking down disease: a progress report on siRNA therapeutics. *Nature Reviews Genetics*, *16*(9), 543–552.

Wong, Y. L., LeBon, L., Basso, A. M., Kohlhaas, K. L., Nikkel, A. L., Robb, H. M., Donnelly-Roberts, D. L., Prakash, J., Swensen, A. M., Rubinstein, N. D., Krishnan, S., McAllister, F. E., Haste, N. V, O'Brien, J. J., Roy, M., Ireland, A., Frost, J. M., Shi, L., Riedmaier, S., … Sidrauski, C. (2019). eIF2B activator prevents neurological defects caused by a chronic integrated stress response. *ELife*, *8*.

Wortel, I. M. N., van der Meer, L. T., Kilberg, M. S., & van Leeuwen, F. N. (2017). Surviving Stress: Modulation of ATF4-Mediated Stress Responses in Normal and Malignant Cells. *Trends in Endocrinology & Metabolism*, *28*(11), 794–806.

Wortham, N. C., Martinez, M., Gordiyenko, Y., Robinson, C. V., & Proud, C. G. (2014). Analysis of the subunit organization of the eIF2B complex reveals new insights into its structure and regulation. *The FASEB Journal*, *28*(5), 2225–2237.

Wortham, N. C., & Proud, C. G. (2015). eIF2B: recent structural and functional insights into a key regulator of translation. *Biochemical Society Transactions*, *43*(6), 1234–1240.

Wortham, N. C., Stewart, J. D., Harris, S., Coldwell, M. J., & Proud, C. G. (2016). Stoichiometry of the eIF2B complex is maintained by mutual stabilization of subunits. *Biochemical Journal*, *473*(5), 571–580.

Yanagiya, A., Svitkin, Y. V., Shibata, S., Mikami, S., Imataka, H., & Sonenberg, N. (2009). Requirement of RNA Binding of Mammalian Eukaryotic Translation Initiation Factor 4GI (eIF4GI) for Efficient Interaction of eIF4E with the mRNA Cap. *Molecular and Cellular Biology*, *29*(6), 1661–1669.

Yang, P., Mathieu, C., Kolaitis, R.-M., Zhang, P., Messing, J., Yurtsever, U., Yang, Z., Wu, J., Li, Y., Pan, Q., Yu, J., Martin, E. W., Mittag, T., Kim, H. J., & Taylor, J. P. (2020). G3BP1 Is a Tunable Switch that Triggers Phase Separation to Assemble Stress Granules. *Cell*, *181*(2), 325-345.e28.

Yang, W., & Hinnebusch, A. G. (1996). Identification of a Regulatory Subcomplex in the Guanine Nucleotide Exchange Factor eIF2B That Mediates Inhibition by Phosphorylated eIF2. *Molecular and Cellular Biology*, *16*(11), 6603–6616.

Youn, J.-Y., Dyakov, B. J. A., Zhang, J., Knight, J. D. R., Vernon, R. M., Forman-Kay, J. D., & Gingras, A.-C. (2019). Properties of Stress Granule and P-Body Proteomes. *Molecular Cell*, *76*(2), 286–294.

Zeng, L.-R., Vega-Sánchez, M. E., Zhu, T., & Wang, G.-L. (2006). Ubiquitination-mediated protein degradation and modification: an emerging theme in plant-microbe interactions. *Cell Research*, *16*(5), 413–426.

Zhang, H., Dai, L., Chen, N., Zang, L., Leng, X., Du, L., Wang, J., Jiang, Y., Zhang, F., Wu, X., & Wu, Y. (2015). Fifteen Novel EIF2B1-5 Mutations Identified in Chinese Children with Leukoencephalopathy with Vanishing White Matter and a Long Term Follow-Up. *PLOS ONE*, *10*(3), e0118001.

Zhang, Y., Liu, L., Qiu, Q., Zhou, Q., Ding, J., Lu, Y., & Liu, P. (2021). Alternative polyadenylation: methods, mechanism, function, and role in cancer. *Journal of Experimental & Clinical Cancer Research*, *40*(1), 51.

Zhao, J., Hyman, L., & Moore, C. (1999). Formation of mRNA 3′ Ends in Eukaryotes: Mechanism, Regulation, and Interrelationships with Other Steps in mRNA Synthesis. *Microbiology and Molecular Biology Reviews*, *63*(2), 405–445.

Zhigailov, A. V., Alexandrova, A. M., Nizkorodova, A. S., Stanbekova, G. E., Kryldakov, R. V., Karpova, O. V., Polimbetova, N. S., Halford, N. G., & Iskakov, B. K. (2020). Evidence That Phosphorylation of the α-Subunit of

eIF2 Does Not Essentially Inhibit mRNA Translation in Wheat Germ Cell-Free System. *Frontiers in Plant Science*, *11*.

Zhou, D., Palam, L. R., Jiang, L., Narasimhan, J., Staschke, K. A., & Wek, R. C. (2008). Phosphorylation of eIF2 Directs ATF5 Translational Control in Response to Diverse Stress Conditions. *Journal of Biological Chemistry*, *283*(11), 7064–7073.

Zhou, J., Lancaster, L., Donohue, J. P., & Noller, H. F. (2014). How the ribosome hands the A-site tRNA to the P site during EF-G–catalyzed translocation. *Science*, *345*(6201), 1188–1191.

Zhou, L., Lu, D.-Q., Wang, Q., Hu, S., Wang, H., Sun, H., & Zhang, X. (2017). An efficient two-photon ratiometric fluorescent probe platform for dual-channel imaging of lysosomes in living cells and tissues. *Sensors and Actuators B: Chemical*, *238*, 274–280.

Zyryanova, A. F., Kashiwagi, K., Rato, C., Harding, H. P., Crespillo-Casado, A., Perera, L. A., Sakamoto, A., Nishimoto, M., Yonemochi, M., Shirouzu, M., Ito, T., & Ron, D. (2021). ISRIB Blunts the Integrated Stress Response by Allosterically Antagonising the Inhibitory Effect of Phosphorylated eIF2 on eIF2B. *Molecular Cell*, *81*(1), 88-103.e6.

Zyryanova, A. F., Weis, F., Faille, A., Alard, A. A., Crespillo-Casado, A., Sekine, Y., Harding, H. P., Allen, F., Parts, L., Fromont, C., Fischer, P. M., Warren, A. J., & Ron, D. (2018). Binding of ISRIB reveals a regulatory site in the nucleotide exchange factor eIF2B. *Science*, *359*(6383), 1533–1536.